Natural Resources Canada | Ressources naturelles Canada

GEOLOGICAL SURVEY OF CANADA
OPEN FILE 8755

Targeted Geoscience Initiative 5: grant program final reports (2018-2020)

Edited by
Targeted Geoscience Initiative Coordination Office

2021

Canada

GEOLOGICAL SURVEY OF CANADA
OPEN FILE 8755

Targeted Geoscience Initiative 5: grant program final reports (2018-2020)

Edited by
Targeted Geoscience Initiative Coordination Office

2021

Permanent link: https://doi.org/10.4095/328978

This publication is available for free download through GEOSCAN (https://geoscan.nrcan.gc.ca/).

Recommended citation
Targeted Geoscience Initiative Coordination Office (ed.), 2021. Targeted Geoscience Initiative 5: grant program final reports (2018-2020); Geological Survey of Canada, Open File 8755, 1 .zip file. https://doi.org/10.4095/328978

Publications in this series have not been edited; they are released as submitted by the author.

CONTENTS

Transport and deposition of sulphide liquid – vectors to ore accumulations

Z.S. Yao, Y.Z. Li, and J.E. Mungall

Yao, Z.S., Li, Y.Z., and Mungall, J.E., 2021. Transport and deposition of sulphide liquid – vectors to ore accumulations; in *Targeted Geoscience Initiative 5:grant program final reports (2018-2020); Geological Survey of Canada, Open File 8755, p. 1–25. https://doi.org/10.4095/328979*

Abstract: This project aims to model the kinetic controls on sulphide composition due to the extraction of chalcophile elements from silicate magmas, and use the numerical models to deepen our knowledge of the physical constraints that govern sulphide dynamic processes (e.g., breakup, coalescence, transport and deposition) in magmatic system. Based on the new understanding obtained from these forward models, we then take the textural and compositional features of sulphide globules from the field investigation at Raglan komatiite-associated deposits for instance, to better understand the control on entrainment, transport and deposition of sulphide liquids within the ore-forming processes.

Department of Earth Sciences, Carleton University, 2115 Herzberg Laboratories,
1125 Colonel By Drive, Ottawa, Ontario K1S 5B6

1. INTRODUCTION

The objective of this project was to use numerical modeling and field observations to address the processes governing the transport, collection, accumulation and composition of magmatic sulphide liquids to form economic Ni-Cu-PGE deposits, with a focus on ore formation at Raglan and Noril'sk mining camps. Base metal sulphide ores form when small droplets of immiscible sulphide liquid form within magmas and are carried in suspension within flowing melt. The compositions of these droplets change with time as they react with the magma to become enriched in ore metals, which we have modeled as a kinetic process. Physical constraints on the size distribution of sulphide blebs via the deformation, breakup or coalescence of sulphide droplets in various fluid dynamic processes (e.g. free settling in a stagnant reservoir, transport in a uniform ascending flow along conduit and/or a horizontal shear flow) have been outlined by the numerical simulations. A quantitative model for the dynamics of mm-scale sulphide droplets in a vertical magmatic conduit was also developed to place empirical inferences about conduit-hosted magmatic sulphide mineralization on a firmer theoretical basis. Sulphide deposition in lateral flow, especially across sudden expansions of conduit cross-sectional area, are also taken into account, which matches the close spatial relationship between the economic ore bodies and embayments in lava flow channels for komatiite-associated Ni-Cu-(PGE) deposits. We have developed a quantitative model for the Raglan deposits for instance, comprising a quantitative model for assimilation of sulphidic substrates during lava emplacement, with consideration of thermodynamics, kinetics and dynamics to trace the compositional variations of externally-derived sulphide liquid droplets during downstream lava flow.

2. KOMATIITE-ASSOCIATED DEPOSITS AT RAGLAN

Komatiite-associated magmatic Ni-Cu-(PGE) sulphide deposits contain ~20% of the world's Ni resources (Hronsky and Schodde, 2006), and the Raglan deposits in Cape Smith Belt, Nunavik, are widely considered as the best preserved and exposed examples of this type of deposit (Lesher, 2007). The Ni-Cu-PGE mineralization within the Raglan formation is associated with poorly differentiated lava flows that are suggested to be co-magmatic with the high-MgO komatiitic basalts at the base of the overlying Chukotat Group (Fig. 1a; Picard et al., 1990; Lesher 2007). Economic mineralization occurs as multiple distinct ore bodies, the majority of which lie in second order embayments at the bases of ultramafic units. In most cases, the massive sulphide ores grade upward into net-textured and disseminated ores. In addition, irregular sulphide blebs (up to ~1 cm) occasionally occur throughout the whole complex, especially above the disseminated ores and/or below the lowermost massive ores. The host sediments contain abundant sulphide phases, which have a heterogeneous texture such as folded thin vein, stringer-type, recrystallized, banded, brecciated or even massive sulphide.

A regional 3D magnetic inversion model (Watts and Osmond, 1999) was used to support a proposition that the ore-bearing conduit facies complexes were parts of a single connected erosive lava flow system extending for >~20 km (Fig. 1b, c). Formation of these ore-bearing ultramafic units was accompanied by ~8-10% assimilation of underlying unconsolidated, sedimentary and pyroclastic rocks of the upper Povungnituk Group by the komatiitic basalt (~18 wt.% MgO) (St-Onge and Lucas, 1994; Lesher et al., 2001; Lesher 2007), which is suggested to have been sulphide-undersaturated during emplacement (Lesher et al., 2001; Lesher, 2007; Mungall, 2007). Meanwhile, the S isotopic compositions of sulphide ores (4-6 $\delta^{34}S$) fall into the range of the footwall sulphide-rich semipelites (Lesher et al., 1999), suggesting that the lavas and/or related shallow sills have assimilated enough sulphur to form ore bodies in multiple episodes (Lesher et al., 1999; Lesher 2007; Williams et al., 2011).

Although the mechanism of triggering sulphide saturation in the parental magma is well understood from a purely geochemical standpoint, the fluid dynamic processes controlling the transport and deposition of magmatic sulphide liquids remain some of the least understood aspects of the genesis of this type of deposit. In addition, the ore bodies are commonly localized in the footwall embayments (Lesher et al., 2001; Lesher, 2007; Williams et al., 2011), suggesting strong influences of fluid dynamics on the spatial distributions of sulphide mineralization in the Raglan deposits. Clues to the transport and deposition of sulphide liquids in magmatic systems can be obtained from studies of size distributions and compositions of sulphide blebs, which have received growing attention as indicators of magmatic processes. The Raglan deposits are characterized by the occurrence of globular sulphide mineralization, which may provide insight into the complex ore-forming processes operating in vigorous magma flows. The sulphide composition and droplet size distribution we observe are the results of a complex set of interacting dynamic processes, and interpretations must be based on a correct, understanding of the shape, composition and size of sulphide droplets in different stages from the initial segregation to final accumulation in dynamic magmatic systems. Hence, we firstly focus on forward modelling of the variations of composition and size of sulphide droplets within different dynamic magmatic processes.

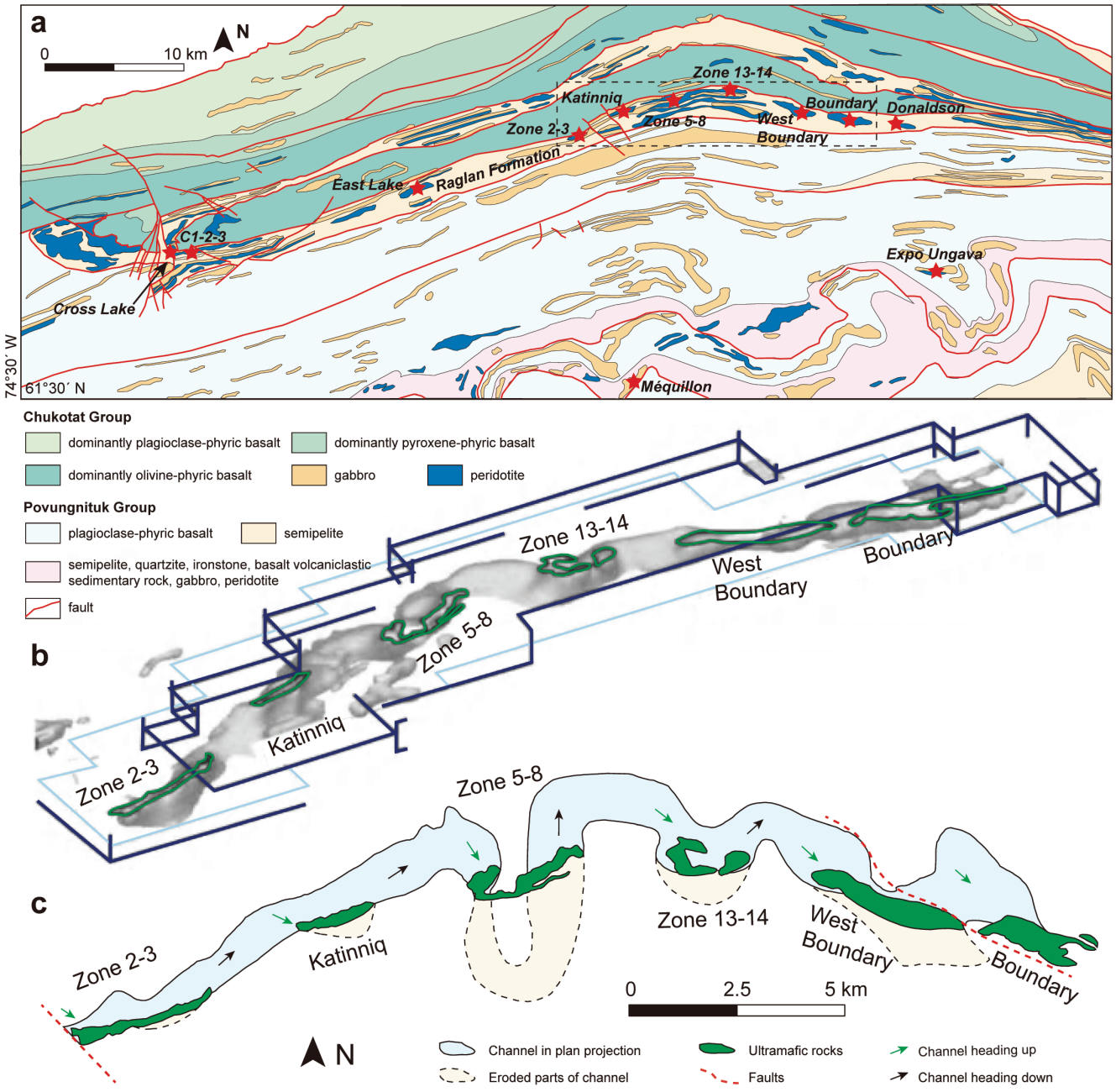

Figure 1. a) Geological map of the eastern part of the Cape Smith Belt (modified from St-Onge and Lucas, 1994, Mungall, 2007). **b)** Regional 3-D magnetic inversion model for the Raglan deposits between the Zone 2-3 and Boundary Complex (dashed box in **a)** (after Watts and Osmond, 1999). The green lines outline the surface expressions of the ore-bearing complexes. **c)** Interpreted model for the Raglan deposits in a meandering lava channel (Green and Dupras, 1999; Lesher, 2007; Williams et al., 2011).

3. KINETIC CONTROLS ON SULPHIDE COMPOSITION

For the Raglan deposits, in almost all situations, the sedimentary sulphides are dominated by pyrite, and would be directly released as nearly-pure FeS liquid droplets into the komatiitic basalts during the process of assimilation. Hence, the saturation of sulphide in parental magma can be reached via two methods: either the sedimentary sulphides are completely dissolved to increase the sulphur content in magma until it reaches the saturation point for sulphide segregation; or alternatively externally derived pure-FeS liquid droplets are released from the S-rich sediments as xenomelts that then collect chalcophile elements from peripheral silicate melt via advection-enhanced diffusive transport. The initial compositions of externally-derived sulphide droplets are close to a pure-FeS liquid; whereas, in contrast, the endogenous sulphides should remain at or near equilibrium with the sulphur-saturated melt and are initially rich in the Ni, Cu and PGE due to their high partition coefficients into sulphide (Mungall, 2002). Although the compositions of these two populations of sulphide droplets are both kinetically controlled, the existing large differences on their initial compositions must result in distinct evolution paths with time.

For comparison, we modeled the compositional variations of these two types of sulphide droplets due to the convection-enhanced diffusive transport of sulphur, oxygen, and metal elements during their free settling in a stagnant system. In this regard, the diffusive transport of Fe, S, Ni, Cu and O was modeled simultaneously, and meanwhile the influence of variation of sulphide composition on the partitioning behaviors of Ni, Cu and O were also taken into account. For the external sulphide droplets, their Ni concentrations maintain sustained growth from the low initial values to the equilibrium value of ~33 wt.% Ni, and the required durations will increase with increase of droplet radius (Fig. 2a) because the larger droplet needs more Ni mass to be transported from silicate melt. The kinetic behavior of Cu is parallel, except that the Cu content will slightly decrease after reaching its maximum (Fig. 2b), because Cu content reaches equilibrium first due to its faster diffusion (Ni et al., 2017), but the subsequent addition of slower-diffusing Ni reduces the relative proportion of Cu. Although the external sulphide droplet immersed in the S-unsaturated komatiitic basalt should experience shrinkage due to the dissolution of sulphur, its size remains nearly constant until its Ni and Cu contents are close to the equilibrium condition (Fig. 2c), because in this period the loss of slow-diffusing sulphur is almost offset by the addition of Ni and Cu from the silicate melt. In contrast, the initial radius of endogenous sulphide droplets after nucleation is taken as 2 μm based on previous experiments (Holzheid, 2010), and their kinetic growth rate is very low because it is assumed that the sulphide composition always approximates to be equilibrated with silicate melt, and hence the compositional gradient in the boundary layer is too small to drive the effective transport of chalcophile elements. For the external sulphide droplet, the time required for reaching equilibrium state is far shorter than the growth of the endogenous droplet from its initial size to the same size (Fig. 2d). Therefore, during the assimilation of sulphidic sediments, both the kinetic growth and upgrading of the endogenous and external sulphide droplets, respectively, are happening at the same time in the magmatic systems, and the latter one wins out in the competition to scavenge chalcophile elements.

Before reaching the final equilibrium state, the compositions of external sulphide droplets change distinctively with time, which in turn can be related to the spatial location-relation of the mineralization and sulphur source if we know the transport and deposition mechanisms of sulphide droplets in the magma lava flows. Taking the stagnant system as a simplified example, the kinetic upgrading of external sulphide droplets will cease when they reach the bottom of a magma reservoir with a crystal-dominated mush at its base. If the maximum thickness of olivine mesocumulates in the Raglan deposits (~200-300 m) is taken as the upper bounding limit to distance of travel, the external sulphide droplet with radius larger than 0.5 mm may not reach the equilibrium condition, and the endogenous sulphide droplet also takes a long time (~10^6 s) to reach ~0.5 mm radius before it falls on the bottom of the magmatic reservoir (Fig. 2d). Dashed portions of the curves illustrate qualitatively the consequences of more extended episodes of equilibration enabled by droplet transport in a turbulently convecting flow, neglecting the effects of shear flow on the length-scales of diffusion but extending the total distance of travel.

4. PHYSICAL CONSTRAINTS ON DROPLET SIZE

The kinetic model above has shown that the dominant control on the composition of a sulphide droplet is its size, which is also the key factor to determine the entrainment, transport, coalescence and deposition of sulphide liquid in magma flows (De Bremond d'Ars et al., 2001; Chung and Mungall, 2009; Robertson et al., 2015). Physical breakup and coalescence induced by the fluid dynamic processes are suggested to be the most rapid and efficient ways to change the size of sulphide droplets (Barnes et al., 2013; Robertson et al., 2015). Deformation and breakup of drops involve several mechanisms (e.g. viscous shear, shearing-off and interfacial instability), which are controlled by the interactions of several dynamic forces: surface tension, buoyancy, and viscous force and/or pressure gradient forces due to the external flow. In the literature, several non-dimensional parameters (defined as the ratios between the external disruptive stresses and cohesive stresses) are usually adopted to identify the predominant force and associated physical mechanism in various fluid dynamic circumstances. For example, Reynolds number (*Re*) is defined as the ratio of momentum advection to viscous force,

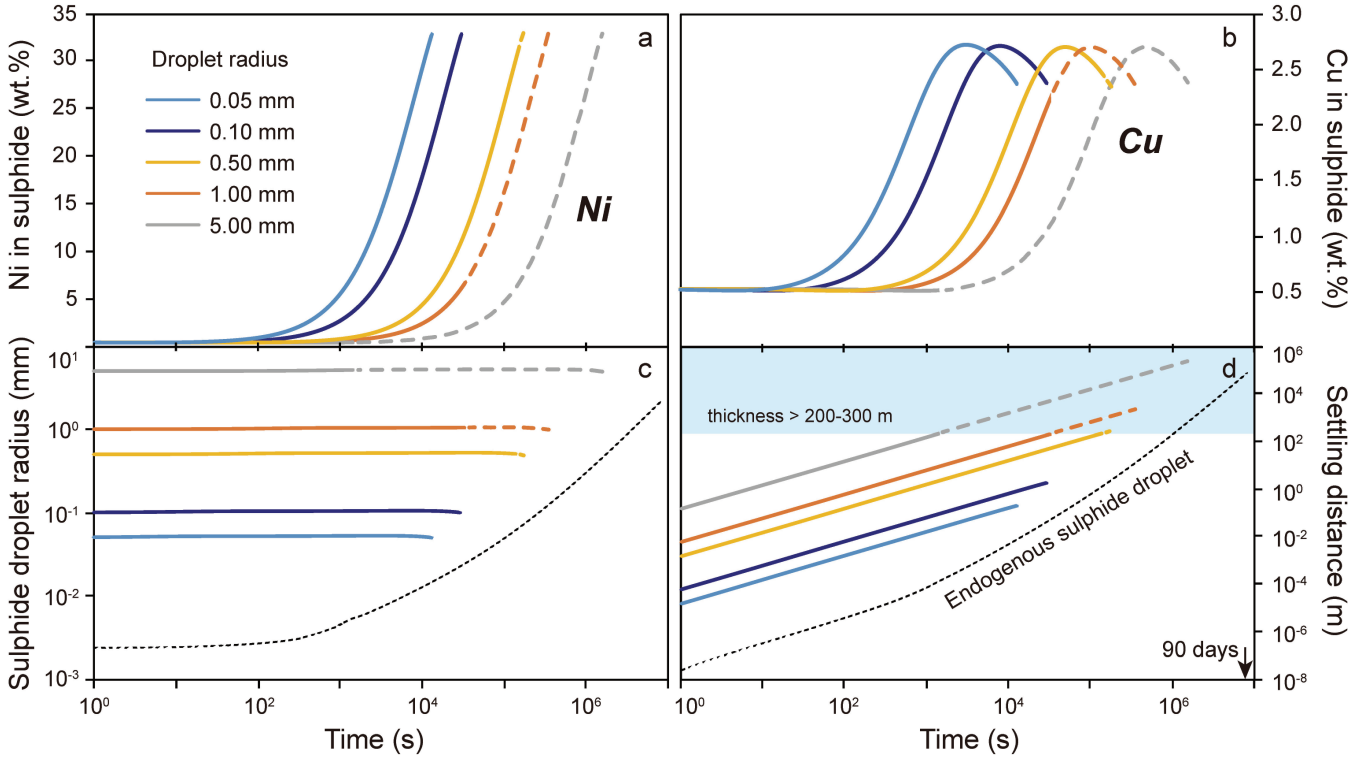

Figure 2. Kinetic fractionation of Ni and Cu into external sulphide droplets via gravitational settling through quiescent komatiitic basalt. Kinetic-controlled variations of **a)** Ni and **b)** Cu concentrations in the external sulphide droplet. The corresponding variations of droplet radius and settling distance before reaching equilibrium concentration are shown in **c)** and **d)**, respectively. The parts of settling distances exceeding the total thickness of ultramafic complex (~200-300 m, blue box in **(d)**) cannot physically exist and are expressed as dashed lines in **(a-d)**, qualitatively representing the histories of droplets repeatedly lofted back into the main flow by turbulence. The kinetic growth and sinking of an endogenous sulphide droplet with a 2 μm initial radius at supersaturation state (x=0.1) are shown as black dashed lines in **(c)** and **(d)**.

$$Re = \frac{\rho_m U L}{\mu_m}$$

where ρ_m and μ_m are the magma density and viscosity, respectively; U is the magma velocity, L is the length scale which is equal to the half-width of magma flow or radius of droplet. For the magma flow, the corresponding *Re* number is a measure of flow regime: low *Re* number (<~10-500) is related to the laminar flow that is dominated by viscous forces; while high Re (>~3000-4500) falls within the regime of turbulent flow with extensive vorticity. When the *Re* number is applied to sulphide droplet, low *Re* corresponds to the Stokes regime of creeping flow in which the inertial force is negligible. As *Re* number increases, the major external disruptive stress will change from the viscous shear stress to inertial forces. On the other hand, Bond number (*Bo*) is a measure of the relative importance of drop buoyancy to surface tension:

$$Bo = \frac{(\rho_s - \rho_m) g r^2}{\sigma_{ms}}$$

where ρ_m and ρ_s are the densities of magma and sulphide liquid, respectively, r is the radius of sulphide droplet, g is the gravitational acceleration, and σ_{ms} is the surface tension between sulphide and basaltic melts (~0.21-0.24 N/m, Mungall et al., 2015). Similarly, the Galilei number (*Ga*) is calculated as the ratio of the gravitational force to the viscous force:

$$Ga = \frac{\rho_m \sqrt{grr}}{\mu_m}$$

where ρ_m and μ_m are the magma density and viscosity, respectively; r is the radius of sulphide droplet, and g is the gravitational acceleration. The ratio of inertial force to surface tension force is equal to the Weber number (*We*):

$$We = \frac{\rho_m U^2 r}{\sigma_{ms}}$$

where ρ_m and σ_{ms} are the magma density and sulphide-magma surface tension, respectively; r is the radius of sulphide droplet, and U is the magma velocity. In an external laminar flow, whether or not the sulphide droplets retain steady shapes in response to flow shearing is qualitatively determined by the ratio of viscous shear stress to surface tension force, which is called the Capillary number (Ca):

$$Ca = \frac{r\mu_m\dot{\gamma}}{\sigma_{ms}}$$

where μ_m and σ_{ms} are the magma viscosity and sulphide-magma surface tension, respectively; r is the radius of sulphide droplet, and γ is the strain rate of magma flow in the vicinity of the sulphide droplet. In this regard, we conducted a series of numerical simulations to outline the physical feedbacks of sulphide droplets to the peripheral fluid dynamics in various reasonable scenarios of magmatic systems, which can be an *a priori* theoretical basis for predicting the morphology and size distribution of sulphide blebs observed in the Raglan deposits and in other magmatic sulphide systems.

4.1 Droplet freely settling in a stagnant magma

Once entering the magmatic system, the sulphide droplets whether nucleated within the silicate melts or released from the sulfidic sediments, tend to settle through their host magma under their own weight. If there is no powerful convection or dynamic flow (i.e. a stagnant environment), the negative buoyancy of dense sulphide droplet may be balanced by a drag force from the surrounding melts, resulting in a constant terminal sinking rate that is proportion to the square of droplet radius (De Bremond d'Ars et al., 2001; Chung and Mungall, 2009). Hence, for slow-settling droplets with a small size, the viscous drag forces can be easily balanced via the surface tension, whereas large droplets may settle fast enough that the Rayleigh-Taylor instability (driven by density difference between two fluids) and/or Kelvin-Helmholtz instability (induced by velocity difference across the interface between two fluids) at the drop surfaces may break the droplet apart (Robertson et al., 2015). Hence, the *Bo* number (drop buoyancy/surface tension) and *Ga* number (drop buoyancy/viscous force) are adopted here (Fig. 3a) to trace whether the sulphide droplets retain steady shapes or experience viscous breakup in response to the flow shearing during free settling.

After the numerical validation of model parameters such as node spacing and time step by comparing results to experimental results or analytical solutions, the shape and breakage of free-settling sulphide droplets within stagnant mafic-ultramafic magma has been investigated via the conservative level set method in more than 60 simulations (Fig. 3). Several features emerge from Figure 3, which is divided into five modes. In Mode I, at low *Bo* and *Ga* numbers, surface tension and viscous stress are stronger than gravity force, and therefore the sulphide drop retains its initial spherical shape (Fig. 3a). With a slight increase of *Bo* number, a very small pinnacle occurs at the top of the drop, but the overall morphology is still approximately spherical. In Mode II, the gravity gradually comes into play along with the increasing *Ga* number, and the sinking drop tends to form a "mushroom-like" shape because growing vorticity at the interface (Fig. 3a) leads to the Kelvin-Helmholtz instability (Arecchi et al., 1989). In Mode III, at high *Ga* but low *Bo* numbers for the small droplet within a low-viscosity magma (Fig. 3a) where the surface tension > body gravity > viscous stress, the spherical droplet becomes a hemisphere with a smooth surface. In contrast, in Mode IV with high *Ga* and *Bo* numbers, the drop starts forming a hollow bowl-shaped hemisphere (a crescent shape in longitudinal section) (Fig. 3a). At the highest *Ga* and *Bo* numbers in Mode V, the sulphide droplet faced with the predominant large gravity, breaks up or undergoes topological changes to form a toroidal shape (Fig. 3a). This unstable toroidal drop will further disintegrate into several smaller daughter droplets.

In order to simplify interpretation of the *Bo* - *Ga* diagram, we replot the deformation regions of sulphide droplets into the magma viscosity – droplet radius diagram (Fig. 3b), because the other remaining parameters in the expressions of *Bo* and *Ga* numbers vary in a very limited scope and can be approximated by fixed values. As shown in Figure 3b, sulphide droplets immersed in viscous mafic magmas (~5-300 Pa·s, Table 1) nearly always retain their primitive spherical shape or experience just slight deformation (in Regions I and II) regardless of the drop size. In contrast, for ultramafic magmas that have extremely low viscosity (~0.01-2 Pa·s, Table 1), the spherical sulphide droplet should be quickly deformed to a "mushroom-like" or "hemisphere-like" drop when it initial radius is less than ~0.75 cm, but the coarser ones can be transformed into a bowl-type drop or even break up into many smaller daughter droplets via the toroidal deformation. Magma viscosity therefore is shown to play a fundamental role in controlling the maximum size of a stable sulphide droplet in free fall.

4.2 Coalescence of free settling droplets

As the opposite of breakup, droplet coalescence can create larger drops and occur via the impingement of droplets on each other, drainage of the liquid film separating them, and rupture of the remaining infinitesimally thin interface. In order to deepen the understanding of

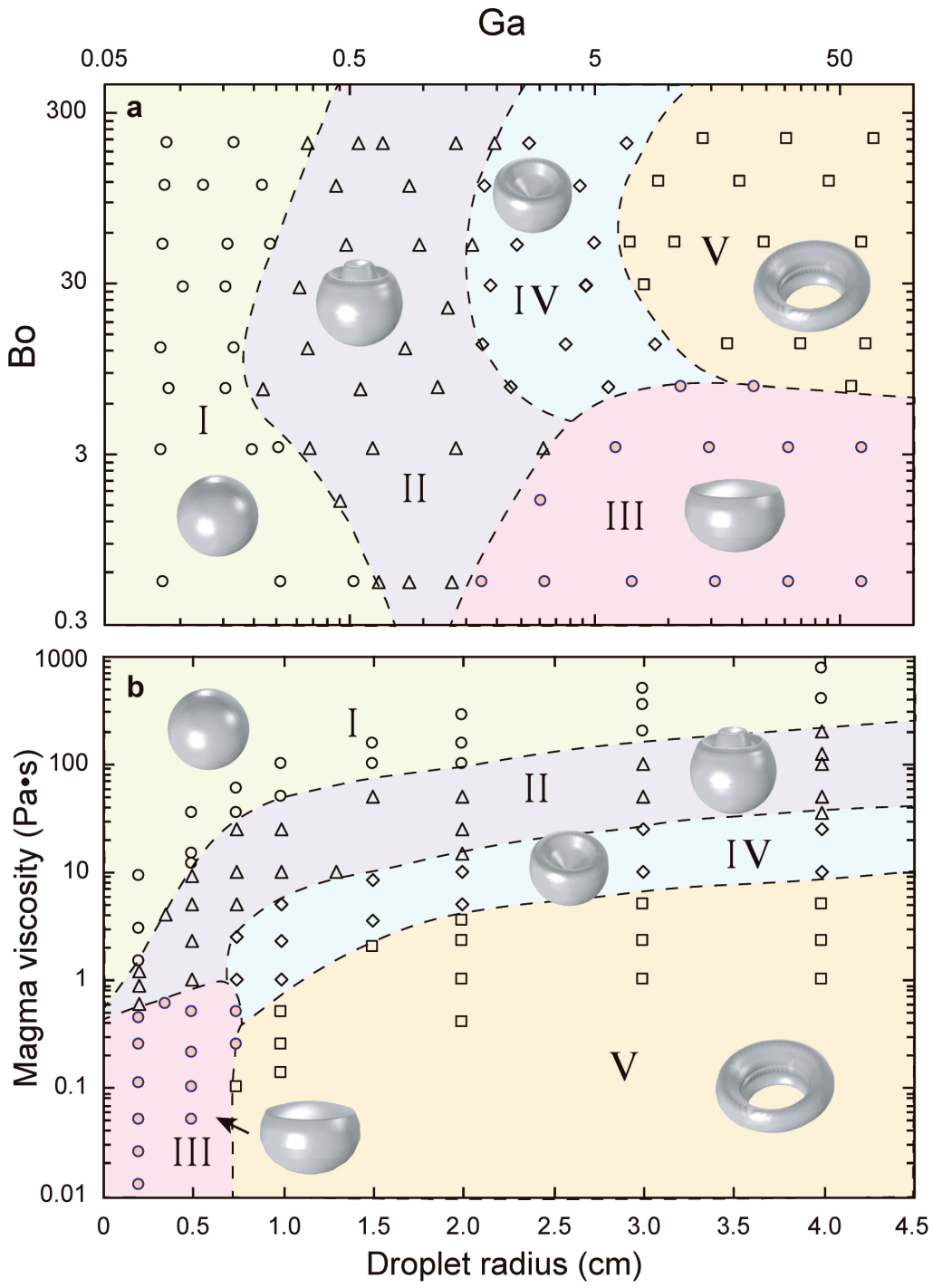

Figure 3. Different regimes of droplet shape and behavior after reaching constant settling velocity are shown in **a)** *Bo* versus *Ga* number and **b)** magma viscosity versus droplet radius. Each symbol represents a single simulation experiment.

Table 1. Viscosity of natural melts spanning the compositional range rhyolite to komatiite (Lesher and Spera, 2015).

	Komatiite	Basalt	Andesite	Dacite	Rhyolite
Temperature (ºC)	1600-1200	1400-1100	1300-1000	1100-800	1000-800
Viscosity (Pa·s)	0.01-2	5-300	300-210^4	810^4-10^8	10^7-710^9

coalescence, free-falling of two sulphide droplets in a vertical line was simulated numerically with the conservative level set method in a robust finite element solver (COMSOL Multiphysics™). Two scenes have been modeled here: first, the radius of the top sulphide droplet is the double of that of the bottom drop, which drives a faster settling velocity for the top drop, resulting in the continuous approach of the upper droplet to the lower one; second, the size of the top sulphide droplet is the same as the bottom drop, and hence, their free-falling should follow the same dynamic process if their interaction is not taken into account. In Figure 4a, the terminal settling velocity of the top sulphide droplet should be four times that of the bottom drop, so the intervening film between them thins to the point where it can break so that the two droplets join together. In the latter scene, there is no velocity difference between the top and bottom sulphide droplets, and the operation of coalescence must come from other mechanisms; a closed toroidal vortex is generated in the wake of settling bottom droplet (Fig. 4b), which drives a small upward tip for the bottom drop and makes the top droplet taper toward its bottom if it enters into the wake region of bottom drop. This mechanism holds for the connection of both droplets along the center vertical line, which further leads to the coalescence of the two sulphide droplets (Fig. 4b). In the first scene, the influence of the closed toroidal vortex in the wake is also observed at the bottom of the top sulphide drop (Fig. 4a). After coalescence, the subsequent dynamic process (e.g. deformation and breakup) of the multi-drop system behaves like an integrated, coarse droplet in both scenes (Fig. 4).

Our primary simulations indicate that droplet coalescence may be favored where population densities of sulphide droplets are high, and where droplets are pressed together to allow drainage of films of host liquid, which can be further enhanced by the interaction between them via the peripheral fluid flow field. In contrast to the previous deduction that the coalescence should take a long time to proceed, this process in our simulations takes only a few seconds under the assistance of the toroidal vortex in the wake of the settling bottom droplet. Therefore, droplet coalescence that acts against the breakup processes is expected to be an active and effective mechanism to determine the sulphide droplet size distributions in dynamic magmatic systems when sulphide droplets are close together.

4.3 Droplet deformation in a sudden ascending magma flow

Presuming the existence of a sulphide-saturated magma reservoir at depth in the crust, the classical conduit model requires this deep-seated staging magma reservoir to rupture and a liquid-driven fracture propagates from chambers to the ore-forming intrusions. When the magma replenishment and reservoir rupture drive the unrest of magma, an ascending magma flow is suddenly triggered, and the ambient melt is forced to flow through the sulphide drops, whereas the heavier drops tend to continue its original state because of the inertia. Therefore, a sudden relative motion between the dense sulphide drop and the surrounding silicate melt is generated that resembles a shock-induced magma flow around a sulphide drop. Similarly, during turbulent flow of magma, a sudden change in direction of motion of the enclosing melt effectively subjects a suspended droplet to an acceleration. The three forces controlling the deformation and breakup of droplets faced with a sudden acceleration are the inertial, viscous, and surface tension forces (Jain et al., 2015; Liao et al., 2018). The former two enhance whereas the latter counteracts breakup. Here, for the dense sulphide droplet, its gravity force should be an important factor, and is also taken into account.

In this project, we present level-set simulations with appropriate densities for mafic-ultramafic magmatic systems and capture the initial breakup of a coarse sulphide droplet with radius of 0.5 cm in a uniform magma flow. The simulation results are plotted in the Weber number (*We*) - Galilei number (*Ga*) diagram, and we recognize three deformation modes (Fig. 5a). Mode I, the teardrop deformation, is the predominant mechanism at low to moderate *Ga* number and a wide range of *We* number (1-1000), in which the motion of the surrounding melt forces the sulphide droplet to taper toward its top, forming a teardrop-like or pear-shaped droplet. For a larger *Ga* number, gravity gradually plays a more important role in the deformation of sulphide drop, and the sharp tail in the wake region becomes shorter and smooth along with the increasing *Ca* number until the drop starts forming a hollow bowl-shaped hemisphere (Mode II in Fig. 5a, bowl-type deformation). At higher *Ca* number, counter-rotating vortices in the wake region move the sulphide liquid outwards from the center of bowl-like drop, which finally drives the drop to form an increasingly thinner core until the pressure exerted on the front pole destabilizes the center of the interface (Mode III, toroidal breakup). The transition from the bowl-type deformation to the initial breakup also occurs for the free

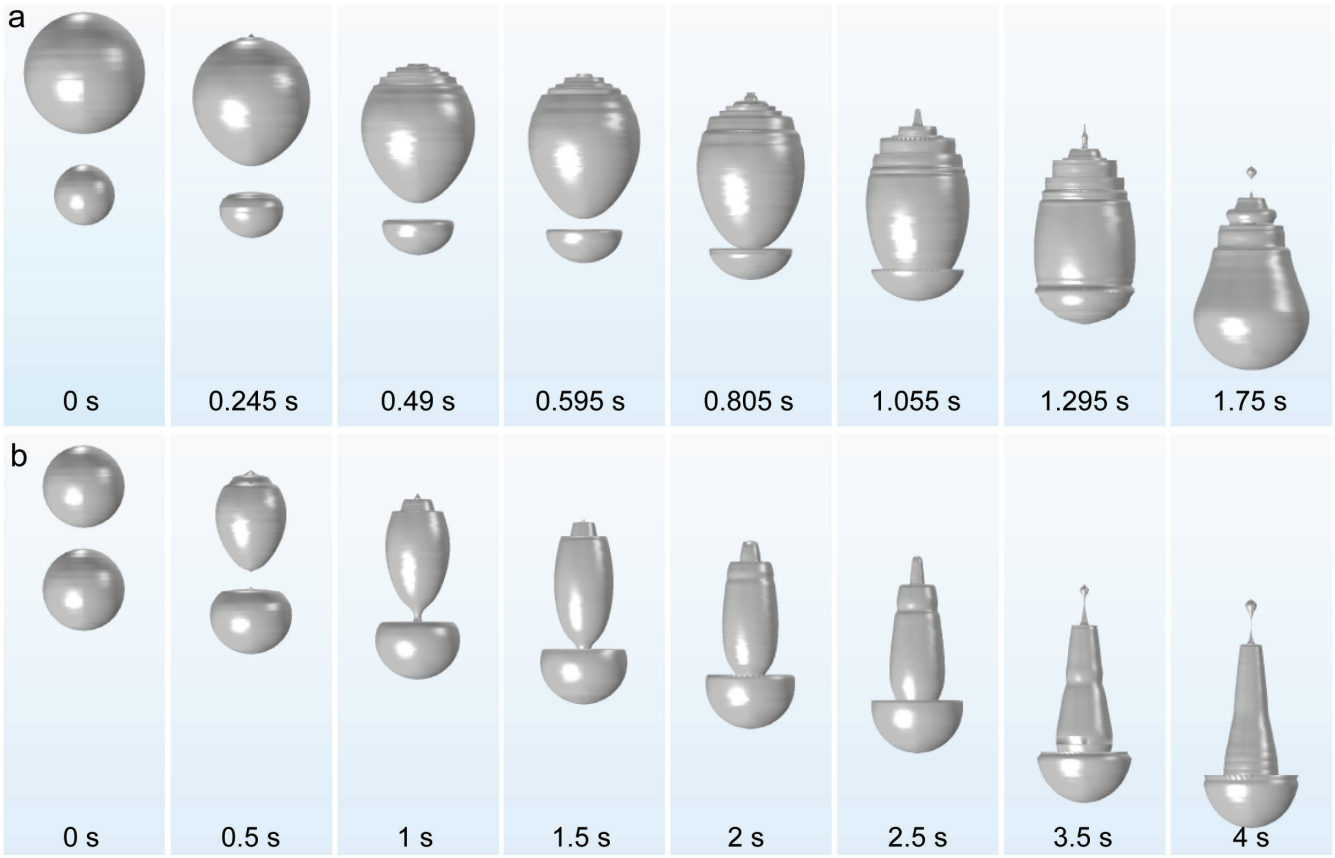

Figure 4. Deformation and coalescence of two sulphide droplets free settling in a vertical line. **a)** Radius of the top sulphide droplet is the double of that of the bottom drop; **b)** Size of the top sulphide droplet is the same as the bottom drop.

settling sulphide droplet at high *Bo*-*Ga* numbers (Fig. 3a), suggesting that at this condition, deformation of a sulphide droplet in a uniform ascending magma flow is mainly controlled by gravity. Because all simulations were conducted for coarse sulphide droplets with the same radius (0.5 cm), the *We* – *Ga* number diagram can be transformed to a plot of magma viscosity and instantaneous velocity as a proxy for whatever random acceleration a drop might encounter in turbulent flow (Fig. 5b). For the accelerated flow of mafic magma, the sulphide droplet always remains in the teardrop-like deformation regime, and no breakup occurs during the conduit propagation. In contrast, in low-viscosity ultramafic magmas, the sulphide droplet can easily go through the bowl-type deformation and even initial breakup at the center of bottom once the velocity of magma flow reaches and exceeds the order of m/s, which may be a common occurrence in natural ultramafic magmas (Huppert and Sparks, 1985). The critical velocities for the transitions between the three deformation regimes rapidly grow with the increase of viscosity for the ultramafic magmas. Hence, in most cases, sulphide droplets experiencing sudden accelerations of the enclosing mafic magma flow in the conduit system should experience obvious deformation without breakup, whereas sulphide droplets in ultramafic flows may be broken up and dispersed by the random accelerations experienced during turbulent flow.

4.4 Drop breakup in shear flows

In reality, the dynamic magma flows that sulphide droplets are subjected to are rarely simple uniform flows, and more chaotic flows need to be considered in magmatic processes occurring in vigorous staging reservoirs, conduit propagation, emplacement and/or surface flows. Hence, the sulphide droplet should travel through a quickly varying velocity field and must be subjected to a variety of dynamic flow conditions. In order to approach a more realistic magma flow configuration, a single sulphide droplet immersed in a simple shear flow serves as an excellent first step to understand the droplet dynamics and can also provide fundamental insights into the more complex fluid dynamics.

Here, we have used the conservative level set method in the COMSOL Multiphysics™ to track the dynamic evolution of sulphide droplets placed in a horizontal shear flow with a uniform vertical gravity field. Based on ~100 simulations, we recognize three principal models for the deformation or breakup of sulphide droplet in shear flow, and plot them in the Capillary number (*Ca*: shear stress/surface tension) versus Bond number (*Bo*: drop buoyancy/surface tension) diagram (Fig. 6) because gravity should be an indispensable factor of drop deformation. In Mode I, (non-breakup) at

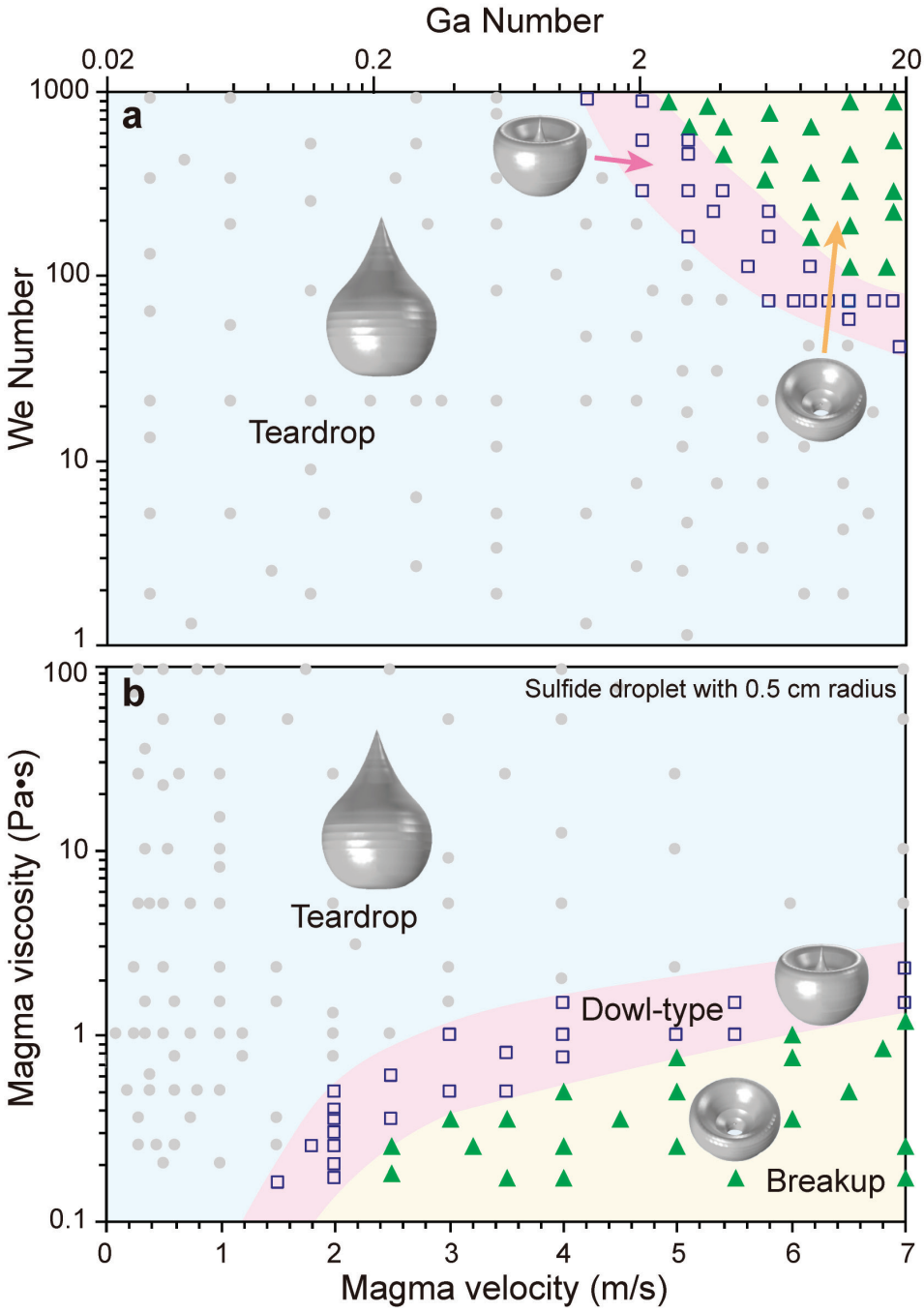

Figure 5. Different regimes of droplet shape and behavior within a sudden ascending magma flow are shown in **a)** *We* versus *Ga* number and **b)** magma viscosity versus velocity.

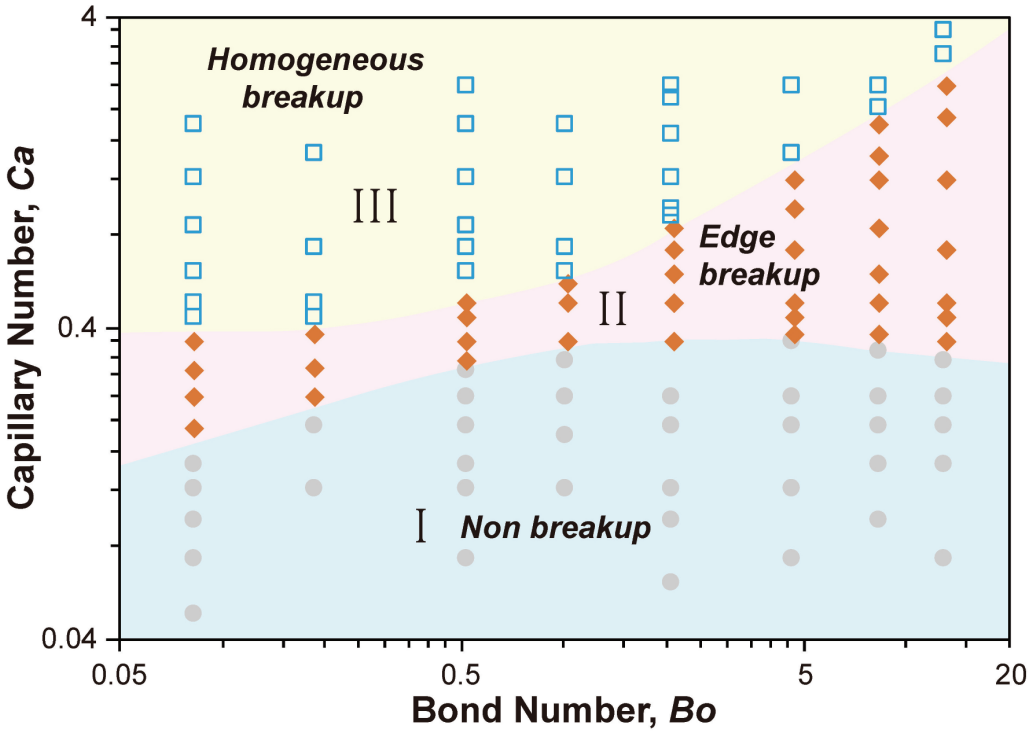

Figure 6. Different regimes of droplet shape and behavior in a horizontal shear flow.

low *Ca* number, the viscous shear stress can be easily balanced by surface tension via the change of morphology, and the sulphide droplet deforms to a downward-sloping tadpole-type drop with a short tail (Fig. 7a). In Mode II, (edge breakup) at a moderate *Ca* number (Fig. 6), along with the increase of viscous forces the sulphide droplet becomes unstable preferentially at its tail, leading to the detachment of smaller droplets from the intact central segment (Fig. 7b). In Mode III, (homogeneous breakup) at higher *Ca* number (Fig. 6), the sulphide droplet is continually elongated due to the large viscous forces until it breaks apart into a large number of daughter drops with similar sizes (Fig. 7c). This breakup mechanism results from the capillary wave instability of the extended drop, which affects the entire droplet and forms homogeneously distributed smaller daughter drops if the *Ca* number exceeds the critical value.

In comparison to the free-settling droplet in stagnant magma, the breakup of a sulphide droplet in a quickly varying velocity field may be the most important mechanism to control the sizes of sulphide droplets. Theoretically, the edge breakup will develop typically bi-modal size distributions with two frequency peaks of drop size, and the smaller size fraction far exceeds the peak for the larger size fraction. In contrast, the homogeneous breakup can produce multiple droplets with similar size, and results in a narrow spread of size distribution with a unimodal frequency after large amounts of shear flows. The most frequent droplet size is suggested to be in one tenth of the initial drop diameter (Barai and Mandal, 2016).

4.5 Upward transport of sulphide droplets in magmatic conduit

For each single sulphide droplet, its upward transport velocity in the ascending magma flow is equal to the difference between the settling velocity and the vertical component of magma velocity. Based on the previous analog experiments and the simulation results from the section 4.1, we confirmed that the settling velocity of dense sulphide droplet obeys the Hadamard-Rybczynski equation, which is expressed as (De Bremond d'Ars et al., 2001):

$$V = \frac{2(\rho_s - \rho_m)gr^2}{3\mu_m} \cdot \frac{\mu_m + \mu_s}{2\mu_m + 3\mu_s}$$

where ρ_m and ρ_s are the densities of magma and sulphide liquid, respectively; μ_m and μ_s are the viscosities of magma and sulphide, respectively; r is the radius of sulphide droplet, and g is the gravitational acceleration. For the sulphide droplet with size less than 1 cm, the maximum settling velocities in mafic and ultramafic magma are ~0.002 and ~0.7 m/s, respectively. In comparison, the ascent rates of natural mafic magma are mostly constrained in the range of 0.0015-0.1 m/s (Rutherford, 2008; Chavrit et al., 2012), and the ultramafic magma can ascend rapidly at velocity on the order of m/s (Huppert and Sparks, 1985; Brett et al., 2015). Hence, in most cases, mm-scale sulphide droplets fall behind the ascending magma flow, but still show net upward

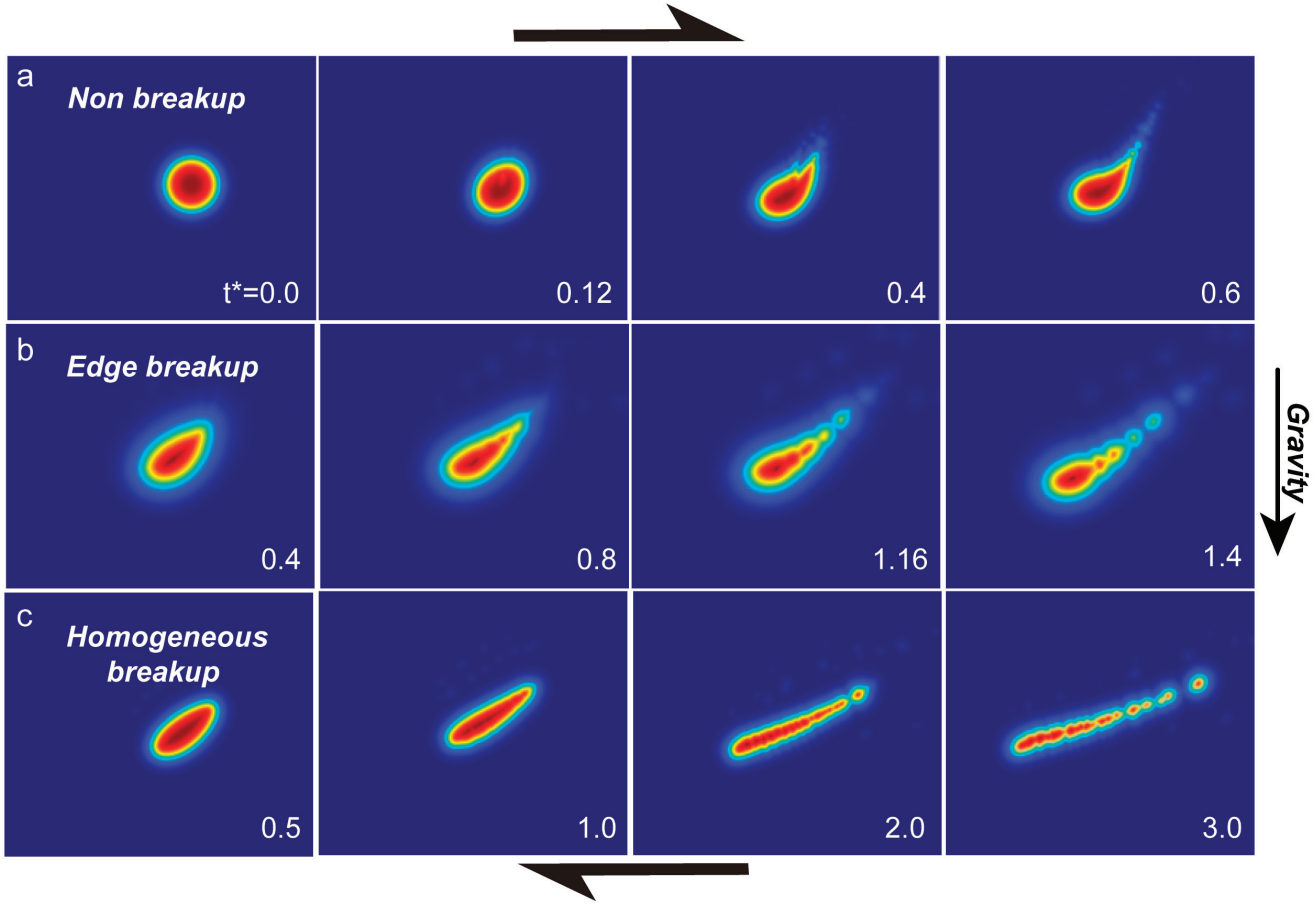

Figure 7. Progressive stages of drop deformations of sulphide droplet in a shear flow at different mode: **a)** non-breakup; **b)** Edge breakup; and **c)** Homogeneous breakup. The normalized time step, t*=γ̇t.

transport relative to the immobile conduit walls because the sulphide drops' settling velocities are lower than the magma ascent rates.

On the other hand, if a group of sulphide droplets is introduced into the ascending flows, the magma as a whole mixture has obvious increases in the density and viscosity, which further results in a complex rheological behavior and strongly influences the dynamic flow through dykes and volcanic conduits. Here, we use the *Confort* 15 (Campagnola et al., 2016) to model the steady-state flow of magma in vertical conduits (Yao et al., 2020). In general, the addition of dense particles into magma not only reduces the density contrast relative to the upper crust which weakens its buoyancy-driven impetus for upward transport, but also enlarges the viscous resistance to flow. We define the maximum carrying capacity for sulphide droplets as the suspended volume fraction above which the driving pressure in magma can no longer overcome the tensile strength of the host rock at the propagating tip and hence the conduit propagation should cease. For sulphide droplets alone, the maximum carrying capacity is relatively low (~2-4 vol% for mafic melt), but it will be strongly improved by the addition of volatiles (~6-9 and 15-18 vol% for the mafic melt at 1 and 2 wt.% H^2O, respectively, Table 2; Yao et al., 2020) which decreases the density and viscosity of silicate melt. When the ascending magma also carries olivine xenocrysts with the same volume fraction of sulphide droplets, the maximum carrying capacity would be cut by 30-38% (Table 2, Yao et al., 2020). On the other hand, during the decompression of magma flow, the occurrence of volatile degassing at low pressure further facilitates sulphide entrainment by reducing bulk magma density via the large generation of low-density vapour bubbles (e.g. the maximum carrying capacity of mafic melt with 3 wt.% H2O that drives volatile exsolution at ~1 kbar can even reach ~30 vol.% for sulphide droplets, Table 2, Yao et al., 2020). In addition, the vapour bubbles should be easily coupled with the existing sulphide droplets to form compound drops, based on the experimental observations of Mungall et al. (2015). Hence, the compound drops may become buoyant, and also increase the potential for upward transfer of sulphide droplets to the overlying parts of the ore-forming systems (Yao et al., 2020; Yao and Mungall, 2020).

Table 2. The carrying load capacity of the Etna and Stromboli basalts for sulphide droplets or sulphide-olivine mixture (volume ratio=1:1) at various H_2O concentrations (from Yao et al., 2020).

Grains type		Sulphide Droplets						Sulphide Droplet : Olivine = 1:1					
Basalts		Etna			Stromboli			Etna			Stromboli		
H_2O (wt.%) in magma		1	2	3	1	2	3	1	2	3	1	2	3
Maximum load (vol.%) at various final depth (~ lithostatic pressure)	0.94 km (~25 MPa)	5.7	15.0	29.9	9.3	17.5	31.4	3.8	9.8	18.4	6.0	11.9	19.8
	1.88 km (~50 MPa)	5.5	10.9	20.2	8.8	13.8	22.9	3.7	7.2	13.3	5.9	~9.0	14.5
	2.82 km (~75 MPa)	5.3	10.7	16.8	8.7	13.6	18.6	~3.6	7.0	10.7	~5.8	8.8	12.2
	3.76 km (~100 MPa)	5.1	10.4	14.9	8.5	13.3	17.5	3.4	6.9	9.7	5.7	8.7	11.3

4.6 Transport and deposit of sulphide in lateral magma flow

We also examined the transport and deposit of sulphide droplets during sill emplacement and related lateral magma flow. Given the relatively high viscosity and low flow rate of mafic magma, its lateral flow falls into the laminar flow region. If the vertical component of flow rate is less than the terminal settling velocity of sulphide droplet, which will be common during lateral magma flow, the gravity regains an important role, and sulphide droplets should settle downward. Meanwhile, the sulphide droplet also has the horizontal velocity due to inertia and drag by the enclosing silicate magma and can be transported a long distance along with the lateral magma flow before its final deposition at the base of the flow. When the sulphide droplet sinks across a varying velocity field in laminar flow, which is most pronounced in the viscous boundary layer at the bottom of the flow, the local strain rate may force the sulphide droplet into the downward-sloping tadpole-type deformation, edge breakup, or even homogeneous breakup with the formation of many daughter droplets, which in turn diminishes the settling velocity of the drops.

Taking the Noril'sk-Talnakh deposits as an example, we used the 2D mixture method to model the deviation of sulphide-laden magma form vertical dykes to near-horizontal sill-like segments (Fig. 8). Once magma flow deflects into sill-like bodies, the discrete sulphide droplets mostly decouple from main mixtures, and converge at low-lying places. Along with continuous injection of sulphide-laden magma, the volume fraction of accumulated sulphide will increase at the bottom and gradually decline upward (Fig. 8). Once formed, the high density and low viscosity of sulphide pools can drive extensive lateral and downward transport under their own hydrostatic head. Furthermore, in the presence of a plane stress field within the thermal aureole immediately beneath a sill (e.g., Mungall et al., 2016), the downward propagating sulphide melt might be expected to be preferentially emplaced in contact-parallel sheets a short distance beneath the base of the sills, as is commonly observed at Noril'sk and other localities.

In contrast to mafic basalt, the ultramafic magmas have lower viscosity (Table 1), and their open-channel flows at surface have been suggested to be turbulent and to have velocities ranging from few m/s to tens of meters per second, depending on slope and flow thickness (Huppert and Sparks, 1985; Rice and Moore, 2001). The dense sulphide droplets would remain in suspension or be sedimented in turbulent ultramafic flows, in measure of the difference between the vertical component of velocity in the turbulent flow and the terminal settling velocity of sulphide droplets. As the local velocity of the turbulent flow is complex and variable, the shearing stress velocity is approximated by the characteristic velocity (U') of turbulent flow:

$$U' = \beta(k/2)^{0.5}U$$

where β is a constant (0.12-0.65), k is the friction coefficient, and U is the average flow velocity. Experiments have confirmed that if this characteristic velocity is larger than the terminal settling velocity (Huppert and Sparks, 1985) the mm-scale dispersed sulphide droplets remain in suspension, and can be carried long distances by turbulent flow. However, if the flow *Re* number falls into the laminar flow regime, sedimentation of sulphide droplets should occur because there are no eddies to suspend the dense drops. On the other hand, when the vortices in turbulent eddy field collide with the sulphide droplet, they will pull out ligaments and sheets of sulphide material, forming extensive daughter drops with fine sizes, which in turn decreases the settling velocity. Here, the droplet breakup in turbulent flow is mostly controlled by the interaction between turbulent inertial stresses and surface tension force, and hence can be parameterized via the We number. Previous experiments confirmed that droplets with *We* number greater than critical values (~1-10) will be broken up quickly (Robertson et al., 2015).

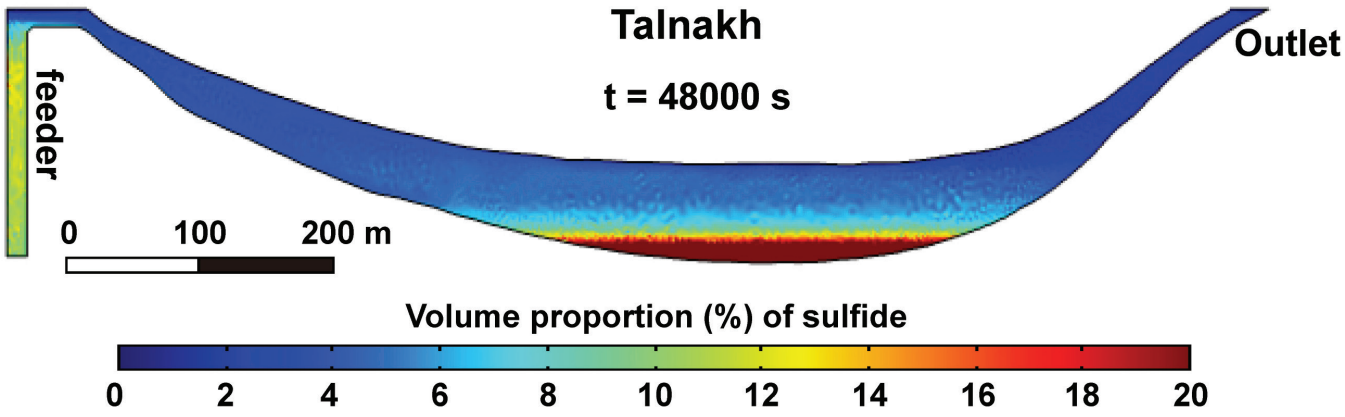

Figure 8. Two-dimensional model simulation of sulphide-laden magma flow in the ore-bearing parts of Talnakh intrusions after 48,000 s. Mixture model was adopted to solve the volume fraction equations for discrete sulphide droplets. Initial sulphide volume fractions at inlet flows are assumed as 10 vol.%. Sulphide droplets have a uniform diameter (0.5 mm), and their sinking follows the Hadamard-Rybczynski equation.

Ore bodies in komatiite-associated deposits are commonly localized in footwall embayments, especially in the Raglan deposits (Lesher et al., 1984, 2001; Lesher, 1989, 2007). When the sulphide and silicate magma inlet flow passes through an expanded section (e.g. embayment), a typical diverging pattern occurs with the result that some flow lines will be diverted into recirculation or free-mixing stall regions (Fig. 9) and follow reverse and/or recirculating paths. The remaining forward flow expands radially, reconnects with the wall, and forms a fully developed outlet flow with a new simple velocity profile as shown at the far right of Figure 9. Sulphide droplets can be partially separated from two-phase flow and occupy the recirculation zone in the transitional region (Fig. 9). In this regard, we model the flow pattern across a sudden expansion of conduit cross-section for the laminar flow of mafic magma (Fig. 10a) and the turbulent flow of ultramafic magma (Fig. 10b). The recirculation zone with low flow velocity is observed in both models and has a larger region in the turbulent flow with high *Re* number. Local strain rate will reach its maximum value at the surface of separation due to the rapid changes of flow velocity between the normal flow and recirculation zone, where homogeneous breakup of sulphide droplets may occur if the viscous stress overcomes surface tension. The other transport and sedimentation of sulphide droplet in these flow patterns still need further simulations in the future.

5. APPLICATION TO THE RAGLAN DEPOSITS

As shown in section 3, the introduction of sulphur into magmatic systems has two methods, and hence the observed populations of globular sulphides in rocks may be either the final productions of nucleation, growth and accumulation of sulphides that segregated from the parental magma after it assimilated and dissolved enough sulphur to reach sulphide saturation, or the remnants of external sulphide droplets released from the S-rich sediment during thermo-mechanical erosion. These distinct starting points will lead to two different compositional evolutions for the globular sulphides. The composition of an external sulphide droplet is kinetically controlled by the residence time since its release (Fig. 2), which can be connected to the flow distance downstream from the sulphur source. Combined with the previous dynamic mode for komatiitic lava emplacement and erosion (Williams et al., 2011), we developed a quantitative model for the assimilation of sulfidic substrates during lava emplacement onto a relatively shallow unobstructed sea floor at a depth of 1 km (pressure, 10 MPa) (Fig. 11) under the consideration of thermodynamics, kinetics and dynamics.

In this erosive lava flow, the kinetic-controlled variations of Ni and Cu concentrations in the external sulphide droplets are given in Figure 12. For fine-grained sulphide droplets (~0.05 mm radius), Ni content increases with flowing downstream distance, and reaches the near-equilibrium state (~22 wt.% Ni) after ~24 km propagation at the 1 m/s initial lava velocity (Fig. 12a). However, the Ni content of fine-grained sulphide droplets only reaches ~9 wt.% Ni after ~30 km propagation if the lava is flowing much faster (e.g. initial velocity 2.5 m/s), because the rapid lava propagation cannot provide enough time for the diffusive transport of Ni before the lava steps into the laminar regime (~4.8 hours) due to the continuous consumption of kinetic energy and the associated decrease of flow velocity during propagation and thermo-mechanical erosion (Fig. 12c). The Cu concentrations of fine-grained sulphide droplets achieve the equilibrium content (~8 wt.% Cu) in both flows due to the larger diffusivity of Cu (Fig. 12b and d). With increasing droplet radius, the Ni and Cu contents in sulphide droplets become farther and farther away from the equilibrium states (Fig. 12). The estimated diffusivities of Pt-Pd-Rh-Ir are slightly larger than Ni, which may drive mild enrichments for these PGEs relative to Ni. The variations of Pt-Pd contents in the external sulphide droplets are modelled for comparison (Fig. 13a), in which the initial Pt-Pd content of parental magma is about 10 ppb (Barnes et al., 1992). But unlike the Cu, there is no obvious

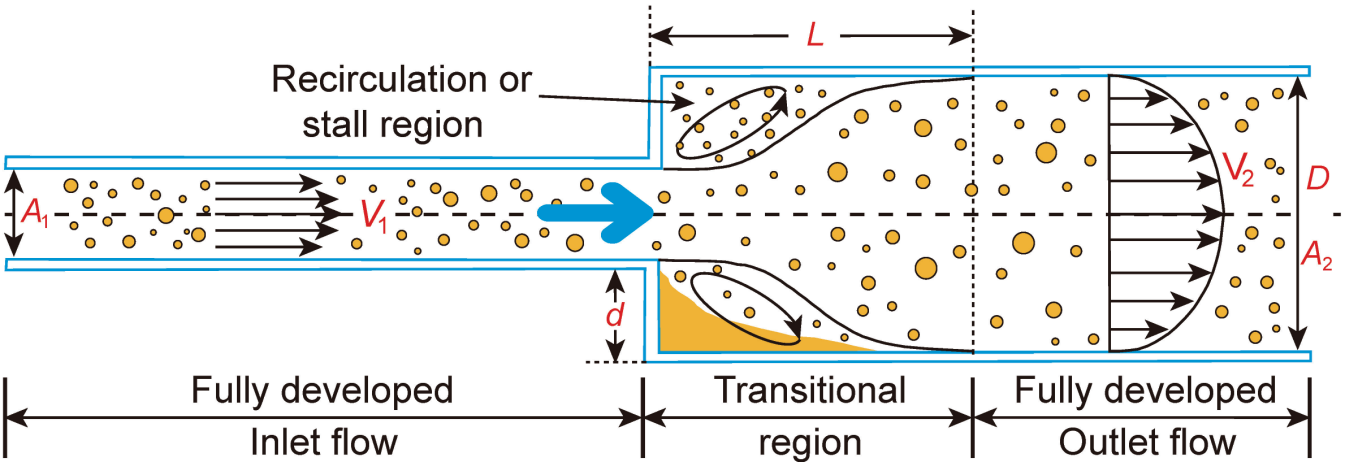

Figure 9. Diagrammatic sections illustrate the dynamics of two-phase sulphide droplet-silicate melt flow through sudden expansions (modified from Aloui and Souhar, 1996; Ahmadpour et al., 2016).

difference between Pt-Pd and Ni behaviors in the external sulphide droplets (Fig. 12 and 13). The modelled apparent R factors for Pt-Pd exhibit trends similar to the evolution of their concentrations (Fig. 13b).

Due to the high energy dissipation of turbulent komatiite flow, the stable droplets at the Raglan should mostly fall below the limit of 0.16 - 0.5 mm, no matter what the initial radii of sulphide droplets released from sediments. Such fine-grained external sulphide droplets (~0.06 mm radius) would contain 4.25% Ni, 2.18% Cu and 840 ppb Pt-Pd at ~1 km downstream, 11.6% Ni, 3.7% Cu and 3890 ppb Pt-Pd at ~5.8 km downstream, 17.1% Ni, 7.2% Cu and 10450 ppb Pt-Pd at ~21.5 km downstream from source when the initial velocity equals to 1 m/s (Fig. 12 and 13). Similar trends of compositional variations of sulphide liquids have also observed in the Raglan formation. For example, the average compositions of disseminated ores recalculated to 100% sulphides in the deposits from the westernmost to easternmost endpoints are as follow: Cross Lake, 4.25-6.31% Ni, 1.31-3.26% Cu, 850-3000ppb Pt-Pd; Zone 2-3, 12.2% Ni, 2.64% Cu, 3125 ppb Pt and 7782 ppb Pd; Katinniq, 11.4% Ni, 3.45% Cu, 4032 ppb Pt and 11878 ppb Pd; Donaldson, 17.1% Ni, 4.16-9.08% Cu, ~6600 ppb Pt and 15408-25261 ppb Pd (Lesher, 2007).

When a 10-m thick komatiitic basalt flow with initial velocity of 2 m/s passes across a sudden expansion in cross section of the conduit, the reattachment length between the fully developed inlet and outlet flows can reach as far as ~42 m, corresponding to a large recirculation zone (Fig. 10b), in which the sulphide droplets are continuously extracted from the through-going magma and tend to settle in a region of vigorous mixing and efficient reaction between the accumulated sulphide drops and the recirculating silicate melts. Hence, the embayments in the lava flow channel are a far more effective means for gathering and enriching sulphide droplets (Fig. 14). Additionally, the sulphide enrichments are strongly enhanced with the increasing sizes of sulphide droplets that are carried by the flowing magmas (Fig. 14). The presence of footwall embayments and associated sedimentation at the downstream of komatiite flow offers the first-order determinant for spatial distributions and compositional variations of sulphide ore bodies, which supports the field observation that embayments are vital to sulphide mineralization in the Raglan deposits (Lesher et al., 1984, 2001; Lesher, 1989, 2007; Houlé et al., 2012).

5.1 Field investigation in sulphide globules

The fieldwork component of the TGI project aims to document the spatial distribution of sulphide globules in several different boreholes. Due to time constraints, the majority of the efforts were placed on orebodies 8M, 14K, 14J and 14G of the Zone 5-8, all of which belong to the Katinniq member of the Raglan formation (Fig. 15).

In general, the 50-100 m thick komatiitic dunite or peridotite of the ca. 1.82-83 Ga (Bleeker and Kamo 2018) lower Chukotat Group are bound by a <10 m thick, sulphide-rich sedimentary unit (Nuvilik Fm.) on the top (Fig. 16a) which shows hornfels development and local peperitic units (Gillies, 1993; Lévesque and Lesher, 2002), which may have resulted from shallow intrusion of the dense komatiitic flows into unconsolidated mud at the seafloor as shown in Figure 11, and often by a greenish gabbroic unit on the bottom. Faults are common in the rock successions and probably responsible for occurrence of some out-of-place massive sulphide units (Fig. 16b). Underlying sulfidic mudstones are rarely found in the cores we have examined but they are abundant in holes flanking the main mineralized ultramafic channels. This can be attributed to the thermal erosion effect when the hot ultramafic magma assimilated the easily fused sedimentary unit (Williams et al., 2011). Features of fast cooling have been found between the ultramafic and gabbroic units where plagioclase crystals are recrystallized into

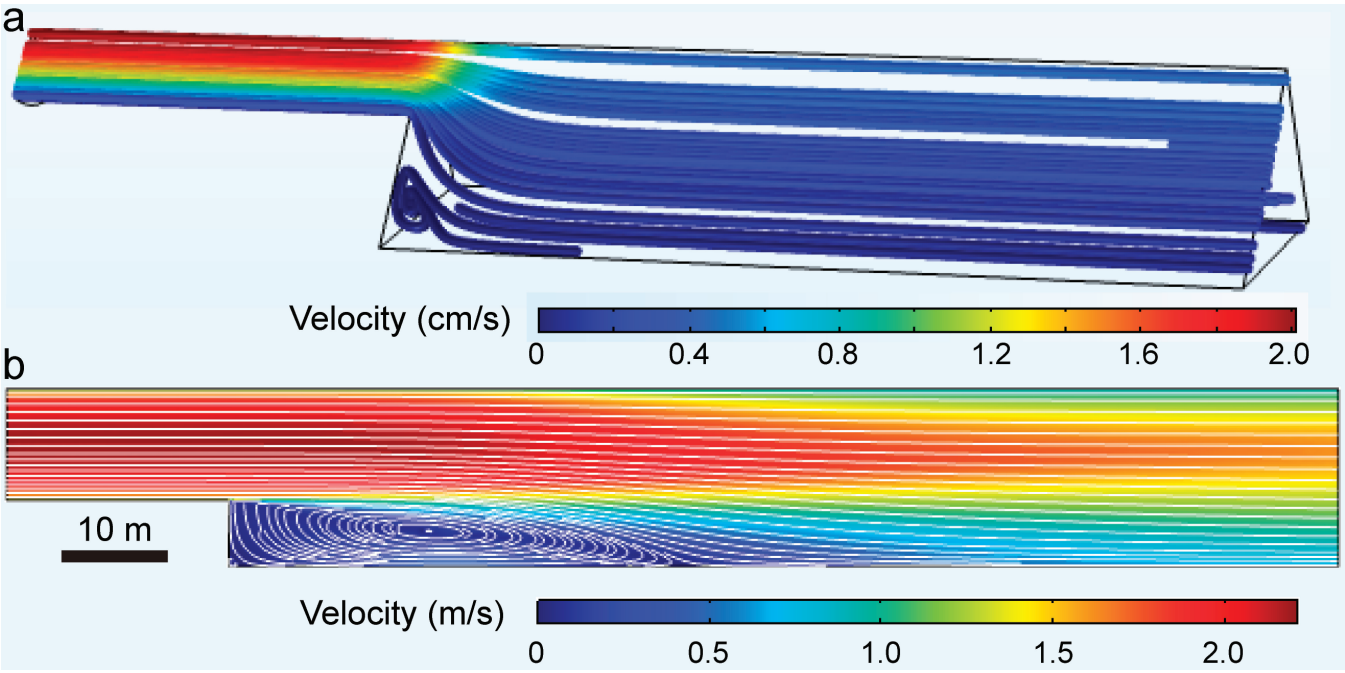

Figure 10. The recirculation region visualized using a velocity streamline plot. **a)** Laminar flow of mafic magma (viscosity, 20 Pa·s; velocity, 0.01 m/s; *Re* number, ~0.7). **b)** Turbulent flow of ultramafic magma (viscosity, 1 Pa·s; velocity, 2m/s; *Re* number, ~54,860).

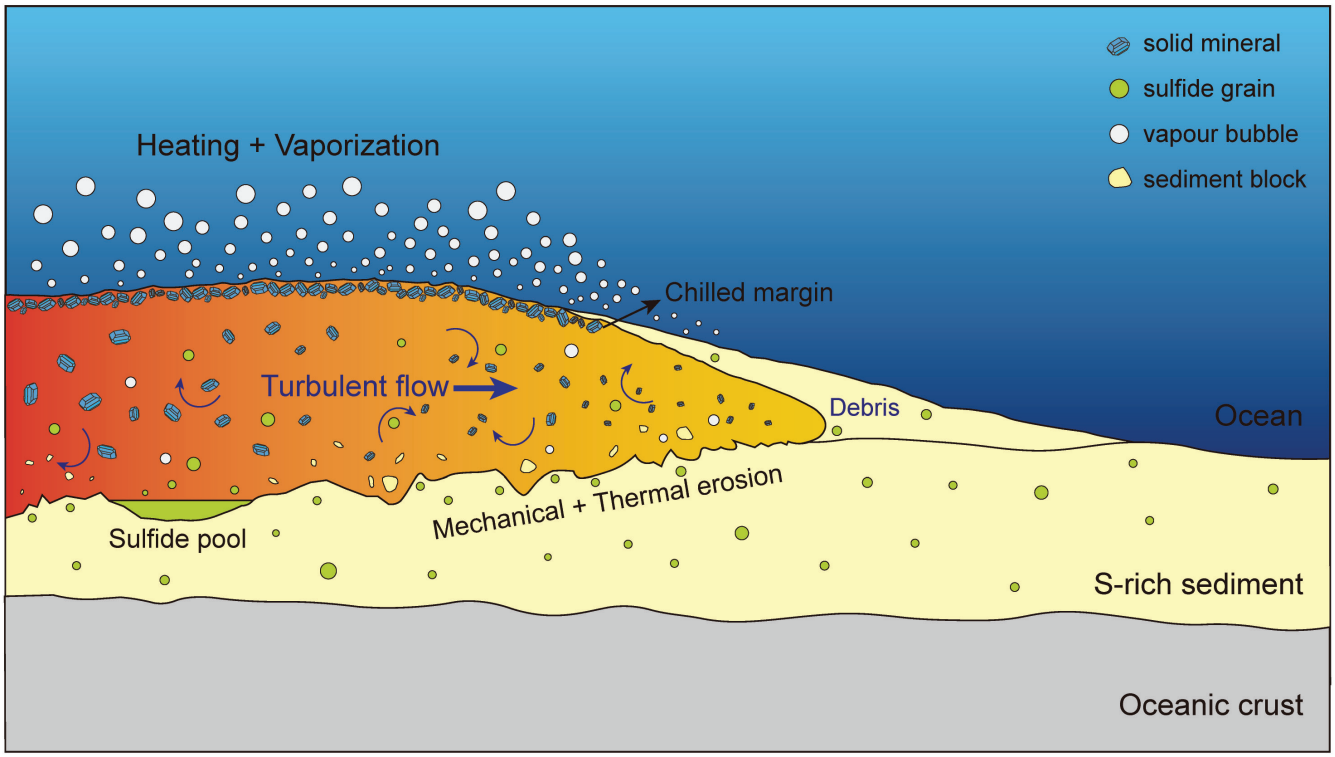

Figure 11. Schematic diagrams for the comprehensive model that the turbulent magma flow erodes the unconsolidated, sulphidic sediments on a seafloor. This schematic figure is out of scale. The color of komatiite flow represents the evolution of magmas from left to right during its propagation and thermal-mechanical erosion.

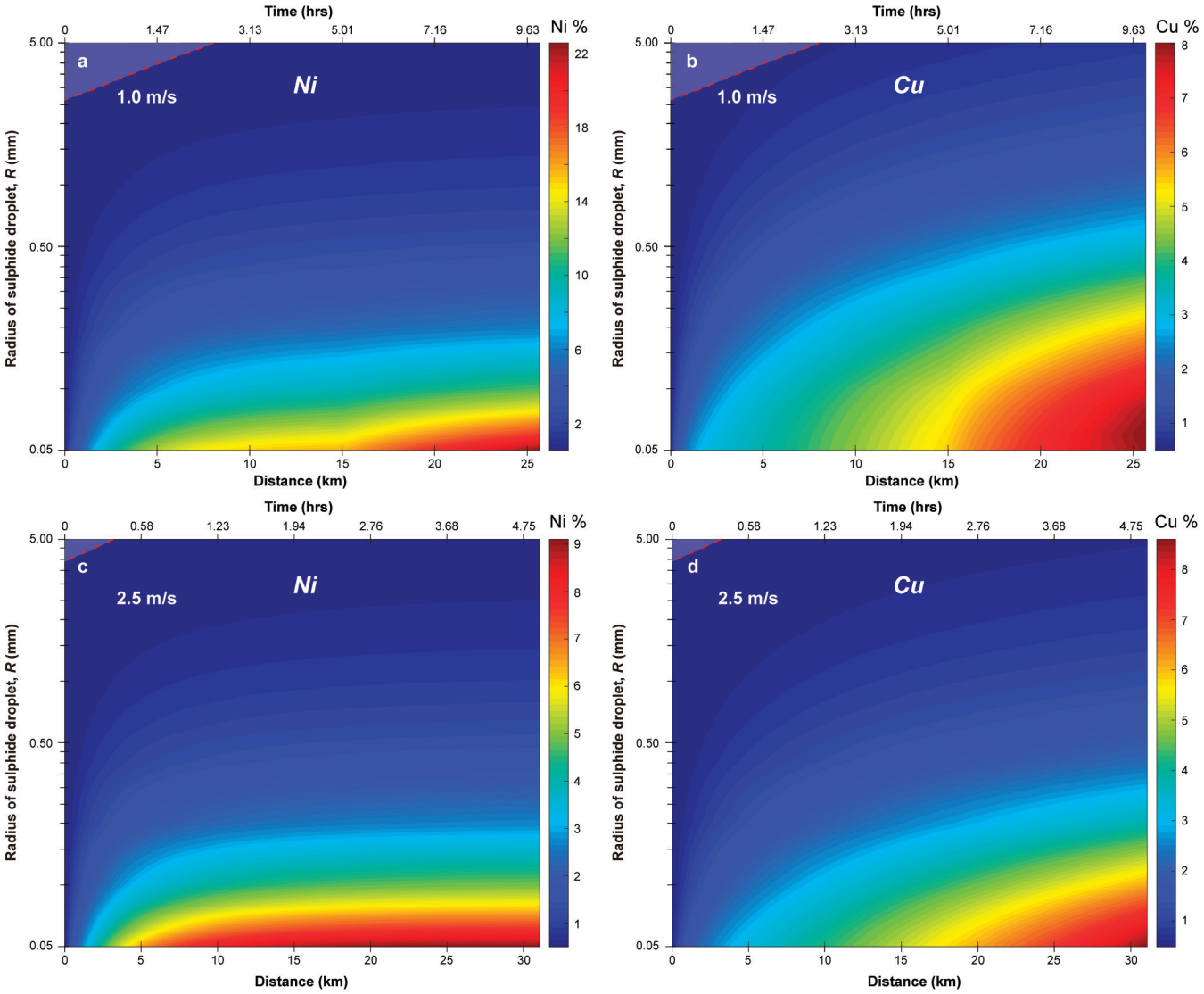

Figure 12. Compositional variations of Ni and Cu in external sulphide droplets with different radii (0.05-5 mm) during downstream turbulent flow. Initial flow velocities in **(a, b)** and **(c, d)** are 1.0 and 2.5 m/s, respectively. The shaded triangle with red dashed borderline in **(a, b)** represents the situation in which the turbulent motion cannot suspend the large sulphide droplets.

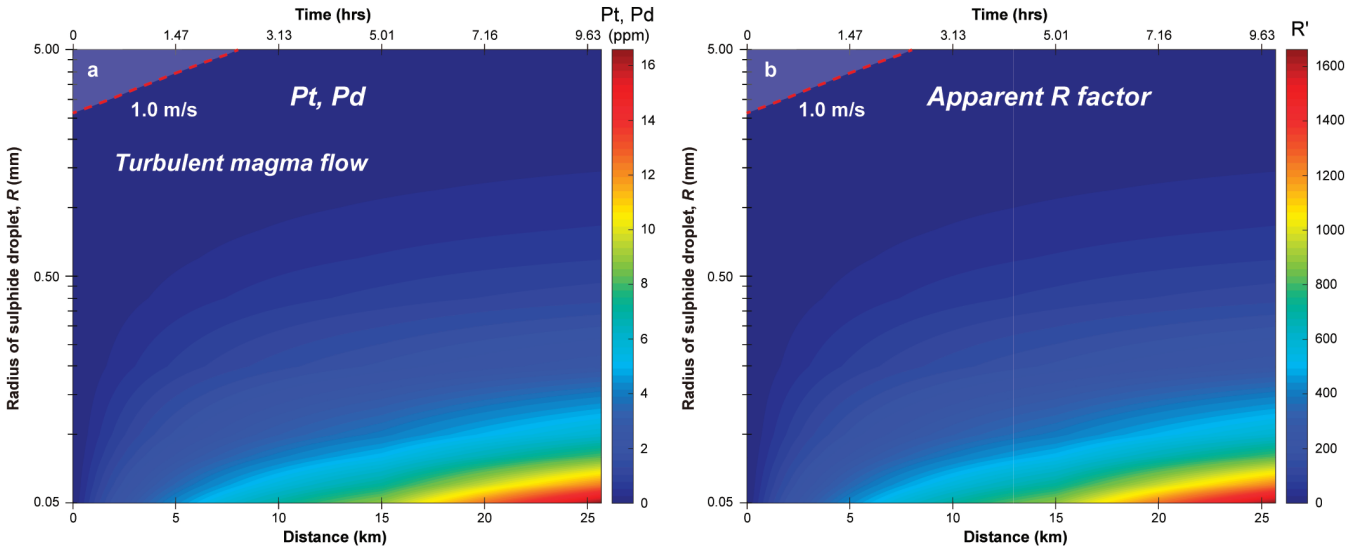

Figure 13. Contour maps for the variations of Pt-Pd concentration in the external sulphide droplets **a)** and the corresponding apparent R factor **b)** in the models of erosive lava flow with an initial velocity of 1 m/s.

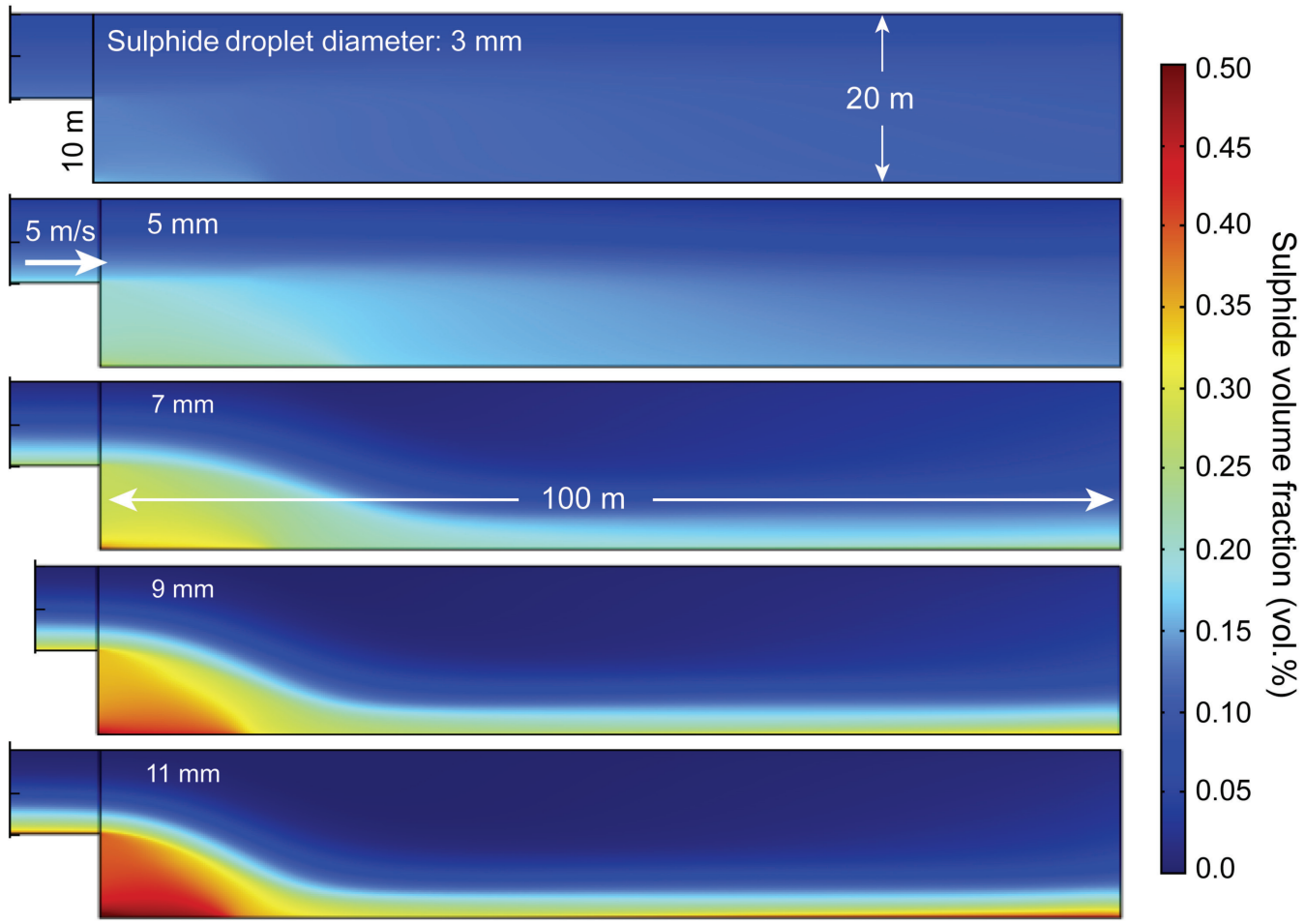

Figure 14. Modelling results show that sulphide enrichments occur at the embayments when the magma carrying 10 vol.% sulphide flows through the back step at a velocity of 5 m/s.

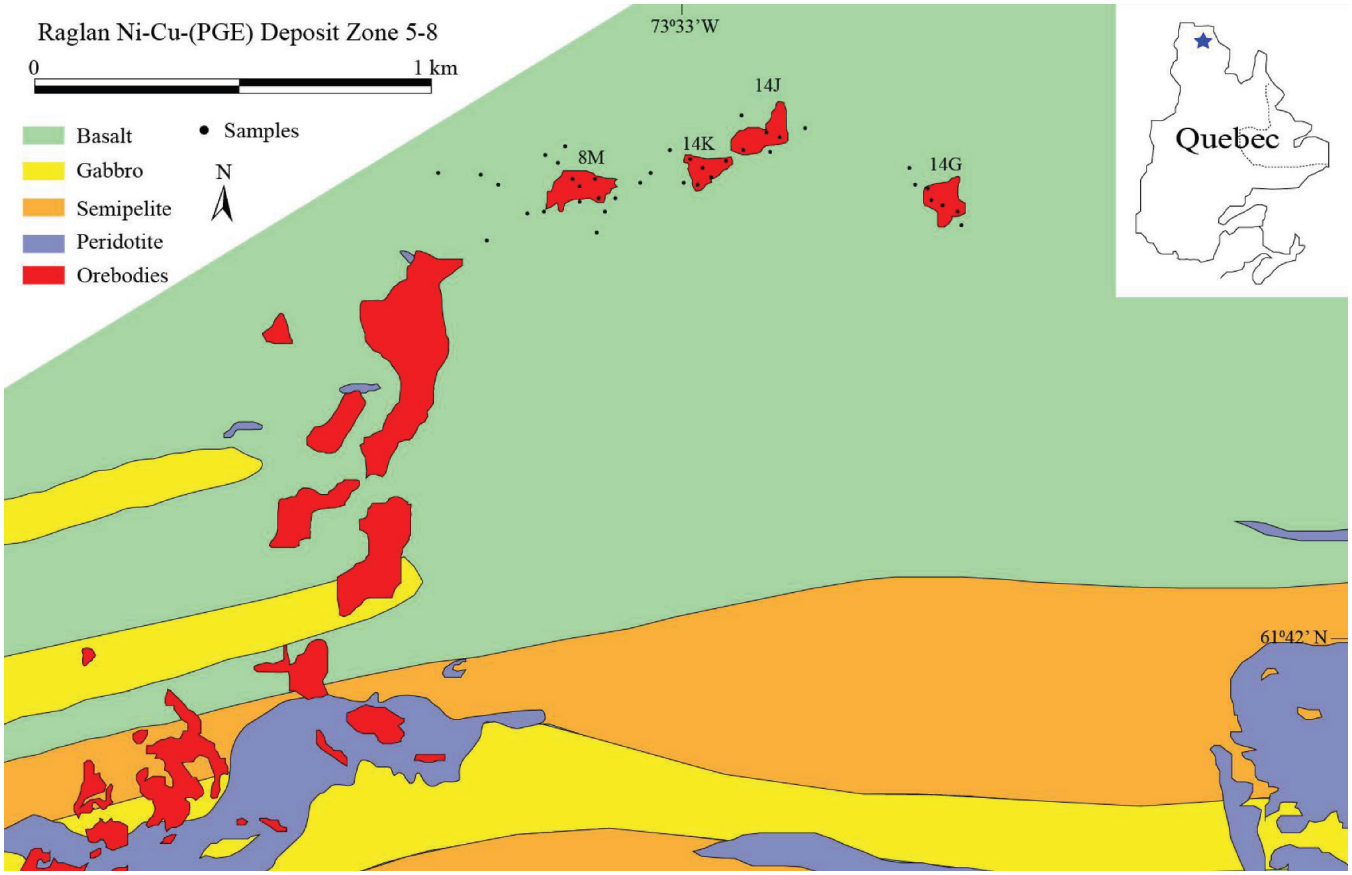

Figure 15. The locations of samples from Raglan Ni-Cu-PGE deposit Zone 5-8, modified after Lesher (2007).

coarser grains (Fig. 16c). Spinifex texture, which is mostly associated with komatiitic flow, can also be seen close to the upper chilled margins.

Near the bases of the ultramafic channels, over thickened portions of the systems corresponding to embayed basal sections, net textured ores (Fig. 16d) commonly sit right above massive sulphides. Sulphide globules are hosted by both peridotite and olivine pyroxenite. Some disseminated sulphides are believed to have been remobilized by later metamorphic fluids because of their textures and proximity to alteration veins (Fig. 16e). Sulphide globules are occasionally found associated with segregation vesicles which is probably caused by the excess volatile released during degassing of the underlying gabbroic unit (Fig. 16f).

The sulphide globules in Raglan formation have received little attention. However, a moderate number of them can be found in most of the drill cores. In general, they appear to be elliptical to subspherical with ragged outlines (Fig. 17a). Most of them fit the description of spheroidal globule discussed above. They range from sub-mm to more than 1 cm in length. Some of them sit directly above the massive sulphide ore, whereas the others are found up to 20 m above the massive ore with no apparent connection to it, and a few occurrences sit near the upper contacts with the metasediments, where in some cases they preserve highly irregular forms suggestive of xenolithic origins. Sulphide globules are sometimes found in associated with disseminated sulphides (Fig. 17b). However, on only one occasion were sulphide globules observed below the massive orebodies (Fig. 17c). It may be worth noting that the number density and sphericity of sulphide globules hosted in the ultramafic unit dramatically increases when there is a felsic to intermediate unit below the ultramafic intrusion (Fig. 18), for as-yet undetermined reasons.

An interesting and unusual texture encountered several times during the course of our field investigation (Fig. 17d) is very similar to "inverted net texture" described in Barnes et al. (2018). The interstitial space between pyrrhotite grains is occupied by interconnected silicate melt (probably intermediate in composition). This may be interpreted as the silicate melt infiltrated into the sulphide orebody when most of the monosulphide solid solution (MSS) had already crystallized (Barnes et al., 2018). Although the texture has been observed elsewhere in both komatiitic and non-komatiitic settings (Staude et al., 2017), it has never seen in such scale and well-developed form. In all cases it was seen to be associated with the presence of partially melted xenoliths, and we infer that silicate melts with low melting points derived from the xenoliths were forced into the partially solidified sulphide bodies, expelling sulphide melt from the space

Figure 16. a) Sulphide-rich sedimentary rocks of Nuvilik Formation. **b)** Fault which is filled up by massive sulphide. **c)** Recrystallized plagioclase crystals in the lower gabbro unit. **d)** "Leopard" net texture ore. **e)** Disseminated and globular sulphide remobilized by small veins. **f)** Sulphide globule with silicate fluid infills (segregation vesicle) on the top, forming a "cap".

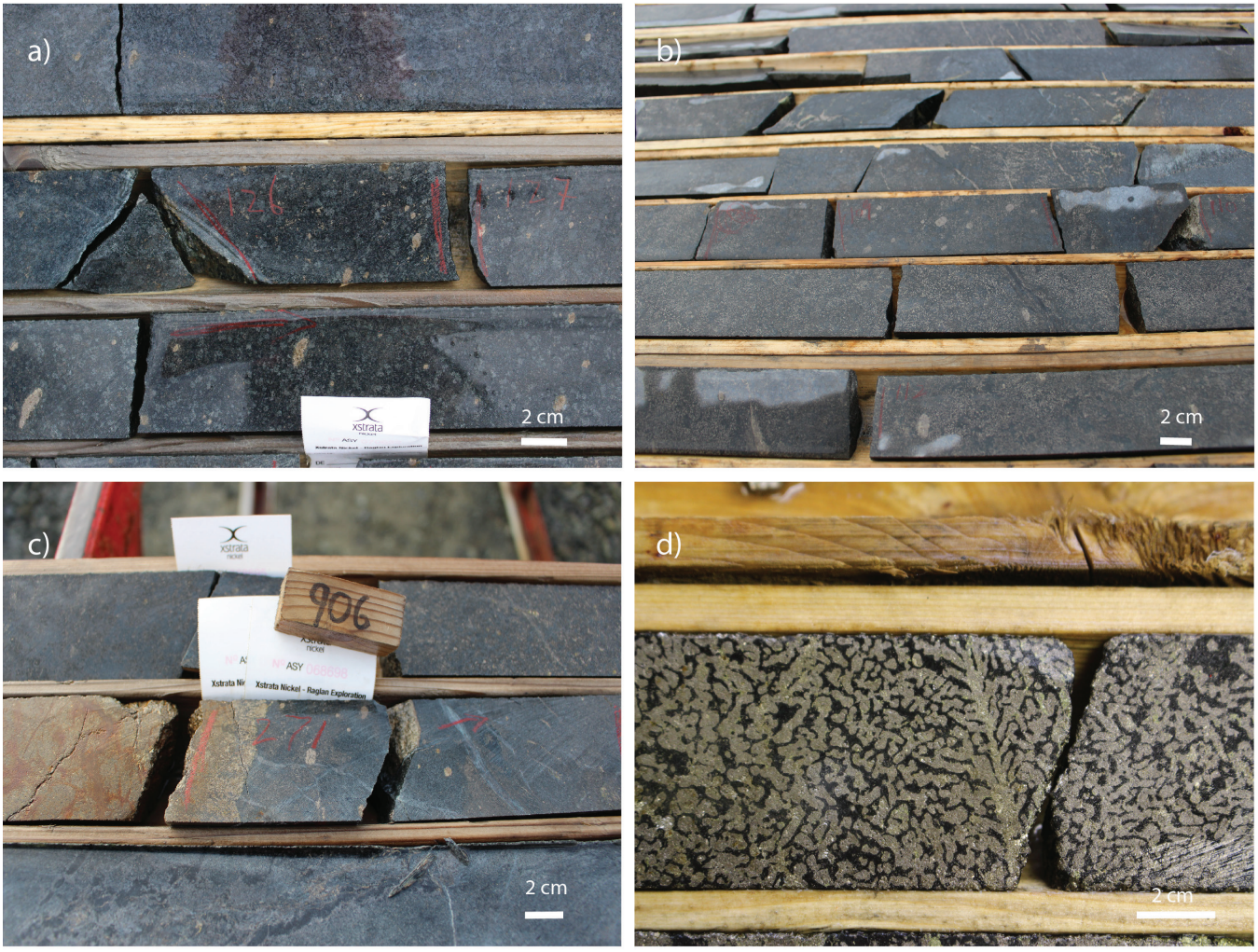

Fig. 17. a) Photo of sulphide globules hosted in olivine-phyric peridotite. **b)** Sulphide globules are in close association with disseminated sulphides. **c)** Sulphide globules are rarely found below the massive orebodies **d)** "Inverted net texture", which has been described by Barnes et al. (2018).

interstitial to growing MSS crystals, and thereby preserving the detailed textures of the incompletely solidified sulphide magma.

6. FUTURE WORK

Crystal size distribution analyses of sulphide globules are underway to document their spatial relationship with the massive orebodies, and to test the validity of numerical modeling shown above. Samples (~15 cm in length) containing sulphide globules from 38 boreholes were collected along longitudinal and lateral traverses spanning entire mineralized ultramafic cooling units, vertically from upper to lower contacts of the ore-bearing intrusions, so that patterns of spatial distribution of globules in both vertical and horizontal dimensions can be examined. Their locations are shown in Figure 15. Around 100 individual samples have been selected and sent to Perth, Australia for crystal distribution analysis of sulphide globules by using the medical X-ray computed tomography scanner, which allows fast and cost-efficient scans of large numbers of samples. Sulphides with clear evidence for post-depositional modification have been avoided. In addition, sulphide globules which are embedded in the net texture are of the lowest priority because it may be difficult to distinguish individual globules from the matrix.

7. CONCLUSION

Erosion and assimilation of sulphur-rich substrates by turbulently flowing lava can result in the production of two populations of sulphide droplets in magmatic systems. Kinetic collection of ore metals by the external sulphide droplets operates at a faster rate than the in sulphides that are endogenously segregated via the complete dissolution of enough crustal sulphur to reach supersaturation. The kinetic upgrading of external sulphide liquid determines the

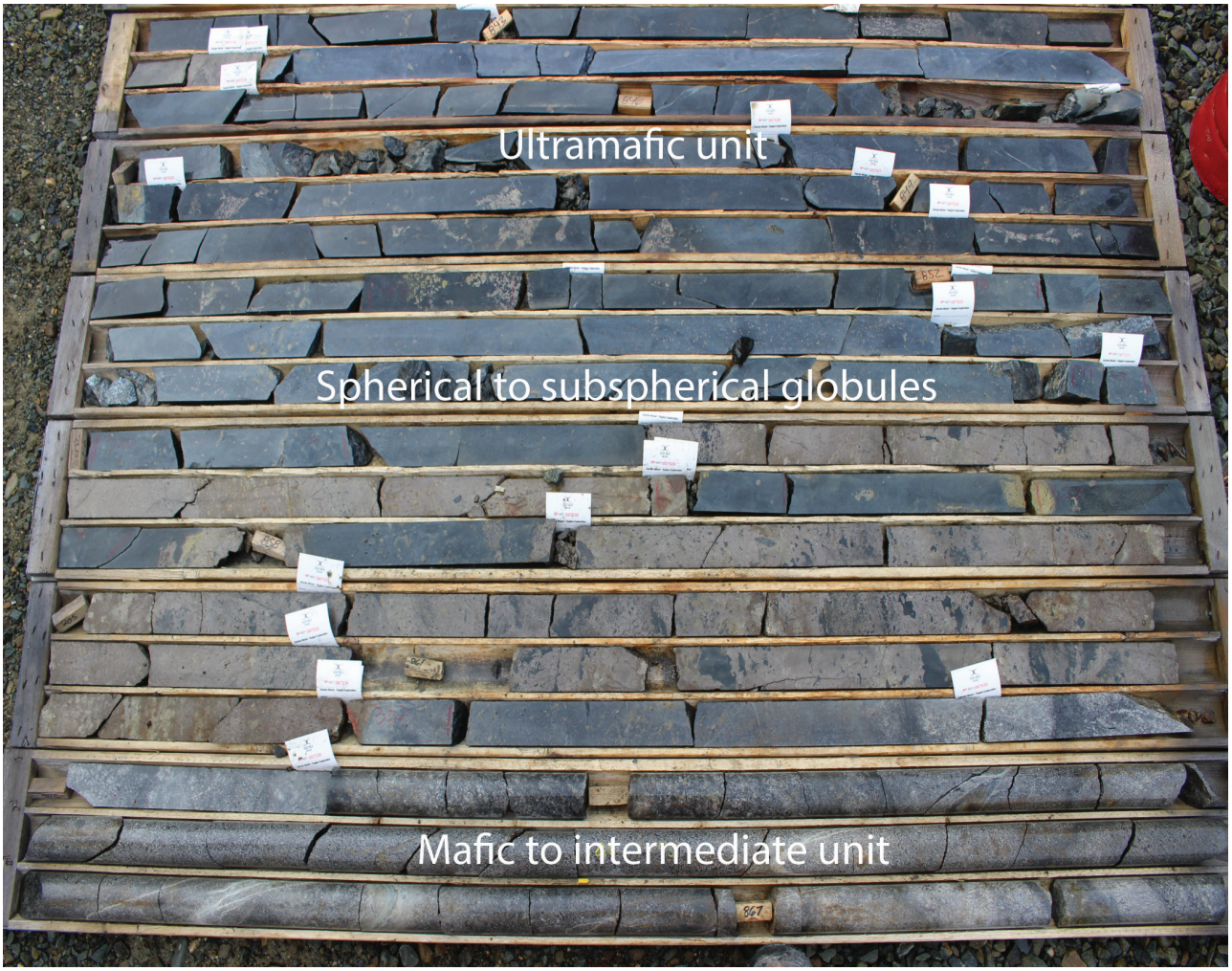

Fig. 18. Drill core photo of borehole 718-3423, showing spherical to subspherical sulphide-bearing ultramafic unit at the top of massive orebody which is further underlaid by the mafic to intermediate unit.

compositional variations of sulphide droplets along with downstream lava flow, and has been combined with the mathematical simulation of erosion to develop a comprehensive model to track the turbulent flow of komatiitic basalt at the Raglan deposit. Numerical simulations that work on the coalescence, breakoff, transport and deposition of sulphide droplet at small scale fluid field have been conducted for many common scenarios in magmatic systems. These dynamic processes of sulphide droplet have been parameterized via a group of non-dimensional parameters in order to scale them up or down to other magmatic systems or to different locations in one dynamic system, which can further connect to the spatial variations of the size distribution of blebby and disseminated sulphides in a given mineralized magmatic suite. Hence, the compositions and size distribution of sulphide droplets contain valuable information about the transport and depositional processes, and can potentially be used as pointers to ore accumulations and mineral explorations.

8. REFERENCES

Ahmadpour, A., Noori Rahim Abadi, S. M. A. and Kouhikamali, R., 2016. Numerical simulation of two-phase gas-liquid flow through gradual expansions/contractions; International Journal of Multiphase Flow, v. 79, p. 31-49.

Aloui, F. and Souhar, M., 1996. Experimental study of a two-phase bubbly flow in a flat duct symmetric sudden expansion- part 2: Liquid and bubble velocities, bubble sizes; International Journal of Multiphase Flow, v. 22, p. 849-861.

Arecchi, F. T., Buah-Bassuah, P. K., Francini, F., Pérez-Garcia, C. and Quercioli, F., 1989. An experimental investigation of the break-up of a liquid drop falling in a miscible fluid; Europhysics Letters, v. 9, p. 333-338.

Barai, N. and Mandal, N., 2016. Breakup modes of fluid drops in confined shear flows; Physics of Fluids, v. 28, 073302.

Barnes, S. -J., Picard, C., Giovenazzo, D. and Tremblay, C., 1992. The composition of nickel-copper sulphide deposits and their host rocks from the Cape Smith Fold Belt, Norther Quebec; Australian Journal of Earth Sciences, v. 39, p. 335-347.

Barnes, S. J., Robertson, J. and Godel, B., 2013. Physical processes in magmatic ore formation: fluid dynamics of sulfide liquid droplets in sulfide-silicate emulsions; 12th SGA Biennial Meeting, p. 944-947.

Barnes, S. J., Staude, S., Le Vaillant, M., Pina R. and Lighfoot, P. C., 2018. Sulfide-silicate textures in magmatic Ni-Cu-PGE sulfide ore deposits: Massive, semi-massive and sulfide-matrix breccia ores; Ore Geology Reviews, v. 101, p. 629-651.

Bleeker, W. and Kamo, S. L., 2018. Extent origin, and deposit-scale controls of the 1883 Ma Circum-Superior large igneous province, northern Manitoba, Ontario, Quebec, Nunavut and Labrador; in Targeted Geoscience Initiative: 2017 report of activities, v.2, N. Rogers (ed.), Geological Survey of Canada, Open File 8373, p. 5-14.

Brett, R. C., Russell, J. K., Andrews, G. D. and Jones, T. J., 2015. The ascent of kimberlite: Insights from olivine; Earth and Planetary Science Letters, v. 424, p. 119-131.

Campagnola, S., Romano, C., Mastin, L. G. and Vona, A., 2016. Confort 15 model of conduit dynamics: applications to Pantelleria Green Tuff and Etna 122 BC eruptions; Contributions to Mineralogy and Petrology, v. 171, 60.

Chavrit, D., Humler, E., Morizet, Y. and Laporte, D. 2012. Influence of magma ascent rate on carbon dioxide degassing at oceanic ridges: Message in a bubble; Earth and Planetary Science Letter, v. 357-358, p. 376-385.

Chung, H. and Mungall, J. M., 2009. Physical constraints on the migration of immiscible fluids through partially molten silicates, with special reference to magmatic sulfide ores; Earth and Planetary Science Letters, v. 286, p. 14-22.

De Bremond d'Ars, J., Arndt, N. T. and Hallot, E., 2001. Analog experimental insights into the formation of magmatic sulfide deposits; Earth and Planetary Science Letters, v. 186, p. 371-381.

Gillies, S. L., 1993. Physical volcanology of the Katinniq Peridotite Complex and associated Fe-Ni-Cu-(PGE) mineralization, Cape Smith Belt, Northern Quebec: M.Sc. Thesis, University of Alabama, p. 146.

Green, A. H. and Dupras, N., 1999. Exploration model for komatiitic peridotite-hosted Ni-Cu-(PGE) mineralization in the Raglan Belt. In: Lesher C. M., (ed) Komatiitic peridotite-hosted Fe-Ni-Cu-(PGE) sulphide deposits in the Raglan area, Cape Smith Belt, New Québec, Guidebook Series 2. Mineral Exploration Research Centre, Laurentian University, Sudbury, p. 187-190.

Holzheid, A., 2010. Separation of sulfide melt droplets in sulfur saturated silicate liquids; Chemical Geology, v. 274, p. 127-135.

Houlé, M. G., Lesher, C. M. and Davis, P. C., 2012. Thermomechanical erosion at the Alexo Mine, Abitibi greenstone belt, Ontario: implications for the genesis of komatiite-associated Ni-Cu-(PGE) mineralization; Mineralium Deposita, v. 47, p. 105-128.

Hronsky, J. M. and Schodde, R.C., 2006. Nickel exploration history of the Yilgarn Craton: from the nickel boom to today; Society of Economic Geologists, Special Publication, v. 13, p. 1-11.

Huppert, H. E. and Sparks, R. S. J., 1985. Komatiites I: eruption and flow; Journal of Petrology, v. 26, p. 694-725.

Jain, M., Prakash, R. S., Tomar, G. and Ravikrishna, R. V., 2015. Secondary breakup of a drop at moderate Weber numbers; Proceedings of The Royal Society A, v. 471, 20140930.

Liao, B., Zhang, G. F., Zhu, Y. J., Li, Z, F., Li, E. Q. and Yang, J. M., 2018. Deformation process of a shocked drop-in-liquid; Science China, v. 61, 104721.

Lesher, C. E. and Spera, F. J., 2015. Thermodynamic and transport properties of silicate melts and magma. In: Sigurdsson, H., Houghton, B., McNutt, S. R., Rymer, H., and Stix, J., (eds) The encyclopedia of volcanoes. Academic Press, p. 113-141.

Lesher, C. M., 1989. Komatiite-associated nickel sulfide deposits. In: Whitney, J. A. and Naldrett, A. J., (eds) Ore deposition associated with magmas. Economic Geology Publishing Company, Reviews in Economic Geology, v. 4, p. 45-101.

Lesher, C. M., 2007. Ni-Cu-(PGE) deposits in the Raglan Area, Cape Smith Belt, New Québec. In: Goodfellow W. D. (ed) Mineral deposits of Canada: a synthesis of major deposit-types, district metallogeny, the evolution of geological provinces, and exploration methods. Geological Association of Canada, Mineral Deposits Division, Special Publication, v. 5, p. 351-386.

Lesher, C. M., Arndt, N. T. and Groves, D. I., 1984. Genesis of komatiite-associated nickel sulphide deposits at Kambalda, Western Australia: A distal volcanic model. In: Buchanan, D. L. and Jones, M. J., (eds) Sulphide deposits in mafic and ultramafic rocks. Institution of Mining and Metallurgy, London, p. 70-80.

Lesher, C. M., Burnham, O. M. and Keays, R. R., 2001. Trace-element geochemistry and petrogenesis of barren and ore-associated komatiites. The Canadian Mineralogy, v. 39, p. 673-696.

Lesher, C. M., Thibert, F., Gillies, S. L., Thacker, J. L. and Williams, D. A., 1999. Lithology and physical volcanology of komatiitic peridotite-gabbro complexes in the Raglan Block. In: Lesher, C. M. (ed) Komatiitic peridotite-hosted Fe-Ni-Cu-(PGE) sulphide deposits in the Raglan area, Cape Smith Belt, New Québec, guidebook series 2. Mineral exploration research center, Laurentian University, Sudbury, p. 43-60.

Mungall, J. E., 2002. Kinetic controls in the partitioning of trace elements between silicate and sulfide liquids; Journal of Petrology, v. 43, p. 749-768.

Mungall, J. E., 2007. Crustal contamination of picritic magma during transport through dikes: the Expo Intrusive Suite, Cape Smith Fold Belt, New Quebec; Journal of Petrology, v. 48, p. 1021-1039.

Mungall, J. E., Brenan, J. M., Godel, B., Barnes, S. J. and Gaillard, F., 2015. Transport of metals and sulphur in magmas by flotation of sulphide melt on vapour bubbles; Nature Geoscience, v. 8, p. 216-219.

Mungall, J. E., Kamo, S. L. and McQuade, S., 2016. U-Pb documents out-of-sequence emplacement of ultramafic layers in the Bushveld Igneous Complex of South Africa; Nature Communications, v. 7, 13385.

Ni, P., Zhang, Y. X., Simon, A. and Gagnon, J., 2017. Cu and Fe diffusion in rhyolitic melts during chalcocite "dissolution": Implications for porphyry ore deposits and tektites; American Mineralogist, v. 102, p. 1287-1301.

Picard, C., Lamothe, D., Piboule, M. and Oliver, R., 1990. Magmatic and tectonic evolution of a Proterozoic basin system: The Cape Smith Thrust-Fold Belt (New-Quebec); Precambrian Research, v. 47, p. 223-249.

Rice, A. and Moore, J. M., 2001. Physical modeling of the formation of komatiite-hosted nickel deposits and a review of the thermal erosion paradigm; The Canadian Mineralogist, v. 39, p. 491-503.

Robertson, J. C., Barnes, S. J. and Le Vaillant, M., 2015. Dynamics of magmatic sulphide droplets during transport in silicate melts and implications for magmatic sulphide ore formation; Journal of Petrology, v. 56, p. 2445-2472.

Rutherford, M. J., 2008. Magma ascent rates; Reviews in Mineralogy and Geochemistry, v. 69, p. 241-271.

Staude, S., Sheppard, S., Parker, P. and Paggi, J., 2017. Long-Victor nickel sulfide complex, Kambalda, Western Australia. In: Phillips, N. (Ed.), Australian Ore Deposits Monograph. Australian Institute of Mining and Metallurgy, Melbourne.

St-Onge, M. R. and Lucas, S. B., 1994. Controls on the regional distribution of iron-nickel-copper-platinum-group element sulfide mineralization in the eastern Cape Smith Belt, Quebec; Canadian Journal of Earth Science, v. 31, p. 206-218.

Watts, T. and Osmond R., 1999. Geophysical model of the Raglan belt. In: Lesher, C. M. and Green, A. H. (eds) Komatiitic peridotite-hosted Fe-Ni-Cu-(PGE) sulphide deposits in the Raglan area, Cape Smith Belt, New Québec, guidebook series 2. Mineral exploration research center, Laurentian University, Sudbury, p. 181-186.

Williams, D. A., Kerr, R. C. and Lesher, C. M., 2011. Mathematical modeling of thermomechanical erosion beneath Proterozoic komatiitic basaltic sinuous rilles in the Cape Smith Belt, New Québec, Canada; Mineralium Deposita, v. 46, p. 943-958.

Yao, Z. S. and Mungall, J. E., 2020. Flotation mechanism of sulphide melt on vapour bubbles in partially molten magmatic systems; Earth and Planetary Science Letters, v. 542, 116298.

Yao, Z. S., Mungall, J. E. and Qin, K. Z., 2020. A preliminary model for the migration of sulfide droplets in a magmatic conduit and the significance of volatiles; Journal of Petrology, v. 61, egaa005.

Origin of chromitites in the Esker Intrusive Complex, Ring of Fire Intrusive Suite, as revealed by chromite trace element chemistry and simple crystallization models

J.M. Brenan[1], K. Woods[1], J.E. Mungall[2], and R. Weston[3]

Brenan, J.M., Woods, K., Mungall, J.E., and Weston, R., 2021. Origin of chromitites in the Esker Intrusive Complex, Ring of Fire Intrusive Suite, as revealed by chromite trace element chemistry and simple crystallization models; in *Targeted Geoscience Initiative 5: grant program final reports (2018-2020), Geological Survey of Canada, Open File 8755, p. 25–43. https://doi.org/10.4095/328981*

Abstract: To better constrain the origin of the chromitites associated with the Esker Intrusive Complex (EIC) of the Ring of Fire Intrusive Suite (RoFIS), a total of 50 chromite-bearing samples from the Black Thor, Big Daddy, Blackbird, and Black Label chromite deposits have been analysed for major and trace elements. The samples represent three textural groups, as defined by the relative abundance of cumulate silicate phases and chromite. To provide deposit-specific partition coefficients for modeling, we also report on the results of laboratory experiments to measure olivine- and chromite-melt partitioning of V and Ga, which are two elements readily detectable in the chromites analysed.

Comparison of the Cr/Cr+Al and Fe/Fe+Mg of the EIC chromites and compositions from previous experimental studies indicates overlap in Cr/Cr+Al between the natural samples and experiments done at >1400°C, but significant offset of the natural samples to higher Fe/Fe+Mg. This is interpreted to be the result of subsolidus Fe-Mg exchange between chromite and the silicate matrix. However, little change in Cr/Cr+Al from magmatic values, owing to the lack of an exchangeable reservoir for these elements. A comparison of the composition of the EIC chromites and a subset of samples from other tectonic settings reveals a strong similarity to chromites from the similarly-aged Munro Township komatiites.

Partition coefficients for V and Ga are consistent with past results in that both elements are compatible in chromite (D_V = 2-4; D_{Ga} ~ 3), and incompatible in olivine (D_V = 0.01-0.14; D_{Ga} ~ 0.02), with values for V increasing with decreasing fO_2. Simple fractional crystallization models that use these partition coefficients are developed that monitor the change in element behaviour based on the relative proportions of olivine to chromite in the crystallizing assemblage; from "normal" cotectic proportions involving predominantly olivine, to chromite-only crystallization. Comparison of models to the natural chromite V-Ga array suggests that the overall positive correlation between these two elements is consistent with chromite formed from a Munro Township-like komatiitic magma crystallizing olivine and chromite in "normal" cotectic proportions, with no evidence of the strong depletion in these elements expected for chromite-only crystallization. The V-Ga array can be explained if the initial magma responsible for chromite formation is slightly reduced with respect to the FMQ oxygen buffer (~FMQ- 0.5), and has assimilated up to ~20% of wall-rock banded iron formation or granodiorite.

Despite the evidence for contamination, results indicate that the EIC chromitites crystallized from "normal" cotectic proportions of olivine to chromite, and therefore no specific causative link is made between contamination and chromitite formation. Instead, the development of near- monomineralic chromite layers likely involves the preferential removal of olivine relative to chromite by physical segregation during magma flow. As suggested for some other chromitite-forming systems, the specific fluid dynamic regime during magma emplacement may therefore be responsible for crystal sorting and chromite accumulation.

[1]Department of Earth and Environmental Sciences, Dalhousie University, Halifax, Nova Scotia
[2]Department of Earth Science, Carleton University, Ottawa, Ontario
[3]Noront Resources, Thunder Bay, Ontario

1.0 INTRODUCTION AND MOTIVATION

Chromite is a nearly ubiquitous accessory mineral in primitive basaltic and komatiitic magmas, yet economically significant accumulations of chromite are so rare that none were known in North America until the discovery of the Ring of Fire Intrusive Suite (RoFIS) deposits less than fifteen years ago. Questions about the ore-forming process responsible for producing ore-grade, high-tonnage accumulations of chromite can be distilled into a choice between two competing hypotheses: 1) chromitite deposits formed predominantly due to fluid dynamical process involving crystal sorting from otherwise unremarkable komatiitic magmas in exceptionally large and/or long-lived conduits (Eales, 2000; Eales and Costin, 2012; Mondal and Mathez, 2007; Voordouw et al., 2009; Marques et al., 2017; Jenkins and Mungall, 2018) or 2) the rarity of chromitite deposits results from a need for komatiitic magmas to have interacted with a highly specific and unusual combination of contaminants, or more evolved magma compositions during transit through the crust (Irvine, 1975, 1977; Spandler et al., 2005; Lesher et al., 2019). As in many scientific controversies, successful resolution may require some degree of synthesis of the two end-member viewpoints. In Phase 1 of this project, it was proposed that the predictions stemming from these two hypotheses could be tested by conducting a series of experiments under controlled conditions of temperature (T), pressure (P), and oxygen fugacity (fO_2), in which a primitive komatiitic melt of the type presumed to have been parental to the EIC deposits was combined with a variety of contaminants (e.g., granodiorite, iron-rich metasediment, banded iron formation) and compared with a base case in which no contamination occurs. Results of that work (Keltie, 2018; manuscript in preparation) have provided additional insights into the chromite-forming process with the important discovery being that iron is the essential additive that reduces the chromite solubility, and a scenario was developed showing that chromite-only precipitation was possible under certain circumstances. Results from Phase 1 also indicate that the major element composition of contaminants may not be sufficiently different to be reflected in the chromite composition. However, by virtue of the different geochemical processes by which they form, the trace element signature of different contaminants may impart a unique chemical fingerprint on any resulting chromite. Therefore, the goals of Phase 2 of this project are two-fold: 1) to expand on the existing database documenting the trace element composition of EIC chromites and 2) to perform laboratory experiments to measure chromite- melt partition coefficients involving a komatiite composition doped with a suite of trace elements readily measurable in the EIC chromites.

In this report, the major and trace element composition of chromites from 50 samples taken from the Black Thor, Black Label, Big Daddy, and Blackbird deposits is presented, augmenting the dataset of Laarman (2014). Along with this data, the existing literature on olivine- and spinel-melt partitioning was surveyed in order to identify certain trace elements that are 1) readily detectable in the EIC chromites and 2) highly compatible in chromite, but incompatible in olivine, and hence sensitive to the proportions of these phases during crystallization. The survey revealed that vanadium (V) and gallium (Ga) share these desirable properties (e.g., Horn et al., 1994; Canil and Fedourtchouk, 2001; Mallmann and O'Neill, 2009; Davis et al., 2013; Wijbrans et al., 2015) and are therefore the prime focus of the partitioning experiments presented. With the so-measured partition coefficients, simple models have been developed to predict the effect of differences in the olivine/chromite crystallization proportions, as well as various contamination scenarios, on the resulting covariation of these elements in chromite.

2.0 GEOLOGICAL SETTING

The Ring of Fire intrusive suite comprises a series of mafic to ultramafic dikes, sills, and layered intrusive bodies of mafic (e.g., Butler intrusion; Kuzmich, 2014) to ultramafic (e.g., Esker intrusive complex, Houlé et al. 2019, Carson et al. 2015) origin emplaced into the McFaulds Lake greenstone belt (MLGB), with the entire succession located within the James Bay Lowlands of Northern Ontario (Figure 1). Age constraints on the ultramafic-dominated subsuite Esker Intrusive Complex (EIC) are derived from zircon U-Pb measurements on the tonalite host rock to the associated Eagle's Nest magmatic sulfide deposit and ferrograbbro, yielding dates of 2773.4 +/- 0.9 and 2734.5 +/- 1 Ma, respectively (Mungall et al., 2010) and for the Black Thor Intrusion of 2734 Ma (Houle et al., 2015). The EIC contains six known chromitite deposits: Black Thor, Big Daddy, Blackbird, Black Label, Black Creek and Black Horse (Figure 1). Together these deposits comprise ~201.3 million tonnes of measured and indicated chromite resources (Aubut, 2015). The deposits are hosted by serpentinised and talc-altered ultramafic rocks, and consist of disseminated to massive chromitite occurring as lenses and conformable continuous layers, in some cases reaching several meters in thickness, and up to km-scale in lateral extent (Azar, 2010; Aubut, 2010; 2012). Detailed studies of the EIC chromitites have been done for Blackbird (Azar, 2010), Black Thor, Black Label, and Big Daddy (Laarman, 2014) and of the Black Thor intrusion, which hosts the Black Thor and Black Label deposits (Carson et al., 2015). Of these studies, only Laarman (2014) has measured the trace element content of individual chromites, reporting on the abundances of 23 trace elements, with the exception of V, which has been determine to be a particularly useful element to unravelling chromitite genesis, as described below.

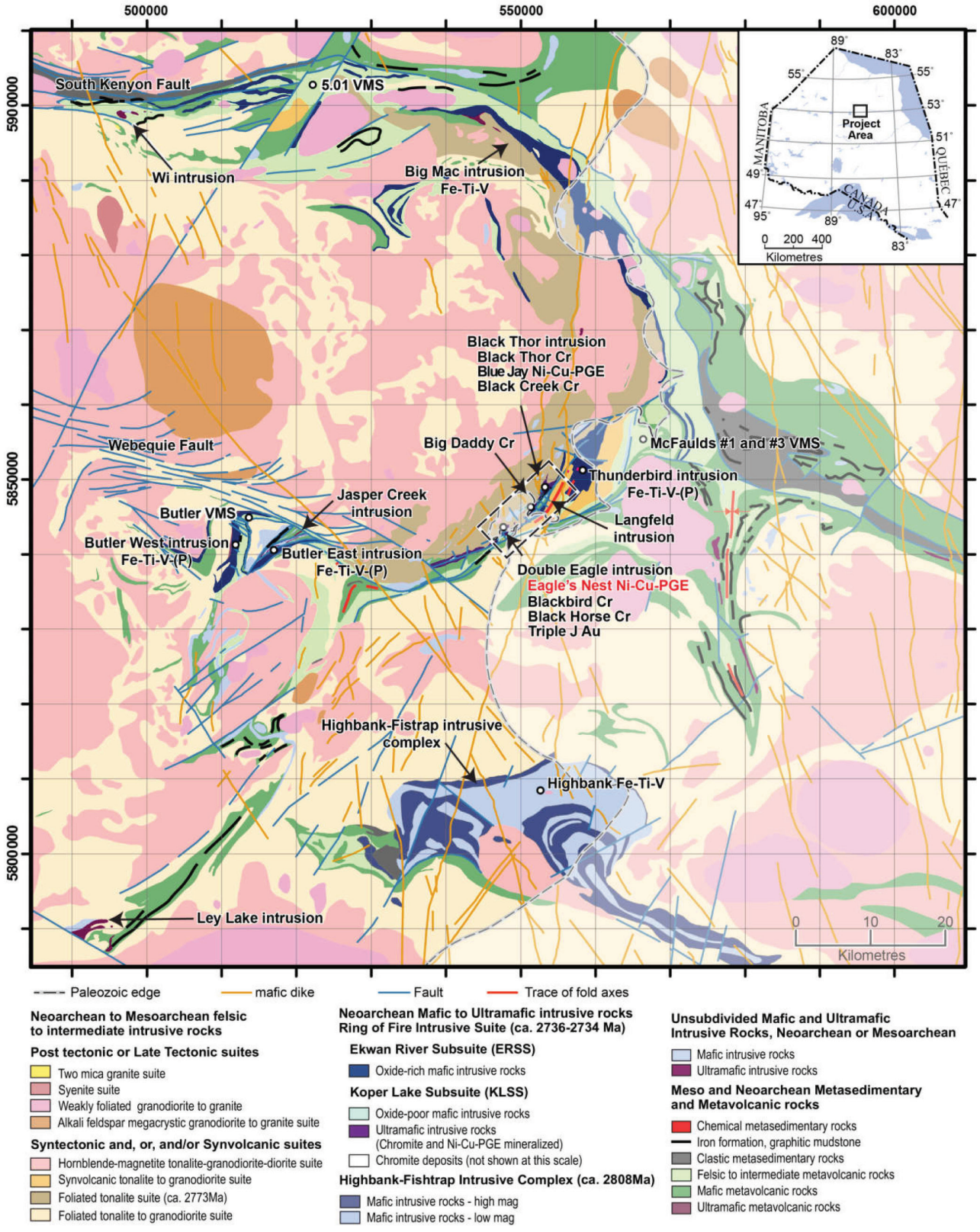

Figure 1. Geological map of the McFaulds Lake greenstone belt showing the spatial distribution of lithologies that comprise the EIC, and the main mineral deposits and occurrences. Colours and symbols are explained in the legend. From Houlé et al. (2019)

3.0 SELECTED SAMPLES

A total of 50 samples were selected for major and trace element analysis, with only three samples (BL162, BL218, BL282) having grains too small (< 25 microns) for laser ablation analysis. Sample textures were characterized by reflected and transmitted light petrography and backscattered electron imaging, with representative examples provided in Figure 2. In all samples, chromite is altered to varying degree to magnetite, in response to low grade metamorphism and the production of magnetite by serpentinization. The extent of magnetite alteration is similar to the Type 1 variety of Barnes (2000) in which chromites show incipient replacement along grain edges and fractures. Apart from the aforementioned three fine-grained samples, samples contain chromites with magnetite-free domains sufficiently large for laser ablation analysis. Chromites are euhedral, exhibiting a remarkably uniform grain size, typically in the range of 50-200 microns. Some samples also contain chromite with spherical inclusions (Figure 2d, e; see also Figure 8 of Azar, 2010, Figures 3.29 and 3.30 of Laarman, 2014), hosting various combinations of albite, enstatite, chlorite, tremolite, phlogopite, and amphibole, similar to reported at other localities (e.g., Muskox, Stillwater and Bushveld; Irvine, 1977; Spandler et al.,2005; Li et al., 2005). Although relict olivine is present in a few samples, the primary silicate mineralogy has been largely replaced by serpentine, talc, a fine dusting of magnetite and in some cases chlorite and carbonate. Samples can be broadly classified into three textural types based on the abundance of chromite relative to the interpreted primary silicate mineralogy, with all exhibiting a cumulate texture. The first, termed chromite-bearing dunite (Figure 2a-c) contains < 10 modal % chromite, and consists of mm-sized olivine pseudomorphs surrounded by chromite grains in a "necklace-like" texture, with altered silicate material interstitial to the chromite. The second, termed "porphyritic" chromitite (Figure 2d-f) is like the first type, but contains significantly more chromite (> 50 modal %), surrounding mm- sized former olivine crystals. Note that former olivine in both textural types contain few or no chromite inclusions, suggesting olivine was the primary liquidus phase, followed by chromite. The third textural type is termed cumulate chromitite (Figure 2g-l), and contains > 90 modal % chromite, in a fine grained matrix of altered silicate material. For each sample, at least 10 analyses were done on the cores of chromite crystals that were selected based on size (at least > 25 microns, which was the minimum useful laser spot size) and lack of silicate inclusions or magnetite rims.

4.0 MAJOR AND TRACE ELEMENT ANALYTICAL PROCEDURE

4.1. Major element analysis

The major element composition of chromite, glass, and olivine were determined using the JEOL JXA-8200 Electron Probe Micro-Analyzer (EPMA) housed in the Robert M. MacKay Electron Microprobe Lab at Dalhousie University. Chromite analyses were done using an accelerating voltage of 15 kV, a beam current of 50 nA, and a focused spot. Primary standards for chromite analysis were chromite (Mg, Fe, Cr, Al), pyrolusite (Mn), rutile (Ti), V metal (V), kaersutite (Ca), sanidine (Si), and GaAs (Ga). Standards used to correct for interferences were Ti metal (first-order interference of Ti on V and fourth-order interference of Ti on Mg), V metal (first-order interference of V on Cr, third-order interference of V on Si, and fourth-order interference of V on Mg), Cr metal (first-order interference of Cr on Mn and third-order interference of Cr on Si), pyrolusite (first-order interference of Mn on Fe), and rutile (third-order interference of Ti on Al). On-peak count times were 20 seconds for Mg, Fe, Cr, and Al, and 60 seconds for Ti, V, Ca, Si, Mn, and Ga. Silicate glass analyses were done using an accelerating voltage of 15kV, a beam current of 10 nA, and a 10 μm defocused beam to limit glass damage. Standards for silicate melt analysis were natural basalt (Si, Ca, Al, Fe, Mg, Na), pyrolusite (Mn), rutile (Ti), and sanidine (K). Count times were 20 seconds on peak for all elements. Olivine analyses were done using an accelerating voltage of 15 kV, a beam current of 12 nA and a 1 μm spot size. Olivine standards were olivine (Fe, Mg,Si), sanidine (Al), chromite (Cr), pyrolusite (Mn), rutile (Ti), and kaersutite (Ca). Count times were 20 seconds on peak for Fe, Mg, Si, Al, Cr, Mn, Ti and 60 seconds for Ca. For all analyses, raw count rates were converted to concentrations using the ZAF data reduction scheme. Table A1 provides a summary of the major element composition of the EIC chromite; Tables A3, A5, and A6 summarize the major element data for the experimental run-product phases.

4.2 Trace element analysis

The trace element composition of chromite, glass, and olivine were determined using the Dalhousie University laser ablation ICP-MS facility located in the Health and Environments Research Centre (HERC) Laboratory. The system employs a frequency quintupled Nd:YAG laser operating at 213 nm, coupled to a Thermo Scientific iCAP Q ICP-MS quadrupole mass spectrometer with He flushing the ablation cell to enhance sensitivity (Eggins et al., 1998). At the start of each analytical session, the ICP was tuned by monitoring the signal from ablated NIST 610 glass until the following three conditions were met: maximum sensitivity was achieved for ^{115}In, $^{238}U/^{232}Th$ signal ratio of ~1, and $^{232}Th^{16}O/^{232}Th<0.005$. Chromites from the EIC, as well as run-product olivines and glasses, were analyzed using

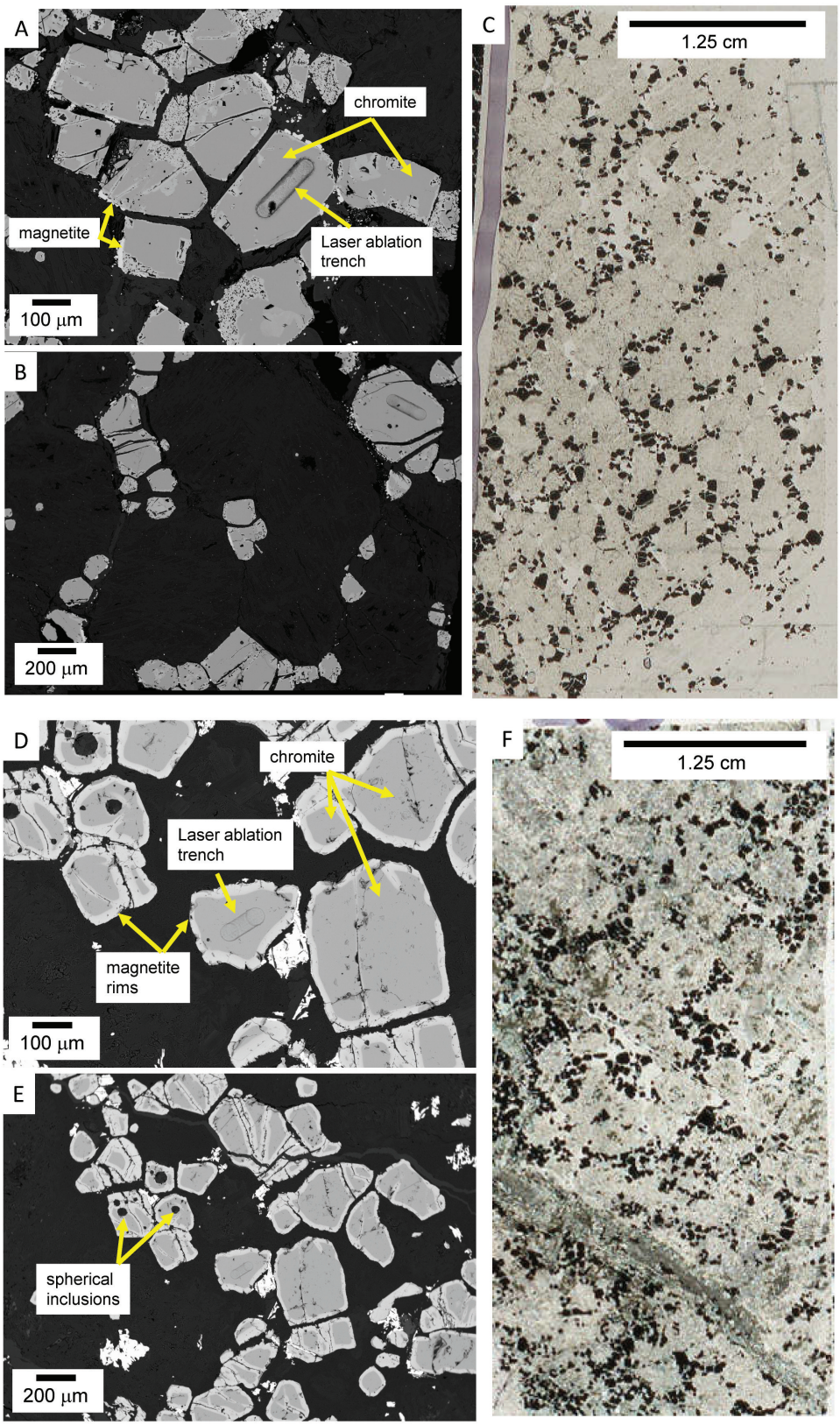

Figure 2. Backscattered electron (A,B,D,E,G,H,J,K) and transmitted light (C,F,I,L) images of polished thin sections showing examples of the textural types for chromite-bearing samples analysed in this study. **A-C)** Chromite-bearing dunite, sample BT31 (Black Thor deposit), comprised of < 10 modal % chromite, and dominated by cumulate-textured olivine. **D-F)** "Porphyritic" chromitite, sample BD282 (Big Daddy deposit) comprised of > 50 modal % chromite, with a bimodal grain size distribution involving larger olivine grains with a finer-grained chromite matrix.

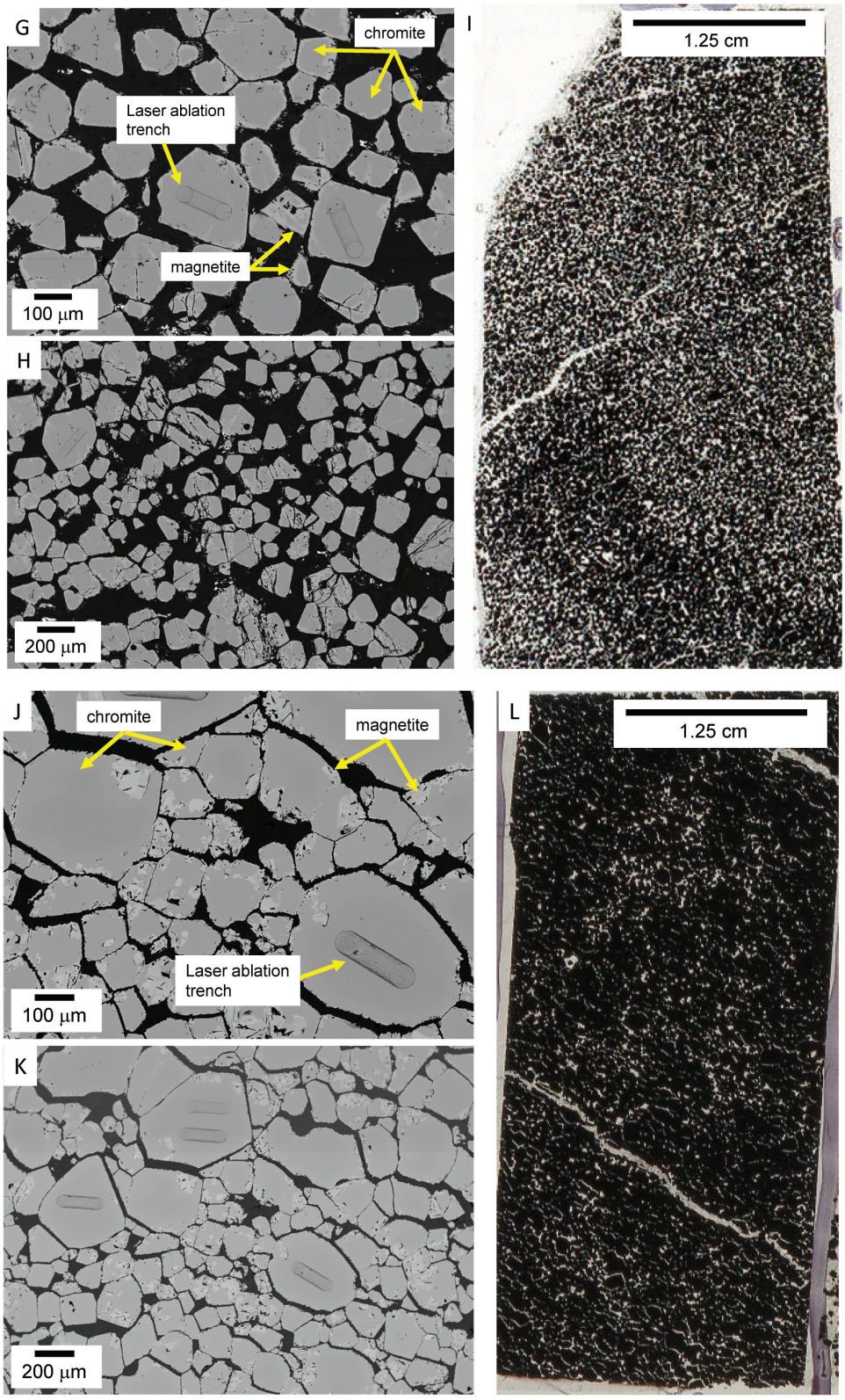

Figure 2. (cont) Backscattered electron (A,B,D,E,G,H,J,K) and transmitted light (C,F,I,L) images of polished thin sections showing examples of the textural types for chromite-bearing samples analysed in this study. **G-L)** Cumulate chromitite, samples BD281 (Big Daddy deposit; **G-I**) and BT32 (Black Thor deposit; **J-L)** comprised of > 95 modal % chromite, and minor interstitial silicates.

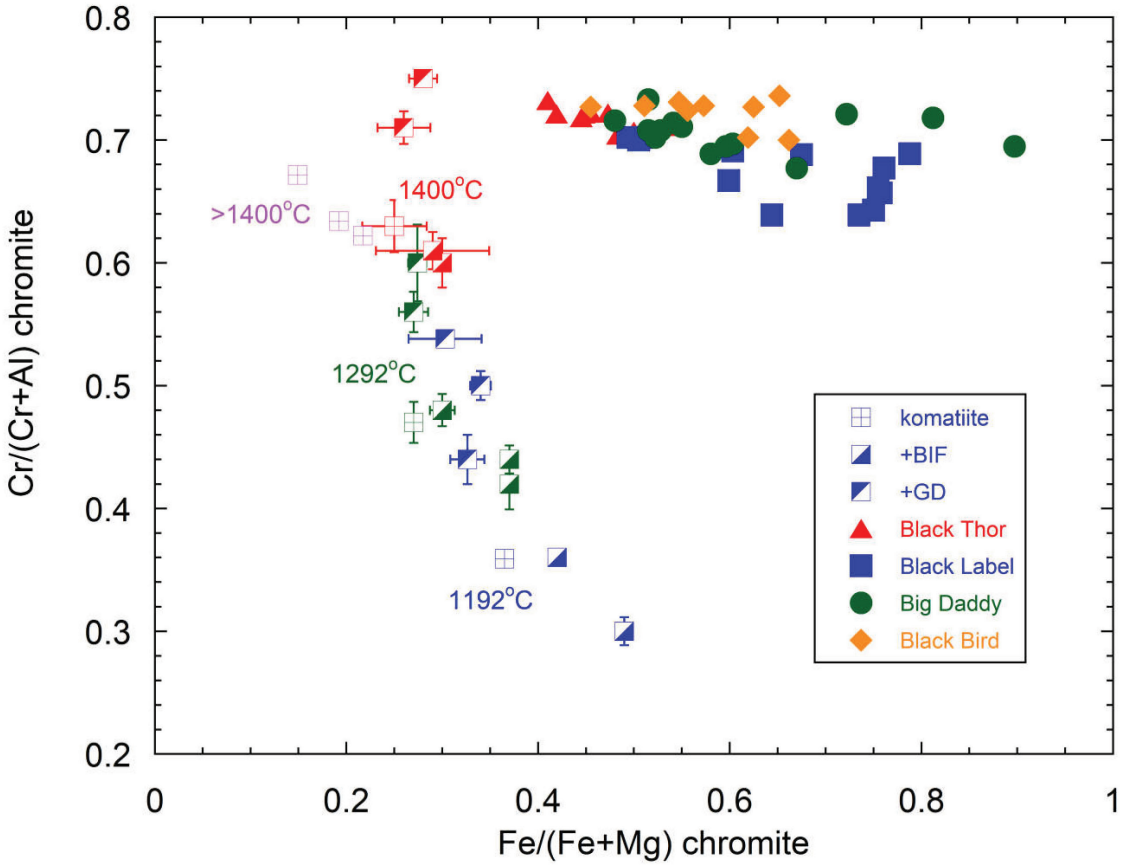

Figure 3. Comparison of the compositions of the EIC chromites, in terms of Cr/Cr+Al and Fe/Fe+Mg, to those produced in experiments involving komatiite compositions, either "as is" or doped with 5-50 wt% banded iron formation (BIF) or granodiorite (GD). For the experimental chromite compositions, the data are colour-coded according to experiment temperature, with the symbols corresponding to the composition. Results for experiments done at 1192, 1292 and 1400°C are from Keltie (2018), and for >1400°C (1450 and 1500°C) are from Murck and Campbell (1986). Error bars represent 1 standard deviation based on multiple analyses.

a laser repetition rate of 10-20 Hz, spot size of 25-75 µm, and laser output of ~8 J/cm2. Because of the small size of the run-product chromite, analyses were done with a 10 µm spot and a rep rate of 5 Hz to collect enough data before the crystal was drilled through. Factory supplied time resolved software was utilized for the acquisition of individual analyses. A typical analysis involved 20 seconds of background acquisition with the ablation cell being flushed with He, followed by laser ablation for 60 seconds, then 60 seconds of cell washout. Analyses were collected in a sequence in which two analyses were done on a standard reference material (NIST610) at the start of the acquisition cycle, then after every 20 analyses on the unknowns. When possible, 10 analyses were done on each sample. Data reduction was done off- line using the Iolite version 3.6 software package. Trace element concentrations were quantified using the NIST610 silicate glass, which contains 69.7 wt% SiO_2, 11.4±0.2 wt% CaO, 413±46 µg/g P, 455±10 µg/g Sc, 452±10 µg/g Ti, 450±9 µg/g V, 458±9 µg/g Fe, 410±10 µg/g Co, 458.7±4 µg/g Ni, 441±15 µg/g Cu, 460±18 µg/g Zn, 433±13 µg/g Ga, 447±78 µg/g Ge, 325±18 µg/g As, 515.5±1 µg/g Sr, 462±11 µg/g Y, 448±9 µg/g Zr, 417±21 µg/g Mo, 270±16 µg/g Cd, 434±19 µg/g In, 430±29 µg/g Sn, 396±19 µg/g Sb, 435±12 µg/g Hf, 446±33 µg/g Ta, 444±29 µg/g W, 426±1 µg/g Pb, 384±26 µg/g Bi, 457.2±1 µg/g Th, and 461.5±1 µg/g U (Jochum et al., 2005).

Ablation yields in chromite were corrected by referencing to the known concentration of Ti as determined by EPMA (Page and Barnes, 2009), whereas Ca was used for the yield correction involving glass and olivine analyses. The following isotopes were measured (italicised species used for quantification when multiple isotopes measured): ^{29}Si, ^{31}P, ^{43}Ca, ^{44}Ca, ^{45}Sc,^{47}Ti, ^{48}Ti, ^{51}V, ^{57}Fe, ^{59}Co, ^{60}Ni, ^{63}Cu, ^{65}Cu, ^{66}Zn, ^{67}Zn, ^{69}Ga, ^{71}Ga, ^{72}Ge, ^{75}As, ^{88}Sr, ^{89}Y, ^{95}Mo, ^{111}Cd, ^{115}In, ^{118}Sn, ^{119}Sn, ^{120}Sn, ^{121}Sb, ^{178}Hf, ^{181}Ta, ^{182}W, ^{208}Pb, ^{209}Bi, ^{232}Th, ^{238}U. Agreement within error was obtained for concentrations of Ga and Zn determined for all the isotopes measured, indicating negligible interference from higher concentration transition metal oxides (i.e., ^{53}Cr^{16}O on ^{69}Ga, etc). Table A2

provides a summary of the trace element composition of the EIC chromite; Tables A2, A4, and A7 summarize the trace element data for the experimental run-product phases.

4.3. External Standards

Two basalts from a suite of USGS reference materials, BHVO-1 and BIR-1, were used to test the accuracy of the LA-ICP-MS glass analyses. Glasses were prepared by fusing powders at 1400°C and 1 GPa for 30 minutes in high purity graphite. Analyses of the BHVO-1 and BIR-1 glasses were done in the same analytical sessions to measure glass unknowns. Included in Table A8 are the results of these measurements and indicates that most measured values agree within less than 10% of the preferred values from Jochum et al. (2005).

5.0 TRACE ELEMENT PARTITIONING EXPERIMENTS

5.1 Starting materials

The komatiite composition used in experiments is taken from Mungall et al. (2010) and corresponds to the model parental liquid composition to the Eagle's Nest magmatic Ni-sulfide deposit hosted by the EIC. To this composition was added 1 wt% $FeCr_2O_4$ to ensure saturation in chromite. This material was prepared by mixing reagent-grade oxides and carbonates in an agate mortar and pestle under ethanol until a well-mixed and very fine-grained powder was achieved. The mixture was then calcined in a Pt crucible at 1000°C in air for 12 hours and reground. The calcined material was then twice fused at 1530°C in air for 30 minutes, with grinding after each fusion. We made two versions of this komatiite, the first nominally trace element free (except for minor impurities in the reagents) and the second doped with ~ 2 wt% each of V, Co, Zn, Ga, Sr, Zr, Sn, Hf, Ta, W and ~0.5 wt% In. Several small fragments of the resultant glasses were retained for subsequent major and trace element analysis, with Table 1 summarizing these compositions. The doped komatiite composition was then diluted by mixing with the undoped komatiite by grinding under ethanol in an agate mortar to produce starting compositions with ~2000, ~500, ~200, and ~100 µg/g of each trace element.

5.2. Experimental procedure

Experiments were conducted using vertical tube gas mixing furnaces housed in the Dalhousie Laboratory for Experimental High Pressure Research. Oxygen fugacity was controlled using mixtures of CO and CO_2, whose proportions were fixed by mass-flow controllers. Oxygen fugacities were measured in the furnace before and after each experiment using a Y-doped zirconia sensor, with the accuracy of the sensor confirmed by equilibrating NiO-MnO mixtures with pure Ni to form $Ni_xMn_{1-x}O$, in which x depends on fO_2 (i.e., the sliding sensor method of Taylor et al., 1992). Oxygen fugacities returned by this method are indistinguishable from those calculated from the zirconia sensor emf output. Temperatures were monitored with the Type S thermocouple housed inside the fO_2 sensor, which is referenced against a Type S thermocouple calibrated against the melting point of pure gold.

In order to limit the loss of iron from the sample to the wire loop used to suspend samples within the furnace, loops were first pre-saturated with iron. To accomplish this, approximately 50 mg of a powdered sample of iron-bearing basalt (same FeO as the komatiite) was mixed with a liquid polyvinyl alcohol "glue" to form a thick slurry which was then attached to a loop made from 0.010" high purity iridium wire, then dried to hardness at 100°C. We used iridium instead of platinum for these experiments because of the much lower solubility of iron in iridium. Because of the extremely brittle nature of the iridium wire, only a single loop was made with the wire, and the remaining straight end was wound onto 0.010" platinum wire for attachment to the silica rod used to suspend the sample in the furnace. Pre-saturation was done by melting the basalt on the loop for the same time-temperature- fO_2 conditions as the partitioning experiments, then removing the resulting glass by dissolution in concentrated HF for 12 hours. Samples for the trace element partitioning experiments were prepared in an identical way as the iron-presaturation step, with the trace element-doped komatiite loaded onto the clean, presaturated, now Fe-Ir alloy loop. Experiments were done by attaching the wire loops to the end of a silica rod, whose shape was fashioned to accommodate up to three loops per experiment.

Experiments were executed by first withdrawing the glass rod to the top of the furnace tube, then sealing the furnace and commencing gas flow. After 30 minutes the sample was slowly lowered into the predetermined hot-spot and remained there for the experiment duration. Experiments were terminated by opening the bottom of the furnace and rapidly lowering the rod through the furnace into a beaker of water placed below the bottom opening. Experiments were done at 1400°C for 48 hours and oxygen fugacities of FMQ-1, FMQ, and FMQ+1 (values of log fO_2 corresponding to those buffers are from O'Neill and Wall, 1987).

6.0 RESULTS AND DISCUSSION

6.1 EIC chromite compositions

Before discussion of the primary igneous compositional variation in the EIC chromites, it is necessary to consider the effects of low temperature alteration to chromite compositions. Following Barnes (1998), we have filtered the data to exclude samples with Fe/Fe+Mg > 0.85 and Mn concentrations that exceed the Barnes (1998) "filter" line in terms

Table 1. Summary of experiments and partition coefficients for V and Ga

Expt ID	log fO_2	% Ko	%Kt_a	ΔFMQ	t(hrs)	D_V chromite	D_V olivine	D_{Ga} chromite	D_{Ga} olivine
we_01	-5.11 ± 0.11	97.4	2.8	FMQ+1	63.0	1.50 (0.11)	0.015(0.006)	3.02(0.24)	0.021(0.005)
wd_01	-5.11 ± 0.11	86.4	13.6	FMQ+1	63.0	1.31 (0.09)	0.011(0.002)	2.39(0.46)	0.016(0.002)
we_02	-6.33 ± 0.01	97.4	2.8	FMQ	45.0	3.77(0.17)	0.032(0.005)	2.54(0.32)	0.021(0.004)
wd_02	-6.33 ± 0.01	86.4	13.6	FMQ	45.0	4.26(0.22)	0.035(0.009)	3.08(0.51)	0.021(0.007)
we_03	-7.13 ± 0.2	97.4	2.8	FMQ-1	62.0	8.06(0.28)	0.135(0.028)	nd	0.044(0.02)
w25_01	-6.39 ± 0.03	99.3	0.7	FMQ	46.0	4.24(0.52)	0.040(0.002)	nd	0.022(0.007)
w50_01	-6.39 ± 0.03	98.6	1.4	FMQ	46.0	4.34(0.44)	0.054 (0.017)	nd	0.016(0.006)

Notes:
nd = not determined, concentration in chromite below detection
%Ko and %Kt_a are the percentages of the trace element free and doped starting materials, respectively, with compositions provided in Tables A6 and A7.
Values in parentheses represent 1-sigma uncertainty based on multiple analyses of minerals and glasses

of variation in Mn vs Fe/Fe+Mg. Both filters are meant to exclude samples whose compositions would be inconsistent with high temperature (>500°C) equilibrium with olivine. A total of five samples (in italics in Table A3) were removed using this data filter. Figure 3 provides a comparison of the compositions of the EIC chromites, in terms of Cr/Cr+Al and Fe/Fe+Mg, to those produced in experiments involving a komatiite composition from the results of Murck and Campbell (1986) and Keltie (2018). In addition to chromites from komatiite, the results of Keltie (2018) also show the array of chromite compositions produced from komatiite compositions contaminated with either granodiorite (containing 2.5 wt% FeO) and banded iron formation (containing 23 wt% FeO). Typical of most komatiite suites (Barnes, 1998) samples from the EIC define sub horizontal arrays with a relatively limited range in Cr/Cr+Al of 0.64 to 0.74 but Fe/Fe+Mg varying from ~0.4 to 0.8. By comparison, the experimental chromites define a diagonal array, extending from Cr/Cr+Al of 0.3 and Fe/Fe+Mg of 0.5 at 1200°C, to Cr/Cr+Al of 0.68 and Fe/Fe+Mg of 0.15 for experiments done at T> 1400°C. Contamination does not significantly shift compositions off this array, but moves those to either higher Cr/Cr+Al and lower Fe/Fe+Mg (granodiorite contamination) or in the opposite sense for BIF contamination. In this context, the high Cr/Cr+Al of the EIC chromites is consistent with origin from a high temperature magma (i.e., >1400°C), but that Fe/Fe+Mg is significantly shifted from expected primary values. Keltie (2018) applied the O'Neill and Wall (1987) olivine-spinel geothermometer to calculate temperatures for coexisting olivine and chromite from the Black Thor deposit, revealing a range of values from 800 to below 500°C. Mass balance calculations show that the trend in chromite compositions in equilibrium with olivine with decreasing temperature is to higher Fe/Fe+Mg, and that the variation in Fe/Fe+Mg observed in the EIC dataset is consistent with re- equilibration over the range of measured temperatures.

We use the MORB-normalised variation diagram (Figure 4) proposed by Pagé and Barnes (2009) to provide some context for the overall chemical characteristics of the EIC samples. In this diagram, the concentration of key major, minor, and trace elements are plotted relative to a reference chromite composition from a Mid-Ocean Ridge Basalt (MORB) emplaced at the East Pacific Rise. Along with this are included the average of four chromite grains from Bonin Island (Pagé and Barnes, 2009), representing magmas produced by high degrees of flux-driven melting in a convergent margin setting, and chromites from olivine- or olivine-pyroxene cumulates from the Alexo mine in the Neoarchean Munro Township (MT) komatiites (Meric, 2018). The EIC samples show clear fractionation of elements relative to the MORB reference, with depletions in Al, Ga, and Ni, and relatively uniform enrichments in Ti, Zn, Co, Mn, Fe/Fe+Mg, V, and Cr/Cr+Al. Whereas some of these differences may be primary features, the high Fe/Fe+Mg (as previously mentioned) and Zn are likely to be due to subsolidus exchange. Although not previously discussed, pervasive elevation in Zn abundances is a common feature of chromitites subject to even the lowest grades of metamorphism (Barnes, 2000). The pattern for the EIC samples also differs from the Boninite chromite, most distinctly in terms of the very low Al, Ga, and Ti and high Sc for the Bonin sample relative to the EIC, MT komatiites and MORB. The Munro Township chromites are very similar to the EIC samples in terms of relative and absolute element abundances, supporting the Mungall et al (2010) assertion that the parental magma to the EIC was derived from a similar refractory mantle source.

6.2 Partition Coefficients

A summary of experiments and partition coefficients for V and Ga is provided in Table 1. The products of experiments to measure element partitioning yielded chromite, olivine, and glass in approximate proportions of 2%, 15-20%, and 80-85%, respectively, with glass amounts somewhat higher

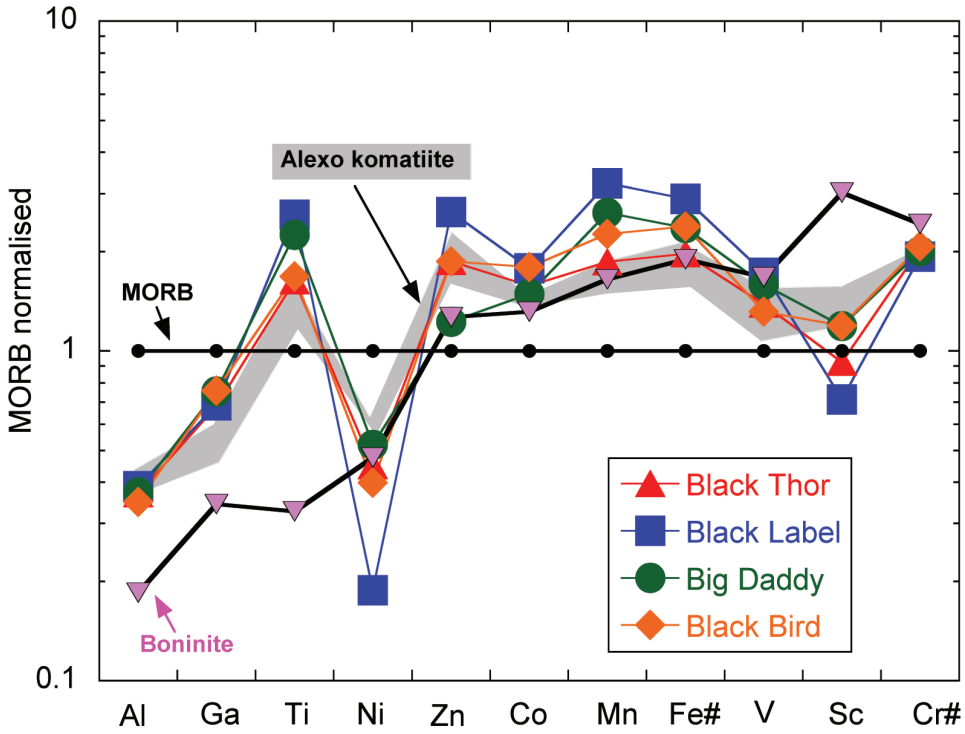

Figure 4. MORB-normalized diagram comparing the major, minor, and trace element composition of the chromites from the EIC with phenocrystic chromite from a boninite of Bonin Island (average of four analyses; Pagé and Barnes, 2009) and olivine- (average of 52 analyses) and olivine-pyroxene (average of 11 analyses) cumulus chromites from Neoarchean Munro Township komatiites of the Alexo mine (gray field; Meric, 2018). MORB normalization values from Pagé and Barnes (2009).

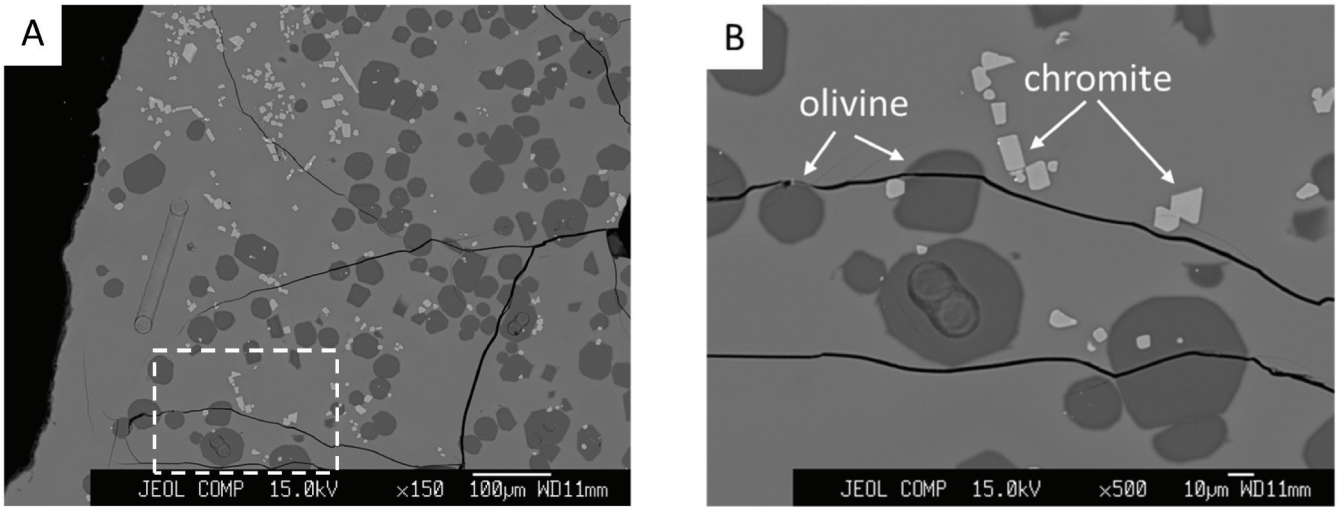

Figure 5. Backscattered electron images of experiment run product W02_e done at FMQ. Panel B) is an enlargement of the white dashed area in panel A). Elongate linear features in glass **(A)** and olivine **(B)** are laser ablation trenches.

in the samples with the higher trace element doping levels. As well, chromite grain sizes were generally smallest in the run at the lowest fO_2 and those with the lower dopant levels. Figure 5 shows the development of texture within a typical run product (in this case, sample W02_e, done at FMQ) producing euhedral olivine and chromite. Whereas run-product olivines were large enough for laser ablation analysis, repeated attempts to analyse chromites yielded signals from elements that were clearly incompatible in chromite (e.g., Ca, Sr) but concentrated in the glass, indicating ablation of a chromite-glass mixture. Therefore, chromite-melt partition coefficients for V and Ga are calculated from measurements on the chromite done with the electron microprobe and glass by LA-ICP-MS. We calculated elemental mass balance on experimental run products by reconstructing the initial composition using the proportions of olivine and glass, with the mass fraction of glass (X_{glass}) estimated by assuming all the calcium in the experiment is concentrated in the glass (i.e., C_{Ca} olivine ~0, and therefore, $X_{glass} = C_{Ca}$initial/C_{Ca} glass). Mass balance calculated in this manner indicates that iron loss from the experiments was less than 2%. In terms of trace elements, abundances of V, Co, Sr, Zr, Hf, and Ta in the run-product glasses are consistent with amounts added, whereas Zn, Ge, In, and Sn were quantitatively lost. Abundances of W also decreased significantly, with the experiment at FMQ+1 experiencing the greatest loss (60-80%) relative to those at lower fO_2 (30-50%). Ga concentrations in the experiments at FMQ and FMQ+1 are consistent with the amounts added, but we estimate > 90% of this element was lost at FMQ-1.

Because of the high doping levels required to obtain accurate and precise partition coefficients for chromite using the electron microprobe, there is the concern that concentration levels may exceed the limits of Henry's Law, and therefore not applicable at natural concentration levels. We have tested this in experiments for which the V and Ga concentrations in the starting material result in chromites with V concentrations ranging from ~800 to ~15,000 µg/g and Ga concentrations from ~1000 to ~8000 µg/g. For both elements, the partition coefficients are nearly indistinguishable over these concentration ranges (Figure 6a and b), and importantly for V, this overlaps with the ~900 to ~1500 µg/g range found in the EIC chromites. For the case of Ga, the concentrations in the experimental chromites are well above the range of 30-50 µg/g for the EIC samples, however, Horn et al (1994) demonstrated constant chromite-melt partitioning of Ga at concentrations from ~6 to ~60,000 µg/g (Figure 6a and b), which encompasses those found in chromites from both the EIC samples, and our experimental run- products. For the case of olivine-melt partitioning, we have not measured the trace element content of olivine from the EIC so it is unclear if the concentration ranges would overlap. However, we note essentially constant partitioning of V and Ga into olivine over a concentration range that spans ~10-fold, and certainly at "trace" levels of ~10-100 µg/g V and ~2-30 µg/g Ga (Figure 6a and b). In terms of the approach to mineral-melt equilibrium in our experiments, we note the following aspects that are consistent with equilibrium: 1) chromite grains show major element homogeneity, although it was not possible to measure traverses across single chromite crystals, the standard deviation of analyses for Cr, Al, and V are each < 10%, and Ga < 20%. The notable exception is the Fe contents of the three experiments, as noted above, with the smallest chromite grains that show standard deviations of 16- 17%, which is larger than the other runs which vary by < 10%. However, the latter could be a grain size effect reflecting secondary fluorescence of Fe from the surrounding melt, 2) Partition coefficients are reproducible for experiments done at different concentration levels, 3) Partition coefficients for V vary in a way expected from thermodynamics in which V^{4+} is significantly less compatible than V^{3+}, with species abundance varying with fO_2 (e.g., Canil 1997; Mallmann and O'Neill, 2009), 4) The estimated length scale for diffusion of highly charged cations (e.g., Ti) into spinel-structured minerals is ~150 microns after 2 days at 1400ºC (using the diffusion parameters provided in Aggarwal and Dieckmann, 2002), which significantly exceeds the typical chromite grain-size of 10-50 microns from the experiments.

Results from experiments show that the chromite-melt partition coefficients for V increase systematically from ~1.4 at FMQ+1 to ~8 at FMQ-1, and values for olivine increase from ~0.01 to 0.14 over the same fO_2 interval (Table 1). Olivine- and chromite-melt partition coefficients for Ga at FMQ and FMQ+1 are essentially identical (Table 1), yielding average values of 0.02 +/- 0.001 and 2.8 +/- 0.3, respectively. The somewhat higher value measured for olivine at FMQ-1 (0.044) is likely due to Ga loss during the experiment, and abundances of this element were too low in chromite from that experiment to calculate a partition coefficient. Figure 7 provides a comparison of results for chromite- and olivine- melt partitioning of V (Figure 7a) and Ga (Figure 7b) between the current study and previous work. For both elements, partition coefficients measured in this study are in very good agreement with past work, and most notably, the increase in values for V with decreasing fO_2 reflects the higher compatibility of V^{3+} relative to V^{4+} as documented in the literature.

6.3 Approach to modelling

The experimental results of Keltie (2018) indicate that the effect of increased iron in the melt is to lower the solubility of chromite, suppress the olivine-in temperature, and reduce the amount of olivine that will form. Therefore, given sufficient chromium in the initial magma, it is possible, through contamination by a Fe-rich component, to reverse the normal order of olivine-first crystallization, and induce chromite to form as the sole liquidus phase over a limited temperature interval. Although these experimental results suggest the plausibility of this process as a mechanism to form monomineralic layers of chromite, the question arises as to the evidence for this process in natural samples. As determined from the variation in Cr with MgO in komatiite

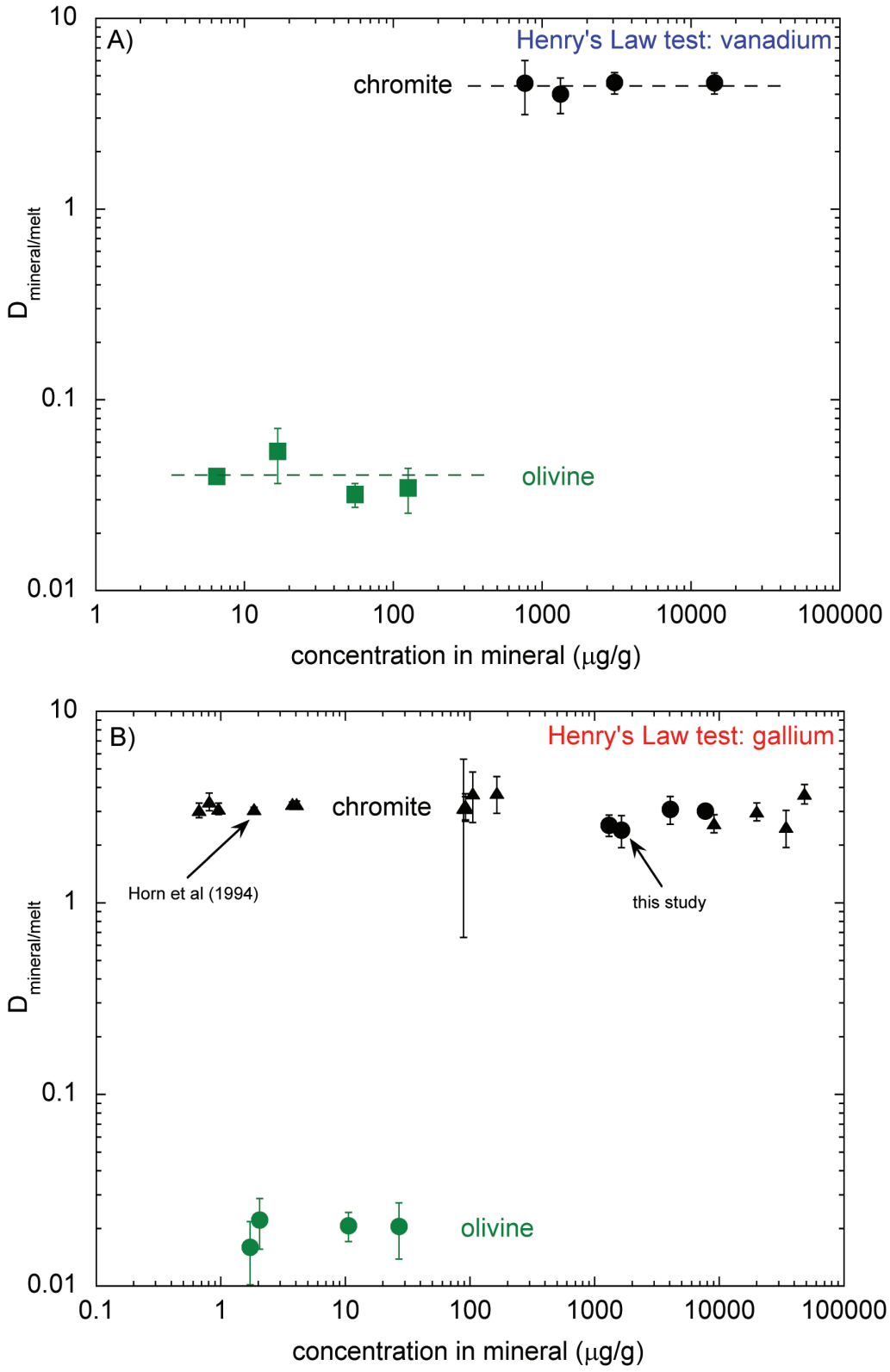

Figure 6. Chromite- and olivine-melt partition coefficients for V **(A)** and Ga **(B)** as a function of the trace element concentration in the mineral phase (experiments for V done at the FMQ buffer). Also shown are the chromite-melt partition coefficients for Ga reported by Horn et al (1994). Note the overall constant partition coefficients over the concentration ranges studied.

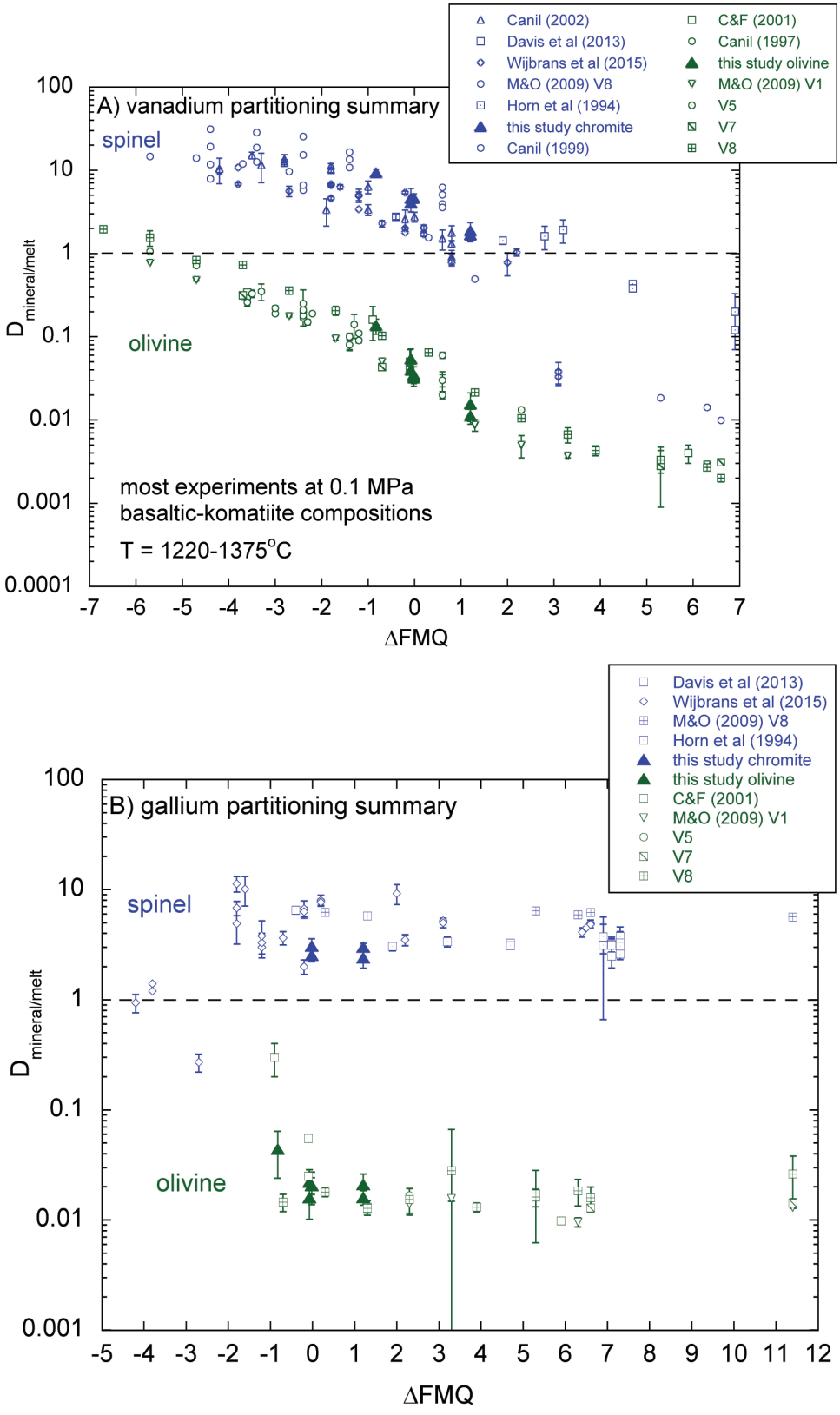

Figure 7. Comparison between partition coefficients for V **(A)** and Ga **(B)** measured in this study with values from past work. Data sources are provided in the legends. Abbreviations for data sources are as follows: M&O = Mallmann and O'Neill; C&F = Canil and Fedortchouk; V1, V5, V7, V8 correspond to the different compositions employed by Mallmann and O'Neill (2009).

suites (Barnes, 1998) the approximate cotectic proportion of olivine/chromite is 50, corresponding to 2 wt% chromite in the crystallizing assemblage. This is also consistent with the experimental results of Murck and Campbell (1986). Therefore, in order to identify chromitites that have formed by segregation from magmas crystallizing the normal olivine/chromite cotectic proportions, from those produced by chromite-only crystallization, evidence should be sought using the covariation of elements with significantly different olivine- and chromite-melt partition coefficients, as is the case for V and Ga documented in our experiments.

The data for V and Ga concentrations in EIC chromites is shown in Figure 8, along with the composition of cumulate chromite in Munro Township komatiites from the Alexo Mine (same samples as plotted in Figure 4), reported by Meric (2018). Open symbols on the diagram denote chromites that occur in the silicate-dominant lithologies as defined in this study (spinel dunite or porphyritic chromitite), whereas filled symbols are silicate-poor chromitites (cumulate chromitite). Three features of the data are of note: 1) compositions show a trend of increasing V with Ga, with relatively coherent behaviour exhibited within each deposit, 2) there is no systematic difference in the V or Ga concentrations between textural types, i.e., for each suite there are chromites from the cumulate chromitites with identical compositions as those from the silicate-dominant samples, and 3) the Munro Township chromites plot within the array exhibited by the EIC samples. We place this dataset into the context of crystallization models by calculating chromite compositional trajectories for the case of 0-50% fractional crystallization involving an assemblage of olivine + chromite (2, 20, and 98% chromite), with model parameters summarized in Table 2 and model curves portrayed in Figure 8A. In the calculations, the initial liquid composition is equivalent to the parental magma composition of the Neoarchean Munro Township komatiite suite, using the compositional data of Sossi et al. (2016), and calculations are done at oxygen fugacities corresponding to FMQ, FMQ+0.8, and FMQ-0.4. The chosen limits of oxygen fugacity are based on the estimate of ~FMQ determine from a suite of Black Thor samples by Keltie (2018) and for the FMQ+0.8 to FMQ-0.4 range estimated for the Munro Township suite using V to lithophile element ratios (Canil, 1997). Chromite compositions are calculated from model liquid compositions by multiplying by the chromite/melt partition coefficient for that element. The chromite data portrayed in Figure 8A show a broad positive correlation between V and Ga, which is consistent with model curves for the normal olivine:chromite cotectic proportions (2% chromite), as the bulk partition coefficient for both elements (defined as the sum of the individual mineral-melt partition coefficients multiplied by their mass fraction in the crystallizing assemblage) is less than 1. A shift in the predicted chromite compositions to higher V at the same Ga content occurs as the fO_2 of crystallization decreases (as V becomes more compatible in chromite, but the bulk D remains <1), and to lower V at higher fO_2 (V less compatible), but in both cases the trends remain the same. Higher proportions of chromite in the crystallizing assemblage raise the bulk partition coefficient, until D_V and D_{Ga} values exceed 1 (corresponding to ~20-30% chromite in the crystallizing assemblage) and the model concentrations of V and Ga both decrease relative to the initial composition. In terms of the fO_2 of crystallization, most of the chromite data lie between the FMQ to FMQ-0.4 model curves, including the Alexo samples. Results of this modeling therefore suggest that the range in V-Ga concentrations of chromite exhibited by the various EIC chromite deposits is consistent with crystallization of a parental magma originating from a depleted mantle source similar to other Neoarchean ultramafic magmas (i.e., the MT suite) with differences between deposits possibly related to magma redox state; the Black Label chromitites reflecting fO_2 ranging from FMQ to ~ FMQ-0.4 (or slightly lower), and the other deposits reflecting crystallization closer to FMQ.

An alternative to closed system crystallization models involving differences in magma redox state is one in which fO_2 remains constant, but the magma composition is shifted as the result of contamination. Both Azar (2010) and Carson et al. (2015) show that the whole-rock lithophile trace element content of chromitite from the Blackbird deposit and the Black Thor intrusive complex are consistent with assimilation of some combination of local country rocks (e.g., granodiorite, banded iron formation). Physical evidence for contamination by banded iron formation comes from the occurrence of partially digested xenoliths in the magmatic host rocks to the Blackbird deposit (Azar, 2010). The effect of contamination has been modelled here by calculating mixtures of Munro Township komatiite with the granodiorite and banded iron formation compositions reported in Mungall et al (2010) and Azar (2010; compositions in Table 2), and the resulting fractional crystallization trajectories are shown in Figure 8B. Both contaminants have lower V but higher Ga than the MT komatiitic parental magma composition, so the starting point for crystallization of komatiite-contaminant mixtures shifts accordingly. In order to reproduce the EIC chromite array, the fO_2 at which crystallization occurs is required to be ~FMQ-0.5, which in the uncontaminated case (Figure 8A) captures the composition of the Black Thor samples with the highest V contents. Both contaminant types shift this model trajectory in a manner consistent with the EIC compositional array, with the larger shift corresponding to the more Ga-enriched BIF composition, although the difference between contaminants is small. While contamination of up to 20% BIF captures nearly the entire EIC chromite array (except 3 Ga-enriched Black Bird samples), Carson et al (2015) has shown that this lithology has certain element ratios (e.g., Th/Yb) that are too low to reproduce the EIC trace element array as the sole contaminant; instead a hybrid contaminant consisting of BIF + local granodiorite + upper continental crust was modeled as more appropriate. For the case of the rare-earth elements (REE) only, Mungall et al (2010) were able to reproduce the chill margin to the associated Eagle's Nest Ni-sulfide deposit as a mixture between MT komatiite and 17% granodiorite. This is

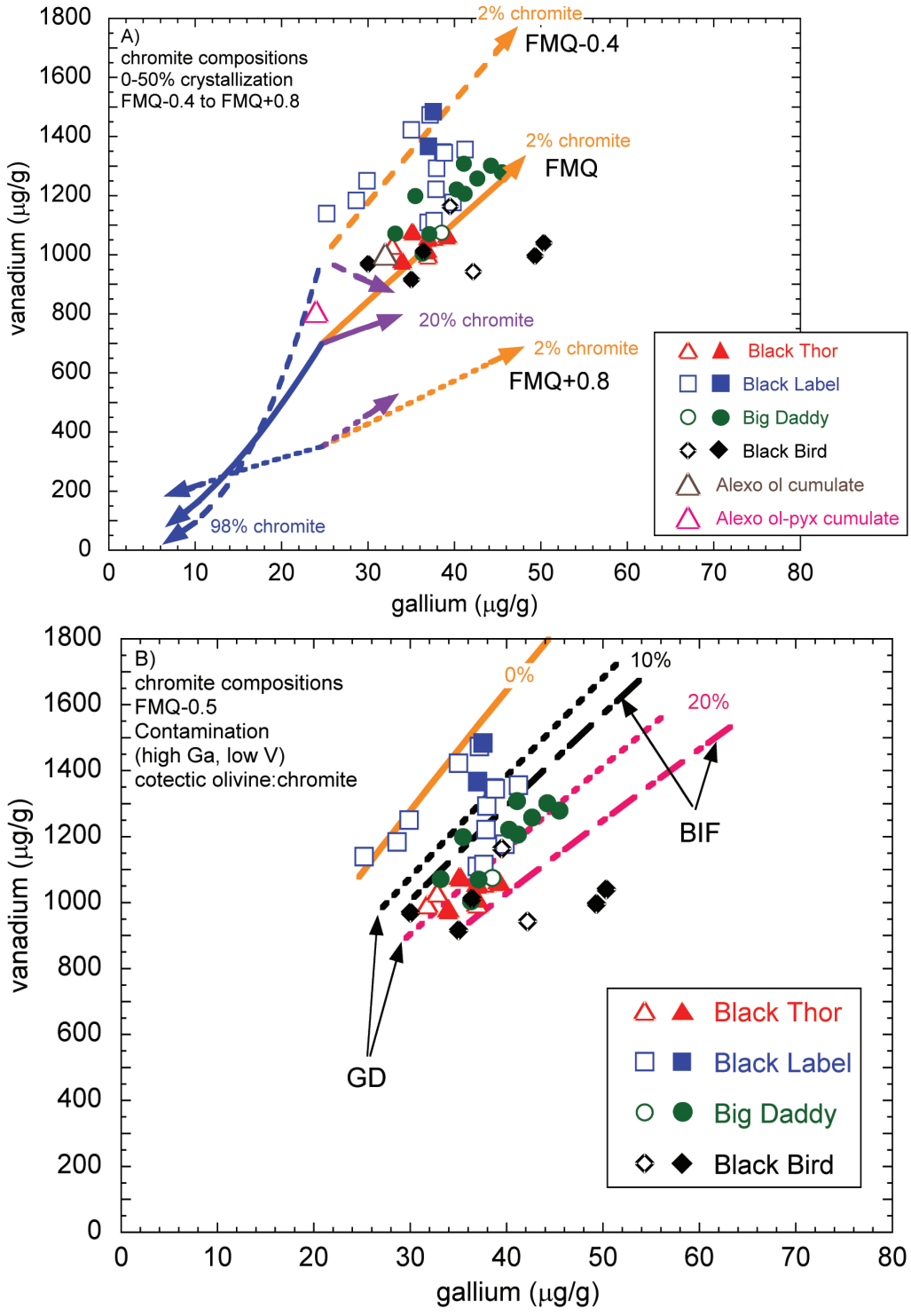

Figure 8. A) V vs Ga covariation diagram for chromites from the EIC compared to compositions produced by 0-50% fractional crystallization (increasing in the direction of the arrow) involving different proportions of chromite in the olivine + chromite crystallizing assemblage at the indicated oxygen fugacity. The initial liquid composition corresponds to a least differentiated Munro Township komatiite (Sossi et al., 2016). All filled symbols are samples that belong to the chromitite textural group, and open symbols correspond to silicate-rich lithologies (*see* Figure 2). For comparison, the average composition of chromites from cumulate samples associated with Munro Township komatiites from the Alexo Mine (Meric, 2018) are also plotted. **B)** V vs Ga covariation diagram with symbols as in A) and model fractional crystallization curves involving the "normal" olivine-chromite cotectic proportions (2% chromite) for komatiite mixed with 0, 10, and 20% of banded iron formation (BIF) and granodiorite (GD). In this model, the oxygen fugacity is set at FMQ-0.5.

Table 2. Summary of model parameters (partition coefficients and trace element composition.

Element	$D^{Olivine/melt}$	$D^{Chromite/melt}$	MunroTownship komatiite*[1]	Banded iron formation[2]	Grano-diorite[3]
V	0.01 (FMQ+1)	1.4	176	14.97	24.75
	0.04 (FMQ)	(FMQ+1)			
	0.14 (FMQ-1)	4.2 (FMQ)			
		8.1 (FMQ-1)			
Ga	0.026	2.5	8.8	24.59	17.53

Notes:
*All trace element compositions are in units of μg/g
1. Munro Township komatiitic primary liquid from Sossi et al (2016)
2. Sample NOT-08-1G79 303 from Azar (2010)
3. Sample NOT-08-1G77 428 from Azar (2010)

similar to the amount suggested by the crystallization models presented in Figure 8B, with all the samples from Black Label and Big Daddy consistent with contamination of up to 20% granodiorite, but somewhat higher levels suggested for some Black Thor and Black Bird samples. In summary, the V-Ga array exhibited by the EIC chromites (including both silicate-dominant, and chromite-dominant samples) can be reproduced with a model involving the crystallization of olivine and chromite in cotectic proportions, with the spread in the array the result of either variable fO_2 during crystallization, or open system behaviour involving a shift in magma composition by assimilation, or possibly a combination of both. Given the presence of partially dissolved country rocks in some EIC samples, along with elevated concentrations of other lithophile trace elements in the silicate rocks associated with the EIC chromitites, we favour the contamination hypothesis as best accounting for the observed compositional variation.

Although there is evidence for contamination in the EIC, as reflected both texturally, and in the trace element chemistry of the chromites, that on its own does not either support or deny a causative link between contamination and chromitite formation. In this context, the link between BIF assimilation, and magnetite "upgrading" as proposed by Lesher et al (2019) seems unlikely based on the work of Keltie (2018), who showed that komatiites have an extraordinary capacity to dissolve FeO. For example, at 1290°C, and the FMQ buffer, a chromite-saturated komatiite can dissolve ~66 wt% FeO before saturating in magnetite, so it is unlikely that this mineral would survive prolonged contact with a komatiite host, even if the host were already saturated in chromite. Importantly, the chromite V-Ga compositional arrays suggest "normal" crystallization of olivine-chromite cotectic proportions, despite contamination. The textural context of the chromites in the samples studied, in terms of their occurrence in silicate poor chromitites, or silicate-rich spinel dunite, bears no relation to the trace element content of the chromite, with samples from either context recording overlapping compositions. This means that the chromites that occur in chromitites were formed by the same extent of crystallization and magma compositions as the chromite-poor lithologies, involving the same proportions of olivine:chromite during crystallization. Therefore, instead of resulting from changes in intensive parameters or magma chemistry, we suggest the EIC chromitites formed by efficient physical separation of olivine from chromite by mechanical sorting within a crystal-liquid slurry.

Segregation within such a slurry, a type of granular flow, has been demonstrated using both numerical and experimental methods (Gray and Hutter, 1997; Ottino and Khakhar, 2000; Forien et al., 2016). A similar style of chromitite formation has been proposed for the Peridotite Zone of the Stillwater Complex (USA; Jenkins and Mungall, 2018), the UG1 and UG2 Horizons of the Critical Zone of the Bushveld Complex (South Africa; Eales, 2000; Mondal and Mathez, 2007; Eales and Costin, 2012;Voordouw et al., 2009; Maier and Barnes, 2008; Maier et al., 2013), and the Main Chromite Layer of the Jacurici Complex (Brazil; Marques et al., 2017). In terms of the specific mechanisms for generating the relevant magma flow regimes, Maier and coworkers (Maier and Barnes, 2008; Maier et al, 2013) have suggested that slumping of unconsolidated ultramafic cumulates may drive crystal sorting within gravity-driven flows following magma chamber subsidence. Others have suggested that chromite crystals may be segregated by turbulent flow within the magma conduit system, then injected as chromite-rich slurries (Eales, 2000; Mondal and Mathez, 2007; Voordouw et al., 2009; Eales and Costin, 2012; Marques et al., 2017; Jenkins and Mungall, 2018). Consistent with the latter, as described by Azar (2010) and Houlé et al (2019), the magmatic architecture of the EIC suggests a sill-hosted conduit style of mineralization. Chromitite beds are lenticular, and discontinuous, as opposed to the relatively thin and laterally continuous chromitite within the Bushveld Complex. Evidence for turbulent magma injection is documented for both the Black Bird and Black label deposits in the form of clastic chromitite and disrupted chromitite layers (Figures 5h and i from Azar, 2010) and magmatic breccia textures (Figures 3.42 and 3.48 from Laarman, 2014), demonstrating the plausibility of the sorting hypothesis.

SUMMARY

The essential results of this research can be summarized as follows:

1) A total of 50 chromite-bearing samples from the Black Thor, Big Daddy, Blackbird, and Black Label chromite deposits have been analysed for major and trace elements. The sample suite represents three textural groups largely defined by the silicate/chromite ratio, the chromite-bearing dunite, the "porphyritic" chromitite, and the cumulate chromitite.

2) V and Ga are elements that are both readily detectable in the EIC chromitites, and show contrasting behaviour in their olivine- and chromite-melt partitioning, each being moderately compatible in chromite, and moderately incompatible in olivine. These partitioning data are used to develop simple fractional crystallization models in which the bulk partition coefficient is varied from olivine-dominant (2% chromite), to chromite-only crystallization.

3) The observed trends in the V and Ga content of EIC chromites reflects crystallization from a komatiitic magma producing olivine and chromite in "normal" cotectic proportions. Textural observations, lithophile trace element geochemistry of the associated silicate rocks and modeling indicate that the overall spread in the V-Ga data is consistent with formation from a magma that has assimilated up to ~20% of wall-rock banded iron formation or granodiorite at an oxygen fugacity of ~FMQ-0.5.

4) Despite the evidence for contamination, the V-Ga trends suggest that cotectic proportions of olivine to chromite are preserved during crystallization, eliminating any causative link between contamination and chromitite formation. Instead, we suggest that physical separation of olivine from chromite has occurred, underscoring the specific fluid dynamic regime during magma emplacement as conducive to crystal sorting and chromite accumulation.

ACKNOWLEDGEMENTS

Funding for this research was generously provided by Targeted Geoscience Initiative grants from Natural Resources Canada. We thank Dan MacDonald for developing the necessary analytical protocols for the EMP analysis of chromite. Michel Houlé is thanked for comments that improved the clarity of this contribution.

REFERENCES

Aggarwal, S., and Dieckmann, R., 2002. Point defects and cation tracer diffusion in $(Ti_xFe_{1-x})3-\delta O_4$: II. Cation tracer diffusion. Physics and Chemistry of Minerals, vol. 29, pp. 707–718.

Aubut, A. June 27, 2012. Big Daddy chromite deposit McFaulds Lake Area, Ontario, Canada. National Instrument 43-101 Technical Report prepared for KWG Resources Inc, 64 pp.

Aubut, A., 2010. McFauld's Lake Area, Ontario, Canada Black Thor Chromite Deposit. National Instrument 43-101 Technical Report prepared for Freewest Resources Canada Inc, 65 pp.

Aubut, A., 2015. Black Thor, Black Label, and Big Daddy chromite deposits, McFaulds lake Area, Ontario, Canada. National Instrument 43-101 Technical Report prepared for Noront Resources Ltd, 146 pp.

Azar, B., 2010. The Blackbird chromite deposit, James Bay Lowlands of Ontario, Canada: Implications for chromitite genesis in ultramafic conduits and open magmatic systems. M.Sc. thesis, University of Toronto, Toronto, Ontario, Canada, 154 pp.

Barnes, S.J., 1998. Chromite in komatiites, 1. Magmatic controls on crystallization and composition. Journal of Petrology, vol. 39, pp. 1689–1720.

Barnes, S.J., 2000. Chromite in komatiites, II. Modification during greenschist to mid-amphibolite facies metamorphism. Journal of Petrology, vol. 41, pp. 387–409.

Canil, D., 1997. Vanadium partitioning and the oxidation state of Archaean komatiite magmas. Nature, vol. 389, pp. 842–845.

Canil, D., 1999. Vanadium partitioning between orthopyroxene, spinel and silicate melt and the redox states of mantle source regions for primary magmas. Geochimica et Cosmochimica Acta, vol. 63, pp. 557–572.

Canil, D., 2002. Vanadium in peridotites, mantle redox, and tectonic environments: Archean to present. Earth and Planetary Science Letters, vol. 195, pp. 75–90.

Canil, D., and Fedortchouk, Y., 2001. Olivine-liquid partitioning of vanadium and other trace elements, with applications to modern and ancient picrites. The Canadian Mineralogist, vol. 39, pp. 319–330.

Carson, H.J.E., Lesher, C.M., and Houlé, M.G., 2015. Geochemistry and petrogenesis of the Black Thor intrusive complex and associated chromite mineralization, McFaulds Lake greenstone belt, Ontario, In: Targeted Geoscience Initiative 4: Canadian Nickel-Copper-Platinum Group Elements-Chromium Ore Systems — Fertility, Pathfinders, New and Revised Models, (ed.) D.E. Ames and M.G. Houlé; Geological Survey of Canada, Open File 7856, pp. 87–102.

Davis, F.A., Humayun, M., Hirschmann, M.M., and Cooper, R.S., 2013. Experimentally determined mineral/melt partitioning of first-row transition elements (FRTE) during partial melting of peridotite at 3 GPa. Geochimica et Cosmochimica Acta, vol. 104, pp. 232–260.

Eales, H.V., 2000. Implications of the chromium budget of the Western Limb of the Bushveld Complex. South African Journal of Geology, vol. 103, pp. 141–150.

Eales, H.V., and Costin, G., 2012. Crustally contaminated komatiite: Primary source of the chromitites and Marginal, Lower, and Critical Zone magmas in a staging chamber beneath the Bushveld Complex. Economic Geology, vol 107, pp. 645–665.

Eggins, S.M., Kinsley, L.P.J., and Shelley, J.M.M., 1998. Deposition and element fractionation processes during atmospheric pressure laser sampling for analysis by ICPMS. Applied Surface Science, vol. 127-129, pp. 278–286.

Forien, M., Tremblay, J., Barnes, S.-J., Burgisser, A., and Pagé, P., 2016. The role of viscous particle segregation in forming chromite layers from slumped crystal slurries: Insights from analogue experiments. Journal of Petrology, vol. 56, pp. 2425–2444.

Gray, J.M.N.T., and Hutter, K., 1997. Pattern formation in granular avalanches. Continuum Mechanics and Thermodynamics, vol. 9, pp. 341–345.

Horn, I., Foley, S.F., Jackson, S.E., and Jenner, G.A., 1994. Experimentally determined partitioning of high field strength and selected transition elements between spinel and basaltic melt. Chemical Geology, vol. 117, pp 193–218.

Houlé, M.G., Lesher, C.M., McNicoll, V.J., Metsaranta, R.T., Sappin, A.-A., Goutier, J., Bécu, V., Gilbert, H.P., and Yang, X.M., 2015. Temporal and spatial distribution of magmatic Cr-(PGE), Ni-Cu-(PGE), and Fe- Ti-(V) deposits in the Bird River–Uchi–OxfordStull–La Grande Rivière–Eastmain domains: a new metallogenic province within the Superior Craton, In: Targeted Geoscience Initiative 4: Canadian Nickel-Copper-Platinum Group Elements-Chromium Ore Systems — Fertility, Pathfinders, New and Revised Models, (ed.) D.E. Ames and M.G. Houlé; Geological Survey of Canada, Open File 7856, pp. 35–48.

Houlé, M.G., Lesher, C.M., Metsaranta, R.T., and Sappin, A.-A., 2019. Architecture of magmatic conduits in chromium-PGE and Ni-Cu-PGE ore systems in Superior Province: example from the 'Ring of Fire' region, Ontario; in Targeted Geoscience Initiative: 2018 report of activities, (ed.) N. Rogers; Geological Survey of Canada, Open File 8549, pp. 441–448.

Irvine, T.N., 1975. Crystallization sequences in the Muskox intrusion and other layered intrusions—II. Origin of chromitite layers and similar deposits of other magmatic ores. Geochimica et Cosmochimica Acta, vol. 39, pp. 991–1020.

Irvine, T.N., 1977. Origin of chromite layers in the Muskox intrusion and other stratiform intrusions: A new interpretation. Geology, vol. 5, pp. 273–277.

Jenkins, M.C., and Mungall, J.E., 2018. Genesis of the Peridotite Zone, Stillwater Complex, Montana, USA. Journal of Petrology, vol. 59, pp. 2157–2190.

Jochum, K.P., Nohl, U., Herwig, K., Lammel, E., Stoll, B., and Hofmann, A.W., 2005. GeoReM: A new geochemical database for reference materials and isotopic standards. Geostandards and Geoanalytical Research, vol. 29, pp. 333–338.

Keltie, E.E., 2018. An experimental study of the role of contamination in the formation of chromitites in the Ring of Fire intrusive suite. M.Sc. thesis, Dalhousie University, Halifax, Nova Scotia, Canada, 146 pp.

Kuzmich, B., 2014. Petrogenesis of the ferrogabbroic intrusions and associated Fe-Ti-V-P mineralization within the McFaulds Lake greenstone belt, Superior Province, northern Ontario, Canada; M.Sc. thesis, Lakehead University, Thunder Bay, Ontario, 486 pp.

Laarman, J.E., 2014. A detailed metallogenic study of the McFaulds Lake chromite deposits, Northern Ontario. Ph.D. thesis, Western University, London, Ontario, Canada, 529 pp.

Lesher, C.M., Carson, H.J.E., and Houlé, M.G., 2019. Genesis of chromite deposits by dynamic upgrading of Fe ± Ti oxide xenocrysts. Geology, vol. 27, pp 207–210.

Li, C.S., Ripley, E.M., Sarkar, A., Shin, D.B., and Maier, W.D., 2005. Origin of phlogopite-orthopyroxene inclusions in chromites from the Merensky Reef of the Bushveld Complex, South Africa. Contributions to Mineralogy and Petrology, vol. 150, pp 119–130.

Maier, W.D., and Barnes, S.-J., 2008. Platinum-group elements in the UGl and UG2 chromitites, and the Bastard reef, at Impala platinum mine, western Bushveld Complex, South Africa: Evidence for late magmatic cumulate instability and reef constitution. South African Journal of Geology, vol. 111, pp. 159– 176.

Maier, W.D., Barnes, S.-J., and Groves, D.I., 2013. The Bushveld Complex, South Africa: formation of platinum–palladium, chrome- and vanadium-rich layers via hydrodynamic sorting of a mobilized cumulate slurry in a large, relatively slowly cooling, subsiding magma chamber. Mineralium Deposita, vol. 48, pp. 1–56.

Mallmann, G., and O'Neill, H.St-C., 2009. The crystal/melt partitioning of V during mantle melting as a function of oxygen fugacity compared with some other elements (Al, P, Ca, Sc, Ti, Cr, Fe, Ga, Y, Zr, and Nb). Journal of Petrology, vol. 50, pp. 1765–1794.

Marques, J.C., Dias, J.R.V.P., Friedrich, B.M., Frantz, J.C., Queiroz, W.J.A., and Botelho, N.F., 2017. Thick chromitite of the Jacurici Complex (NE Craton São Francisco, Brazil): Cumulate chromite slurry in a conduit. Ore Geology Reviews, vol. 90, pp. 131–147.

Meric, J., 2018. Le ruthenium (Ru), iridium (Ir), osmium (Os) et rhodium (Rh) et les elements traces dans des chromites de komatiites issues de la zone Alexo t de la zone Hart (Abitibi, Ontario) – Un outil diagnostique pur l'exploration de systems fertiles. M.Sc. thesis, Université du Québec à Chicoutimi, Chicoutimi, Quebec, Canada, 185 pp.

Metsaranta, R.T., Houle, M.G., McNicoll, V.J., and Kamo, S.L., 2015. Revised geological framework for the McFaulds Lake greenstone belt, Ontario, *In*: Targeted Geoscience Initiative 4: Canadian Nickel-Copper- Platinum Group Elements-Chromium Ore Systems — Fertility, Pathfinders, New and Revised Models, (ed.) D.E. Ames and M.G. Houlé; Geological Survey of Canada, Open File 7856, pp. 61–73.

Mondal, S.K., and Mathez, E.A., 2007. Origin of the UG2 chromitite layer, Bushveld Complex. Journal of Petrology, vol. 48, pp. 495–510.

Mungall, J.E., Harvey, J.D., Balch, S.J., Azar, B., Atkinson, J., Hamilton, M.A. (2010) Eagle's Nest: A Magmatic Ni-Sulfide Deposit in the James Bay Lowlands, Ontario, Canada. Society of Economic Geologists, Special Publication 15, pp. 539–557.

Murck, B.W., and Campbell, I.H., 1986. The effects of temperature, oxygen fugacity and melt composition on the behaviour of chromium in basic and ultrabasic melts. Geochimica et Cosmochimica Acta, vol. 55, pp. 1871–1877.

O'Neill, H.St.C., and Wall, V.J., 1987. The olivine—orthopyroxene—spinel oxygen geobarometer, the nickel precipitation curve, and the oxygen fugacity of the Earth's upper mantle. Journal of Petrology, vol. 28, pp. 1169–1191.

Ottino, J.M., and Khakhar, D.V., 2000. Mixing and segregation of granular materials. Annual Reviews of Fluid Mechanics, vol. 32, pp 55–91.

Pagé, P., and Barnes, S.-J., 2009. Using trace elements in chromites to constrain the origin of podiform chromitites in the Thetford Mines ophiolite, Québec, Canada. Economic Geology, vol. 104, pp. 997– 1018.

Sossi, P.A., Eggins, S.M., Nesbitt, R.W., Nebel, O., Hergt, J.M., Campbell, I.H., O'Neill, H.St.C., Van Kranendonk, M., and Davies, D.R., 2016. Petrogenesis and geochemistry of Archean komatiites. Journal of Petrology, vol. 57, pp 147–184.

Spandler, C., Mavrogenes, J., and Arculus, R., 2005. Origin of chromitites in layered intrusions: Evidence from chromite-hosted melt inclusions from the Stillwater Complex. Geology, vol. 33, pp. 893–896.

Taylor, J.R., Wall, V.J., and Pownceby, M.I., 1992. The calibration and application of accurate redox sensors. American Mineralogist, vol. 77, pp. 284–295.

Voordoux, R., Gutzmer, J., and Beukes, N.J., 2009. Intrusive origin for Upper Group (UG1, UG2) stratiform chromitite seams in the Dwars River area, Bushveld Complex, South Africa. Mineralogy and Petrology, vol. 97, pp 79–94.

Wijbrans, C.H., Lemee, S., Berndt, J., and Vollmer, C., 2015. Experimental determination of trace element partition coefficients between spinel and silicate melt: the influence of chemical composition and oxygen fugacity. Contributions to Mineralogy and Petrology, vol. 169, pp 45–78.

APPENDIX A

Links to Appendix Tables: Tables A1_A2 ROFIS Chromite data_revised 20 Oct 2021.xlsx
Tables A3_A8 Run Product Major and Trace Element Compositions_revised 2 June.xlsx

Evaluating white mica as an indicator mineral for lithium bearing pegmatites, Wekusko Lake pegmatite field, Manitoba, Canada

D. Benn[1], R. Linnen[1], and T. Martins[2]

Benn, D., Linnen, R., and Martins, T., 2021. Evaluating white mica as an indicator mineral for lithium bearing pegmatites, Wekusko Lake pegmatite field, Manitoba, Canada; in *Targeted Geoscience Initiative 5: grant program final reports (2018-2020), Geological Survey of Canada, Open File 8755, p.45–58. https://doi.org/10.4095/328982*

Abstract: This project investigates the potential use of white micas as an indicator mineral within Li-bearing pegmatites and the potential of field portable techniques, such as Raman spectroscopy and Laser Induced Breakdown Spectroscopy (LIBS) as real-time techniques in exploration. The pegmatites in the Wekusko Lake field, Manitoba, Canada, display five zones of varying mineralization. White micas display two textures in the field (primary igneous and secondary) and four textures were identified by backscattered electron imaging (poor zonation, rimmed, patchy and exsolution). The white micas were analysed by Electron Probe Micro-Analysis (EPMA) and Laser Ablation Induction-Coupled Plasma Mass Spectroscopy (LA-ICP-MS) and the results show a strong correlation in the Li content of the white mica and the whole rock Li_2O obtained from the assays of drill core. The K/Rb vs. Cs contents of the white mica indicate that the most prospective dikes contain moderate to highly evolved grains. The use of portable Raman Spectrometer, while useful for mineral identification, was not able to detect a significant Li signature at the concentrations tested (1500-6000 ppm).

[1]Department of Earth Sciences, Western University, 1151 Richmond Street North, London, Ontario
[2]Manitoba Geological Survey, 360-1395 Ellice Avenue, Winnipeg, Manitoba

INTRODUCTION

The emergence of new technologies in electric cars and renewable energies have led to an increased demand for lithium (Li) for use in Li-ion batteries. As a result, Li has become a highly sought-after resource and is included in the Canada – US joint action plan on critical metals (Natural Resources Canada, 2020). There are two primary sources for Li: pegmatites (e.g., Greenbushes, Australia) and brines (e.g., Salar de Atacama, Chile). Of these, pegmatites contain the highest Li grades; spodumene, petalite and Li-bearing micas are the main Li-bearing ore minerals in pegmatites.

In Canada, the primary source for Li is Li-Cs-Ta (LCT) pegmatites. This includes the Whabouchi pegmatite in Quebec, which is scheduled to come into production, and the world-class Tanco pegmatite in Manitoba, a former Li producer.

The Wekusko Lake pegmatite field in Manitoba is currently being explored for Li potential (Far Resources Ltd., 2017, 2018, 2019). The Green Bay group of pegmatite dikes (Černý et al., 1981) in the Wekusko Lake pegmatite field is the focus of this study.

The field area contains at least 13 pegmatite dikes (Far Resources Ltd., 2019), of which 8 are included in this study. These dikes consist of variable proportions of five zones: a border zone, wall zone, intermediate zone, central zone, and core zone (Benn et al., 2018a). These zones differ in mineralogy, degree of alteration and Li content. The central zone contains the highest concentration of the Li-bearing mineral spodumene. The 13 pegmatite dikes differ greatly in their overall Li contents. However, white micas are prevalent throughout all dikes and all zones in the dikes. White micas in pegmatites commonly range in composition from muscovite ($KAl_2[AlSi_3O_{10}][F,OH]_2$) to polylithionite ($KLi_2Al[Si4O_{10}][F,OH]_2$), where the two are in solid solution as Li is incorporated into the octahedral site (Tindle and Webb, 1990). This solid solution is herein referred to as white mica, which has the potential to reflect the whole rock Li content and be a useful vector in mineral exploration.

The heterogeneity and complex mineralogy of pegmatite dikes poses an issue during exploration. There are a variety of white minerals in pegmatites such as albite, microcline, petalite, amblygonite, Cs-beryl and pollucite. If they are sub to anhedral, their identification in the field can be difficult. It is also possible that dikes are barren of Li mineralization at surface, but are mineralized at depth, or that the central zone, which contains the highest concentrations of spodumene, is not intersected by drilling. However, if an indicator mineral like white mica (a ubiquitous mineral in pegmatites) can be developed, real time analyses of white micas could be an important exploration tool to evaluate mineral potential in the field. Commonly used tools such as field portable X-ray fluorescence (pXRF) instruments are not capable of detecting lighter elements such as Li. However, less common portable techniques such as Raman spectroscopy, and Laser Induced Breakdown Spectroscopy (LIBS) show potential for detecting Li minerals or Li, respectively. Raman Spectroscopy uses molecular vibrations to detect physical and chemical changes in the molecular structure of minerals and is capable of identifying minerals. This technique can potentially detect the changes in white mica as it incorporates the Li into its molecular structure. Laser Induced Breakdown Spectroscopy is a newer technique that is becoming more widespread. This uses a laser to produce a plasma state on the surface of the material, as the plasma cools, it produces a spectrum based on the chemical composition of the material. An example of an application of LIBS is to determine the Li content of spodumene and its alteration products in pegmatites dikes in Australia (Sweetapple and Tassios, 2015). The focus of the current study is to investigate the use of white mica as an indicator mineral for lithium pegmatite exploration and to evaluate different methods for determining the Li content of white micas in the field.

GEOLOGICAL SETTING

The Wekusko Lake pegmatite field is located in central Manitoba approximately 25 km east of Snow Lake (Figure 1). This pegmatite field is part of the 1.91 – 1.83 Ga Flin-Flon – Glennie Complex (Connors et al., 2002) in the Trans-Hudson orogen (THO; Figure 1). The THO is a well-preserved Paleoproterozoic collisional belt between the Archean-aged Superior province and the Rea-Hearne craton (Hoffman, 1989), which spans from Scandinavia and through Canada and into the central United States (Schnieder et al., 2007). The central Canada portion cuts through northern Manitoba and Saskatchewan (Figure 1). The Flin Flon – Glennie complex displays a metamorphic gradient from lower greenschist at the southern boundary to upper amphibolite at the northern boundary (Černý et al., 1981).

The Wekusko Lake area has undergone four deformational events (D1–D4) as defined in Connors et al. (1999). Regional peak metamorphism occurred at 1.81 Ga (Gordon et al., 1990; David et al., 1996; Schneider et al., 2007). The final deformation event (D4) records northwest-trending compression, which caused brittle to ductile deformation (Černý et al., 1981; Lucas et al., 1994; Conners et al., 1999). The age of the D4 deformation event is unknown. However, the Green Bay group pegmatite dikes, dated at 1.78 Ga, are interpreted to be associated with the brittle-ductile phase of the D4 event (Benn et al., 2019).

GREEN BAY GROUP PEGMATITES

The study area was the focus of bedrock mapping at a scale of 1:4 000 (Figure 2; Benn et al., 2018b) to investigate surface zoning, morphology and structural controls of the pegmatite dikes. The primary host rock of the studied pegmatite dikes is a meta-andesite, with a small portion of Dike 1 hosted in the quartzofeldspathic gneiss of the Missi

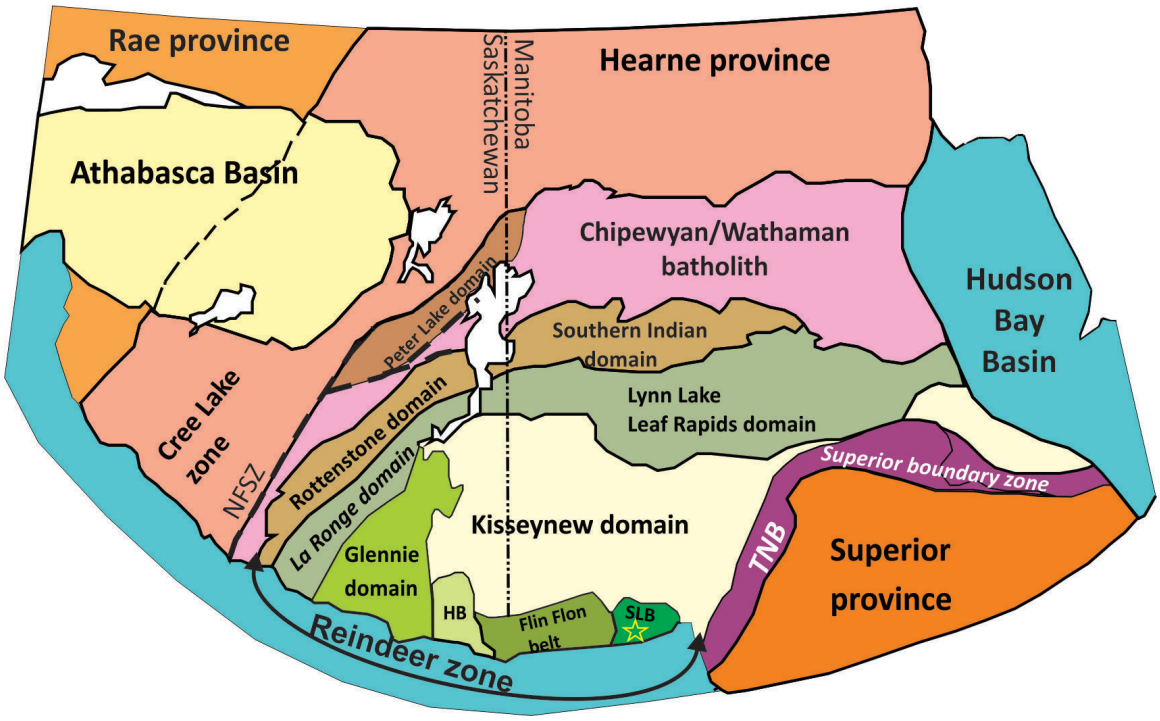

Figure 1. Simplified geology of northern Saskatchewan and Manitoba, showing the main lithotectonic subdivisions and major structural boundaries (after Hoffman, 1988). Abbreviations: HB, Hanson Lake block; NFSZ, Needle Falls shear zone; SLB, Snow Lake block; TNB, Thompson nickel belt. The star overlies the field area of this study.

Group (NATMAP Shield Margin Project Group, 1998; Benn et al., 2018b). Along with a garnet biotite gneiss of the Burntwood Group, these units make up the Roberts Lake fault block (Figure 2). The Roberts Lake fault block is bound by a north-northeast-trending fault to the west and a broadly east-trending fault to the south (Figure 2).

The pegmatite dikes in the Green Bay Group were classified in Benn et al. (2018a) as belonging to the rare-element (REL) class, REL-Li subclass, complex type, spodumene subtype, based on the Černý and Ercit (2005) classification scheme. The pegmatites consist of quartz, albite, K-feldspar, white mica, spodumene and tourmaline, with accessory beryl, apatite, Fe-Mn phosphate minerals, garnet, zircon and columbite-group minerals (Benn et al., 2018a).

Dike size varies with host lithology. The largest dike, Dike 1, has a strike length of 300 m at surface and ranges between 1 – 15 m in width, where hosted in the mafic volcanic rock. However, where Dike 1 crosses into the quartzofeldspathic gneiss the width tapers to 10 cm before terminating.

Dikes crosscut S3 north-northeast trending foliations (as defined by Connors et al., 2002) in the host mafic volcanic rock. The pegmatite dikes are folded over several metres (Benn et al., 2018a). Thinner dikes, such as Dike 7, are folded to a greater extent than the thicker Dike 1 and the folding in these dikes can be more extreme (i.e., they display ptygmatic folds; Figure 3); their thickness also changes due to pinching and swelling (Benn et al., 2018a).

METHODS

The studied pegmatite dikes were sampled from quartered drill core and are representative of all drilled dikes and zones. Polished thin sections were cut for petrographic analysis using a transmitted light microscope. These were then carbon coated and analyzed for major and minor elements on the JEOL JXA-8530F field-emission electron probe micro-analyzer at Western University, London, ON. Operating conditions were an accelerated voltage of 15 kV and a beam current of 100 nA. Transects were taken from core to rim, to determine the nature of chemical zonation, where present. Laser Ablation Inductively Coupled Plasma Mass Spectrometry (LA-ICP-MS) was conducted at the Element and Heavy Isotope Analytical Laboratories (EHIAL) at the University of Windsor. The instrument used was a Photon Machine 193 nm short pulse width Analyte Excite excimer laser ablation system coupled with an Agilent 7900 quadrupole mass spectrometer. Transects were once again taken from core to rim. The values from electron probe micro-analysis (EPMA) and LA-ICP-MS were averaged for comparison with field portable techniques.

Polished quartered pieces of drill core were kept for *in situ* measurements with field portable instruments. Raman measurements were performed *in situ* using a DeltaNu field portable RockHoundTM 785 nm wavelength Raman spectrometer and a custom-built laboratory 514 nm wavelength Raman spectrometer at the High-Pressure Diamond Anvil

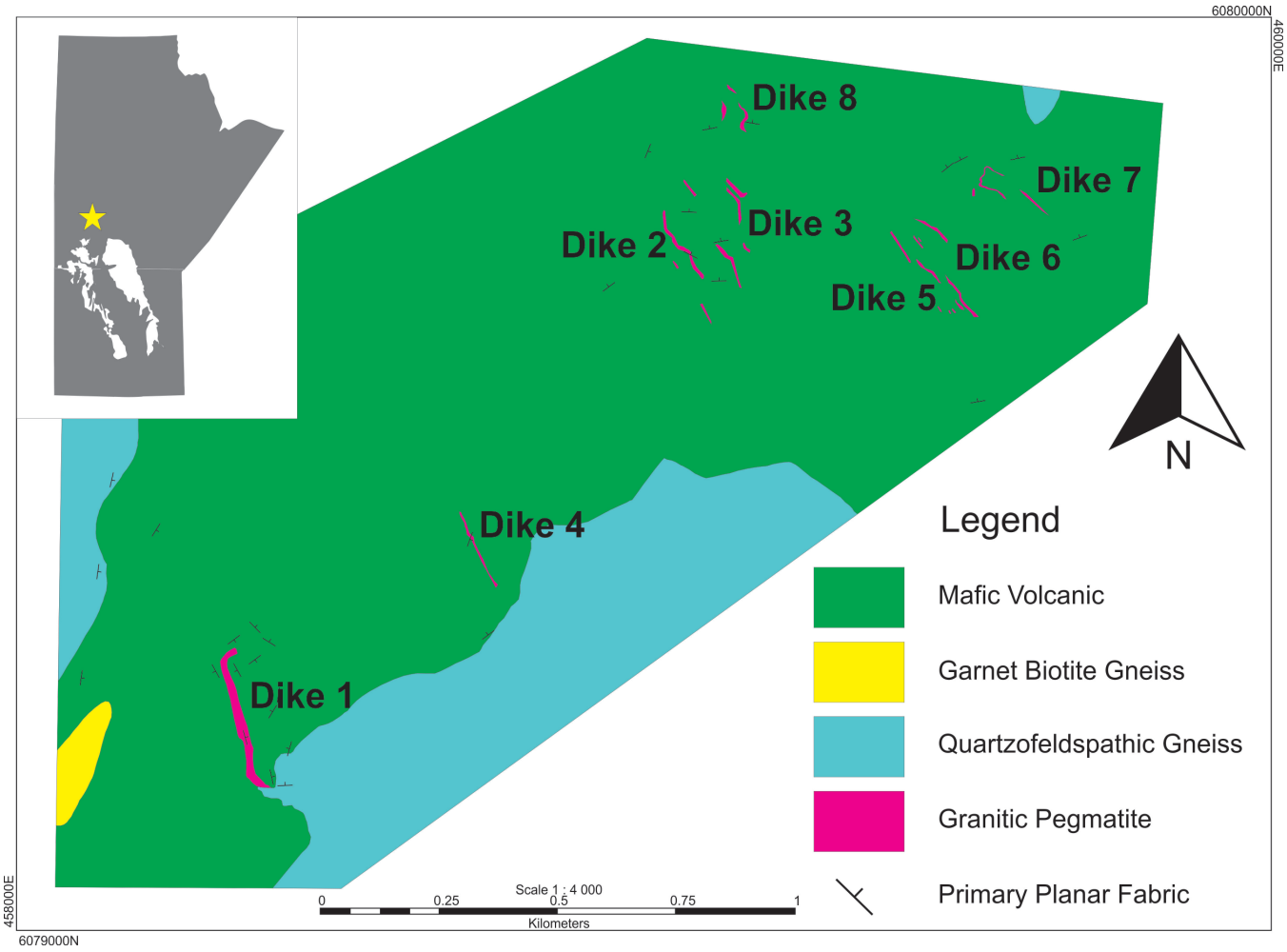

Figure 2. Simplified bedrock geological map of Wekusko Lake pegmatite field (northeastern block), central Manitoba, modified from Benn et al. (2018b).

Figure 3. Field photograph of a folded pegmatite belonging to the Green Bay group. Hammer for scale.

Cell (HPDAC) Mineral Physics Laboratory at Western University. The data was processed using Peakfit® to remove background noise. The data from both spectrometers were compared to reference spectra obtained from RRUFF™ spectral database.

Whole rock geochemistry concentrations of Li_2O are from Far Resources, Ltd obtained from metre-spaced drill core samples. The data for each dike were averaged to evaluate exploration potential for the pegmatite dikes. Dikes with high Li_2O values were given higher rankings in this study. In cases of dikes having similar Li_2O values, the thicker dike was ranked higher. The dike rankings from most prospective to least prospective are: Dike 1, Dike 8, Dike 5, Dike 7, Dike 2, Dike 4. Dikes 3 and 6 were not drilled and therefore were not included in the ranking.

RESULTS

White Mica Geochemistry

The white mica was divided into primary igneous and secondary white mica, based on textures observed in the field and petrographic analyses. Primary white mica is brown, coarse-grained (>0.5 cm), in book structures with well-defined contacts with magmatic minerals such as albite and perthite. Secondary white mica is green-brown, fine-grained (<0.5 cm), and occurs as flaky masses that typically have replaced feldspars.

Four textural types of white mica were observed from backscattered electron images acquired during EPMA analyses. Figure 4A is an example of a white mica that lacks zonation. Rimmed grains show a brighter outer rim due to Cs enrichment (Figure 4B). Patchy textured grains show irregular bright regions that are enriched in Fe and Cs (Figure 4C) and some white mica contain thin, rod-shaped inclusions of a Cs-rich mica (Figure 4D).

White mica geochemistry data obtained from EPMA and LA-ICP-MS were used to calculate atoms per formula unit (apfu). Grain averages of major and minor elements from EPMA and Li, Mn and Ba from LA-ICP-MS were used to calculate apfu assuming 20 oxygens and 4 (OH, F) per formula unit. This data was plotted on a $[(Fe_{tot} + Mn + Ti) - Al]$ vs $[Mg - Li]$ mica classification scheme (Tischendorf et al., 2007; Figure 5), which shows that all white micas plot in the muscovite field with a trend towards an intermediate composition between the polylithionite and zinnwaldite fields.

Lithium shows a negative correlation with octahedral Al (^{VI}Al; Figure 6A) and no correlation with tetrahedral Al (^{IV}Al; Figure 6B). This suggests that Li is primarily substituting into the octahedral site of the white mica.

Since Dike 1 is the largest dike and has the most drill core available for study, EPMA results of mica grains from Dike 1 were subdivided by pegmatite zone, texture and whether the mica grain is primary or secondary (Figure 7A-C). The Li vs F graph was used for comparison because F content typically correlates linearly with Li concentrations in white mica (Tindle and Webb, 1990; Tischendorf et al, 1997). The Li content in the white mica from the wall zone range from 0.38 to 0.7 wt% Li_2O with an outlier value at 1.31 wt% Li_2O; white mica in the intermediate and central zones are very similar with Li contents that range from 0.34 to 1.38 wt% Li_2O (Figure 7A). White mica grains with exsolution textures have the lowest average Li_2O concentrations of the four textures and range from 0.47 to 0.65 wt% Li_2O (Figure 7B). White mica with rimmed textures has the greatest range in average Li_2O content, from 0.38 to 1.31 wt% Li_2O. White mica with poor or no zoning has the least range and the lowest maximum in average Li_2O concentrations, ranging from 0.34 to 1.07 and a mean value of 0.70 wt% Li_2O, respectively. White mica with patchy textures has Li contents ranging from 0.51 to 1.38 and mean value of 0.83 wt% Li_2O, respectively (figure 7B).

The range of Li contents in primary versus secondary white mica overlap (Figure 7C), however, the primary white micas have a wider range of compositions with a higher maximum Li concentration, up to 1.31 wt% Li_2O. Data from LA-ICP-MS show that white mica from the most prospective dike, Dike 1, ranges in Li content from 1500 ppm to 6500 ppm with an average concentration of 3400 ppm (Figure 8A). The least prospective dike, Dike 4, has an average Li concentration of 2598 ppm. Dike 5 is ranked as the third most prospective (Figure 8A). However, its white mica contains the lowest Li content of all dikes, ranging from 250 ppm to 1200 ppm, with an average of 500 ppm (Figure 8A). The studied white micas are also enriched in Nb and Ta. The Nb contents range from 250 ppm to 1000 ppm with most of the dikes averaging between 625 ppm and 875 ppm Nb. Dike 5 is an exception with Nb ranging from 150 ppm to 250 ppm and an average of 225 ppm (Figure 8B). The Ta values in white mica from Dikes 1, 5 and 8 range from 25 ppm to 475 ppm. The Ta values in white mica from other dikes range from 50 ppm to 125 ppm. Dike 5 has the highest concentrations of Ta ranging from 200 ppm to 475 ppm, with an average of 425 ppm (Figure 8C).

Portable Raman Spectroscopy

Raman spectra are characterized by peak positions and peak heights or areas. These parameters are used to compare spectra of different minerals and to identify different minerals. Some pegmatite minerals that are commonly misidentified are petalite, albite and K-feldspar. The portable Raman in this study was used to establish whether this technique is a viable method for identifying minerals in the field. Albite can be distinguished from microcline using Raman spectra by differences in peaks in the ranges of 260 to 330 cm^{-1}, 450 to 510 cm^{-1} and 1000 to 1100 cm^{-1} (Figure 9A, B). An unknown red-colored feldspar from the Wekusko lake pegmatites was compared to reference spectra of microcline and albite and identified as albite (Figure 9A, C). A

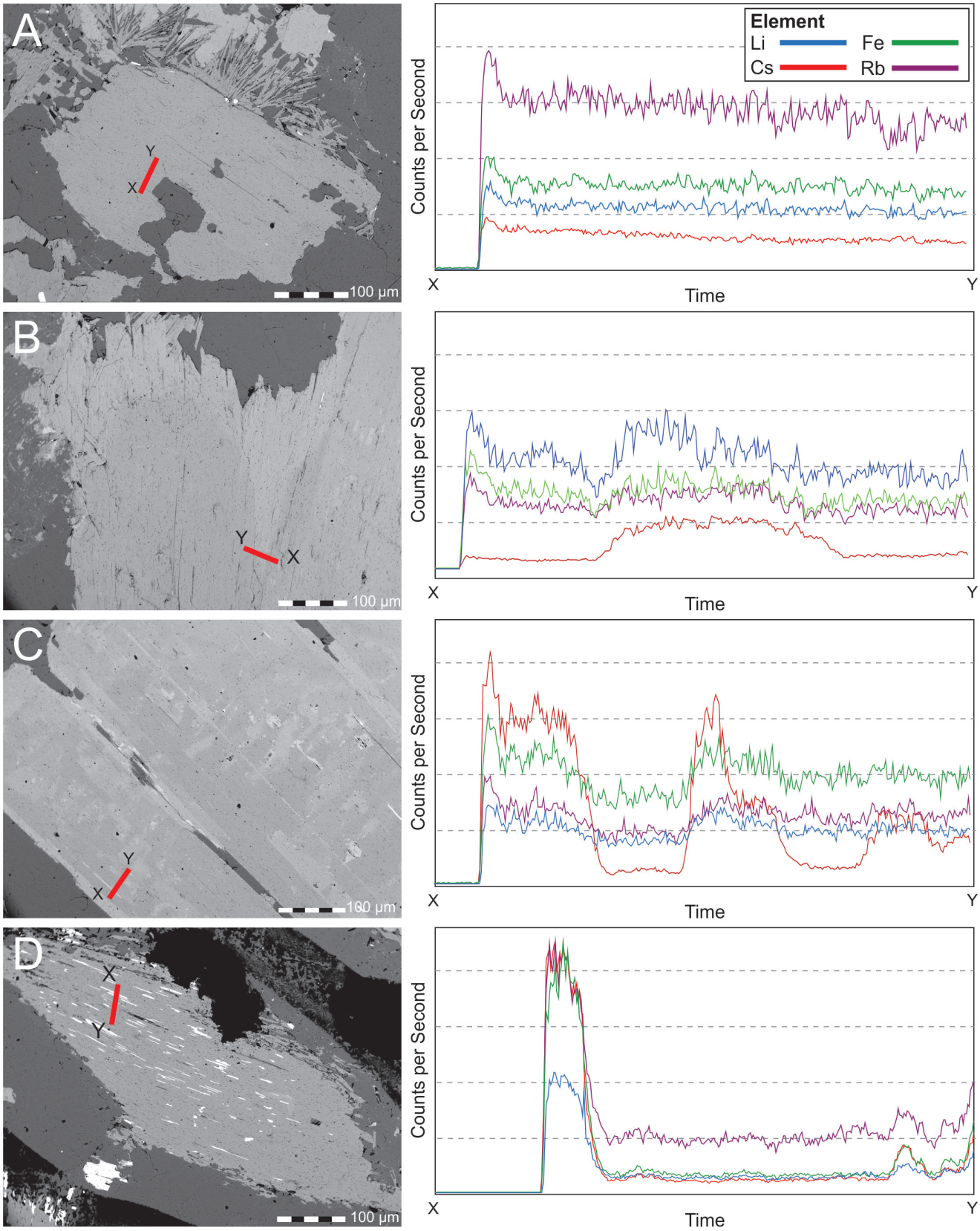

Figure 4. Backscattered electron images of white mica grains showing different textures and laser profiles showing selected element concentrations: **A)** no zonation **B)** rimmed **C)** patchy **D)** mica with rod-shaped inclusions. Red lines depict laser transects from X to Y. Corresponding LA-ICP-MS results in counts per second vs time.

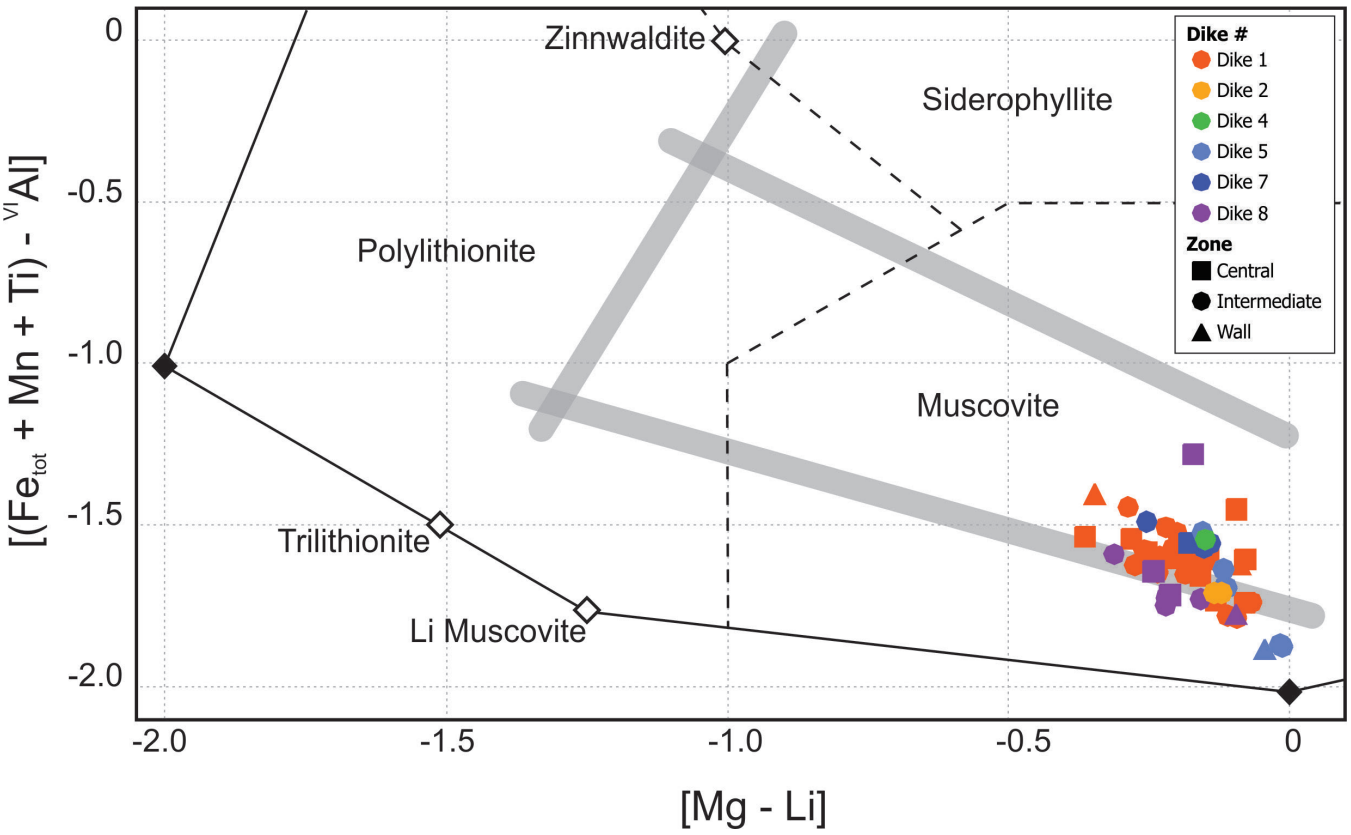

Figure 5. Classification scheme for micas Fe-Al vs Mg-Li in apfu (after Tischendorf et al., 2007). Calculated apfu values were halved to fit the classification scheme calculated at 10 oxygens and 2 (OH, F) apfu. Filled diamonds represent endmember composition; Hollow diamonds represent ideal member composition; Grey lines show ideal evolutionary paths of muscovite.

spodumene sample from La Corne, Canada was positively identified by characteristic peaks at 355cm^{-1}, 393 cm^{-1}, 522 cm^{-1} and 706 cm^{-1}, and samples of white petalite from Bikita, Zimbabwe were also tested and positively identified characteristic peaks at 283 cm^{-1}, 491 cm^{-1}, and 1132 cm^{-1}.

Muscovite has major Raman peaks at 260 cm^{-1}, 406 cm^{-1}, and 700 cm^{-1}. By contrast, polylithionite and trilithionite have major Raman peaks at 190 cm^{-1}, 263 cm^{-1}, and 711 cm^{-1} (Figure 10). Since muscovite forms a solid solution with trilithionite, a gradual change in the Raman spectrum between the two mineral phases would be expected. As a white mica becomes more Li enriched, it would be expected the structural changes in the white mica would cause the 190 cm^{-1} peak to appear, the 406 cm^{-1} peak to shift, and the 700 cm^{-1} peak to shift towards 711 cm^{-1}.

The Raman spectra of white mica grains from this study containing high Li_2O and low Li_2O are similar and most minor peaks are hidden by background noise. Therefore, Raman spectroscopy cannot be used to distinguish Li contents at the 1500 to 6500 ppm Li range.

DISCUSSION

There seems to be a consistent increase in the average Li concentrations in the white mica from the barren dikes (4 and 2) to the intermediate dike (5 and 7), to the enriched dikes (1 and 8) (Figure 8A). This suggests that Li concentrations in white mica could be an indicator for Li mineralization in pegmatite dikes. However, within a single dike there is little difference in Li content between a white mica from the central zone (>10% spodumene) and the intermediate zone (<10% spodumene) (Figure 7A). This may be caused by availability of Li in the pegmatitic melt. For example, high concentrations of Li in the melts preferentially form Li rich minerals such as spodumene before this element is incorporated into the white mica structure. However, if a melt from which the two zones crystallized were of similar composition and temperature, then spodumene saturation could buffer the Li content of the white mica. The overlap of Li content in white micas between intermediate and enriched dikes from 2500 to 4500 ppm Li indicates that multiple grains of white mica should be analyzed and an average calculated. It is also interesting that the more enriched dikes display greater variability in concentration of Li in white mica, but more work needs to be completed to assess whether this variability is significant.

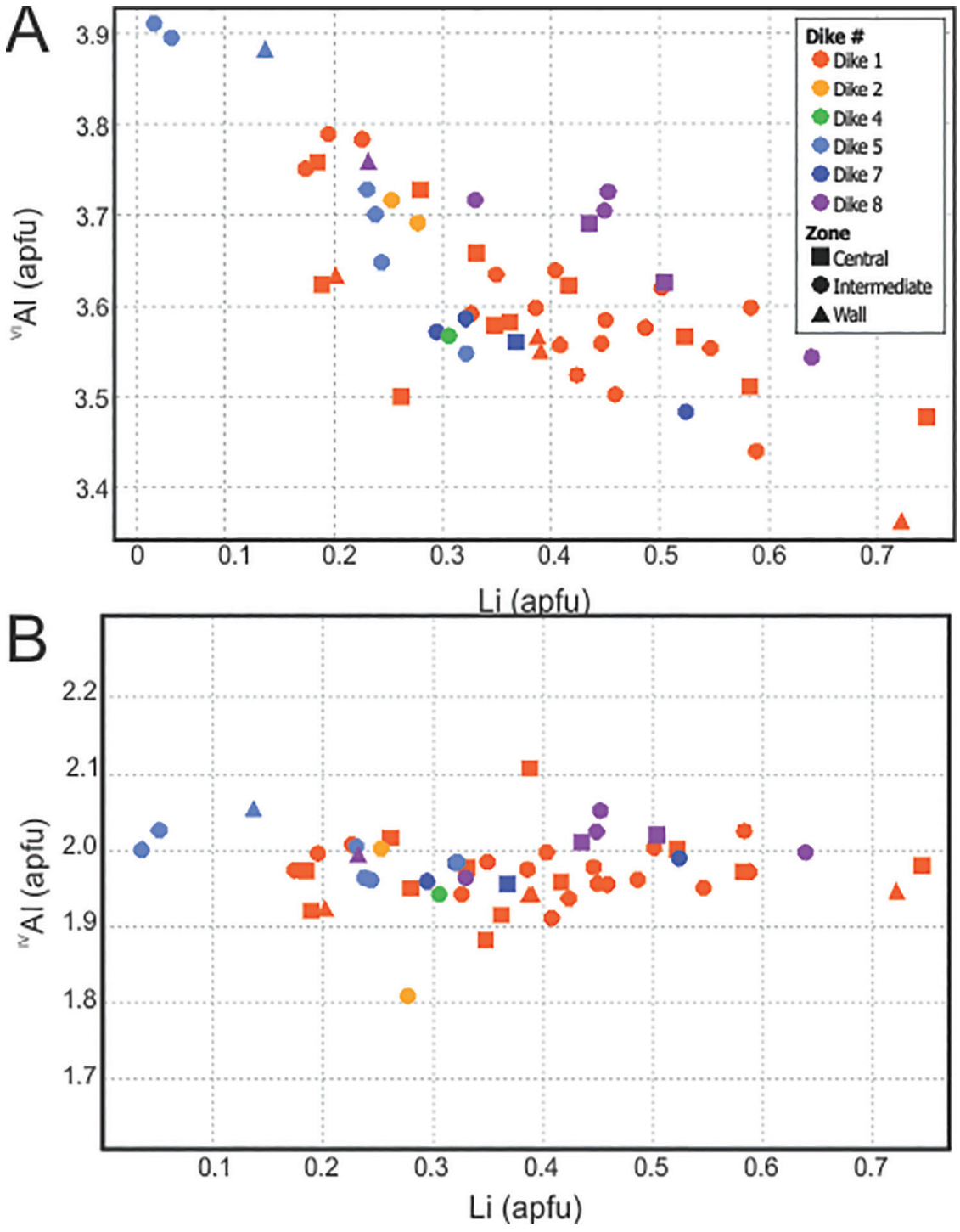

Figure 6. Lithium and Al substituions in white mica: **A)** Li vs. ^{VI}Al ; **B)** Li vs. ^{IV}Al. All values in apfu.

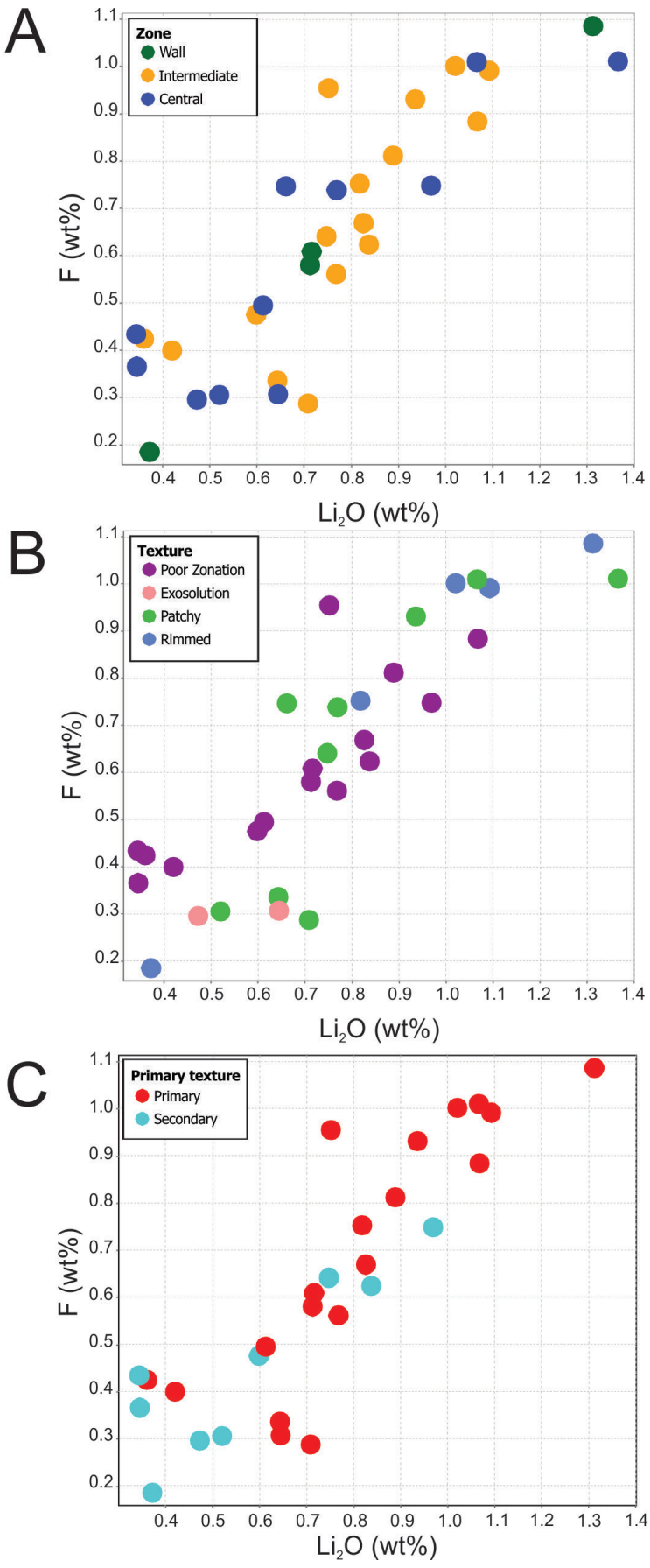

Figure 7. Content of Li_2O vs. F (wt%) comparison of Dike 1 by: **A)** pegmatite zone **B)** grain texture **C)** primary vs. secondary.

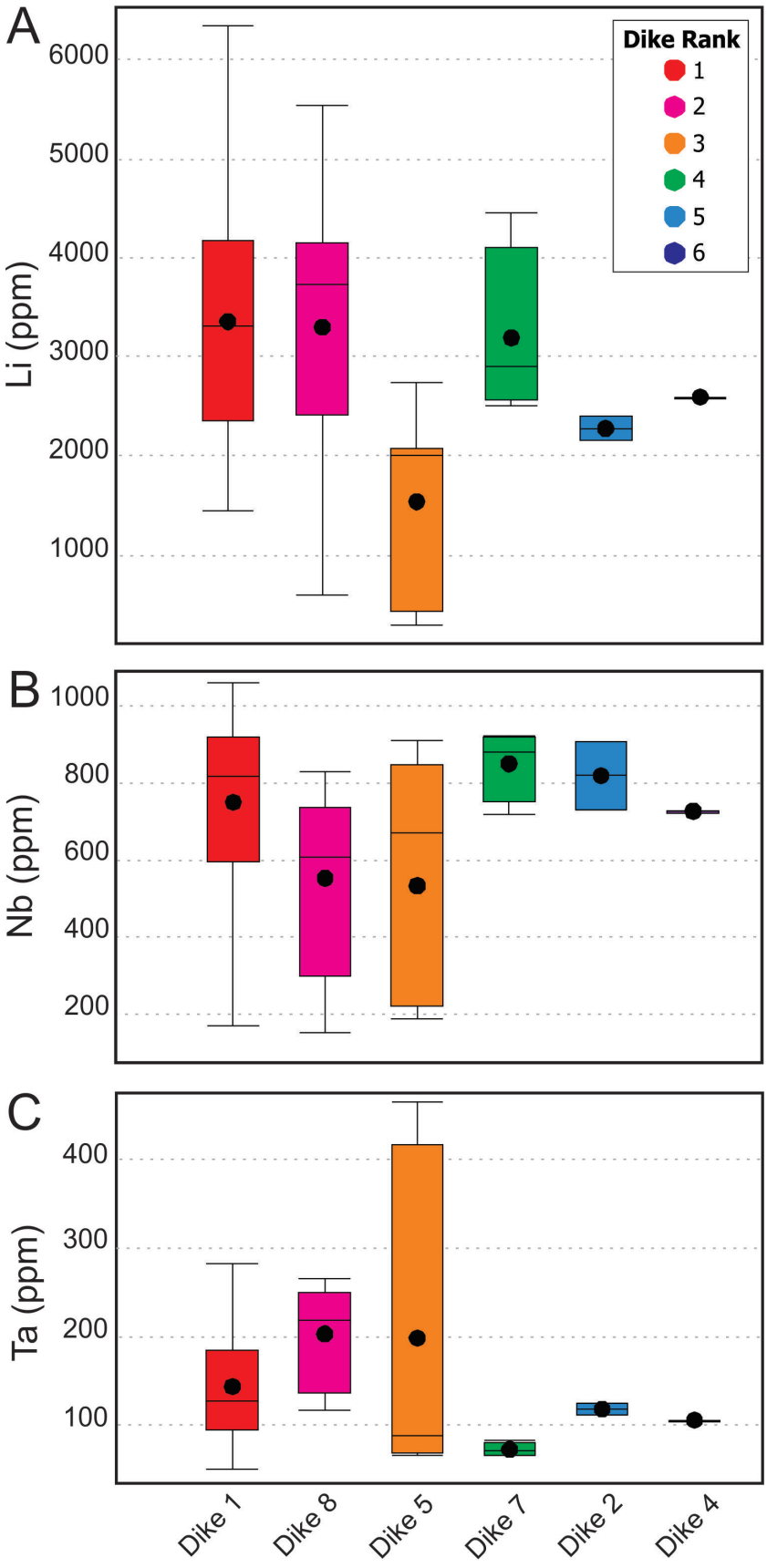

Figure 8. Concentration ranges from LA-ICP-MS analyses of white mica grains in each dike: **A)** Li, **B)** Ta and **C)** Nb concentrations (ppm). Dikes are ordered by rank of increasing Li_2O mineralization. Center line is median, black dot is mean.

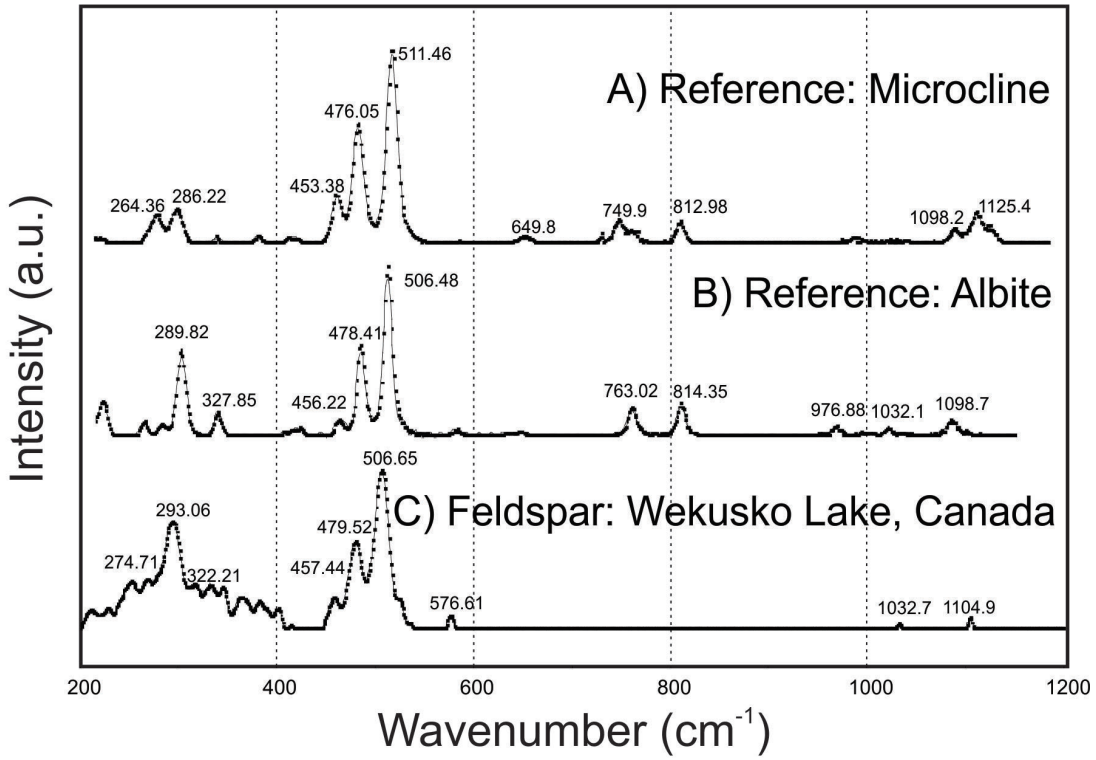

Figure 9. Reference Raman spectra and portable Raman spectra (RRUFF, 2019a;b, Microcline R040154; Albite R040068) for **A)** microcline **B)** albite and **C)** unknown feldspar from Wekusko Lake pegmatites.

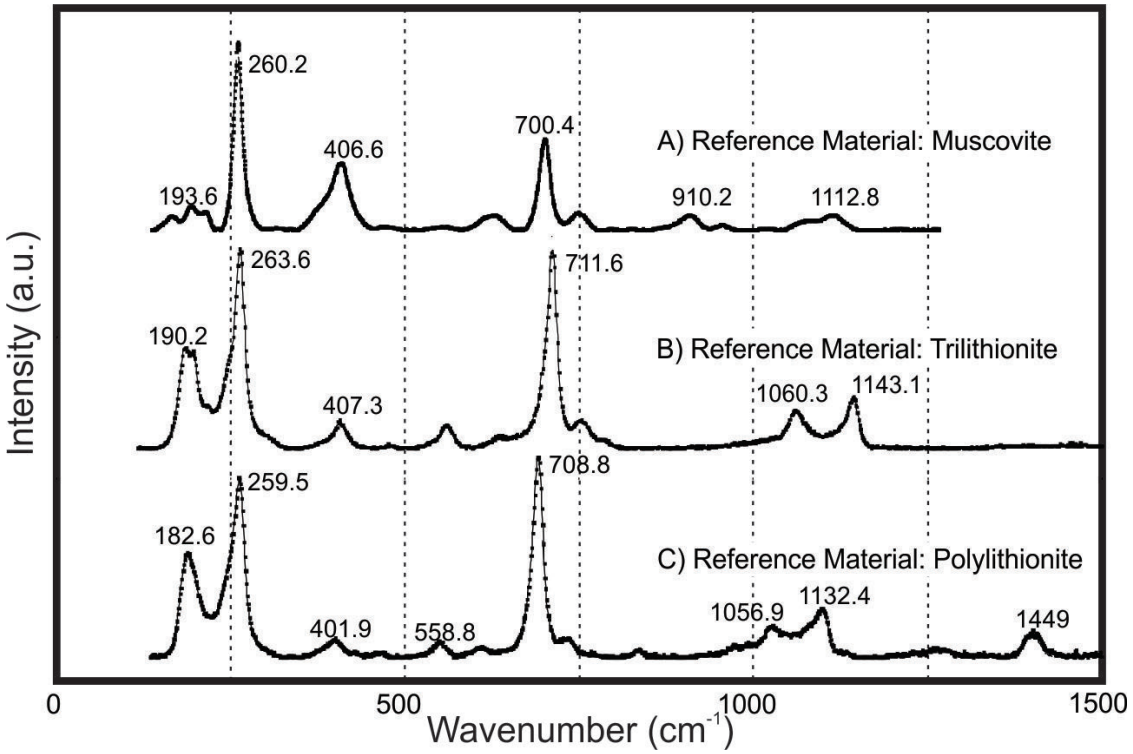

Figure 10. Raman spectra of reference white micas **A)** muscovite (RRUFF Muscovite R040104, 2019c), **B)** trilithionite (RRUFF Trilithionite R040101, 2019d), **C)** polylithionite (RRUFF Polylithionite R050132, 2019e).

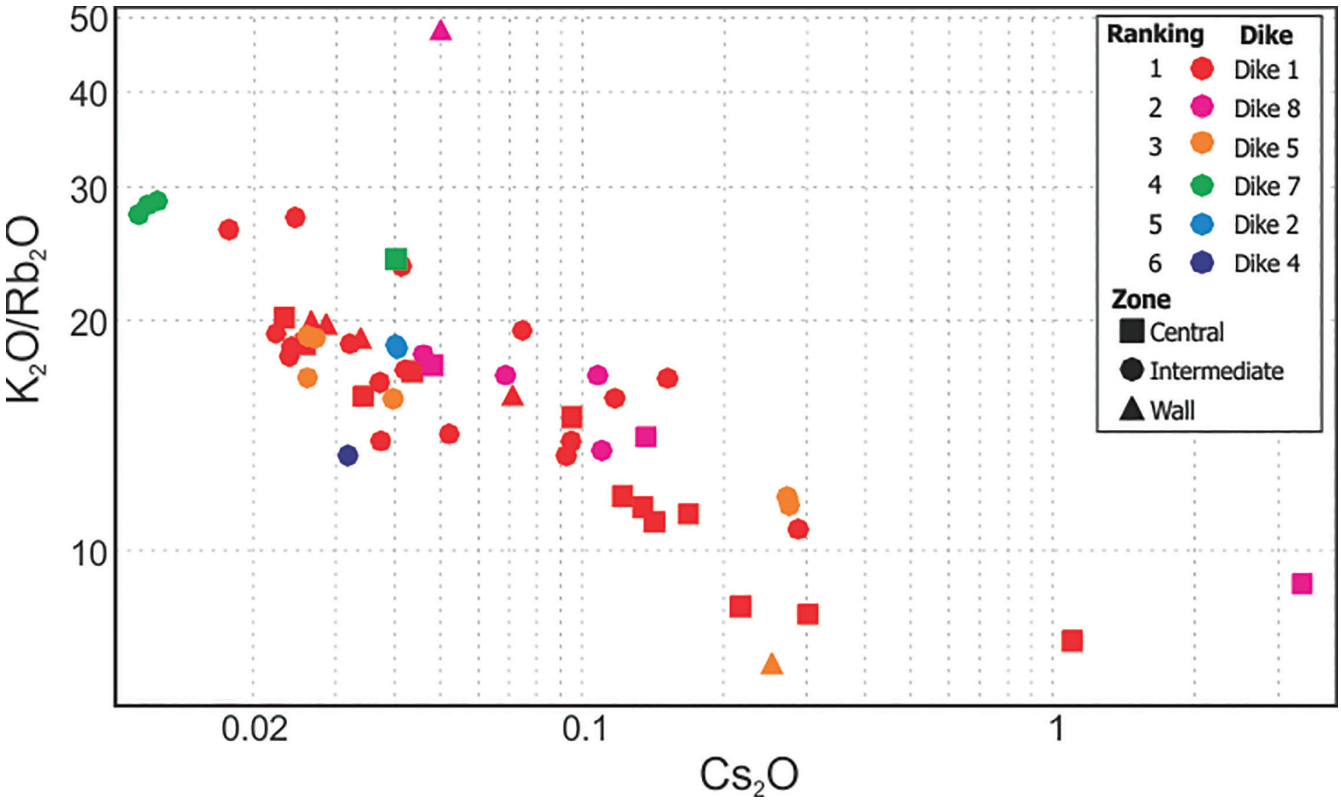

Figure 11. Log scale graph of white mica grains showing K_2O/Rb_2O vs Cs_2O (wt%). Colour describes dike sampled and are listed in order of ranking. Shape describes sampled zone.

Within a single dike, white micas from the wall zone are the least evolved, and white micas from the central zone are the most evolved. This result is somewhat expected taking into account the zonation described for the studied pegmatites (Benn et al., 2018a). The variations between the zones show that the Li content of white mica and other incompatible elements (i.e., Nb and Ta) overlaps but also increases toward the central zone. This may suggest that incorporation of Li in white mica is also controlled by the crystallization of other Li minerals and not only its availability in the melt.

The ratio K/Rb vs Cs has been used extensively to determine the degree of chemical evolution of white mica in pegmatites (e.g., Černý and Burt 1984; Černý et al. 1985; Lichtervelde et al, 2007) (Figure 11). Our results show that Dike 5 is the most evolved (low K/Rb and high Cs), followed by Dike 1 and 8. Dikes 4, 7 and 2 all plot as primitive. Our data shows that there is no clear direction of fractionation for the Green Bay Group of pegmatites. Dikes 1 and 8 are the most southwestern and northeastern dikes on the studied area, respectively (Figure 2) and are the most fractionated of the dikes. Dike 5 is in the middle of the dike swarm, with the less evolved dikes between Dike 1, 5 and 8. However, fractionation has not been studied at a regional level for the entire pegmatite field. It is possible that fractionation is a factor of depth of emplacement and the dikes have been cut at different levels (i.e. Dike 5 was emplaced above Dike 2 but at surface we are seeing the very bottom of Dike 5 and the top of Dike 2). Regional folding is another factor to consider when determining fractionation direction.

Much of the chemical variation with white mica is not evident through field observations. White mica grains can range greatly in average Li_2O composition between primary white mica grains or within white mica grains from the same zone. The textural variation observed through backscattered imaging cannot be assessed in the field. As a result, to ensure the chemical variance between white mica grains is accounted for, a statistically significant number of white mica grains should be tested before a targeted pegmatite dike is assessed for potential Li mineralization.

The comparison of spectra from high and low Li white mica with the Raman field portable device does not show difference in peak height ratios or peak shift that is readily visible. This may be due to the high degree of background noise, which overwhelms any of the expected changes, or the range of Li contents observed in this study.

CONCLUSION

White mica shows promise to be an effective indicator mineral for identifying prospective Li-bearing pegmatites. For the studied pegmatites, it does not matter from which

zone of the pegmatite the samples are collected, but chemical variation should be accounted for by testing a statistically significant number of white mica grains. Multiple white mica samples are required with both field and laboratory techniques as there is an overlap of Li concentrations between prospective and non-prospective dikes. It is easiest to obtain reliable results with field techniques if larger grains are selected for analyses. Mineral chemistry of white mica is also useful for identifying dikes with potential for rare metals such as Nb and Ta. This is very useful as columbite group minerals are typically very fine-grained and can be difficult to identify in the field.

The field portable Raman spectrometer, while useful for mineral identification, was not able to detect a significant Li signature at the concentrations tested (1500-6000ppm). The use of portable LIBS to detect Li contents within white mica is a promising technique. It is currently being used successfully in Australia to map the Li concentrations of spodumene in pegmatites (Sweetapple and Tassio, 2015). The use of field portable techniques and real-time results in exploration will provide geologists with a powerful tool for more effective drilling and field exploration.

FUTURE STUDIES

The Li contents of white micas are currently being acquired using a portable LIBS. These results will be compared to the LA-ICP-MS and EPMA results. The use of short wavelength infrared was not investigated in this study, in part because it is difficult to quantify F-OH variation in OH sites, which is needed to estimate lithium contents.

ACKNOWLEDGEMENTS

This study is supported by a Targeted Geoscience Initiative Phase 5 Program grant to R. Linnen from the Department of Natural Resources Canada. FAR Resources Ltd. is thanked for access to drill core and field support. Field and logistical support from the Manitoba Geological Survey are also gratefully acknowledged.

REFERENCES

Benn, D., Linnen, R.L. and Martins, T., 2018a. Geology and bedrock mapping of the Wekusko Lake pegmatite field (northeastern block), central Manitoba (part of NTS 63J13); *in* Report of Activities 2018, Manitoba Growth, Enterprise and Trade, Manitoba Geological Survey, p. 79–88.

Benn, D., Martins, T., Linnen, R.L., Ziehlke, J. and Singh, J., 2018b. Bedrock geology of the Wekusko Lake pegmatite field (northeastern block), central Manitoba (part of NTS 63J13); Manitoba Growth Enterprise and Trade, Preliminary Map PMAP2018-2, scale 1:4000.

Benn, D., Martins, T. and Linnen, R.L., 2019. Interpretation of U-Pb isotopic dates of columbite-group minerals in pegmatites, Wekusko Lake pegmatite field, central Manitoba (part of NTS 63J13); *in* Report of Activities 2019, Manitoba Agriculture and Resource Development, Manitoba Geological Survey, p. 52–59.

Černý, P., and Burt D. M., 1984. Paragenesis, crystallochemical characteristics, and geochemical evolution of micas in granite pegmatites. in Micas SW, Bailey (ed) Reviews *in* Mineralogy, vol 13, p 257–292.

Černý, P. and Ercit, T. S., 2005. The classification of granitic pegmatites revisited. The Canadian Mineralogist, v. 43, p. 2005-2026.

Černý, P., Trueman, D. L., Zeihlke, D. V., Goad, B. E. and Paul, B. J., 1981. The Cat Lake-Winnipeg River and the Wekusko Lake pegmatite fields, Manitoba. Winnipeg, Man.: Manitoba, Dept. of Energy and Mines, Mineral Resources Division

Černý, P., Meintzer R. E., and Anderson A. J., 1985. Extreme fractionation in rare-element granitic pegmatites: selected examples of data and mechanisms. Canadian Mineralogist, v.23, p. 381–421.

Connors, K., Ansdell, K. and Lucas, S., 1999. Coeval sedimentation, magmatism, and fold-thrust development in the Trans-Hudson Orogen: Propagation of deformation into an active continental arc setting, Wekusko Lake area, Manitoba. Canadian Journal of Earth Sciences, v. 36, p. 275-291.

Connors, K., Ansdell, K. and Lucas, S., 2002. Development of a transverse to orogen parallel extension lineation in a complex collisional setting, Trans-Hudson Orogen, Manitoba, Canada. Journal of Structural Geology, v. 24, p. 89-106.

David, J., Bailes, A. H., and Machado, N., 1996. Evolution of the Snow Lake portion of the Paleoproterozoic Flin Flon and Kisseynew belts, Trans-Hudson Orogen, Manitoba, Canada. Precambrian Research, v. 80, p. 107-124

FAR Resources Ltd., 2017. Phase 3 Drilling; FAR Resources Ltd. URL <https://www.farresources.com/phase-3-drilling/> [August, 2018]

FAR Resources Ltd., 2018. Phase 4 Drilling; FAR Resources Ltd. URL <https://www.farresources.com/phase-4-drilling/> [August, 2018]

FAR Resources Ltd., 2019. Far Resources discovers five new pegmatite dykes and significantly expands pegmatite field at the Zoro Lithium Project, Manitoba; FAR Resources Ltd., URL <https://farresources.com/news/2019/2/18/far-resources-discovers-five-new-pegmatite-dykes-and-significantly-expands-pegmatite-field-at-the-zoro-lithium-project-manitoba/> [March, 2019].

Gordon, T. M., Hunt, P. A., Bailes, A. H., and Syme, E. C., 1990. U-pb ages from the Flin Flon and Kisseynew belts, Manitoba; chronology of crust formation at an early Proterozoic accretionary margin. Special Paper - Geological Association of Canada, v. 37, p. 177-199.

Hoffman, P., 1989. Precambrian geology and tectonic history of North America. The Geology of North America—An Overview, Geological Society of America, The Geology of North America, v. A, p. 447–512.

Hoffman, P., 1988. United Plates of America, The Birth of a Craton: Early Proterozoic Assembly and Growth of Laurentia. Annual Review of Earth and Planetary Sciences, v. 16, p. 543–603.

Lichtervelde, M. V., Grégoire, M., Linnen, R. L., Béziat, D., and Salvi, S., 2007. Trace element geochemistry by laser ablation ICP-MS of micas associated with Ta mineralization in the Tanco pegmatite, Manitoba, Canada. Contributions to Mineralogy and Petrology, v. 155, p. 791–806.

Lucas, S., White, D., Hajnal, Z., Lewry, J., Green, A., Clowes, R., Zwanzig, H., Ashton, K., Schledewitz, D., Stauffer, M., Norman, A., Williams, P., and Spence, G., 1994. Three-dimensional collisional structure of the Trans-Hudson Orogen, Canada. Tectonophysics, v. 232, p. 161–178.

NATMAP Shield Margin Project Working Group, 1998. Geology, NATMAP shield margin project area (Flin Flon Belt), Manitoba/Saskatchewan; Geological Survey of Canada, Map 1968A, scale 1:100 000.

Natural Resources Canada, 2020. The Canadian Minerals and Metals Plan, Action Plan, 2020. Introducing the Pan-Canadian Initiatives., URL <https://www.minescanada.ca/sites/default/files/cmmp-actionplan2020_rev52_feb_29_2020-a_en.pdf> [March 2020]

RRUFF™, 2019a. *Microcline R040154*., URL <https://rruff.info/microcline/display=default/R040154> [March, 2019]

RRUFF™, 2019b. *Albite R040068*. URL <https://rruff.info/albite/display=default/R040068> [March, 2019]

RRUFF™, 2019c. *Muscovite* R040104., URL <http://rruff.info/muscovite/display=default/R040104> [March 2019]

RRUFF™, 2019d. *Polylithionite* R050132. URL <http://rruff.info/polylithionite/display=default/R050132> [March 2019]

RRUFF™, 2019e. *Trilithionite* R040101. URL <http://rruff.info/trilithionite/display=default/R04010> [March 2019]

Schneider, D., Heizler, M., Bickford, M., Wortman, G., Condie, K., and Perilli, S., 2007. Timing constraints of orogeny to cratonization: Thermochronology of the Paleoproterozoic Trans-Hudson Orogen, Manitoba and Saskatchewan, Canada. Precambrian Research, v. 153, p. 65–95.

Sweetapple, M. T., and Tassios, S., 2015. Laser-induced breakdown spectroscopy (LIBS) as a tool for in situ mapping and textural interpretation of lithium in pegmatite minerals. American Mineralogist, v. 100, p. 2141–2151.

Tindle, A. G., and Webb, P. C., 1990. Estimation of lithium contents in trioctahedral micas using microprobe data: application to micas from granitic rocks. European Journal of Mineralogy, v. 2, p. 595–610.

Tischendorf, G., Gottesmann, B., Förster, H.-J., and Trumbull, R. B., 1997. On Li-bearing micas: estimating Li from electron microprobe analyses and an improved diagram for graphical representation. Mineralogical Magazine, v. 61, p. 809–834.

Tischendorf, G., Förster, H.-J., Gottesmann, B., and Rieder, M., 2007. True and brittle micas: composition and solid-solution series. Mineralogical Magazine, v. 71, p. 285–320.

The geochemistry of thallium and its isotopes in rare-element pegmatites

I.J. Jacques[1], A.J. Anderson[1], and S.G. Nielsen[2,3]

Jacques, I.J., Anderson, A.J., and Nielsen, S.G., 2021. The geochemistry of thallium and its isotopes in rare-element pegmatites; in *Targeted Geoscience Initiative 5: grant program final reports (2018-2020), Geological Survey of Canada, Open File 8755, p. 59–84. https://doi.org/10.4095/328983*

Abstract: The Tl isotopic and trace element composition of K-feldspar, mica, pollucite and pyrite from 13 niobium-yttrium-fluorine (NYF)-type and 14 lithium-cesium-tantalum (LCT)-type rare-element pegmatites was investigated. In general, the ε^{205}Tl values for K-feldspar in NYF- and LCT-type pegmatites increases with increasing magmatic fractionation. Both NYF and LCT pegmatites display a wide range in ε^{205}Tl (-4.25 to 9.41), which complicates attempts to characterize source reservoirs. We suggest ^{205}Tl-enrichment during pegmatite crystallization occurs as Tl partitions between the residual melt and a coexisting aqueous fluid or flux-rich silicate liquid. Preferential association of ^{205}Tl with Cl in the immiscible aqueous fluid may influence the isotopic character of the growing pegmatite minerals. Subsolidus alteration of K-feldspar by aqueous fluids, as indicated by the redistribution of Cs in K-feldspar, resulted in ε^{205}Tl values below the crustal average (–2.0 ε^{205}Tl). Such low ε^{205}Tl values in K-feldspar is attributed to preferential removal and transport of ^{205}Tl by Cl-bearing fluids during dissolution and reprecipitation. The combination of thallium isotope and trace element data may be used to examine late-stage processes related to rare-element mineralization in some pegmatites. High ε^{205}Tl and Ga in late-stage muscovite appears to be a favorable indicator of rare-element enrichment LCT pegmatites and may be a useful exploration vector.

[1]Department of Earth Sciences, St. Francis Xavier University, Antigonish, Nova Scotia, Canada
[2]NIRVANA laboratories, Woods Hole Oceanographic Institute, Woods Hole, MA, USA
[3]Department of Geology and Geophysics, Woods Hole Oceanographic Institution, Woods Hole, MA, USA

INTRODUCTION

Non-traditional isotopes such as Li, Mg, Si, Cl, Cr, Re, Ni, Cu, Zn, Ge, Se, Mo, Hg and Tl (Teng et al., 2017) are increasingly used as geochemical tracers in ore deposit investigations. The stable isotopes of thallium are the heaviest of the non-traditional isotopes and their mass difference is small enough to negate mass fractionation during magmatic processes (Nielsen et al., 2006a, 2007, 2009a, 2015, 2016, 2017b; Prytulak et al., 2016; Shu et al., 2017; Blusztajn et al., 2018). Recent studies of igneous rocks and associated ore deposits display a large range of thallium isotope ratios, which is attributed in part to hydrothermal alteration processes (Baker et al., 2010; Hettmann et al 2014a,b; Nielsen et al., 2015; Fitzpayne et al., 2018; Rader, 2018).

Compared to previous Tl isotopic studies of ore deposits (Baker et al., 2010; Hettmann et al., 2014a,b; Fitzpayne et al., 2018), the study of granitic pegmatites offer several advantages. These include: 1) high concentrations of Tl in highly evolved pegmatites (Černý et al. 1985), 2) most of the Tl in the melt is concentrated in K-feldspar and mica, and 3) Tl behaves as a lithophile element because granitic pegmatites contain negligible amounts of sulfur.

In the present study, we examine the trace element and Tl isotopic compositions of K-feldspar and muscovite from different rare element pegmatites. Primary, blocky K-feldspar crystals were sampled from 14 Lithium-Cesium-Tantalum (LCT) type pegmatites, 13 Niobium-Yttrium-Fluorine (NYF)-type rare element pegmatites, 1 mixed-type pegmatite and 1 anatectic pegmatite. Isotopic variations within the Tanco pegmatite, Manitoba, and the Kamativi pegmatite district, Zimbabwe, were evaluated in light of mineral paragenesis, subsolidus alteration, and the degree of fractionation of the pegmatite melt.

BACKGROUND

Thallium Geochemistry

Thallium is the 87th element in the periodic table with an estimated concentration of 1-2 ppb in the mantle (Prytulak et al., 2017), 10's to 100's of ppb in igneous systems (McDonough and Sun, 1995; Prytulak et al., 2017; Rader et al., 2018) and approximately 490 ppb in the continental crust (Heinrichs et al., 1980). Thallium occurs as one of two stable isotopes: ^{203}Tl and ^{205}Tl, with abundances of about thirty and seventy percent, respectively (Hoefs, 2009; Rader et al., 2018). Thallium exists in either the monovalent or the trivalent state but occurs predominantly as Tl^+ (Schauble, 2007; Nielsen et al., 2009b, 2017; Prytulak et al., 2017). Although Tl displays both chalcophile and lithophile tendencies, Tl^+ tends to behave geochemically like a large ion lithophile element such as rubidium and tends to proxy for K^+ in K-bearing minerals (Rankama, 1949; Hettman et al., 2014a; Prytulak et al., 2017). Despite the similar ionic radii of Tl^+ and Rb^+ (1.49 Å), the much higher electronegativity of Tl (1.5 compared to 0.8 for Rb) makes it less stable in the feldspar structure than Rb, resulting in similar distribution patterns as Cs (Heier, 1962; Heinrichs et al., 1980).

The variation in Tl isotopes is reported as ε^{205}Tl units, which is the difference in ^{205}Tl to ^{203}Tl relative to a standard such as NIST SRM 997 (Nielsen et al., 2017). Epsilon ^{205}Tl units are formally expressed as

$$\varepsilon^{205}Tl_{sample} = 10^4 \times \left(\frac{\left(\frac{^{205}Tl}{^{203}Tl}\right)_{sample}}{\left(\frac{^{205}Tl}{^{203}Tl}\right)_{standard}} - 1 \right) \quad (1)$$

Fractionation of Tl isotopes is due mainly to a nuclear field shift (NFS) effect (Bigeleison, 1996; Schauble, 2007; Moynier et al., 2013; Yang and Liu, 2015; Fuji et al., 2013). The NFS is the result of differences in the size and surface charge density of the nucleus, and the electron density between isotopes, which causes the ground state to shift (Bigeleison, 1996). Theoretical work (Fujii et al., 2011) and experimental studies of aqueous Tl^+ and Tl^{3+} in HCl and $C_2H_4Cl_2$ at room temperature (Fujii et al., 2013) indicates fractionation of Tl isotopes by NFS can occur by redox state changes and association with various ligands. For redox-related isotope fractionation, ^{205}Tl is more energetically favourable as Tl^{3+} while ^{203}Tl is more energetically favourable as Tl+ (Schauble, 2007; Peacock and Moon, 2012; Yang and Liu, 2016; Fang and Liu, 2019). Redox change-induced isotope fractionation is proposed as the mechanism by which birnessite (Na,Ca)0.5(Mn^{4+},Mn^{3+})2O4 · 1.5 H2O preferentially incorporates ^{205}Tl (Peacock and Moon, 2012; Nielsen et al., 2013). Fang and Liu (2019) show that the reduction in electronic density at the Tl nucleus by bonding to anions can cause preferential bonding to ^{205}Tl such that the relative preference for heavy Tl is O2- < F- < Cl- < Br-.

Previous investigations show that the average ε^{205}Tl for the continental crust and mantle is –2.0 ± 0.5 (Nielsen et al., 2005, 2006a,b, 2007). According to Prytulak et al. (2016), magmatic processes have little effect on Tl isotope fractionation. Consequently, several studies have used Tl isotopes to trace subducted Fe-Mn-rich sediments (Rekhämper et al., 2002; Nielsen et al., 2006a, 2007, 2009a, 2015, 2016, 2017b; Shu et al., 2017; Blusztajn et al., 2018). Generally, these studies show that variability of ε^{205}Tl in subduction-related lavas may be attributed to inheritance of Fe-Mn sediments.

Variations in ε^{205}Tl in igneous rocks may also be due to subsolidus processes. Studies of altered oceanic crust show that Tl isotope signatures are likely inherited from Fe-Mn-bearing, sediment-derived fluids (Nielsen et al., 2015). Hettmann et al (2014a) proposed that Tl isotope fractionation in the alkaline Ilimaussaq complex, Greenland, occurred during the exsolution of an aqueous phase from the magma, which then caused alteration of early magmatic

units. Similarly, the correlation between Tl/As ratios and ε^{205}Tl of sulfide minerals from the Lengenbach sulfide deposit suggests that the interaction of hydrothermal fluids with the remaining sulfide melt resulted in ^{205}Tl enrichment in the remaining melt (Hettmann et al., 2014b). Studies of porphyry Cu deposits suggest late fluids affected Tl isotope ratios due to either fluid-mineral partitioning or P-T-X-*f*O2 evolution of hydrothermal fluids (Baker et al., 2010; Fitzpayne et al., 2018). Rader et al. (2018) suggested that variations in ε^{205}Tl is related to crystal-chemical controls. Their results show that in a variety of rock types, Fe-rich micas, feldspar and sulfides display low, intermediate and high ε^{205}Tl values, respectively. In a study of the waste products from pyrite smelting, Liu et al (2020) demonstrated that mass fractionation might cause light Tl isotopes to partition into a volatile phase while heavy Tl condenses.

Pegmatites

The term "pegmatite" is used to describe a rock with grain sizes typically greater than 2.5 cm. London (2008) proposed the following definition:

> "An essentially igneous rock, commonly of granitic composition, that is distinguished from other igneous rocks by its extremely coarse grain-size, or by an abundance of crystals with skeletal, graphic, or other strongly directional growth-habits. Pegmatites occur as sharply bounded homogenous to zoned bodies within igneous or metamorphic hosts."

This study examines granitic pegmatites and thus all references to pegmatites refer to granitic bulk compositions. Pegmatites are divided into five classes: Abyssal, Muscovite, Muscovite–Rare-element, Rare-element and Miarolitic, and the rare-element class is divided into three families, which denote geochemistry and source rocks: lithium-cesium-tantalum (LCT), niobium-yttrium-fluorine (NYF) and mixed (Černý, 1991; Černý and Ercit, 2005). As their names imply, LCT pegmatites contain Li, Cs and Ta minerals and are the fractionation products of granitic melts derived by partial melting of crustal rocks in orogenic settings. In contrast, NYF pegmatites are noted for the presence in Nb-, Y- and F-bearing minerals and are generally associated with A-type magmatism (Martin and de Vito, 2005; Černý, 1991a,b; Černý and Ercit, 2005). Mixed pegmatites are those that exhibit both LCT and NYF characteristics.

The traditional view of pegmatite petrogenesis is that they are derived from a parental granite via fractional crystallization (Černý, 1991b); however, formation by direct anatexis has also been proposed (Stewart, 1978; Simmons et al., 2016; Webber et al., 2019). Fractionation of pegmatite forming melts results in an enrichment in incompatible elements and volatile components such as H_2O, B, F and P (Jahns and Burnham, 1969; London, 1987; Kontak et al., 2001; London, 2008; Simmons and Webber, 2008; Nabelek et al., 2010). The concentration of these components affects melt viscosity, nucleation rates, solidus temperatures, electrical conductivity, compressibility and diffusivity (Pichavant 1981; Holtz et al. 1993; Nabelek et al. 2010; Manning, 2018). The most evolved and volatile-rich melts may migrate further from their source into distal country rocks (Baker, 1998; Nabelek et al., 2010), resulting in regional zonation (Černý, 1991b). Despite the enrichment in fluxes and rare elements, the bulk composition of pegmatites is essentially the same as in normal granites (Černý, 1991a; see Stilling et al., 2006 and Roda-Robles et al., 2015).

The internal evolution of pegmatites is summarized in three main petrogenetic models. Jahns and Burnham (1969) proposed that pegmatites are the product of crystallization of H_2O-saturated silicate melt that formed by early crystallization of primarily anhydrous phases. London (2008) proposed that pegmatite textures formed by constitutional zone refining. According to this model, undercooling of a pegmatite melt results in rapid crystallization and the accumulation of fluxes and incompatible elements in a boundary layer at the crystallization front. This H2O-undersaturated boundary layer facilitates rapid diffusion of essential components and the growth of large crystals. A third model proposes that an initially homogeneous granitic melt separates into two immiscible silicate liquids of different compositions (type-A and type-B melts). Large crystals typical of pegmatites crystallize from a hydrous alkaline type-B melt (Borisova et al., 2012; Thomas and Davidson, 2008; Veksler et al., 2002).

Local Geology of the Tanco Pegmatite

The Tanco pegmatite, located 110 miles northeast of Winnipeg, Manitoba, at Bernic lake (Crouse and Černý, 1972), is an important rare metal deposit with a reserve of 7.3 Mt of Li_2O, 2.1 Mt of Ta_2O_5, 0.3 Mt of Cs_2O, 0.9 Mt of BeO and 0.1 Mt of Rb_2O (Černý, 1991a and references therein). Since the mid 1950's, the Tanco pegmatite has been mined for Li, Cs, Ta and Rb (Brown, 2001; Crouse and Černý, 1972). The 2640 Ma (Stilling et al., 2006; Camacho et al., 2012) pegmatite belongs to the petalite subtype of the LCT rare-element pegmatites (Brown, 2001). It occurs within the metagabbro, metadiorite and granodiorite of the Bernic Lake Formation of the 2750-2715 Ma Bird River Greenstone Belt within the Superior Province (Brown, 2001; Stilling et al., 2006). Tanco contains 9 zones (Fig. 1): 1) border zone of albite, quartz and tourmaline; 2) wall zone of albite, quartz, microcline-perthite and tourmaline; 3) albitic aplite containing albite and quartz; 4) the lower intermediate zone contains microcline-perthite, albite, quartz, spodumene and amblygonite; 5) the upper intermediate zone consists of spodumene, quartz, amblygonite and petalite; 6) the central intermediate zone with an assemblage of microcline-perthite, albite, quartz, beryl and wodginite; 7) quartz zone; 8) pollucite zone; 9) lepidolite zone (Crouse and Černý, 1972).

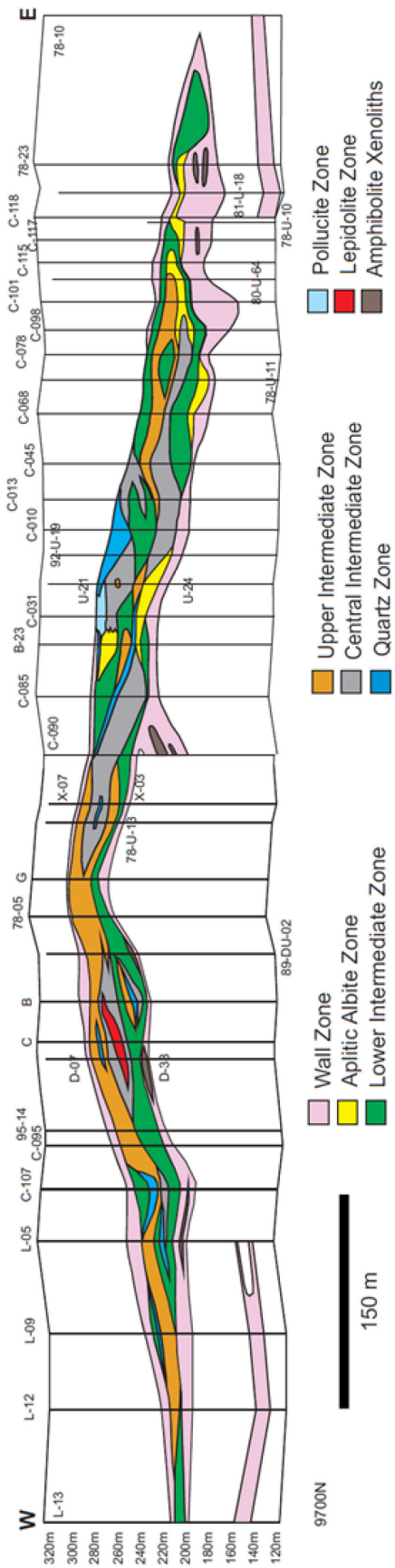

Figure 1. Cross section of the Tanco pegmatite modified after Černý et al. (2005).

Local Geology of the Pegmatites at Kamativi

The LCT pegmatites at Kamativi, Zimbabwe, occur within the Dete-Kamativi Inlier and are hosted in the supracrustal gneisses and pelitic schists of the Palaeoproterozoic Magondi Belt. The Dete-Kamativi inlier consists of granodioritic gneisses, granites and metamorphosed supracrustal sequences that are divided in four northeast-southwest belts known as the Kamativi, Tshontanda, Inyantue and Malaputese formations (Lockett 1979). Cassiterite and spodumene-bearing pegmatites at Kamativi occur mainly as near horizontal sheets that range up to 30 m in thickness and pinch out along strike. Spodumene, which constitute up to 15% of the pegmatite, is the dominant Li mineral. Cassiterite occurs in quartz-muscovite assemblages at the contacts and as smaller crystals disseminated in aplitic units. The average Sn grade of the pegmatites was 0.114% Sn. About 60 tons of Ta concentrates were produced at Kamativi (Melcher et al., 2015)

METHODOLOGY

Materials

Thallium isotopic ratios were determined for muscovite and K-feldspar, which are major sinks for Tl in granitic pegmatites. Blocky K-feldspar crystals were collected from 14 LCT, 13 NYF, 1 mixed-type pegmatite, and 1 anatectic pegmatite. The location of each pegmatite is shown in Figure 2. Pollucite, pyrite, and different paragenetic types of mica were sampled from the Tanco pegmatite and muscovite from several pegmatites at the Kamativi mine, Zimbabwe, were analyzed. Thallium isotopic ratios were also determined for obsidian from Lake County, Oregon (LCO) and from Macusani, Peru (JV-1). Thin sections of all minerals were examined using a polarizing microscope in order to identify alteration and inclusion-free sites for laser ablation analysis, and for textural characterization. Thin, inclusion-free sheets of mica were separated under a binocular microscope for Tl isotopic analysis.

Analytical methods

Electron probe microanalysis

Major element analyses of mineral grains were made using a JEOL JXA-733 electron probe microanalyzer (EPMA) at the Microscopy and Microanalysis Laboratory, University of New Brunswick. The microprobe was operated at an accelerating voltage of 15 kV and a probe current of approximately 30 nA using Geller MicroAnalytical dSpec

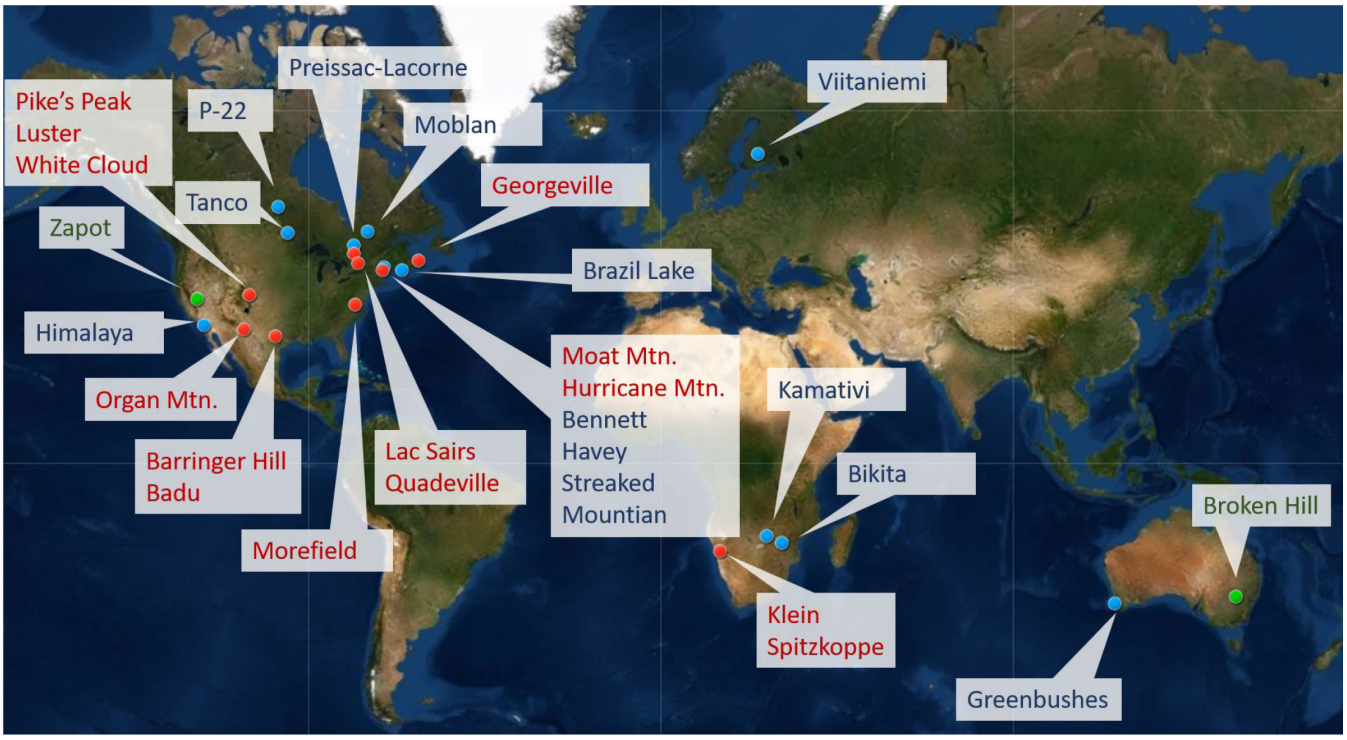

Figure 2. Locations of pegmatites sampled for this study. Blue points and text refer to LCT-type pegmatites, red points and text refer to NYF-type pegmatites, and green points refer to a mixed-type (Zapot) and an anatectic pegmatite (Broken Hill). Scale ~ 1:170M Using: ArcGIS Enterprise 10.8.1 Redlands, CA: Environmental Systems Research Institute, Inc, 2020.

v. 4.36.0 and dQuant32 v 4.36.0 automation. Elemental concentrations were calculated from measured intensity ratios using CITZAF v 4.01 (California Institute of Technology) (Armstrong, 1982; 1984). Potassium-feldspar and mica samples were analyzed 3-5 times on average. Backscatter electron images were obtained for all K-feldspar samples except for sample PMB-19. Major element concentrations for Tanco K-feldspar are from Brown (2001). Various primary and secondary standards were employed based on the major elements and sample mineralogy to ensure data quality.

Inductively coupled plasma-mass spectrometry

The major element concentration for the muscovite samples from the Kamativi pegmatites were measured using a SCIEX ELAN ® model *250* inductively coupled plasma mass spectrometer (ICP-MS) at Memorial University of Newfoundland. A standard HF/HNO_3 solution was used to digest 0.1 g of sample, followed by analysis of the solution by ICPMS. Any sample material not dissolved in HF/HNO_3 was reacted with HCl/HNO3 and any remaining sample was filtered for insoluble residue prior to analyses. A reagent blank and CANMET geological reference standard SY-2 syenite (Gladney and Roelandts, 2007) was added for quality control.

Laser ablation- ICP-MS

A Resonetics S-155-LR 193mm Excimer laser ablation system coupled with an Agilent 7700x quadrupole ICP-MS with an external rotary pump at the University of New Brunswick, Earth Sciences Department was used to measure trace element concentrations. Ultra pure nitrogen (2 mL/min), ultra pure helium (300 mL/min) and argon (930 mL/min) were used as carrier gasses. Samples were ablated for 40 seconds using an ablation spot size of 45µm, at a pulse rate of 3.5 Hz and laser fluence of 4 J/cm². Data reduction was conducted using Iolite software (Paton et al. 2011) which converts the raw counts per second into parts per billion (ppb) using National Institute of Standards and Technology Standard Reference Material (NIST SRM 610 and 612). Major oxide ($Al2O_3$ and SiO_2) data obtained from EMPA were used for internal standardization of LA-ICP-MS analyses.

Trace element distribution maps were produced using LA-ICP-MS by rastering the laser along a 2-dimenstional grid on the sample. Mapping of samples with LA-ICP-MS was done using a spot size of 24 µm, a repetition rate of 10 Hz and a scan speed of 8 µm/s. The high sensitivity of the LA-ICPMS technique afforded mapping of all trace elements. Areas within K-feldspars from Bikita, Lac Sairs, Cross Lake and Morefield were mapped. Standard reference glasses were measured between rows in the grid to correct for instrument drift.

Multi-collector–ICP-MS

Thallium isotope ratios were measured using a multi-collector–inductively coupled plasma–mass spectrometer (MC-ICP-MS) at Woods Hole Oceanographic Institute. For MC-ICP-MS analysis, Tl is isolated by anion exchange chromatography in HF or HCl using an AG 1-X8 anion exchange resin. The solution is oxidized by adding water, which brings Tl into the trivalent state, allowing the formation of Tl-halide complexes. A resin is then introduced to the solution, causing the compounds to collect as precipitates and the halides are removed by adding a reducing agent. This process may be repeated more than once if necessary. For a more detailed explanation of the isolation of Tl, the reader is referred to Nielsen et al. (2017). After chemical isolation of Tl, the product is put into solution and a standard reference material, typically NIST SRM 981 Pb or 997, is admixed. Because Pb and Tl fractionate similarly, the known starting isotope concentrations of Pb can be used to correct for any isotope partitioning the MC-ICP-MS may incur. The solution is then introduced into the MC-ICP-MS to analyze the isotope concentrations. Procedural blanks were used to monitor for contamination (Nielsen et al., 2017).

RESULTS

Subsolidus Textures

Various perthite textures were observed in thin section and characterized according to Eyal and Shimshilashvili (1988). The samples include 4 coarse vein-patch perthite, 1 medium vein perthite, 8 coarse vein perthite (Fig. 3a), 2 fine vein perthite, 1 fine patch perthite (Fig. 3b), 1 coarse patch perthite, 3 vein perthite, 3 patch perthite (Fig. 3c),1 medium perthite and 2 coarse braid perthite (Fig. 3d). The percentage of the albite component of the perthite was determined by image analysis for some samples and visually estimated for others. The albite component of perthite ranged from about 7% in GB-12 to 42% in Barringer Hill. Most samples contained about 20-25% albite. There is no apparent correlation between the perthite textures and ε^{205}Tl.

Thallium Isotope Results

Thallium isotope data for 52 K-feldspar, 22 mica, 2 pollucite, 1 sulphide and 2 obsidian samples are presented in Tables 1-3. Isotope values range from -4.3 to 9.4 ε^{205}Tl units with an analytical precision of ± 0.5. K-feldspars from LCT pegmatites range -4.3 to 9.4 ε^{205}Tl while those from NYF pegmatites range -1.7 to 5.1 ε^{205}Tl. The ε^{205}Tl of mica range from -0.4 to 5.4. Primary micas from Tanco give a range of ε^{205}Tl from 1.9 to 2.4 ε^{205}Tl while secondary mica fall between 2.1 to 4.7 ε^{205}Tl. Kamativi muscovite range from -0.4 to 5.4.

Potassium-feldspar from LCT and NYF rare element type pegmatites exhibit some of the highest ε^{205}Tl values in crustal rocks. Rare element pegmatites show a large range in ε^{205}Tl values with some pegmatites exhibiting greater values than pelagic clays. However, the average ε^{205}Tl for pegmatites is indistinguishable from island arc basalts and ocean island basalts (Fig. 4).

Major and Trace Element Analyses

Major and trace element concentrations for K-feldspar (n=63), mica (n=22), pollucite (n=2), pyrite (n=1) and obsidian (n=2) from 29 pegmatites were measured. Tables listing all geochemical data are given in the appendices.

Figure 5 shows plots of K/Rb vs ε^{205}Tl, and Ga, Cs and Tl for K-feldspar. In agreement with previous studies (e.g., Černý et al. 1985), Ga, Cs, and Tl increase with decreasing K/Rb ratios. Figures 6-9 show the distribution of Rb and Cs within 1 × 1.4 mm areas in four K-feldspar samples (Bikita, LS-1, MOR-1, P-22). All samples show a heterogeneous distribution of B, Ca, Ba, Fe, Li, Mg, Mn, Sr and Ti, whereas Na, K, Rb, Si, Ga, Ge, Tl and Pb concentrations appear to be distributed uniformly. The distribution of Cs in K-feldspar from the Bikita and Morefield pegmatites is highly variable, whereas samples from Cross Lake (P-22) and Lac Sairs (LS-1) show no significant variability in Cs (Figs. 6-9). The concentration of Cs in sample P-22 and LS-1 is uniform except along fractures that served as conduits for late hydrothermal fluids. The samples with a heterogeneous distribution of Cs have low ε^{205}Tl values (-0.84 for MOR-1 and -2.54 for Bikita) whereas those with a homogeneous distribution have high ε^{205}Tl values (5.06 for LS-1 and 9.22 for P-22).

Major and trace element data for mica samples from the Tanco pegmatite and the Kamativi mine are given in Appendix B. According to the classification diagram of Tischendorf et al. (1997), all of the studied mica samples are muscovite, except for two Li-muscovite samples collected from zone 90 of the Tanco pegmatite (Fig. 10). Large (2-4 cm in diameter), tabular book-type muscovite crystals are interpreted to be primary magmatic in origin whereas fine-grained mica within fractures and replacing K-feldspar is designated as secondary.

The K/Rb ratios in mica samples from the Tanco pegmatite range between 2 and 23, and Kamativi muscovite samples range between 7 and 23. The concentration of Li, Cs, Tl and Ga increase with decreasing K/Rb in all mica (Fig. 11).

Analyses of pollucite from the Tanco pegmatite are shown in Appendix C. Pollucite has high concentrations of Rb (7112-9648 ppm), P (1589-1598 ppm), and Tl (89.5-129 ppm).

Major and trace element analyses on a pyrite sample from Tanco are given in Appendix D. The pyrite sample (S-40) is As-rich and shows variable concentrations in Sb

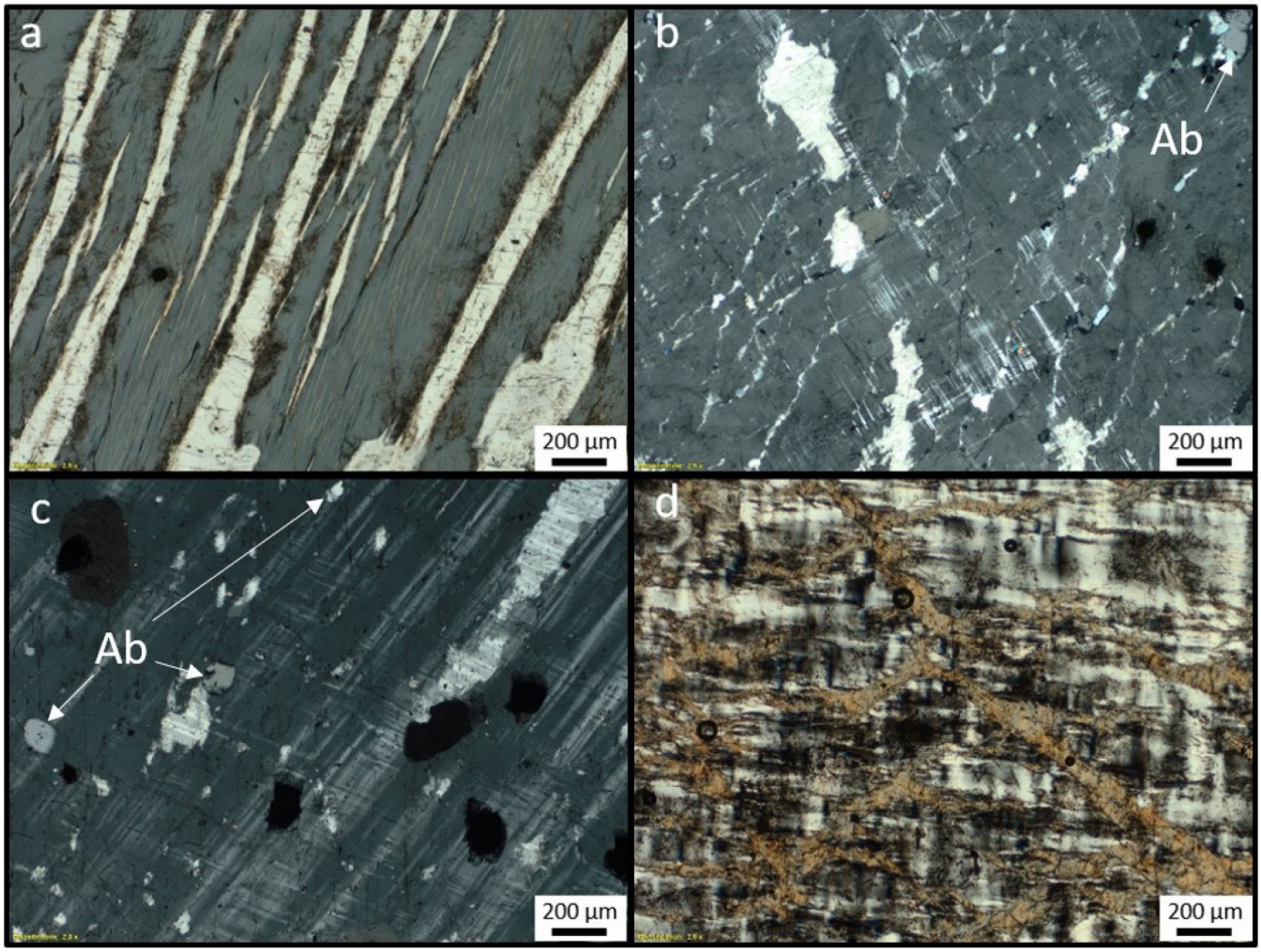

Figure 3. Photomicrographs of some perthite textures in cross polarized light for **a)** Coarse vein perthite from Barringer Hill, Texas, **b)** fine patch perthite from Brazil Lake, Nova Scotia, **c)** patch perthite from Moblan, Quebec, and **d)** Coarse braid perthite from White Cloud, Colorado. Inclusions of albite (Ab) are often present.

Table 1 Thallium isotope data for K-feldspar samples.

Sample	Pegmatite	Location	Age (Ma)	Tl (ppm)	ε^{205}Tl
SLW-1B	Tanco	Bernic Lake, MB	2640	127	4.1
SLW-1B dup					3.5
SLW-2B	Tanco	Bernic Lake, MB	2640	87.6	-0.1
SLW-2B dup					0.4
12-15-2C	Tanco	Bernic Lake, MB	2640	101	1.5
12-15-2C dup					1.7
12-15-2E	Tanco	Bernic Lake, MB	2640	103	1.5
12-15-2E dup					1.8
C-090-B	Tanco	Bernic Lake, MB	2640	142.3	2.6
92-11-L	Tanco	Bernic Lake, MB	2640	130	2.3
92-11-L dup					2.3
C-033-H	Tanco	Bernic Lake, MB	2640	161.4	2.7
3A-Ksp	Tanco	Bernic Lake, MB	2640	145.3	2.9
86-07-C	Tanco	Bernic Lake, MB	2640	185	3
86-07-C dup					2.5
C-090-J	Tanco	Bernic Lake, MB	2640	160.3	4.2
C-090-J dup					3.7
12-15-12-	Tanco	Bernic Lake, MB	2640	211.5	5.1
12-15-5-	Tanco	Bernic Lake, MB	2640	136.2	3.1
10 25 1	Tanco	Bernic Lake, MB	2640	145.3	2.6
10 25 1 dup					2.7
12 15 17	Tanco	Bernic Lake, MB	2640	169.09	3.5
12 15 17 dup					4.2
12 15 23	Tanco	Bernic Lake, MB	2640	173.7	3
P-22	Pegmatite 22	Cross Lake, MB	2760	67.1	9.4
Quadeville-fs*	Quadeville Beryl Pit	Quadeville, ON	990-1000	37.1	4.1
BL-1	Brazil Lake	Yarmouth County, NS	378	28.9	-2.2
GV-G*	Georgeville	Georgeville, NS	580	12.8	1.7
PL-1	Preissac Lacorne	Preissac, QB	2596-2615	93.6	-1.1
LS-1*	Lac Sairs	Kipawa Region, QB	980-1050	10.9	5.1
PMB-1	Moblan	Moblan Lake, QB	2500	105.2	0.5
H-1	Harding	Taos County, NM	1336	131.1	3.4
OrganB	Organ Mountain	S. Dona Ana County, NM	<32.8	1.4	-0.9

Table 1 (cont.) Thallium isotope data for K-feldspar samples.

Sample	Pegmatite	Location	Age (Ma)	Tl (ppm)	ε^{205}Tl
Him-3	Himalaya	Mesa Grande District, CA	93-143	31.1	-4.3
Badu	Badu	Llano County, TX	1100	2.1	-1.7
Barringer	Barringer Hill	Llano County, TX	1090	2	-0.2
Bennett	Bennett	Oxford County, ME		13.4	-1.4
Sample	Pegmatite	Location	Age (Ma)	Tl (ppm)	ε205Tl
Havey	Havey	Androscoggin County, ME	200-250	31.7	1.2
StrkMtn	Streaked Mountain	Oxford County, ME	283-264	7.4	-0.4
Hurricane Mtn	Hurricane Mountain	Carroll County, NH	183	5	1.7
Moat Mtn	Moat Mountain	N. Conway, NH	155	4.9	-0.5
Mor-1*	Morefield	Amelia, VA	265	17.1	-0.8
LG-PikesPeak	Pike's Peak	Front Ranges, CO	1000	5.7	4.4
Luster4	Luster	Jefferson County, CO	1040	3.6	-1.6
WhiteCloud3	White Cloud	South Platte, CO	1040	2.7	-0.9
ZAP-1 *	Zapot	Hawthorne, NV	72-200	65.9	-0.2
ZAP-1 dup*					-0.4
Bikita	Bikita	Masvingo, Zimbabwe	2500	119.5	-2.5
K-33	Chingahari section	Kamativi, Zimbabwe	990	31.8	0.5
K-33 dup					1.3
K-Sec-6	Section 6	Kamativi, Zimbabwe	990	47.4	0.4
Kama-147	Section 2	Kamativi, Zimbabwe	990	39.9	-0.1
KF-K-148	Section 7	Kamativi, Zimbabwe	990		1.3
K100 dup	Chingahari section	Kamativi, Zimbabwe	990	33.9	-0.1
K146	Chingahari section	Kamativi, Zimbabwe	990	99.9	0.7
K170	Section 7	Kamativi, Zimbabwe	990	112.7	-0.9
K692	Chingahari Section	Kamativi, Zimbabwe	990	72.4	0.6
K733	Section 7	Kamativi, Zimbabwe	990	45.9	-0.4
Viitaniemi	Viitaniemi	Eräjärvi, Finland	1800	22.9	1.8
Spitz2	Klein Spitzkoppe	Damaraland, Namibia	100-160	8.9	-1.3
GB-12	Greenbushes	W. Australia	2527	247.9	3.4
GB-17					1
BH-1	Broken Hill	NSW, Australia	1540	14.2	-2.6

dup - duplicate. Values used in the study are in bold.
*amazonite sample.

Table 2 Thallium isotope data for mica, pollucite and pyrite samples.

Sample	Pegmatite	Location	Age (Ma)	Tl (ppm)	ε^{205}Tl
7A	Tanco (muscovite)	Bernic Lake, MB	2640	55.9	2.4
13A	Tanco (muscovite)	Bernic Lake, MB	2640	47.3	2.2
38A*	Tanco (muscovite)	Bernic Lake, MB	2640	59.3	2.1
22Aa	Tanco (muscovite)	Bernic Lake, MB	2640	41	2.3
22Ab	Tanco (muscovite)	Bernic Lake, MB	2640	65.4	2.1
3A*	Tanco (muscovite)	Bernic Lake, MB	2640	51.6	3.6
30A	Tanco (muscovite)	Bernic Lake, MB	2640	42.8	2.2
31A	Tanco (muscovite)	Bernic Lake, MB	2640	73.26	1.9
TL-56*	Tanco (muscovite)	Bernic Lake, MB	2640	117.31	4.7
LEP-80*	Tanco (muscovite)	Bernic Lake, MB	2640	162.83	3.3
2C-04	Tanco (Li-muscovite)	Bernic Lake, MB	2640	156.48	2.4
5C-02	Tanco (Li-muscovite)	Bernic Lake, MB	2640	139.78	2.5
S-40	Tanco (pyrite)	Bernic Lake, MB	2640	120.9	1.8
Pol-80	Tanco (pollucite)	Bernic Lake, MB	2640	129	4.2
Pol-FX	Tanco (pollucite)	Bernic Lake, MB	2640	89.5	3.3
KAMA-72	Kamativi (muscovite)	Kamativi, Zimbabwe	990	39.9	3.6
KAMA-120	Chingahari (muscovite)	Kamativi, Zimbabwe	990	13.7	1.6
KAMA-148	Section 7 (muscovite)	Kamativi, Zimbabwe	990	49.4	5.1
KAMA-163	Chingahari (muscovite)	Kamativi, Zimbabwe	990	19.8	0.1
KAMA-165	Chingahari (muscovite)	Kamativi, Zimbabwe	990	28.3	2.5
KAMA-183	Chingahari (muscovite)	Kamativi, Zimbabwe	990	56.5	4.1
KAMA-616	Chingahari (muscovite)	Kamativi, Zimbabwe	990	16.3	0.8
KAMA-655	Chingahari (muscovite)	Kamativi, Zimbabwe	990	52.3	4.1
KAMA-725	Section 6 (muscovite)	Kamativi, Zimbabwe	990	36.1	-0.4
KAMA-726	Quartz vein (muscovite)	Kamativi, Zimbabwe	990	17.7	3.5
*secondary muscovite					

Table 3 Tl isotope data for obsidian and selected reference samples.

Sample	Pegmatite	Location	Age (Ma)	Tl (ppm)	ε^{205}Tl
JV-1	Macusani obsidian	Macusani, Peru	4	10.2	2.8
LCO	Lake County obsidian	Lake County, Oregon	5-6	0.9	2.5
G-2	Westerly granite	Bradford, RI	276	0.9[1]	-2.3[1]
BC-76 feldspar	Birch Creek granite	Birch Creek, NV	82	0.9[2]	-3.6[2]
BC-76 biotite	Birch Creek granite	Birch Creek, NV	82	2.4[2]	-3.3[2]
NIST SRM 607	Kingman pegmatite	NV	1680	2.6[1]	-3.1[1]
[1]from Brett et al (2018). [2]from Rader et al (2018).					

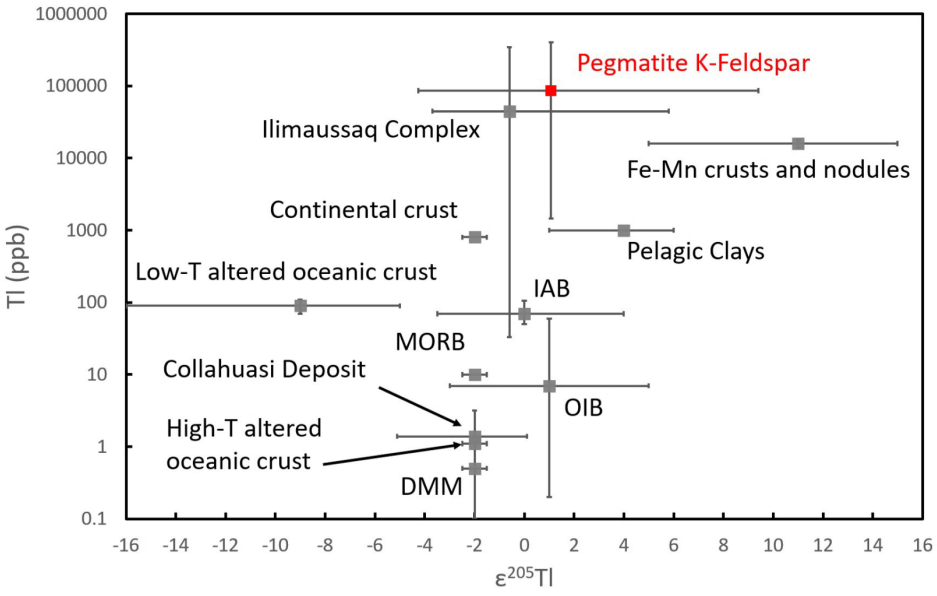

Figure 4. Thallium isotopes compared with Tl concentrations in ppb for a variety of rock types including mid-ocean ridge basalts (MORB), depleted MORB mantle (DMM), ocean island basalts (OIB) and island arc basalts (IAB). The data in red is for pegmatite K-feldspar measured in this study. The data in gray is sourced from Rehkämper et al. (2002, 2004); Nielsen et al. (2005a, 2006b,c, 2010, 2014, 2015, 2016); Baker et al. (2010); Prytulak et al. (2013); Hettmann et al. (2014a).

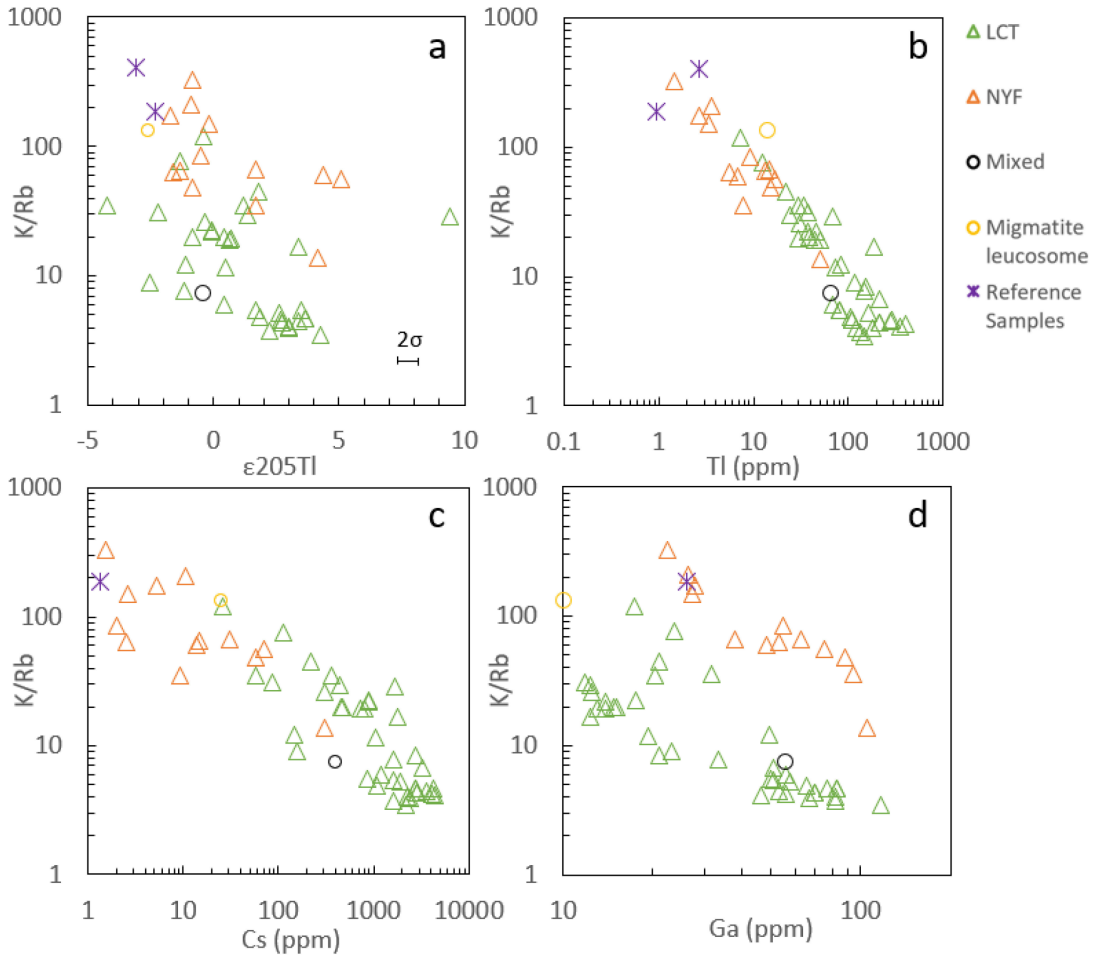

Figure 5. K/Rb versus ε205Tl (a), Tl (b), Cs (c), and Ga (d) for all K-feldspar samples.

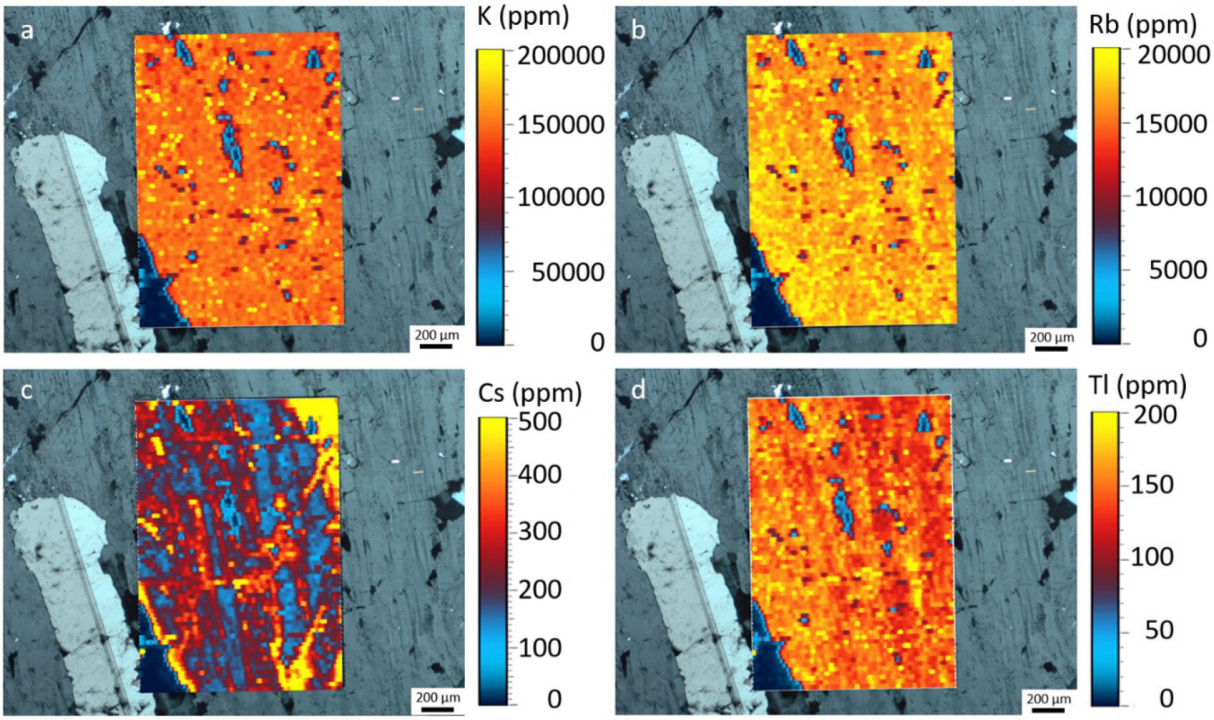

Figure 6. Laser ablation maps for K (a), Rb(b) Cs (c) and Tl (d) superimposed on the photomicrograph of the K-feldspar sample from the Bikita pegmatite in cross polarized light. The mineral inclusion in the lower left-hand corner of the photo is albite.

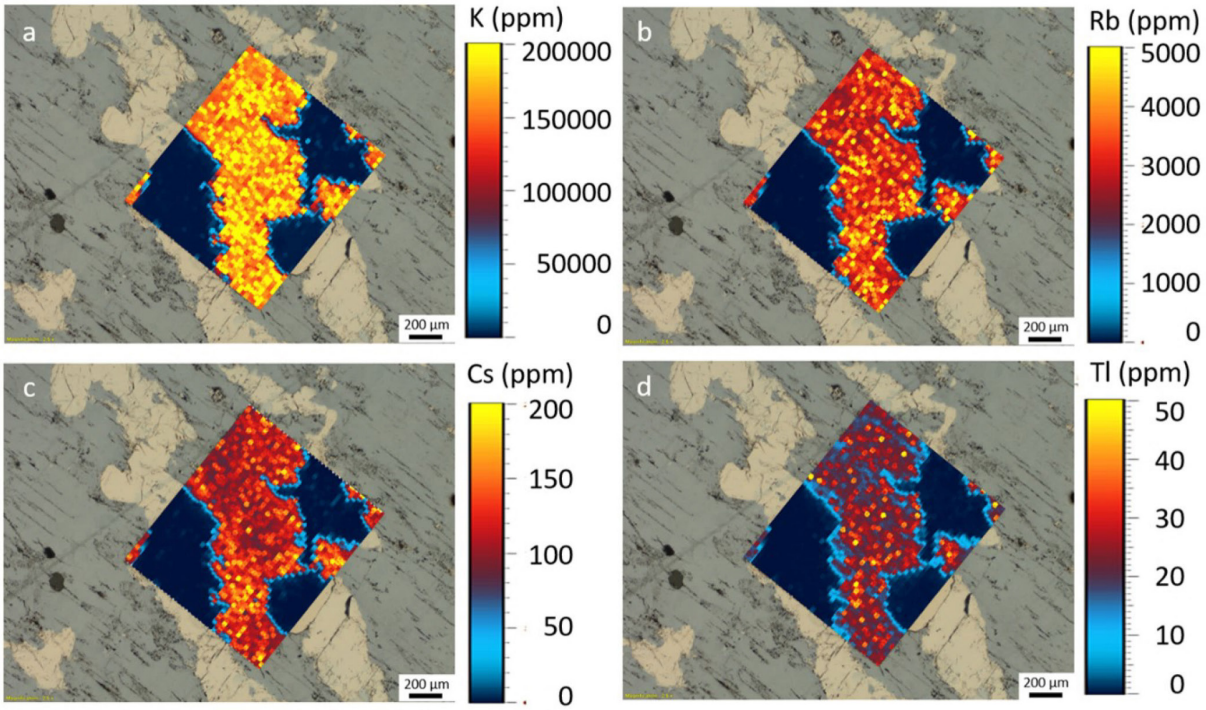

Figure 7. Laser ablation maps for K (a), Rb (b) Cs (c) and Tl (d) superimposed on the photomicrograph of the coarse vein perthite sample from the Lac Sairs pegmatite in cross polarized light.

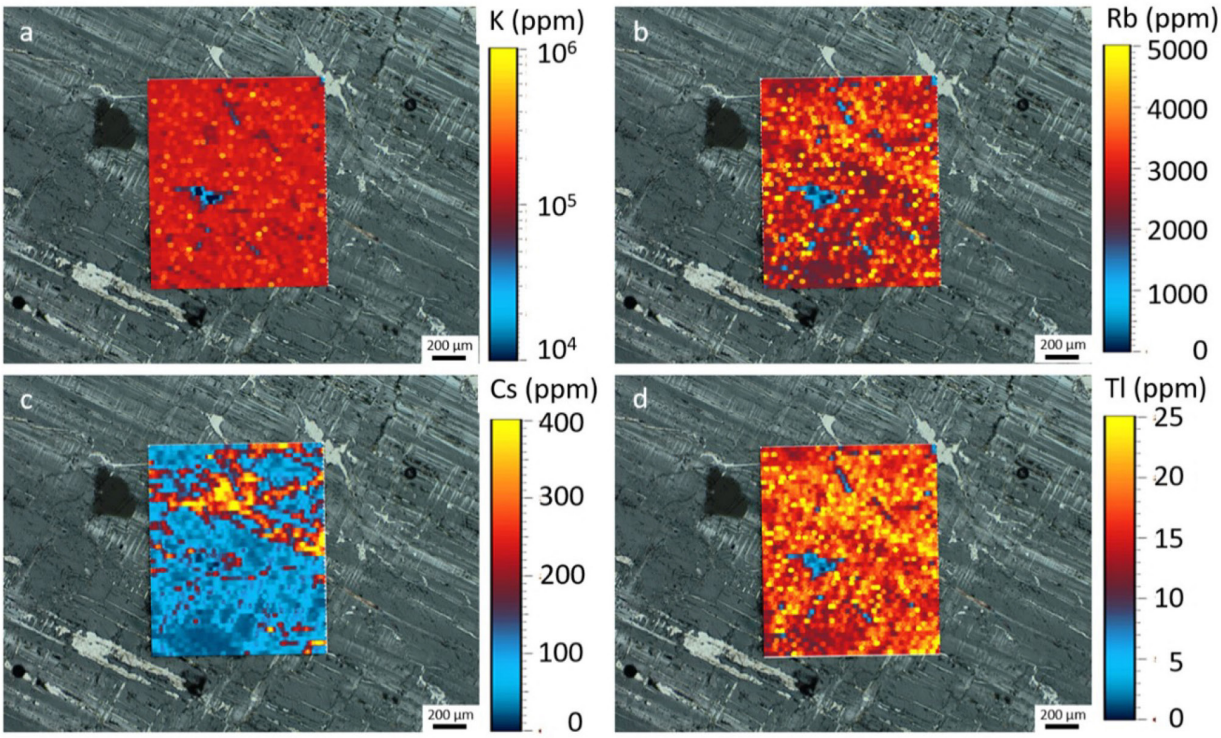

Figure 8. Laser ablation maps for K (a), Rb(b) Cs (c) and Tl (d) superimposed on the photomicrograph of the K-feldspar sample from the Morefield pegmatite displaying tartan twinning in cross polarized light. Black spots are laser ablation sites.

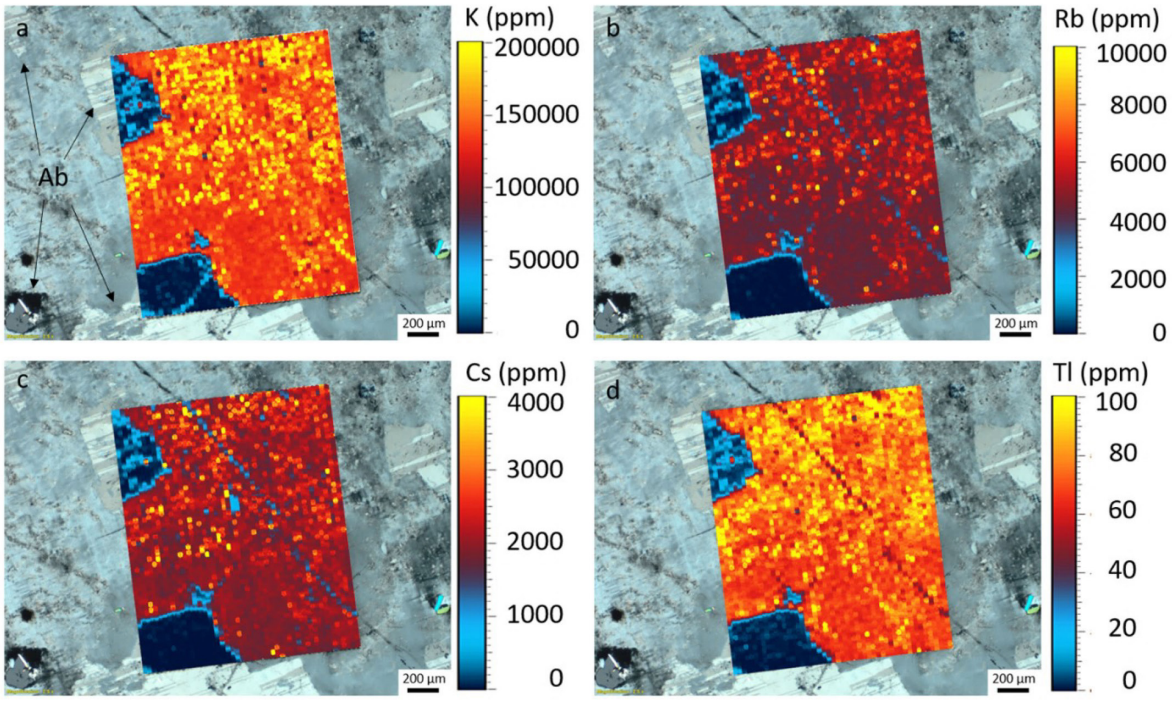

Figure 9. Laser ablation maps for K (a), Rb(b) Cs (c) and Tl (d) superimposed on the photomicrograph of the K-feldspar sample from pegmatite 22 of Cross Lake in polarized light. Albite (Ab) inclusions are common.

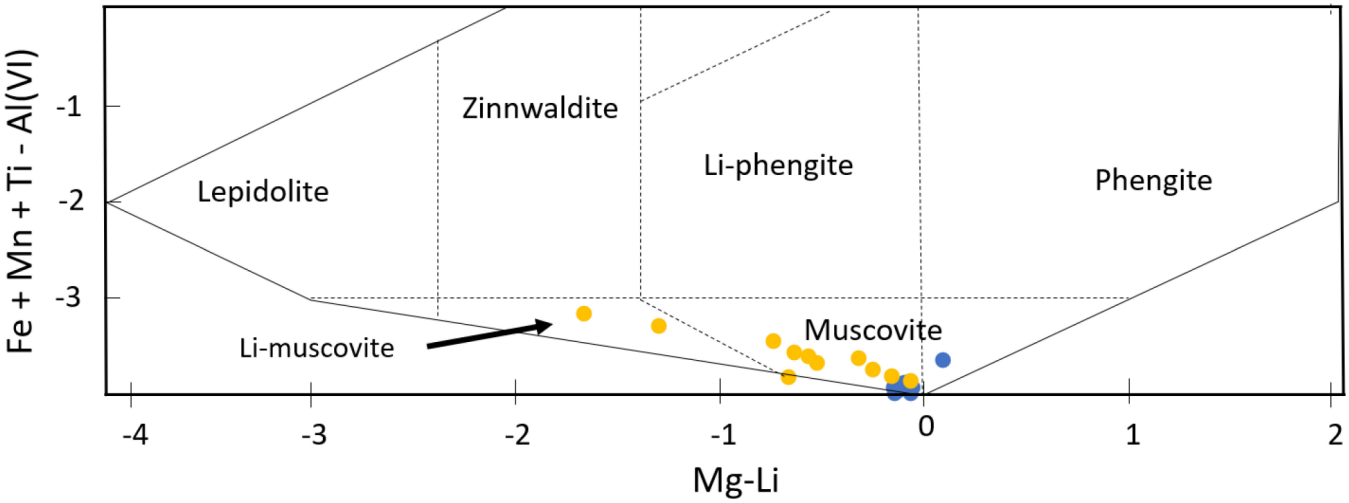

Figure 10. Interlayer site occupancy Mg-Li vs. Fe+Mn+Ti-Al(VI) for mica classification (Tischendorf et al., 1997). The blue points represent Kamativi mica samples and the yellow spots represent Tanco mica. Units are in atoms per formula unit (APFU) calculated from EPMA and ICP-MS data.

(356-4420 ppm), Tl (7-738 ppm) and Pb (49-924 ppm). Figure 12 shows a synchrotron XRF map of Tl in sample S-40 from the central intermediate zone (60) of the Tanco pegmatite.

Major and trace element analyses for obsidian samples are listed in Appendix E. Sample JV-1 (obsidian from Macusani, Peru) shows notable concentrations of B (651 ppm), Li (3304 ppm), Rb (1160 ppm) and Cs (561 ppm). It has K/Rb and Rb/Cs ratios of 25 and 2, respectively, while LCO (obsidian from Lake County, Oregon) K/Rb and Rb/Cs ratios are 247 and 57, respectively.

Quality of trace element data

Trace elements were measured using both LA-ICP-MS and MC-ICP-MS techniques in order to identify any mineral inclusions or contaminants that could potentially affect Tl isotope results. Figure 13 shows the close agreement for measured Tl concentrations obtained by these techniques.

Geochemical Trends

Plots of various fractionation indicators (Černý et al., 1985; Moller and Morteani, 1987; Černý, 1991a) vs ε^{205}Tl show an increase in ε^{205}Tl with decreasing K/Rb, Rb/Cs, K/Cs and Al/Ga (Fig. 14). A plot of K/Rb vs Ga displays separate trends for K-feldspar from different NYF and LCT pegmatites (Fig. 5d) The observed trends reflect different degrees of fractionation of melts derived from distinct sources for NYF and LCT pegmatites (see Whalen et al., 1987). A plot of K/Rb vs. ε^{205}Tl for reference material NIST SRM 607, alkali feldspar from the Kingman Quarry, NV (Brown, 2010), shows that this feldspar falls within the NYF pegmatite trend.

Gallium is a relatively incompatible and immobile element (Černý et al., 1985). Plots of Ga vs fluid mobile, large ion lithophile elements, therefore, provide a means to assess the effects of subsolidus alteration (Sánchez-Muñoz et al. 2017). The plot Rb/Cs vs Ga/Tl shows a magmatic trend (Sánchez-Muñoz et al. 2017), however some K-feldspar samples deviate from the trend, likely due to a loss of Cs during alteration (Figure 15).

K-feldspar and muscovite within a single pegmatite exhibit a similar trend with respect increasing magmatic fractionation and ε^{205}Tl. Samples from the Kamativi Sn mine, Zimbabwe, and from the Ta-rich Tanco mine, Manitoba, show a large range in ε^{205}Tl (Fig. 16). For both Tanco and Kamativi, the muscovite samples show an increase in ε^{205}Tl with decreasing Rb/Cs indicating co-enrichment of heavy Tl and Cs. A plot of Rb/Cs vs Ga/Tl shows parallel fractionation trends for the micas and K-feldspars (Fig. 17).

Thallium isotopic variability in the Tanco pegmatite

A plot of the sequence of crystallization of the zones at Tanco (Černý et al., 1996) against ε^{205}Tl (Fig. 18), shows that K-feldspar in the latest zones tend to have the highest ε^{205}Tl values. An exception is sample SLW-1B from the border zone, which has an ε^{205}Tl value of 3.5. This K-feldspar, however, contains minute sulphide inclusions that may contribute to its high ε^{205}Tl value. Two pollucite samples from zone 80 give ε^{205}Tl values of 4.2 and 3.3. These results show that minerals in the latest and most fractionated zones of the Tanco pegmatite yield the highest ε^{205}Tl values.

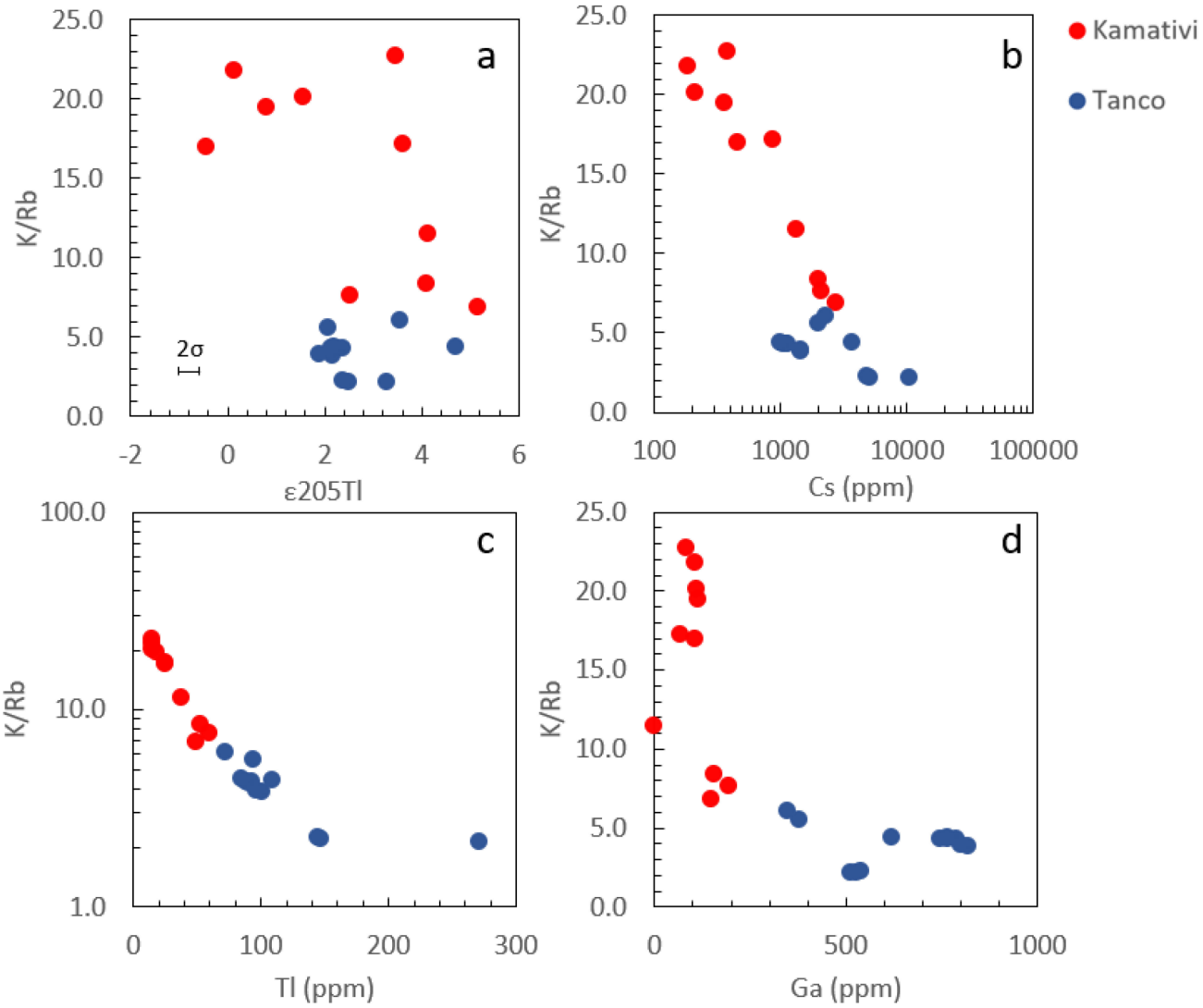

Figure 11. K/Rb vs ε^{205}Tl (a), Cs (b), Tl (c), and Ga (d) for mica from the Kamativi and Tanco pegmatites.

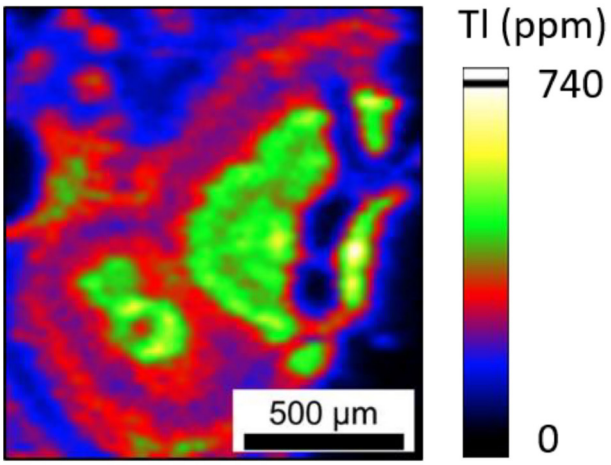

Figure 12. SXRF map showing the distribution of Tl in pyrite grain S-40 from zone 60 of the Tanco pegmatite, Manitoba..

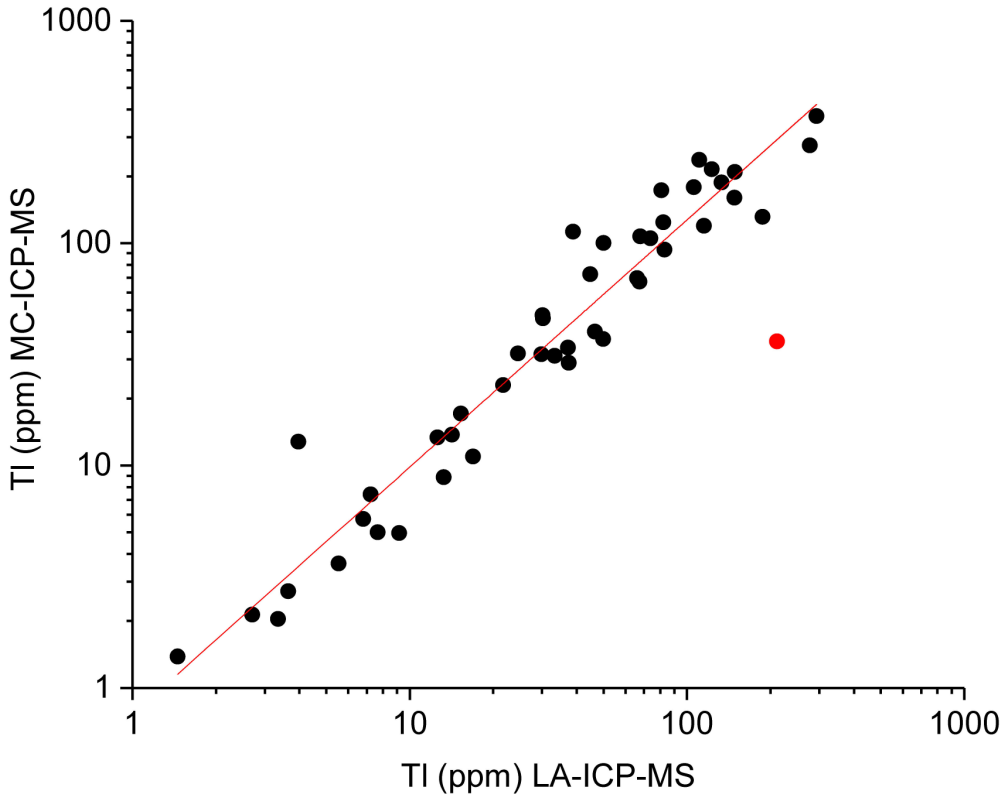

Figure 13. Thallium concentrations obtained by LA-ICP-MS vs MC-ICP-MS for all K-feldspar samples measured in this study.

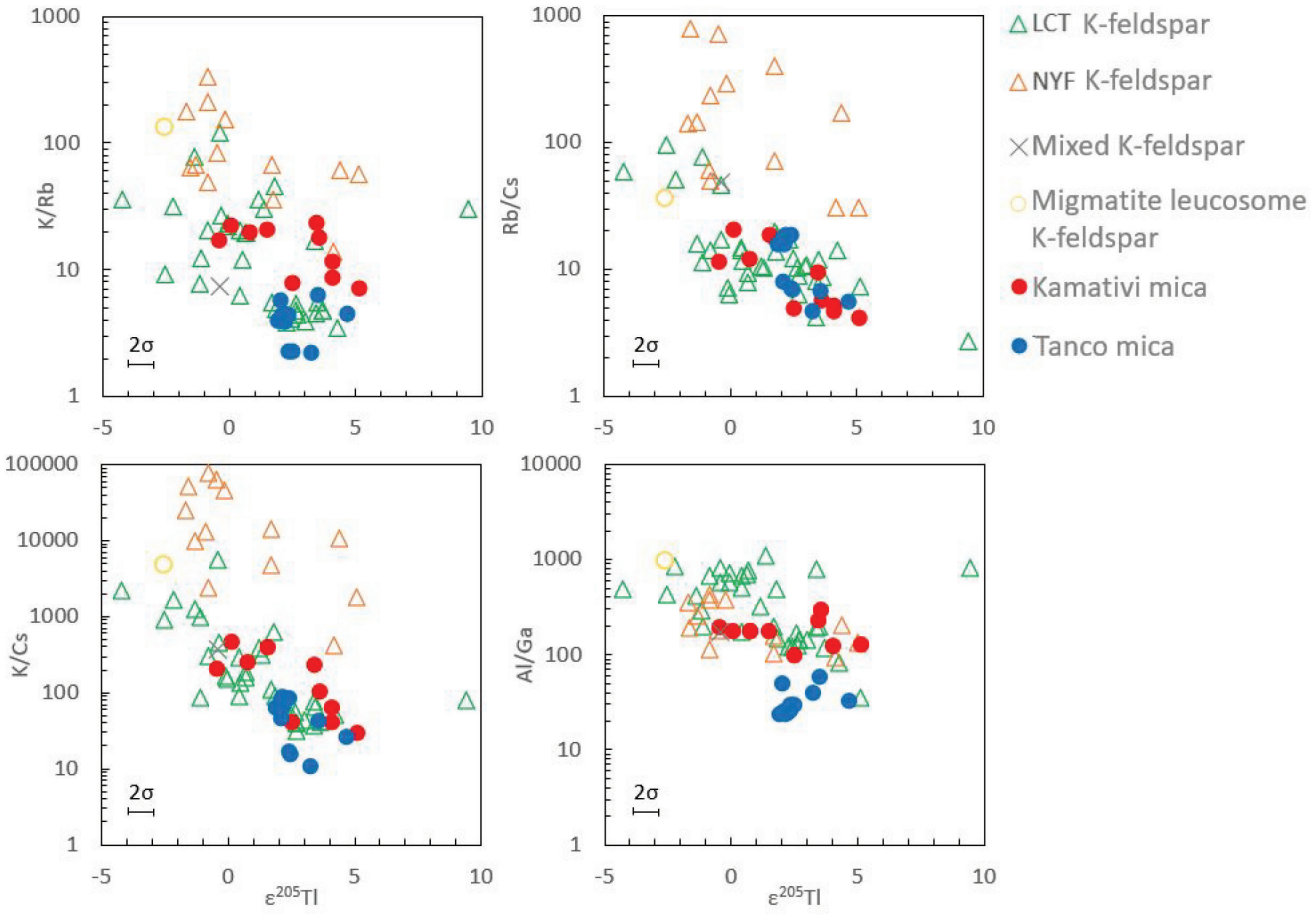

Figure 14. Plots show K/Rb versus ε^{205}Tl (a), Rb/Cs versus ε^{205}Tl (b), K/Cs versus ε^{205}Tl (c) and Al/Ga versus ε^{205}Tl (d) for K-feldspar and muscovite samples.

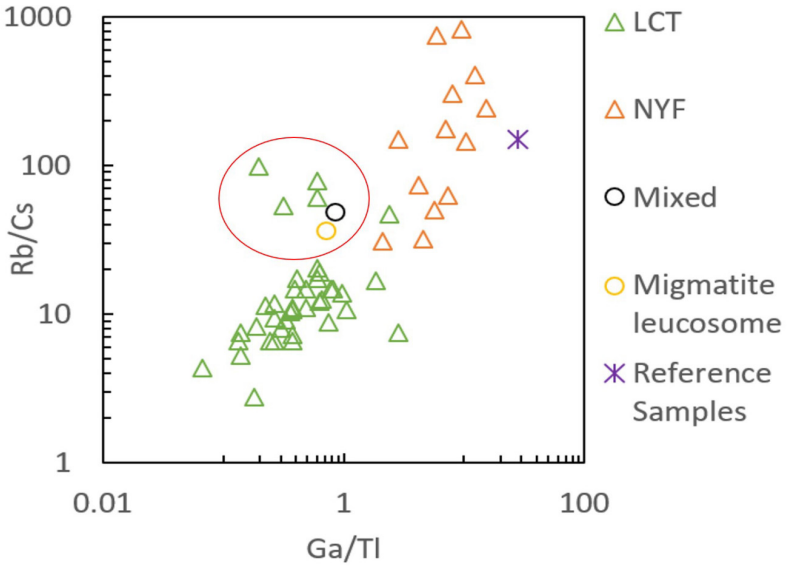

Figure 15. Comparison of Ga/Tl and Rb/Cs for K-feldspar samples. Samples circled in red are suspected to have been disturbed by alteration.

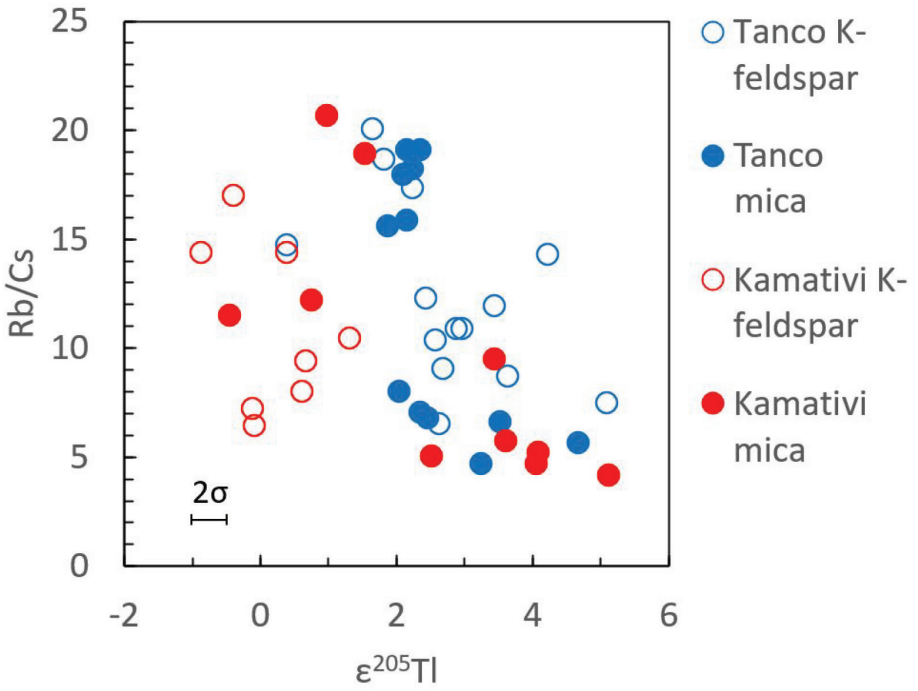

Figure 16. Comparison of Tl isotopes with Rb/Cs ratios for K-feldspar and mica samples from the Kamativi and Tanco pegmatites.

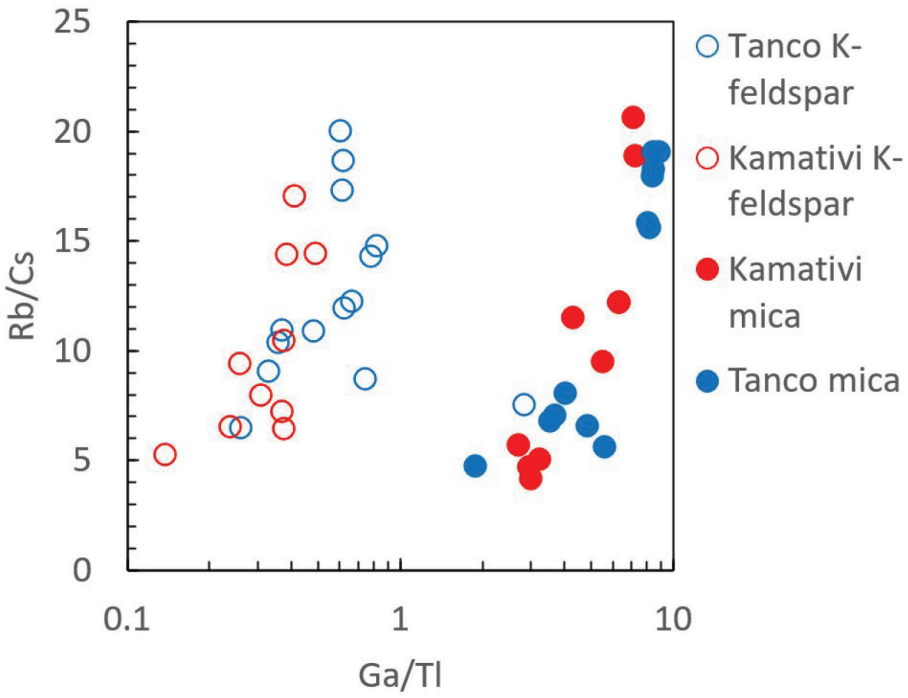

Figure 17. Plot Rb/Cs vs Ga/Tl for K-feldspar and mica from the Kamativi and Tanco pegmatites.

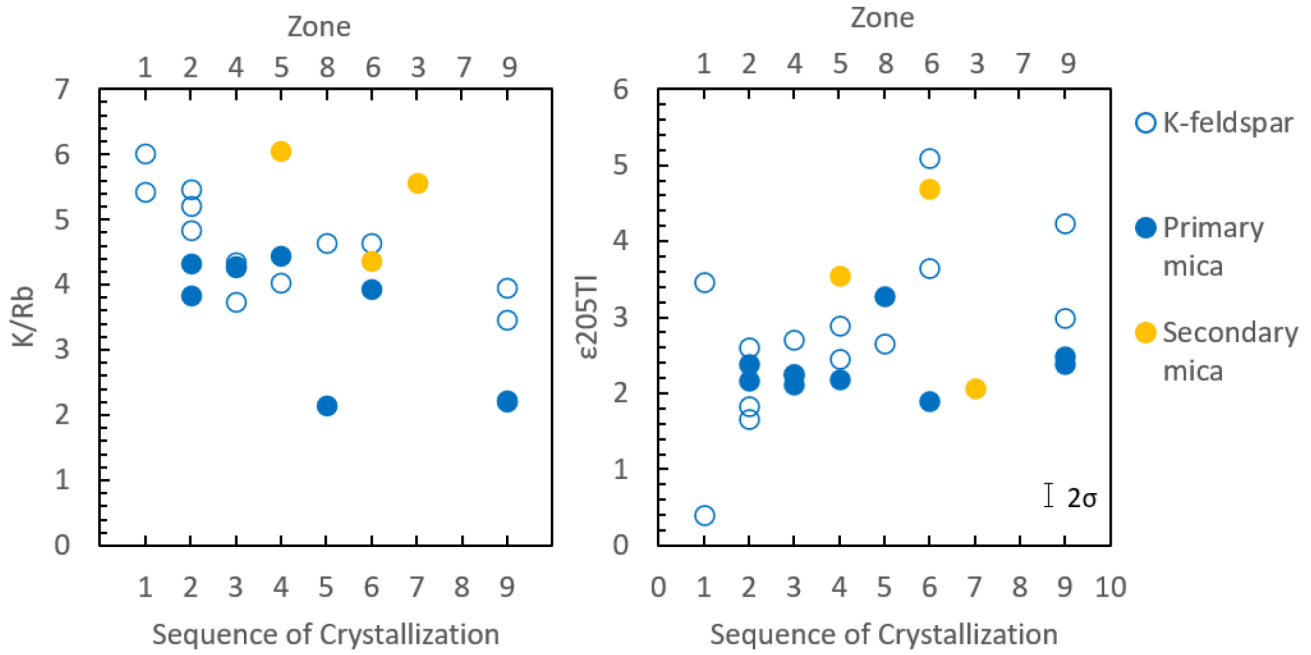

Figure 18. Comparison of the sequence of crystallization for the Tanco pegmatite and Tl isotopes for K-feldspar and muscovite samples. The zones are shown on the upper X-axis.

In contrast to K-feldspar, primary mica in all zones at Tanco give nearly constant ε^{205}Tl values of 2.0 ± 0.5. Secondary muscovite, however, exhibits significantly higher ε^{205}Tl. These results suggest that Tl isotopic fractionation occurred during subsolidus alteration of the pegmatite.

Thallium isotopic variability in the pegmatites at Kamativi

Muscovite samples were obtained from the quartz-muscovite hanging wall assemblage and from the core of three separate flat-lying pegmatites in the Sn-rich Chingahari section of the mine. Muscovite from the hanging wall is characterized by relatively high Rb/Cs ratios and low ε^{205}Tl, whereas muscovite from the core of the pegmatite exhibit a low Rb/Cs and high ε^{205}Tl (Fig. 19). The distance between the hanging wall and core zone in the Chingahari section is generally between 1 and 2 m.

All K-feldspar samples at Kamativi exhibit low (–0.85 to 1.28) ε^{205}Tl values relative to those of from the Tanco pegmatite. Thin section petrography indicates that each K-feldspar has been sericitized to varying degrees, which suggests the lower ε^{205}Tl values may be due in part to deuteric alteration. The hydrous nature of the pegmatites in the Chingahari section of the Kamativi mine is indicated by the high modal abundance of muscovite and local greisenization. Kamativi K-feldspar exhibits moderate to extensive sericitization, which may have affected ε^{205}Tl values.

DISCUSSION

Tl isotope fractionation in rare element pegmatites

Although Tl concentrations in K-feldspar and muscovite increase with decreasing K/Rb, ε^{205}Tl appears to be more closely related to increasing Cs relative to Rb and Tl. Previous studies show that Cs may be enriched in hydrothermal fluids relative to other LILEs (Ellis, 1967; Ellis and Mahon, 1977, Keith et al., 1983; Busigny et al., 2003; Bebout., 2016).

The Rb/Cs ratio of the Tanco pegmatite is 2.03 with most zones having Rb > Cs (Stilling et al., 2006). Quartz-hosted, primary and secondary fluid inclusions from Tanco, however, have Rb/Cs ratios between 0.16 and 0.24 (Der Channer and Spooner, 1992). Analysis of coexisting fluid and melt inclusions in granitic rocks show that Cs partitions favorably into the aqueous fluid and the fluid/melt partition coefficient for Rb is between 0.1 and 1 (Zajacs et al., 2008). The volatile nature of Tl favours partitioning into an aqueous phase (Bebie et al., 1998). Indeed, Audétat and Zhang (2019) reported Tl concentrations of up to 150 ppm in quartz-hosted fluid inclusions in mineralized granitic rocks. It is therefore likely that Cs and Tl behave similarly in high-temperature, magmatic fluids (Kaplan and Mattigod, 1998).

The Hard-Soft Acids and Bases (HSAB) theory predicts that a hard acid will preferentially bond to a hard base and a soft acid to a soft base in a competitive environment

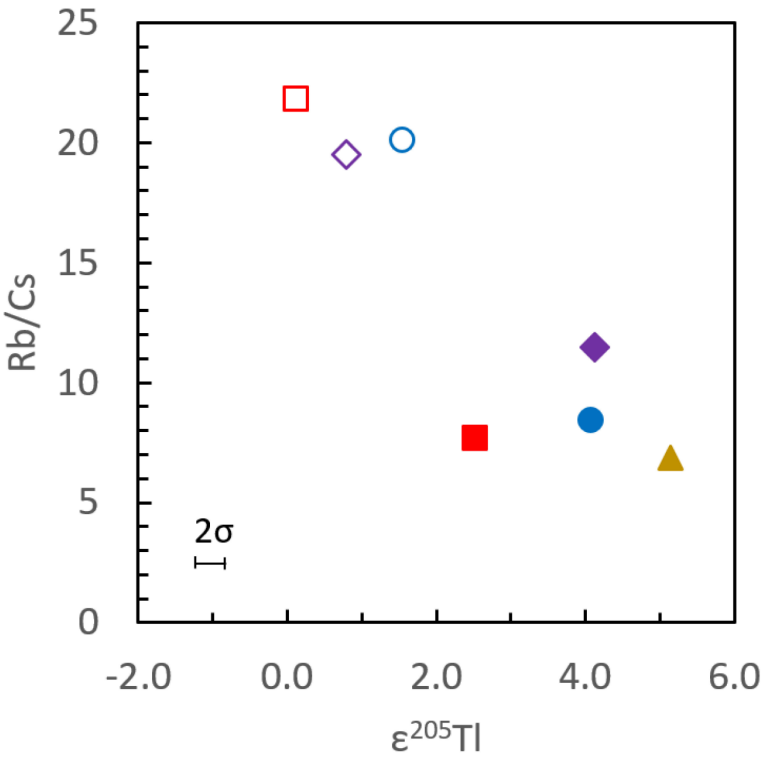

Figure 19. Comparison of muscovite samples from the Kamativi mine. The different colour and symbol shapes represent different pegmatites. Muscovite from the hanging wall assemblages are shown as open symbols while those from the core of the pegmatite are designated by filled symbols.

(Pearson, 1963). However, a soft acid can complex with a hard base in the absence of a soft base. The classification of Pearson (1963) indicates Cs^+ is a hard acid while Tl^+ is a soft acid. Thallium (I) will preferentially bond with a soft base such as I- or Br-, while Cs^+ will associate with a hard base such as F^- and OH^- (Wood and Samson, 1998). However, in hydrothermal fluids CsCl0 is typically the dominant Cs species (Ellis, 1967; Ellis and Mahon, 1977). Due to the softer nature of Cs, compared to other hard acids, it may preferentially bond to the intermediate base, Cl^- (Pearson, 1963; Wood and Samson, 1998). Spectrophotometric determination of the stability of thallium (I) chloride complexes in aqueous solution (Bebie et al 1998) suggest that the neutral chloride complex, $TlCl^0$, is the dominant species at temperatures greater than 200°C. Given that Cl is 30 to 40 times more abundant than Br in inclusion fluids at Tanco (Der Channer and Spooner, 1992), it is probable that Tl in late fluids was transported as a chloride complex.

The experiments of Maneta and Anderson (2018) show that aqueous fluids play an important role in the growth of primary mica and K-feldspar crystal in H2O-saturated, granitic melts. Their experiments indicate that an immiscible aqueous phase facilitated the rapid transfer of ions to the growing K-feldspar crystals. If an aqueous fluid or hydrous silicate liquid was involved in the growth of pegmatite crystals, then preferential partitioning of Cs and Tl into this fluid may explain why both Ga/Tl and Ga/Cs correlate similarly with respect to ε^{205}Tl while Ga/Rb does not (Fig. 20).

Proposed mechanisms of Tl isotope fractionation

Given that ε^{205}Tl values increase with decreasing Rb/Cs ratios in mica and K-feldspar (Fig. 14b), we suggest the enrichment of Cs relative to Rb and Tl in evolved pegmatite melts is due to a separate aqueous fluid or hydrous silicate liquid present during crystallization. This interpretation is supported by studies showing normal magmatic processes have little or no effect on Tl isotope fractionation (Baker et al., 2010; Prytulak et al., 2016; Nielsen et al., 2017a,b). Baker et al., (2010), Hettmann et al., (2014a,b), Nielsen et al. (2015) and Fitzpayne et al. (2018), however, suggest ε^{205}Tl variability in igneous rocks may be related to the activity of an aqueous phase. Compared to typical magmas, fractionation of Tl isotopes in pegmatite melts may differ because of their enrichment in water and other fluxes.

Rader et al. (2018) suggested that crystal chemical controls govern Tl isotope ratios in minerals. Based on their results, the crystallization of Fe-rich biotite should cause an increase in ε^{205}Tl in the residual melt while the crystallization of feldspar and sulfide minerals should cause a decrease in ε^{205}Tl. However, K-feldspar and mica from the Tanco and Kamativi pegmatites exhibit similar ranges in ε^{205}Tl. Rader et al. (2018) also noted that sulphide samples consistently yielded the highest ε^{205}Tl values. At Tanco, pyrite occurs a small (~1 mm diameter) mounds on the surface of vug quartz crystals. One pyrite sample (S-40) from the

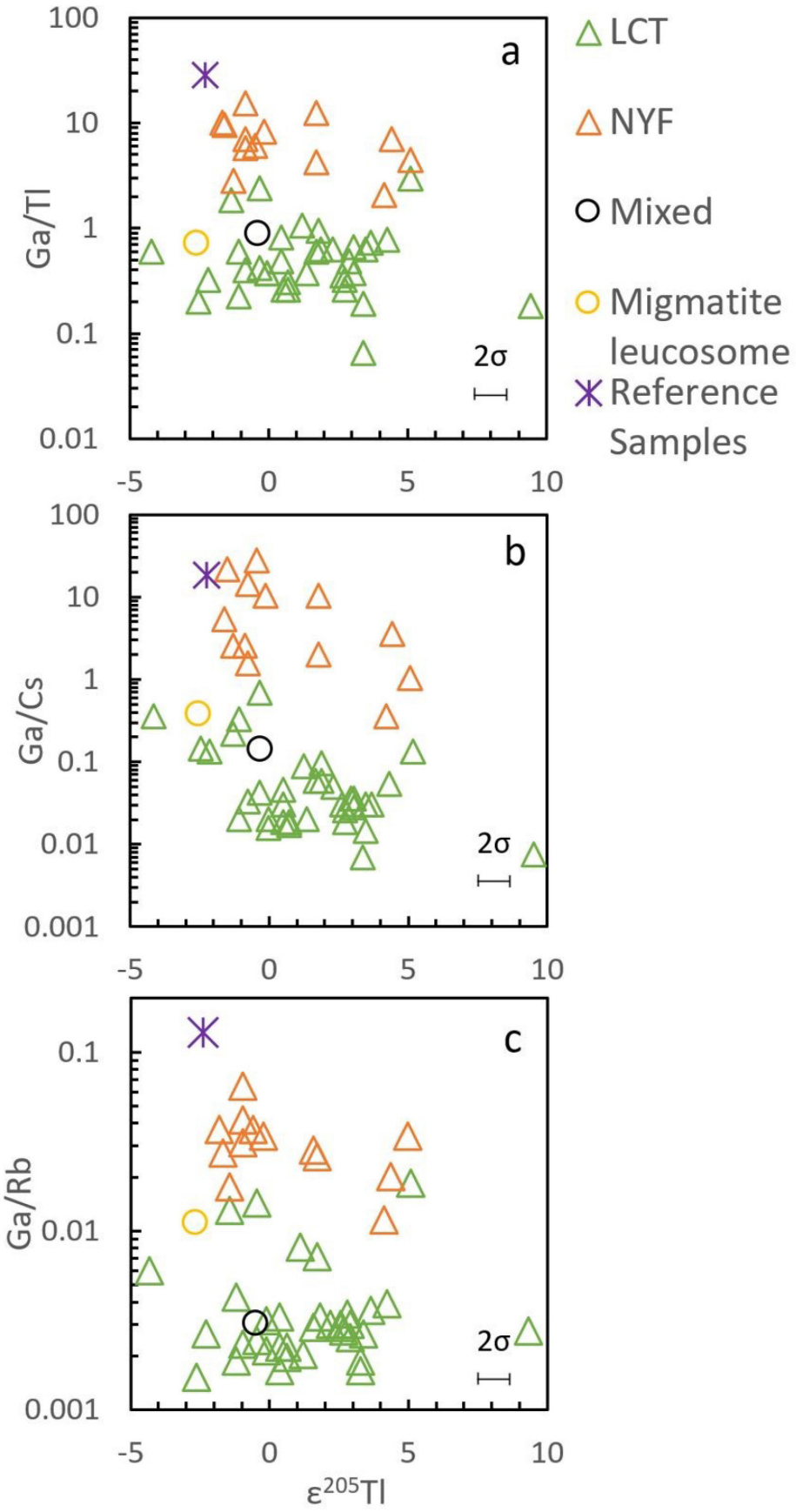

Figure 20. Comparison of Tl isotopes with Ga relative to Tl (a), Rb (b) and Cs (c) for K-feldspar samples.

central intermediate zone (60) gave an ε^{205}Tl value of 1.8, which is within error of the primary mica and some primary K-feldspar at Tanco.

Most work on Tl isotopes state that mass fractionation has a negligible effect (Bigeleison, 1996; Schauble, 2007; Moynier et al., 2013; Yang and Liu, 2015; Fuji et al., 2013). However, obsidian from Lake County (2.5 ε^{205}Tl) and Macusani (2.8 ε^{205}Tl), is 4 to 5 ε^{205}Tl units greater than the average for the continental crust and mantle (–2.0 ε^{205}Tl). The heavy Tl-enriched obsidian may reflect incorporation of ^{205}Tl-enriched crustal source rocks. The other explanation is that isotope fractionation occurred during volatile loss from the glass (Liu et al., 2020).

At high temperatures, the nuclear field shift effect is believed to be a dominant mechanism affecting Tl isotope variation (Bigeleison, 1996; Fujii et al., 2013; Yang and Liu, 2015). Mechanisms of Tl isotope fractionation caused by nuclear field shift effects include redox reactions and bonding in an aqueous phase. Previous studies indicate a redox reaction can cause Tl isotope fractionation (Schauble, 2007; Peacock and Moon, 2012; Nielsen et al., 2013; Fang and Liu, 2019), but because of the dominance of Tl (I) in magmatic and hydrothermal systems, such a mechanism is unlikely. Nuclear field shift effects may occur by ligand exchange reactions in an aqueous phase (Fujii et al., 2011, 2013). The other means by which nuclear field shift can occur is by the bonding of Tl^{+} to $O2^{-}$, F^{-}, Cl^{-} or Br^{-} (Fang and Liu, 2019). According to Fang and Liu (2019), the association of Tl^{+} with Cl^{-}, results in a decrease in electron density at the nucleus, resulting in preferential bonding of heavy Tl to Cl relative to bonding with O.

Tl isotope fractionation via complexing in an aqueous phase

Of the proposed mechanisms of Tl isotope fractionation, a possible cause for the observed variation in ε^{205}Tl in pegmatite K-feldspar and muscovite is ligand exchange reactions between a silicate melt and a separate aqueous phase or hydrous silicate liquid. Fang and Liu (2019) have shown that the association of Tl with Cl, Br and F may promote the fractionation of Tl isotopes. Of these possible ligands, Cl- is the dominant anion in primary fluid inclusions in granitic pegmatites (Der Channer and Spooner, 1992; Gammel and Nabelek, 2016). Chlorine may therefore preferentially transport ^{205}Tl to growing K-feldspar and muscovite via a separate aqueous fluid or hydrous silicate liquid.

A number of pegmatite K-feldspar samples have ε^{205}Tl values that are significantly lower than the average continental crust and mantle. These K-feldspar samples tend to be more altered than those with high ε^{205}Tl values. Element distribution maps show that K-feldspar samples with a heterogeneous distribution of Cs have low ε^{205}Tl values. The homogeneous distribution of Rb in these samples suggests Cs was lost to late-stage fluids. It is likely that these fluids preferentially removed ^{205}Tl by a dissolution-reprecipitation process (Parsons et al. 2009a,b). Loss of ^{205}Tl occurs due to a reduction in the electron density at the Tl nucleus caused by the association of Tl and Cl (Fang and Liu, 2019).

Most K-feldspar samples obtained from miarolitic pockets in NYF pegmatites show low ε^{205}Tl values. Non-amazonite K-feldspar show variable degrees of sericitization. In contrast, amazonite samples are pristine and exhibit higher ε^{205}Tl than non-amazonite varieties (see Table 1).

Geochemical indicators of alteration

As shown above, K-feldspar samples with low ε^{205}Tl values exhibit a uniform distribution in K and Rb and a heterogeneous distribution for Cs and, to a lesser extent, Tl. Moreover, there is a correlation between Ga/Cs vs. ε^{205}Tl but not for Ga/Rb vs. ε^{205}Tl (Fig. 20), indicating that the concentration of Cs and Tl is more sensitive to fluid alteration. When examining geochemical indicators of magmatic fractionation, some samples tend to deviate from the typical fractionation trend for rare element pegmatites (Černý et al., 1985). An example of this is the plot Rb/Cs vs Ga/Tl, in which there is a grouping of K-feldspar samples that depart from the magmatic trend and display low ε^{205}Tl values (Fig. 15). Samples Bikita, HIM-3, BL-1, BH-1, ZAP-1, PL-1, Spitz-2, Luster4 and MoatMtn all fall below the trend. Of those listed, samples Bikita, Spitz2, Luster4 and MoatMtn show a greatest degree of alteration.

CONCLUSIONS

This is the first comprehensive study of Tl isotopes in minerals from rare element granitic pegmatites. Pegmatite minerals exhibit some of the highest ε^{205}Tl values found to date, with K-feldspar samples ranging between –4.3 to 9.4 and mica samples ranging between –0.4 and 5.1 ε^{205}Tl units. A possible mechanism governing Tl isotope fractionation in pegmatites is the separation of an aqueous fluid from the granitic melt. Heavy thallium preferentially bonds to Cl- (Fang and Liu, 2020) resulting in an enrichment of ^{205}Tl in the coexisting H2O-rich phase. Minerals crystallizing in the presence of the H2O-rich phase may therefore incorporate more ^{205}Tl. Low ε^{205}Tl in pegmatite K-feldspar appears to be related to subsolidus alteration.

According to the model of Jahns and Burnham (1969), the coexistence of an aqueous phase and silicate melt is essential for the formation of pegmatite textures. It is therefore possible that significant fractionation of Tl isotopes may occur at the time of fluid exsolution. Alternatively, isotopic fractionation may occur during the formation of an exceedingly H2O-rich melt that evolves during pegmatite crystallization. Our results indicate that the most evolved

and economically interesting LCT-type pegmatites tend to yield high ε^{205}Tl values. We suggest that heavy Tl enrichment in late-stage muscovite and K-feldspar is a favorable indicator of rare element enrichment. The combination of thallium isotope and trace element data, for example K/Rb versus Ga, is useful for discriminating NYF- and LCT-type pegmatites and for assessing the rare element potential of an individual pegmatite.

ACKOWLEDGEMENTS

Support for this study was provided through the Targeted Geoscience Initiative Phase 5 Program (TGI-5). Project's Activity: Delineating the source(s) of rare element granitic pegmatites with application to exploration for tantalum, tin and lithium.

We are grateful to Mary Besaw and Olivia Pushie for their preliminary work on K-feldspar samples. We would also like to thank David Lentz and Chris MacFarlane (University of New Brunswick), Mark Badham (Queen's University), Karen Ferreira (University of Manitoba), Tania Martins (Manitoba Department of Natural Resources) and Michael Wise (Museum of Natural History Smithsonian Institute) for providing some of the samples used in this study. Mike Gadd provided insightful comments on an early version of this report.

REFERENCES

Armstrong, J.T., 1982. New ZAF and a-factor correction procedures for the quantitative analyses of individual microparticles, in: Microbeam Analysis-1982, K.F.J. Heinrich, ed., San Francisco Press, p. 175-180.

Armstrong, J.T., 1984. Quantitative analysis of silicate and oxide minerals. A reevaluation of the ZAF corrections and for new Bence-Albee coefficients, in: Microbeam Analysis-1984, D.E. Newbury, ed., San Francisco Press, p. 208-212.

Audétat, A. and Zhang, D., 2019. Abundances of S, Ga, Ge, Cd, In, Tl and 32 other major to trace elements in high-temperature (350–700°C) magmatic-hydrothermal fluids; Ore Geology Reviews, v. 109, p. 630-642.

Baker, D.R., 1998. Granitic melt viscosity and dike formation; Journal of Structural Geology v. 20, p. 1395-1404.

Baker, R.G.A., Rehkämper, M., Ihlenfeld, C., Oates, C.J. and Coggon, R., 2010. Thallium isotope variations in an ore-bearing continental igneous setting: Collahuasi Formation, northern Chile; Geochimica et Cosmochimica Acta v. 74, p. 4405-4416.

Bebie, J., Seward, T.M. and Hovey, J.K., 1998. Spectrophotometric determination of the stability of thallium (I) chloride complexes in aqueous solution up to 200°C; Geochimica et Cosmochimica Acta v. 62, p. 1643-1651.

Bebout, G.E., 2016. Cesium. In: White W (ed) Encyclopedia of Geochemistry; Encyclopedia of Earth Sciences Series. Springer, Cham.

Bebout, G.E., Ryan, J.G., Leeman, W.P. and Bebout, A.E., 1999. Fractionation of trace elements by subduction-zone metamorphism – effect of convergent-margin thermal evolution; Earth and Planetary Science Letters v. 171, p. 63-81.

Bigeleisen, J. 1996. Nuclear Size and Shape Effects in Chemical Reactions. Isotope Chemistry of the Heavy Elements; Journal of American Chemical Society v. 118, p. 3676-3680.

Blusztajn, J., Nielsen, S.G., Marschall, H.R., Shua, Y., Ostranderf, C.M. and Hanyu, T., 2018. Thallium isotope systematics in volcanic rocks from St. Helena – Constraints on the origin of the HIMU reservoir; Chemical Geology v. 476, p. 292-301.

Borisova, A.Y., Thomas, R., Salvi, S., Candaudap, F., Lanzanova, A. and Chmeleff, J., 2012. Tin and associated metal and metalloid geochemistry by femtosecond LA-ICP-QMS microanalysis of pegmatite–leucogranite melt and fluid inclusions: new evidence for melt–melt–fluid immiscibility; Mineralogy Magazine v. 76, p. 91-113.

Brown, J.A., 2001. Mineralogy and geochemistry of alkali feldspars from the Tanco pegmatite, southeastern Manitoba (Unpublished master's thesis). University of Manitoba, Fall. <https://mspace.lib.umanitoba.ca/xmlui/handle/1993/2693>.

Brown, T.J.A., 2010. Geology and geochemistry of the Kingman Feldspar, Rare Metals and Wagon Bow pegmatites. M.Sc. thesis. University of New Orleans.

Černý, P. and Ercit, T.S., 2005. The classification of granitic pegmatites revisited; The Canadian Mineralogist v. 43, p. 2005-2026.

Černý, P., Meintzer, R.E. and Anderson, A.J., 1985. Extreme fractionation in rare-element granitic pegmatites; selected examples of data and mechanisms; Canadian Mineralogist v. 23, p. 381-421.

Černý, P., 1991a. Rare-element Granitic Pegmatites. Part I: Anatomy and Internal Evolution of Pegmatite Deposits; Geoscience Canada v. 18, p. 49-67.

Černý, P., 1991b. Rare-element granitic pegmatites. Part II: Regional to global environments and petrogenesis; Geoscience Canada v. 18, p. 68-81.

Černý, P., Ercit, T.S. and Vanstone, P.T., 1996. Petrology and mineralization of the Tanco rare-element pegmatite, southeastern Manitoba – Field Trip Guidebook A4; Geological Association of Canada/Mineralogical Association of Canada Annual Meeting. Winnipeg, Manitoba, May 27-29, 1996.

Černý, P., Blevin, P.L., Cuney, M. and London, D., 2005. Granite-related ore deposits; Economic Geology, 100th Anniversary Volume, p. 337-370.

Crouse, R.A. and Černý, P., 1972. The Tanco pegmatite at Bernic Lake, Manifoba I. Geology and paragenesis; The Canadian Mineralogist v. 11, p. 591-608.

Der Channer, D.M. and Spooner, E.T.C., 1992. Analysis of fluid inclusion leachates from quartz by ion chromatography; Geochimica et Cosmochimica Acta v. 56, p. 249-259.

Ellis, A.J., 1967. The chemistry of some explored geothermal systems In Varnes, H.L. (ed) Geochemistry of Hydrothermal Ore Deposits; Holt, Rinehart and Winston, Inc, p. 465-514.

Ellis, A.J. and Mahon, W.A.J., 1964. Natural hydrothermal systems and experimental hot water/rock interactions; Geochimica et Cosmochimica Acta v. 28, p. 1323-1357.

Eyal, M. and Shimshilashvili, E., 1988. A comparative album for quantitative study of perthite textures; Israelian Journal of Earth Science v. 37, p.171-180.

Fang, T. and Liu, Y., 2019. Equilibrium thallium isotope fractionation and its constraint on Earth's late veneer; Acta Geochimica v. 38, p. 459-471.

Fitzpayne, A., Prytulak, J., Wilkinson, J.J., Cooke, D.R., Baker, M.J. and Wilkinson, C.C., 2018. Assessing thallium elemental systematics and isotope ratio variations in porphyry ore systems: a case study of the Bingham Canyon District; Minerals v. 8, p. 1-21.

Fujii, T., Moynier, F., Agranier, A., Ponzevera, E. and Abe, M., 2011. Nuclear field shift effect of lead in ligand exchange reaction using a crown ether; Proc Radiochim Acta v. 1, p. 387-392.

Fujii, T., Moynier, F., Agranier, A., Ponzevera, E., Abe, M., Uehara, A. and Yamana, J., 2013. Nuclear field shift effect in isotope fractionation of thallium; Journal of Radioanalytical Nuclear Chemistry v. 296, p. 261-265.

Gammel, E.M. and Nabelek, P.I., 2016. Fluid inclusion examination of the transition from magmatic to hydrothermal conditions in pegmatites from San Diego County, California; The American Mineralogist v. 101, p. 1906-1915.

Gladney, E.S. and Roelandts, I., 2007. 1988 compilation of elemental concentration data for CCRMP reference rock samples SY-2, SY-3 and MRG-1; Geostandards and Geoanalytical Research, v. 14, p. 373-458.

Heier, K.S., 1962. Trace elements in feldspars – a review; Norsk Geologisk Tidsskrift, v. 42, p. 415-454.

Heinrichs, H., Schulz-Dobrick, B. and Wedepohl, K.H., 1980. Terrestrial geochemistry of Cd, Bi, Tl, Pb, Zn and Rb; Geochimica et Cosmochimica Acta, v. 44, p. 1519-1533.

Hettmann, K., Marks, M.A.W., Kreissig, K., Zack, T., Wenzel, T., Rehkämper, M., Jacob, D.E. and Markl, G., 2014a. The geochemistry of Tl and its isotopes during magmatic and hydrothermal processes: The peralkaline Ilimaussaq complex, southwest Greenland; Chemical Geology, v. 366, p. 1-13.

Hettmann, K., Kreissig, K., Rehkämper, M., Wenzel, T., Mertz-Kraus, R. and Markl, G., 2014b. Thallium geochemistry in the metamorphic Lengenbach sulfide deposit, Switzerland: thallium-isotope fractionation in a sulfide melt; The American Mineralogist v. 99, p. 793-803.

Hoefs, J., 2009. Isotope Fractionation Processes of Selected Elements *In* Hoefs, J., Stable Isotope Geochemistry; Springer International Publishing, p. 35–92.

Holtz, F., Dingwell, D.B., Behrens, H., 1993. Effects of F, B_2O_3 and P^{205} on the solubility of water in haplogranite melts compared to natural silicate melts; Contributions to Mineralogy and Petrology, v. 113, p. 492-501.

Jahns, R.H. and Burnham, W.C., 1969. Experimental Studies of Pegmatite Genesis: A Model for the Derivation and Crystallization of Granitic Pegmatite; Economic Geology v. 64, p. 863-864.

Kaplan, D.I. and Mattigod, S.V., 1998. Aqueous geochemistry of thallium; Advances in Environmental Science and Technology v. 29, p. 15-30.

Keith, T.E.C., Thompson, J.M. and Mays, R.E., 1983. Selective concentration of cesium in analcime during hydrothermal alteration, Yellowstone National Park, Wyoming; Geochimica et Cosmochimica Acta v. 47, p. 795-804.

Kontak, D.J., Ansdell K., Dostal J., Halter W., Martin R. and Williams-Jones A.E. 2001. The nature and origin of pegmatites in a fluorine-rich leucogranite, East Kemptville Tin Deposit, Nova Scotia, Canada; Transactions of the Royal Society of Edinburgh: Earth Sciences v. 92, p. 173-200.

Liu, J., Yin, M., Xiao, T., Zhang, C., Tsang, D.C.W., Bao, Z., Zhou, Y., Chen, Y., Luo, X., Yuan, W. and Wang, J., 2020. Thallium isotopic fractionation in industrial process of pyrite smelting and environmental implications; Journal of Hazardous Materials, v. 384, p. 121378.

Lockett, N.H. (1979) The Geology of the Country around Dett. Rhodesia Geological Survey,

Bulletin No. 85; Salisbury; 199 p.

London, D., 1987. Internal differentiation of rare-element pegmatites: effects of boron, phosphorous and fluorine; Geochimica et Cosmochimica Acta v. 51, p. 403-420.

London, D., 2008. Pegmatites; The Canadian Mineralogist, Special Publication v. 10, p. 347.

Maneta, V., Baker, D.R. and Minarik, W., 2015. Evidence for lithium-aluminosilicate supersaturation of pegmatite-forming melts; Contributions to Mineralogy and Petrology v. 170, no. 4.

Maneta, V. and Anderson, A.J., 2018. Monitoring the crystallization of water-saturated granitic melts in real time using the hydrothermal diamond anvil cell; Contributions to Mineralogy and Petrology v. 173, no. 83.

McDonough, W.F. and Sun, S.S., 1995. The composition of the Earth; Chemical Geology v. 120, p. 223-253.

Melcher, F., Graupner, T., Gäbler, H., Sitnikova, M., Henjes-Kunst, F., Oberthür, G.A. and Dewaele, S., 2015 Tantalum–(niobium–tin) mineralisation in African pegmatites and rare metal granites: Constraints from Ta–Nb oxide mineralogy, geochemistry and U–Pb geochronology; Ore Geology Reviews v. 64, p. 667-719.

Moller, P. and Morteani, G., 1987. Geochemical Exploration Guide for Tantalum Pegmatites; Economic Geology v. 82, p. 1888-1897.

Moynier, F., Fujii, T., Brennecka, G.A. and Nielsen, S.G., 2013. Nuclear field shift in natural environments; C. R. Geoscience v. 345, p. 150-159.

Nabelek, P.I., Whittington, A.G. and Sirbescu, M.C., 2010. The role of H2O in rapid emplacement and crystallization of granite pegmatites: resolving the paradox of large crystals in highly undercooled melts; Contributions to Mineralogy and Petrology v. 160, p. 313-325.

Nielsen, S.G., Mar-Gerrison, S., Gannoun, A., LaRowe, D., Klemm, V., Halliday, A.N., Burton, K.W. and Hein, J.R., 2009b. Thallium isotope evidence for a permanent increase in marine organic carbon export in the early Eocene; Earth and Planetary Science Letters v. 278, p. 297-307.

Nielsen, S.G., Gannoun, A., Marnham, C., Burton, K.W., Burton, K.W., Halliday, A.N. and Hein, J.R., 2011b. New age for ferromanganese crust 109D-C and implications for isotopic records of lead, neodymium, hafnium, and thallium in the Pliocene Indian Ocean; Paleoceanography v. 26, no. 2.

Nielsen, S.G., Goff, M., Hesselbo, S.P., Jenkyns, H.C., LaRowe, D.E. and Lee, C.A., 2011. Thallium isotopes in early diagenetic pyrite –A paleoredox proxy? Geochimica et Cosmochimica Acta v. 75, p. 6690-6704.

Nielsen, S.G., Klein, F., Kadin, T., Blusztajn, J. and Wickham, K., 2015. Thallium as a tracer of fluid–rock interaction in the shallow Mariana forearc; Earth and Planetary Science Letters v. 430, p. 416-426.

Nielsen, S.G., Prytulak, J., Blusztajn, J., Shu, Y., Auro, M., Regelous, M. and Walker, J., 2017b Thallium isotopes as tracers of recycled materials in subduction zones: Review and new data for lavas from Tonga-Kermadec and Central America; Journal of Volcanology and Geothermal Research v. 339, p. 23-40.

Nielsen, S.G., Rehkämper, M., Brandon, A.D., Norman, M.D., Turner, S. and O'Reilly, S.Y., 2007. Thallium isotopes in Iceland and Azores lavas—Implications for the role of altered crust and mantle geochemistry; Earth and Planetary Science Letters v. 264, p. 332-345.

Nielsen, S.G., Rehkämper, M., Norman, M.D., Halliday, A.N. and Harrison, D., 2006a. Thallium isotopic evidence for ferromanganese sediments in the mantle source of Hawaiian basalts; Nature v. 439, p. 314-317.

Nielsen, S.G., Rehkämper, M., Porcelli, D., Andersson, P., Halliday, A.N., Swarzenski, P.W., Latkoczy, C. and Günther, D., 2005. Thallium isotope composition of the upper continental crust and rivers – An investigation of the continental sources of dissolved marine thallium; Geochimica et Cosmochimica Acta v. 19, p. 2007-2019.

Nielsen, S.G., Rehkämper, M., Teagle, D.A.H., Butterfield, D.A., Alt, J.C. and Halliday, A.N., 2006b. Hydrothermal fluid fluxes calculated from the isotopic mass balance of thallium in the ocean crust; Earth and Planetary Science Letters v. 251, p. 120-133.

Nielsen, S.G., Wasylenski, L.E., Rehkämper, M., Peacock, C.L., Xue, Z. and Moon, E.M., 2013. Towards an understanding of thallium isotope fractionation during adsorption to manganese oxides; Geochimica et Cosmochimica Acta v. 117, p. 252-265.

Nielsen, S.G., Williams, H.M., Griffin, W.L., O'Reilly, S.Y., Pearson, N. and Viljoen, F., 2009 Thallium isotopes as a potential tracer for the origin of cratonic eclogites; Geochimica et Cosmochimica Acta v. 73, p. 7387-7398.

Nielsen, S.G., Yogodzinski, G., Prytulak, J., Plank, T., Kay, S.M., Kay, R.W., Blusztajn, J., Owens, J.D., Auro, M. and Kading, T., 2016. Tracking along-arc sediment inputs to the Aleutian arc using thallium isotopes; Geochimica et Cosmochimica Acta v. 181, p. 217-237.

Nielson, S.G., Rehkämper, M. and Prytulak, J., 2017. Investigation and Application of Thallium Isotope Fractionation; Reviews in Mineralogy and Geochemistry, v. 82, p. 759-798.

Parsons, I. and Lee, M.R., 2009a. Mutual replacement reactions in alkali feldspars I: microtextures and mechanisms; Contributions to Mineralogy and Petrology v. 157, p. 641-661.

Parsons, I., Magee, C.W., Allen, C.M., Shelley, J.M.G. and Lee, M.R., 2009b. Mutual replacement reactions in alkali feldspars II: trace element partitioning and geothermometry; Contributions to Mineralogy and Petrology v. 157, p. 663-687.

Peacock, C.L. and Moon, E.M., 2012. Oxidative scavenging of thallium by birnessite: Explanation for thallium enrichment and stable isotope fractionation in marine ferromanganese precipitates; Geochimica et Cosmochimica Acta v. 84, p. 297-313.

Pearson, R.G., 1963. Hard and Soft Acids; Journal of the American Chemical Society v. 85, p. 3533-3539.

Pichavant, M., 1981. An experimental study of the effect of boron on a water-saturated haplogranite at 1 kbar vapour pressure; Contributions to Mineralogy and Petrology v. 76, p. 430-439.

Pretorius, W., Weis, D., Williams, G., Hanano, D., Kieffer, B. and Scoates, J., 2005. Complete trace elemental characterisation of granitoid (USGS G-2, GSP-2) reference materials by high resolution inductively coupled plasma-mass spectrometry; Geostandards and Geoanalytical Research v. 30, p. 39-54.

Prytulak, J., Brett, A., Webb, M., Plank, T., Rehkämper, M., Savage, P.S. and Woodhead, J., 2017. Thallium elemental behaviour and stable isotope fractionation during magmatic processes; Chemical Geology v. 448, p. 71-83.

Putnis, A., 2002. Mineral replacement reactions: from macroscopic observations to microscopic mechanisms; Mineralogy Magazine v. 66, p. 689-708.

Putnis, A. and Putnis, C.V., 2007. The mechanism of reequilibration of solids in the presence of a fluid phase; Journal of Solid State Chemistry v. 180, p. 1783-1786.

Rader, S.T., Mazdab, F.K. and Barton, M.D., 2018. Mineralogical thallium geochemistry and isotope variations from igneous, metamorphic and metasomatic systems; Geochimica et Cosmochimica Acta v. 243, p. 42-65.

Rankama, K., 1949. A note on the geochemistry of thallium; Journal of Geology v. 57, no. 6, p. 608-613.

Rekhämper, M., Frank, M., Hein, J.R., Porcelli, D., Halliday, A., Ingri, J. and Liebetrau, V., 2002. Thallium isotope variations in seawater and hydrogenetic, diagenetic, and hydrothermal ferromanganese deposits; Earth and Planetary Science Letters v. 197, p. 65-81.

Rekhämper, M., Frank, M., Hein, J.R. and Halliday, A., 2004. Cenozoic marine geochemistry of thallium deduced from isotopic studies of ferromanganese crusts and pelagic sediments; Earth and Planetary Science Letters v. 219, p. 77–91.

Roda-Robles, E., Simmons, W., Pesquera, A., Gil-Crespo, P.P., Nizamoff, J. and Torres-Ruiz, J., 2015. Tourmaline as a petrogenetic monitor of the origin and evolution of the Berry-Havey pegmatite (Maine, U.S.A.); The American Mineralogist v. 100, p. 95-109.

Sáchez-Muñoz, L., Müller, A., Andrés, S.L., Martin, R.F., Modreski, P.J. and Moura, O.J.M., 2016. The P-Fe diagram for K-feldspars: a preliminary approach in the discrimination of pegmatites; Lithos v. 272-273, p. 116-127.

Schauble, E.A., 2007. Role of nuclear volume in driving equilibrium stable isotope fractionation of mercury, thallium, and other very heavy elements; Geochimica et Cosmochimica Acta v. 71, p. 2170-2189.

Schauble, E.A., 2013. Modeling nuclear volume isotope effects in crystals. Proceedings of the National Academy of Science v. 110, p. 17714-17719.

Shu, Y., Nielsen, S.G., Zeng, Z., Shinjo, R., Blusztajn, J., Wang, X. and Chen, S., 2017. Tracing subducted sediment inputs to the Ryukyu arc-Okinawa Trough system: Evidence from thallium isotopes; Geochimica et Cosmochimica Acta v. 217, p. 462-491.

Simmons, W.B. and Webber, K.L., 2008. Pegmatite genesis: state of the art; European Journal of Mineralogy v. 20, p. 421-438.

Stilling, A., Černý, P. and Vanstone, P.J., 2006. The Tanco pegmatite at Bernic Lake, Manitoba. XVI. Zonal and bulk compositions and their petrogenetic significance; The Canadian Mineralogist v. 44, p. 599-623.

Teng, F., Dauphas, N. and Watkins, J.M., 2017. Non-traditional stable isotopes: retrospective and prospective; Reviews in Mineralogy and Geochemistry v. 82, p. 1-26.

Thomas, R. and Davidson, P., 2008. Water and melt/melt immiscibility, the essential components in the formation of pegmatites; evidence from melt inclusions; Z. Geol. Wiss v. 36, p. 347-364.

Veksler, I.V., Thomas, R. and Schmidt, C., 2002. Experimental evidence of three coexisting immiscible fluids in synthetic granitic pegmatite; The American Mineralogist v. 87, p. 775-779.

Webber, K.L., Simmons, W.B., Falster, A.U. and Hanson, S.L., 2019. Anatectic pegmatites of the Oxford County pegmatite field, Maine, USA; The Canadian Mineralogist v. 57, p. 811-815.

Whalen, J.B., Currie, K.L. and Chappel, B.W., 1987. A-type granites: geochemical characteristics, discrimination and petrogenesis; Contributions to Mineralogy and Petrology v. 95, p. 407-419.

Wood, S.A. and Samson, I.M., 1998. Solubility of ore minerals and complexation of ore metals in hydrothermal solutions; Reviews in Economic Geology v. 10, p. 33-80.

Yang, S. and Liu, Y., 2015. Nuclear volume effects in equilibrium stable isotope fractionations of mercury, thallium and lead; Scientific Reports v. 5, p. 12.

Zajacz, Z., Halter, W.E., Pettke, T. and Guillong, M., 2008. Determination of fluid/melt partition coefficients by LA-ICPMS analysis of co-existing fluid and silicate melt inclusions: Controls on element partitioning; Geochimica et Cosmochimica Acta v. 72, p. 2169–2197.

Link to Appendix Tables: of_8755_appendix_tables.xlsx

APPENDIX A – K-FELDSPAR COMPOSITIONS

APPENDIX B – MICA COMPOSITIONS

APPENDIX C – POLLUCITE COMPOSITIONS

APPENDIX D – PYRITE COMPOSITION

APPENDIX E – OBSIDIAN COMPOSITIONS

The role of enigmatic deep crustal and upper mantle structures on Au and magmatic Ni–Cu–PGE–Cr mineralization in the Superior Province

L.B. Harris[1], P. Adiban[1], and E. Gloaguen[1]

Harris, L.B., Adiban, P., and Gloaguen, E., 2021. The role of enigmatic deep crustal and upper mantle structures on Au and magmatic Ni–Cu–PGE–Cr mineralization in the Superior Province; in *Targeted Geoscience Initiative 5: grant program final reports (2018-2020), Geological Survey of Canada, Open File 8755, p. 85–128. https://doi.org/10.4095/328984*

Abstract: Aeromagnetic and ground gravity data for the Canadian Superior Province, filtered to extract long wavelength components and converted to pseudo-gravity, highlight deep, N-S trending regional-scale, rectilinear faults and margins to discrete, competent mafic or felsic granulite blocks (i.e. at high angles to most regional mapped structures and sub-province boundaries) with little to no surface expression that are spatially associated with lode ('orogenic') Au and Ni–Cu–PGE–Cr occurrences. Statistical and machine learning analysis of the Red Lake-Stormy Lake region in the W Superior Province confirms visual inspection for a greater correlation between Au deposits and these deep N-S structures than with mapped surface to upper crustal, generally E-W trending, faults and shear zones. Porphyry Au, Ni, Mo and U-Th showings are also located above these deep transverse faults.

Several well defined concentric circular to elliptical structures identified in the Oxford Stull and Island Lake domains along the S boundary of the N Superior proto-craton, intersected by N- to NNW striking extensional fractures and/or faults that transect the W Superior Province, again with little to no direct surface or upper crustal expression, are spatially associated with magmatic Ni–Cu–PGE–Cr and related mineralization and Au occurrences. The McFaulds Lake greenstone belt, aka. 'Ring of Fire', constitutes only a small, crescent-shaped belt within one of these concentric features above which 2736-2733 Ma mafic-ultramafic intrusions bodies were intruded. The Big Trout Lake igneous complex that hosts Cr-Pt-Pd-Rh mineralization west of the Ring of Fire lies within a smaller concentrically ringed feature at depth and, near the Ontario-Manitoba border, the Lingman Lake Au deposit, numerous Au occurrences and minor Ni showings, are similarly located on concentric structures. Preliminary magnetotelluric (MT) interpretations suggest that these concentric structures appear to also have an expression in the subcontinental lithospheric mantle (SCLM) and that lithospheric mantle resistivity features trend N-S as well as E-W. With diameters between ca. 90 km to 185 km, elliptical structures are similar in size and internal geometry to coronae on Venus which geomorphological, radar, and gravity interpretations suggest formed above mantle upwellings. Emplacement of mafic-ultramafic bodies hosting Ni-Cr-PGE mineralization along these ring-like structures at their intersection with coeval deep transverse, ca. N-S faults (viz. *phi structures*), along with their location along the margin to the N Superior proto-craton, are consistent with secondary mantle upwellings portrayed in numerical models of a mantle plume beneath a craton with a deep lithospheric keel within a regional N-S compressional regime. Early, regional ca. N-S faults in the W Superior were reactivated as dilatational antithetic (secondary Riedel/R') sinistral shears during dextral transpression and as extensional fractures and/or normal faults during N-S shortening. The Kapuskasing structural zone or uplift likely represents Proterozoic reactivation of a similar deep transverse structure.

Preservation of discrete faults in the deep crust beneath zones of distributed Neoarchean dextral transcurrent to transpressional shear zones in the present-day upper crust suggests a 'millefeuille' lithospheric strength profile, with competent SCLM, mid- to deep, and upper crustal layers. Mechanically strong deep crustal felsic and mafic granulite layers are attributed to dehydration and melt extraction. Intra-crustal decoupling along a ductile décollement in the W Superior led to the preservation of early-formed deep structures that acted as conduits for magma transport into the overlying crust and focussed hydrothermal fluid flow during regional deformation. Increase in the thickness of semi-brittle layers in the lower crust during regional metamorphism would result in an increase in fracturing and faulting in the lower crust, facilitating hydrothermal and carbonic fluid flow in pathways linking SCLM to the upper crust, a factor explaining the late timing for most orogenic Au.

Results provide an important new dataset for regional prospectively mapping, especially with machine learning, and exploration targeting for Au and Ni-Cr-Cu-PGE mineralization. Results also furnish evidence for parautochthonous development of the S Superior Province during plume-related rifting and cannot be explained by conventional subduction and arc-accretion models.

[1]Institut national de la recherche scientifique (INRS-ETE), 490 de la Couronne, Québec, QC, G1K 9A9 Canada
*Corresponding author: Lyal Harris (email: lyal.harris@inrs.ca)

INTRODUCTION

Whilst geological mapping in Canada has traditionally focused on documenting features at or, through drilling and conventional geophysics, close to the Earth's surface, this project aims at mapping faults (especially those at a high angle to mapped geological trends), regional-scale circular to elliptical structures, and the contacts between geological domains or sub-province boundaries in the mid- to lower crust to determine their relationship to lode ('orogenic') Au and magmatic Ni-Cr-Cu-PGE occurrences in the Superior Province in Canada. The study combines the extraction and enhancement of deep-source components of aeromagnetic data and their interpretation, along with the preliminary processing and interpretation of magnetotelluric (MT) data for the W Superior Province (Fig. 1a) in 2D and 3D to establish the geometry of structures in the subcontinental lithospheric mantle (SCLM). Results of regional aeromagnetic enhancements and interpretations and a case study incorporating NRCan ground Bouguer gravity data and statistical analysis in the Red Lake-Stormy area of the W Superior (Fig. 1c) are presented; a comparison is also made with deep structural controls established in the NE Superior Province, where detailed analysis is presented by Cleven et al. (2020a,b) for the Eeyou Istchee Baie-James region (Fig. 1c). Additional detailed studies in SE Ontario, especially the Schrieber area (Fig. 1c), which included the Hemlo Au deposit, and Québec (Rivière Delay, Fig. 1c), the extension of Archean structures beneath the Cape-Smith - Ungava Orogen and SE Churchill Province (Fig. 1b), and satellite gravity disturbances for the Superior Province and surrounds south of 60°N also undertaken in this TGI project will be presented in subsequent articles and a MSc thesis. Research outcomes will help the understanding of the origin and setting of mineral deposits, and hence aid regional mineral exploration targeting; this research also has implications for tectonic models in the absence of plate tectonics, not only for the Superior Province, but for all Archean terrains.

BACKGROUND

Long-lived deep crustal and SCLM structures exert primary controls on cratonic architecture and the localisation of mineral deposits in diverse tectonic settings (e.g. Watson and O'Hara, 1980; Konstantinov et al., 1999; Favorskaya and Vinogradov, 1991; Hildenbrand et al., 2000; Kutinia et al., 2003; Bierlein et al., 2006; Begg, 2009; Begg et al., 2010; Hronsky, 2013). Discrete structures in metasomatized SCLM and in the deep crust may focus the flow of volatile-rich mantle-sourced fluids and magmas related to a range of mineral deposit types (Groves and Santosh, 2015; Groves et al., 2016); their reactivation creates both faults and/or broad corridors of increased deformation induced permeability (Hronsky, 2020) in the mid- to upper-crust and host structures for mineralization, whose geometry may differ from those developed in the absence of such pre-existing weaknesses. Hronsky (2011) concludes that '…ore formation is the by-product of transient, and rather rare, periods of anomalous dynamics during the evolution of large-scale fluid flux systems. Large-scale geodynamics, patterns of lithospheric architecture and the lithosphere history provide the critical spatial context for these dynamic systems'. Mapping deep structures and establishing their geodynamic and lithospheric setting and reactivation history is an important element in exploration targeting strategies using a systematic mineral systems approach (Hronsky and Groves, 2008; McCuaig and Hronsky, 2014) and is a recommendation of the Australian Academy of Sciences (2010) *Think Tank* 'Searching the Deep Earth: The Future of Australian Resource Discovery and Utilisation'.

Despite their importance for mineral exploration, deep structures are not readily identified using conventional techniques at the deposit to district scales of mapping: Hronsky's presentation included in the Australian Academy of Sciences (2010) report states that lithospheric scale structures that exert fundamental controls on giant metal deposits never manifest themselves as major faults in the near surface environment and have cryptic or complex geophysical signatures, hence there are often difficulties in recognising the most important structures in high resolution geophysical data. This is most likely why they have not previously been documented in the W Superior Province, at least in the public domain; specialised treatments of geophysical data not generally undertaken are required to map them, as described below.

METHODS

Geophysical enhancements

Regional NRCan aeromagnetic for the whole Canadian Superior Province and NRCan-MERN TGI Abitibi aeromagnetic data (Keating et al., 2010), aeromagnetic 'supergrid' data (Ontario Geological Survey, 2017), MERN Québec detailed aeromagnetic data accessed through SIGÉOM[2] (Fig. 1), and NRCan Bouguer gravity for the W Superior (at an average station spacing between 12 and 15 km) were filtered and enhanced to portray structures at different crustal levels using Oasis Montaj software by Geosoft. Aeromagnetic data were first reduced to the pole to centre anomalies over their source (Baranov and Naudy, 1964; Blakely, 1995). Aeromagnetic data were also converted to pseudo-gravity (magnetic potential). In doing so, a dipolar magnetic field is converted to a monopolar field resembling gravity (Baranov, 1957; Blakely, 1995) to highlight regional, deep-source anomalies representing tectono-stratigraphic domain or terrane boundaries and distinct lithological units and intrusions in the deep crust. Features in pseudo-gravity images still, however, reflect initial differences in magnetic susceptibility.

[2]SIGÉOM: Système d'information géominière of Québec, https://sigeom.mines.gouv.qc.ca/signet/classes/I1102_indexAccueil?l=f

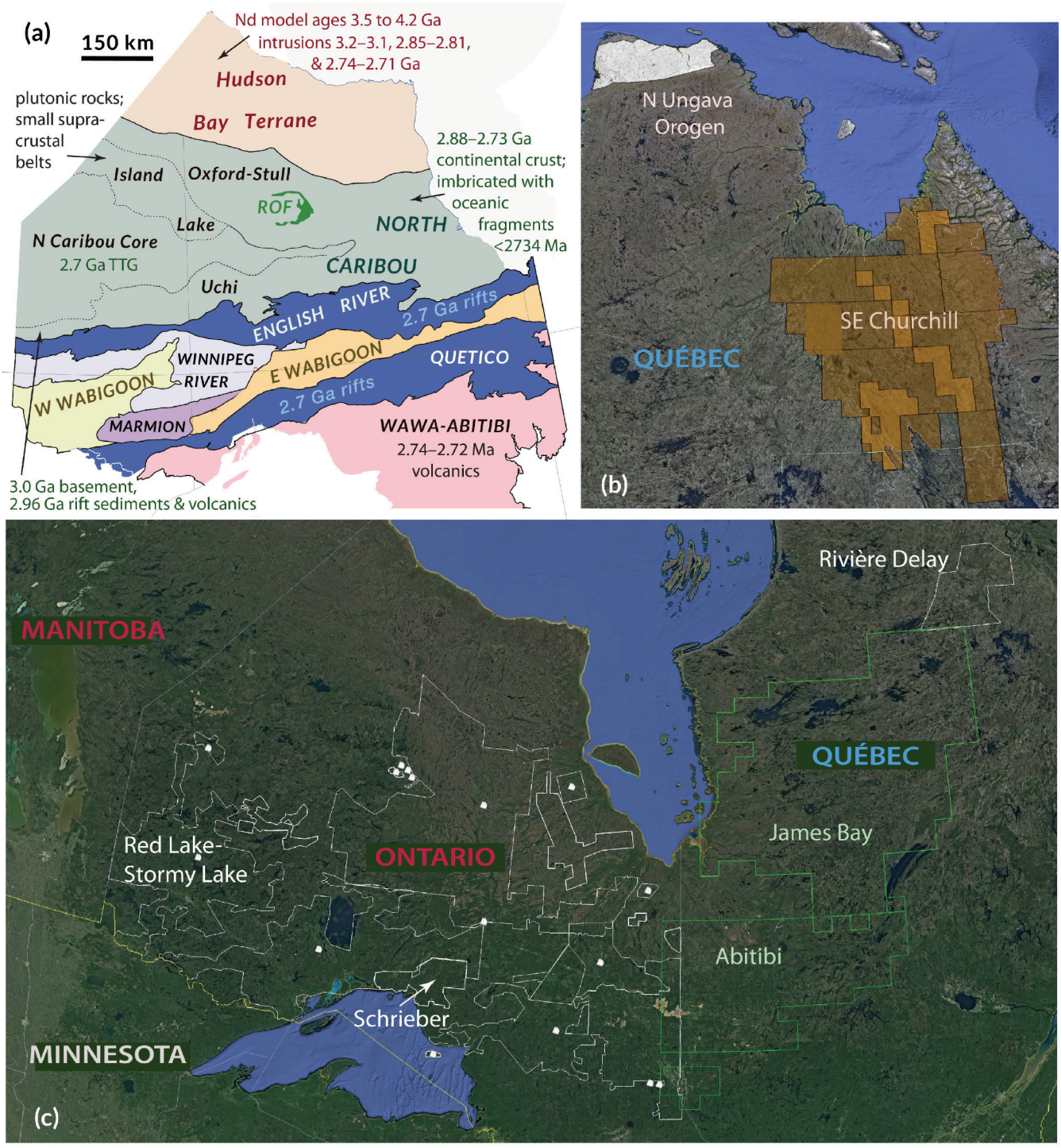

Figure 1. (a) Western Superior subprovinces in Ontario (modified after Stott, 2011). ROF = Ring of Fire (McFaulds Lake greenstone belt). **(b)** and **(c)** Location of detailed aeromagnetic images used in this project. White lines: location of Ontario Geological Survey (2017) 'supergrids', all of which were filtered and enhanced in this project; detailed interpretations, statistical analysis and machine learning carried out in the Red Lake - Stormy Lake are discussed in this report. Green and orange: MERN Québec (James Bay and SE Churchill) and TGI Abitibi data provided by NRCan enhanced in prior studies in the Superior and SE Churchill respectively. Detailed studies in the Schrieber area (especially over the Hemlo district) and the Ungava Orogen - Cape Smith Belt (white filled area), Rivière Delay and SE Churchill Province using MERN data will be presented in subsequent publications. Satellite images are from Google Earth.

Components corresponding to different source depths were extracted through interactive filtering using a butterworth filter based on changes in slope of the radially averaged power spectrum (Spector and Grant, 1970; Cowan and Cowan, 1993; Likkason, 2011; Kalberg et al., 2015); this is a standard geophysical technique in regional studies (e.g. Sadek et al., 1984; Naidu et al., 1998a,b; Urquhart, 2009), but appears to be little used in N America apart from by major exploration companies. Each component was subsequently enhanced using local phase filters (Cooper and Cowan, 2006), especially tilt angle (Miller and Singh, 1994; Salem et al., 2007; Blakely et al., 2016) and theta map/angle (Wijns et al., 2005) to better define geological contacts, faults, shear zones, etc., and to enhance subtle features for geological interpretation (using principals outlined by Dentith et al., 2000 and Isles and Rankin, 2013). Components with source depths of ca. 10 km or less were used to interpret structures and establish the deformation regime in rocks within the present-day upper crust. Structures and lithological contacts in aeromagnetic images processed to highlight deeper features have a maximum source depth of ca. 50 km, possibly even deeper. Depth values are derived from calculations within Oasis Montaj over the average of the slope of the energy spectrum (s) over 5 points where the depth (h) to a statistical ensemble of sources is determined by the expression, $h=s/4\pi$ (Geosoft, 2015). Based on crustal depth averages between 40 km and 41 km in the western Superior (Musacchio et al., 2004), and similar Moho depths determined in the Abitibi (Clowes et al., 1996), from these depth calculations based on power spectra the long wavelength 'deep-source' aeromagnetic images portray structures down to, and even possibly beneath, the base of the crust. This deep maximum source depth estimate is compatible with detailed Curie depth studies in the Quebec portion of the Superior Province (B. Giroux, INRS, unpublished data) and other Archean cratons have comparable or even greater source depths, e.g. in Australia (Chopping and Kennett, 2015).

NRCan magnetotelluric (MT) data, provided in table form by J. Craven (NRCan) and described by Roots and Craven (2017) were gridded using a minimum curvature method for different crustal depths. Horizontal gradients were also calculated to highlight circular and linear features in map view (as undertaken by Fishwick and Rawlinson, 2012 and Ramachandran, 2012). Preliminary resistivity isosurfaces extracted from voxels created by 3D gridding were combined with other map and geophysical data for 3D visualisation in Oasis Montaj. Analysis of MT data has been restricted to the lithosphere, which in the central and western Superior Province south of the Hudson Bay Terrane (Fig. 1a), has a maximum depth of ca. 200 km (Darbyshire et al., 2007). Available MT resistivity data is low resolution, especially in the northern part of the study area (station locations are provided in Roots and Craven, 2017). These authors state that data from over half of the stations collected had to be excluded due to lack of computer memory and software limitations; MT results and interpretations are therefore tentative and inverting all MT data is required to validate any conclusions made herein.

To portray the form of the N Superior proto-craton keel, S-wave seismic tomography data (Godey et al., 2003, 2004) were gridded as 3D voxels and isosurfaces were calculated and portrayed in Oasis Montaj. The full interactive 3D model is available as supplementary data to Harris and Bédard (2014b) and a depth slice at 120 km for the whole Superior Province is presented in Bédard and Harris (2014).

Statistical analysis and machine learning

A test case was undertaken to use machine learning algorithms to produce predictive maps of hydrothermal-type Au deposits and to rank the importance of regional scale structures of different orientations on mineralisation on a local-scale at the Red Lake-Stormy Lake area (corresponding to the Ontario Geological Survey's 'supergrid' of this name, Fig. 1c) in the western Superior Province.

Training a machine learning model involves finding the parameters that can fit the input "x" (evidential features in Fig. 3) and make predictions based on labels "y". The ensemble tree method combines decision trees, which provides a flexible approach to the bias-variance trade-off (Kohavi and Wolpert, 1996). The bias error is defined as erroneous assumptions from the data where the correlations between evidential features and labels are not recognized (i.e. the model is underfitting the data). A high variance may result in the model predicting noise in the data and therefore not able to generalize the relationship between features and label. In this case the model is overfitting the data.

Decision Trees

A decision tree (DT) is a set a hierarchical nodes where the data is split depending on the value of its evidential feature (e.g. pixels are categorized based on the magnetic intensity value assigned to them). Once the data is split at a given node, it receives a prediction score, also known as gain. The gain of the split determines the quality of the split. The aim of each split is to reduce the variance and eventually perfectly split the data into their correct labels, viz. perfectly determine the node condition that splits data into gold and non-gold pixels (Breiman et al., 1984). It is difficult to capture all the relationships within a given dataset with a single decision tree. The tree can either become too complex as it grows deeper and overfits the data or the decision tree will be unable to capture the interaction between all evidential features and labels if it heavily regularized. Random Forest (RF) and Gradient Boosted Decision Trees (GBDT) are two common methods of combining DTs into an ensemble tree method.

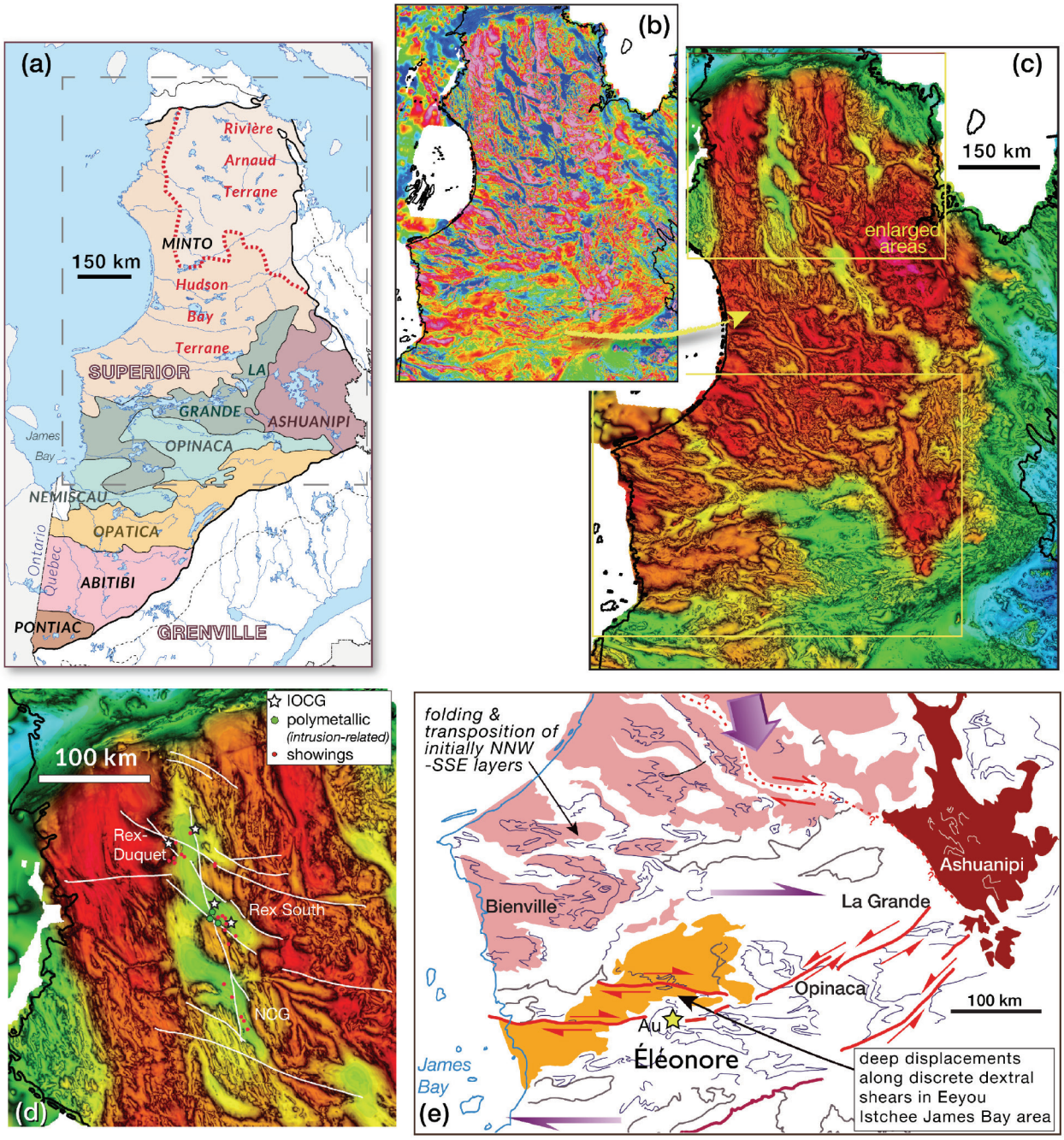

Figure 2. (a) Subprovinces of the eastern Superior Province, modified after SIGÉOM, MERN (Québec) and Boily et al. (2009). Dashed box = location of images in (b) and (c). **(b)** Unprocessed image of NRCan aeromagnetic data for the NE Superior Province. **(c)** Pseudo-gravity image (see Methods section) filtered to highlight deep crustal structures. Boxes = locations of the image in (d) and its interpretation in (e). **(d)** Enlargement of (c) showing mineral occurrences in the 'Rex Trend' of Azimut Exploration Inc. (Lulin et al, 2012; Lulin, 2016) that are located on the margins to deep crustal blocks, offset from and oblique to mapped domain boundaries and near-surface aero-magnetic trends. Simplified structural interpretation showing faults formed late in the deformation history of the NE Superior localised by these basement discontinuities which appear spatially associated with mineralization. **(e)** Schematic interpretation of the southern part of the image in (c) covering the Eeyou-Istchee-James Bay area. Whilst aeromagnetic images enhanced to portray upper crustal deformation illustrate distributed ductile deformation during dextral transpression in the Opinaca - southern La Grande sub-provinces (Cleven et al., 2020a, b), discrete dextral shears displace a competent crustal unit (orange) interpreted as anhydrous felsic granulite (due to lack of any associated gravity anomaly) *beneath* a regional ductile dextral transpressional shear zone (Cleven et al., 2020a). Undoing displacement on dextral shears shows this orange unit was initially elongated ca. N-S, i.e. parallel to regional lithological and structural trends in the northern Minto Subprovince, implying this subprovince constitutes basement to the Opinaca and La Grande subprovinces which formed during mantle plume or OUZO-related rifting. The Éléonore (Roberto) Au deposit occurs at the intersection of dextral regional and sinistral (antithetic) faults in the deep crust.

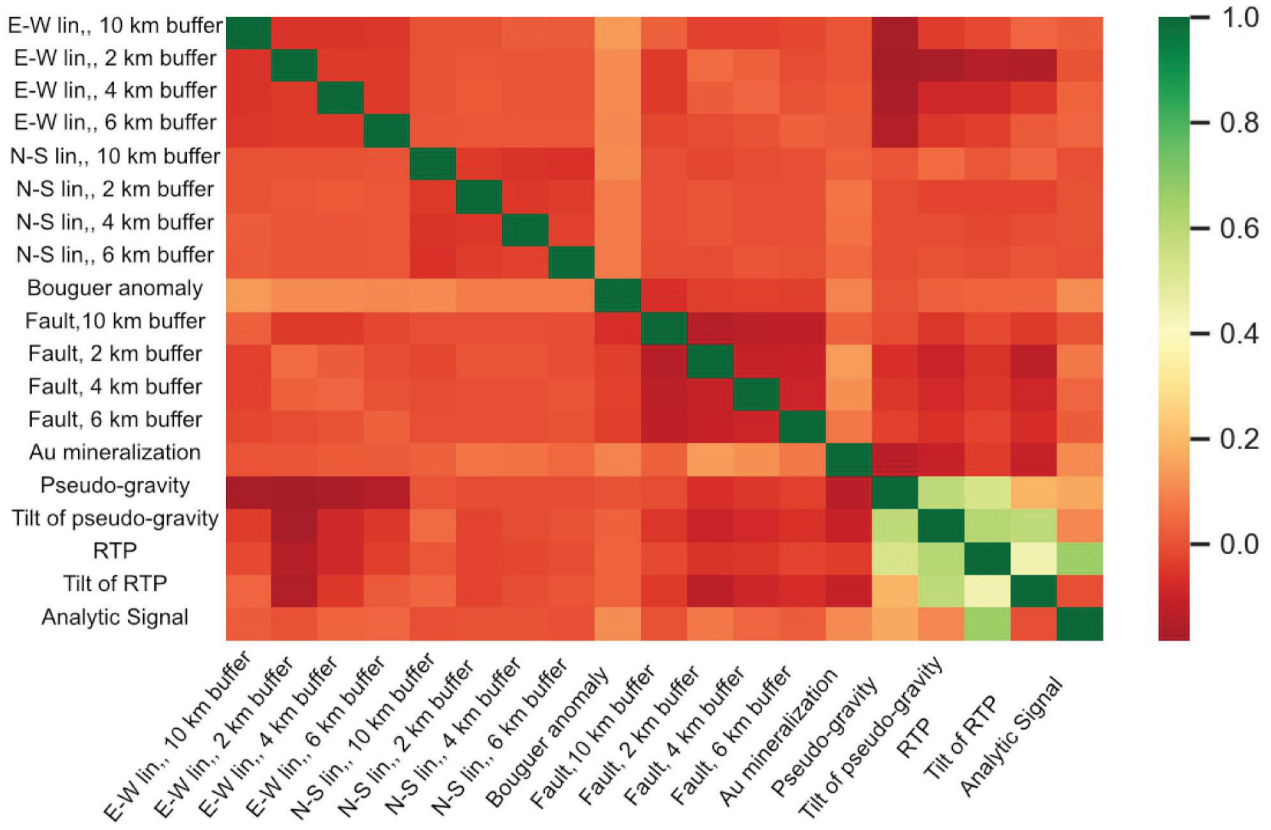

Figure 3. Correlation matrix of all the evidential features training the machine learning model, where the features are all in raster format. The lineaments and structural data are defined by Boolean values where the pixels contained within the designated buffer is equal to 1 and those outside of the buffer region are equal to 0. Buffer distance refers to the maximum distance from line features where the buffer area is defined. The end of line round with a radius equal to the maximum distance. The buffer area is defined by a maximum value of the buffer distance and a minimum value of the buffer distance (previous buffer increment). In addition, the mean, median, minimum, maximum, variance, standard deviation, skew, and kurtosis of all features were calculated and used as evidential features. In this figure, there appears to be very little to no correlation between the different variables. This indicates that it is unlikely that there would be a linear relationship between a feature and the label (Au mineralization). However, machine learning algorithms are capable of combining various features to potentially identify complex relationship between the features and the label. Furthermore, ensemble tree methods can identify non-linear relationship due partly to the chain metrics of decision trees and randomization elements of combining trees and treating the data.

Gradient Boosting Decision Trees

The goal of any model is to produce a prediction ŷ given input x. In Gradient Boosting Decision Trees (GBDT) the parameters applied to the input x are contained within a "tree function", where k is the number of trees. For the i-th example of the input data, the prediction ŷ is:

$$\sum_{k=1}^{K} T_k(x_i). \tag{1}$$

The tree parameters are a set of functions such that $\Theta = [T_1, T_2,\ldots, T_k]$. In supervised learning the goal is to optimize an objective function defined as $obj(\Theta) = L(\Theta) + \Omega(\Theta)$ (Chen, 2014). $L(\Theta)$ is the loss function that measures the accuracy of the model and $\Omega(\Theta)$ is the regularization function that measures its complexity. The objective function can be further simplified to:

$$\sum_{i=1}^{n} l(y_i - \hat{y}_i) + \sum_{k=1}^{K} \Omega_k(T) \tag{2}$$

where l is a function that compares the predicted value ŷ to the actual value y, and the regularization function Ω is applied to the summation of trees. The boosting process (Fig. 4) begins with one DT followed by further DTs added to optimize the objective function. The optimization process involved calculating the residual error of the model and adding trees that solve for those residual errors (Friedman, 2001).

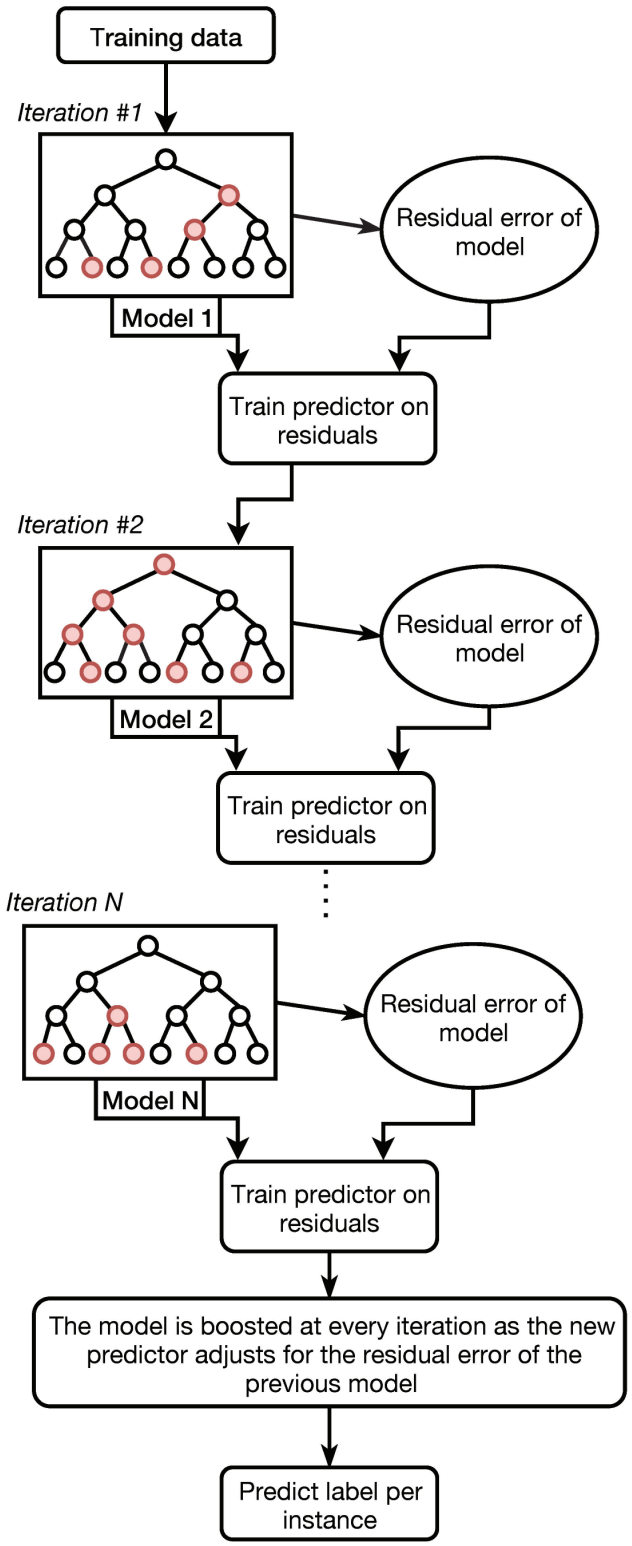

Figure 4. Flow chart of the boosting process. Boosting is an iterative process where the training data is fit with a decision tree to start and then additional trees (also referred to as "weak learners") are applied to adjust for the residual error. This process is repeated N times depending on conditions set by the user. To test the model, data that was put aside (testing data) is applied to the sum of all the trees and the predicted labels are compared to the true label.

eXtreme Gradient Boosting

eXtreme Gradient Boosting (XGB) was proposed as an alternative method to GBDT by (Chen and Guestrin, 2016). XGB applies calculates L1 and L2 norms (GBDT with typically one of the two) in the regularization function therefore penalizing complexity at each node. In GBDT and XGB row subsampling of the training set (i.e. using a portion of the input data) during tree growth adds a randomization factor that reduces variance. XGB adds column subsampling of the features, therefore adding another element of randomness and decreasing variance while increasing bias. The aforementioned regularization functions prevent overfitting of the model to the data. XGB uses the Newton-Raphson method of optimization for the loss function (Galántai, 2005) which uses the second order derivative in order to find a minima of a function. The limitation is that the loss function must be a function where its second derivative exists. However, it is more accurate and the model is able to better capture the relationship between labels and features.

Random Forest

Random Forest (RF) is an ensemble tree method that combines K number of DTs using bootstrap aggregation (bagging) and the final prediction is decided by a voting process for the most popular class (Breiman, 2001). Bagging (Fig. 5) is a process where the training data is randomly split into K independent subsets with a consistent distribution as the original data (Breiman, 1996). For an input vector x, a DT develops parameters in the form of a function T(x) that result in a prediction $\hat{y}$. Bagging reduces variance while retaining bias, therefore producing a more robust model (Breiman, 1996) compared to a single DT as it is adaptable to slight variations in the data. Bagging is also applied to the features while training individual trees. At each node, the best split/best feature is chosen from a subset of all features that went through the bagging process.

Data Sampling

The XGBoost and RF algorithm models were trained on an oversampled dataset and an under-sampled dataset. A pixel (representing a 2 km x 2 km area on the raster image) was classified as gold-bearing at a low threshold of 2 showings/occurrences, nonetheless, the unsampled dataset remains highly imbalanced (positive labels make up 5,240 data points of the overall 39,424). Balancing the data is possible by under-sampling the majority class (i.e. remove non-gold pixels until we reach the desired balance between positive and negative targets) or oversample the minority class (i.e. add points to the data set based on the relationship between the points). By under-sampling majority data, the model will lose information on that class, and the power of prediction decreases; oversampling the data, however, may

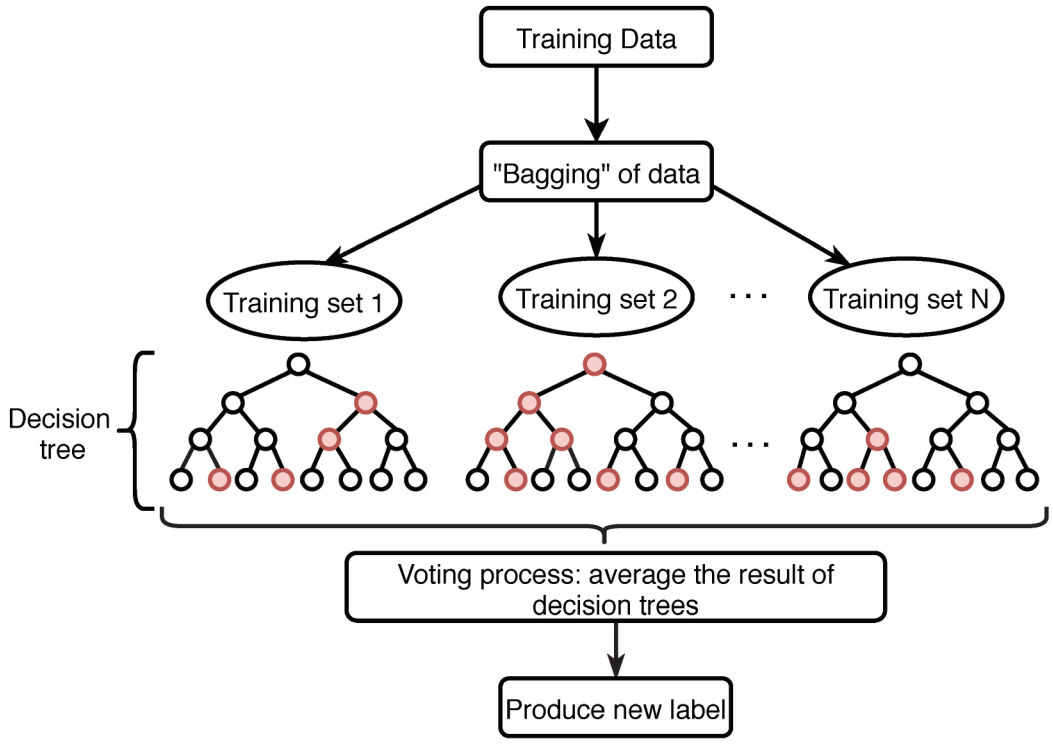

Figure 5. Flow chart of the bagging process. The training data is is randomly split into N different sets while maintaining a similar distribution as the original data. Each set is assigned a decision tree and the result of all decision trees are compiled. Testing data is applied to the compilation of trees and a prediction label is produced through a voting process.

result in overfitting and lowers the ability of the model to generalize a relationship. This study uses simple oversampling and simple undersampling. In simple oversampling, pixels containing gold were randomly duplicated until the number of gold pixels were equal to the number of non-gold pixels. In simple under-sampling, pixels without gold were randomly eliminated until the number of gold containing and empty pixels were equal.

RESULTS

Deep transverse faults and concentric elliptical structures in the western Superior

NRCan total field (TMI) aeromagnetic data over the W Superior Province (Fig. 6a) was filtered to extract different source depth components and converted to pseudogravity (as explained in the Methods section above) to show both near surface structural and lithological trends, faults and shear zones and mid- to deep crustal structures. Images of the short wavelength component representing sources in the upper 10 km of the crust, such as the grayscale tilt angle image in Figure 6b, show that the faults and shear zones in this aeromagnetic image correspond to regional faults mapped by the Ontario and Manitoba geological surveys. Ternary images combining pseudo-gravity horizontal and vertical gradient grids for the western Superior Province (Fig. 6c), highlight N-S to NNW-SSE striking faults that cross-cut the entire western Superior Province in the deep crust. Most are oblique to mapped surface structures (Fig. 6d). They appear most pronounced in the North Caribou Terrane, although some extend beneath southern sub-provinces, and several of these transverse structures were also identified in the Hudson Bay Terrane (see Fig. 1a for a subprovinces map). Concentric elliptical structures were also identified in this image: the most prominent are 4 concentric, circumferential features ca. 90 -185 km in diameter within the Oxford-Stull and Island Lake domains in, from W to E, the Norway House (#1), Lingham Lake (#2), Big Trout Lake (#3) and the Ring of Fire (#4) areas (Fig. 6c); another potential elliptical structure may occur immediately SW of feature #1. The striking N-S to NNW-SSE rectilinear faults at a high angle to regional geological trends that splay from the Lingham Lake and Big Trout Lake elliptical features (Fig. 6c) have no expression in the tilt angle image of the upper 10 km 'shallow-source' aeromagnetic component (Fig. 6b) and, for the most part, do not correspond to mapped faults (Fig. 6d). Both rectilinear transverse and concentric structures are also seen in images (especially the tilt angle) of aeromagnetic

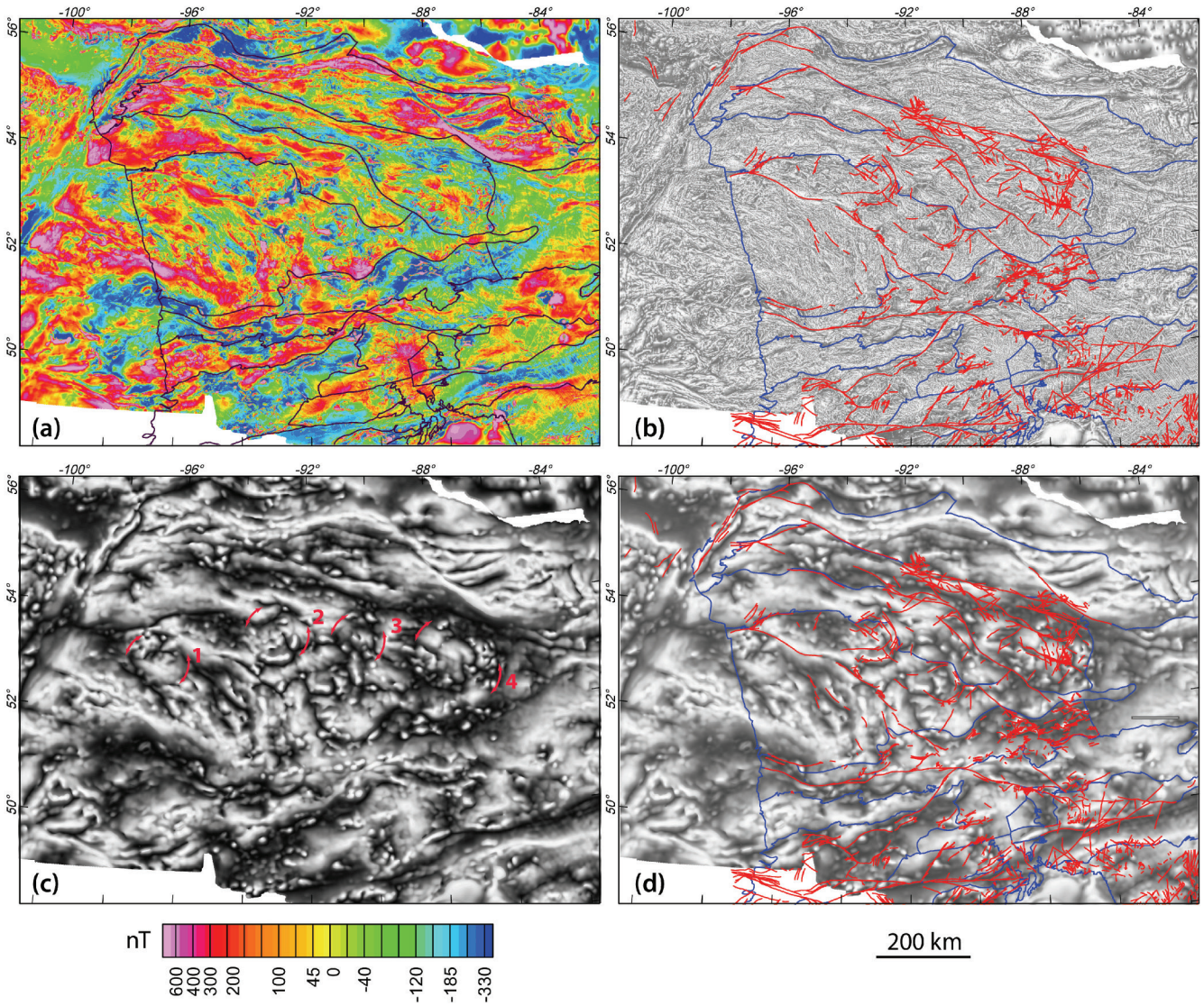

Figure 6. Aeromagnetic and pseudo-gravity images for the W Superior Province. **(a)** Original NRCan aeromagnetic image with sub-province boundaries (see Fig. 1a for names, not shown here for clarity). **(b)** Short wavelength (= upper 10 km source depths) aeromagnetic grayscale tilt image portraying upper crustal structures overlain by mapped faults (OGS and Manitoba Geological Survey). **(c)** & **(d)** Pseudo-gravity ternary gradient image highlighting (i) deep concentric elliptical structures, whose main, well defined outer rims are partially outlined in (c): #1 = Norway House, #2 = Lingham Lake, and #3 = Big Trout Lake; the Big Trout Lake Cr-PGE-(Ni) occurrence occurs on the rim of this structure. The 'Ring of Fire' (Fig. 1a) occurs within elliptical structure #4, named the Greater Ring of Fire (enlarged in Fig. 7). (ii) Deep N- to NNW-striking faults oblique to those mapped at the surface (e.g. centre of the image in d), including several prominent faults that intersect the elliptical structures. Additional, but less well defined elliptical features may be present, e.g. SW of structure #1. See text for discussion and interpretations.

source components with > 10 km source depths, however they are much clearer in the filtered grayscale pseudo-gravity image in Figure 6c and d.

The NE part of the western Superior Province that includes elliptical structures #3 and #4 of Figure 6c, enlarged in Figure 7, illustrates the potential economic significance of recognising these structures in Ni–Cu–PGE–Cr exploration. This area includes the crescent-shaped McFaulds Lake greenstone belt, *aka*. 'Ring of Fire' (ROF) where the discovery of mafic-ultramafic complexes hosting Cr-Ni-PGE mineralisation (Metsaranta and Houlé, 2012, 2020; Laarman, 2014; Houlé et al., 2015; Metsaranta et al., 2015), and subsequent Au discoveries, resulted in considerable exploration interest and claim staking. The ROF is clearly shown in total field as well as first vertical derivative (1VD) and edge-enhanced short wavelength aeromagnetic images (Figs 7a, b, and d). Overlying the NRCan geological map on the pseudo-gravity ternary gradient image in Figure 7c shows that the ROF is situated in the eastern part of much larger concentric elliptical structures (#4 in Fig. 6c) constituting what we term the 'Greater Ring of Fire'. Upper mantle MT resistivity

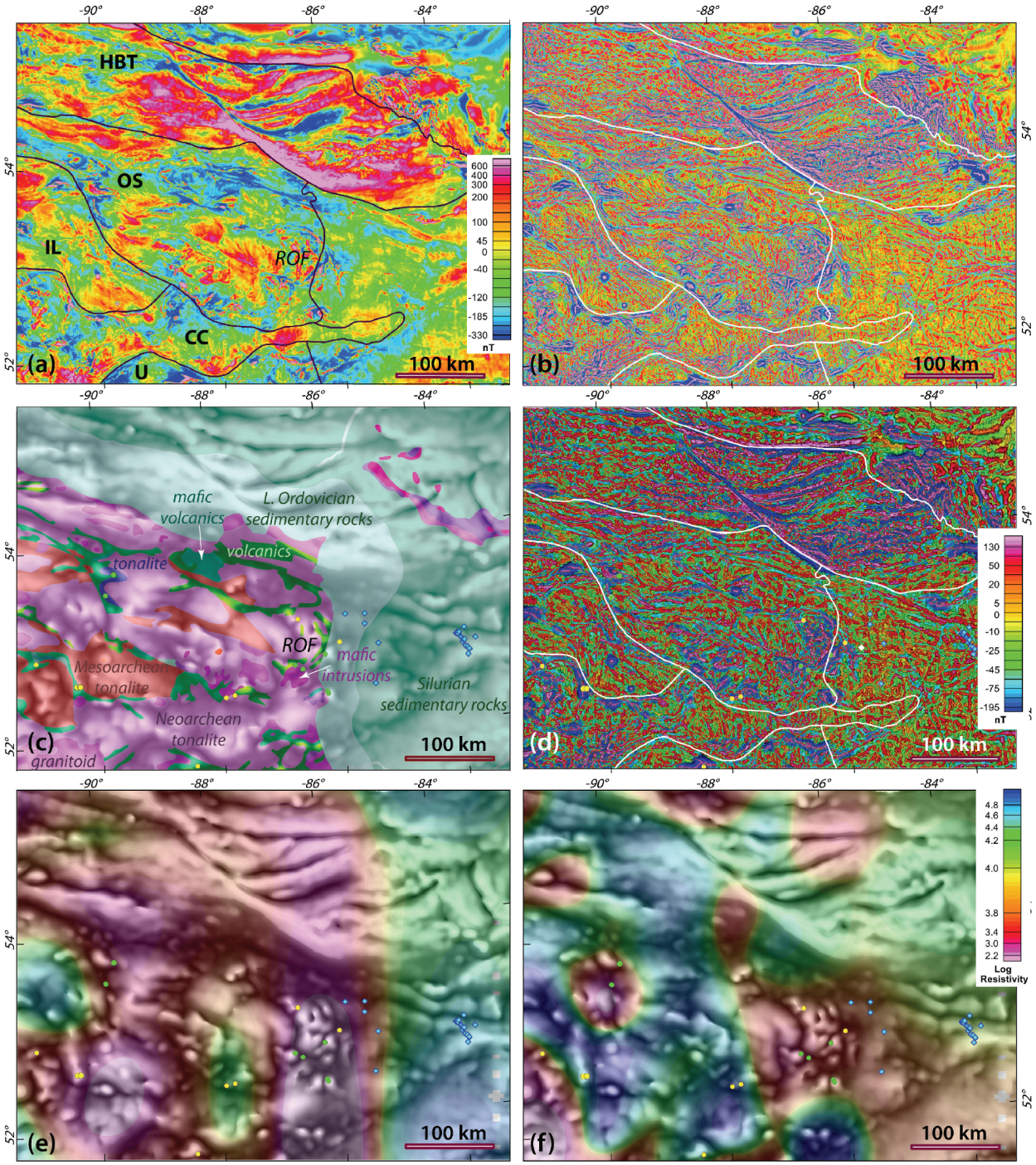

Figure 7. Enlargement of the area containing elliptical structures #3 (Big Trout Lake) and #4 (Greater Ring of Fire) identified in Fig. 6c. **(a)** Total magnetic intensity (TMI), with sub-province boundaries: HBT = Hudson Bay Terrane, OS = Oxford-Stull, CC = Caribou Core, IL = Island Lake, U = Uchi. **(b)** First vertical aeromagnetic derivative (1VD), with subprovince boundaries in white. **(c)** Simplified regional geology (from NRCan), showing the McFaulds Lake Greenstone belt, *aka*. Ring of Fire (ROF), within the eastern part of elliptical feature #4; the gray background image is an enlargement of the pseudo-gravity gradient image in Fig. 6c. **(d)** Edge-enhanced short wavelength aeromagnetic image highlighting crustal structures in the upper 10 km (presenting a clearer image, with less noise, than the normally used 1VD) — there is no indication of the larger concentric structures. **(e)** & **(f)** Magnetotelluric (MT) resistivity depth slices at 120 km (i.e. in SCLM) and 42 km (base of the crust), respectively. Mineral occurrences (Ontario Geological Survey database): Ni: green, Au: yellow: A; blue diamonds = kimberlites. Aeromagnetic enhancements in background images to (c), (e) & (f) portray deep crustal structures. N-S trends in MT data in (e), and the SE part of (f), parallel structures in deep-source aeromagnetics. Au and Ni occurrences lie on elliptical and or N-S faults. Note the circular MT anomaly centred on the western elliptical feature (#3, Big Trout Lake) on whose margin the Big Trout Lake Ni occurrences occur. MT data is described in Roots and Craven (2017).

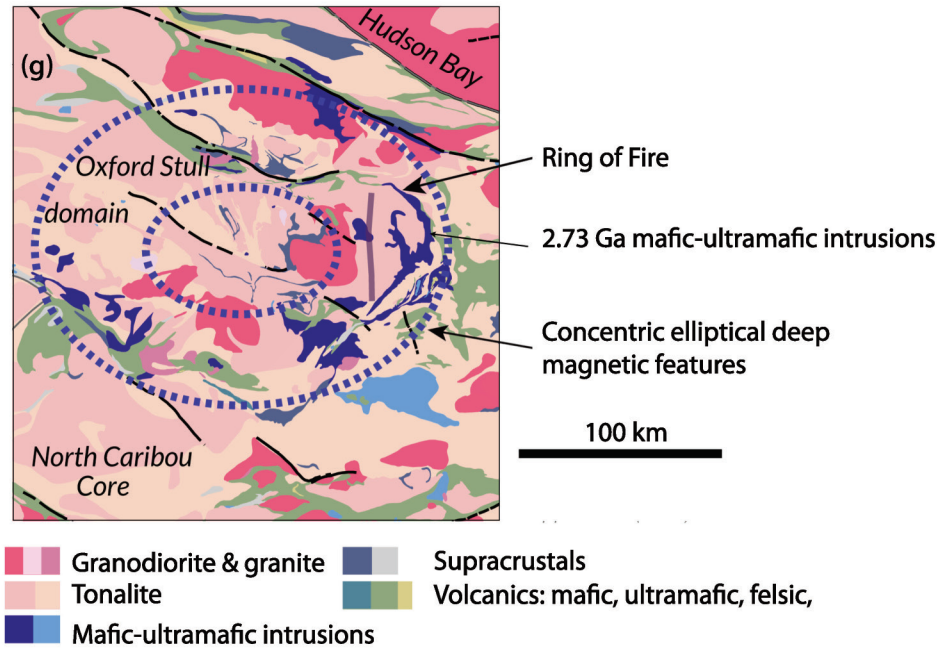

Figure 7 (cont.). Enlargement of the area containing elliptical structures #3 (Big Trout Lake) and #4 (Greater Ring of Fire) identified in Fig. 6c. **(g)** Ca. 2.73 Ga mafic-ultramafic intrusions lie within the periphery of the outer concentric ring of the Greater Ring of Fire feature; the McFaulds Lake greenstone belt (Ring of Fire) is a much smaller horseshoe-shaped feature in the eastern part of the larger structure. Geological map simplified after Sappin et al. (2015).

depth slices at 120 km and 42 km are superposed on this pseudo-gravity image in Figures 7e and f. N-S structures in the deep crust clearly defined in the pseudo-gravity ternary gradient image correspond to the margins of two N-S bands of lower resistivity in the SCLM (Fig. 7e). Both N-S and E-W trends are apparent in the eastern half of the MT image at the base of the crust in Figure 7f; a prominent N-S contact between domains of different resistivity occurs within the Greater Ring of Fire. A circular low resistivity anomaly directly correlates with the Big Trout Lake concentric feature in the pseudo-gravity image (#3 in Fig. 6c).

Most mafic-ultramafic complexes of the same age as Ring of Fire intrusions (2736-2733 Ma; Metsaranta and Houlé, 2020) in the detailed map of the ROF area in Sappin et al. (2015) lie within, and close to the margin of, the outer ellipse of feature #4 (Fig. 7g). These larger concentric elliptical structures in the Greater Ring of Fire' are not, however, apparent in the 1VD and enhanced short wavelength aeromagnetic images, and regional lithological units and faults continue across them (Fig. 7c). As can be expected, because of the different scale of observation and their focus on imaging near surface geology, there is no indication of these larger structures in detailed geophysical studies of the Ring of Fire by Rainsford et al. (2017). The Big Trout Lake Cr-PGE occurrence in NW Ontario 420 km northeast of Red Lake (Whittaker, 1986) in layered and anorthositic gabbro, dunite, peridotite, and serpentinite, interpreted as a sill-like synvolcanic layered intrusion in the Oxford-Stull Terrane in a similar setting to the Ring of Fire (Laarman, 2014), also lies on the margins of the smaller Big Trout Lake deep elliptical structure (#3 in Fig. 6c).

An association between the N-S faults that intersect in and cut concentric elliptical structures in Figures 7e and f and mineralization is identified. The Big Trout Lake and an adjacent Ni occurrences lie on one such N-S fault, one of a set of en relais stepping N-S structures, and some Ni and Au occurrences occur on one of its elliptical rings. A SSW-NNE oriented fault cross-cutting the Ring of Fire is mentioned by Vaillancourt (2003) and modelling of the form of ultramafic intrusions hosting the Eagle's Nest Ni-Cu-(PGE) occurrence in the ROF based on high resolution aeromagnetic data and drillhole information by Laudadio et al. (2018) illustrates a control of N-S structures on magma emplacement in the Double Eagle intrusive complex in the ROF. These observations suggest that both sets of structures were initiated prior to or syn-mineralization, and that faults remained active, or new parallel faults were formed, post-mineralization.

MT images in Figures 7e-f and 8 show a N-S orientation of resistivity anomalies in both the SCLM and crust. The elliptical feature #4 containing the ROF occurs in a zone of N-S resistivity anomalies at different depths (Figs 7e-f and 8c and d), the elliptical, Big Trout Lake feature #3e has an coincident, sub-circular MT high anomaly at 42 km (Fig. 7f) and 35 km (Fig. 8a). Feature #2, N of Red Lake, has a coincident negative resistivity anomaly at 35 km but a positive anomaly at 109 km. Horizontal resistivity gradients at 128 km in Figure 8c define a larger ellipse around the Lingham Lake (#2) concentric feature. The association of MT anomalies with concentric elliptical structures is not yet clearly understood, and 3D visualisation is being undertaken to better understand the form of these anomalies).

Comparison of structures portrayed by the enhanced 'deep source' aeromagnetic image with MT resistivity data and its horizontal gradient in Figure 8 show that MT

anomalies in the lower crust and, to a lesser extent in SCLM at a depth of at 109 km, are aligned both parallel and at a high angle to sub-province boundaries (note, however, the limitations of this MT data in the Methods section above). N-S resistivity anomalies parallel structures in the deep aeromagnetic image (Figs 7e, f and 8), and some terminate at sub-province boundaries (Fig. 8). The horizontal resistivity gradient image in Figure 8c shows both linear features that parallel deep N-S crustal faults in the grayscale, deep aeromagnetic image and concentric circular features that correspond remarkably well to the concentric rings of the Lingham Lake feature, from which several prominent faults radiate. Horizontal gradient anomalies in the SCLM correspond to sub-province boundaries in the northern map area (Fig. 8d, and to a lesser extent, Fig. 8c). A similar elliptical gradient anomaly in the western extremity of the Superior Province in Figure 8c increases the likelihood that the less-well defined deep aeromagnetic structure noted above, but not highlighted in Figure 6c, may indeed be significant.

Despite the low resolution of this data, the correspondence between features derived from aeromagnetic data and MT resistivity in Figures 7e, f and 8, appears to be more than fortuitous and suggests that the rectilinear and concentric

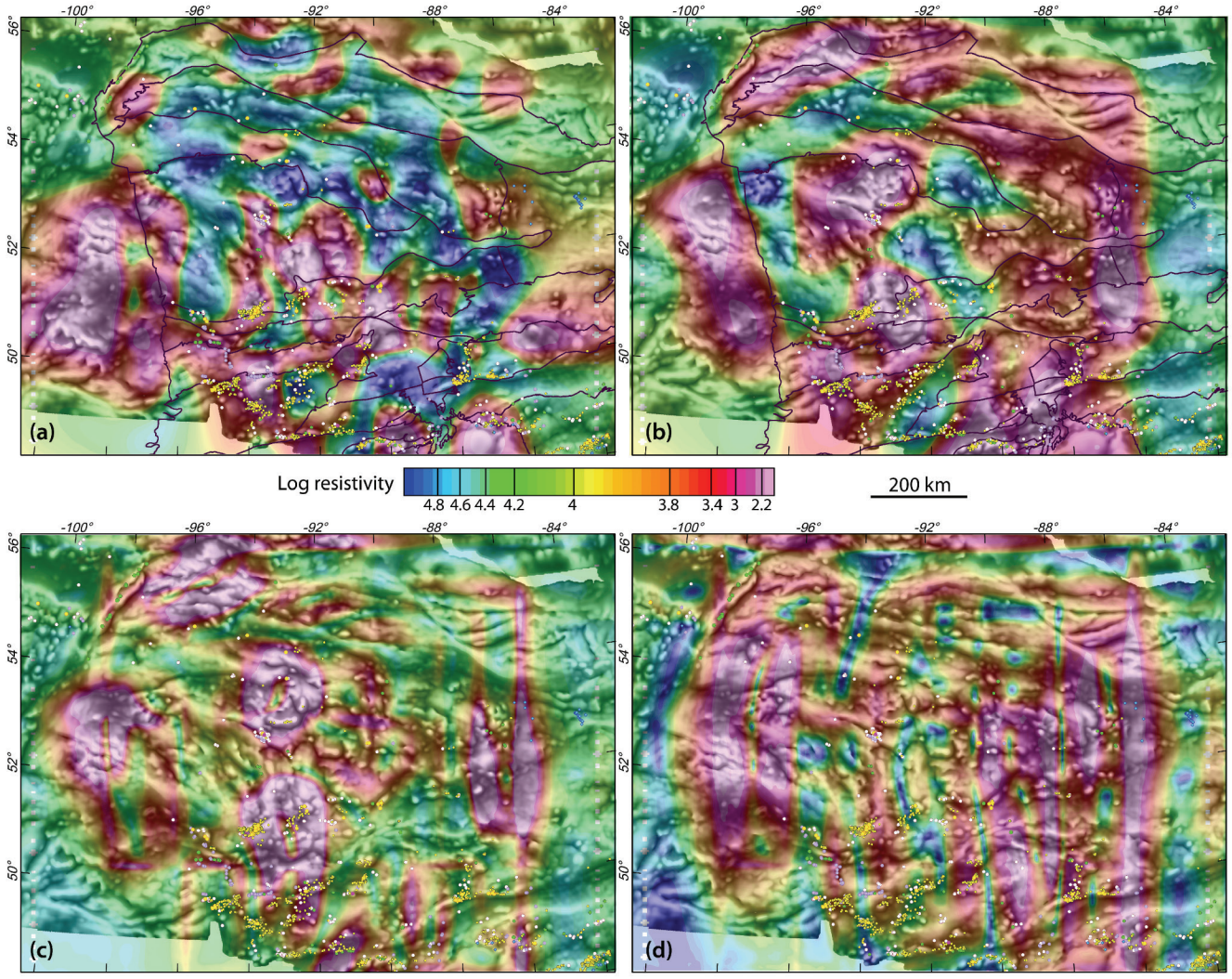

Figure 8. Relationships between mineral deposits with deep crustal faults transverse to regional trends and concentric elliptical and rectilinear transverse structures (seen in the background enhanced grayscale pseudo-gravity gradient image) and MT resistivity data at 35 km and 109 km in **(a)** & **(b)** and the horizontal gradient of MT resistivity at 128 km (SCLM) and 207 km (approximate base of SCLM according to Darbyshire et al., 2007) in **(c)** & **(d)**. Although some MT anomalies terminate against or are parallel to subprovince boundaries, as noted by Roots and Craven (2017), MT data also suggests that there are upper mantle and crustal structures at a high angle to main structural trends and subprovince boundaries (note the limitations, however, of this MT data discussed in the Methods section). In (c), circular features in the resistivity horizontal gradient at 128 km directly overlay the Norway House and Lingham Lake circular features (#1 and #2 in Fig. 6c). Au: large yellow circles = deposits, small = occurrences, porphyry-hosted deposits: pink circles, Ni deposits and occurrences: green circles, molybdenum showings (often spatially related to Au): white circles, and U-Th deposits: mauve circles, from NRCan and Ontario Geological survey databases. See text for further details.

structures have an expression in MT data for both the lowermost crust/Moho depth and in the underlying SCLM. Inversion of the whole dataset (see Methods section), at least in key areas, is hence required to confirm these preliminary results and to better understand these enigmatic structures identified for the first time in the W Superior.

Interpretations

Interpretations of ternary gradient pseudo-gravity and long wavelength aeromagnetic tilt images and their comparison with mapped faults, from the Hudson Bay Terrane to the northern Winnipeg River Subprovince, centred over the most prominent transverse structures, are portrayed in Figure 9. Au, Ni, U-Th and Mo mineralization and a kimberlite occur along or in proximity to these deep transverse structures (discussed in the following section). Although regional maps (e.g. Fig. 9b) do not show mapped N-S faults, detailed mapping and interpretation of geophysical images in the Ear Falls area immediately S of Red Lake (figs 12 and 13 of Ravenelle, 2013) shows a large number of minor ca. N-S fractures and faults. Some ca. N-S faults mapped at the surface are likely caused by reactivation of similarly oriented mid- to deep crustal discontinuities; their mapping may therefore provide evidence for the presence of deep structures.

A 'cartoon' of the key structural elements interpreted for the W Superior Province (irrespective of mapped subprovinces) in Figure 10a summarizes structures observed in the top ca. 10 km depth slice of aeromagnetic data and Lithoprobe reflection seismic profiles for the upper crust in map and section views respectively and compares them to those interpreted in the deeper crust. In the upper crust, extensional shear zones (blue) parallel and mark sub-province boundaries and open folds, bracketed to have formed between 2.691 and 2.68 Ga (Hrabi and Cruden, 2006; their D3). In the Uchi and English River subprovinces, extensional shears displace an early bedding parallel foliation and isoclinal folds that folded it during N-S shortening (Calvert et al., 2004; Hrabi and Cruden, 2006). Their D2 folds are not shown on this figure due to the limitations of scale. It is also likely that these extensional shears may reactivate early rift-bounding structures formed during sedimentation and volcanism associated with basin formation throughout the W Superior (*c.f.* the rift models of Bédard and Harris, 2014 and Mints 2017). The dominant regional shear zones and folds interpreted from aeromagnetic images (shown in red) are attributed to a distributed regional dextral transpression event at ca. 2.67 Ga (Bethune et al., 2006); this displacement sense is based on the orientation and sigmoidal curvature of fold axial traces into parallelism with generally E-W trending shears and NW and NNE-striking shears interpreted as primary and secondary Riedel shears (R and R'; Riedel, 1929; Tchalenko, 1970). No evidence was seen in aeromagnetic images for E-W sinistral D4 shear zones of Hrabi and Cruden (2006). Dextral transpression is also interpreted in the Caribou Core from field and microstructual studies (Gagnon et al., 2026) as well as in our aeromagnetic interpretations in southern sub-provinces. Broad dextral transpressional shear zones are also interpreted in the Opinaca and LaGrande subprovinces in the Eeyou Istchee-James Bay region (Cleven et al., 2020a, b) and in the Abitibi subprovince (Harris and Bédard, 2014a). Although dextral deformation is widespread and not defined solely to discrete shears, earlier extensional shears and sub-province boundaries are reactivated in this event (shown schematically at 3 in Fig. 10a). Lode Au deposits in the W Superior dated at ca. 2.7 Ga (Dubé et al., 2000, 2004) and 2.68 Ga (reported in Anderson, 2008) likely formed in this dextral transpression event, although this deformation regime may not be recognized at the outcrop or mine scale given the regional scale of its constituent structures. Cross-cutting conjugate discrete brittle-ductile to brittle shear zones imply late N-S shortening; late hydrothermal activity is also reported by Gulson et al. (2011) at 2660 ± 10 Ma (although in which event is yet uncertain). The deep concentric and transverse structures described above that, due to their control on mafic-ultramafic intrusion emplacement in the Ring of Fire, formed prior to 2.74 Ga, and hence pre-date regional deformation of the upper crust; their preservation requires the presence of a ductile décollement in the competent mid-lower crust. Note that the depth of this décollement depicted in Figure 10a is approximate, and based on lithospheric strength profiles presented in Figure 10b and lithoprobe seismic interpretations.

Relationship between mineral and kimberlite occurrences and deep structures

Figure 8 shows that many lode Au and porphyry deposits and minor Au, Ni, Mo and U-Th occurrences in the W Superior are located along N-S to NNW-SSE trending faults and concentric elliptical structures in the mid- to deep crust, especially at their intersections, and at the intersections of these transverse deep faults and mapped structures defining and paralleling sub-province boundaries. Preliminary enhancements of MT data suggest that there is also a likely relationship between mineralization and ca. N-S features in SCLM. Many lode Au, porphyry, Ni and Mo and U-Th occurrences and the western cluster of kimberlites in NE Ontario lie on resistivity horizontal gradients in both the 120 km and 207 km depth slices (Figs 8c,d). [The lack of mantle features associated with the kimberlites in the easternmost part of images in Figure 8 may be due to the decrease in data locations towards the margins of the MT survey area (Roots and Craven, 2017).]

In order to quantify these relationships, a statistical and machine learning study was undertaken over the Red Lake - Stormy Lake area (Fig. 1b) which lies within the southern part of the interpretive map of deep structures and mapped regional faults in Figure 9. The regional geology, Au occurrences and the area covered by the Red Lake - Stormy Lake high resolution aeromagnetic data are portrayed in

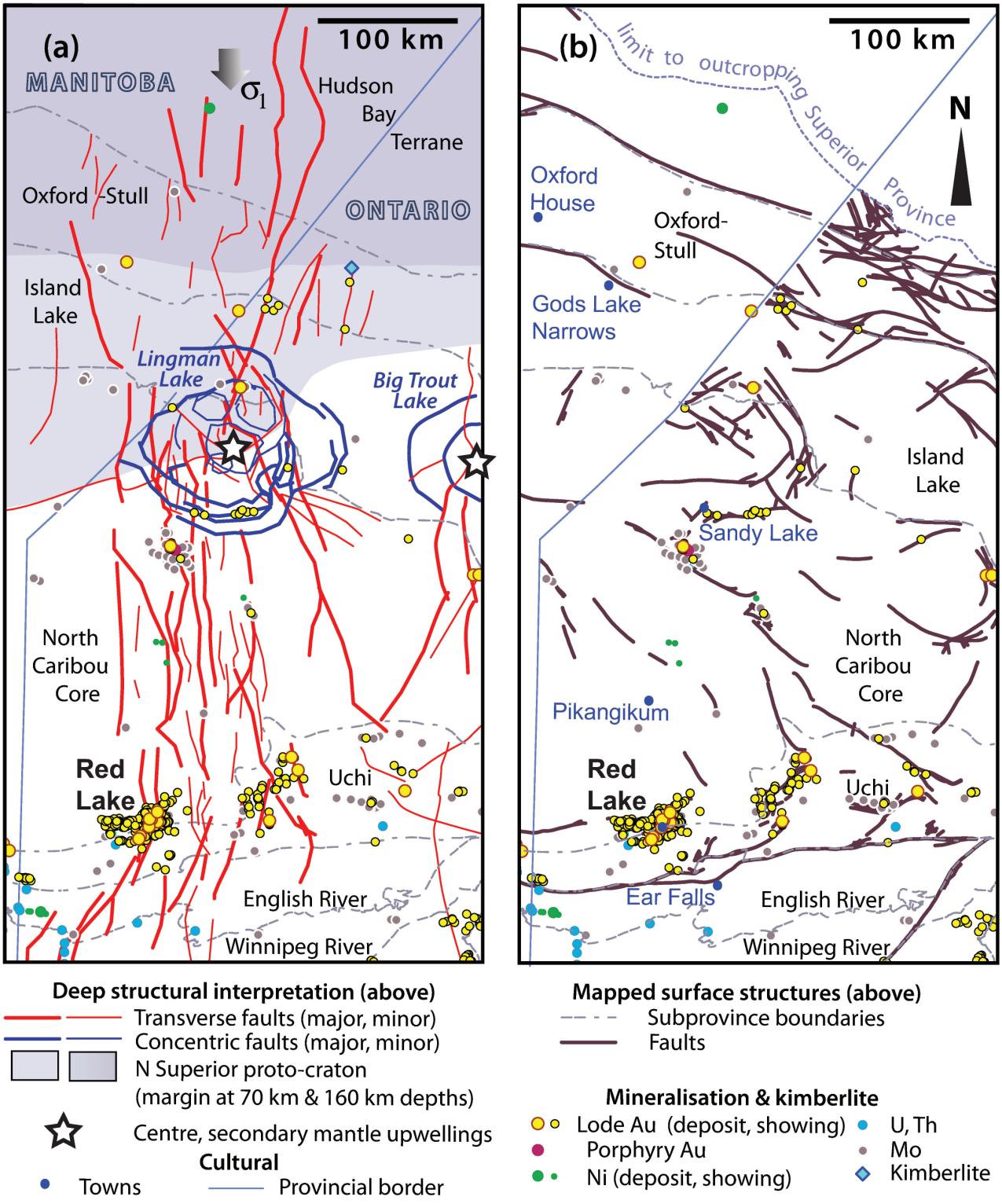

Figure 9. Maps of a N-S transect from the the Hudson Bay Terrane to the northern Winnipeg River Subprovince centred on the prominent transverse structures that cross the Red Lake area that intersect in the concentric Lingman Lake and the western margin of Big Trout Lake structures (identified in Fig. 6c). **(a)** Interpretation of deep transverse rectilinear structures (red) and concentric structures (blue) over interpreted secondary mantle upwellings (c.f. Fig. 16). Au, Ni, U-Th and Mo mineralization and a kimberlite occur along or in close proximity to these deep transverse structures. Concentric structures are centred on the surface projection of the southernmost SCLM of the Northern Superior proto-craton portrayed in Figure 17a.

Figure 11. Most Au occurs in mafic, felsic and intermediate metavolcanics, mafic metavolcanic-metasediment packages, and foliated to undeformed TTGs. This well-studied, approximately 400 km x 300 km region hosts several world class gold deposits at the intersection of E-W (i.e. along and paralleling subprovince boundaries) and N-S deep faults (Figs 8, 9). In the Red Lake area, N-S structures were also identified in previous, preliminary geophysical interpretations (L.B. Harris, unpublished report for Laurentian Goldfields Ltd., 2009), in lineament studies using other data sets by Galkin (2015) and in exploration mapping (Premier Gold Mines Limited, 2009). In the Red Lake mine, although main mapped shear zones and regional foliation strike NW-SE, some structures hosting Au strike 340° and ore shoots develop at their intersection with 110° striking structures; post-ore lamprophyre dykes strike both E-W and N-S and there is evidence for some Au remobilisation post their emplacement (Twomey, 2000). Of interest to our project in seeking to define deep regional structures controlling mineralization, Twomey (2000) notes that "the first-order regional structure common to most Archean gold camps… seems to be missing from the Red Lake belt". Mineral potential mapping using a GIS-based system using evidence maps in binary format of the Red Lake area (J.R. Harris et al., 2006) has not included much structural (especially fault and shear zone) information, and no deep faults were previously recognized.

The dataset prepared for developing a mineral prospectivity map consisted of the location of previously mapped faults, E-W lineaments, N-S striking deep lineaments (i.e. perpendicular to the dominant structural trend and subprovince boundaries) and images of the reduced to the pole (RTP) total magnetic field and its tilt angle (Fig. 12), its derived pseudo-gravity and its tilt angle, the Bouguer gravity anomaly (in colour, combined with intermediate source aeromagnetic in gray in Fig. 13), and the analytical signal. Statistical properties mean, minimum, maximum, median, variance, standard deviation, skewness, and kurtosis of each map were calculated over 5 pixel x 5 pixel (equivalent to 10 km x 10 km) rolling window.

Red Lake area structural overview

Interpretation of aeromagnetic data in Figure 12 shows that the obliquity of fold axial traces to regional E-W high strain zones (i.e. a regional S/C relationship; *c.f.* in mylonites, Berthé et al., 1979; Lister and Snoke, 1984) along with antithetic NE-SW trending sinistral shear zones implies early ductile deformation within a regional dextral transpressional regime. E-W structures in the English River, Winnipeg River, and Wabigoon subprovinces mark the boundaries between subprovinces. Aeromagnetic images highlighting deep features portray three major N-S structures extend from the North Caribou Core subprovince through the Uchi, English, River and Winnipeg subprovinces at a high angle the regional E-W trend (Figs 9, 12, 13) in addition to subparallel minor structures. Au deposits and showings tend to cluster in areas of higher Bouguer anomaly and along a N-S to NE-SW trending deep magnetic lineament (Fig. 13). There are no deposits/showings in the Winnipeg River and English River Basin subprovinces in the NRCan and OGS databases used.

Figure 10. Relationships between structures and crustal strength at different depths. (a) Schematic 3D representation of key structural elements interpreted for the Western Superior Province reflecting the strength profiles shown in **(a)**, where brittle ductile transitions occur both in the mid-crust and in the lower crust. The southern part of the N-S cross-section is inspired by Calvert et al.'s (2004) Lithoprobe seismic interpretation, and relatively higher density, resistivity and seismic velocity domains are based on (but with a different tectonic interpretation to) fig. 11 in Percival et al. (2012) and refraction seismic studies by Musacchio et al. (2004), along with studies of mantle domains from long wavelength gravity (Harris, unpublished data). Upper crustal features are decoupled across a ductile décollement 1 from those with a different geometry and implied age preserved in the deeper crust. Differences in structures in SCLM for those in the deep crust imply that decoupling with the SCLM has also occurred in the lower crust 2. Dextral deformation in the upper crust is widespread and extensional shears and sub-province boundaries were reactivated in this event (shown schematically at 3). Some faults are likely caused by reactivation of similarly oriented basement discontinuities, as at 4. Beneath the mid-crustal ductile décollement, early-formed coeval concentric circumferential and intersecting ca. N-S faults and/or fractures 5 are preserved. Au deposits are spatially associated with deep transverse faults, as well as structures paralleling subprovince boundaries. Mafic-ultramafic intrusion hosted Ni-Cr-PGE deposits occur within the outer concentric structures above contemporaneously formed N-S transverse faults. See text for detailed description and discussions of structures and geostatistical/machine learning analysis. Strength profiles and differences between deformation interpreted at different depths in the Superior Province. **(b)** Strength profiles calculated for the Abitibi Subprovince at 2.55 Ga by Mareschal and Jaupart (2006); see text for details. The Abitibi Subprovince lithosphere is, however composed of a range of different lithologies (listed to the right of the figure); differences in strength profile between homogeneous and different thickness differentiated crust are shown in the set of profiles on the right. Note the presence of two brittle-ductile transitions. Following previous sweet food analogies for strength profiles, viz, crème-brulé and jelly sandwich (Burov and Watts, 2006) and banana split (Bürgmann and Dresen, 2008), the term millefeuille, after a French cake with 3 strong pâte feuilletée /puff pastry layers separated by weak crème pâtissière / custard cream (sketch in lower right), is used to describe this strength profile.

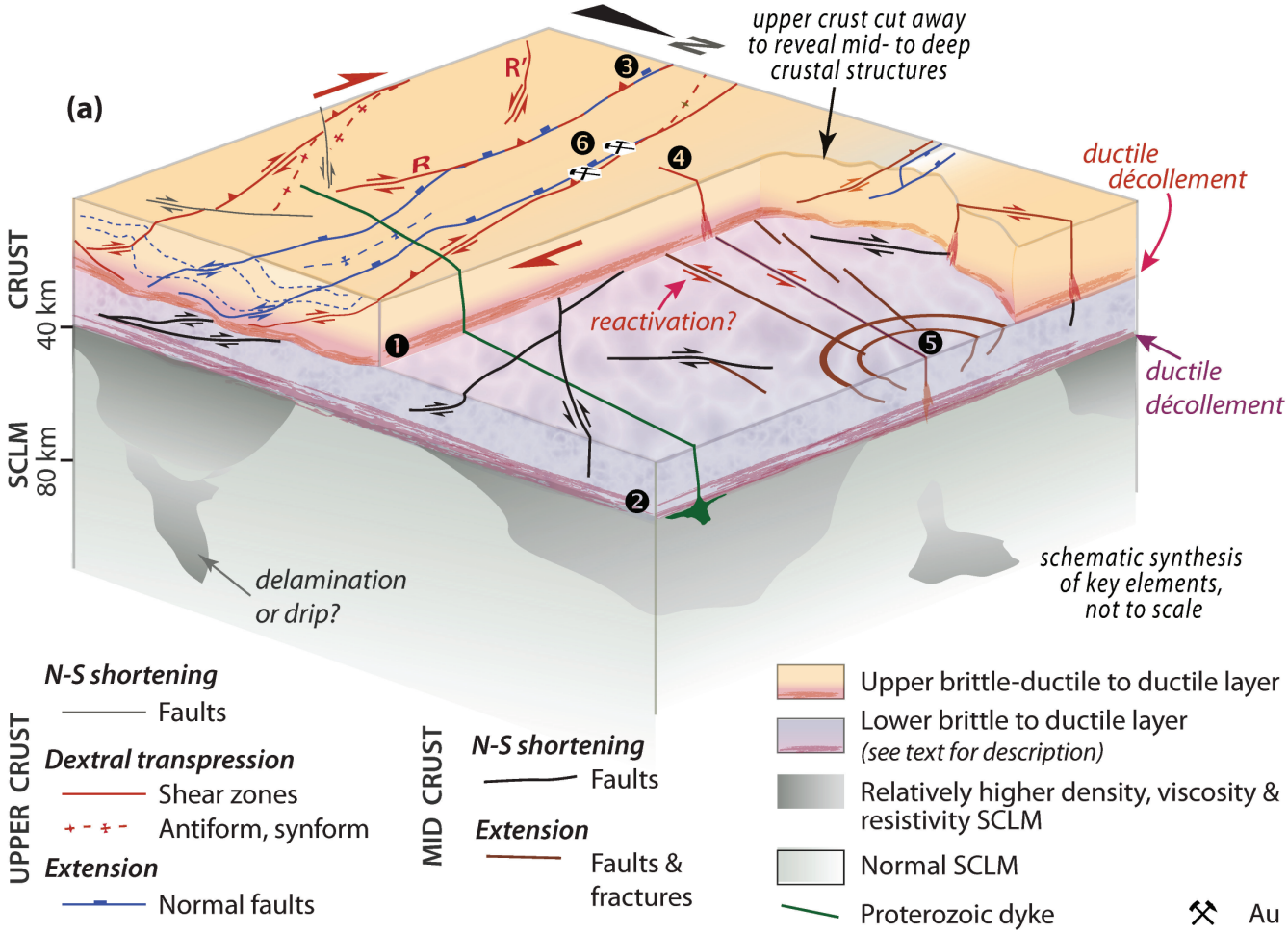
(a)
upper crust cut away to reveal mid- to deep crustal structures
ductile décollement
reactivation?
ductile décollement
CRUST 40 km
SCLM 80 km
delamination or drip?
schematic synthesis of key elements, not to scale
R'
R
UPPER CRUST
N-S shortening
Faults
Dextral transpression
Shear zones
Antiform, synform
Extension
Normal faults
MID CRUST
N-S shortening
Faults
Extension
Faults & fractures
Upper brittle-ductile to ductile layer
Lower brittle to ductile layer
(see text for description)
Relatively higher density, viscosity & resistivity SCLM
Normal SCLM
Proterozoic dyke
Au

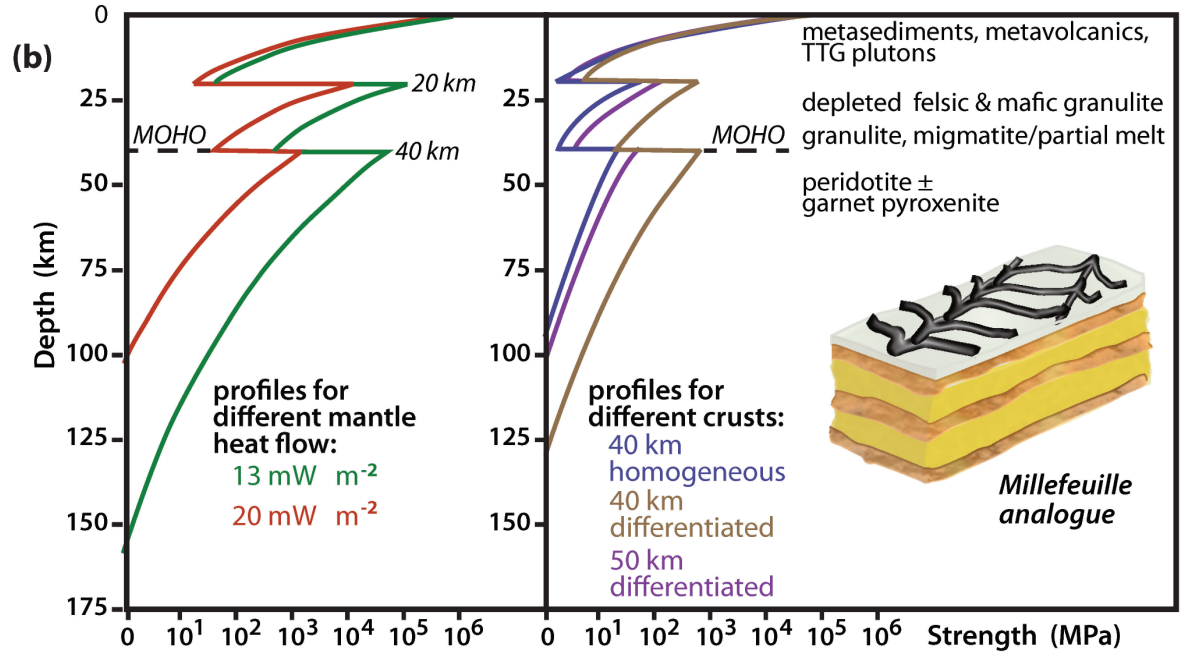
(b)
Depth (km)
0
25
50
75
100
125
150
175
MOHO
20 km
40 km
profiles for different mantle heat flow:
13 mW m-2
20 mW m-2
0 10^1 10^2 10^3 10^4 10^5 10^6
profiles for different crusts:
40 km homogeneous
40 km differentiated
50 km differentiated
metasediments, metavolcanics, TTG plutons
depleted felsic & mafic granulite
granulite, migmatite/partial melt
peridotite ± garnet pyroxenite
Millefeuille analogue
Strength (MPa)

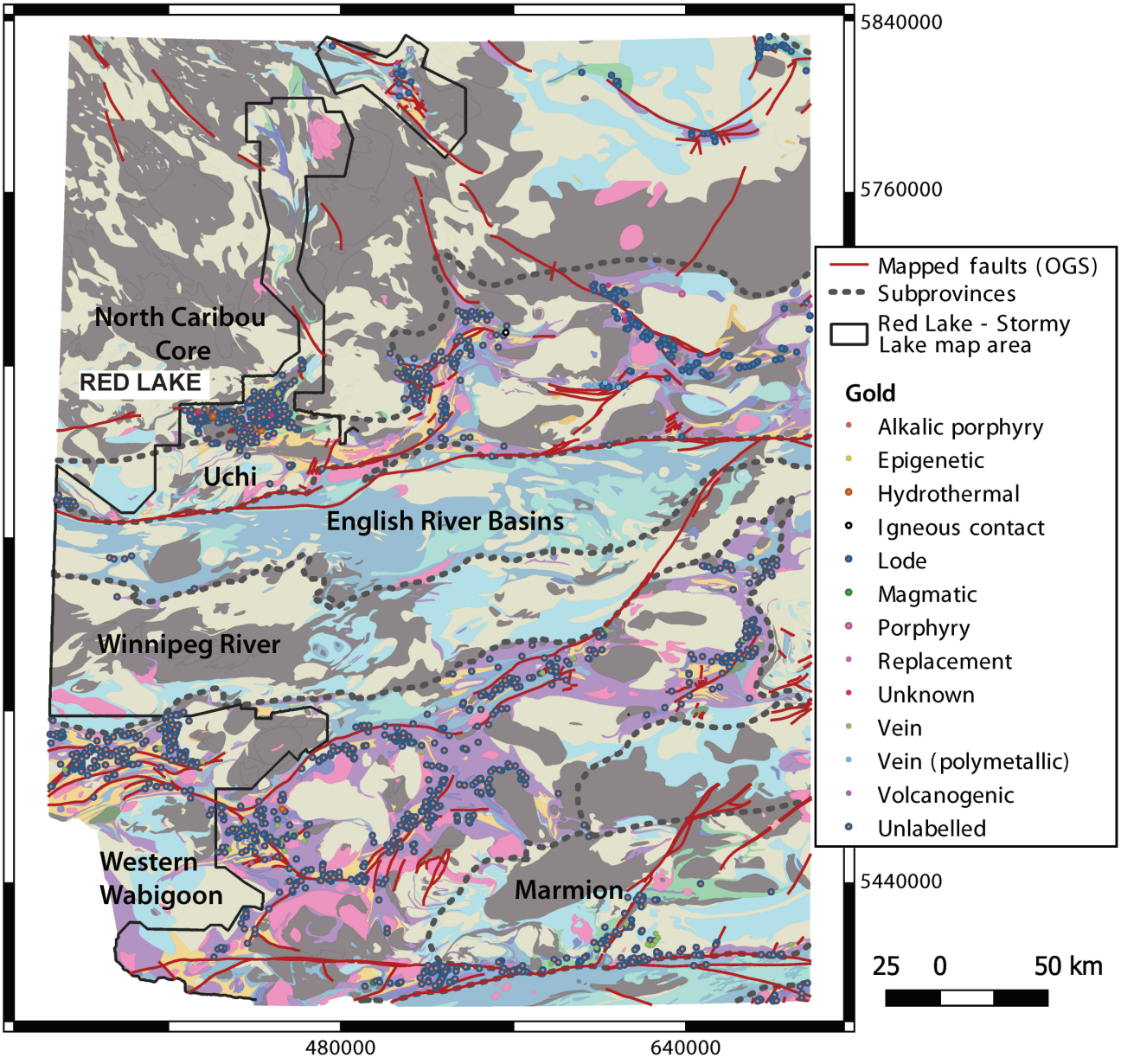

Unit name (OGS)

- Coarse clastic metasediments
- Diorite-monzondiorite-granodiorite
- Felsic to intermediate metavolcanic
- Felsic to intermediate metavolcanic
- Foliated tonalite
- Gneissic tonalite
- Hornblendite - nepheline syenite
- Mafic - ultramafic
- Mafic dikes & related intrusives
- Mafic metavolcanic & metasediments
- Mafic to intermediate metavolcanics
- Mafic to ultramafic metavolcanics
- Massive granodiorite to granite
- Metasediments
- Metasediments & mafic - ultramafic metavolcanics
- Migmatized supracrustals
- Muscovite-bearing granites

Figure 11. Regional geological map with the location of lode Au deposits and showings (1772 in number) classified by style according to the OGS. The solid black line shows the perimeter of the OGS Red Lake-Stormy Lake aeromagnetic 'supergrid' used in this analysis. Note that there are no regional-regional-scale N-S faults mapped, and only few NNW-SSE faults are mapped in the N-central part of the map area.

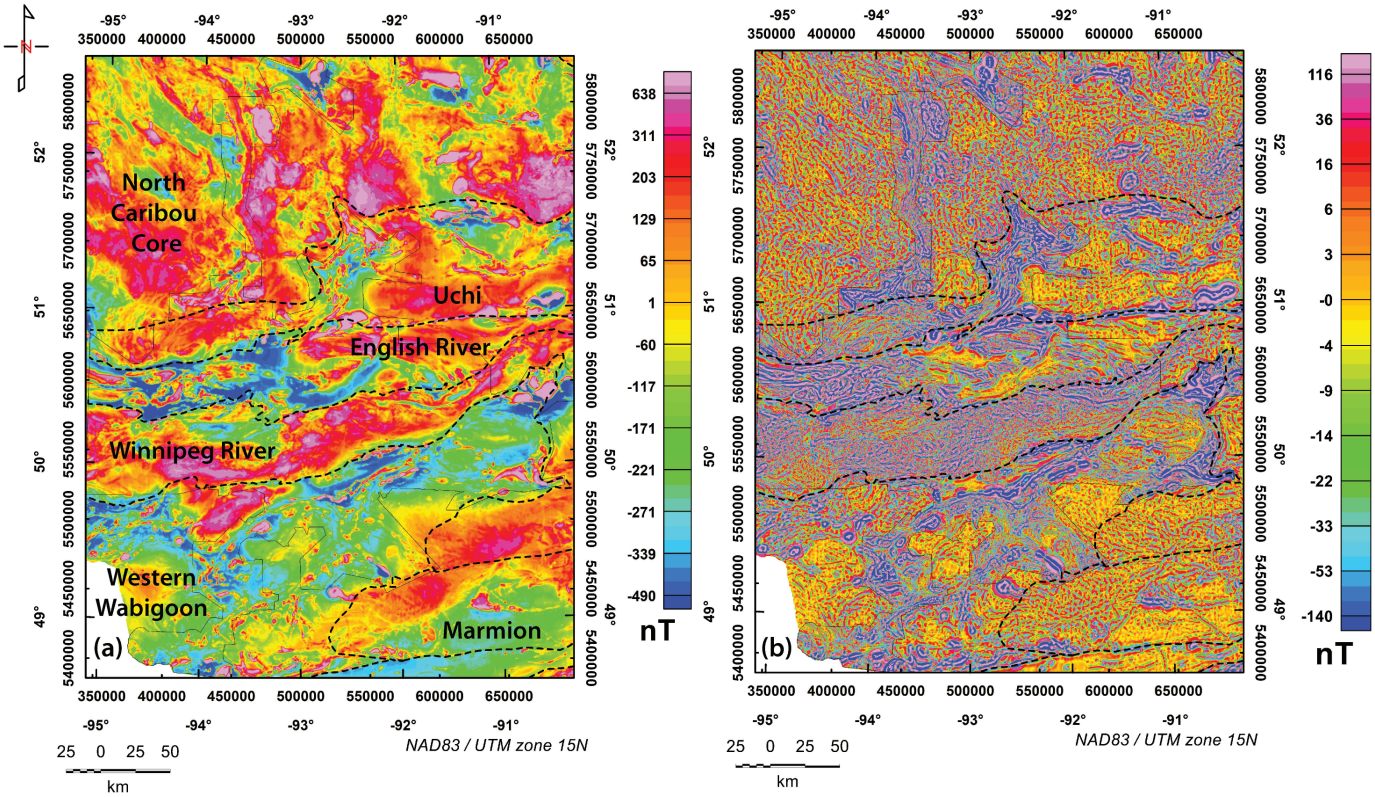

Figure 12. Aeromagnetic images of the Superior Province in central western Ontario over the map area in Figure 11. **(a)** Reduced to pole total magnetic intensity map superposing the Red Lake – Stormy Lake OGS 'supergrid' on NRCan regional data. **(b)** Short wavelength component of the Red Lake – Stormy Lake OGS 'supergrid' with source depths in approximately the upper 10 km of the crust.

Machine Learning

The XGBoost model with an oversampled dataset was best at recovering pixels that are gold-bearing, whereas the Random Forest (RF) model with an under-sampled dataset was the most precise in identifying whether each pixel was gold-bearing (Table 1, Figure 14).

Feature importances, calculated using the Shapley Additive Explanation (SHAP), which determines the average contribution of each feature through several permutations, showed that the deep N-S trending shear zones are rated higher than those trending E-W. The aim of this research was also to explore the relationship between deep lineaments and occurrences. In SHAP dependence measurements, N-S lineaments showed a positive correlation with relation to gold deposit, whereas the East-West lineaments were not influential. In Figure 15, which compares the relationship of E-W lineaments and N-S lineaments with gold deposits/showings in the region, the N-S lineaments correspond to a higher number of deposits at all buffer distances whereas the E-W lineaments have the majority of deposits at a 10 km buffer distance. N-S lineaments are hence seen as better indicators of the likelihood for Au deposits or showings due to their consistency and this may be one of the reasons that the model identifies them as stronger features. Further, there is a positive correlation between N-S structures and gold deposits/showings (positive classification by the model). The results for the oversampled and undersampled data were similar with variations of 1% to 3% in their scores. Comparing the RF and XGBoost models, RF has a propensity to overfit as it has a higher recall rate, but lower precision. Furthermore, RF consistently has a 9% difference between the training and testing accuracy respectively, showing its tendency to overfit the training data and inability to generalize as well as the XGBoost model (higher precision compared to RF and 3% to 4% difference in accuracy between training and testing). Another method of under-sampling is by removing areas further than 15 km from faults and lineaments manually, however there is a risk of overtraining the data around structures, losing positive results outside of the buffer regions, which risks losing information for negative results (i.e. areas where there are no Au occurrences).

Results suggest that the 'missing first-order regional structures' in the Red Lake belt (Twomey, 2000) are indeed the deep N-S faults not apparent at the surface but recognized in our study.

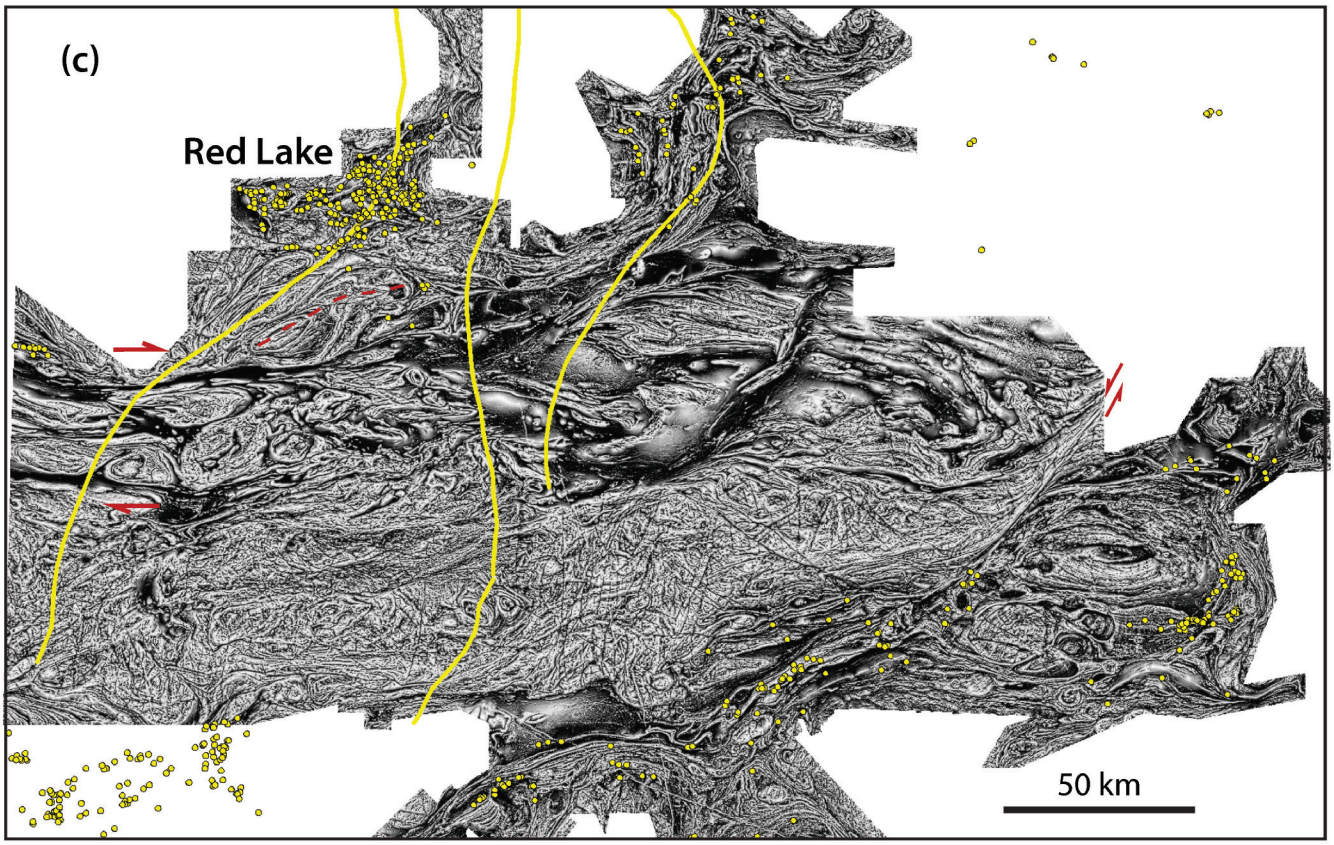

Figure 12. (cont.) Aeromagnetic images of the Superior Province in central western Ontario over the map area in Figure 11. **(c)** The 3 main deep ca. N-S structures (yellow), interpreted from intermediate wavelengths (mid-crustal source depths) shown in Fig. 13, overlain on the tilt angle of the short wavelength Red Lake – Stormy Lake OGS 'supergrid' data. Au deposits and showings are in yellow circles. The obliquity of fold axial traces at 45° to the dominant E-W structural trend (e.g. in the NW part of the image S of Red Lake, dashed red line), the 'drag' of foliations into E-W deformation zones, and the presence of a NE-SW sinistral (i.e. antithetic) shear zone in the eastern part of the image indicate a ductile dextral transpressional deformation regime. Mid- to deep crustal structures are not affected, implying intra-crustal decoupling.

DISCUSSION

Links between mantle upwellings, concentric elliptical structures, and transverse faults and fractures − comparisons with coronae on Venus

Origin of concentric elliptical structures, emplacement of mafic-ultramafic intrusions, and related Ni mineralisation

This is the first time large, deep concentric elliptical structures described above have been recognized in the W Superior Province from enhanced aeromagnetic data, although a comparable elliptical feature in the SE Superior Province is also interpreted using different aeromagnetic enhancements by Prevec et al. (2005) oblique to, and underlying the impact-related Sudbury Structure[3]. The dimensions of the greater elliptical structure that encloses the Ring of Fire is also comparable to elliptical domes in the Douglas Harbour domain of the NE Superior for which Bédard et al. (2003) ascribe a vertical tectonic model involving mantle upwelling and ensuing delamination of cumulates and restite. The geometry and dimensions of the concentric elliptical structures identified in the Superior Province are also identical to those of many coronae on Venus (e.g. Figs 16a, d) which are attributed to upwelling mantle 'hot spots' or plumes (Stofan et al., 1992; Phillips and Hansen, 1994; Ernst and Desnoyers 2004) or hot mantle diapirs (Krassilnikov et al., 2012). Many coronae are thought to be presently active based on their low bouguer gravity anomalies comparable to those over Iceland, an example of an active mantle plume on Earth (Harris and Bédard, 2014b), and based on comparisons between their morphology and thermomechanical numerical simulations (Gülcher et al., 2020). It has been previously suggested that Venus coronae lack (e.g. Ernst and Desnoyers, 2004) or have few (Buchan and Ernst, 2016) terrestrial analogues. Buchan and Ernst (2018) and Lopez et al. (1997) however propose that domal uplifts on Earth above some mantle plumes may be analogous to early stages of the formation of coronae on Venus, and Archean East Pilbara basins have been attributed to collapse after arching above a mantle plume by Nijman et al. (2017).

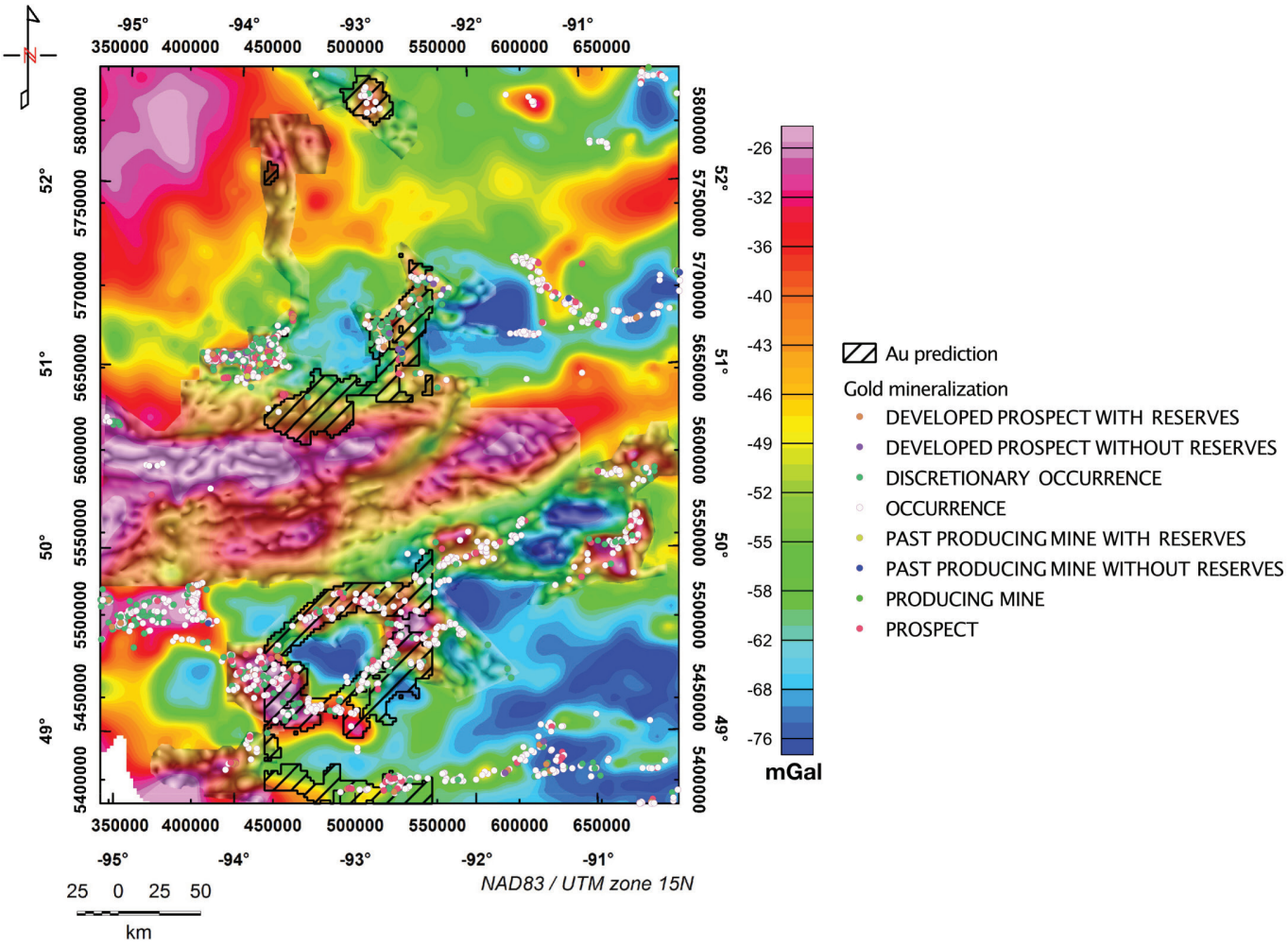

Figure 13. NRCan Bouguer gravity (colour) and tilt angle of intermediate wavelength OGS aeromagnetics (gray). N-S structures are apparent west of centre in the gray aeromagnetic image. The Winnipeg River and English River subprovinces show relatively higher bouguer anomaly values. The prediction of Figure 9b is overlain in orange shows a correlation between previously unmapped N-S trending structures interpreted from the aeromagnetics and Au.

Mantle upwellings, whether mantle plumes, heat pipes (Moore and Webb, 2013) or overturn upwelling zones (OUZOs of Bédard, 2018) played an especially important role in the Archean Earth (Barley et al., 1998; Rey et al,, 2003; Harris and Bédard, 2014a and references therein; Mints, 2017; Bédard, 2018) and concentric crustal structures akin to those we interpret in the W Superior Province were produced in numerical models of mantle upwellings for Venus and the Archean Earth (Göğüş and Pysklywec, 2008; Gerya, 2014a, b; Johnson et al., 2014; Fischer, 2016; Fischer and Gerya, 2016; Göğüş et al., 2017). Intrusion of mafic magma portrayed within the concentric structures developed above a mantle upwelling in the numerical models of Gerya (2014a) is comparable to the location of mafic-ultramafic intrusions within the greater ring of fire in Figure 7g. A mantle upwelling model to explain the formation of the concentric structures interpreted in the W Superior and associated intrusions is supported by the interpretation of Kuzmich (2009) that ferro-gabbroic intrusions in the ROF originated from a shallow depleted mantle source, possibly related to a plume event.

Neoarchaean volcano-sedimentary sequences and Ni occurrences in the Superior Province within the BUOGE domain of Houlé et al. (2015) along the southern margin of the N Superior proto-craton occur in an analogous position to greenstone sequences and komatiite-hosted Ni deposits in the Eastern Goldfields province of the Yilgarn Craton, Western Australia, along the E margin of the older Youanmi Terrane (also termed the Western Yilgarn Craton by Begg

[3]'Giant ring structures' have, however, been proposed in the Superior Province by Watchorn (2019), as well as in other Archean cratons, although the enhancement technique used (based on processing of published images using 'PowerPoint Texture enhancing' and not original data) is highly unconventional and its validity is contentious, given the possibilities for creating artefacts and the brain's propensity to visualise circles; despite this, some of his interpreted ring structures may be valid and his interpretations require further evaluation using other data and software. Preservation and reactivation of structures with a Hadean impact origin is interpreted by Watchorn (2019) for his interpreted ring structures, with which we do not agree.

Table 1. Evaluating Extreme Gradient Boosting and Random Forest classifiers using training and testing accuracy, recall, and precision, where training accuracy is the accuracy of the model at predicting the training data, testing accuracy is the accuracy of the model at predicting the test data (data it has not seen before), recall refers to the rate at which the positive outcome is true, and precision indicates the percentage of results that are relevant.

	XGBoost classifier				**Random Forest classifier**			
	Training Accuracy	Testing Accuracy	Recall	Precision	Training accuracy	Testing Accuracy	Recall	Precision
Undersampling	80%	76%	69%	53%	80%	71%	84%	42%
Oversampling	80%	77%	69%	52%	81%	72%	85%	39%

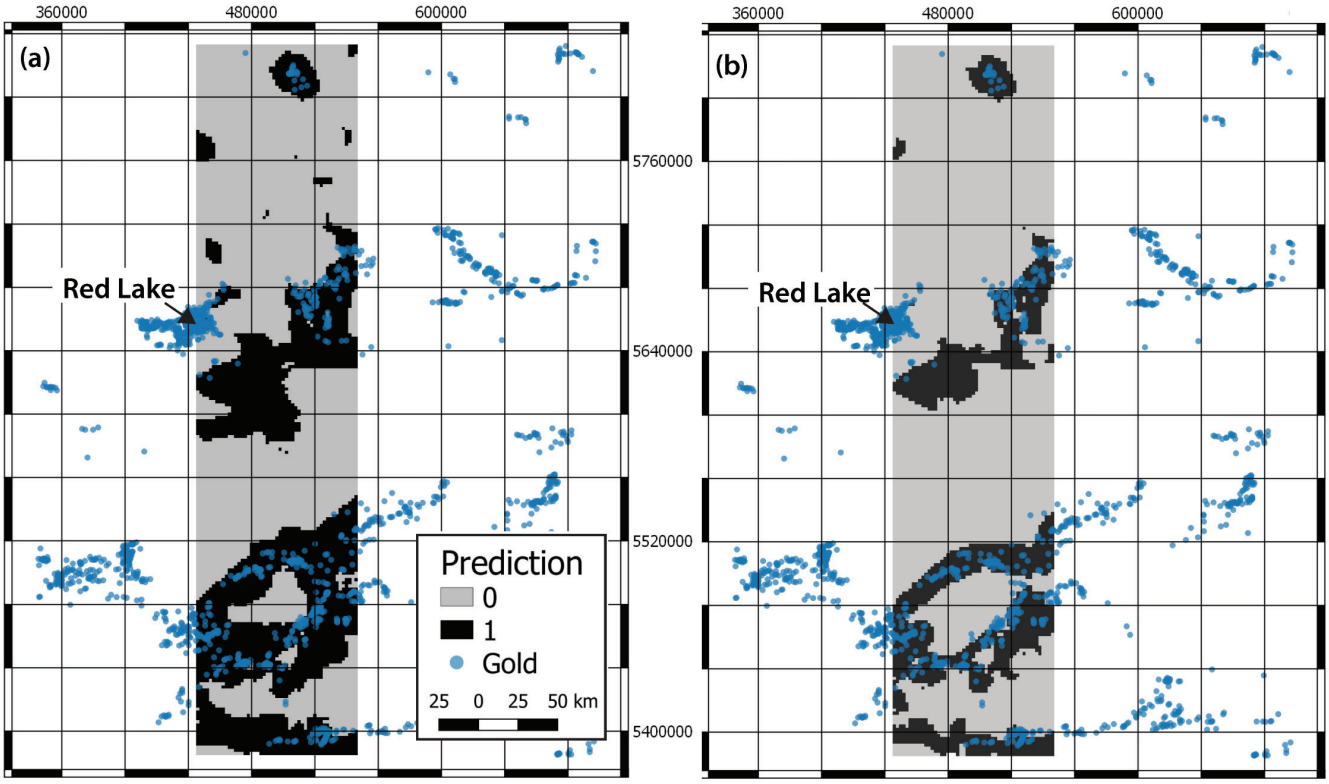

Figure 14. Prediction maps of potential deposits. **(a)** Map generated using the Random Forest algorithm with the oversampled data. **(b)** Prediction map of potential deposits generated using the XGBoost algorithm. Compared to (a) the positive predictions are more precise in identifying known occurrences as reflected in Table 1. The XGBoost model is however more prone to missing deposits compared to the RF model (as reflected by the recall rates of the models in Table 1). The prediction produces a "1" or "0" value where "1" indicates that the probability of a gold occurrence is greater 55% whereas "0" has a probability of less than 55%. Overall, the two models agree on the location of gold prospects and highlight similar areas of the map. The extents of the black and grey area highlight the testing data (i.e. data the algorithm had not seen previously). In most cases the model was able to predict the location of occurrences. Areas where there are no known occurrences may be due to the inaccuracies of the model or that those regions haven't been thoroughly explored, hence suggesting new exploration target areas.

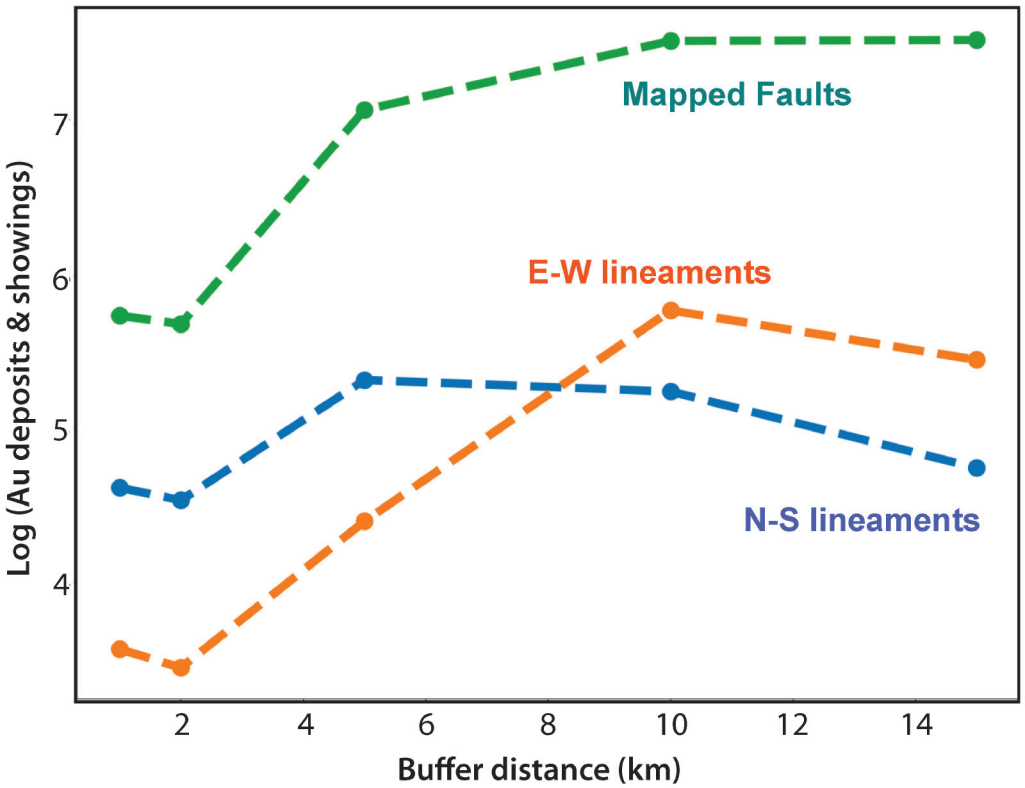

Figure 15. Number of deposits/showings at difference buffer distances from mapped faults, N-S trending lineaments, and E-W trending lineaments. The mapped faults are consistently higher as they have a higher coverage of the region. Deposits have a tendency to form closer to N-S structures compare the E-W structures. The E-W structures occurred predominantly in the English River Basin and Winnipeg River subprovinces, where there were no mapped deposits or showings.

Figure 16. Radial and concentric circumferential structures associated with mantle upwellings on Venus and Earth that appear identical to early structures preserved in the competent mid- to lower crust of the western Superior Province, suggesting the same origin. **(a)** Fatua Corona, located in Alpha Regio (V-32 quadrangle) on Venus, provides an example of corona formation within a regional compressive stress field; structural data are extracted and simplified from the geological map of this quadrangle by Bethell et al. (2019). The principal maximum stress direction σ1 (determined by Bethell et al., 2017) is indicated by the broad gray arrows. Wrinkle ridges (analogous to folds on Earth) are orthogonal to the local orientation of σ1. The superposed high contrast false colour Magellan radar image (whose location is shown by the brown rectangle on the map) shows that structures in the Brynhild Fossae regional graben-fissure system merge with circumferential and radial structures within Fatua Corona, and were hence coeval. **(b)** Radiating faults or fractures (less prominent lineaments are dashed) in the western USA (combining interpretations in Glen and Ponce, 2002 and Ponce and Glen, 2002) intersect at the interpreted Miocene position of the Yellowstone plume centre. Epithermal Au deposits in Nevada (Ponce and Glen, 2002) appear to be spatially associated with these structures. **(c)** Numerical modelling of predicted maximum principal stress trajectories (= expected tensile fracture patterns) around one (top) and three (lower figure) 'holes' in a thin plate during regional shortening. From McKenzie et al. (1992), who applied these models to interpreting coronae on Venus and graben-fissure systems and dyke emplacement on Venus and Earth. **(d)** High contrast false colour radar image portraying multiple coronae with concentric tensile fractures and ridges that are linked by radar bright structures in Bereghinya Planitia (V-8 quadrangle on Venus mapped by McGill, 2004). The 146 km diameter Trotula corona, which includes a smaller set of concentric structures slightly offset from its centre, is of similar geometry and size to the Greater Ring of Fire in Ontario (Figs 6 and 7). The smaller Yaroslavna Corona has approximately the same diameter as the interpreted Big Trout Lake concentric features in the W Superior (Figs 6 and 7), and its distance from the Trotula Corona is comparable to that between Big Trout Lake and the Greater Ring of Fire. Original grayscale 75 m per pixel resolution Magellan radar images in (a) and (d) were downloaded from Astropedia (USGS); a false colour table and enhancements were undertaken using Fiji-ImageJ.

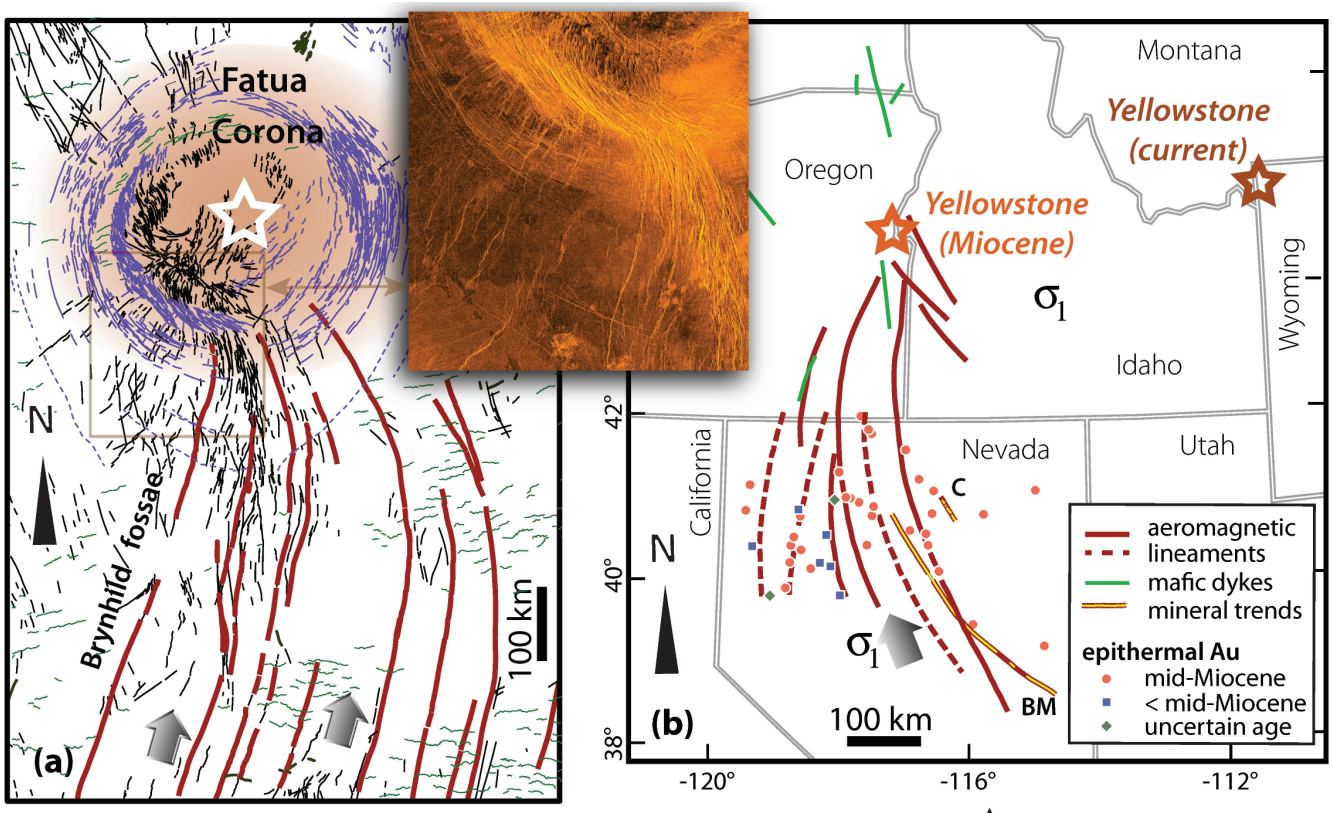

radar lineaments: extensional faults or fractures:
regional, radiating concentric minor

wrinkle ridges:

plume or ouzo: centre
head *(schematic)*

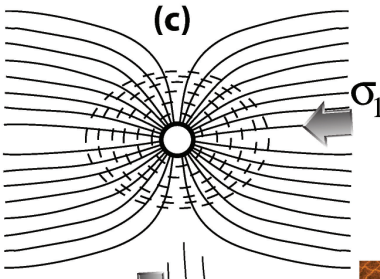

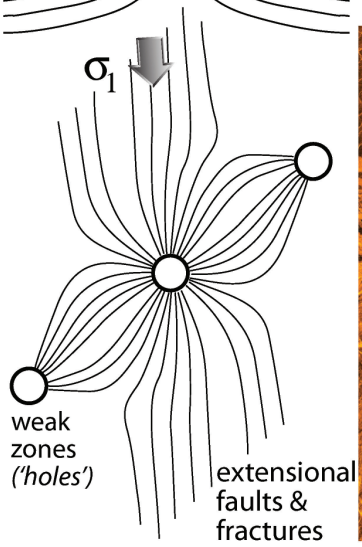

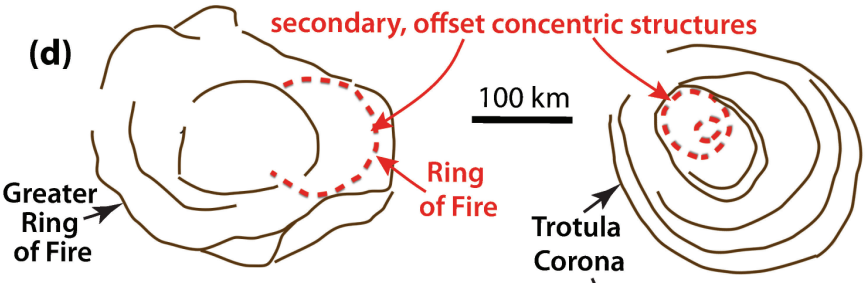

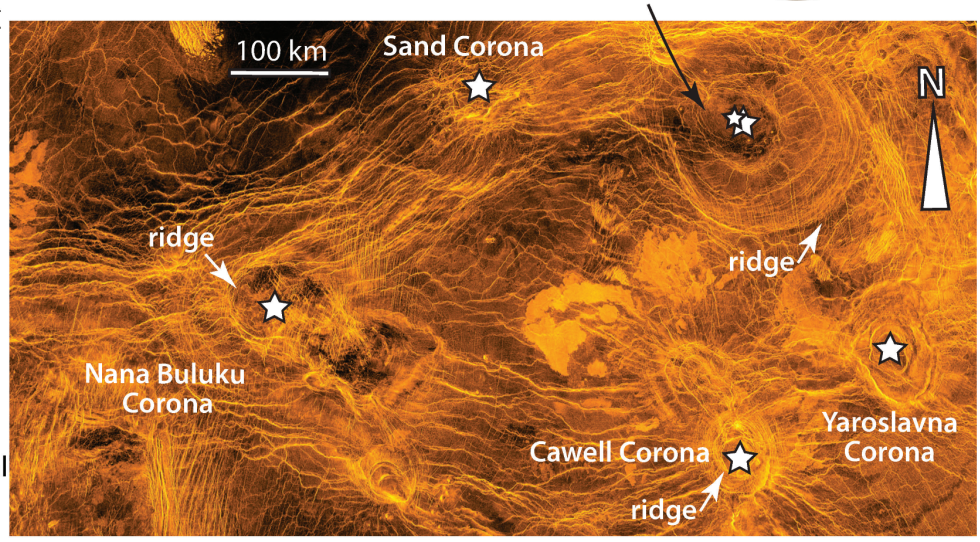

et al., 2010). In the autochthonous model for the Yilgarn Craton, rifting and komatiite volcanism in the Eastern Goldfields superterrane are attributed by Mole et al., (2013), Barnes and Van Kranendonk (2014), and Witt et al. (2020) to crustal extension and melting due to diversion of a mantle plume head beneath the Youanmi Terrane towards the craton margin (*c.f.* the generalized model for Ni-Cu mineralization of Maier and Groves, 2011; their fig 7c). In the Yilgarn, basement faults at a high angle to a NNW-trending basement rift on the margin of the Youanmi 'protocraton' interpreted from gravity data are spatially related to both ultramafic and mafic intrusions and volcanics and Au deposits (Connors et al., 2002; Miller et al., 2010; Harris and Bédard, 2015), especially at the intersection of rift and transfer faults (Begg et al., 2018).

Camp and Hanan (2008) provide a younger example where plume impingement at the base of the lithosphere in the eastern USA is interpreted to have lead to successive stages of lithospheric delamination, volcanism (producing the Columbia River Basalt Group) and intrusion at the N American Precambrian craton margin. A superplume origin is also proposed for concentric Paleozoic ring structures interpreted in Kazakhstan by Baibatsha (2020) on which Au, Cu, and Cr-Pt deposits are located (although data to independently verify the interpreted structures is not provided, hence further validation is required).

Origin of transverse faults and their relationship to concentric elliptical structures in the W Superior

Studies of structures associated with Venus coronae and terrestrial analogues help explain the formation and timing of the deep crustal transverse faults that cross the W Superior and intersect in and displace elliptical structures. Fatua Corona (Fig. 16a), located in Alpha Regio (V-32 quadrangle) on Venus mapped by Bethell et al. (2019), provides an example of corona formation within a regional compressive stress field (Bethell et al., 2017). Structures comprising a regional graben-fissure system that extends from Fatua Corona for ca. 1,700 km southwards (Bethell et al., 2017) merge with circumferential and radial structures within Fatua Corona (see inset radar image in Figure 16a) and were hence coeval. A similar example of regional extensional faults or fractures in the western USA (Fig. 16b) interpreted from aeromagnetic images radiating from the depicted Miocene position of the Yellowstone mantle plume is presented by Glen and Ponce (2002) and Ponce and Glen (2002); the pattern of their aeromagnetic lineaments resembles the graben-fissure system of Brynhild Fossae radiating from Fatua Corona in Figure 16a. Epithermal Au deposits in Nevada (Fig. 16b) are located along these structures (Ponce and Glen, 2002) in a similar manner to Au and many other mineral occurrences appearing spatially associated with the transverse structures intersecting in the concentric, corona-like features in the W Superior. The curvature of lineaments intersecting in an interpreted plume centre in both the Yellowstone and Fatua Corona examples is seen in the predicted maximum principal stress trajectories (equating to expected tensile fracture patterns) around a "hole" in a thin plate during regional compression in the upper numerical model of McKenzie et al. (1992) in Figure 16c, undertaken to model coronae on Venus and graben-fissure systems and dyke emplacement on Venus and Earth. Numerical models that also show faults that propagate for large distances into the thinner lithosphere away from a plume centre at a craton margin on Earth (fig. 8.1 in Wang, 2015), faults are oriented at a high angle to the craton margin, and only start to change in orientation and radiate sideways near the extremities of the craton. The pattern of aeromagnetic lineaments in the W Superior in Figure 9a is therefore interpreted to have similarly formed; lineaments consequently represent regional extensional faults or fractures formed in a regional stress field with the principal compressive stress oriented N-S, coeval with the formation of circular to elliptical concentric structures on the southern margin of the N Superior proto-craton. Corroborating evidence comes from mafic-ultramafic intrusions hosting Ni-Cr-Cu-PGE deposits that show a strong spatial association with N-S faults (Fig. 7) suggesting faults existed prior or contemporaneous to their emplacement: N-S faults cross-cut units of the ca. 2736–2732 Ma Ring of Fire intrusive suite (Houlé et al., 2019 - see maps therein) and in the Eagle's Nest Ni-Cu-(PGE) occurrence, detailed 3D reconstructions from drilling show intrusions form N-S to NE-SW lobes/keels (Laudadio et al., 2018) suggesting faults in these orientations controlled their emplacement. The Big Daddy Chromite deposit 5 km northeast of the Eagle's Nest is also delimited by N-S striking faults. In the Big Trout Lake igneous complex, a large layered intrusion with an unfolded strike length of up to 93 km and a thickness of up to 7 km within the smaller concentric feature W of the Ring of Fire, primarily igneous layering in the basal ultramafic sequence strikes N-S and N-S shears are present in equal numbers to E-W shears (Burnside & Associates, 2005). In the Lingman Lake concentric structure (Fig. 9a), serpentinized pyroxenite ultramafic rocks with elevated nickel and copper are present, however any relationship to N-S structures is not known. Neoarchean gabbro-anorthosite intrusions in the Red Lake area also occur on deep N-S faults (P. Adiban, unpublished data).

The lower model in Figure 16c shows the predicted maximum principal stress treajectories where the regional maximum compressive stress is oriented at 45° to three aligned holes simulating coronae. Multiple coronae in Bereghinya Planitia (V-8 quadrangle on Venus mapped by McGill, 2004) with concentric tensile fractures and compressional annual ridges are shown in Figure 16d. The 146 km diameter Trotula corona, which includes a smaller set of concentric structures slightly offset from its centre, is of similar geometry and size to the Greater Ring of Fire in Ontario described herein, where the McFaulds Lake greenstone belt (Ring of Fire) is similarly offset from the centre of the much larger circumferential structures. The smaller Yaroslavna

Corona has approximately the same diameter as the interpreted Big Trout Lake concentric features in the W Superior, and its distance from the Trotula Corona is comparable to that between Big Trout Lake and the Greater Ring of Fire. Gerya (2014) interprets such linked, coeval coronae as forming above secondary mantle upwellings above a single, large and wide mantle plume. Instead of forming a ring structure (as portrayed by Gerya (2004), the alignment of concentric structures in the W Superior is taken as similar secondary structures but where the main plume underlies the older, N Superior proto-craton. Coronae in Figure 16d, linked by radar bright structures, provide an example equating to the lower numerical model in Figure 16c and the pattern of rifts created between upwellings in analogue models described by Harris et al. (2004). The morphology of structures linking coronae in Figure 16d, including the *en échelon* stepping of minor structures along them, and comparisons with numerical models in Figure 16c and by Mériaux and Lister (2002), and with analogue models of Harris et al. (2004), suggest they were formed due to tensile fracturing and are not "wrinkle ridges" indicative of shortening as interpreted by McGill (2004).

Tectonic interpretation

From the observations and comparisons above, there is compelling evidence that both the previously largely unmapped concentric and the N-S to NNW-SSE structures at a high angle to regional trends and subprovince boundaries in the W Superior result from mantle upwellings due to a mantle plume beneath the N Superior proto-craton (whose 3D form in the study area is shown in Fig. 17a), as proposed by Mints (2017) and illustrated in Figure 17b; no evidence is available to support an alternative bolide impact origin commonly attributed to some concentric geological features (e.g. the Vredefort crater in South Africa, the largest impact crater on Earth). The regional lithospheric to crustal-scale processes envisaged for the western Superior Province described above and portrayed in Figure 17b combine elements of:

(i) A numerical model by Koptev et al. (2016; their figs 6 and 7) where an upwelling mantle plume beneath a pre-existing craton, with splitting and lateral flow of the plume head, produces lateral displacement of the craton and rifting adjacent to one if its margins and thermal erosion of SCLM beneath the craton.

(ii) The model of Guillou-Frottier et al. (2012, their fig. 2b) where a laterally spreading plume head may give rise to several second order mantle upwellings beneath thinner lithosphere abutting a deeper lithospheric block. The elliptical structures described in this report are likely to mark such smaller, 2nd order mantle upwellings, each developing concentric rings as in models of single and multiple mantle upwellings by Fischer (2016) and Fischer and Gerya (2016).

(iii) Rifting, where rifts develop along the protocraton margin linking mantle upwellings, plus formation of coeval faults at a high angle to rift margins.

The proposed model for mantle upwelling strengthens analogues proposed between the tectonics of Venus and the Archean Earth (Harris and Bédard, 2014a, b and references therein).

There is substantial evidence for the presence of older basement to the southern Superior Province (Harris and Bédard, 2014a), including inherited zircons in high-grade rocks of the Kapuskasing structural zone >2760 Ma, interpreted by Benn and Kamber (2009) as indicating the presence of a thick, metamorphic crust formed in a large igneous province in the lower crust. Pre-2.8 Ga protoliths have been documented in the W Superior Province in Manitoba (Heaman et al., 1999), and analyses of ca. 2.7 Ga diamonds from Archean metavolcanic rocks in SW Wawa sub-province indicate the presence of a thick SCLM (Stachel et al., 2006), providing support for an autochthonous model for formation of the Abitbi–Wawa sub-province proposed by Thurston (2002). Some deep N-S faults may also hence represent structures in Mesoarchean basement along or parallel to an early N-S trending protocraton margin interpreted from seismic tomography (Frederiksen et al., 2007; Bédard and Harris, 2014), subsequently reactivated during rifting and formation of younger volcano-sedimentary sequences in the W Superior.

Concentric and intersecting transverse structures were formed by 2736 Ma, based on the age of emplacement of mafic-ultramafic bodies in the Ring of Fire between 2736 and 2733 Ma (Metsaranta and Houlé, 2020). However, the age of their inception and for the earliest mantle upwellings that led to subsequent corona-like structures is not known. It is hence plausible that older vocanosedimentary sequences on the S margin to the N Superior proto-craton are also related to early stages of mantle upwelling, The interpretation that supracrustal rocks in the Oxford-Stull Domain (Stott et al., 2010) and Island Lake Domain (Anderson, 2008), in which the deep concentric features described above are located, formed in an intracratonic rift between the North Caribou and Hudson Bay terranes may be equivalent to the extensional features that link coronae on Venus portrayed in Figure 16d. That the W Superior was undergoing regional N-S shortening during formation of concentric and transverse structures, as implied from the relationship between extensional, N-S and concentric structures on Venus and numerical models in Figure 16c, is consistent with regional structural interpretations: Metsaranta and Houlé (2020) describe a period of folding and thrusting on the S margin of the Hudson Bay terrane pre-2728 Ma that folds, and possibly thrusts, mafic volcanics and supracrustals dated at 2820–2797 Ma and 2783–2780 Ma, i.e. formed prior to emplacement of the Ring of Fire mafic-ultramafic intrusions. In an eastwards correlation of the same belt in the Eeyou Istchee James-Bay region, a period of N-S shortening

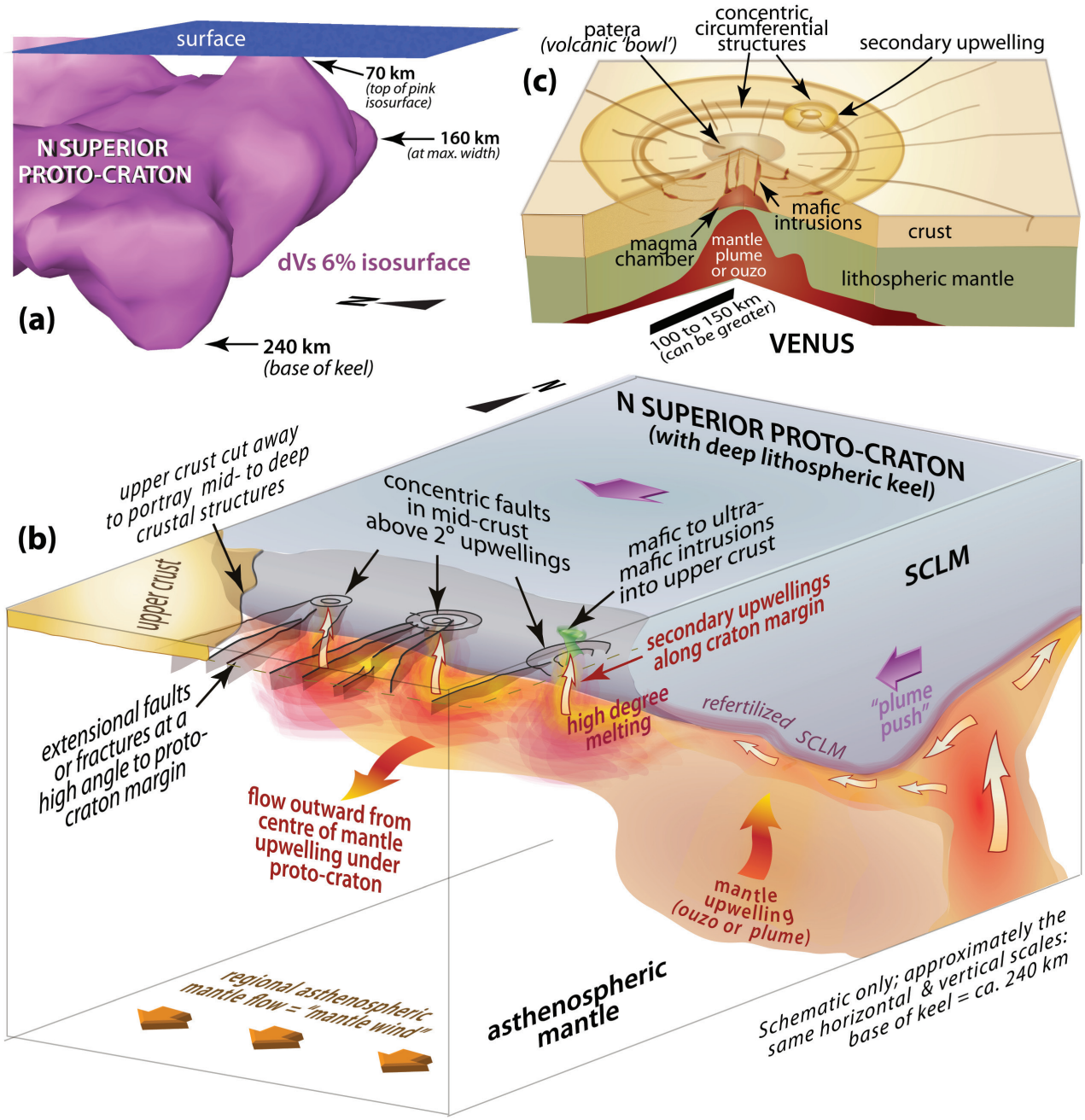

Figure 17. Geometry and conceptual model of the coeval formation of concentric circumferential and transverse rectilinear structures in the W Superior Province. **(a)** Oblique view portraying the 3D form of the Northern Superior proto-craton (shaded 6% dVs isosurface in pink), of which the Hudson Bay Terrane is part, calculated from S-wave seismic tomographic data of Godey et al. (2003, 2004). The blue surface rectangle corresponds to the area covered by aeromagnetic data over the western Superior in Figure 3. **(b)** Schematic 3D 'cartoon' of how several secondary mantle upwellings develop along the southernmost margin at depth of the Northern Superior proto-craton due to lateral mantle flow created by a much larger mantle upwelling (plume or ouzo) beneath the N Superior proto-craton. Concentric extensional structures (akin to coronae associated with mantle upwellings on Venus in (c) form along with regional transverse structures that intersect them, with the same geometry as regional structures paralleling the maximum compressive stress trajectory in examples from Earth and Venus and numerical models in Figure 16c. **(c)** 3D representation of extensional structures associated with coronae on Venus. Note that some coronae also have one or more concentric annular ridge(s) (e.g. Fig. 16d, as mapped by McGill, 2004), created by localised shortening due to upwarping/doming of the central part of the corona (c.f. Krasilnikov et al., 2001; Krassilnikov, 2002). Some radial structures within the corona may extend far beyond its margins where there is a regional compressive stress (i.e. as in Fig. 15). Features defining the corona proper were traced from a 3D sketch by Bethell (2016).

and thrusting of the 2820 to 2806 Ma Guyer Group (David, 2012) over the 2751–2732 Ma Yasinski Group (i.e. the same age as supracrustals in the Island Lake Subprovince of the W Superior) at the S margin of the Hudson Bay Terrane at 2727 ± 11 Ma is also documented by Cleven et al. (2020b, c). Significantly, geochemical studies by Sappin et al. (2018) led them to conclude that both the Guyer and Yasinski groups were formed during plume-related rifting which marks the onset of autochthonous greenstone belt formation throughout the NE Superior Province, after assembly of the Hudson Bay and Rivière Arnaud terrains that constitute the N Superior proto-craton (Maurice et al., 2008). Mafic-ultramafic and TTG pluton emplacement in the NE Superior Province reached their paroxysm between 2.75 and 2.71 Ga (Maurice et al., 2008).

Early regional shortening on the S margin to the N Superior proto-craton may be related to 'plume-push' (*c.f.* Lithgow-Bertelloni and Silver, 1998; Cande and Stegman, 2011; Harris and Bédard, 2014b) from a mantle upwelling then situated near the northern margin of the proto-craton and/or regional mantle flow (Fig. 17b), both acting against the deep keel of the proto-craton (Bédard et al., 2013; Harris and Bédard, 2014a). This early shortening event in the Eeyou Istchee Baie-James region took place prior to rifting and sediment deposition in a rift setting in the Opinaca Sub-Province between 2716 to 2695 Ma (Cleven et al., 2020b, c). Other pre-tectonic volcanosedimentary and sedimentary sequences further south from the proto-craton margin in the W Superior, such as in the English River (2720-2710 Ma; Corfu et al.,1995; Sanborn-Barrie et al., 2001), Quetico (between 2698 ± 3 Ma and 2688 ± 4 Ma; Davis et al., 1990), and Abitibi (pre-2750 to ca. 2695; Thurston et al., 2008) subprovinces, penecontemporaneous or which overlap the time of sedimentation in the Opinaca, are interpreted as being deposited in rifts during southwards mantle flow as illustrated by Bédard and Harris (2014), Harris and Bédard (2014a) and Mints (2017), where outward flow from mantle upwellings is deflected into the regional mantle flow, analogous to the present day E Africa-Red Sea-Arabia region (Fig. 18). A ca. 2682 Ma mafic and ultramafic volcanic event synchronous with the deposition of the Pontiac subprovince sedimentary rocks is also attributed to plume-related extension in the Pontiac Subprovince by Rehm (2020). Both the English River (Corfu et al.,1995; Pan and Therens, 2000) and the laterally equivalent Opinaca sequences in the NE Superior (Côté-Roberge, 2018) underwent high temperature - low pressure metamorphism shortly after their deposition during continued crustal extension prior to their folding and shearing during dextral transpression.

Evidence presented therefore points to widespread rift-related, concentric and transverse faulting, deposition of volcanosedimentary sequences and intrusion of mafic-ultramafic bodies across the southern Superior Province, as well as localized shortening on the margin of the N Superior proto-craton, between ca. 2.88 and 2.7 Ga related to multiple mantle upwellings that are related to one or more larger mantle plumes or OUZOs. The proposed model however differs to that of Mints (2017), which did not take into account the presence of a pre-existing mantle keel to the N Superior proto-craton. Instead, Mints' (2017) model portrays delamination and removal of SCLM beneath the Hudson Bay Terrane; whilst this may be applicable to other Archean cratons, potentially the Slave Craton, where Davis et al. (2003) propose its Mesoarchean SCLM was not preserved prior to Neoarchean tectonism, this is nevertheless not the case in the Superior Province. The localisation of mantle upwellings over the surface projections (Fig. 9) of the widest margin to the mantle keel (Fig. 17a) confirms the presence of a rigid/anhydrous and buoyant SCLM root to the N Superior proto-craton by the Neoarchean, and its preservation until the present day. This conclusion was also reached by Frederiksen et al. (2007) who document two distinct domains from S-wave seismic tomography in the mantle beneath the N Superior proto-craton. This is separated from a shallower, anisotropic and more fertile and metasomatized mantle (established from mantle xenoliths) beneath Neoarchean southern sub-provinces by a sharp E-W velocity discontinuity (also noted by Faure et al., 2011, Harris and Bédard, 2014a and Bédard and Harris 2014). Our observations and interpretations concur with conceptual models for the control on craton or proto-craton geometry on mantle plume-related Ni deposits (Begg et al., 2010; Maier and Groves, 2011; Griffin et al., 2013); the role of a proto-craton's margins within a larger Archean craton are exemplified by seismic tomography and gravity mapping of lithospheric controls on emplacement of the Bushveld complex and coeval plutons in South Africa (see 3D model in fig. 2 of Harris, 2017 and Harris and Moyen, 2017).

The deflection and flattening of mantle flow associated with upwelling mantle plumes beneath the present day Red Sea in Figure 18 illustrates that large region away from the plume's head may be affected by mantle thermal anomalies associated with mantle plumes. For the Red Sea example, deflection of the mantle flow has resulted in off-axis volcanism NE of the Red Sea rift. If, similarly, the second order mantle upwellings in the W Superior were deflected horizontally and merged with regional southwards mantle flow from the plume beneath the N Superior proto-craton (Fig. 17b), the interpreted deep ca. N-S structures may overlie a thermal anomaly created by deflected secondary upwellings that in turn may drive hydrothermal systems in the overlying crust, increasing the likelihood for Au mineralization and late intrusion emplacement in broad corridors above which these transverse structures lie.

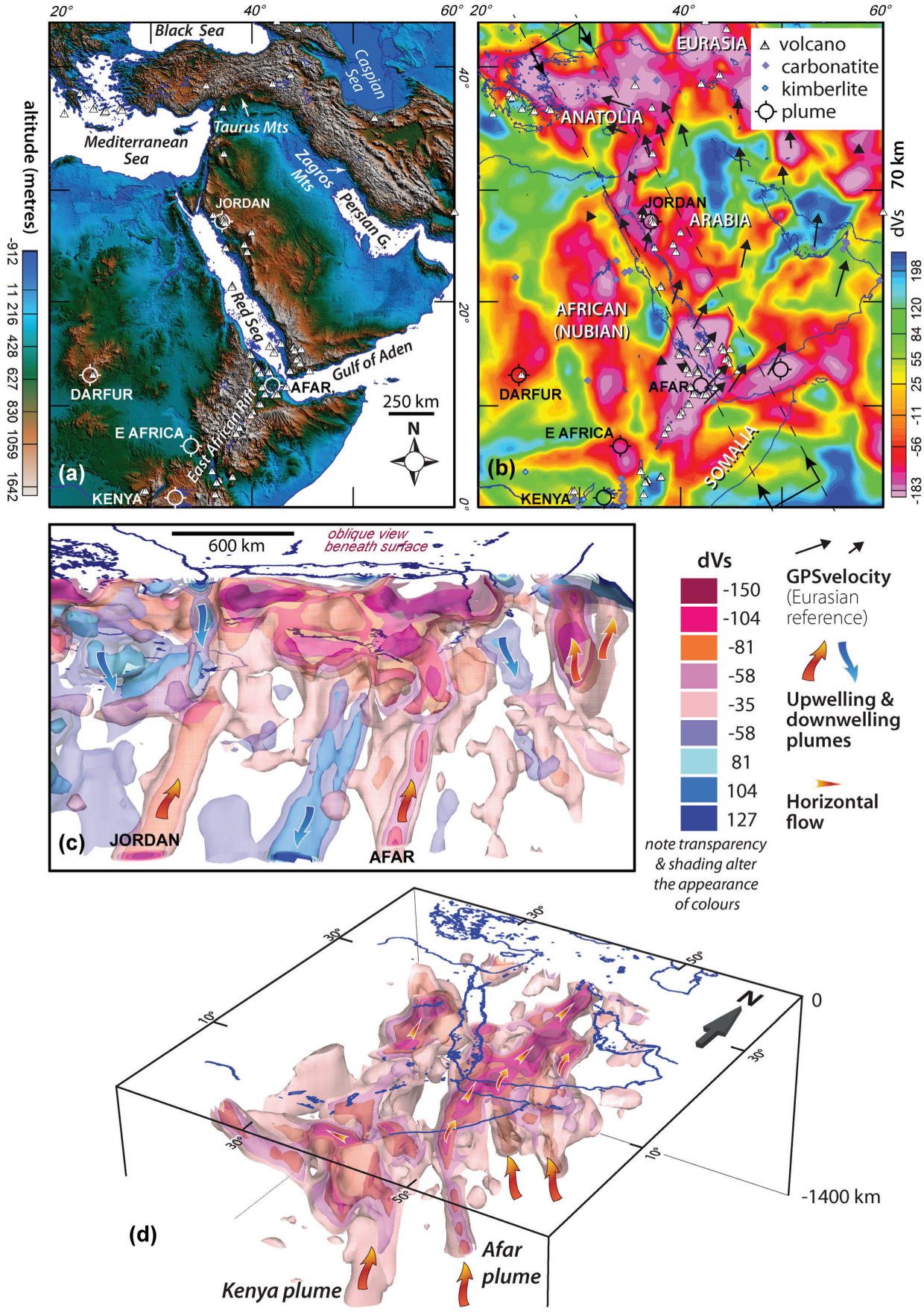
20°
40°
60°
Black Sea
Caspian Sea
Mediterranean Sea
Taurus Mts
Zagros Mts
Persian G.
JORDAN
Red Sea
Gulf of Aden
DARFUR
AFAR
E AFRICA
East African Rift
KENYA
250 km
N
(a)
altitude (metres)
-912
11
216
428
627
830
1059
1642
EURASIA
ANATOLIA
ARABIA
AFRICAN (NUBIAN)
SOMALIA
volcano
carbonatite
kimberlite
plume
(b)
70 km
dVs
198
120
84
55
25
-11
-56
-183
600 km
oblique view beneath surface
(c)
dVs
-150
-104
-81
-58
-35
-58
81
104
127
note transparency & shading alter the appearance of colours
GPSvelocity (Eurasian reference)
Upwelling & downwelling plumes
Horizontal flow
30°
50°
10°
N
0
-1400 km
(d)
Kenya plume
Afar plume

Thermal mantle downwelling, drips and delamination

Whilst the observations and interpretations above have focussed on features attributable to mantle upwellings, dynamically linked, commensurate downwellings are likely to also have played a role in deformation of the Superior Province, including the areas described herein. 3D seismic tomographic isosurface images shown in Figure 18 for active mantle circulation beneath and near the Red Sea, show both planar and more sheet-like mantle higher velocity (colder) downwellings in addition to the well documented slower velocity (hot) mantle upwellings associated with mapped mantle plumes, and smaller previously unmapped upwellings. In contrast to extension above mantle upwellings, shortening would occur above downwellings, producing folds and potentially thrusts in local regions, in addition to those formed by regional shortening (described in the next section). A complex interplay between melting above an upwelling mantle plume, formation of Tonalite-trondhjemite-granodiorite (TTGs), and delamination and dripping or restite and cumulates in the Archean, the catalytic delamination-driven model of Bédard (2006), is corroborated by numerical models of mantle plume interaction with an Archean lithosphere (Fischer, 2016; Fischer et al., 2016).

Neoarchean shearing and reactivation

Regional, distributed ductile shearing interpreted in the present-day surface and upper crust in a dextral transpressional regime interpreted for the S Superior from field studies (Tabor and Hudleston, 1991; Poulsen et al., 1992; Hudleston and Bauer, 1995) and aeromagnetic data pre-dates formation of discrete ductile to brittle-ductile shear zones during N-S shortening (Harris and Bédard, 2014a and references therein; Hendrickson, 2016; Cleven et al., 2020a, b; P. Adiban, unpublished data). Structures developed during regional shortening are attributed to southwards displacement of the N Superior proto-craton driven by a combination of southwards directed regional mantle flow (Bédard and Harris, 2014a; Harris and Bédard, 2014a; Bédard, 2018), the 'mantle wind' of Davies (1993, discussed in detail by Bédard et al., 2013) and plume push (Cande and Stegman, 2011; van Hinsbergen et al., 2011), as shown schematically in Figure 17b.

Preliminary analysis suggests that the same structural features indicative of dextral transpression are likely diachronous across the Superior Province (further development of this idea is beyond the scope of this article). Irregularities in the shape of the proto-craton margin (Fig. 17a) could result in lateral extrusion that may create localized dilatational sites focussing hydrothermal fluids responsible for Au mineralization (Bédard, 2018). Sinistral displacements noted on some ca. N-S structures in the deep crust at a high angle to regional trends in the W Superior are consistent with antithetic shearing (i.e. displacement on R' structures; Fig. 19a) within the overall regional dextral transpressional regime. This proposed regional structural geometry resembles that of high-angle cross faults, antithetic to regional dextral shears in the Denali-Tintina Fault Zone (Sanchez et al., 2014) which extends from Alaska into northern British Columbia. Groves et al. (2018) suggests displacement along the antithetic sinistral shears in the Denali-Tintina Fault Zone 'leads to focussed ore-fluid flux into dilation zones along suitably-aligned pre-existing structures and deposition of high-grade gold ores within those structures and more disseminated mineralization and alteration zones adjacent to them'. Similarly, Au mineralization in the western (and potentially other parts of the) Superior may be associated with dilatational reactivated N-S faults in the deep crust which focussed hydrothermal fluid flow into the greenstone cover (Fig. 19).

The origin of late NE-SW shortening documented by Percival et al. (2003) in the Wabigoon Subprovince and by Leclerc et al. (2012) in the NE Abitibi is unknown.

Figure 18. Upwelling hot and downwelling cold mantle plumes and their regional effects in the E Africa-Red Sea-Arabia region. Maps and 3D isosurfaces present S wave velocity data from Chang & Van der Lee (2011) compared to reference model 'MEAN' of Marone et al. (2004). **(a)** Elevation. The majority of the interpreted mantle plumes from Chang & Van der Lee (2011) and a compiled list of plume locations (see Anderson: http://www.mantleplumes.org/CompleateHotspot.html) correspond to areas of elevated topography. **(b)** Velocity differences at 70 km depth. Warm colours correspond to higher temperatures that are interpreted as mantle upwelling by Chang & Van der Lee (2011). **(c)** and **(d)** 3D isosurfaces of velocity differences from 50 to 1400 km depth. Data portrayed in (c) show hot upwelling and downwelling cold plumes along a slice parallel to the Red Sea, dashed lines, indicated by the arrows in (b), viewed from below the Earth's surface (i.e. looking upwards at the map of the Red Sea). Isosurfaces in (d), viewed looking down obliquely NW, show upwelling mantle plumes being deflected to flow horizontally northwards by the regional mantle flow ('mantle wind'). This deflection explains the volcanism on the margin and away from the Red Sea rift. A similar horizontal deflection from the secondary and main mantle upwellings is envisaged for the W Superior (shown schematically in Fig. 17) to explain volcanism and rifting S of, as well as along, the southern margin to the N Superior proto-craton. The N- to NNW-striking structures intersecting concentric structures above mantle upwellings in the W Superior (illustrated in Fig. 17) would overlie broad linear thermal anomalies, akin to the deflected mantle plumes (with triangles indicating horizontal flow) in (d), which would likely facilitate high temperature mixed aqueous and carbonic fluid circulation associated with Au mineralization along these structures in the overlying crust.

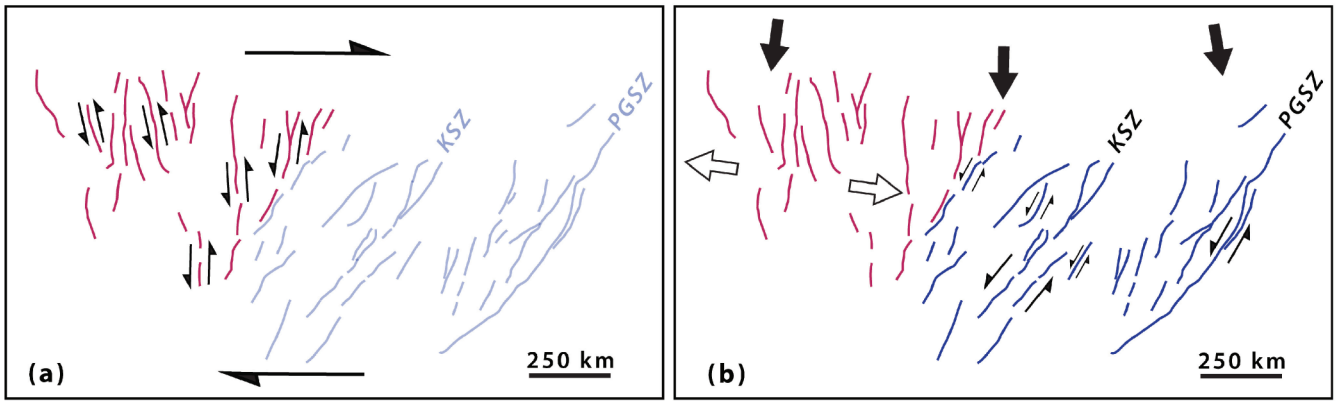

Figure 19. Schematic illustration from the W Superior across the Abitibi Subprovince to the Grenville Front. Deep, ca. N-S structures (red), formed during early plume-related rifting in the western Superior Province, possibly controlled by inherited basement weaknesses, would have been potentially sinistrally reactivated as secondary Riedel (R') shears within an early dextral transcurrent or transpressional regime in (**a)** or as extensional fractures or normal faults during subsequent bulk N-S shortening (filled black arrows) in **(b).** Their dilatation during both stages may have focussed hydrothermal fluid associated with lode Au mineralization. Sinistral displacement along NE-SW structures (blue) in (b) occurred during N-S shortening. KSZ = Kapuskasing structural zone, PGSZ = proto-Grenville shear zone (see Harris and Bédard, 2014a). The PGSZ may have been localised (at least in part) by a plume-related aulacogen during formation of rifts in which the Abitibi sub-province and Belomorian belt in the Kola Peninsula (placed against the Superior in tectonic reconstructions) were formed (Dufréchou et al., 2013; Harris and Bédard, 2014a). Whether other NE structures formed during N-S shortening or whether some may have an older origin, possibly having been rotated from a more N-S orientation during dextral shearing in (a), is not known.

Lithospheric strength profiles — a neglected element in metallogenic models

There is evidence for the presence of a semi-brittle mid- to deep crustal layer, as required to explain the preservation of early-formed structures described above, and other studies of the Superior Province where differences between deep and upper crustal structures similarly imply intra-crustal decoupling (e.g. Moser et al., 1996) and lateral crustal flow in the middle to lower crust in the W Superior has been proposed by Hill et al. (2020) from interpretation of MT data. In the NE Superior Province in Quebec (Fig. 2a), NRCan aeromagnetic data (Fig. 2b), transformed into pseudogravity (see Methods section) to show deep crustal domains in Figures 2c and d, highlight deep domain boundaries that are oblique to trends in the upper crust and to lithostratigraphic boundaries derived from surface mapping, so a semi-brittle mid-crustal layer must have existed early in the region's history. In the northern Minto and Rivière Arnaud terranes (Fig. 2a), distinct changes in colour of the enlarged, edge enhanced pseudogravity image in Figure 2b define crustal domains whose contacts are oblique to those mapped at the surface (e.g. in Bédard, 2006). Polymetallic, intrusion-related (Cu-Au-W-Sn-Bi) and late Archean or Paleoproterozoic IOCG mineral occurrences in the "Rex Trend" (Lulin et al., 2012; Lulin, 2016) are located on the margins to these deep crustal blocks, at their intersection with late strike-slip faults localized by their irregular margins (Fig. 2d, whose location is shown in Fig. 2c). Whilst interpreted by these authors as a suture, at least in part of the area's history, research in our TGI project suggests rifting to create the domain green-yellow central domain of Figure 2d. In the La Grande and Opinaca sub-provinces, where ca. N-S surface trends of the NE Superior change to a generally E-W orientation, high resolution enhanced short wavelength aeromagnetic data portray regional distributed ductile deformation of amphibolite to granulite facies gneisses during E-W dextral transpression (Cleven, 2017; Cleven et al., 2020a, b). An interpretation (Fig. 2e) of the southern part of the pseudogravity image in Figure 2b of underlying, deep crustal structures, however, portrays several discrete E-W dextral shear zones that displace the initially N-S margins of an elongate, semi-rigid block (ca. 170 km from N to S; Fig. 2e). Similarly, in the central Abitibi, comparisons of bouguer gravity and aeromagnetic data show that discrete E-W faults offsetting the N-S margins of units with high gravity signatures, interpreted as mafic deep crustal rocks, underlie broad ductile dextral shear zones (Harris and Bédard, 2014a; Fayol, 2016). Differences in deformation responses and the amount of likely decoupling in the mid crust between the western Superior, where decoupling appears complete, as shown in the 3D diagram in Fig. (10a), and the eastern Superior, where there is evidence for only partial decoupling as basement blocks beneath zones of penetrative ductile shearing are displaced along discrete faults (Fig. 2; Fayol, 2016; Cleven, 2017; Cleven et al., 2020a,b) may reflect differences in age and nature of the SCLM (see seismic tomographic 3D images and cross-sections in Harris and Bédard, 2014a). Whereas rifted fragments of an older, possibly Hudson Bay Terrane crust are preserved in the W Superior (see Bédard and Harris, 2014 and evidence for old basement ages outlined above), the Abatibi-Opatica

has juvenile mantle signature, likely formed in a rift environment and is similar to a modern oceanic plateau (Benn and Moyen, 2008; Bédard et al., 2013).

The presence of rigid deep crustal domains preserving early-formed structures underlying ductile structures in the present day upper crust is inferred for other Archean cratons. For example, regional faults beneath the classical diapiric granitoid-gneiss domes in the Pilbara Craton, Western Australia, created during a partial convective overturn, are preserved below depth in mafic crustal basement (Harris, 2017; Harris and Lu, 2018). Enhanced gravity images also show basement to the Yilgarn Craton in Western Australia preserves an early rift geometry; overlying transpressional to transcurrent shear zones are localized by rift margins Harris and Bédard, 2015). Mechanically strong deep crustal units in the Superior Province, Pilbara and Yilgarn Craton are interpreted as anhydrous felsic and mafic granulites formed through intense dehydration and melt extraction (c.f. Yakymchuk and Brown, 2014; Diener and Fagereng, 2014), which is likely to have been greater in the Archean compared to younger crust due to higher radiogenic crustal heat production (Condie and Benn, 2006; Flament et al., 2008).

Strength profiles calculated for the Abitibi Subprovince at 2.55 Ga by Mareschal and Jaupart (2006), as shown in Fig. 6b, also illustrate the presence of two brittle-ductile transitions and the presence of a semi-brittle crustal layer. The strength profiles of Mareschal and Jaupart (2006) on the left of Figure 10b are based on their calculated temperature profiles, the stress required to maintain their estimated strain rate of 10-15 s-1 for a dry granitic upper crust, a granulite lower crust, and dry dunite for mantle for two different heat flows. The lithosphere was, however composed of a range of different lithologies (listed to the right of Fig. 10b) so local deviations from this strength profile would occur; differences in strength profile between homogeneous and different thickness differentiated crust (right set of profiles). Strength profiles by other researchers for the Abitibi (e.g. Guillou et al.,1994; Benn, 2006), and more general models of Gueydan et al. (2014), Gouiza and Heron et al. (2016) and Gouiza and Paton (2019) all show two brittle-ductile transitions, although their depths differ, e.g. Benn (2006) and Gouiza and Paton (2019) show the transition to a strong granulite crust at 35 km and Heron et al. (2016) at 24 km, instead of 20 km in the figures of Guillou et al. (1994), Mareschal and Jaupart (2006), and Perry et al. (2006), and in profiles for medium and high strain rates by Gueydan et al. (2014).

Common end-member lithospheric strength profiles for the Earth's lithosphere are (i) the crème-brûlée analogue, where a strong, uppermost brittle crustal layer overlies weak lower crust and upper mantle and (ii) the jelly sandwich model, where lithospheric strength resides in both the elastic-ductile SCLM and brittle-elastic upper crust and the mid- and lower crust are considered to be ductile (Burov and Watts, 2006) and (iii) the banana split model (Bürgmann and Dresen, 2008), which includes weakness of major crustal fault zones throughout the thickness of the lithosphere, caused by various strain weakening and feedback processes. Discrete faults in the upper crust are routinely portrayed as broadening with depth into brittle-ductile shear zones then mylonites (e.g. Mattauer, 1974; Fossen and Cavalcante, 2017); the lower crust is generally depicted as undergoing pervasive ductile deformation, including in Archean terrains where Au mineralization commonly thought to occur at a single brittle-ductile crustal transition (e.g. Colvine et al., 1988; Eisenlohr et al., 1989; Groves, 1993). Our results and comparison with other Archean cratons clearly shows classical models of a simple progression from a brittle upper crust to a ductile lower crust and conceptual, physical and numerical models for a weak Archean 'crème-brûlée' lithosphere (Cagnard et al., 2006; Chardon et al., 2009; Gerya, 2012; Gapais et al., 2014; Gapais, 2018; Poh et al., 2020) are not applicable in the Superior Province and most likely not in other Neoarchean terrains. Such models that interpret a crème-brûlée lithospheric strength profile as a result of the higher heat flow in the Archean due to the increasing abundance of radiogenic elements within the mantle and continental crust (e.g. Condie and Benn, 2006) do not take into account the ensuing enhanced dehydration and melt extraction as discussed above and that granulite facies metamorphic conditions would be achieved at a shallower crustal depth compared to in a younger Earth. A crème-brûlée lithospheric strength profile is not supported by observations of structures at different depths on potential field geophysics images in the Superior, Yilgarn, and Pilbara cratons, and the formation and preservation of planar and pipe-like fluid flow pathways linking the mantle to the upper crust that correlate with Archean Au deposits imaged in MT studies in Archean terrains (e.g. Yilgarn Craton; Dentith et al., 2013; Dentith, 2019), the results of modelling strength profiles discussed above, and the observations of Condie and Benn (2006) for rigid Archean lithosphere since ca. 2.9 Ga and for the formation of cratons with deep lithospheric keels, preserved until the present day, at the same time or before the formation overlying crust (despite this article being cited in support for a weak Archean lithosphere by Poh et al., 2020).

Following previous sweet food analogies for strength profiles, the term millefeuille, after a French cake with 3 strong pâte feuilletée /puff pastry layers separated by weak crème pâtissière / custard cream (Harris et al., 2018d; sketch in lower right of Fig. 10b), is proposed to describe the strength profile we attribute to the Superior Province.

Metallogenic implications

Whilst a transition from viscous to plastic deformation in the mid-crust is significant in localising a detachment surface that may act as a seal to hydrothermal fluid flow (Drummond et al., 2004), it is difficult to reconcile ideas of a continuous thick ductile mid- to lower-crust with those of many economic and tectonic researchers and exploration geologists, cited in the background section above, that long-lived deep crustal structures exert primary controls on cratonic architecture and the localisation of mineral deposits, are commonly

linked with SCLM discontinuities that focus the flow of mantle-sourced fluids and igneous intrusions (as confirmed from recent MT studies in South Australia; e.g. Heinson et al., 2018; Wise and Thiel, 2018 and the Yilgarn cited above). Deep crustal discontinuities, and discrete shear zones and faults above them, are spatially related to Au, polymetallic, VMS, IOCG and REE occurrences in the overlying crust in the NE Superior (Fig. 2d; Harris et al., 2018b,c) and with late alkaline plutons and Au mineralization in the central Abitibi (eg. Lac Bachelor deposit: Fayol, 2016; Fayol and Jébrak, 2017). In the Eeyou Istchee James Bay area, the Éléonore Au deposit is situated at the intersection of one of the deep E-W dextral faults offsetting a rigid, initially N-S crustal block, on the margin of a pluton intruded on its eastern margin, and at the intersection of an antithetic, sinistral shear zone (Fig. 2e). Similarly, in the eastern Yilgarn, basement horst and graben localize transpressional sinistral and superposed dextral transcurrent shearing during which Au deposits were formed; Au mineralization appears spatially related to preserved deep, 'fossil' transfer faults developed during rifting (Harris and Bédard, 2015). Au and other mineral occurrences are located above the basement structures in the Pilbara Craton especially on overlying, upper crustal diapir margins (Harris, 2017; Harris and Lu, 2018). Mapping boundaries and structures developed in strong, deep crustal layers from enhanced geophysical images is thus shown to be especially important for mineral exploration in Archean terrains.

As the presence of a strong mid- to lower crustal felsic of mafic restite is attributed to dehydration and migration of melt and radiogenic elements into overlying crust (as discussed above), it is likely that the crustal strength profile may have changed progressively during a tectonothermal event, i.e. there may have been an increase in rigidity and thickness of a competent mid- to deep crustal layer which enhanced fracturing and faulting late or post regional metamorphism, providing fluid and magma conduits between discontinuities in metasomatized SCLM and the mid- to upper crust. This therefore provides a factor that helps explain the commonly documented late timing of orogenic Au mineralisation (Jemielita et al., 1990; Kerrich and Cassidy, 1994; Gaboury, 2019 and Groves et al., 2000 and references therein), which Groves et al. (2000) state "… is pivotal to geologically-based exploration methodologies", and which explains the lithospheric scale fluid pathways imaged by MT studies.

The Kapuskasing structural zone - inception as an Archean transverse fault?

Although this project focussed on the Archean geology and tectonics related to mineralization, it also has implications for the origin of the NNE-SSW Kapuskasing structural zone/uplift/line (KSZ), that crosses the central-southern Superior Province from James Bay to Lake Superior, where high-grade Archean crust is exhumed (Truscott and Shaw, 1990). The KSZ shows evidence for multiple reactivation episodes with diverse displacements (Watson, 1980; Percival and Card, 1983; Percival et al., 1991; Percival and West, 1994; Heather et al., 1995). The KSZ parallels other deep crustal structures that cross-cut the W Superior identified in this study, and includes faults that extend to at least 30 km depth; the KSZ may thus have been localized by an early-formed transverse Archean fault as described above in the W Superior, possibly subsequently rotated to a more eastern strike during Neoarchean shortening and dextral transpression.

Several observations support Archean initiation of the KSZ. From the ductile deflection of their foliation, gneisses of the KSZ were interpreted by Watson (1980) to record sinistral ductile transpressional shearing that predates formation of semi-brittle to brittle structures at ca. 1.9 Ga (Percival and Card, 1983; Percival, 1991; Percival and West, 1994), also predating shallowly NW-dipping thrust faults described by Perciva (2018). Formation of a crustal root (Boland, 1989; Percival, 2018) and anomalous 48 km thick crust (Darbyshire et al., 2007) beneath the KSZ is interpreted to have occurred at ca. 1.9 Ga during thrusting (Percival and West, 1994) or dextral transpression (Heather et al., 1995), however these interpretations do not fit all available data. Instead of shortening, mafic underplating along a localized rift (c.f. Thybo and Artemieva, 2013) is thought to be more likely; deep linear structures (which cannot be explained in previous models) would then represent earlier weaknesses that localized rifting or were developed in this extensional event. Whilst the timing of underplating is not well established, exhumation along the KSZ took place after intrusion of NW-striking ca. 2.45 Ga Matachewan dykes (Halls and Zhang, 1998). Whilst some mafic underplating may have occurred in the Archean (as suggested by Truscott and Shaw, 1990), it is likely that extension along the KSZ and (further?) mafic underplating was contemporaneous with emplacement of the 2.1 Ga Marathon dykes during a 'long-lived mantle plume event' along the southern Superior Province margin, for which the plume centre is interpreted to lie about 400 km SW of the southern termination of the KSZ (Halls et al., 2008). This mafic underplate would then have acted as a rigid block during Paleoproterozoic shortening, localising thrusting at higher crustal levels on the edge and over this pre-existing lithospheric heterogeneity (as in analogue models of Calignano et al., 2015).

The demise of plate tectonic models for the Superior Province?

Project results are impossible to reconcile with putative conventional arc accretion models for the Superior Province as developed by Card (1990), Poulsen et al. (1992), and Percival et al. (2006, 2012), but support non-plate tectonic models as reviewed by Bédard et al. (2013 and references therein), Harris and Bédard (2014a), Bédard (2018). Studies of Venus presented herein and in Harris and Bédard (2014a, b) show that plate tectonics is not required to produce many

salient features of Archean deformation, including rifting, regional shortening, polyphase deformation, lateral transcurrent and transpressional shear zones, where shortening can be linked to rift zones produced by mantle upwelling. Upwelling mantle plumes combined with regional mantle flow and plume push produces horizontal compressive stress trajectories over large regions resulting in thrust and strike-slip faulting far from the plume centres: Supplementary Figure 2 in Harris and Bédard (2014b) illustrates how deformation related to the Iceland plume is interpreted in Britain and Norway and multiple plumes in the E Africa-Red-Sea-Arabia region portrayed in Fig. 18 are linked to the formation of the Zagros Mountains by Mouthereau et al. (2012). On Venus, transcurrent and transpressional shear zones and fold and thrust belts occur on the margins of craton-like domains, which gravity data require to be largely constituted by felsic crust (Harris and Bédard, 2014a).

Recent isotope data do not fit the multiple subduction zone-accretion construct for the Superior Province and the Australian Yilgarn Craton. In the SW Superior, Bjorkman (2017) suggests that the consistency in Hf and O isotope measurements 'favours autochthonous growth of the craton, because disparate evolutionary paths are expected for a collage of exotic terranes amalgamated by younger tectonic processes'. Subsequent isotope studies by Li et al. (2020) from the N Caribou to Winnipeg River subprovinces are consistent with models that suggest recycling of pre-existing mature crust > 3 Ga. Isotope studies by Mole et al. (2012) required revision of tectonic and metallogenic models for the Yilgarn Craton in Western Australia, pointing to break-up of the Yilgarn proto-continent (equivalent to the term proto-craton used herein), the formation of rift-zones during plume-lid and mantle drip tectonics (Mole et al., 2013, 2019), which we also propose for the Superior Province. The results of Bjorkman (2017) and Li et al. (2019) similarly provide a new framework and evolutionary model for the W Superior consistent with the structural and tectonic interpretations presented herein, thus requiring a re-evaluation of metallogenic models presently based on a plate tectonic paradigm, such as illustrated in Mercier-Langevin et al. (2007). The models we propose for the controls on lode Au deposits in the W Superior challenge the postulate of Groves et al. (2020) for "… the ubiquitous occurrence of orogenic gold deposits in subduction-related orogenic belts". Isotope studies as undertaken in the Yilgarn Craton currently being undertaken by David Mole in the Superior Province will provide valuable new data for better understanding Superior Province evolution. In the models of Bédard and Harris (2014), Harris and Bédard (2014a), Bjorkman (2017) and Mints (2017), older metamorphic basement remnants in and beneath the W Superior, such as the Winnipeg River terrane which contains >3.5 Ga rocks (Melnyk et al., 2006) and the Minnesota River Valley Terrane in the USA where tonalite gneiss is dated at 3.42 Ga (Schmitz et al., 2006), are interpreted as rifted fragments of the N Superior proto-craton / Hudson Bay Terrane which were subsequently reassembled. Some basement to the central and western Superior may have therefore preserved structures equivalent to those in the NE Superior which were subsequently reactivated in the Neoarchean. Preservation of deep N-S structures beneath the Opinaca and LaGrande sub-provinces of the Eeyou Istchee James Bay area of the NE Superior interpreted by Cleven (2017), Cleven et al. 2020 a, b) and Harris et al. (2018b, c) from aeromagnetic and gravity data, spatially associated with mineralization, supports an autochthonous model, similar to the western Superior and provide another example of the controls of preserved basement structures on focussing hydrothermal fluids and magma into the overlying crust. Recent studies in the adjoining Nemiscau Subprovince led Pérez et al. (2020) to consider all three subprovinces constitute the same tectonometamorphic unit and to dismiss accretionary prism, back-arc, and collision-accretion models in favour of the models of Stern (2008), Bédard et al. (2013) and Bédard and Harris (2014). Whilst further refinement of non-plate tectonic models is required, our study along with much recent research suggest the imminent demise of plate tectonic accretionary models for the Superior Province will furnish new mineral exploration constructs and hence opportunities.

Reflections

A relationship between large ring-shaped faults cross-cut by regional fault or shear zones which appear to cross domain, sub-province and even province boundaries (termed phi / Φ structures by O'Driscoll and Campbell, 1996 and Lambert, 2018) and mineral occurrences has long been suggested from gravity, aeromagnetic, satellite image, seismic tomographic and digital terrain (elevation) models, especially in Precambrian terrains or areas with Precambrian basement (Gintov, 1973; Witschard, 1984; O'Driscoll, 1992; O'Driscoll and Campbell, 1996; Bourne and Twidale, 2007 and references therein; Lambert, 2018). O'Driscoll (1992) suggests "sub-crustal pressure resulting in crustal upwelling" for the origin of ring structures he interpreted in Australia, with which our research on the W Superior Province concurs. However, the diverse origins proposed for concentric ring structures (including bolide impact, alkali ring complex, diapir, dome, caldera, and mantle plume, etc.) along with commonly simplistic 'stick and ball' and/or 'overzealous' interpretation of numerous poorly defined circular and linear structures has often lead to scepticism, even rejection, of lineament and 'giant ring' interpretation in general (*c.f.* Wise, 1982). If care is not taken, concentric artefacts/short wavelength reverberations may be introduced in filtering of potential field data in the frequency domain, such as where there are sharp steps or spikes in the data (Dentith and Mudge, 2014) or by imposing too sharp filter cutoffs, known as Gibbs Phenomenon, Gibbs Effect or simply as '*ringing*' (Billings and Richards, 2000; Pan, 2001). Interpretation of circular and linear structures, especially from poor initial data, may sometimes also be in part due to the human brain's propensity to imagine and interpret the

presence of linear and especially circular shapes (Ohla et al., 2005), including for geophysics images when no real circular objects may be present (Dentith and Mudge, 2014, pp. 65-67). This is illustrated by Nock (undated) and Hamilton (undated) from studies of human visual perception. The concentric ring structures in the Oxford Stull and Island Lake domains (some of which are also associated with circular MT anomalies) and sharp, straight faults and fractures intersecting them that cut the North Caribou Core area, which are spatially related to Au and N-Cu-PGE occurrences, are so well imaged in the present study in aeromagnetic (including derived pseudo-gravity) data, where there no ringing artefacts were introduced in their processing, and MT data and whilst not previously mapped and are difficult to explain given conventional geological interpretations, their alignment along the margin of the deep keel to the N Superior proto-craton is precisely where mantle upwelling are predicted in models cited above; it therefore concluded they indeed represent real features.

We are mindful that the presence of elliptical structures elsewhere in the Superior Province, possible SCLM controls on transverse fault formation, fault reactivation and linking from 'source to trap' and their 3D structure, and many other aspects presented herein require further study, especially better defining depths at which the structures we describe occur, however our results have immediate mineral exploration implications. In their presentations in Australian Academy of Sciences (2010) to address the fundamental needs of the Australian mineral exploration industry, Neil Williams (past CEO of Geoscience Australia) and Jon Hronsky (Director, Western Mining Services and Chairman of the Australian Geoscience Council) support Woodall's (1994) ideas on 'empiricism and concept in successful mineral exploration' in pointing out that, whilst we do not understand the origin of regional lineaments by O'Driscoll and others cited above, interpreting these cryptic features played a major role in the discovery the world-class Olympic Dam IOCG-U deposit in South Australia. As expressed by Hronsky (2013), in linking trans-lithospheric structures to mineral deposits: 'The big lesson from the history of tectonics *(is)*: we see patterns long before we understand mechanisms'. In a similar vein, Phillips et al. (2019), in discussing the role of geoscience breakthroughs in gold exploration success, posit that '… openness to new ideas may correlate with the massive and ongoing exploration success witnessed in the Yilgarn goldfields' (Western Australia). Whilst not yet fully understood, research in this TGI project has provided the first stage in developing a new, deep structural framework to the Superior Province which has major implications for mineral exploration, and further research is underway to better substantiate certain interpretations herein and to provide more precise estimates to their formation depth and timing.

Recommendations for future research

All current Metal Earth transects, along with the majority of previous Lithoprobe and Discover Abitibi deep crustal reflection seismic profiles (Naghizadeh et al., 2019) are sub-parallel to the deep transverse structures described in this report. At least one regional E-W seismic profile and MT profile imaging the upper mantle crossing the ca. N-S to NE-SW striking deep faults are required to better establish the nature of the structures described in this report and their relationship with structures and plutons in the (present-day) upper crust (unfortunately, given the results of recent MT profiles in Australia showing the importance of upper mantle structures, MT profiles undertaken in Metal Earth do not image the SCLM). Our study concurs with Roots and Craven (2017) that inversion of *all* MT data for the western Superior, to provide better definition of SCLM and deep crustal structures, is definitely warranted.

3D numerical and/or physical modelling SCLM features, decoupling horizons in the lithosphere and deep crustal structures at a high angle to mapped surface trends are required to better understand trans-lithospheric fluid pathways. Isotope and geochronological studies are required to test possible differences in basement deep crust and upper mantle on either side of the identified N-S structures.

CONCLUSIONS

Early-formed deep crustal structures with little to no upper crustal expression at a high angle to sub-province boundaries and mapped surface structures and coeval concentric elliptical structures in the W Superior resembling Venus coronae, identified for the first time in the Canadian Superior Province, are spatially related to orogenic/lode and intrusion-related Au and magmatic Ni-Cu-PGE-Cr deposits. Statistical analysis and machine learning applied to the Red Lake - Stormy Lake area shows a these N-S structures play a greater role in localising Au mineralization than mapped, E-W structures. This study therefore provides important new data for regional exploration targeting, especially using machine learning. These early-formed deep transverse structures are thought to have been reactivated throughout the Neoarchean and, as exemplified by the Kapuskasing Structural Zone, Paleoproterozoic. Decoupling between deformation in the deep and mid- to upper crust is required to explain preservation of these deep structures beneath penetratively deformed overlying crust. In focussing hydrothermal fluids and magma into the overlying crust they represent key elements in a mineral systems approach linking source to trap (*c.f.* Hronsky et al., 2012 and Hronsky, 2020). Their formation accompanying secondary mantle upwellings arising from a mantle plume or OUZO beneath the N Superior proto-craton and the early development and preservation of transverse structures beneath subprovinces of

the W Superior are incompatible with conventional arc-accretion models which, as a consequence, requires revision of metallogenic models.

ACKNOWLEDGEMENTS

Support for the project 'The role of deep crustal structures on Au and Magmatic Ni–Cu–PGE–Cr mineralization in the Superior Province and and its extension beneath the southeast Churchill Province' was provided through NRCan's Targeted Geoscience Initiative Program (TGI): 'Increasing Deep Exploration Effectiveness', for which this is a contribution.

Preliminary research in parts of the W Superior was funded by Laurentian Goldfields Ltd. J. Craven (NRCan) is thanked for providing MT data in a different format to that published suitable for our processing. N. Cleven and C. Guilmette contributed to the interpretations of NRCan data for the James Bay area where research was funded by the MERN Québec. Parham Adiban was a recipient of an NSERC MSc scholarship. Oasis Montaj® (Seequent) and software provided by P. Keating (NRCan, retired) were used for geophysical processing. Tectonic interpretations of concentric elliptical structures in the western Superior and Venus benefited from discussions with, among many others, J. Bédard (NRCan), O. Göğüş (Istanbul Technical University, Eurasia Institute of Earth Sciences), and T. Gerya (ETH, Zürich). The structural map in Fig. 16 was adapted from the open access geological map by Bethell et al. (2019), distributed under the terms of the Creative Commons Attribution License.

REFERENCES

Anderson, S.D., 2008. Orogenic gold deposits in the Superior Province of Manitoba; Manitoba Mining and Minerals Convention 2008, Orogenic Gold Short Course, https://www.manitoba.ca/iem/geo/shortcourse/2008/anderson.pdf.

Benn, K., 2006. Tectonic delamination of the lower crust during Late Archean collision of the Abitibi-Opatica and Pontiac terranes, Superior Province, Canada; Geophysical Monograph Series, American Geophysical Union, v. 16, p. 267-282.

Australian Academy of Sciences, 2010. Searching the Deep Earth: The Future of Australian Resource Discovery and Utilisation; Proceedings, Theo Murphy High Flyers Think Tank, https://www.science.org.au/files/userfiles/events/documents/2010-thinktank-proceedings.pdf.

Baibatsha, A., 2020. Geotectonics and geodynamics of Paleozoic structures from the perspective of plume tectonics: a case of Kazakhstan; International Journal of GEOMATE, v. 19, p.194 -202.

Baranov, V., 1957. A new method for interpretation of aeromagnetic maps: pseudo-gravimetric anomalies; Geophysics, v. 22, p. 359–383.

Baranov, V. and Naudy, H., 1964. Numerical calculation of the formula of reduction to the magnetic pole; Geophysics, v. 29, p. 67–79.

Barley, M.E., Krapež, B., Groves, D.I., and Kerrich, R., 1998. The Late Archaean bonanza: metallogenic and environmental consequences of the interaction between mantle plumes, lithospheric tectonics and global cyclicity; Precambrian Research, v. 91, p. 65-90.

Barnes, S.J. and Van Kranendonk, M.J., 2014. Archean andesites in the east Yilgarn craton, Australia: Products of plume-crust interaction?; Lithosphere v. 6, p. 80-92.

Bédard, J.H., 2006. A catalytic delamination-driven model for coupled genesis of Archaean crust and sub-continental lithospheric mantle; Geochimica et Cosmochimica Acta, v. 70, p. 1188-1214.

Bédard, J.H., 2018. Stagnant lids and mantle overturns: Implications for Archaean tectonics, magmagenesis, crustal growth, mantle evolution, and the start of plate tectonics; Geoscience Frontiers, v. 9, p. 19-49.

Bédard, J.H., Brouillette, P., Madore, L., and Berclaz, A., 2003. Archaean cratonization and deformation in the northern Superior Province, Canada: an evaluation of plate tectonic versus vertical tectonic models; Precambrian Research, v. 127, p. 61-87.

Bédard, J.H. and Harris, L.B., 2014. Neoarchean disaggregation and reassembly of the Superior craton; Geology, https://doi.org/10.1130/G35770.1.

Bédard, J.H., Harris, L.B., and Thurston, P., 2013. The hunting of the snArc; Precambrian Research, v. 229, p. 20–48.

Begg, G.C., 2009. The lithospheric architecture of Africa: Seismic tomography, mantle petrology, and tectonic evolution; Geosphere, v. 5, p. 23–50.

Begg, G.C., Hronsky, J.A.M., Arndt, N.T., Griffin, W.L., O'Reilly, S.Y., and Hayward, N., 2010. Lithospheric, cratonic, and geodynamic setting of Ni-Cu-PGE sulfide deposits; Economic Geology, v. 105, p. 1057–1070.

Begg, G.C., Hronsky, J.A.M., Griffin, W.L., and O'Reilly, S.Y., 2018. Global- to deposit-scale controls on orthomagmatic Ni-Cu(-PGE) and PGE reef ore formation, in: Processes and Ore Deposits of Ultramafic-Mafic Magmas through Space and Time, (eds) S.K. Mondal and W.L. Griffin, Elsevier, p. 1-46, https://doi.org/10.1016/B978-0-12-811159-8.00002-0.

Benn, K., 2006. Tectonic delamination of the lower crust during Late Archean collision of the Abitibi-Opatica and Pontiac terranes, Superior Province, Canada; Geophysical Monograph Series, American Geophysical Union, v. 16, p. 267-282.

Benn, K. and Kamber, B.S., 2009. In situ U/Pb granulite-hosted zircon dates, Kapuskasing structural zone, Ontario: A late Archean large igneous province (LIP) as a substrate for juvenile crust; The Journal of Geology, v. 117, p. 519-541.

Benn, K. and Moyen, J.-F., 2008. The Late Archean Abitibi-Opatica terrane, Superior Province: A modified oceanic plateau; Geological Society of America Special Papers, v. 440, p.173–197.

Berthé, D., Choukroune, P., and Jegouzo, P., 1979. Orthogneiss, mylonite and non-coaxial deformation of granites: The example of the south Armorican shear zone; Journal of Structural Geology, v. 1, p. 31–42.

Bethell, E.M., 2016. Circumferential dyke swarms (image); 47th Lunar and Planetary Science Conference, https://pbs.twimg.com/media/CeUfSG1UAAAYBJB?format=jpg&name=medium

Bethell, E.M., Ernst, R.E, and Samson, C., 2019. Geological Map of the Alpha Regio (V-32) quadrangle, Venus; Journal of Maps, v. 1, p. 474-486, https://doi.org/10.1080/17445647.2019.1614489

Bethell, E.M., Ernst, R.E, Samson, C., and Buchan, K.L., 2017. Detailed mapping of graben-fissure systems associated with Fatua Corona, Venus: implications for magmatism and the regional stress field. Lunar and Planetary Science, v. XLVIII, https://www.hou.usra.edu/meetings/lpsc2017/pdf/2177.pdf.

Bierlein, F.P., Groves, D.I., Goldfarb, R.J., and Dubé, B., 2006. Lithospheric controls on the formation of provinces hosting giant orogenic gold deposits; Mineralium Deposita, v. 40, p.1432-1866.

Billings, S. and Richards, D., 2000. Quality control of gridded aeromagnetic data; Exploration Geophysics, v. 31, p. 611-616, https://doi.org/10.1071/EG00611.

Bjorkman, K.E., 2017. 4D crust-mantle evolution of the Western Superior Craton: implications for Archaean granite-greenstone petrogenesis and geodynamics. PhD thesis, The University of Western Australia, https://doi.org/10.4225/23/5a39c88a2f559.

Blakely, R.J., 1995. Potential theory in gravity and magnetic applications. Cambridge University Press, 464 p.

Boily, M., Leclair, A., Maurice, C., Bédard, J.H., and David, J., 2009. Paleo- to Mesoarchean basement recycling and terrane definition in the Northeastern Superior Province, Québec, Canada; Precambrian Research, v. 168, p. 23-44.

Boland, A.V., 1989. A geophysical analysis of the Kapuskasing Structural Zone. PhD thesis, University of British Columbia, https://open.library.ubc.ca/cIRcle/collections/ubctheses/831/items/1.0052973.

Bourne, J.A. and Twidale, C.R., 2007. Crustal Structures and Mineral Deposits: E.S.T. O'Driscoll's Contribution to Mineral Exploration. Rosenberg Publishing, Australia.

Breiman, L., 1996. Bagging predictors; Machine Learning, v. 24, p. 123-140, https://doi.org/10.1007/BF00058655.

Breiman, L., 2001. Random Forests; Machine Learning, v. 45, p. 5-32.

Breiman, L., Friedman, J., Stone, C.J., and Olshen, R.A., 1984. Classification and regression trees; CRC press, 368 p.

Buchan, K.L. and Ernst, R.E., 2016. Giant circumferential dyke swarms on Earth as possible analogues of coronae on Venus; 47th Lunar and Planetary Science Conference, https://www.hou.usra.edu/meetings/lpsc2016/pdf/1183.pdf

Buchan, K.L. and Ernst, R.E., 2018. Giant circumferential dyke swarms, Catalogue and characteristics; in Dyke Swarms of the World: A Modern Perspective, Springer, p. 1-44.

Bürgmann, R. and Dresen, G., 2008. Rheology of the lower crust and upper mantle: evidence from rock mechanics, geodesy, and field observations; Annual Review of Earth and Planetary Sciences, v. 36, p. 531–567, https://doi.org/10.1146/annurev.earth.36.031207.124326.

Burnside, R.I. and Associates Limited, 2005. Supplementary report on multi-criteria analysis, Big Trout Lake exploration property, District of Kenora, Ontario, NTS 53H/12. http://www.geologyontario.mndm.gov.on.ca/mndmfiles/afri/data/imaging/20000000256/20001048.pdf

Burov, E.B. and Watts, A.B., 2006. The long-term strength of continental lithosphere: "jelly sandwich" or "crème brûlée"?; GSA Today, v. 16, p. 4-10.

Cagnard, F., Durrieu, N., Gapais, D., Brun, J.-P., and Ehlers C., 2006. Convergence tectonics within weak lithospheres: a working hypothesis with particular reference to Precambrian times; Terra Nova, v. 18, p. 72–78.

Calignano, E., Sokoutis, D., Willingshofer, E., Gueydan, F., and Cloetingh, S., 2015. Strain localization at the margins of strong lithospheric domains: Insights from analog models; Tectonics, v. 34, p. 396–412.

Calvert, A.J., Cruden, A.R., and Hynes, A., 2004. Seismic evidence for preservation of the Archean Uchi granite–greenstone belt by crustal-scale extension; Tectonophysics, v. 388, p. 135–143.

Camp, V.E. and Hanan, B.B., 2008. A plume-triggered delamination origin for the Columbia River Basalt Group; Geosphere, v. 4, p. 480–495.

Cande, S.C. and Stegman, D.R., 2011. Indian and African plate motions driven by the push force of the Réunion plume head. Nature, 475, 47–52.

Card, K.D., 1990. A review of the Superior Province of the Canadian Shield, a product of Archean accretion; Precambrian Research, v. 48, p. 99-156.

Carranza, E.J.M. and Laborte, A.G., 2015. Data-driven predictive mapping of gold prospectivity, Baguio district, Philippines: Application of random forests algorithm; Ore Geology Reviews, v. 71, p. 777-787, https://doi.org/10.1016/j.oregeorev.2014.08.010.

Chang, S.-J. and Van der Lee, S. 2011. Mantle plumes and associated flow beneath Arabia and East Africa; Earth and Planetary Science Letters, v. 302, p. 448–454.

Chardon, D., Gapais, D., and Cagnard, F., 2009. Flow of ultra-hot orogens: a view from the Precambrian, clues for the Phanerozoic; Tectonophysics, v. 477, p. 105–118.

Chen, T., 2014. Introduction to Boosted Trees. University of Washington Computer Science & Engineering.

Chen, T. and Guestrin, C., 2016. XGBoost: A scalable tree boosting system; Proceedings of the 22nd ACM SIGKDD International Conference on Knowledge Discovery and Data Mining: San Francisco, California, USA, Association for Computing Machinery, p. 785–794, https://doi.org/10.1145/2939672.2939785.

Chopping, R. and Kennett, B.L.N., 2015. Maximum depth of magnetisation of Australia, its uncertainty, and implications for Curie depth; Geophysical Research Journal, v. 7, p. 70-77.

Cleven, N.R., 2017. Application of gravity and pseudo-gravity geophysical treatments to structural targeting in the Eeyou Istchee Baie-James region, Québec Superior Province: Preliminary interpretations; MB 2017-14, Ministère de l'Énergie et des Ressources naturelles, Québec.

Cleven, N.R., Harris, L.B., and Guilmette, C., 2020a. Structural interpretation of enhanced high-resolution aeromagnetic depth slices of the Eeyou Istchee James Bay region, Québec Superior Province; Ministère de l'Énergie et des Ressources naturelles, Québec, MB 2020-02, 82 p.

Cleven, N.R., Harris, L.B., Guilmette, C., and Davis, D., 2020b. Timing of crustal deformation in Archean rocks along the northern boundary of the Opinaca and La Grande subprovinces, Eeyou Istchee Baie-James region, Québec Superior Province; Ministère de l'Énergie et des Ressources naturelles, Québec, MB 2020-03, 52p.

Cleven, N.R., Guilmette, C., Davis, D.W, and Côté-Roberge, M., 2020c. Geodynamic significance of Neoarchean metasedimentary belts in the Superior Province: detrital zircon U-Pb LA-ICP-MS geochronology of the Opinaca and La Grande subprovinces; Precambrian Research, v. 347, 105819, https://doi.org/10.1016/j.precamres.2020.105819.

Clowes, R.M., Calvert, A.C, Eaton, D.W., Hajnal, Z., Hall, J., and Ross, G.M., 1996. LITHOPROBE reflection studies of Archean and Proterozoic crust in Canada; Tectonophysics, v. 264, p. 65-88.

Colvine, A.C., Fyon, J.A., Heather, K.K., Soussan Marmont, P.M., Smith, P.M., and Troop, D.G., 1988. Archean lode gold deposits in Ontario; Ontario Geological Survey Miscellaneous Paper, v. 139, 136 pp.

Condie, K.C., and Benn, K., 2013. Archean geodynamics: similar to or different from modern geodynamics? American Geophysical Union (AGU), p. 47–59, https://doi.org/10.1029/164GM05.

Connors, K., Stolz, E. and Hanneson, J.E., 2002. Early fault architecture at St. Ives: Implications for Au and Ni mineralisation, in: Applied structural geology for mineral exploration and mining, (ed.) S. Vearncombe; Australian Institute of Geoscientists, 29–31.

Cooper, G.R.J. and Cowan, D.R., 2006. Enhancing potential field data using filters based on the local phase, Computers & Geosciences, v. 32, p. 1585–1591, https://doi.org/10.1016/j.cageo.2006.02.016.

Corfu, F., Stott, G.M., and Breaks, F.W., 1995. U-Pb geochronology and evolution of the English River Subprovince, an Archean low P-high T metasedimentary belt in the Superior Province; Tectonics, v. 14, p. 1220-1233, https://doi.org/10.1029/95TC01452.

Côté-Roberge, M., 2018. Contexte tectonométamorphique du nord-ouest du Complexe de Laguiche, sous-province d'Opinaca, Eeyou Itschee Baie-James; MSc thesis, Université Laval, http://hdl.handle.net/20.500.11794/34575.

Cowan, D.R. and Cowan, S., 1993. Separation filtering applied to aeromagnetic data; Exploration Geophysics, v. 24, p. 429-436.

Darbyshire, F.A., Eaton, D.W., Frederiksen, A.W., and Ertolahti, L., 2007. New insights into the lithosphere beneath the Superior Province from Rayleigh wave dispersion and receiver function analysis; Geophysical Journal International, v. 169, p. 1043–1068.

David, J., Simard, M., Bandyayera, D., Goutier, J., Hammouche, H., Pilote, P., Leclerc, F., and Dion, C., 2012. Datations U-Pb effectuées dans les provinces du Supérieur et de Churchill en 2010-2011. Ministère des Ressources naturelles et de la Faune, Québec, RP 2012-01, pp. 33.

Davis, W.J., Jones, A.G., Bleeker, W., and Grütter, H., 2003. Lithosphere development in the Slave craton: a linked crustal and mantle perspective; Lithos, v. 71, p. 575-589.

Davis, D.W., Pezzutto, F., and Ojakangas, R.W., 1990. The age and provenance of metasedimentary rocks in the Quetico Subprovince, Ontario, from single zircon analyses: implications for Archean sedimentation and tectonics in the Superior Province; Earth and Planetary Science Letters, v. 99, p. 195-205.

Dentith, M., 2019. Geophysical responses from orogenic gold mineral systems; Acta Geologica Sinica, v. 93, p. 239-240.

Dentith, M., Evans, S., Thiel, S., Gallardo, L., Joly, A. and Romano, S.S., 2013. A magnetotelluric traverse across the southern Yilgarn Craton; Geological Survey of Western Australia, Report 121, 43 p.

Dentith, M. and Mudge, S.T., 2014. Geophysics for the Mineral Exploration Geoscientist. Cambridge University Press.

Diener, J.F.A. and Fagereng, Å.,2014. The influence of melting and melt drainage on crustal rheology during orogenesis, Journal of Geophysical Research Solid Earth, v. 119, p. 6193–6210, https://doi.org/10.1002/2014JB011088.

Drummond, B.J., Hobbs, B.E., and Goleby, B.R., 2004. The role of crustal fluids in the tectonic evolution of the Eastern Goldfields Province of the Archaean Yilgarn Craton, Western Australia; Earth Planets Space, v. 56, p. 1163–1169.

Dufréchou, G. and Harris, L.B., 2013. Tectonic models for the origin of regional transverse structures in the Grenville Province of SW Quebec interpreted from regional gravity; Journal of Geodynamics, v. 64, p. 15– 39.

Eisenlohr, B., Groves, D.I., and Partington, G.A., 1989. Crustal-scale shear zones and their significance to Archaean gold mineralization in Western Australia; Mineralium Deposita, v. 24, p.1-8.

Ernst, R.E. and Bleeker, W., 2010. Large igneous provinces (LIPs), giant dyke swarms, and mantle plumes: significance for breakup event within Canada and adjacent regions from |2.5 Ga to the present; Canadian Journal of Earth Sciences, v. 47, |p. 695–739.

Ernst, R.E. and Desnoyers, D.W., 2004 Lessons from Venus for understanding mantle plumes on Earth; Physics of the Earth and Planetary Interiors, v. 146, p. 195–229.

Faure, S., Godey, S., Fallara, F., and Trépanier, S., 2011. Seismic architecture of the Archean North American mantle and its relationship to diamondiferous kimberlite fields; Economic Geology, v. 106, p. 223–240.

Favorskaya, M.A. and Vinogradov, N.V., 1991. Geological evolution of ore-concentrating lineaments; Global Tectonics and Metallogeny, v. 4, p. 75-84.

Fayol, N., 2016. Les minéralisations aurifères associées aux intrusions alcalines néoarchéennes de la sous-province de l'Abitibi, Canada : exemple de la mine d'or Lac Bachelor, Abitibi : modèle génétique et guides d'exploration; PhD thesis, UQÀM, Québec, https://archipel.uqam.ca/8819/.

Fayol, N. and Jébrak, M., 2017. Archean sanukitoid gold porphyry deposits: A new understanding and genetic model from the Lac Bachelor gold deposit, Abitibi, Canada; Economic Geology, v. 112, p. 1913-1936.

Fischer, R., 2016. From early Earth plume-lid tectonics to present-day plate tectonics: A high-resolution 3D numerical modelling approach. PhD thesis, ETH Zürich, No. 2337, https://science.egoat.ch/publications/FischerPhDThesis.pdf.

Fischer, R. and Gerya, T., 2016. Early Earth plume-lid tectonics: A high-resolution 3D numerical modelling approach; Journal of Geodynamics, v. 100, https://doi.org/10.1016/j.jog.2016.03.004.

Fishwick, S. and Rawlinson, N., 2012. 3-D structure of the Australian lithosphere from evolving seismic datasets; Australian Journal of Earth Sciences, v. 59, p. 809-826, https://doi.org/10.1080/08120099.2012.702319.

Flament, N., Coltice, N., and Rey, P.F., 2008. A case for late-Archaean continental emergence from thermal evolution models and hypsometry; Earth and Planetary Science Letters, v. 275, p. 326–336.

Fossen, H. and Cavalcante, G.C.G., 2017. Shear zones – a review; Earth-Science Reviews, v. 171, p. 434-455.

Frederiksen, A.W., Miong, S.-K., Darbyshire, F.A., Eaton, D.W., Rondenay, S., and Sol, S., 2007. Lithospheric variations across the Superior Province, Ontario, Canada: Evidence from tomography and shear wave splitting: Journal of Geophysical Research, v. 112, B07318, https://doi.org/10.1029/2006JB004861

Friedman, J.H., 2001. Greedy function approximation: A gradient boosting machine; Annals of Statistics, v. 29, p. 1189-1232.

Gagnon, É., Schneider, D.A., Kalbfleisch, T., Habler, G., and Biczok, J., 2016. Characterization of transpressive deformation in shear zones of the Archean North Caribou greenstone belt (NW Superior Province) and the relationship with regional metamorphism. Tectonophysics, v. 693, p. 261-276.

Gaboury, D., 2019. Parameters for the formation of orogenic gold deposits; Applied Earth Science, Transactions of the Institutions of Mining and Metallurgy, v. 128, p. 124-133, https://doi.org/10.1080/25726838.2019.1583310.

Galántai, A., 2000. The theory of Newton's method; Journal of Computational and Applied Mathematics, v. 124, Issues, p. 25-44.

Galkin, V., 2015. Complex structural study of the West Red Lake area northwestern Ontario, Canada; https://www.slideshare.net/VadimGalkine/structural-study-of-the-west-red-lake-area-53747535.

Gapais, D., 2018. Tectonics-mineralisation relationships within weak continental lithospheres: a new structural framework for Precambrian cratons; BSGF - Earth Sciences Bulletin, v. 189, 14p., https://doi.org/10.1051/bsgf/2018014.

Gapais, D., Jaguin, J., Cagnard, F., and Boulvais, P., 2014. Pop-down tectonics, fluid channelling and ore deposits within ancient hot orogens; Tectonophysics, v. 618, p. 102–106.

Geosoft, 2015. Calculating the energy spectrum in MAGMAP; MAGMAP filtering how-to guide, http://updates.geosoft.com/downloads/files/how-to-guides/Calculating_the_Energy_Spectrum_in_MAGMAP.pdf

Gerya, T.V., 2014a. Plume-induced crustal convection: 3D thermomechanical model and implications for the origin of novae and coronae on Venus; Earth and Planetary Science Letters, v. 391, p. 183–192.

Gerya, T.V., 2014b. Precambrian geodynamics: Concepts and models; Gondwana Research, v. 25, p. 442–463.

Gintov, O.B., 1973, Ring structures in the Precambrian of the Ukraine; Geotectonics, v. 7, p. 288-292.

Glen, J.M.G. and Ponce, D.A., 2002a. Large-scale fractures related to inception of the Yellowstone hotspot; Geology, v. 30, p. 647–650.

Glen, J.M.G. and Ponce, D.A., 2002b. Relationship of epithermal gold deposits to large-scale fractures in northern Nevada; Economic Geology, v. 97, p. 3–9.

Godey S., Deschamps, F., Trampert, J., and Snieder, R., 2004. Thermal and compositional anomalies beneath the North American continent; Journal of Geophysical Research, v. 109, B01308, https://doi.org/10.1029/2002JB002263.

Godey, S., Snieder, R., Villasenor, A., and Benz, H.M., 2003. Surface wave tomography of North America and the Caribbean using global and regional broad-band networks: phase velocity maps and limitations of ray theory; Geophysical Journal International, v. 152, p. 620–632.

Göğüş O.H. and Pysklywec, R.N., 2008. Near-surface diagnostics of dripping or delaminating lithosphere; Journal of Geophysical Research: Solid Earth, v. 113, https://doi.org/10.1029/2007JB005123.

Göğüş O.H., Pysklywec, R.N., Şengör, A.M.C., and Gün, E., 2017. Drip tectonics and the enigmatic uplift of the Central Anatolian Plateau; Nature Communications, https://doi.org/10.1038/s41467-017-01611-3.

Griffin, W.L., Begg, G.C., and O'Reilly, S.Y., 2013. Continental-root control on the genesis of magmatic ore deposits; Nature Geoscience, v. 6, p. 905–910.

Grindrod, P.M. and Hoogenboom, T., 2006. Venus: The corona conundrum; Astronomy and Geophysics, v. 47, p. 3.16–3.21, https://doi.org/10.1111/j.1468-4004.2006.47316.x.

Groves, D.I., 1993. The crustal continuum model for late-Archaean lode-gold deposits of the Yilgarn Block, Western Australia; Mineralium Deposita, v. 28, p. 366-374.

Groves, D.I., Goldfarb, R.J., Knox-Robinson, C.M., Ojala, J., Gardoll, S., Yun, G.Y., and Holyland, P., 2000. Late-kinematic timing of orogenic gold deposits and significance for computer-based exploration techniques with emphasis on the Yilgarn Block, Western Australia; Ore Geology Reviews, v. 17, p. 1-38.

Groves, D.I. and Santosh, M., 2015. Province-scale commonalities of some world-class gold deposits: Implications for mineral exploration; Geoscience Frontiers, v. 6, p. 389-399.

Groves, D.I., et al., 2020. A holistic model for the origin of orogenic gold deposits and its implications for exploration; Mineralium Deposita, v. 55, p. 275–292.

Groves, D.I., Santosh, M., and Goldfarb, R.J., 2016. The conjunction of factors that lead to formation of giant gold provinces and deposits in non-arc settings; Geoscience Frontiers, v. 7, p. 303-314.

Groves, D.I., Santosh, M., Goldfarb, R.J., and Zhang, L., 2018. Structural geometry of orogenic gold deposits: Implications for exploration of world-class and giant deposits; Geoscience Frontiers, v. 9, p. 1163-1177.

Gueydan, F., Précigout, J., and Montési, L.G.J., 2014. Strain weakening enables continental plate tectonics; Tectonophysics, v. 631, p. 189–196.

Guillou-Frottier, L., Burov, E., Cloetingh, S., Le Goff, E., Deschamps, Y., Huet, B., and Bouchot, V., 2012. Plume-induced dynamic instabilities near cratonic blocks: Implications for P-T-t paths and metallogeny; Global and Planetary Change, v. 90-91, p. 37-50, https://doi.org/10.1016/j.gloplacha.2011.10.007.

Gouiza, M. and Paton, D., 2019. The role of inherited lithospheric heterogeneities in defining the crustal architecture of rifted margins and the magmatic budget during continental breakup; Geochemistry Geophysics Geosystems, https://doi.org/10.1029/2018GC007808.

Guillou, L., Mareschal, J.-C., Jaupart, C., Gariépy, C., Bienfait, G., and Lapointe, R., 1994. Heat flow, gravity and structure of the Abitibi belt, Superior Province, Canada: Implications for mantle heat flow; Earth and Planetary Science Letters, v. 122, p. 103-123.

Gulson, B.L., Mizon, K.J., and Atkinson, B.T., 2011. Source and timing of gold and other mineralization in the Red Lake area, northwestern Ontario, based on lead-isotope investigations; Canadian Journal of Earth Sciences, v. 30, p. 2366-2379, https://doi.org/10.1139/e93-205.

Halls, H.C., Davis, D.W., Stott, G.M., Ernst, R.E., and Hamilton, M.A., 2008. The Paleoproterozoic Marathon Large Igneous Province: new evidence for a 2.1 Ga long-lived mantle plume event along the southern margin of the North American Superior Province; Precambrian Research, v. 162, p. 327-353.

Halls, H.C. and Zhang, B., 1998. Uplift structure of the southern Kapuskasing zone from 2.45 Ga dike swarm displacement; Geology, v. 26; p. 67–70.

Hamilton, T., undated. Perception; How your mind understands sensory information, https://slideplayer.com/slide/8090597/.

Harris, J.R., Sanborn-Barrie, M., Panagapko, D.A., Skulski, T., and Parker, J.R., 2006. Gold prospectivity maps of the Red Lake greenstone belt: application of GIS technology; Canadian Journal of Earth Sciences, v. 43, p. 865–893.

Harris, L.B., 2009. Basement controls on mineralization in the New Quebec Orogen and the Voisey's Bay Deposit, Canada; *in*: 10th Biennial SGA Meeting of The Society for Geology Applied to Mineral Deposits, (ed.) P.J. Williams et al.; Smart science for exploration and mining, v. 2, p. 818-820.

Harris, L.B., 2017a. Deep structures in the Pilbara Craton and their relationship to overlying deformation, mineralization and kimberlite emplacement; *in*: SGTSG Denmark 2017 Abstract Volume, Biennial Meeting of the Specialist Group in Tectonics and Structural Geology, Geological Society of Australia, (compiler): M.A. Pearce; Geological Survey of Western Australia, Record 2017/17, p. 51.

Harris, L.B., 2017b. Controls of "proto-craton" boundaries and deep faults on the intrusion of mafic-ultramafic complexes hosting Ni-PGE-Cr mineralisation, Kaapvaal and Superior cratons; Mineral Resources to Discover - 14th SGA Biennial Meeting 2017, Volume 2, p. 459-462.

Harris, L.B. and Bédard, J.H., 2014a, Crustal evolution and deformation in a non-plate-tectonic Archaean Earth: Comparisons with Venus; *in*: Evolution of Archean crust and early life, (eds) Y. Dilek and H. Furnes; Modern Approaches in Solid Earth Sciences, v. 7, p. 215–291, https://doi.org/10.1007/978-94-007-7615-9_9.

Harris, L.B. and Bédard, J.H., 2014b, Interactions between continent-like 'drift', rifting, and mantle flow on Venus: Gravity interpretations and Earth analogues; *in*: Volcanism and tectonism across the inner solar system, (eds) T. Platz, T., et al.; Geological Society of London Special Publication, v. 401, p. 327-356, https://doi.org/10.1144/SP401.9.

Harris, L.B. and Bédard, J.H., 2015. Implications from geophysical data for the structural and tectonic evolution of the Superior and Yilgarn cratons, AGU-GAC-MAC-CGU Joint Assembly, Montréal, Paper/35640.

Harris, L.B., Byrne, D.R., Wetherly, S., and Beeson, J., 2004. Analogue modelling of structures developed above single and multiple mantle plumes: applications to brittle crustal deformation on Earth and Venus; *in*: GeoMod 2004 - From mountains to sedimentary basins: modelling and testing geological processes, (eds) G. Bertotti, S. Buiter, P. Ruffo, and G. Schreurs, Bolletino di Geofiscia teorica ed applicata; v. 45, Supp. 1, p. 301-303.

Harris L.B., Cleven N., and Guilmette C., 2018a. Deep crustal to SCLM controls on Ni-PGE-Cr and Au mineralisation, northern Superior Province, Canada. Australian Geoscience Council Convention (AGCC) 2018 - Big Issues & Ideas in Geoscience, Adelaide, Australia. Abstract Volume, p. 744.

Harris L.B., Cleven N., and Guilmette C., 2018b. Deep lithological domains, structures, and reconstructions for the eastern Superior Province, Canada: implications for mineral exploration and tectonic models. Australian Geoscience Council Convention (AGCC) 2018 - Big Issues & Ideas in Geoscience, Adelaide, Australia. Abstract Volume, p. 769.

Harris L.B., Cleven N., and Guilmette C., 2018c. Deep lithological domains, structures & reconstructions, Quebec Superior Province: implications for mineral exploration and tectonic models. Abstract Volume, Québec Mines.

Harris L.B., Cleven N., and Guilmette C., 2018d. Implications of a 'millefeuille' lithospheric strength model for mineral exploration in Archean terrains; in: CTG 2018 Program with Abstracts, (eds) A. Tremblay, D. Corrigan, and M. Perrot; p.15, https://tinyurl.com/y2dy6wcf.

Harris L.B. and Lu, Y-J., 2018. Deep structures in the Pilbara Craton, WA, and their relationship to overlying deformation, mineralisation and kimberlite emplacement. Australian Geoscience Council Convention (AGCC) 2018 - Big Issues & Ideas in Geoscience, Adelaide, Australia, Abstract Volume, p. 745.

Harris, L.B. and Moyen, J.-F., 2017. Lithospheric, 'proto-craton' controls on the intrusion of the Bushveld Complex and diamondiferous kimberlites, South Africa, *in*: Target 2017, Perth, Australia, (eds) S. Wyche and W.K. Witt, Geological Survey of Western Australia Record, v. 2017/6, p. 54-55.

Heinson, G., Didana, Y., Soeffky, P., Thiel, S., and Wise, T., 2018. The crustal geophysical signature of a world-class magmatic mineral system; Scientific Reports, v.8, 10608, https://www.nature.com/articles/s41598-018-29016-2.

Heaman, L.M., Böhm, Ch.O., Corkery, M.T., and Creaser, R.A.,1999. Re-examining the northwest Superior Province margin; Manitoba Energy and Mines, Geological Services, Open File Report OF99-11, 6 p.

Heather, K.B., Percival, J.A., Moser, D., and Bleeker, W., 1995. Tectonics and metallogeny of Archean crust in the Abitibi - Kapuskasing - Wawa region. Field Trip Guidebook, Geological Survey of Canada Open File, v. 3141.

Hendrickson, M.D., 2016. Structural analysis of aeromagnetic data from the Rainy River Block,Wabigoon subprovince, Minnesota, USA and Ontario, Canada: Strain partitioning along a Neoarchean terrane boundary and implications for mineral exploration; Precambrian Research, v. 286, 20-34.

Heron, P.J., Pysklywec, R.N., and Stephenson, R., 2016. Identifying mantle lithosphere inheritance in controlling intraplate orogenesis; Journal of Geophysical Research Solid Earth, v. 121, 6966–6987, https://doi.org/10.1002/2016JB013460.

Hildenbrand, T.G., Berger, B., Jachens, R.C., and Ludington, S., 2000. Regional crustal structures and their relationship to the distribution of ore deposits in the western United States, based on magnetic and gravity data; Economic Geology, v. 95, p. 1583-1603.

Hill, G., et al., 2020. Lateral crustal flow along discrete flat-lying lower crustal shear zones during Archean continent construction; 22nd EGU General Assembly, id.7051, https://ui.adsabs.harvard.edu/abs/2020EGUGA..22.7051H/abstract.

Holden, D., Archibald, N.J., Boschetti, F., and Jessell, M.W., 2000. Inferring geological structures using wavelet-based multiscale edge analysis and forward models; Exploration Geophysics, v. 31, p. 617-621.

Houlé, M.G., Lesher, C.M., McNicoll, V.J., Metsaranta, R.T., Sappin, A.-A., Goutier, J., Bécu, V., Gilbert, H.P., and Yang, X.M., 2015. Temporal and spatial distribution of magmatic Cr-(PGE), Ni-Cu-(PGE), and Fe-Ti-(V) deposits in the Bird River–Uchi–Oxford-Stull–La Grande Rivière–Eastmain domains: a new metallogenic province within the Superior Craton; *in*: Targeted Geoscience Initiative 4: Canadian Nickel-Copper-Platinum Group Elements-Chromium Ore Systems — Fertility, Pathfinders, New and Revised Models, (eds) D.E. Ames and M.G. Houlé; Geological Survey of Canada, Open File 7856, p. 35–48.

Houlé, M.G., Lesher, C.M., Metsaranta, R.T., Sappin, A.-A., 2019. Architecture of magmatic conduits in chromium-PGE and Ni-Cu-PGE ore systems in Superior Province: example from the 'Ring of Fire' region, Ontario, *in*: Targeted Geoscience Initiative: 2018 report of activities; (ed.) N. Rogers, Geological Survey of Canada, Open File, v. 8549, p. 441-448, https://doi.org/10.4095/313678.

Hronsky, J.M.A., 2011. Self-organized critical systems and ore formation: The key to spatial targeting?; Society of Economic Geologists Newsletter, v. 84, https://www.segweb.org/pdf/views/2011/01/SEG-Newsletter-Views-Jon-Hronsky.pdf.

Hronsky, J.M.A., 2013. Understanding major trans-lithospheric structures, their evolution and relationship to ore deposits; Presentation, CCFS Lithosphere Dynamics Workshop, Perth, WA, http://ccfs.mq.edu.au/Workshops/PDF/Hronsky.pdf.

Hronsky, J.M.A., 2020. Deposit-scale structural controls on orogenic gold deposits: an integrated, physical process–based hypothesis and practical targeting implications; Mineralium Deposita, v. 55, p. 197–216, https://doi.org/10.1007/s00126-019-00918-z.

Hronsky, J.M.A. and Groves, D.I., 2008. Science of targeting: definition, strategies, targeting and performance measurement; Australian Journal of Earth Sciences, v. 55, 3-12.

Hudleston P.J. and Bauer R.L., 1995. Kinematics of shear zones in the southern Superior Province; in: Basement Tectonics 10, (eds) R.W. Ojakangas, A.B. Dickas, J.C. Green; Proceedings of the International Conferences on Basement Tectonics, v 4, Springer, Dordrecht, p. 359-366.

Isles, D.J. and Rankin, L.R., 2013. Geological interpretation of aeromagnetic data; Australian Society of Exploration Geophysicists, https://www.aseg.org.au/publications/geological-interpretation-aeromagnetic-data.

Jemielita, R.A., Davis, D.W., and Krogh, T.E., 1990. U-Pb evidence for Abitibi gold mineralization postdating greenstone magmatism and metamorphism; Nature. 346:831–834, https://doi.org/10.1038/346831a0.

Johnson, T.E., Brown, M., Kaus, B.J.P., and VanTongeren, J.A., 2014. Delamination and recycling of Archaean crust caused by gravitational instabilities; Nature Geoscience, v. 7, p. 47–52.

Kalberg, T., Gohl, K., Eagles, G., and Spiegel, C., 2015. Rift processes and crustal structure of the Amundsen Sea Embayment, West Antarctica, from 3D potential field modelling; Marine Geophysical Research, 17pp., https://doi.org/10.1007/s11001-015-9261-0.

Keating, P., Dubé, B., and Lacroix, S., 2010. Use of high-resolution geophysical data to help mineral exploration and geological mapping in the Abitibi Greenstone Belt; TGI-3 Workshop: Public geoscience in support of base metal exploration programme and abstracts. Geological Association of Canada, Cordilleran Section, p. 19-22.

Kerrich R. and Cassidy K.F. 1994. Temporal relationships of lode gold mineralization to accretion, magmatism, metamorphism and deformation - Archean to present: A review; Ore Geology Reviews, v. 9, p. 263–310, https://doi.org/10.1016/0169-1368(94)90001-9.

Kohavi, R. and Wolpert, D.H., 1996. Bias plus variance decomposition for zero-one loss functions; in: ICML'96: Proceedings of the thirteenth international conference on machine learning, (ed) L. Saitta, Morgan Kaufmann Publishers Inc., p. 275-283.

Konstantinov, M.M., Cherkasov, S.V., Dankovtsev, R.F., and Egorkin, A.V., 1999. Specific crustal features of large and superlarge endogenic gold deposits (Siberia and Far East regions); Global Tectonics and Metallogeny, v. 7, p. 143 - 147.

Koptev, A., Burov, E., Calais, E., Leroy, S., Gerya, T., Guillou-Frottier, L., and Cloetingh, S., 2016. Contrasted continental rifting via plume-craton interaction: Applications to Central East African Rift; Geoscience Frontiers, v. 7, p. 221-236.

Krassilnikov, A.S., 2002. Tectonics and evolution of novae and coronae on Venus: tectonophysical modeling based on gravitational models; Solar System Research, v. 36, p. 293–321.

Krasilnikov, A.S., Galkin, V.A., and Basilevsky A.T., 2001. Tectonics and evolution of coronae on Venus: preliminary results of tectonophysical modeling; Solar System Research, v. 35, p.103–116.

Krassilnikov, A.S., Kostama, V.-P., Aittola, M., Guseva, E.N., and Cherkashina, O.S., 2012. Relationship of coronae, regional plains and rift zones on Venus; Planetary and Space Science, v. 68, p. 56–75, https://doi.org/10.1016/j.pss.2011.11.017.

Kutinia, J., Pei, R., and Heyl, A.V., 2003. The role of deep lithospheric structure in the genesis and distribution of giant and supergiant concentrations of metals in the crust; Global Tectonics and Metallogeny, v. 8, 9-49.

Kuzmich, B.N., 2009. Petrogenesis of the ferrogabbroic intrusions and associated Fe-Ti-V-P mineralization within the McFaulds Greenstone belt, Superior Province, Canada. MSc thesis, Lakehead University, https://knowledgecommons.lakeheadu.ca/handle/2453/768

Laarman, J.E., 2014. A detailed metallogenic study of the McFaulds Lake chromite deposits, northern Ontario. PhD thesis, University of Western Ontario, Electronic Thesis and Dissertation Repository 1966, https://ir.lib.uwo.ca/etd/1966.

Lambert, A., 2018. The hunt for phi structures; European Geologist Journal, v. 45, p. 6-11.

Laudadio, A.B., Schetselaar, E., Houlé, M.G., and Samson, C., 2018. 3D geological modelling of the Double Eagle–Black Thor intrusive complexes, McFaulds Lake greenstone belt, Ontario; *in* Targeted Geoscience Initiative: 2017 report of activities, volume 2, (ed.) N. Rogers; Geological Survey of Canada, Open File 8373, p. 35–41.

Leclerc, F., Harris, L.B., Bédard, J.H., van Breemen, O., and Goulet, N., 2012. Structural and stratigraphic controls on magmatic, volcanogenic, and syn-tectonic mineralization in the Chapais-Chibougamau Mining Camp, northeastern Abitibi, Canada; Economic Geology, v. 107, p. 963–989, https://doi.org/10.2113/econgeo.107.5.963.

Li, D., Hollings, P., Chen, H., Sun, X., Tan, C., and Zurevinski, S., 2020. Zircon U–Pb and Lu–Hf systematics of the major terranes of the Western Superior Craton, Canada: Mantle-crust interaction and mechanism(s) of craton formation; Gondwana Research, v. 78, p. 261-277.

Lister, G.S. and Snoke, A.W., 1984. S-C Mylonites; Journal of Structural Geology, v. 6, p. 617-638, https://doi.org/10.1016/0191-8141(84)90001-4.

Likkason, O.K., 2011. Spectral analysis of geophysical data, advances in data, methods, models and their applications in geoscience, (ed.) D.M. Chen, ISBN: 978-953-307-737-6, InTech, http://www.intechopen.com/books/advances-in-data-methods-models-and-their-applications-in-geoscience/spectral-analysis-of-geophysical-data.

Lithgow-Bertelloni, C. and Silver, P. G. 1998. Dynamic topography, plate driving forces and the African superswell; Nature, v. 395, p. 269–272.

Lopez, I., Marquez, A., and Oyarzun, R.,1999. Are coronae restricted to Venus?: Corona-like tectonovolcanic structures on Earth; Earth Moon Planets, v. 77, p.125–137.

Lulin, J.-M., 2016. Country-Scale Target Generation using Big Data, presentation, PDAC Convention, http://azimut-exploration.com/mining_documents/AZIMUT_PDAC_BIG%20DATA_2016_EN-p.pdf

Lulin, J.-M., Bissonnette, F., Delpech, E., Fortin, J., Pelletier, P.-A., Philippin, M., and Wülser, P.A., 2012. The Rex Trend: A new mineral province in northern Québec, http://azimut-exploration.com/en/presentations/AZM_the%20_rex_trend_sept_2012.pdf.

Maier, W.D. and Groves, D.I., 2011. Temporal and spatial controls on the formation of magmatic PGE and Ni–Cu deposits; Mineralium Deposita, v. 46, p. 841-857.

Manitoba Mineral Resources (MMR), 2013. Bedrock geology, Manitoba Map Gallery – Geoscientific Maps, Manitoba Mineral Resources, Government of Manitoba.

Mareschal, J.-C. and Jaupart, C., 2006. Archean thermal regime and stabilization of the cratons; Archean Geodynamics and Environments, Geophysical Monograph Series, American Geophysical Union, v. 16, p. 61-73.

Marone, F., van der Lee, S., and Giardini, D. 2004. Three-dimensional upper-mantle S-velocity model for the Eurasia–Africa plate boundary region; Geophysical Journal International, v. 158, p. 109–130.

Mattauer, M., 1974. Les déformations des matériaux de l'écorce terrestre. Hermann, 493 p.

McCuaig, T.C. and Hronsky, J.M.A., 2014. The mineral system concept: The key to exploration targeting, in: Building Exploration Capability for the 21st Century, (eds) K.D. Kelley and H.C. Golden, Chapter 8, Society of Economic Geologists Special Publication, v. 18, p. 153–175, https://doi.org/10.5382/SP.18.08.

McGill, G.E., 2004. Geologic Map of the Bereghinya Planitia Quadrangle (V–8), Venus; Geologic Investigations Series I–2794, map and pamphlet, USGS.

McKenzie, D., McKenzie, J.M., and Saunders, R.S. 1992. Dike emplacement on Venus and on Earth; Journal of Geophysical Research, v. 97E, 15977-915990.

Melnyk, M., Davis, D., Cruden, A., and Stern, R., 2006. U-Pb ages of magmatism constraining regional deformation in the Winnipeg River Subprovince and Lake of the Woods greenstone belt: evidence for Archean terrane accretion in the Western Superior Province; Canadian Journal of Earth Sciences, v. 43, p. 967–993.

Mercier-Langevin, P., Dubé, B., Hannington, M.D., Davis, D.W., Lafrance, B., and Gosselin, G., 2007. The LaRonde Penna Au-rich volcanogenic massive sulfide deposit, Abitibi Greenstone Belt, Quebec; Economic Geology, v. 102, p. 611–631.

Mériaux, C. and Lister, J.R., 2002. Calculation of dike trajectories from volcanic centers; Journal of Geophysical Research, v. 107, No. B4, 2077, https://doi.org/10.1029/2001JB000436.

Metsaranta, R.T. and Houlé, M.G., 2012. Progress on the McFaulds Lake ("Ring of Fire") region data compilation and bedrock geology mapping project, *in*: Summary of Field Work and Other Activities 2012; Ontario Geological Survey, Open File Report, v. 6280, p.43-1–43-12.

Metsaranta, R.T. and Houlé, M.G. 2020. Precambrian geology of the McFaulds Lake "Ring of Fire" region, northern Ontario; Ontario Geological Survey, Open File Report, v. 6359, 260 p.

Metsaranta, R.T., Houlé, M.G., McNicoll, V.J., and Kamo, S.L., 2015. Revised geological framework for the McFaulds Lake greenstone belt, Ontario, *in*: Targeted Geoscience Initiative 4: Canadian Nickel-Copper-Platinum Group Elements-Chromium Ore Systems — Fertility, Pathfinders, New and Revised Models, (ed.) D.E. Ames and M.G. Houlé; Geological Survey of Canada, Open File, v. 7856, p. 61–73.

Miller, J., Blewett, R., Tunjic, J., and Connors, K.A., 2010. The role of early formed structures on the development of the world class St Ives Goldfield, Yilgarn, WA; Precambrian Research, v. 183, p. 292-315., https://doi.org/10.1016/j.precamres.2010.08.002

Mints, M.V., 2017. The composite North American Craton, Superior Province: Deep crustal structure and mantle-plume model of Neoarchaean evolution; Precambrian Research, v. 302, p. 94-121.

Mole, D.R. et al., 2012. Spatio-temporal constraints on lithospheric development in the southwest—central Yilgarn Craton, Western Australia; Australian Journal of Earth Sciences, v. 59, p. 625–656.

Mole, D.R., et al., 2013. Crustal evolution, intra-cratonic architecture and the metallogeny of an Archaean craton, *in*: Ore Deposits in an Evolving Earth, (eds) G.R.T. Jenkin, P.A.J. Lusty, I. McDonald, M.P. Smith, A.J. Boyce, and J.J. Wilkinson; Geological Society, London, Special Publications, v. 393, http://dx.doi.org/10.1144/SP393.8.

Moore, W.B. and Webb, A.A.G., 2013. Heat-pipe Earth; Nature, v. 501, p. 501-505, https://doi.org/10.1038/nature12473.

Moser, D.E., Heaman, L.M., Krogh, T.E., and Hanes, J.A., 1996. Intracrustal extension of an Archean orogen revealed using single-grain U-Pb zircon geochronology; Tectonics, v. 15, p. 1093-1109.

Musacchio, G., White, D.J., Asudeh, I., and Thomson, C.J., 2004. Lithospheric structure and composition of the Archean western Superior Province from seismic refraction/wide-angle reflection and gravity modeling; Journal of Geophysical Research, v. 109, B03304, https://doi.org/10.1029/2003JB002427.

Mouthereau, F., Lacombe, O., and Vergés, J., 2012. Building the Zagros collisional orogen: Timing, strain distribution and the dynamics of Arabia/Eurasia plate convergence; Tectonophysics, v. 532–535, p. 27-60.

Naghizadeh, M., et al., 2019. Acquisition and processing of wider bandwidth seismic data in crystalline crust: Progress with the Metal Earth project; Minerals, v. 9, 145, https://doi.org/10.3390/min9030145.

Naidu, P.S. and Mathew, M.P., 1998a. Chapter 3: Power spectrum and its applications, in: Analysis of Geophysical Potential Fields, Advances in Exploration Geophysics, v. 5, p. 75-143, https://doi.org/10.1016/S0921-9366(98)80004-2.

Naidu, P.S. and Mathew, M.P., 1998b. Chapter 4: Digital filtering of maps, in: Analysis of Geophysical Potential Fields, Advances in Exploration Geophysics, v. 5, p. 145-221, https://doi.org/10.1016/S0921-9366(98)80005-4.

Natekin, A. and Knoll, A., 2013. Gradient boosting machines, a tutorial; Frontiers in Neurorobotics, https://doi.org/10.3389/fnbot.2013.00021.

Nijman, W., Kloppenburg, A., and de Vries, S.T., 2017. Archaean basin margin geology and crustal evolution: an East Pilbara traverse; Journal of the Geological Society, v. 174, p. 1090-1112.

Nock, M., undated. Visual art and the nature of perception, https://slideplayer.com/slide/4233087/.

O'Driscoll, E.S.T, 1992. Elusive trails in the basement labyrinth, in: Basement Tectonics 9, (eds) M.J. Rickard, H.J. Harrington, and P.R. Williams, Proceedings of the International Conferences on Basement Tectonics, v. 3. Springer, Dordrecht, https://doi.org/10.1007/978-94-011-2654-0_7.

O'Driscoll, E.S.T. and Campbell, I.B., 1996. Mineral deposits related to Australian continental ring and rift structures with some terrestrial and planetary analogies; Global Tectonics and Metallogeny, v. 6, p. 83 - 101.

Ohla, K., Busch, N.A., Dahlem, M.A., and Herrmann, C.S., 2005. Circles are different: The perception of Glass patterns modulates early event-related potentials; Vision Research v. 45, p. 2668-2676, https://doi.org/10.1016/j.visres.2005.03.015.

Ontario Geological Survey (OGS), 2011. 1:250 000 scale bedrock geology of Ontario: Ministry of Northern Development and Mines, Government of Ontario Miscellaneous Release–Data 126 - Revision 1, scale 1:250 000.

Ontario Geological Survey, 2017. Magnetic supergrids; Geophysical Data Set 1037—Revised, http://www.geologyontario.mndm.gov.on.ca/mndmaccess/mndm_dir.asp?type=pub&id=GDS1037-REV.

Pan, C., 2001. Gibbs Phenomenon removal and digital filtering directly through the Fast Fourier Transform;

Pan, Y. and Therens, C., 2000. The Werner Lake Co-Cu-Au deposit of the English River Subprovince, Ontario, Canada: evidence for an exhalative origin and effects of granulite facies metamorphism; Economic Geology, v. 95, p. 1635–1656. IEEE transactions on signal processing, v. 49, p. 444-448.

Percival, J.A., 2018. The Kapuskasing uplift: a deep crust natural laboratory; International Symposium on Deep Earth Exploration and Practices Beijing, China, https://onlinelibrary.wiley.com/doi/pdf/10.1111/1755-6724.14139.

Percival, J.A., Bursnall, J.T., Moser, D.E., and Shaw, D.M. 1991. Site survey for the Canadian Continental Drilling Program's pilot project in the Kapuskasing Uplift; Ontario Geological Survey, Open File Report, v. 5790, 34 p.

Percival, J.A. and Card, K.D., 1983. Archean crust as revealed in the Kapuskasing uplift, Superior Province, Canada; Geology, v. 11, p. 323-326.

Percival, J.A., Sanborn-Barrie, M., Skulski, T., Stott, G.M., Helmstaedt, H., and White, D.J., 2006. Tectonic evolution of the western Superior Province from NATMAP and Lithoprobe studies; Canadian Journal of Earth Sciences, v. 43, p. 1085–1117, https://doi.org/10.1139/e06-062.

Percival, J.A., Skulski, T., Sanborn-Barrie, M., Stott, G.M., Leclair, A.D., Corkery, M.T., and Boily, M., 2012. Geology and tectonic evolution of the Superior Province, Canada, *in*: Tectonic styles in Canada: The Lithoprobe perspective, (eds) J.A. Percival, et al.; Geological Association of Canada Special Paper, v. 49, p. 321–378.

Percival, J.A. and West, G.F., 1994. The Kapuskasing uplift: a geological and geophysical synthesis; Canadian Journal of Earth Sciences, v. 31, p. 1256-1286.

Percival, J.A., McNicoll, V., Brown, J.L., and Whalen, J.L., 2004. Convergent margin tectonics, central Wabigoon subprovince, Superior Province, Canada; Precambrian Research, v. 132, p. 213-244.

Pérez, R.P., Tremblay, A., Daoudene, Y., and Bandyayera, D., 2020. Étude géochimique, structurale et géochronologique de la Sous-province de Nemiscau, Baie-James, Québec : implications quant à l'origine et l'évolution tectonique d'un domaine sédimentaire archéen; MERN Québec, MB 2020-07, 82 p., http://gq.mines.gouv.qc.ca/documents/EXAMINE/MB202007/MB202007RAP001.pdf.

Perry, H.K.C., Mareschal, J.-C., and Jaupart, C., 2006. Variations of strength and localized deformation in cratons: The 1.9 Ga Kapuskasing uplift, Superior Province, Canada; Earth and Planetary Science Letters, v. 249, p. 216–228.

Phillips, G.N. et al., 2019. The role of geoscience breakthroughs in gold exploration success: Yilgarn Craton, Australia. Ore Geology Reviews, v. 112, https://doi.org/10.1016/J.OREGEOREV.2019.103009.

Phillips, R.J. and Hansen, V.L., 1994. Tectonic and magmatic evolution of Venus; Annual Review of Earth and Planetary Science, v. 22, p. 597–654.

Poh, J., Yamato, P., Duretz, T., Gapais, D., and Ledru, P., 2020. Precambrian deformation belts in compressive tectonic regimes: A numerical perspective; Tectonophysics, v. 777, https://doi.org/10.1016/j.tecto.2020.228350.

Poulsen, K.H., Card, K.D., and Franklin, J.M., 1992a. Archean tectonic and metallogenic evolution of the Superior Province of the Canadian Shield; Precambrian Research, v. 58, p. 25-54.

Poulsen, K.H., Robert, F., and Card, K.D., 1992b. Transpressive tectonics and the Archean gold deposits of Superior Province, Canadian Shield, *in*: Basement Tectonics 8, (eds) M.J. Bartholomew, D.W. Hyndman, D.W. Mogk, R. Mason; Proceedings of the International Conferences on Basement Tectonics, v. 2. Springer, Dordrecht, 615-623.

Premier Gold Mines Limited, 2009. Premier provides Red Lake update; http://www.24hgold.com/francais/article-compagnie-or-argent-provides-red-lake-update.aspx?articleid=423976

Prevec, S.A., Cowan, D.R., and Cooper, G.R.J., 2005. Geophysical evidence for a pre-impact Sudbury dome, southern Superior Province, Canada; Canadian Journal of Earth Sciences, v. 42, p. 1–9.

Rainsford, D.R.B., Diorio, P.A., Hogg, R.L.S., and Metsaranta, R.T., 2017. The Use of geophysics in the Ring of Fire, James Bay Lowlands –The chromite story, *in*: Proceedings of Exploration 17: Sixth Decennial International Conference on Mineral Exploration, (ed) V. Tschirhart and M.D. Thomas, p. 649–662, http://tinyurl.com/y3enbe2e.

Ramachandran, K., 2012. Constraining fault interpretation through tomographic velocity gradients: application to northern Cascadia; Solid Earth, v3, p. 53–61, 2012, https://doi.org/10.5194/se-3-53-2012.

Ravenelle, J.-F., 2013. Phase 1 Geoscientific Desktop Preliminary Assessment, Lineament Interpretation, Township of Ear Falls, Ontario; Nuclear Waste Management Organization, 68 p., https://www.nwmo.ca/~/media/Site/Files/PDFs/2015/11/04/17/36/2221_apm-rep-06144-0022_earfalls_geoscience_lineament_w.ashx?la=en

Rehm, A.G.N., 2020. Emplacement history of mafic-ultramafic volcanic rocks in the northern Pontiac subprovince, Quebec, Canada; MSc thesis, Laurentian University, https://zone.biblio.laurentian.ca/handle/10219/3502.

Rey, P.F., Philippot, P., and Thébaud, N., 2003. Contribution of mantle plumes, crustal thickening and greenstone blanketing to the 2.75–2.65 Ga global crisis; Precambrian Research, v. 127, p. 43-60.

Riedel, W., 1929. Zur Mechanik Geologischer Brucherscheinungen; Zentral-blatt für Mineralogie, Geologie und Paläontologie B, p. 354 –368.

Robert, F., 1989. Internal structure of the Cadillac tectonic zone southeast of Val d'Or, Abitibi greenstone belt, Quebec; Canadian Journal of Earth Sciences, v. 26, p. 2661-2675.

Rodriguez-Galiano, V., Sanchez-Castillo, M., Chica-Olmo, M., and Chica-Rivas, M., 2015. Machine learning predictive models for mineral prospectivity: An evaluation of neural networks, random forest, regression trees and support vector machines; Ore Geology Reviews, v. 71, p. 804-818, https://doi.org/10.1016/j.oregeorev.2015.01.001.

Roots, E. and Craven, J.A., 2017. 3-D modelling of magnetotelluric data from the western Superior Province, Ontario; Geological Survey of Canada, Open File 8237 (revised), https://doi.org/10.4095/306191.

Sadek, H.S., Rashad, S.M., and Blank, H.R., 1984. Spectral analysis of aeromagnetic profiles for depth estimation principles, software, and practical application; USGS Open File Report, v. 84-849, https://pubs.usgs.gov/of/1984/0849/report.pdf.

Sanchez, M.G., Allan, M.M., Hart, C.J.R., and Mortensen, J.K., 2014. Extracting ore-deposit-controlling structures from aeromagnetic, gravimetric, topographic, and regional geologic data in western Yukon and eastern Alaska; Interpretation, v. 2, No. 4, p. SJ75–SJ102, http://dx.doi.org/10.1190/INT-2014-0104.1.

Sappin, A.-A., Houlé, M.G., Lesher, C.M., Metsaranta, R.T., and McNicoll, V.J., 2015. Regional characterization of mafic-ultramafic intrusions in the Oxford-Stull and Uchi domains, Superior Province, Ontario, *in*: Targeted Geoscience Initiative 4: Canadian Nickel-Copper-Platinum Group Elements-Chromium Ore Systems — Fertility, Pathfinders, New and Revised Models, (ed.) D.E. Ames and M.G. Houlé, Geological Survey of Canada, Open File 7856, p. 75–85.

Sappin, A.-A., Guilmette, C., Goutier, J., and Beaudoin, G., 2018. Geochemistry of Mesoarchean felsic to ultramafic volcanic rocks of the Lac Guyer area, La Grande Subprovince (Canada): Evidence for plume-related magmatism in a rift setting; Precambrian Research, v. 316. p. 83–102.

Schaffer, C., 1993. Overfitting avoidance as bias; Machine Learning, v. 10, p. 153-178, https://doi.org/10.1007/BF00993504.

Schmitz, M.D., Bowring, S.A., Southwick, D.L., Boerboom, T., and Wirth, K.R., 2006. High-precision U-Pb geochronology in the Minnesota River Valley subprovince and its bearing on the Neoarchean to Paleoproterozoic evolution of the southern Superior Province; Geological Society of America Bulletin, v. 118, p. 82–93, https://doi.org/10.1130/B25725.1.

Spector, A. and Grant, F.S., 1970. Statistical models for interpreting aeromagnetic data; Geophysics, v. 35, p. 293–302.

Stachel, T., Banas, A., Muehlenbachs, K., Kurszlaukis, S., and Walker, E.C., 2006. Archean diamonds from Wawa (Canada): samples from deep cratonic roots predating cratonization of the Superior Province; Contributions to Mineralogy and Petrology, v. 151, article 737, https://doi.org/10.1007/s00410-006-0090-7.

Stern, R.J., 2008. Modern-style plate tectonics began in Neoproterozoic time: An alternative interpretation of Earth's tectonic history; *in*: When did plate tectonics begin on planet Earth, Special Paper, Geological Society of America, v. 440, p. 265–280.

Stofan, E. R., Scharpton, V. L., Schubert, G., Baer, G., Bindschadler, D. L., Janes, D.M., and Squyres, S.W., 1992. Global distribution and characteristics of coronae and related features on Venus: Implications for Origin and Relation to Mantle Processes; Journal of Geophysical Research, v. 97, p. 13347–13378.

Stott, G.M., 2011. A revised terrane subdivision of the Superior Province in Ontario; Ontario Geological Survey, Ministry of Northern Development and Mines, Government of Ontario Miscellaneous Release—Data 27.

Stott, G.M., Corkery, M.T., Percival, J.A., Simard, M. and Goutier, J., 2010. A revised terrane subdivision of the Superior Province; in Summary of Field Work and Other Activities 2010, Ontario Geological Survey, Open File Report, v. 6260, p. 20-1–20-10.

Tabor, J.R. and Hudleston, P.J., 1991. Deformation at an Archean subprovince boundary, northern Minnesota. Canadian Journal of Earth Sciences, v. 28, p. 292-307.

Tchalenko, J.S., 1970. Similarities between shear-zones of different magnitudes. Geological Society of America Bulletin, v. 81, p. 1625–1640.

Thurston, P.C., 2002. Autochthonous development of Superior Province greenstone belts?; Precambrian Research, v. 115, p. 11–36.

Thurston, P., Ayer, J.A., Goutier, J., and Hamilton, M.A., 2008. Depositional gaps in Abitibi greenstone belt stratigraphy: a key to exploration for syngenetic mineralization; Economic Geology, v. 103, p. 1097–1134.

Thybo, H. and Artemieva, I.M., 2013. Moho and magmatic underplating in continental lithosphere; Tectonophysics, v. 609, p. 605-619.

Truscott, M.G. and Shaw, D.M., 1990. Average composition of lower and intermediate continental crust, Kapuskasing Structural Zone, Ontario, in: Exposed Cross-Sections of the Continental Crust, (eds) M.H. Salisbury, D.M. Fountain, p. 421-436, https://doi.org/10.1007/978-94-009-0675-4_16.

Twomey, T., 2000. The geological setting and estimation of gold grade of the high-grade zone, Red Lake mine, Goldcorp Inc.; Exploration and Mining Geology, v. 10, p. 19-34, https://doi.org/10.2113/10.1-2.19.

Urquhart, W.E.S., 2009. Geophysical airborne survey frequency domain filtering, http://www.geoexplo.com/airborne_survey_workshop_filtering.htm.

van Hinsbergen, D.J.J., Steinberger, B., Doubrovine, P., and Gassmöller, R., 2011. Acceleration and deceleration of India – Asia convergence since the Cretaceous: roles of mantle plumes and continental collision; Journal of Geophysical Research, v. 116, B06101, https://doi.org/10.1029/2010JB008051.

Wang, H., 2015. Numerical simulation of subcontinent lithosphere dynamics: craton stability, evolution and formation; Durham E-Theses Online, http://etheses.dur.ac.uk/11173/.

Watchorn, R., 2019. Research of the North America Greater Archaean Craton using seismic tomography; https://www.geotreks.com.au/work/giant-ring-structures/north-america/superior-craton-seismic-tomography-60-km-depth/ (unpublished).

Watson, J., 1980. The origin and history of the Kapuskasing structural zone, Ontario, Canada; Canadian Journal of Earth Sciences, v.17, p.866-875.

Watson, J.V. and O'Hara, M.J., 1980. Metallogenesis in relation to mantle heterogeneity; Philosophical Transactions of the Royal Society of London, Series A, v. 297, p. 347-352.

Whittaker, P.J., 1986. Chromite deposits in Ontario; Ontario Geological Survey, Study 55, 97 p.

Wise, D., 1982. Linemanship and the practice of linear geo-art; Geological Society of America Bulletin, v. 93, p. 886-888.

Wise, T. and Thiel, S., 2018. Imprints of tectonic processes imaged with magnetotellurics and seismic reflection, ASEG Extended Abstracts 2018, p. 1-7.

Witschard, F., 1979. Large-magnitude ring structures on the Baltic Shield - metallogenic significance; Economic Geology, v. 79, p. 1400-1405.

Witt, W.K., Cassidy, K.F., Lu, Y.-J., and Hagemann, S.G., 2020. The tectonic setting and evolution of the 2.7 Ga Kalgoorlie–Kurnalpi Rift, a world-class Archean gold province; Mineralium Deposita, v. 55, p. 601–631, https://doi.org/10.1007/s00126-017-0778-9.

Woodall, R., 1994. Empiricism and concept in successful mineral exploration; Australian Journal of Earth Sciences, v. 41, p. 1-10.

Yakymchuk, C. and Brown, M., 2014. Consequences of open-system melting in tectonics; Journal of the Geological Society, London, v. 171, p. 21–40, http://dx.doi.org/10.1144/jgs2013-039.

Ore mineralogy, pyrite chemistry, and S isotope systematics of magmatic-hydrothermal Au mineralization associated with the Mooshla Intrusive Complex (MIC), Doyon-Bousquet-LaRonde mining camp, Abitibi greenstone belt, Québec

K. Neyedley[1*], J.J. Hanley[1#], P. Mercier-Langevin[2], and M. Fayek[3]

Neyedley, K., Hanley, J.J., Mercier-Langevin, P., and Fayek, M., 2021. Ore mineralogy, pyrite chemistry, and S isotope systematics of magmatic-hydrothermal Au mineralization associated with the Mooshla Intrusive Complex (MIC), Doyon-Bousquet-LaRonde mining camp, Abitibi greenstone belt, Québec; in *Targeted Geoscience Initiative 5: grant program final reports (2018-2020), Geological Survey of Canada, Open File 8755, p. 129–148. https://doi.org/10.4095/328985*

Abstract: The Mooshla Intrusive Complex (MIC) is an Archean polyphase magmatic body located in the Doyon-Bousquet-LaRonde (DBL) mining camp of the Abitibi greenstone belt, Québec. The MIC is spatially associated with numerous gold (Au)-rich VMS, epizonal 'intrusion-related' Au-Cu vein systems, and shear zone-hosted (orogenic?) Au deposits. To elucidate genetic links between deposits and the MIC, mineralized samples from two of the epizonal 'intrusion-related' Au-Cu vein systems (Doyon and Grand Duc Au-Cu) have been characterized using a variety of analytical techniques.

Preliminary results indicate gold (as electrum) from both deposits occurs relatively late in the systems as it is primarily observed along fractures in pyrite and gangue minerals. At Grand Duc gold appears to have formed syn- to post-crystallization relative to base metal sulphides (e.g. chalcopyrite, sphalerite, pyrrhotite), whereas base metal sulphides at Doyon are relatively rare. The accessory ore mineral assemblage at Doyon is relatively simple compared to Grand Duc, consisting of petzite (Ag_3AuTe_2), calaverite ($AuTe_2$), and hessite (Ag_2Te), while accessory ore minerals at Grand Duc are comprised of tellurobismuthite (Bi_2Te_3), volynskite ($AgBiTe_2$), native Te, tsumoite (BiTe) or tetradymite (Bi_2Te_2S), altaite (PbTe), petzite, calaverite, and hessite.

Pyrite trace element distribution maps from representative pyrite grains from Doyon and Grand Duc were collected and confirm petrographic observations that Au occurs relatively late. Pyrite from Doyon appears to have been initially trace-element poor, then became enriched in As, followed by the ore metal stage consisting of Au-Ag-Te-Bi-Pb-Cu enrichment and lastly a Co-Ni-Se(?) stage enrichment. Grand Duc pyrite is more complex with initial enrichments in Co-Se-As (Stage 1) followed by an increase in As-Co(?) concentrations (Stage 2). The ore metal stage (Stage 3) is indicated by another increase in As coupled with Au-Ag-Bi-Te-Sb-Pb-Ni-Cu-Zn-Sn-Cd-In enrichment. The final stage of pyrite growth (Stage 4) is represented by the same element assemblage as Stage 3 but at lower concentrations. Preliminary sulphur isotope data from Grand Duc indicates pyrite, pyrrhotite, and chalcopyrite all have similar $\delta^{34}S$ values (~1.5 ± 1 ‰) with no core-to-rim variations. Pyrite from Doyon has slightly higher $\delta^{34}S$ values (~2.5 ± 1 ‰) compared to Grand Duc but similarly does not show much core-to-rim variation.

At Grand Duc, the occurrence of Au concentrating along the rim of pyrite grains and associated with an enrichment in As and other metals (Sb-Ag-Bi-Te) shares similarities with porphyry and epithermal deposits, and the overall metal association of Au with Te and Bi is a hallmark of other intrusion-related gold systems. The occurrence of the ore metal-rich rims on pyrite from Grand Duc could be related to fluid boiling which results in the destabilization of gold-bearing aqueous complexes. Pyrite from Doyon does not show this inferred boiling texture but shares characteristics of dissolution-reprecipitation processes, where metals in the pyrite lattice are dissolved and then reconcentrated into discrete mineral phases that commonly precipitate in voids and fractures created during pyrite dissolution.

[1]Department of Geology, Saint Mary's University, 923 Robie Street Halifax, Nova Scotia
[2]Geological Survey of Canada, 490 De la Couronne Street, Québec, Quebec
[3]Department of Geological Sciences, University of Manitoba, 125 Dysart Road, Winnipeg, Manitoba
*corresponding author; (email: kevinneyedley@gmail.com); #activity leader

INTRODUCTION

The Mooshla Intrusive Complex (MIC) is an Archean polyphase magmatic body located in the Doyon-Bousquet-LaRonde (DBL) mining camp of the Abitibi greenstone belt, Québec. The MIC is spatially associated with numerous gold (Au)-rich VMS, epizonal 'intrusion-related' Au-Cu sulphide-rich vein systems and shear zone-hosted (orogenic?) Au deposits. Previous studies (e.g. Gosselin, 1998; Mercier-Langevin, 2007a; Galley and Lafrance, 2014; Yergeau, 2015) highlight a possible genetic link between the MIC and mineral deposits in the area based on geochronology, mapping/field relations, petrography, and lithogeochemistry. To elucidate the possible role of coeval magmatic systems in the development of high Au tenor mineral deposits, integration of field-based studies and in-situ analytical techniques are required to provide first-order constraints on the evolution of potentially causative magmas. Specifically, the study of the metal tenors, metal associations, and accessory mineralogy of Au and S-rich ore styles, when combined with S isotope and trace element mapping of base metal sulfides, has been shown to be powerful in elucidating the genetic links between ores and causative magmas. In this study, these characteristics within vein-hosted, high-grade Au deposits within the MIC and/or associated volcanic rocks (Doyon, Grand Duc) in the DBL mining camp were investigated with the aim of determining if the metal associations are genetically linked to the MIC (as a potential causative magmatic source).

BACKGROUND

Regional and Local Geology

The regional geology of the DBL mining camp and geological setting of its contained mineral deposits (Fig. 1) have been described in detail by Gunning (1941), Fillion et al. (1977), Valiant and Hutchinson (1982), Marquis et al. (1990), Trudel et al. (1992), Lafrance et al. (2003, 2005), Mercier-Langevin et al. (2004, 2005, 2007b, 2011), Galley and Lafrance (2014), and Yergeau (2015). The mining camp contains > 28 Moz of Au, making it one of the world's largest Archean Au districts, and contains two world-class Au-rich VMS deposits (LaRonde Penna and Bousquet 2-Dumagami), two major Au-rich sulphide vein deposits (Bousquet 1 and Westwood), epizonal "intrusion-related" Au-Cu vein systems (Doyon and Westwood Zone 2 Extension), and shear-hosted Au deposits (Mouska and Mic Mac), along with a number of smaller Au occurrences (Lafrance et al., 2003; Mercier-Langevin, 2007b, 2009, 2011; Yergeau, 2015).

The DBL mining camp occurs in the eastern portion of the Blake River Group (2704-2695 Ma; McNicoll et al., 2014) of the Archean Abitibi greenstone belt in the Superior Province (Mercier-Langevin, et al., 2007a; Galley and Lafrance, 2014). In the mining camp, the Blake River Group strikes east-west and is a steeply dipping, south-facing homoclinal volcanic sequence (Lafrance et al., 2003; Mercier-Langevin et al., 2007a, Galley and Lafrance, 2014). The Blake River Group in the DBL camp consists of the Hébécourt Formation in the north and the Bousquet Formation in the south (Fig. 1; Lafrance et al., 2003). Along the northern contact of the Blake River Group is the Lac Parfouru Fault, which separates the Hébécourt Formation from the sedimentary rocks of the Kewagama Group (<2686 Ma; Davis, 2002). Along the southern contact of the Blake River Group, the Bousquet Formation is disconformably overlain by the sedimentary rocks of the Cadillac Group (<2687.4 ± 1.2 Ma; Lafrance et al., 2005). The Hébécourt Formation represents the base of the Blake River Group in the DBL camp, and overlying the Hébécourt Formation is the Bousquet Formation. The Bousquet Formation is divided into two members: the 2699-2698 Ma tholeiitic to transitional lower member and the 2698-2697 Ma transitional to calc-alkaline upper member (Lafrance et al., 2005; Mercier-Langevin, 2007b). For detailed descriptions of the Bousquet Formation see Mercier-Langevin et al. (2007b, c).

Emplacement of the MIC occurred along the contact between the Hébécourt and Bousquet Formations in the western portion of the DBL camp (Fig. 1; Galley and Lafrance, 2014). The MIC is subdivided into two distinct stages of formation: (i) the Mouska stage, which consists of six intrusive phases (A to E) that range from gabbroic to tonalitic in composition; and (ii) the Doyon stage, which comprises five intrusive phases (F to I) that range from tonalitic to trondhjemitic in composition (Fig. 1; Galley and Lafrance, 2014). Galley and Lafrance (2014) distinguished the various phases by studying their chemical compositions, intrusion styles, and overprinting relationships.

The synvolcanic age of the MIC and coeval nature of the Bousquet Formation has been documented through field relationships and geochemistry (Galley and Lafrance, 2014), as well as U-Pb geochronology. Zircon U-Pb geochronology of the Doyon-stage trondhjemite (phase H) yielded an age of 2696.9 ± 1 Ma (Lafrance et al., 2005), which demonstrates that Phase H, and by association the Doyon-stage of the MIC, is synchronous with the upper member of the Bousquet Formation (2698−2696 Ma; Lafrance et al., 2005; Mercier-Langevin et al., 2007b, 2011; McNicoll et al., 2014). Zircon U-Pb geochronology of the Phase C quartz diorite yielded an age of 2698.5 ± 0.4 Ma (McNicoll et al., 2014), which is synchronous with the glomeroporphyritic dacite of the lower Bousquet member (unit 4.2; host to part of the Doyon Au-Cu deposit), which has an age of 2698.3 ± 0.9 Ma (Lafrance et al., 2005).

At least three phases of deformation affected the lithologies of the DBL mining camp (Langshur, 1990; Savoie et al., 1991; Belkabir and Hubert, 1995). A weak, moderately inclined northeast-southwest foliation defines the first phase of deformation (D_1). A strong penetrative east-west fabric, with shear planes and faults that dip steeply to the south represents the second phase of deformation (D_2). Dextral

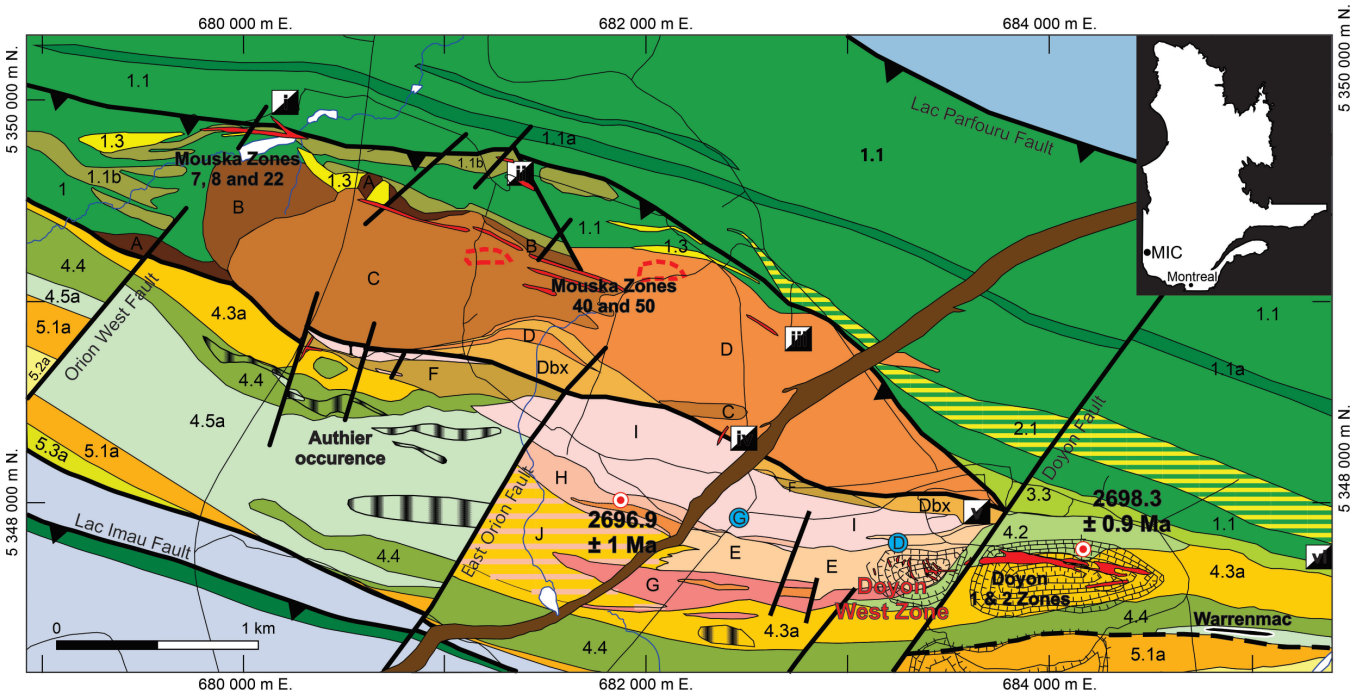

Intrusive rocks

- Proterozoic diabase

Mooshla intrusive complex

Doyon stage

- I: Aphyric to quartz porphyritic trondhjemite
- J: Interlayered Phase H and I in Unit 4.3a
- H: Plagioclase-quartz porphyritic trondhjemite
- G: Plagioclase porphyritic tonalite
- F: Plagioclase-hornblende porphyritic tonalite

Mouskla stage

- E: "Doyon quartz diorite": pendant of Dbx
- Dbx: Xenolith-rich tonalite: Phase D hangingwall contact
- D: Tonalite
- C: Quartz diorite
- B: Layered gabbro
- A: Aphyric/feldspar porphyritic diorite

Sedimentary rocks

- **Cadillac sedimentary rocks**
- **Kewagama sedimentary rocks**

Volcanic rocks

Bousquet Formation

Upper Bousquet

- 5.3a: **Bousquet-Ferris QFP rhyolite**
- 5.2a: **Doyon rhyodacite-rhyolite**
- 5.1a: **Doyon dacite-rhyodacite**

Lower Bousquet

- 4.5a: **Warrenmac rhyodacite** Rhyodacitic schist
- 4.4: **Bousquet heterogeneous unit** Basaltic to andesitic schist
- 4.3a: **Doyon mine felsic Unit** Dacitic to rhyolitic schist
- 4.2: **Doyon glomeroporphyritic** dacite
- 3.3: **Bousquet scoriaceous tuff** Andesite and dacite
- 2.1: **Bousquet felsic sills swarm** Rhyolite

Hébécourt Formation

- 1.3: Rhyolite
- 1.1b: Magnetite-rich basalt and basaltic andesite
- 1.1a: Glomerporphyritic basalt and basaltic andesite
- 1.1: Basalt and basaltic andesite flows

Mineralization

- Gold mine: i: Mouska; ii: Mic Mac iii: Mooshla B; iv: Mooshla A; v: Doyon; vi: Westwood
- Gold lens
- Anomalous gold zone
- Massives sulfides zone
- Massives sulfides horizon
- VMS stringer mineralization
- Open Pit

Sample locations

- Sample locations: D = Doyon West Zone; G = Grand Duc

Figure 1: Geological map of the Mooshla intrusive complex (modified from Galley and Lafrance, 2014). Zircon dates are from Lafrance et al., 2005 and McNicoll et al., 2014.

transpressive brittle-ductile faults related to the third phase of deformation (D_3) overprint D_2. Regional metamorphism in the camp ranges from greenschist- to amphibolite-facies and is approximately coeval with D_2. However, in the MIC, unorientated actinolite and biotite porphyroblasts suggest that peak metamorphism postdates D_2 (Marquis et al., 1990; Belkabir and Hubert, 1995; Dubé et al., 2004; Mercier-Langevin, 2005).

Epizonal "intrusion-related" Au-Cu vein deposits

Epizonal "intrusion-related" Au-Cu vein deposits in the DBL camp are Doyon, Grand Duc, and the Zone 2 Extension, which occur in the western portion of the camp in close proximity to or are hosted by the MIC (Guha et al., 1982; Gosselin, 1998; Yergeau, 2015).

Mineralization at Doyon occurs in three different zones, two (Zones 1 and 2) of which occur in highly altered sericite schists in felsic and mafic volcanic rocks, in the upper portions of the lower member of the Bousquet Formation (units 4.2-4.4; Guha et al., 1982; Gosselin, 1998). The third mineralized zone of Doyon (i.e. West Zone) crosscuts Phase E of the MIC (Fig. 1; Gosselin, 1998; Galley and Lafrance, 2007, 2014). Mineralization in Zone 1 of Doyon is characterized by mm- to cm-wide pyrite-quartz veinlets that contain ~20 vol% sulphides (Guha et al., 1982; Savoie et al., 1991). Chalcopyrite, sphalerite, galena, arsenopyrite, and chalcocite have also been observed in these thin veinlets (Guha et al., 1982). Gold is present as native gold and Au-tellurides and is disseminated and interstitial to pyrite (Guha et al., 1982). Mineralization in the Zone 1 of Doyon and the West zone consists of brecciated pyrite-quartz veins that contain 10-75 vol% sulphides and vary between a few cm to 10s of cm in width (Savoie et al., 1991). Chalcopyrite can locally occur as abundant as pyrite but other sulphides are relatively rare (e.g. sphalerite, pyrrhotite, galena, arsenopyrite, bornite, and chalcocite; Savoie et al., 1991). Similar to Zone 1, gold in Zone 2 and the West zone occurs as native gold and Au-tellurides (Guha et al., 1982; Savoie et al., 1991). Importantly, Gosselin (1998) showed that auriferous veins and their alteration halo at Doyon pre-date all deformation events and therefore suggested veins could be of a synvolcanic (i.e. syn-intrusion) origin.

Little reporting is present for Grand Duc, but it occurs approximately 1 km to the west of the Doyon West Zone and mineralized veins occur within Phase I of the MIC. Mineralization at Grand Duc is characterized by mm- to cm-wide pyrite-quartz veins that contain ~10-30 vol% sulphides.

KEY ACTIVITY HIGHLIGHTS

Methodology

All samples were characterized petrographically using transmitted and reflected light on a Nikon Eclipse H550L microscope. All samples were carbon-coated and analyzed with a TESCAN MIRA 3 LMU Variable Pressure Schottky Field Emission Scanning Electron Microscope (SEM) at Saint Mary's University. The SEM is equipped with a back-scattered electron (BSE) detector coupled with an energy dispersive X-ray (EDS) functionality. For the latter, a solid-state, 80 mm² X-max Oxford Instruments EDS detector was used. A beam voltage of 20 kV and an approximate working distance of 17 mm was used for all analyses. The SEM-EDS was used to characterize different types of zoning in pyrite, to identify other sulphide minerals present, and to document the textural settings of gold and identify accessory minerals. Petrography and SEM-EDS were used as the basis to select specific pyrite grains for laser ablation inductively-coupled plasma mass spectrometry (LA-ICP-MS) and secondary ion mass spectrometry (SIMS) analyses.

Mineralized vein samples from Grand Duc and Doyon were analyzed at the Ontario Geoscience Laboratories for bulk metal concentrations. All samples were pulverized using either an Al oxide ball mill or high chrome steel mills. Following mill prep, samples were subjected to an aqua regia digestion followed by ICP-MS analysis (OGS package IML-101). Select samples that were over range for Cu by ICP-MS were analyzed again by AAS (OGS package AAF-101). Samples contain highly anomalous Au underwent lead fire assay with gravimetric finish (OGS package GFA-PBG).

Pyrite trace element distribution maps were determined by LA-ICP-MS at the University of New Brunswick, Canada using a Resonetics M-50 193 nm excimer laser system connected, via Nylon tubing, to an Agilent 7700x quadrupole ICP-MS equipped with dual external rotary pumps (McFarlane and Luo, 2012). Samples and standards were loaded together into a two-volume, low-volume Laurin Technic Pty sample cell that was repeatedly evacuated and backfilled with ultra-pure He to remove traces of air from the cell after each sample exchange. Pyrite trace element mapping used a 17 µm beam diameter, a stage scan speed of 6 µm/s, and a 10 Hz repetition with the laser fluence regulated at ~3 J/cm². A He carrier gas was used at a flow rate of 300 mL/min that transported the ablated material out of the ablation cell and mixed downstream with 2 mL/min N2 (to enhance sensitivity) and 930 mL/min Ar (from the ICP-MS) prior to reaching the ICP-MS torch. Oxide production rates were maintained below 0.3 % by monitoring ThO/Th. Trace elements measured in represent sulfide-compatible ore and accessory elements that are typically investigated in similar studies of pyrite in gold systems (Neyedley et al., 2017). Dwell times for all measured isotopes (^{33}S, ^{55}Mn, ^{56}Fe, ^{57}Fe, ^{63}Cu, ^{66}Zn, ^{72}Ge, ^{75}As, ^{82}Se, ^{95}Mo, ^{111}Cd, ^{115}In, ^{118}Sn, ^{121}Sb, ^{125}Te, ^{202}Hg, ^{208}Pb, ^{209}Bi) was 10 ms except for ^{59}Co, ^{60}Ni,

$^{107}Ag^{195}Pt$, and ^{182}W were 15 ms and 197Au was 30 ms. Trace element concentrations in unknowns were calibrated against sulfide reference material MASS-1 (to calibrate analyte sensitivities) and an internal standard of 46.5 wt % Fe for ideal pyrite. At the end of the ablation sequence, the laser log file and ICP-MS intensity data file were synchronized using Iolite™ (Paton et al., 2011) running as a plug in for Wave metrics Igor Pro 6.22™. For trace element maps, non-pyrite material was removed using the Fe CPS elemental map as a guide; concentration scales for each map portray internally standardized absolute ppm levels.

Sulfur isotope ratios ($^{34}S/^{32}S$) of pyrite, pyrrhotite, and chalcopyrite from mineralized veins were collected using a CAMECA 7f SIMS at the University of Manitoba, Winnipeg, Canada. Samples and spot locations were chosen based on their representative textures of the different generations of pyrite. A cesium (Cs+) primary beam with a 3 nA current was accelerated (+10 kV) onto the sample surface with a sputtering diameter of ~15 μm. The instrument operated with a 200 V offset for sulfur, –9 kV secondary accelerating voltage, and a mass resolving power of 350. For a detailed description of operating conditions and strategy for correction of instrumental mass fractionation and matrix effects, see Riciputi et al. (1998) for sulfur isotope analysis. Balmat pyrite ($\delta^{34}S$ = 15.1 ± 0.3‰; Riciputi et al., 1998), Anderson pyrrhotite ($\delta^{34}S$ = 1.4 ± 0.2‰; Crowe and Vaughan, 1996) and Trout Lake chalcopyrite ($\delta^{34}S$ value of 0.3 ± 0.2‰; Crowe and Vaughan, 1996) were used as the pyrite, pyrrhotite, and chalcopyrite reference materials, respectively. Spot-to-spot reproducibility for Balmat pyrite was 0.4‰ and was 0.3‰ for both Anderson pyrrhotite and Trout Lake chalcopyrite. Precision for individual analysis was 0.4‰ for pyrite and 0.3‰ for pyrrhotite and chalcopyrite, therefore, 1σ errors for pyrite and pyrrhotite and chalcopyrite are 0.4‰ and 0.3‰, respectively. SIMS results from the reference materials were compared to the accepted isotopic compositions in order to calculate correction factors that were applied to the unknowns measured during the same analytical session (e.g. Holliger and Cathelineau, 1988).

RESULTS AND DATA ANALYSIS

Bulk rock geochemistry

Mineralized veins from Grand Duc and Doyon show an enrichment in a variety of metals (Table 1). Grand Duc samples are divided into high-grade (Au >10 g/t; sample = 18KN03) and low-grade (Au < 10 g/t; samples 18KN07, 08, 09, 11). Both samples from Doyon are high-grade. The high-grade sample from Grand Duc returned 297.88 g/t Au and high-grade samples from Doyon returned 30.45 and 23.80 g/t Au. Silver concentration in the high-grade Grand Duc vein is 46.67 g/t, and between 23.80 and 2.92 g/t in Doyon high-grade samples. Low-grade samples from Grand Duc range between 0.89 and 5.93 g/t Au and 0.54 to 2.21 g/t Ag. Bismuth is highly enriched in the Grand Duc high-grade sample with almost 600 ppm and Te is > 40 ppm (over range). Bismuth content is relatively the same between low-grade samples from Grand Duc and high-grade Doyon samples, ranging from 0.36 to 2.55 ppm. Tellurium is highly enriched in Doyon (25-29 ppm) compared to low-grade Grand Duc samples (0.98-4.74 ppm). Within the high-grade Grand Duc sample, Co, Cu, Zn, Pb, Sb, In, Sn, and Cd are highly enriched relative to all samples from Grand Duc and Doyon. Comparing low-grade Grand Duc and high-grade Doyon samples, As, Cu, Se, Cd, In, Sn, and Te are enriched in Doyon while Co and Pb are enriched in low-grade Grand Duc samples.

Doyon quartz vein and ore mineralogy

Two mineralized quartz-pyrite veins from the Doyon West Zone that crosscuts Phase E (tonalite) of the MIC were sampled for this study. Both veins have sharp contacts with the host tonalite and vary between 5 and 20 cm in width (Fig. 2A-B). The modal proportions of minerals vary between and within individual veins. Quartz and pyrite are the most abundant minerals in the mineralized veins, with quartz comprising 20-80 vol% and pyrite 20-80 vol%. Minor amounts of what is likely highly altered wallrock have been incorporated in the veins, comprising 0-5 vol% (Fig. 2C-D). These wallrock fragments have been strongly chloritized and sericitized.

Two different textural variations (possibly representing different generations) of quartz are identified, and are termed Q1 and Q2. Individual grains of Q1 vary in size from 100-2000 μm and display some evidence of intracrystalline plastic strain (e.g. undulose extinction). Generation Q2 is finer-grained quartz (< 100 μm) and occurs as isolated grain aggregates, or along the margins of Q1 grains as polycrystalline "ribbons". Minor amounts of muscovite and chlorite are present within the mineralized veins as well. Muscovite grains range in size from 50 to 600 μm and occurs along the grain boundaries of all minerals in the veins, and rarely as inclusions within pyrite. Chlorite grains are 50-500 μm in size and are commonly found along the margins of pyrite grains, with rare occurrences along the interstices of quartz grains. Chlorite also appears to be replacing muscovite.

Mineralized veins in Doyon contain the sulphide assemblage pyrite + chalcopyrite ± pyrrhotite. Pyrite ranges in size from 100-4000 μm and is not or only weakly sieved and/or fractured (Fig. 3A). No clear zonation was observed in pyrite prior to and after etching the samples with nitric acid, but individual grains were variably effected by the acid etching (Fig. 3B). Locally, pyrite cores are sieved and contain abundant inclusions of chalcopyrite ± pyrrhotite ± pyrite ± magnetite ± tellurides ± gold (Figs. 3B, 4A). These sieved cores generally transition to clean (i.e. sieve-free), inclusion-free pyrite towards the edge of an individual grain (Fig. 3A-B). Acid etching affected the sieved core and sieve-free rim the same amount for individual grains (Fig. 3B). In the

Table 1. Bulk rock geochemistry for mineralized samples from Grand Duc and Doyon West Zone

Deposit	Grand Duc	Grand Duc	Grand Duc	Grand Duc	Grand Duc	Doyon	Doyon	
Sample #	18KN03	18KN07	18KN08	18KN09	18KN11	18KN05	18KN06	Detect Limit
Au[1] (g/t)	297.88					30.45	23.80	0.47
Ag	46.67					23.34	2.92	2.92
Au[2] (ppm)	>100	5.928	0.885	3.936	1.578	37.433	32.258	0.002
Ag	40.87	2.21	0.54	1.65	0.77	38.56	21.05	0.2
As	13	3.5	3.9	3.3	4.6	107.2	34.2	0.7
Bi	596.16	1.72	0.36	2.51	0.76	1.03	2.55	0.02
Cd	1.4	0.07	0.07	0.04	0.05	0.13	0.14	0.02
Co	97.6	34.6	13.8	29.9	22.5	4.2	7.6	0.03
Cu	16840[a]	217	174	126	116	335	807	0.6
In	3.74	0.084	0.033	0.04	0.048	0.692	1.172	0.002
Mo	1.44	0.71	0.78	0.53	0.76	1.55	0.86	0.06
Pb	85.3	5.5	3.1	6.5	6.6	1.6	2.3	0.2
Sb	0.47	0.06	0.08	0.06	0.05	0.05	0.02	0.009
Se	9	2.1	1.1	3.5	1.2	4.6	9.1	0.2
Sn	2.8	0.3	0.6	0.3	0.4	1.6	4.4	0.06
Te	>40	3.13	0.98	4.74	1.91	24.64	29.4	0.02
Tl	0.054	0.015	0.01	0.013	0.013	0.008	0.01	0.001
Zn	354	9	18	16	10	12	2	2

[1] = Gravimetric Fire Assay; [2] = ICP-MS; [a] = AAS: Atomic Absorption Flame

sieve-textured portions of pyrite grains, inclusions typically fill voids and display planar grain margins, indicative of open space filling (Fig. 3B). Acid etching exposed the presence of a later generation of pyrite (inclusions) that filled the voids of early, sieved pyrite (Fig. 3B).

The textural features and semi-quantitative composition of ore minerals were determined by SEM-BSE and SEM-EDS. Ore minerals identified include gold (as electrum), petzite (Ag_3AuTe_2), calaverite ($AuTe_2$), and hessite (Ag_2Te) and representative SEM-EDS analyses of ore minerals are presented in Table 2. Gold occurs in six textural settings: 1) composite inclusions in pyrite composed of gold + petzite ± calaverite is the most common textural occurrence (Fig. 4A-E); 2) along fractures of pyrite (Fig. 4F); 3) along grain boundaries between pyrite and quartz (Fig. 4G-H); 4) inclusions within pyrite (Fig. 4I); 5) within quartz fractures; and 6) inclusions in chalcopyrite (Fig. 4J). Additionally, some gold-bearing grains present within quartz and pyrite fractures are composed of a mixture of petzite and gold, but with no well-defined grain boundaries (Fig. 4K). The Au:Ag ratio (at. %) of gold ranges from 72:28 to 95:5 and is variable across all textural settings (Table 2).

The composite inclusions of gold + petzite ± calaverite are generally 5-10 μm in size but can be up to 85 μm (Fig. 4A-E). Inclusions typically have a bleb-like morphology, with some inclusions displaying open-space filling textures with sharp crystal faces in contact with the host pyrite (Fig. 4B). The percentage each mineral phase occupies within the composite inclusions is highly variable, with gold occupying 2-38 vol%, petzite 58-92 vol%, and calaverite 24-66 vol% (n=12). Apart from co-existing with gold, petzite occurs as separate inclusions in pyrite, along fractures and grain boundaries of pyrite, along fractures in quartz, and rarely in contact with chalcopyrite or pyrrhotite as inclusions in pyrite (Fig. 4E, I). Calaverite is present as inclusions within pyrite and along fractures of quartz, and hessite is present as composite grains with petzite occurring as inclusions in pyrite. Other minerals identified as inclusions in pyrite include magnetite and cassiterite. Both of these minerals are present in contact with pyrrhotite and chalcopyrite in voids within sieved pyrite (Fig. 4L).

Grand Duc quartz vein and ore mineralogy

All veins studied from Grand Duc range form a few mm to a few cm in width, and have relatively sharp but undulating contacts with the host rocks (Fig. 2E-G). The modal proportions of minerals vary between and within individual veins. Quartz, carbonate, and pyrite are the most abundant minerals in the mineralized veins, with quartz + carbonate comprising 70-90 vol% and pyrite 10-30 vol%. Alteration of the wallrock adjacent to mineralized veins consists of sericite, chlorite, and carbonate (Fig. 4F-G).

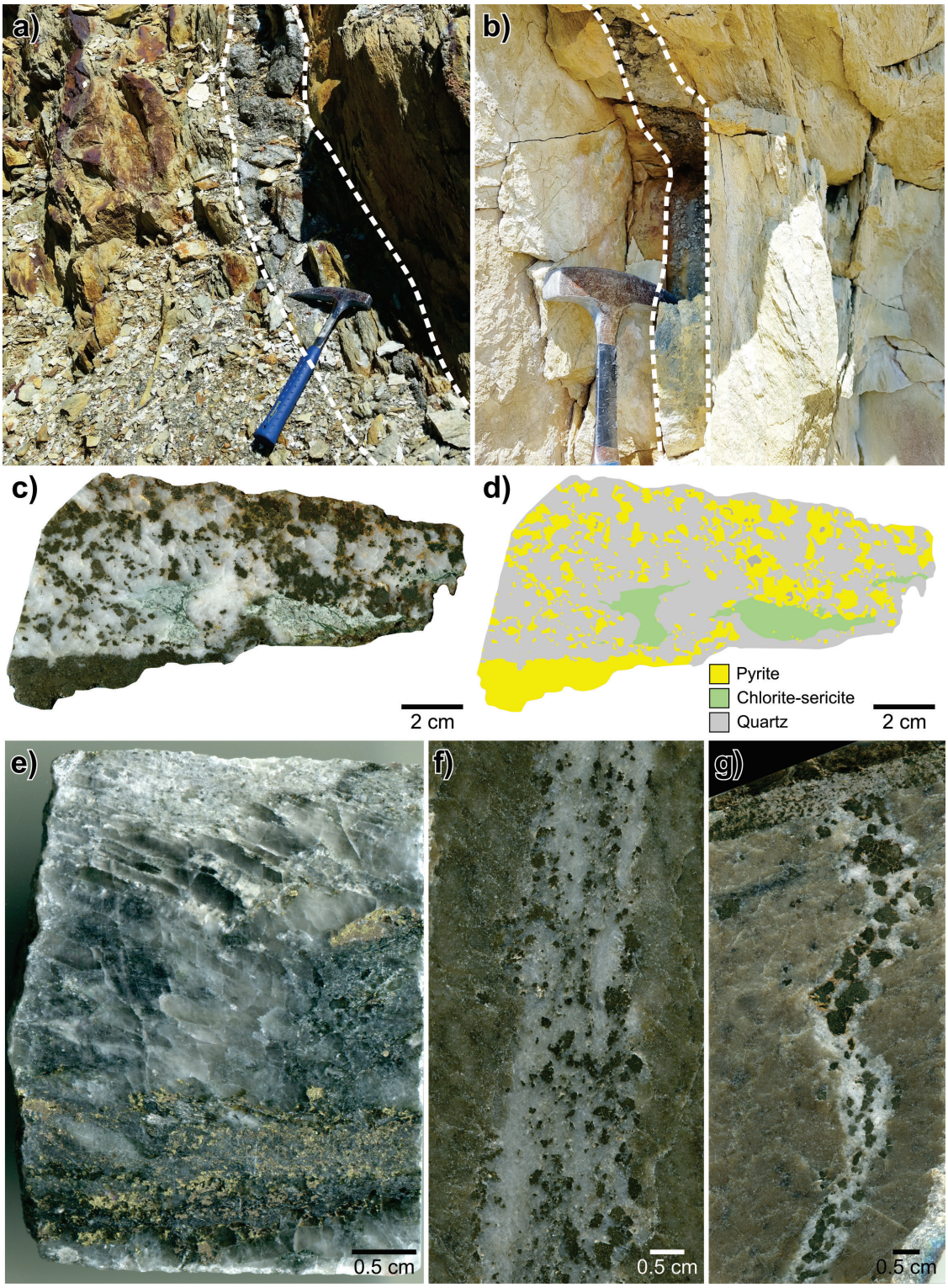

Figure 2: Field photographs of the Doyon West Zone veins sampled for this study and representative slab scans from Doyon and Grand Duc. **a)** Mineralized Doyon vein from which sample 18KN05 was taken. **b)** Mineralized Doyon vein from which sample 18KN06 was taken. **c)** Representative slab from Doyon (18KN05). **d)** Outline of the slab in C to highlight the distribution of pyrite in the sample. **e)** High-grade mineralized vein from Grand Duc (18KN03), note the greater proportion of chalcopyrite compared to Doyon samples (frame C) and other Grand Duc veins (F-G). **f)** Moderate-grade mineralized vein from Grand Duc (18KN07). C) Moderate-grade mineralized vein from Grand Duc (18KN09). White dashed lines in frames A and B represent the surface exposure of the mineralized vein at surface.

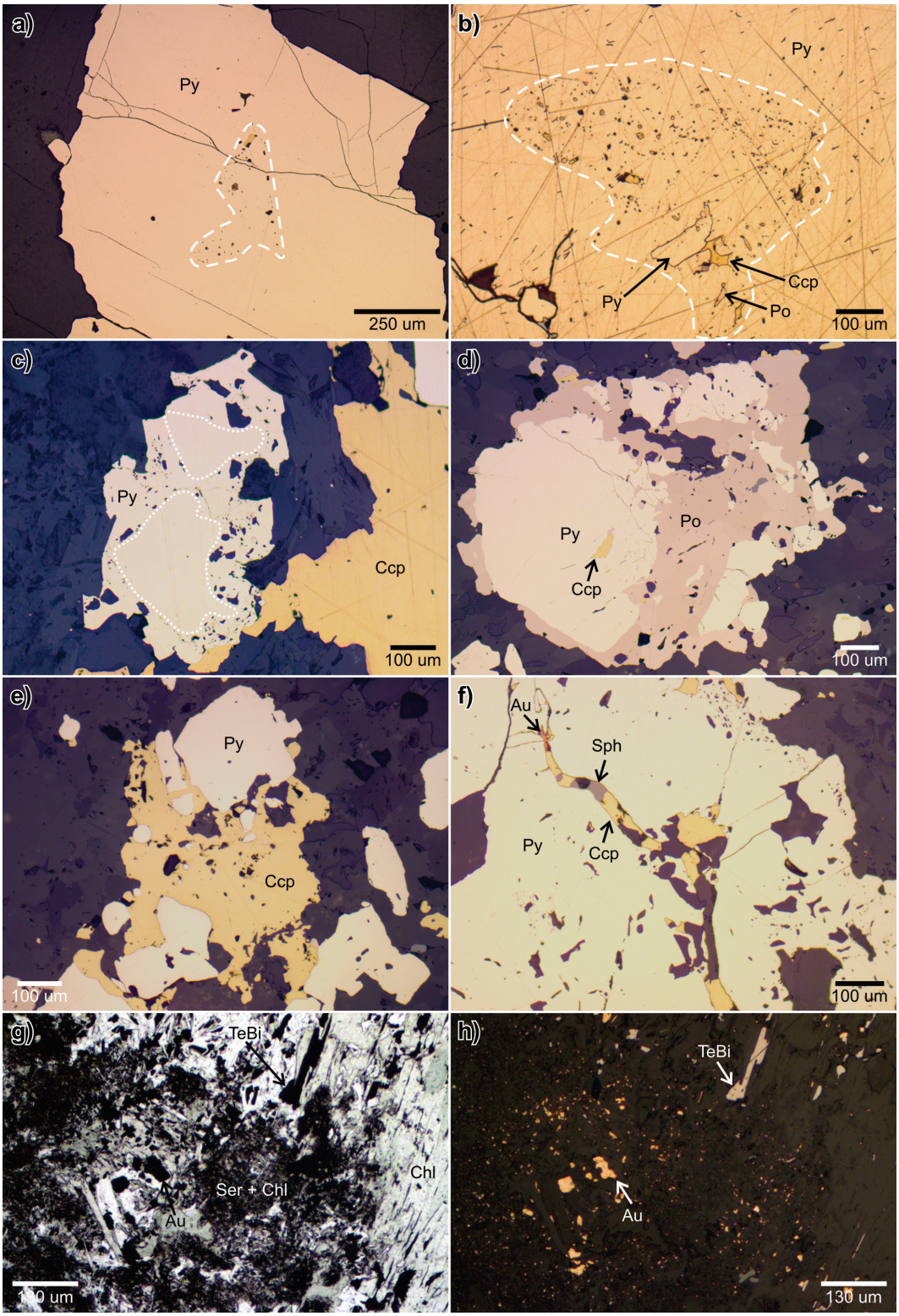

Figure 3: Representative sulphide textures from Doyon (A-B) and Grand Duc (C-H). **a)** Zoned pyrite grain from Doyon with an inclusion-rich core and an inclusion-free rim (18KN06; reflected light [RL]). **b)** Pyrite grain from Doyon that was etched with nitric acid. Note that the etching effected the inclusion-rich core and the inclusion-free rim to the same degree (18KN05; RL). **c)** Pyrite from Grand Duc that has an inclusion-free core and a sieved rim (18KN03; RL). **d)** Pyrite from Grand Duc that is replaced by pyrrhotite indicated pyrrhotite is forming after pyrite (18KN03; RL). **e)** Pyrite from Grand Duc that is replaced by chalcopyrite indicating chalcopyrite is forming after pyrite (18KN03; RL). **f)** A fracture in pyrite from Grand Duc that is infilled with chalcopyrite, sphalerite, and gold (18KN03; RL). E) Representative image of the patchy chlorite alteration from Grand Duc (18KN03; plane polarized light). F) Same image as in E but taken in RL to show the presence of gold and tellurobismuthite. Au = gold; Chl = Chlorite; Py = pyrite; Ccp = chalcopyrite; Po = pyrrhotite; Ser = sericite; Sph = sphalerite; TeBi = tellurobismuthite.

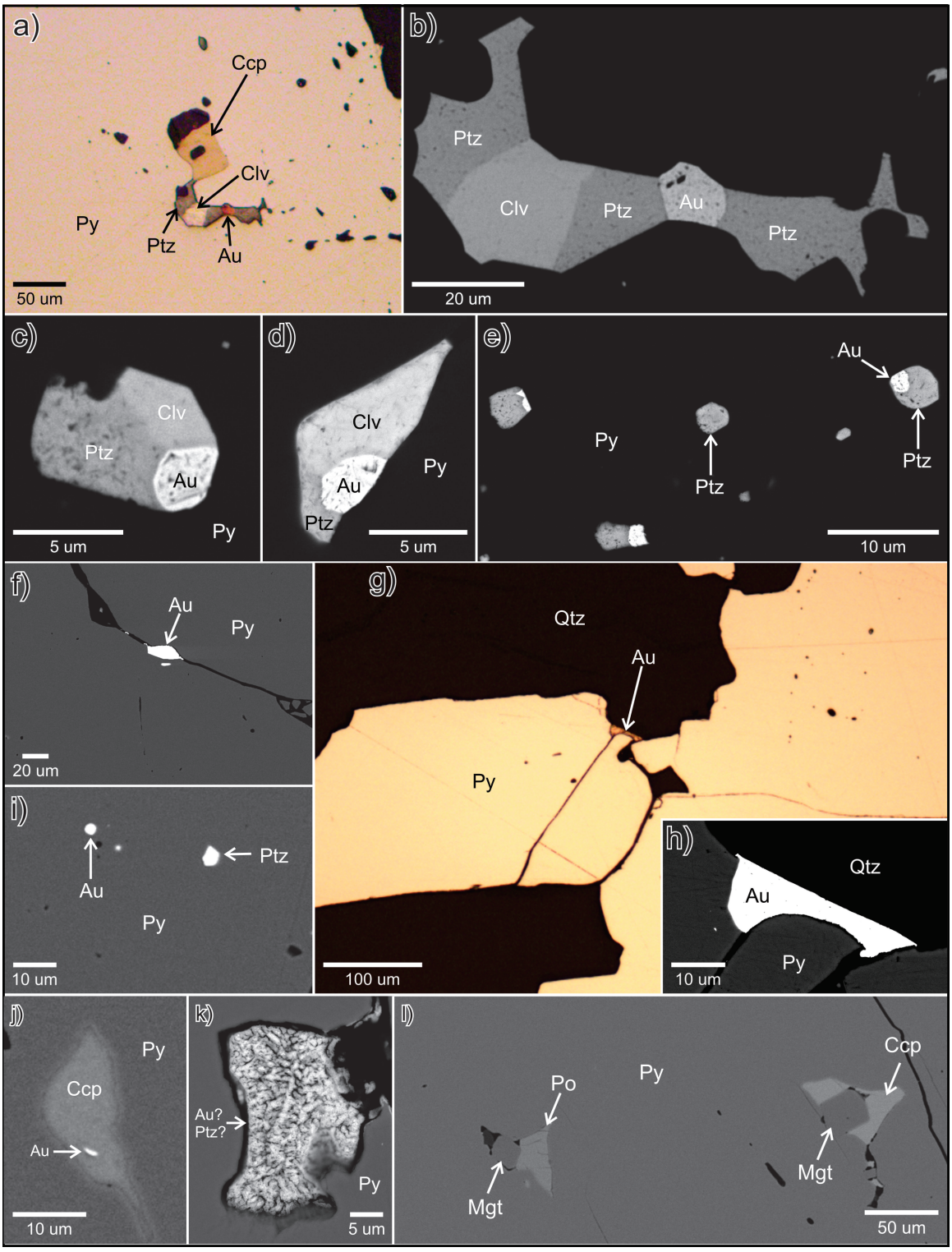

Figure 4: Representative reflected light and SEM-BSE images of the various textural settings of gold in mineralized veins from the Doyon West Zone. **a-b)** Composite inclusion in pyrite composed of gold, petzite, calaverite, and chalcopyrite. Note the planar grain edges formed by the ore minerals suggestive of open space filling. **c-d)** Composite inclusions in pyrite composed of gold, petzite, and calaverite. **e**) Multiple composite inclusions composed of gold and petzite as well as inclusions of only petzite present in pyrite. **f)** Gold present along a fracture running through pyrite. **g-h)** Gold present along the grain boundary of quartz and pyrite. **j)** Inclusion of chalcopyrite in pyrite that contains a small grain of gold. **k)** Ore mineral occurring along a fracture in pyrite that has a composition that is a mixture gold and petzite. **l)** Multiple voids in pyrite infilled with pyrrhotite, chalcopyrite, and magnetite. Au = gold; Clv = calaverite; Ccp = chalcopyrite; Mgt = magnetite; Po = pyrrhotite; Py = pyrite; Ptz = petzite; Qtz = quartz.

Table 2: Representative SEM-EDS analyses of ore minerals from the Doyon west zone

Texture	Mineral	Au (at. %)	Ag	Te	Pb
Composite inclusion in Py	Gold	88.8	11.2		
	Ptz	16.4	50.5	33.1	
	Clv	35.6		64.4	
Composite inclusion in Py	Gold	88.5	11.5		
	Ptz	17.5	49.7	32.8	
Composite inclusion in Py	Gold	79.9	19.1		
	Ptz	17.7	49.9	32.5	
	Alt			52.3	47.7
Py fracture	Gold	88.8	11.2		
Py fracture	Gold	87.9	12.1		
Py-qtz boundary	Gold	88.2	11.8		
Inclusion in Py	Gold	82.1	17.9		
Qtz fracture	Gold	82.4	17.6		
Inclusion in Ccp	Gold	82.2	17.8		
Composite inclusion in Py	Ptz	17.4	50.3	32.3	
	Clv	33.4	66.6		
Composite inclusion in Py	Ptz	12.6	53.7	33.7	
	Hs		62.4	37.6	
Composite inclusion in Py	Ptz	17.6	49.4	33	
	Hs		61.8	38.2	
Inclusion in Py	Ptz	17.7	49.5	17.8	
Inclusion in Qtz	Ptz	16.9	50.5	32.6	
Py grain boundary	Ptz	10.3	53.5	36.2	
Composite inclusion in Qtz	Ptz	17.4	50.6	32	
	Hs	66.6	33.4		
Inclusion in Py	Clv	34.1	65.9		
Qtz fracture	Clv	34.7	65.3		
Py fracture	Gold-Ptz	59.7	27.2	13.1	
Py fracture	Gold-Ptz	40.2	56.3	3.5	
Qtz fracture	Gold-Ptz	38.8	47.7	13.5	

Abbreviations: Alt = altaite; Ccp = chalcopyrite; Clv = calaverite; Hs = hessite; Ptz = petzite; Py = pyrite; Qtz = quartz; Gold-Ptz = gold-petzite intergrowth

Figure 5: Representative SEM-BSE images of the various textural settings of ore in mineralized veins from the Grand Duc deposit. **a)** Sieved grain of pyrite that contains an inclusion of gold along the outer grain margin. Numerous grains of tellurobismuthite and a grain of altaite occur along the grain margin of pyrite (18KN03). **b)** Fracture in pyrite that has been infilled with gold, sphalerite, and chalcopyrite. Note how gold extends into fractures perpendicular to the main fracture (18KN03). **c)** Gold occurring along the grain boundaries of pyrrhotite and calcite. Numerous grains of tellurobismuthite and altaite occur as inclusions filling in voids in pyrite (). **d)** Sieved area in pyrrhotite that has been infilled with gold, tellurobismuthite, and calcite (18KN03). **e)** Gold occurring along fractures in calcite (18KN03). **f)** Composite and individual grains of gold and tellurobismuthite occurring in strong, patchy chlorite alteration (18KN03). **g-h)** Grains of gold and tellurobismuthite occurring along grain boundaries of chlorite and sericite (18KN03). **i)** Composite inclusion filling in a void in pyrite composed of gold, chalcopyrite, sphalerite, and pyrrhotite (18KN07). **j)** Composite inclusion in pyrite composed of pyrrhotite, gold, petzite, tellurobismuthite, and native Te (18KN09). **k)** Composite inclusion in pyrite composed of gold, petzite, and calaverite (18KN07). **l)** Magnetite, pyrrhotite, chalcopyrite, calcite, and chlorite filling in voids in pyrite (18KN07).

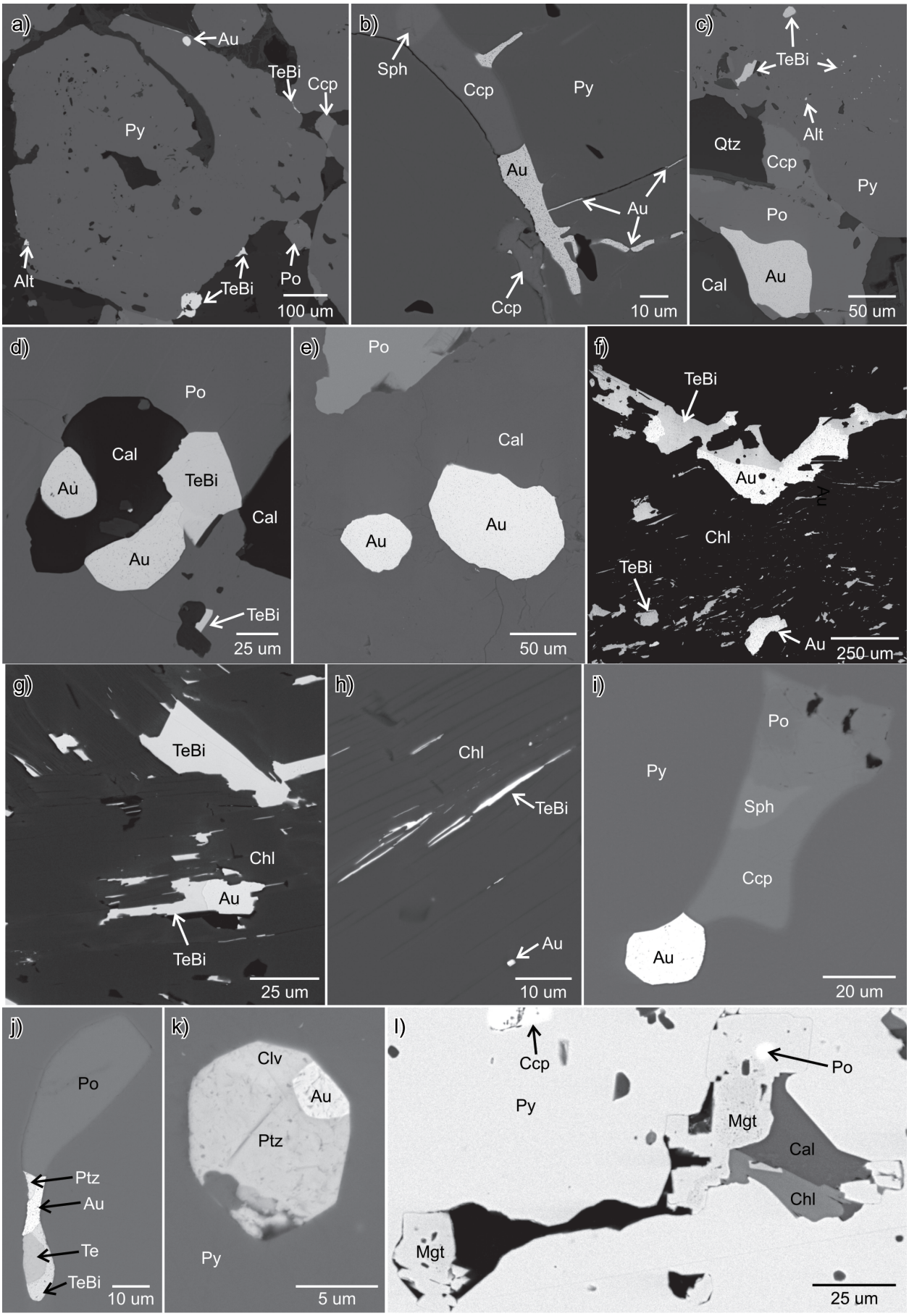
a)
Au
TeBi
Ccp
Py
Alt
TeBi
Po
100 um
b)
Sph
Ccp
Py
Au
Au
Ccp
10 um
c)
TeBi
Alt
Qtz
Ccp
Py
Po
Cal
Au
50 um
d)
Po
Cal
Au
TeBi
Cal
Au
TeBi
25 um
e)
Po
Cal
Au
Au
50 um
f)
TeBi
Au
Alt
Chl
TeBi
Au
250 um
g)
TeBi
Chl
Au
TeBi
25 um
h)
Chl
TeBi
Au
10 um
i)
Po
Py
Sph
Ccp
Au
20 um
j)
Po
Ptz
Au
Te
TeBi
10 um
k)
Clv
Au
Ptz
Py
5 um
l)
Ccp
Po
Py
Mgt
Cal
Chl
Mgt
25 um

Gangue mineralogy in mineralized veins from Grand Duc consists predominately of quartz and carbonate minerals (mainly Mg-bearing ankerite with minor amounts of Fe-Mn-bearing calcite) with minor amounts of chlorite and sericite (Fig. 4E-G). Proportions of quartz and carbonate vary from vein to vein, comprising 20-40 vol% and 60-80 vol% of the gangue, respectively. Carbonate post-dates quartz as it is observed to have planar crystal boundaries with quartz, suggesting open space filling, and carbonate is present interstitial to quartz. Minor amounts of chlorite occur in mineralized veins and generally is only present in contact with sulphides along vein margins with the wallrock or in wallrock fragments within the vein. Muscovite is closely associated with chlorite and can be partially to completely replaced by chlorite.

Mineralized veins at Grand Duc contain the sulphide assemblage pyrite + chalcopyrite + pyrrhotite ± sphalerite and sulphide proportions vary from vein to vein, depending on the grade of the vein.

High-grade vein:

Pyrite occurs as large aggregate masses composed of multiple grains or as individual, isolated grains. Individual pyrite grains range in size from 40 to 2000 μm, but grains predominately range from 100 to 500 μm. In some pyrite grains, cores are moderately sieved while the rims are clean and sieve-free but other grains show sieve-free cores and sieved rims, suggesting multiple stages of pyrite growth (Figs. 3C, 5A). After etching samples with nitric acid, some pyrite grains displayed zoning with non-etch cores and weakly etched rims. However, the majority of grains were variably etched and no qualitative correlation could be made between grains that were etched versus grains that were not etched. Interestingly, inclusions of tellurobismuthite (Bi2Te3) in pyrite (*see* SEM results below) that were exposed at surface prior to acid etching were no longer present after etching, suggesting that they were plucked out/dissolved during the etching. Pyrrhotite occurs along grain boundaries/margins and fractures of pyrite and filling in voids in sieved pyrite (Fig. 4D). Pyrrhotite can display sieve texture but are less the sieved compared to pyrite. Chalcopyrite shares the same textural settings as pyrrhotite in the high-grade vein (Fig. 4E-F). Both pyrrhotite and chalcopyrite locally display textures that are indicative of replacing pyrite in the high-grade vein (Fig. 4D-E). Rare sphalerite is present, occurring in fractures of pyrite and along grain margins of pyrite, pyrrhotite, and chalcopyrite (Fig. 4F).

Gold occurs in five different textural settings within the vein: 1) filling in voids in sieved pyrite (Fig. 5A); 2) along fractures in pyrite with or without pyrrhotite, chalcopyrite, and/or sphalerite (Fig. 5B); 3) along grain boundaries of pyrrhotite, chalcopyrite, and/or sphalerite or quartz and/or carbonate (Fig. 5C); 4) filling in voids in sieved pyrrhotite (Fig. 5D); and 5) along grain boundaries and/or fractures of quartz and carbonate (Fig. 5E).

In addition to gold present within quartz-carbonate veins, gold is associated with strong chlorite and sericite alteration in the wallrock with minor pyrite, pyrrhotite, and chalcopyrite (Fig. 5F-H). Tellurobismuthite (see SEM results below) is also present in the strong chlorite alteration halo, sharing similar grain morphology to gold and can occur as composite grains with gold (Fig. 5F-H). Both gold and tellurobismuthite appear to be present along grain boundaries of chlorite and sericite (Fig. 5G-H).

The textural features and semi-quantitative composition of ore minerals were determined by SEM-BSE and -EDS. Ore minerals identified include gold (as electrum), tellurobismuthite, altaite (PbTe), and tsumoite (BiTe) or tetradymite (Bi_2Te_2S). Due to the small grain size and close association with base metal sulphides, it is difficult to determine if the mineral is tsumoite or tetradymite. Representative SEM-EDS analyses of ore minerals are presented in Table 3. The Au:Ag ratio (at. %) of gold ranges from 81:19 to 91:9 and is variably across all textural settings (Table 3). Composite grains of gold + tellurobismuthite are present in the strong chlorite alteration as well as in voids in sieved pyrite (Fig. 5F-G). Composite grains of gold + altaite are also present but were only observed in the chlorite alteration. Tellurobismuthite and altaite share the same textural settings as gold, while tsumoite (or tetradymite) is predominately observed in the chlorite alteration with one instance of it observed filling in a void in sieved pyrite.

Moderate-low grade veins:

Pyrite in moderate to low-grade veins is relatively coarser-grained (100-2000 um) and shows more distinct sieved cores and clean rims compared to pyrite from the high-grade vein. A second generation of pyrite is present occurring as clean, sieve-free grains along the margins of sieved-pyrite. Similar to the high-grade veins, individual pyrite grains were variably affected by nitric acid etching and no qualitative correlations could be made. Pyrrhotite and chalcopyrite are present in trace amounts filling in voids in sieved pyrite and rarely, chalcopyrite occurs on the margins of pyrite.

In one of the low-grade veins (18KN09) two generations of pyrite-quartz-carbonate veins crosscut each other. The gangue and sulphide mineralogy of both veins is comparable to all other veins described above, but textural differences exist between the two veins. Pyrite size and morphology are similar between the two veins but one vein contains strongly sieved and fractured pyrite, while the other vein contains relatively “clean”, weakly sieved, and fractured pyrite. Pyrite in both veins contains inclusions of pyrrhotite and chalcopyrite that are filling in voids in the sieved areas. Crosscutting relationships suggest the “clean” pyrite vein is younger than the strongly sieved pyrite vein.

Table 3: Representative SEM-EDS analyses of ore minerals from Grand Duc

Sample/Grade	Location	Texture	Mineral	Au (at. %)	Ag	Bi	Te	Pb
18KN03/	Patchy Chl Alt	Chl-Ser grain boundary	Gold	85.2	14.8			
High grade	Patchy Chl Alt	Chl-Ser grain boundary	Gold	88.3	11.7			
	Patchy Chl Alt	Composite grain; Chl grain boundaries	Gold	84.5	15.5			
			Alt				52.5	47.5
	Patchy Chl Alt	Composite grain; Po-Chl grain boundary	Gold	88.6	11.4			
			TeBi			44.9	55.1	
	Patchy Chl Alt	Chl-Ser grain boundary	TeBi			39.8	60.2	
	Patchy Chl Alt	Chl grain boundaries	TeBi			41.5	58.5	
	Patchy Chl Alt	Chl grain boundaries	Alt				52.6	47.4
	Patchy Chl Alt	Chl grain boundaries	Ts/Tt			50.1	49.9	
	Patchy Chl Alt	Chl grain boundaries	Ts/Tt			50.3	49.7	
	Vein	Po-Ccp grain boundary	Gold	84.4	15.6			
	Vein	Po-Py grain boundary	Gold	83.4	16.6			
	Vein	Ccp-Py grain boundary	Gold	85.5	14.5			
	Vein	Sph-Py grain boundary	Gold	84.7	15.3			
	Vein	Po-Cal grain boundary	Gold	85.4	14.6			
	Vein	Fracture in Py	Gold	84.4	15.6			
	Vein	Fracture in Py w/ Sph and Ccp	Gold	83.8	16.2			
	Vein	Py-Qtz grain boundary	Gold	85.5	14.5			
	Vein	Void in Py	Gold	87.4	12.6			
	Vein	Fracture in Qtz	Gold	86.7	13.3			
	Vein	Fracture in Qtz	Gold	86.5	13.5			
	Vein	Composite grain; Void in Py	Gold	88.4	11.6			
			TeBi			40.2	59.8	
18KN07/	Vein	Void in Py	Gold	92.2	7.8			
Moderate grade	Vein	Composite grain; Void in Py	Gold	88.8	11.2			
			Clv	35.2			64.8	
	Vein	Void in Py	TeBi			39.6	60.4	
	Vein	Void in Py	Alt				50.9	49.1
	Vein	Py-Py grain boundary	Gold	71.2	28.8			
	Vein	Py-Qtz grain boundary	Gold	73.1	26.9			
18KN09/	Sieved pyrite vein	Void in Py	Gold	93.3	6.7			
Moderate grade	Sieved pyrite vein	Composite grain; Void in Py	Gold	85.1	14.9			
			Ptz	17.8	49.4		32.8	
			TeBi			39.6	60.4	
			Te				100	
	Sieved pyrite vein	Py-Py grain boundary	Gold	74.4	25.6			
	Sieved pyrite vein	Fracture in Qtz	Gold	69.1	30.9			
	Sieved pyrite vein	Composite grain; Void in Py	Voly		25.7	24.9	49.4	
			Hs		67.5		32.5	
	Sieved pyrite vein	Void in Py	TeBi			40.6	59.4	
	Clean pyrite vein	Fracture in pyrite	Gold	71.7	28.3			
	Clean pyrite vein	Py-Py grain boundary	Gold	84.5	15.5			

Abbreviations: Alt = altaite; Cal = calcite; Ccp = chalcopyrite; Chl = chlorite; Clv = calaverite; Hs = hessite; Ptz = petzite; Py = pyrite; Qtz = quartz; Ser = sericite; Sph = sphalerite; Te = native Te; TeBi = tellurobismuthite; Ts/Tt = Tsumoite or Tetradymite Voly = volynskite

Representative analyses of gold and accessory minerals are presented in Table 3. Gold occurs in three textural settings: 1) filling in voids in sieved pyrite (Fig. 5I-K); 2) along grain boundaries of pyrite and gangue; and 3) along fractures in pyrite, quartz, and carbonate. The Au:Ag (at%) ratio of gold ranges from 60:40 to 78:22 for grains that occur along grain boundaries and fractures but gold occurring in voids within sieved pyrite is more Au-rich with Au:Ag ratio between 85:15 to 93:7 (Table 3). In sample 18KN09, gold occurs in both pyrite-quartz-carbonate vein generations along grain boundaries and fractures, but gold only occurs in voids in the strongly sieved pyrite vein. Gold can be present by itself in sieved pyrite voids or associated with base metals sulphides (chalcopyrite ± pyrrhotite ± sphalerite; Fig. 5J) and/or accessory minerals (e.g. calaverite). Accessory minerals present in the moderate-low grade veins include: tellurobismuthite, petzite, calaverite, altaite, volynskite ($AgBiTe_2$), hessite, and native Te. All accessory minerals occur in voids in pyrite, except for hessite, which also occurs along pyrite grain boundaries (Fig. 5I-K). Numerous types of composite inclusions occur in pyrite voids such as, calaverite + gold, petzite + calaverite, tellurobismuthite + petzite, volynskite + hessite, and gold + petzite + tellurobismuthite + native Te + chalcopyrite (Fig. 5I-K). No accessory minerals were observed in the "clean" pyrite vein in sample 18KN09. Other minerals observed in sieved pyrite include magnetite, which occurs in voids with pyrrhotite, chlorite, and/or carbonate (Fig. 5L).

LA-ICP-MS trace element mapping of pyrite

Two pyrite grains from the Doyon West Zone and four from Grand Duc (two from the high grade vein [18KN03] and two from a lower grade vein [18KN07]) were mapped by LA-ICPMS. Representative pyrite trace element maps from Doyon and Grand Duc are shown in Figure 6 and 7, respectively. Element maps show variable patterns between the two deposits, but are relatively consistent within each system.

For pyrite from the Doyon West Zone (Fig. 6), trace element maps display complex metal zonation involving four distinct stages of metal association. Initially, pyrite is trace element poor with no notable enrichments in the core (Stage 1) followed by Stage 2 which is defined by enrichment in As. Stage 3 represents the ore-metal assemblage with Au-Ag-Te-Bi-Pb followed by late stage Co-Ni (Stage 4). Selenium is at or below detection limits throughout the majority of the pyrite grain, but is above detection in a Co-rich area in Stage 4 (top right corner of pyrite grain). Zinc, Sb, In, Cd, and Sn are all depleted in pyrite from Doyon.

Pyrite from Grand Duc can show nice core to rim zoning (Fig. 7) but also displays complex zoning similar to pyrite from Doyon, but with different metal associations for each stage. Stage 1 metal associations for Grand Duc are characterized by Co-Se-As followed by an increase in As and Co(?), while Se concentration stays relatively the same in Stage 2 compared to Stage 1. Stage 3 in Grand Duc pyrite also represents the ore-metal assemblage with a sharp rim forming around the Co-As-Se core. Stage 3 is characterized by a sharp increase in As with accompanied with the appearance of Au-Ag-Bi-Te-Sb-Pb-Ni-Cu-Zn-Sn-Cd-In. Stage 4 is characterized by a similar element assemblage as Stage 3 but in relatively lower concentrations.

Sulphur isotope composition of pyrite, pyrrhotite, and chalcopyrite

Preliminary S isotope measurements were collected on representative pyrite from Doyon and pyrite, pyrrhotite, and chalcopyrite from Grand Duc. A summary of all $\delta^{34}S$ values are presented in Table 4. Overall pyrite from Doyon has relatively consistent $\delta^{34}S$ ranging from +1.1 to +4.8 ‰ (+2.6 ± 0.9 ‰; 1σ; n=29; Fig. 8A) and no major differences were observed between the different pyrite generations. However, one pyrite grain showed subtle $\delta^{34}S$ variation from core to rim and a pyrite inclusion within this pyrite grain with heavier values (Fig. 8B). Rim $\delta^{34}S$ values of this pyrite grain are between +1.3 and +2.6 ‰, while the core ranges from +1.9 to +3.3 ‰ and the pyrite inclusion has $\delta^{34}S$ between +3.7 and +4.8 ‰.

Pyrite from the high-grade Grand Duc vein has $\delta^{34}S$ values ranging from -0.6 to +2.1 ‰ (+0.9 ± 0.7 ‰; n=19; Fig. 8A, C) with small variations in $\delta^{34}S$ values for the different textural generations and between core and rim of individual grains. Pyrite from the lower grade veins at Grand Duc has similar $\delta^{34}S$ composition (+0.8 ± 0.5 ‰; n=28) compared to the high-grade vein. Pyrrhotite and chalcopyrite from the high-grade sample have average $\delta^{34}S$ values of +1.7 ± 0.6 ‰ (n=15) and +1.6 ± 0.2 ‰ (n=11), respectively. No differences are shown in $\delta^{34}S$ values from pyrrhotite in the vein (~1.5 ± 0.6 ‰; n=11), compared to pyrrhotite in the strong chlorite alteration halo (~1.7 ± 0.6 ‰; n=6). Similarly, measurements on chalcopyrite from the vein and the strong chlorite alteration halo show overlapping $\delta^{34}S$ values with ~+1.6 ± 0.2 ‰ (n=7) and +1.7 ± 0.2 ‰ (n=4), respectively.

PRELIMINARY INTERPRETATIONS AND CONCLUSIONS

Mineralization at Doyon and Grand Duc have some similarities but distinct differences in the alteration, accessory mineral and base metal sulfide assemblages, trace element composition and zoning in pyrite, and bulk rock geochemistry are noted.

In terms of major minerals that compose mineralized veins in each system, both are predominately composed of quartz and pyrite but Grand Duc has a large carbonate component to the vein, while no carbonate minerals were observed at Doyon. Veins at Grand Duc also have a higher,

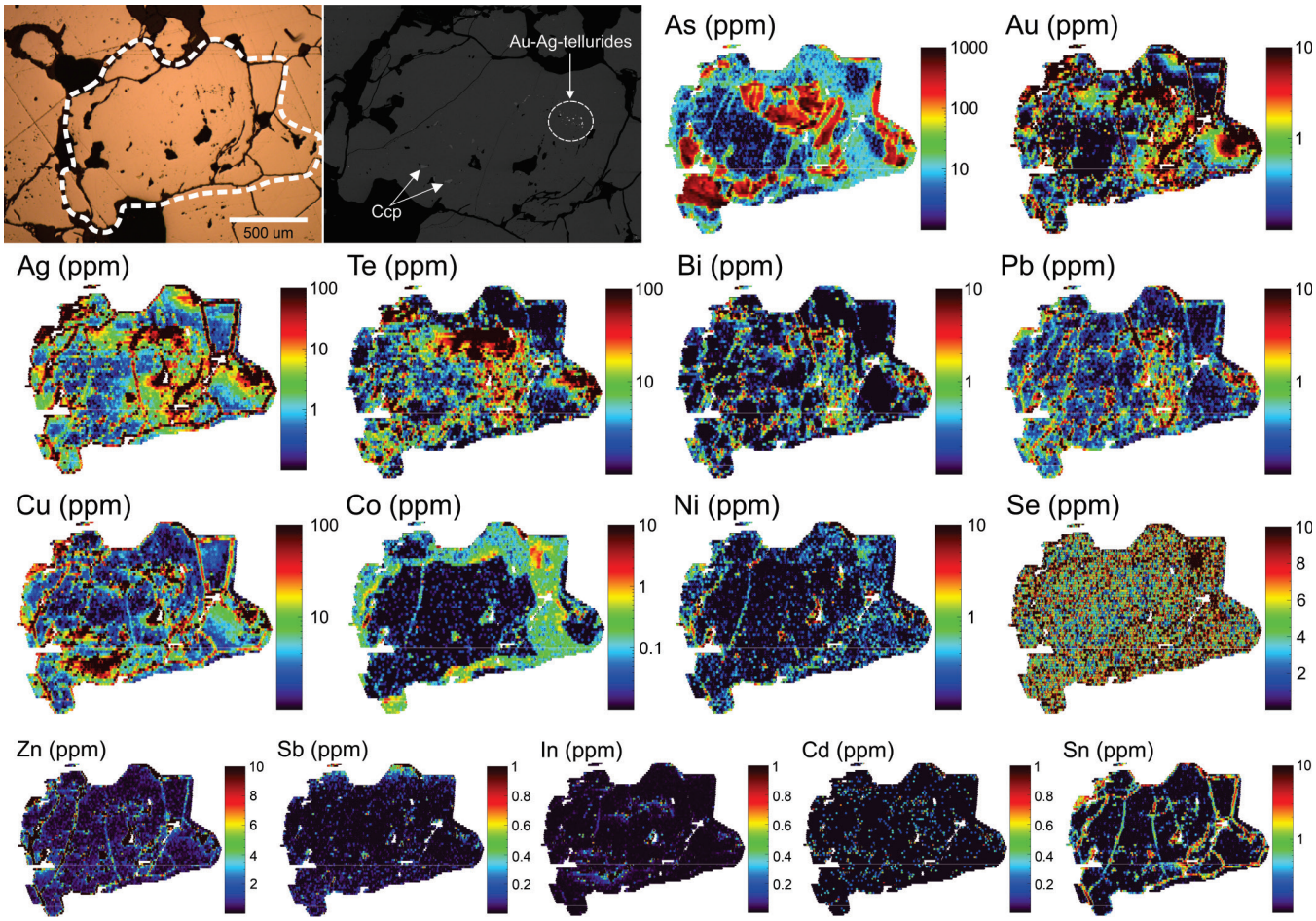

Figure 6: Reflected light, SEM-BSE image, and trace element LA-ICPMS map of pyrite from the Doyon West Zone (18KN05).

and more complex, base metal sulphide (pyrrhotite, chalcopyrite, and sphalerite) component than veins at Doyon (cf. pyrite ± trace pyrrhotite, chalcopyrite). Some accessory ore minerals are present at both Doyon and Grand Duc (petzite, calaverite, hessite and gold). The Au:Ag ratio is fairly consistent between the two systems as well. However, numerous accessory ore minerals identified in Grand Duc veins are not present at Doyon, notably Bi- and Pb-tellurides (tellurobismuthite, native Te, volynskite, tsumoite or tetradymite, and altaite). Additionally, at Grand Duc, a strong chlorite alteration halo occurs on the margins of mineralized veins with abundant gold and tellurides in the alteration halo; this style of mineralization is not observed at Doyon.

Pyrite trace element maps show variable patterns between the two systems but the ore metal associations are relatively the same. Gold in both systems is associated with Ag-Te-Bi-Pb enrichment, but at Grand Duc the Au is associated with a larger and more complex suite of accessory elements (As-Sb-Ni-Cu-Zn-Sn-Cd-In). Based on petrographic observations and pyrite trace element maps, gold mineralization at both Doyon and Grand Duc is relatively late compared to initial vein and pyrite formation as is commonly observed in many orogenic, and magmatic-epithermal gold systems (Cook et al., 2009; LeForte et al., 2011; Velásquez et al., 2014; Franchini et al., 2015; Fougerouse et al., 2016; Sykora et al., 2018; Hastie et al., 2020).

The occurrence of Au concentrating along the rim of pyrite and associated with an enrichment in As and other metals (Sb-Ag-Bi-Te) from Grand Duc shares similarities with porphyry and epithermal deposits (LeForte et al., 2011; Petersen and Mavrogenes, 2014; Franchini et al., 2015; Sykora et al., 2018). Additionally, the overall metal association of Au with Te and Bi is a hallmark of other intrusion-related gold systems (e.g. Lang and Baker, 2001; Maloof et al., 2001; Hart et al, 2004; Mair et al., 2006, 2011). In these porphyry and epithermal systems, the metal-enriched pyrite rim could be the result of fluid boiling, causing fluctuations in the stability of gold-bearing aqueous complexes. Gold is most commonly carried as a bisulphide complex and when boiling occurs, H_2S strongly partitions into the non-aqueous phase (i.e. vapor phase) therefore destabilizing gold bisulphide complexes and promoting gold precipitation (Huang et al., 1985; D'Amore and Truesdell, 1988; Naden and Shepherd, 1989). In situ S isotope work on these

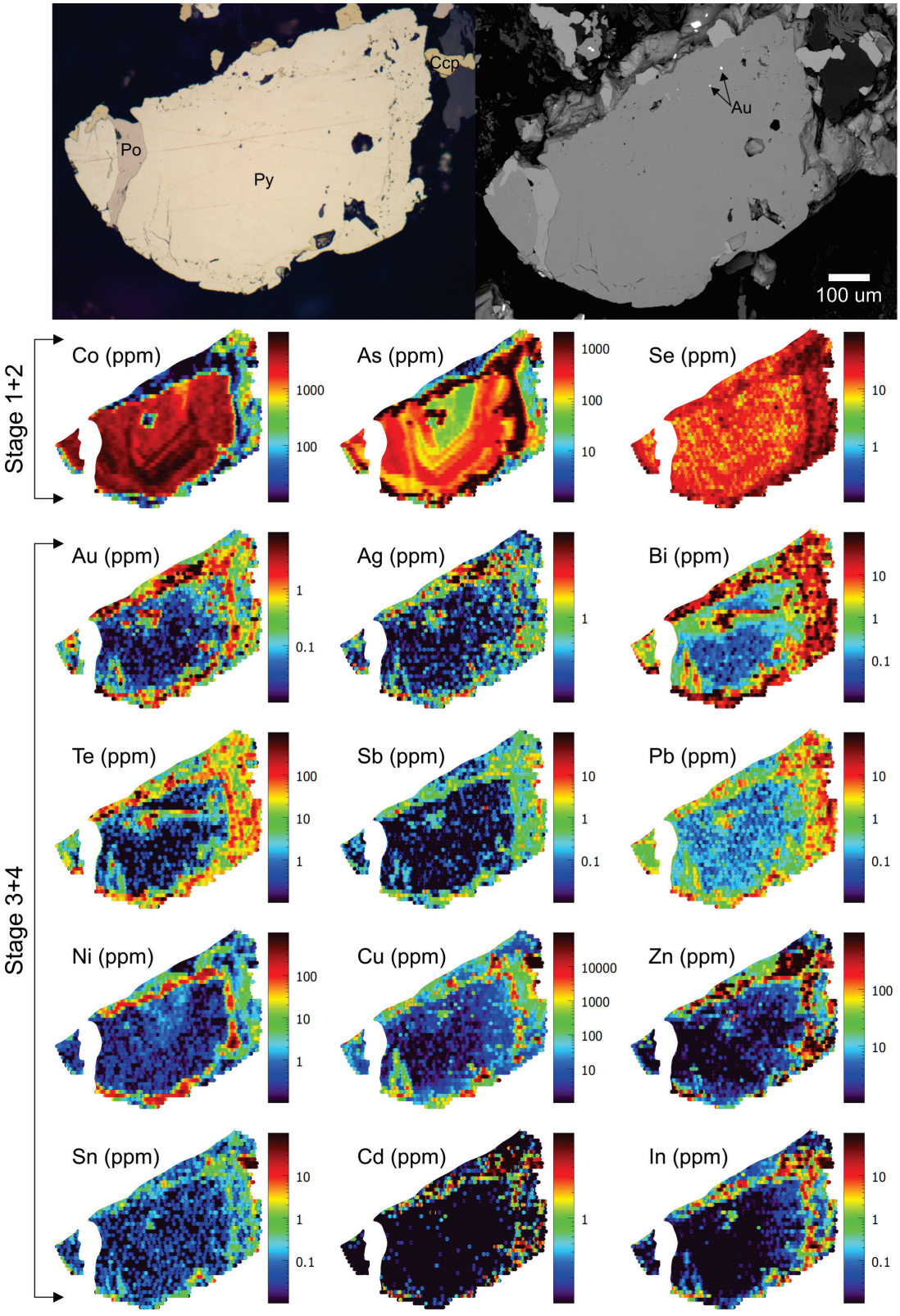

Figure 7: Reflected light, SEM-BSE image, and trace element LA-ICPMS map of pyrite from Grand Duc (18KN03). Note, pyrite was etched with nitric acid.

Table 4. Summary of pyrite, pyrrhotite, chalcopyrite δ34S (‰ VCDT) composition

Sample	Sample location/ description	Mineral	Avg. $\delta^{34}S$	1σ	σ_M	min	max	n
18KN03	Grand Duc; high grade mineralization	Ccp	1.6	0.2	0.05	1.4	1.9	11
18KN03	Grand Duc; high grade mineralization	Po	1.7	0.6	0.20	0.5	2.7	15
18KN03	Grand Duc; high grade mineralization	Py	0.9	0.7	0.20	-0.6	2.1	19
18KN07	Grand Duc; low grade mineralization	Py	1.0	0.4	0.10	0.5	1.9	13
18KN09	Grand Duc; low grade mineralization	Py	0.6	0.5	0.10	-0.4	1.8	15
18KN05	Doyon West Zone; high grade mineralization	Py	2.6	0.9	0.20	1.1	4.8	29
σ_M - standard error of the mean; Ccp = chalcopyrite; Po = pyrrhotite; Py = pyrite								

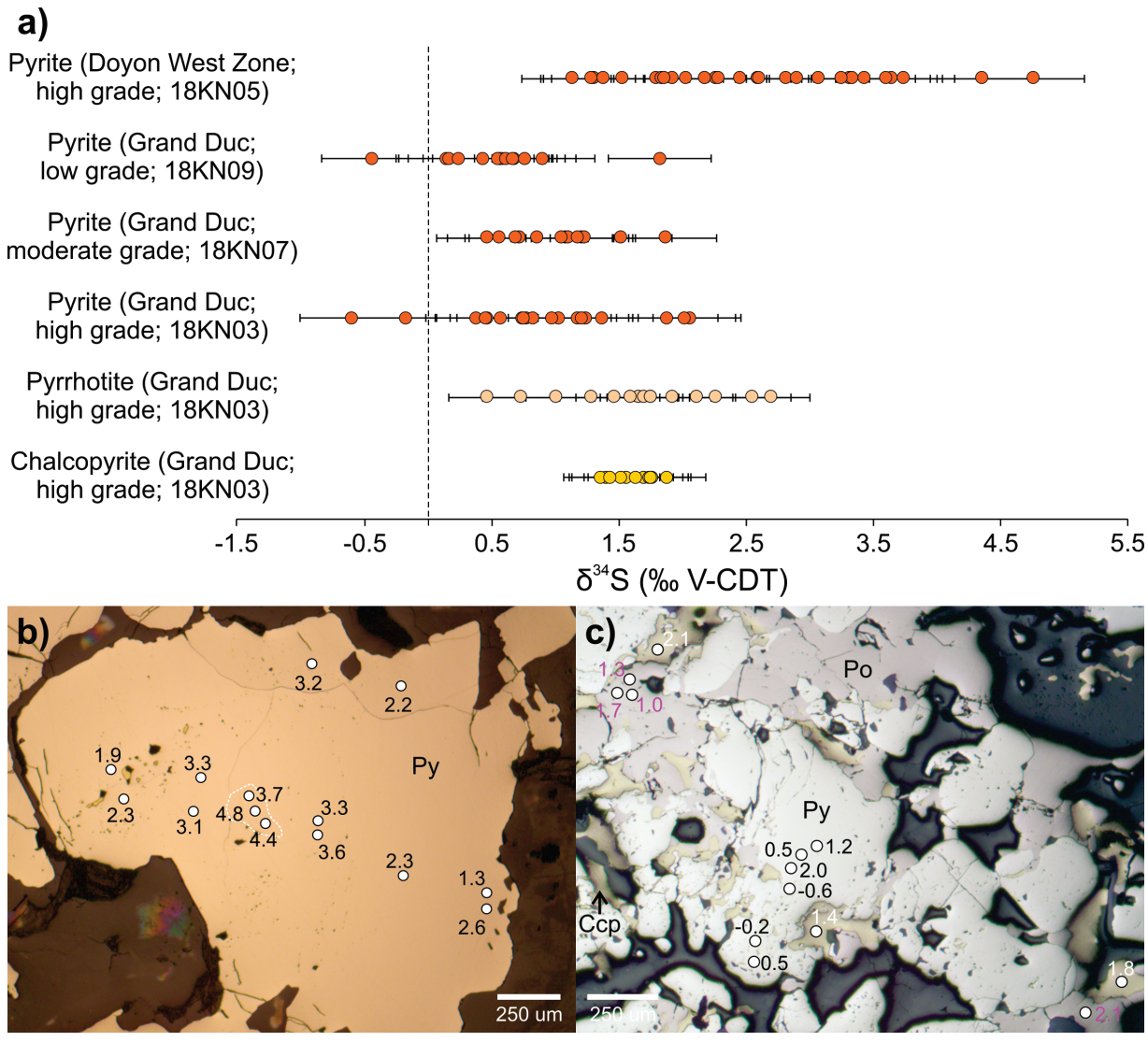

Figure 8: Select spot location $\delta^{34}S$ values for pyrite from Doyon and pyrite, pyrrhotite, and chalcopyrite from Grand Duc and a graphical summary of $\delta^{34}S$ composition for all samples from Doyon and Grand Duc. **a)** Graphical summary of all $\delta^{34}S$ analyses from Doyon and Grand Duc. Error bars represent 1σ. **b)** Pyrite from Doyon (18KN05), note the relatively higher $\delta^{34}S$ values in the core compared to the edge of the grain. The white dashed line near the core outlines a small pyrite inclusion. **c)** Pyrite (black text), pyrrhotite (purple text), and chalcopyrite (yellow text) $\delta^{34}S$ values from Grand Duc (18KN03).

metal-bearing and metal-barren zones could identify boiling processes because during boiling, S^{34} is preferentially enriched in the vapour phase compared to S^{32}, causing the aqueous fluid phase to become depleted in S^{34} and would therefore have a relatively lower $\delta^{34}S$ value than the original fluid (McKibben and Eldridge, 1990). Therefore, pyrite precipitating from an aqueous phase syn-boiling would have a relatively lower $\delta^{34}S$ than pyrite precipitating from pre-boiling fluids (McKibben and Eldrigde, 1990; Petersen and Mavrogenes, 2014). However, based on preliminary $\delta^{34}S$ values of pyrite cores and rims, we do not observe consistently lower $\delta^{34}S$ values on the rim, indicating boiling may not be a crucial depositional process for Au and other metals. Additional $\delta^{34}S$ work (see Next Steps section below) will be targeting specific trace element-rich and -poor zones to provide more detail on any $\delta^{34}S$ variability between different trace element zones in pyrite.

Dissolution reprecipitation processes involve the liberation of Au (and other metals such as Ag, Te, Bi) from the pyrite lattice during dissolution of pyrite and reconcentrate these elements into discrete mineral phases that commonly precipitate into voids and fractures created during dissolution (e.g. Cook et al., 2009; Velásquez et al., 2014; Fougerouse et al., 2016; Hastie et al., 2020). With Au-Ag-Te-bearing minerals (i.e. electrum, petzite, calaverite, hessite) and pyrite trace element maps for Au-Ag-Te-Bi showing a very strong correlation with sieved pyrite and fractures, it is likely that coupled dissolution-reprecipitation processes were an important process in the development of the Doyon ore system. Pyrite at Doyon does not appear to have been initially enriched in Au-Ag-Te-Bi but this does not mean coupled dissolution-reprecipitation processes were not occurring as it could suggest highly efficient liberation of those metals from early pyrite. Mineralized veins at Doyon are interpreted to have formed prior to deformation events as these events modified the veins and their alteration halos, indicating that the mineralization is intrusion-related (Gosselin, 1998). In this study, while identification of coupled dissolution-reprecipitation processes is likely related to deformation events post-vein formation, the Doyon Au-Bi-Te endowment is consistent with an intrusion-related mineralizing system (e.g. Lang and Baker, 2001; Maloof et al., 2001; Hart et al, 2004; Mair et al., 2006, 2011). Therefore, the results of this study further implicate the MIC and its associated volcanics as a possible source for ore metals. Further studies to explore this relationship are warranted.

NEXT STEPS

In the Archean, the S isotope composition of all S reservoirs were similar and had a narrow range ($\delta^{34}S_{V\text{-}CDT} \sim 0$ ‰) because the S cycle was dominated by igneous S; therefore, in Archean ore-forming systems, the use of $\delta^{34}S$ to discriminate sulphur source is of limited use (Jamieson et al., 2006; Seal, 2006). However, in an oxygen-poor atmosphere it has been shown that mass-independent fractionation (MIF) of sulphur occurred due to photochemical reactions, producing anomalous amounts of S^{33} that would cause the $\delta^{33}S$ value to deviate from the mass-dependant fraction line; this deviation is expressed as $\Delta^{33}S$ (Farquhar et al., 2000). To overcome this problem, more detailed sulphur isotope work will be conducted at the University of Alberta where S^{34}, S^{33}, and S^{32} will be determined by SIMS in pyrite and pyrrhotite from Doyon and Grand Duc. The goal of obtaining these data will be to evaluate whether other sulphur sources (e.g. seawater sulphate) were involved in the evolution of the mineralizing systems (Jamieson et al., 2006). Additionally, this sulphur isotope work will be reconciled with the interpreted boiling textures (i.e. As-rich rims) in pyrite from Grand Duc to establish if any variability in $\delta^{34}S$ is present between accessory metal-poor and metal-rich zones within the pyrite.

ACKNOWLEDGEMENTS

The authors would like to thank Iamgold Corporation and the Westwood Mine geology department for allowing access to collect mineralized drillcore and surface samples for the project. Ryan Sharpe (University of Manitoba) and Brandon Boucher (University of New Brunswick) are thanked for the SIMS and LA-ICPMS analyses, respectively. Thank you to Jean-Luc Pilote for a constructive review that improved the contributions significantly.

REFERENCES

Belkabir, A., and Hubert, C., 1995, Geology and structure of a sulfide-rich gold deposit: an example from the Mouska gold mine, Bousquet district, Canada: Economic Geology, v. 90, p. 1064-1079.

Crowe, D.E., and Vaughn, R.G., 1996, Characterization and use of isotopically homogeneous standards for in situ laser microprobe analysis of $^{34}S/^{32}S$ ratios: American Mineralogist, v. 81, p. 187-193.

Cook, N.J., Ciobanu, C.L., and Mao, J., 2009, Textural control on gold distribution in As-free pyrite from the Dongping, Huangtuliang and Hougou gold deposits, North Chine Craton (Hebei province, China): Chemical Geology, v. 264, p. 101-121.

D'Amore, F., and Truesdell, A.H., 1988, A review of equilibrium constants for gaseous species of geothermal interest: Science Geologique Bulletin, v. 41, p. 309-332.

Davis, D.W., 2002, U-Pb geochronology of Archean metasedimentary rocks in the Pontiac and Abitibi subprovinces, Quebec, constraints on timing, provenance, and regional tectonics: Precambrian Research, v. 115, p. 97−117.

Dubé, B., Mercier-Langevin, P., Hannington, M.D., Davis, D.W., and Lafrance, B., 2004, Le gisement de sulfures massifs volcanogènes aurifères LaRonde, Abitibi, Québec: Altération, minéralisations, genèse et implications pour l'exploration: Ministère des Ressources naturelles, de la Faune et des Parcs, Québec Report MB 2004-03, 112 p.

Farquhar, J., Bao, H.M., and Thiemens, M., 2000, Atmospheric influence of Earth's earliest sulfur cycle: Science, v. 289, p. 756-758.

Fillion, M., Vallee, M., and Lavoie, C., 1977, Les gisements d'or de la SOQUEM Silverstack, Canton Bousquet, Quebec: CIM Bulletin, v. 70, p. 159−172.

Fougerouse, D., Micklethwaite, S., Tomkins, A.G., Mei, Y., Kilburn, M., Guagliardo, P., Fisher, L.A., Halfpenny, A., Gee, M., Paterson, D., and Howard, D.L., 2016, Gold remobilisation and formation of high grade ore shoots driven by dissolution-reprecipitation replacement and Ni substitution into auriferous arsenopyrite: Geochimica et Cosmochimica Acta, v. 178, p. 143–159.

Franchini, M., McFarlane, C., Maydagán, L., Reich, M., Lentz, D.R., Meinert, L., and Bouhier, V., 2015, Trace metals in pyrite and marcasite from the Agua Rica porphyry-high sulfidation epithermal deposits, Catamarca, Argentina: textural features and metal zoning at the porphyry to epithermal transition: Ore Geology Reviews, v. 66, p. 366-387.

Galley, A.G., and Lafrance, B., 2007, Évolution et métallogénie du pluton de Mooshla: Ministère des Ressources naturelles et de la Faune, ET 2007-02, 31 p.

Galley, A.G., and Lafrance, B., 2014, Setting and evolution of the Archean synvolcanic Mooshla Intrusive Complex, Doyon-Bousquet-LaRonde mining camp, Abitibi greenstone belt: emplacement history, petrogenesis, and implications for Au metallogenesis: Economic Geology, v. 109, p. 205-229.

Gosselin, G., 1998, Veines de quartz aurifères précoces à la zone ouest de la mine Doyon, canton de Bousquet, Preissac, Abitibi: M.Sc. thesis, Université du Québec à Chicoutimi, 125 p.

Guha, J., Gauthier, A., Vallée, M., Descarreaux, J., and Lange-Brard, F., 1982, Gold mineralization at the Doyon mine (Silverstack), Bousquet, Quebec, in Hodder, R.W., and Petruk, W., eds., Geology of Canadian Gold Deposits: Canadian Institute of Mining and Metallurgy, Special Volume 24, p. 50-57.

Gunning, H.C., 1941, Region de Bousquet-Joannes, Quebec: Geological Survey of Canada Memoir 206, 80 p.

Hart, C.J.R., Mair, J.L., Goldfarb, R.J., and Groves, D.I., 2004, Source and redox controls on matallogenic variations in intrusion-related ore systems, Tombstone-Tungsten Belt, Yukon Territory, Canada: Transactions of the Royal Society of Edinburgh: Earth Sciences, v. 95, p. 339-356.

Hastie, E.C.G., Kontak, D.J., and Lafrance, B., 2020, Gold remobilization: insights from gold deposits in the Archean Swayze Greenstone Belt, Abitibi subprovince, Canada: Economic Geology, v. 115, p. 241-277.

Holliger, P., and Cathelineau, M., 1988, In situ U-Pb age determination by secondary ion mass spectrometry: Chemical Geology, v. 70, p. 173.

Huang, S.S., Leu, A.D., Ng., H.J., and Robinson, D.B., 1985, The phase behavior of two mixtures of methane, carbon dioxide, hydrogen sulfide and water: Fluid Phase Equilibria, v. 19, p. 21-32

Jamieson, J.W., Wing, B.A., Hannington, M.D., and Farquhar, J., 2006, Evaluating isotopic equilibrium among sulfide mineral pairs in Archean ore deposits: case study from the Kidd Creek VMS deposit, Ontario, Canada: Economic Geology, v. 101, p. 1055-1061.

Lafrance, B., Moorhead, J., and Davis, D.W., 2003, Cadre géologique du camp minier de Doyon-Bousquet-LaRonde: Ministère des Ressources naturelles, de la Faune et des Parcs, Québec Reports ET 2002-07, 45 p., and ET 2002-07 C001 1:20,000 map sheet.

Lafrance, B., Davis, D.W., Goutier, J., Moorhead, J., Pilote, P., Mercier-Langevin, P., Dubé, B., and Galley, A., 2005, Nouvelles datations isotopiques dans la portion québecoise du Groupe de Blake River et des unités adjacentes: Ministère des Ressources naturelles et de la Faune, Québec Report RP 2005-01, 26 p.

Lang, J.R., and Baker, T., 2001, Intrusion-related gold systems: the present level of understanding: Mineralium Deposita, v. 36, p. 477-489.

Langshur, A., 1990, The geology, geochemistry and structure of the Mooshla intrusion, Bousquet mining centre, Quebec: Unpublished M.Sc. thesis, Ottawa, Canada, University of Ottawa, 172 p.

LeForte, D., Hanley, J.J., and Guillon, M., 2011, Subepithermal Au-Pd mineralization associated with an alkalic porphryr Cu-Au deposits, Mount Milligan, Quesnel terrane, British Columbia, Canada: Economic Geology, v. 106, p. 781-808.

Mair, J.L., Goldfarb, R.J., Johnson, C.A., Hart, C.J.R., and Marsh, E.E., 2006 Geochemical constraints on the genesis of the Scheelite Dome intrusion-related gold deposit, Tombstone Gold belt, Yukon, Canada: Economic Geology, v. 101, p.523-553.

Mair, J.L., Farmer, G.L., Groves, D.I., Hart, C.J.R., and Goldfarb, R.J., 2011, Petrogenesis of postcollisional magmatism at Scheelite Dome, Yukon, Canada: evidence for a lithospheric mantle source for magmas associated with intrusion-related gold systems: Economic Geology, v. 106, p. 451-480.

Maloof, T.L., Baker, T., and Thompson, J.F.H., 2001, The Dublin Gulch intrusion gold deposit, Tombstone plutonic suite, Yukon Territory, Canada: Mineralium Deposita, v. 36, p. 583-593.

Marquis, P., Hubert, Brown, A.C., and Rigg, D.M., 1990, An evaluation of genetic models for gold deposits of the Bousquet district, Quebec, based on their mineralogical, geochemical and structural characteristics: Canadian Institute of Mining and Metallurgy Special volume 24, p. 383−399.

McFarlane, C., Luo, Y., 2012. U–Pb geochronology using 193 nm excimer LA–ICP-MS optimized for in situ accessory mineral dating in thin section. Geoscience Can. 39, 158–172.

McKibben, M.A., and Eldridge, C.S., 1990, Radical sulfur isotope zonation of pyrite accompanying boiling and epithermal gold deposition: A SHRIMP study of the Valles Caldera, New Mexico: Economic Geology, v. 85, p. 1917-1925.

McNicoll, V., Goutier, J., Dubé, B., Mercier-Langevin, P., Ross, P-S., Dion, C., Monecke, T., Legault, M., Percival, J., and Gibson, H., 2014, U-Pb geochronology of the Blake River Group, Abitibi greenstone belt, Quebec, and implications for base metal exploration: Economic Geology, v. 109, p. 27–59.

Mercier-Langevin, P., 2005, Géologie du gisement de sulfures massifs volcanogènes aurifères LaRonde, Abitibi, Québec: Unpublished Ph.D. thesis, Quebec, Canada, Institut National de la Recherche Scientifique, Centre Eau, Terre et Environnement, 689 p.

Mercier-Langevin, P., Dubé, B., Hannington, M.D., Davis, D.W., Lafrance, B., 2004, Contexte geologique et structural des sulfures massifs volcanogenes auriferes du Gisement LaRonde, Abitibi: Ministere des Ressources naturelles, de la Faune et des Parcs, Quebec, Report ET 2003-03, 47 p.

Mercier-Langevin, P., Dubé, B., Lafrance, B., Hannington, M., Galley, A., Moorhead, J., and Gosselin, P., 2007a, Metallogeny of the Doyon-Bousquet-LaRonde mining camp, Abitibi greenstone belt, Quebec: Geological Association of Canada, Mineral Deposits Division, Special Publication 5, p. 673−701.

Mercier-Langevin, P., Dubé, B., Hannington, M.D., Richer-Laflèche, M., and Gosselin G., 2007b, The LaRonde Penna Au-rich volcanogenic massive sulfide deposit, Abitibi greenstone belt, Quebec: Part 2. Lithogeochemistry and paleotectonic setting: Economic Geology, v. 102, p. 611−631.

Mercier-Langevin, P., Dubé, B., Hannington, M.D., Davis, D.W., Lafrance, B., and Gosselin, G., 2007c, The LaRonde Penna Au-rich volcanogenic massive sulfide deposit, Abitibi greenstone belt, Quebec: Part 1. Geology and geochronology: Economic Geology, v. 102, p. 585−609.

Mercier-Langevin, P., Wright-Holfeld, A., Dubé, B., Bernier, C., Houle, N., Savoie, A., and Simard, P., 2009, Stratigraphic setting of the Westwood-Warrenmac ore zones, Westwood project, Doyon-Bousquet-LaRonde mining camp, Abitibi, Quebec: Geological Survey of Canada Current Research Paper 2009-03, 20 p.

Mercier-Langevin, P., Goutier, J., Ross, P.-S., McNicoll, V., Monecke, T., Dion, C., Dubé, B., Thurston, P., Becu, V., Gibson, H., Hannington, M., and Galley, A., 2011, The Blake River Group of the Abitibi greenstone belt and its unique VMS and gold-rich VMS endowment: Geological Survey of Canada Open File Report 6869, 61 p.

Naden, J., and Shephard, T.J., 1989, Role of methane and carbon dioxide in gold deposition: Nature, v. 342, p. 793-795.

Neyedley, K., Hanley, J.J., Fayek, M., and Kontak, D.J., 2017, Textural, Fluid Inclusion, and Stable Oxygen Isotope Constraints on Vein Formation and Gold Precipitation at the 007 Deposit, Rice Lake Greenstone Belt, Bissett, Manitoba, Canada: Economic Geology, v. 112, p. 629-660.

Peterson, E.C., and Mavrogenes, J.A., 2014, Linking high-grade gold mineralization to earthquake-induced fault-valve processes in the Porgera gold deposit, Papua New Guinea: Geology, v. 42, p. 383–386.

Riciputi, L.R., Paterson, B.A., and Ripperdan, R.L., 1998, Measurement of light stable isotope ratios by SIMS: Matrix effects for oxygen, carbon, and sulfur isotopes in minerals: International Journal of Mass Spectrometry, v. 178, p. 81–112.

Savoie, A., Trudel, P., Sauve, P., Hoy, L., and Lao, K., 1991, Geologie de la mine Doyon (region de Cadillac): Ministere de l'Energie et des Ressources, Quebec, Report ET 90-05, 80 p.

Seal II, R.R., 2006, Sulfur isotope geochemistry of sulfide minerals: Reviews in Mineralogy and Geochemistry, v. 61, p. 633-677.

Sykora, S., Cooke, D.R., Meffe, S., Stephanov, A.S., Gardner, K., Scott, R., Selley, D., and Harris, A., 2018, Evolution of pyrite trace element compositions from porphyry-style and epithermal conditions at the Lihr gold deposit: implications for ore genesis and mineral processing: Economic Geology, v. 113, p. 193-208.

Trudel, P., Sauve, P., Tourigny, G., Hubert, C., and Hoy, L., 1992, Synthèse des caractéristiques géologiques des gisements de la région de Cadillac (Abitibi): Ministère des Ressources naturelles, Québec, Report MM 91-01, 106 p.

Valiant, R.I., and Hutchinson, R.W., 1982, Stratigraphic distribution and genesis of gold deposits, Bousquet region, northwestern Quebec: Canadian Institute of Mining and Metallurgy Special Volume 24 p. 27−40.

Velásquez, G., Béziat, D., Salvi, S., Siebenaller, L., Borisova, A.Y., Pokrovski, G.S., and de Parseval, P., 2014, Formation and deformation of pyrite and implications for gold mineralization in the El Callao district, Venezuela: Economic Geology, v. 109, p. 457–486.

Yergeau, D., 2015, Géologie du gisement synvolcanique aurifère atypique Westwood, Abitibi, Québec: Unplublished Ph.D. thesis, Quebec, Canada, Canada, Institut National de la Recherche Scientifique, Centre Eau, Terre et Environnement, 671 p.

Accessory mineral thermobarometry, trace element chemistry, and stable O isotope systematics, Mooshla Intrusive Complex (MIC), Doyon-Bousquet-LaRonde mining camp, Abitibi greenstone belt, Québec

K. Neyedley[1*], J.J. Hanley[1#], Z. Zajacz[2], and M. Fayek[3]

Neyedley, K., Hanley, J.J., Zajacz, Z., and Fayek, M., 2021. Accessory mineral thermobarometry, trace element chemistry, and stable O isotope systematics, Mooshla Intrusive Complex (MIC), Doyon-Bousquet-LaRonde mining camp, Abitibi greenstone belt, Québec; in *Targeted Geoscience Initiative 5: grant program final reports (2018-2020), Geological Survey of Canada, Open File 8755, p. 149–168. https://doi.org/10.4095/328986*

Abstract: The Mooshla Intrusive Complex (MIC) is an Archean polyphase magmatic body located in the Doyon-Bousquet-LaRonde (DBL) mining camp of the Abitibi greenstone belt, Québec, that is spatially associated with numerous gold (Au)-rich VMS, epizonal 'intrusion-related' Au-Cu vein systems, and shear zone-hosted (orogenic?) Au deposits. To elucidate the P-T conditions of crystallization, and oxidation state of the MIC magmas, accessory minerals (zircon, rutile, titanite) have been characterized using a variety of analytical techniques (e.g., trace element thermobarometry). The resulting trace element and oxythermobarometric database for accessory minerals in the MIC represents the first examination of such parameters in an Archean magmatic complex in a world-class mineralized district.

Mineral thermobarometry yields P-T constraints on accessory mineral crystallization consistent with the expected conditions of tonalite-trondhjemite-granite (TTG) magma genesis, well above peak metamorphic conditions in the DBL camp. Together with textural observations, and mineral trace element data, the P-T estimates reassert that the studied minerals are of magmatic origin and not a product of metamorphism. Oxygen fugacity constraints indicate that while the magmas are relatively oxidizing (as indicated by the presence of magmatic epidote, titanite, and anhydrite), zircon trace element systematics indicate that the magmas were not as oxidized as arc magmas in younger (post-Archean) porphyry environments.

The data presented provides first constraints on the depth and other conditions of melt generation and crystallization of the MIC. The P-T estimates and qualitative fO_2 constraints have significant implications for the overall model for formation (crystallization, emplacement) of the MIC and potentially related mineral deposits.

[1]Department of Geology, Saint Mary's University, 923 Robie Street, Halifax, Nova Scotia
[2]Department of Geological Sciences, University of Geneva, Geneva, Switzerland
[3]Department of Geological Sciences, University of Manitoba, 125 Dysart Road, Winnipeg, Manitoba
*corresponding author; (email: kevinneyedley@gmail.com); #activity leader

INTRODUCTION

The Mooshla Intrusive Complex (MIC) is an Archean polyphase magmatic body located in the Doyon-Bousquet-LaRonde (DBL) mining camp of the Abitibi greenstone belt, Québec. The MIC is spatially associated with numerous gold (Au)-rich VMS, orogenic- and suspected sub-seafloor epithermal-style Au deposits. Previous studies (e.g., Gosselin, 1998; Mercier-Langevin, 2007a; Galley and Lafrance, 2014; Yergeau, 2015) highlight a possible genetic link between the MIC and mineral deposits in the area based on geochronology, mapping/field relations, petrography, and lithogeochemistry. To elucidate the possible role of coeval magmatic systems in the development of high Au tenor mineral deposits, integration of field-based studies and in-situ analytical techniques is required to provide first order constraints on the evolution of potentially causative magmas. Specifically, the physical and chemical conditions at the time of magma formation, crystallization, emplacement, and volatile loss are critically sought parameters. The physical conditions of magma evolution can be resolved from accessory minerals through the acquisition and application of mineral trace element chemical data to well established thermobarometry calibrations (e.g., Ti-in-quartz thermometer: Thomas et al., 2010; Ti-in-zircon thermometer: Ferry and Watson, 2007; Zr-in-titanite thermometer: Hayden et al., 2008; Zr-in-rutile thermometer: Tomkins et al, 2007). For example, by using the method of intersecting isopleths for Ti-in-quartz and Zr-in-titanite thermometric calibrations, the point where these two independent isopleths intersect provides an estimate of magma crystallization P and T (*cf* Thomas et al., 2010).

The chemical characteristics of potentially causative magmas are also important to constrain. For example, oxygen fugacity (fO_2) while the MIC is crystallizing is an important factor to constrain as it has direct influence on the magmas carrying capacity of Au (Jugo, 2009; Botcharnikov et al., 2011; Zajacz et al., 2012). It has been shown that the greatest potential for silicate melt to carry gold is when redox conditions are near the sulphide-sulphate transition (~ΔFMQ+1; Jugo, 2009; Botcharnikov et al., 2011; Zajacz et al., 2012). Additionally, the highest gold solubility in a silicate melt is expected to occur when both S^{2-} and S^{6+} are both dissolved in the melt (Botcharnikov et al., 2011; Zajacz et al., 2012). However, the highest gold solubility is observed when S^{2-} is the main dissolved S species (not when total S is highest) and this occurs between ΔFMQ+0.5 to ΔFMQ +1 (Botcharnikov et al., 2011). At more oxidizing conditions, ^{S6}+ becomes the dominant S species and Au-S-O complexes are no longer stable resulting in a sharp decrease in Au solubility (Botcharnikov et al., 2011). The qualitative fO_2 value of a magmatic system can be inferred by the presence of certain minerals (e.g., anhydrite; Audétat and Pettke, 2006; Stern et al., 2007; Chambefort et al., 2008; Luhr, 2008) but it can also be estimated (quantitatively, in absolute and relative terms) based on the Eu and Ce anomalies of zircon (Ballard et al., 2002; Trail et al., 2012; Dilles et al., 2015; Smythe and Brenan, 2016). To constrain the conditions of magma evolution associated with the MIC, a systematic study of the trace element chemistry of magmatic zircon, titanite, rutile, and quartz was undertaken.

BACKGROUND

Regional Geology of the DBL Camp

The regional geology of the DBL mining camp and geological setting of its contained mineral deposits (Figure 1) have been described in detail by Gunning (1941), Fillion et al. (1977), Valiant and Hutchinson (1982), Marquis et al. (1990), Trudel et al. (1992), Lafrance et al. (2003, 2005), Mercier-Langevin et al. (2004, 2005, 2007b, 2011), Galley and Lafrance (2014), and Yergeau (2015). The mining camp contains > 28 Moz of Au, making it one of the world's largest Archean Au districts and contains two world-class Au-rich VMS deposits (LaRonde Penna and Bousquet 2-Dumagami), two major Au-rich sulphide vein deposits (Bousquet 1 and Westwood), epizonal "intrusion-related" Au-Cu vein systems (Doyon and Westwood Zone 2 Extension), and shear-hosted Au deposits (Mouska and Mic Mac), along with a number of smaller Au occurrences (Lafrance et al., 2003; Mercier-Langevin, 2007b, 2009, 2011; Yergeau, 2015).

The DBL mining camp occurs in the eastern portion of the Blake River Group (2704-2695 Ma; McNicoll et al., 2014) of the Archean Abitibi greenstone belt in the Superior Province (Figure 1; Mercier-Langevin, et al., 2007b; Galley and Lafrance, 2014). In the mining camp, the Blake River Group strikes east-west and is a steeply dipping, south-facing homoclinal volcanic sequence (Lafrance et al., 2003; Mercier-Langevin et al., 2007b, Galley and Lafrance, 2014). The Blake River Group in the DBL camp consists of the Hébécourt Formation in the north and the Bousquet Formation in the south (Figure 1; Lafrance et al., 2003). Along the northern contact of the Blake River Group is the Lac Parfouru Fault, which separates the Hébécourt Formation from the sedimentary rocks of the Kewagama Group (<2686 Ma; Davis, 2002) and along the southern contact the Bousquet Formation is disconformably overlain by the sedimentary rocks of the Cadillac Group (<2687.4 ± 1.2 Ma; Lafrance et al., 2005).

The Hébécourt Formation represents the base of the Blake River Group in the DBL camp and is predominantly composed of massive to pillowed tholeiitic basaltic and basaltic andesite flows and sills (Lafrance et al., 2003; Mercier-Langevin et al., 2007b; Galley and Lafrance, 2014). The earliest evidence of VMS mineralization in the DBL camp is present in minor rhyolite dome complexes near the upper contact of the Hébécourt Formation (Mouska and Mic Mac deposits; Belkabir and Hubert, 1995).

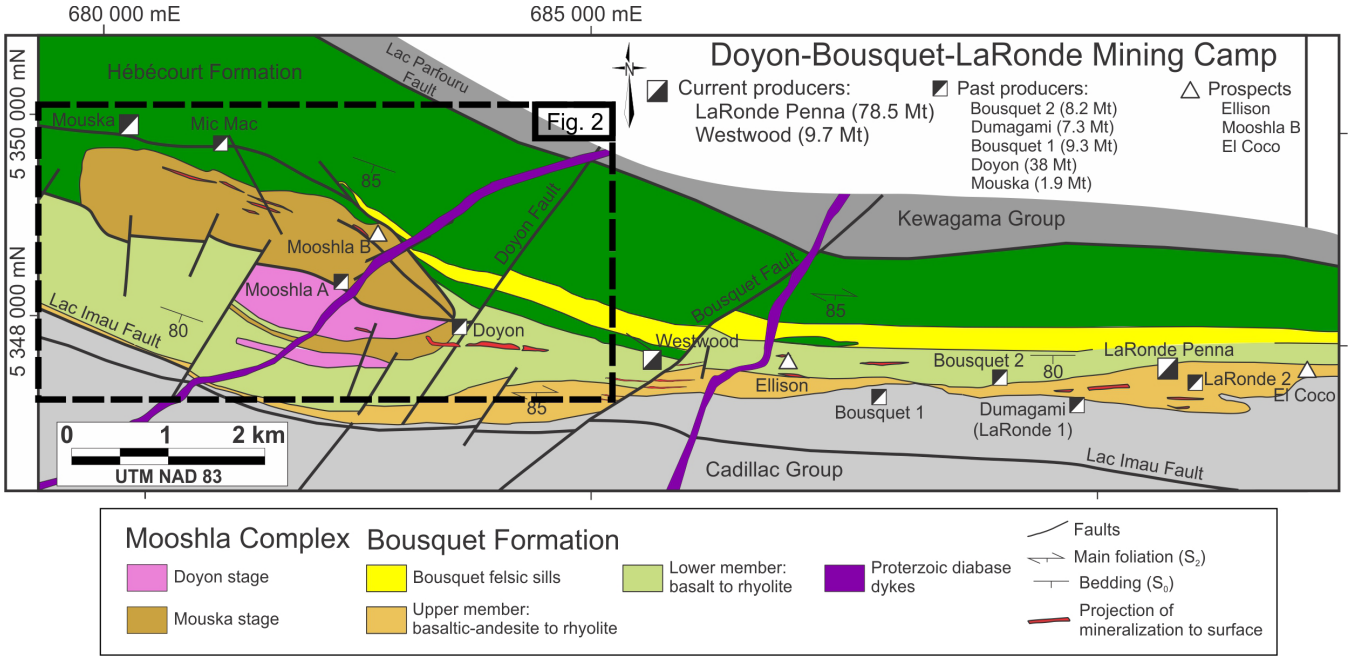

Figure 1: Simplified geology map of the Doyon-Bousquet-LaRonde mining camp showing the location of the Mooshla intrusive complex and spatial relationship to mines in the area. Modified from Mercier-Langevin, 2009.

Overlying the Hébécourt Formation is the Bousquet Formation which is divided into two members: the 2699-2698 Ma tholeiitic to transitional lower member and the 2698-2697 Ma transitional to calc-alkaline upper member (Lafrance et al., 2005; Mercier-Langevin, 2007c). In the western portion of the DBL camp quartz porphyritic rhyolite sills (unit 2.1) intruded along the upper contact of the Hébécourt Formation and represent the lowermost unit of the lower Bousquet Formation (Galley and Lafrance, 2014). Above unit 2.1, intermediate scoriaceous tuffs and tuff breccias predominantly containing basaltic to andesitic fragments occurs (unit 3.3; Mercier-Langevin, 2008). These tuffs are overlain by a glomeroporphyritic dacite (unit 4.2; 2698.3 ± 0.9 Ma, Lafrance et al., 2005). Overlying the glomeroporphyritic dacite is rhyolitic to dacitic schists (unit 4.3a), which is host to the Zone 1 and a portion of the Zone 2 lenses of the Doyon Au-Cu deposit (Savoie et al., 1991; Galley and Lafrance, 2014). A series of tholeiitic to transitional schistose massive to pillowed, mafic to intermediate flows compose the upper portion of the lower member of the Bousquet Formation (Lafrance et al., 2003). The upper member of the Bousquet formation is composed of dacitic to rhyodacitic flows, lobes, and flow breccias (Lafrance et al., 2003; Mercier-Langevin, 2007a, c). It is the upper member of the Bousquet Formation that is host to a majority of the Au-rich VMS deposits in the DBL camp (Figure 1; i.e., LaRonde Penna, Bousquet 2-Dumagami; Dubé et al., 2007; Mercier-Langevin et al., 2007a, 2009).

At least three phases of deformation affected the lithologies of the DBL mining camp (Langshur, 1990; Savoie et al., 1991; Belkabir and Hubert, 1995). A weak, moderately inclined northeast-southwest foliation defines the first phase of deformation (D1). A strong penetrative east-west fabric, with shear planes and faults that dip steeply to the south represents the second deformation phase (D2). Dextral transpressive brittle-ductile faults related to the third phase of deformation (D3) overprint D2. Regional metamorphism in the camp ranges from greenschist- to amphibolite-facies (with P-T conditions at peak of ~2-4 kbar, and ~400-550°C; Tourigny et al., 1989; Marquis et al., 1990; Mercier-Langevin, 2005; Yergeau, 2015) and is approximately coeval with D2. However, in the MIC, unorientated porphyroblasts of actinolite and biotite suggest peak metamorphism post-dates D2 (Marquis et al., 1990; Belkabir and Hubert, 1995; Dubé et al., 2004; Mercier-Langevin, 2005).

Local Geology of the Mooshla Intrusive Complex

The emplacement of the MIC occurred along the contact between the Hébécourt and Bousquet Formations in the western portion of the DBL camp and has an oval form of ~4x2 km (Figure 2; Galley and Lafrance, 2014). The MIC is grouped into two distinct stages of formation: (i) Mouska stage consisting of six intrusive phases (phases A-E) ranging from gabbro to tonalite; and (ii) Doyon stage comprising five intrusive phases (phases F-I) ranging from tonalite to trondhjemite (Figure 2; Galley and Lafrance, 2014). Galley and Lafrance (2014) distinguished each distinct intrusive phase from each other by chemical composition, variable intrusion style, and by distinctive overprinting relationships. They provide visual representations of the magmatic emplacement and evolution of the MIC demonstrating that the Mouska stage intrusive phases were emplaced along the

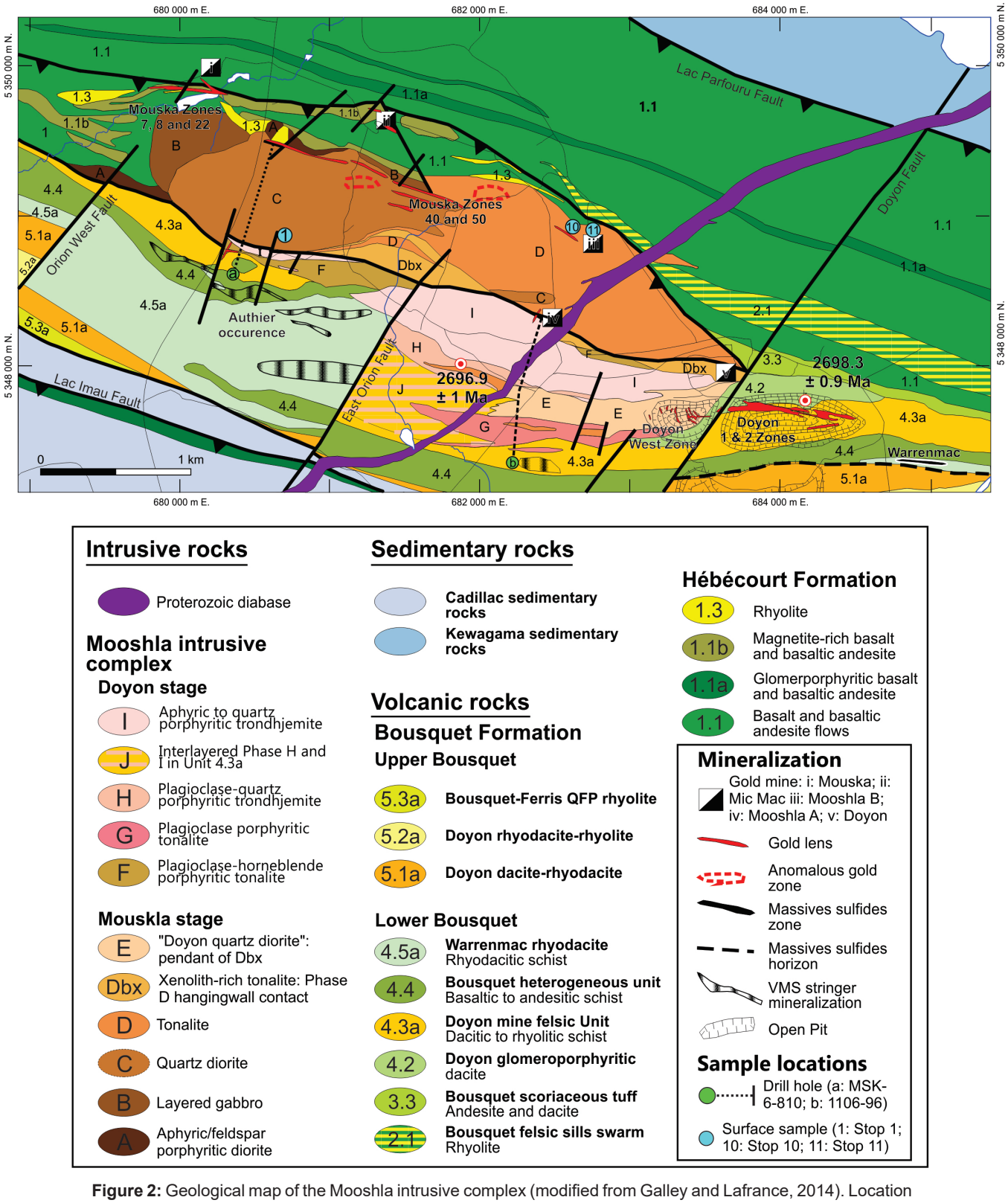

Figure 2: Geological map of the Mooshla intrusive complex (modified from Galley and Lafrance, 2014). Location of drillholes and surface samples utilized in the study are indicated on the map. Age dates are from Lafrance et al., 2005 and McNicoll et al., 2014.

contact of the Hébécourt Formation and the lower member of Bousquet Formation, whereas the Doyon stage phases crosscut the Mouska stage and the lower member of the Bousquet Formation (*see* Figure 12 and 13 in Galley and Lafrance, 2014). The MIC is crosscut by a large Proterozoic diabase dyke and D2 shear zones crosscut and bound the intrusion to the north and south (Figure 2; Galley and Lafrance, 2014). As well, a number of late north-south brittle-ductile faults dislocated the upper part of the MIC that is currently adjacent to the Lower Bousquet member (Orion fault; Galley and Lafrance, 2014). The Orion fault may have been synvolcanic and was possibly active during the latest (Doyon) stage of the MIC emplacement because the fault does not appear to affect the northern (older, Mouska) portion of the MIC (Galley and Lafrance, 2014).

The synvolcanic age of the MIC and coeval nature with the Bousquet Formation has been documented through field relationships and geochemistry (Galley and Lafrance, 2014), as well as U-Pb geochronology. Lafrance et al. (2005) conducted U-Pb geochronology on zircon from a Doyon-stage trondhjemite (Phase H) that yielded an age of 2696.9 ± 1 Ma, demonstrating that Phase H, and by association, the Doyon-stage of the MIC are synchronous with the upper member of the Bousquet Formation (2698−2696 Ma; Lafrance et al., 2005; Mercier-Langevin et al., 2007b, 2011; McNicoll et al., 2014). McNicoll et al. (2014) obtained an age of 2698.5 ± 0.4 Ma from U-Pb dating on zircon from a Mouska-stage quartz diorite (Phase C), which is synchronous with the glomeroporphyritic dacite of the lower Bousquet member (unit 4.2; host to part of the Doyon Au-Cu deposit), which has an age of 2698.3 ± 0.9 Ma (Lafrance et al., 2005).

KEY ACTIVITY HIGHLIGHTS

Methodology

Sample collection

Sampling was done in July and August, 2016, and involved sampling of outcrop and drill core. Outcrop samples were taken as far away from known quartz veining and/or dykes/sills (when present) to try and obtain an unaltered or minimally altered sample. Drill core samples were collected from two drill holes that are interpreted to represent an almost complete stratigraphic column of the entire MIC (Galley and Lafrance, 2014; A. Galley, communication, 2016). Drill hole MSK-6-810 contains Phase A, B, and C of the Mouska stage and drill hole 1106-96 contains Phase E of the Mouska stage and Phases G, H, and I of the Doyon stage. Phase F and D were not present in either of these drill holes and a drill hole that contains Phase F could not be located, but Phase D was collected from outcrop and where possible, representative samples of each intrusive phase were collected. Figure 2 shows the location of surface samples (blue circles) and drill core collars (green circles and associated drill hole traces). Representative images of most lithologies are shown in Figure 3, for lithologies not shown here, we refer the reader to Galley and Lafrance (2014) for a more comprehensive image library. Additionally, comprehensive lithogeochemical data and igneous setting classification/discrimination for the MIC is also summarized by Galley and Lafrance (2014).

Zircon and titanite mineral separation and imaging

Seven samples from four phases of the MIC were selected for zircon and/or titanite mineral separation based on transmitted light petrography. Samples were sent to Boise State University for separation, mineral picking, mounting, and CL imaging of zircon. Titanite was only recovered from two samples (Stop 10; Stop 11) both from the Phase D tonalite of the MIC. After zircon separation, half of the zircon grains picked underwent high temperature annealing in a muffle furnace (~900°C for 60 hours) to enhance the CL response, whereas the other half were not annealed to preserve any silicate and/or sulphide melt inclusions that may be trapped in the zircon. Cold cathodoluminescence (CL) images of annealed zircon grains was obtained with a JEOL JSM-1300 scanning electron microscope (SEM) and Gatan MiniCL. Titanite was not annealed and SEM-BSE images were collected using a TESCAN MIRA 3 LMU Variable Pressure Schottky Field Emission SEM equipped with a BSE detector at Saint Mary's University, Halifax, Nova Scotia.

Laser ablation ICP-MS analyses of accessory minerals and quartz

The major, minor, and trace element composition of accessory minerals (zircon, titanite, rutile, and quartz) was determined by LA-ICP-MS at the Magmatic and Ore-Forming Processes Research Laboratory at the University of Toronto. A New Wave Research® 193 nm ArF Excimer laser ablation system attached to an Agilent 7900 quadrupole mass spectrometer was used. The instrument was tuned to maximum sensitivity while maintaining robust plasma conditions (U≈Th on National Institute of Standards and Technology Standard Reference Material 610 silicate glass (NIST610) and low oxide and doubly charge ion production rates (ThO/Th < 0.3%; Mass 21/42 < 0.3%). Helium was used as a carrier gas at a flow rate of 1.0 L/min. The reference standard NIST610, commonly used in LA-ICPMS studies of silicate mineral chemistry (e.g., Gagnon et al., 2008) was used for the quantification of element concentration ratios and calibration of analyte sensitivities. Analyses of ~16 unknowns were bracketed by 2 standard analyses at the beginning and the end of each analysis block. During analytical sessions where zircon trace elements were collected, 91500 and Plesovice zircon standards (Wiedenbeck et al., 2004; Sláma et al., 2008) were used as external quality control standards during trace element quantification. Trace element quantification of minerals was performed using the

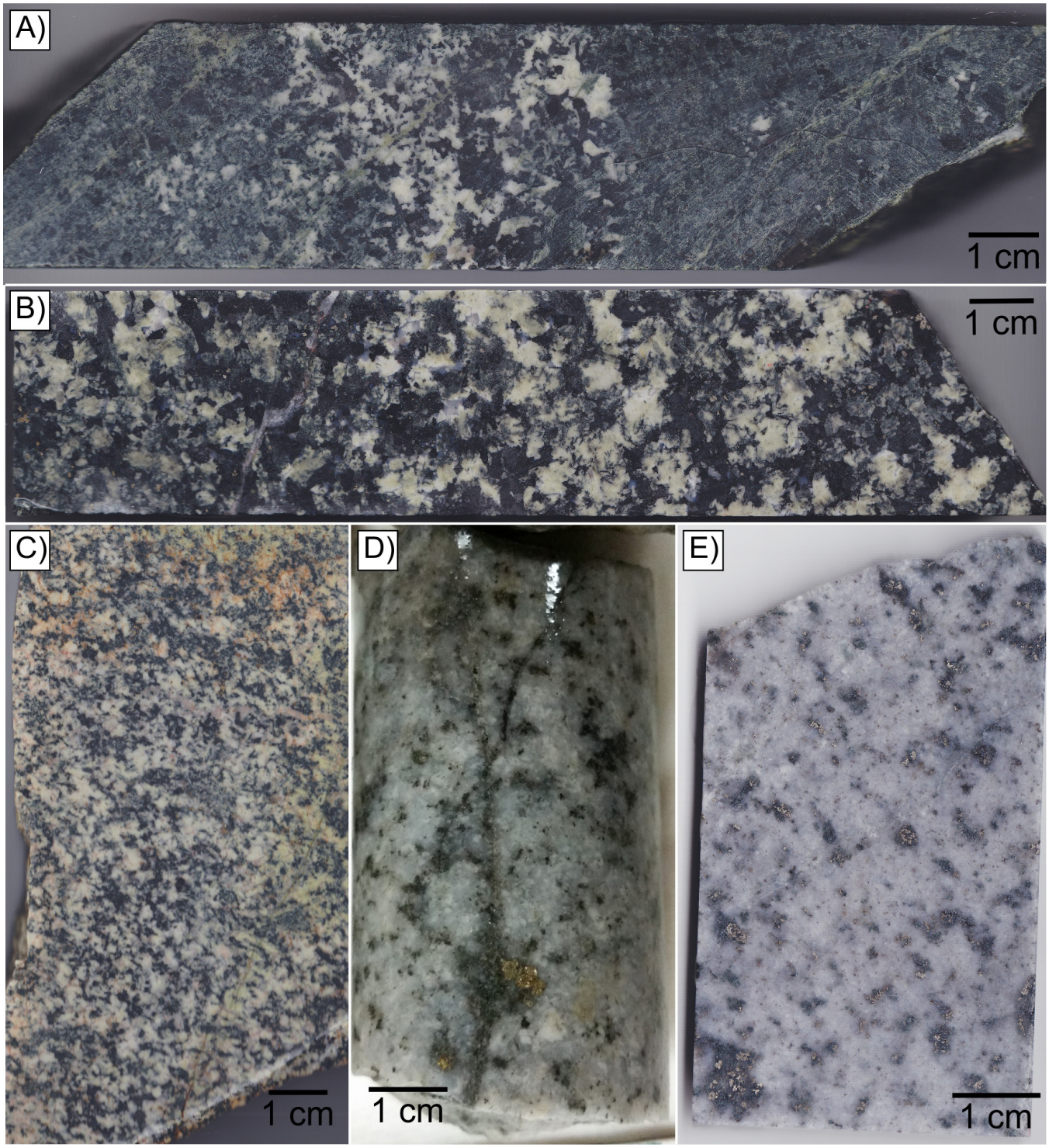

Figure 3: Representative slabs of various lithologies from the MIC. A) Coarse-grained section within Phase B. Possible that this coarser grained section is associated with Phase C as it is more felsic than the surrounding gabbro, but margins are diffuse so could also be an isolated coarser-grained patch of Phase B. MSK-715.6. B) Coarse-grained section of Phase C quartz diorite. MSK-493.7. D) Slab of Phase D tonalite. Margins of the sample are slightly altered because this sample was taken from surface. Stop 11. D-E) Representative core of Phase I trondhjemite. 1106-96-1444.5 (D) and 1106-96-459.4 (E).

software SILLS (Guillong et al., 2008). For quartz, an internal standard of 99.99 wt% SiO_2 was used, 67.2 wt% ZrO_2 for zircon, 30.6 SiO_2 wt% for titanite, and 99 wt% TiO_2 for rutile based on ideal stoichiometry. Dwell times for all elements were 10 ms, except for zircon analyses Ti was 50 ms and La and Pr were 30 ms, and in titanite Zr was 40 ms, and Cr, Cu, Zn, As, Mo, and Sn were 20 ms.

Trace element distribution maps (ppm) for zircon were obtained using a Resonetics COMPexPro® 102 ArF 193 nm Excimer laser ablation system, with a set output energy of 170 mJ at 50% attenuation, coupled to an Agilent 7700 quadrupole ICP-MS at the University of New Brunswick, Fredericton, New Brunswick. Maps were generated using a beam spot size of 17 μm, scan speed 10 μm/s and repetition rate of 10 Hz. Each ablation line scan was bracketed by 20 s of background (laser off, gas blank). The raw data (count rates vs. time) from traverses were imported into the Iolite3™ software package (Hellstrom et al. 2008; Paton et al. 2011), an add-in for Wavemetrics Igor Pro v.6.32™. Trace element maps were quantified using the CellSpace Image function in Iolite with ideal SiO_2 = 32.7 wt% as an internal standard, and using NIST610 for the calibration of analyte sensitivities.

Secondary Ion Mass Spectrometry (SIMS) of zircon

Oxygen isotope ratios ($^{18}O/^{16}O$) of zircon grains from the MIC were collected using a CAMECA 7f® SIMS at the University of Manitoba, Winnipeg, Manitoba. A cesium (Cs+) primary beam with a 6.5 nA current was accelerated (+10 kV) onto the sample surface with a sputtering diameter of ~25 μm. The instrument operated with a 200 V offset for oxygen, –9 kV secondary accelerating voltage, and a mass resolving power of 350. For a detailed description of operating conditions and strategy for correction of instrumental mass fractionation and matrix effects, see Sheahan et al., (2016) for oxygen isotope analysis.

Grains of Temora 2 zircon with a $\delta^{18}O$ value of 8.2 ‰ (Black et al., 2004) were used as the zircon reference material for oxygen isotope analysis and had a spot-to-spot reproducibility of 0.6‰. All isotopic data are presented using standard δ-notation relative to the appropriate standards, Vienna Standard Mean Ocean Water (V-SMOW) for $^{18}O/^{16}O$.

Results and data analysis

Petrography

Quartz occurs in many lithologies forming a variety of textures. For example, in Phase B and C, quartz occurs as a coarse-grained interstitial magmatic phase to amphibole (replacing pyroxene?) and plagioclase, whereas in Phase I quartz occurs as texturally-earlier subhedral grains, or in graphic intergrowth with feldspar. The cathodoluminescence colour range of magmatic quartz is blue, whereas metamorphic quartz is generally purple or red-brown in amphibolite to greenschist facies rocks, respectively (Götze et al., 2001 and references therein). Cathodoluminescence colour response for quartz from Phase C and I in the MIC show short-lived blue colours representative of magmatic quartz.

Zircon in all units comprises euhedral to subhedral grains between ~50 and 620 μm in diameter. It occurs typically as an included phase (Figure 4A) along grain boundaries between quartz, plagioclase and other phases. Zircon also occurs spatially associated with rutile (Figure 4K), occurring as ~10-60 μm-diameter, anhedral to subhedral grains. Zircon from all MIC phases display oscillatory and sector zoning (Figure. 4D-G). Melt inclusions in zircon confirm that it is of magmatic origin. Zircon characteristics from each sample are summarized in Table 1. Spot locations for LA-ICP-MS analyses were selected based on transmitted light petrography and CL images.

Titanite is present in two samples of Phase D tonalite (Stop 10 and Stop 11). Titanite in both samples shows the same textural characteristics, occurring as weakly to moderately fractured, subhedral grains (and grain aggregates). Grains are 100-700 μm in diameter and occur interstitial to plagioclase and quartz (Figure 4B). Rare remnant (i.e., remaining from partial replacement by titanite) inclusions, or partial inclusions, of Fe-Ti-oxides (ilmenite, magnetite, rutile) are present in titanite (Figure 4C). Where these inclusions show symplectic intergrowths of two oxides (Figure 4C), these are interpreted to be the result of oxidation of primary magmatic oxides, as is common in mafic-intermediate igneous rocks (e.g., Tan et al., 2015) and consistent with partial replacement by primary titanite during crystallization. SEM-BSE images show titanite can have oscillatory zoning (Figure 4H), whereas other grains show broad or very weak zoning that is likely an artifact of the orientation of the grain in the polished mount. Oscillatory or broad zoning can be truncated by sector zoning, which can also be broadly zoned. Spot locations for LA-ICP-MS analyses were selected based on transmitted light and SEM-BSE petrography.

Epidote was observed as a magmatic accessory phase in Phases D and I, occurring as anhedral to subhedral grains interstitial to plagioclase and quartz, and sharing grain boundaries with accessory (magmatic) titanite (Figure 3I). Allanite (Figure 4J) also occurs as an interstitial accessory phase in Phase D.

Rutile is a common mineral in Phase I and has been observed in contact with (or in close association with) zircon (Figure 4K). Two textural varieties of rutile occur in Phase I. The first variety (Rutile1; Rtl1) consists of individual rutile grains 20-400 μm in diameter, usually anhedral to subhedral, and rarely euhedral. Rutile1 mainly occurs interstitial to anhydrite-quartz, quartz-quartz, and quartz-feldspar grain boundaries and as inclusions within quartz, feldspar, and

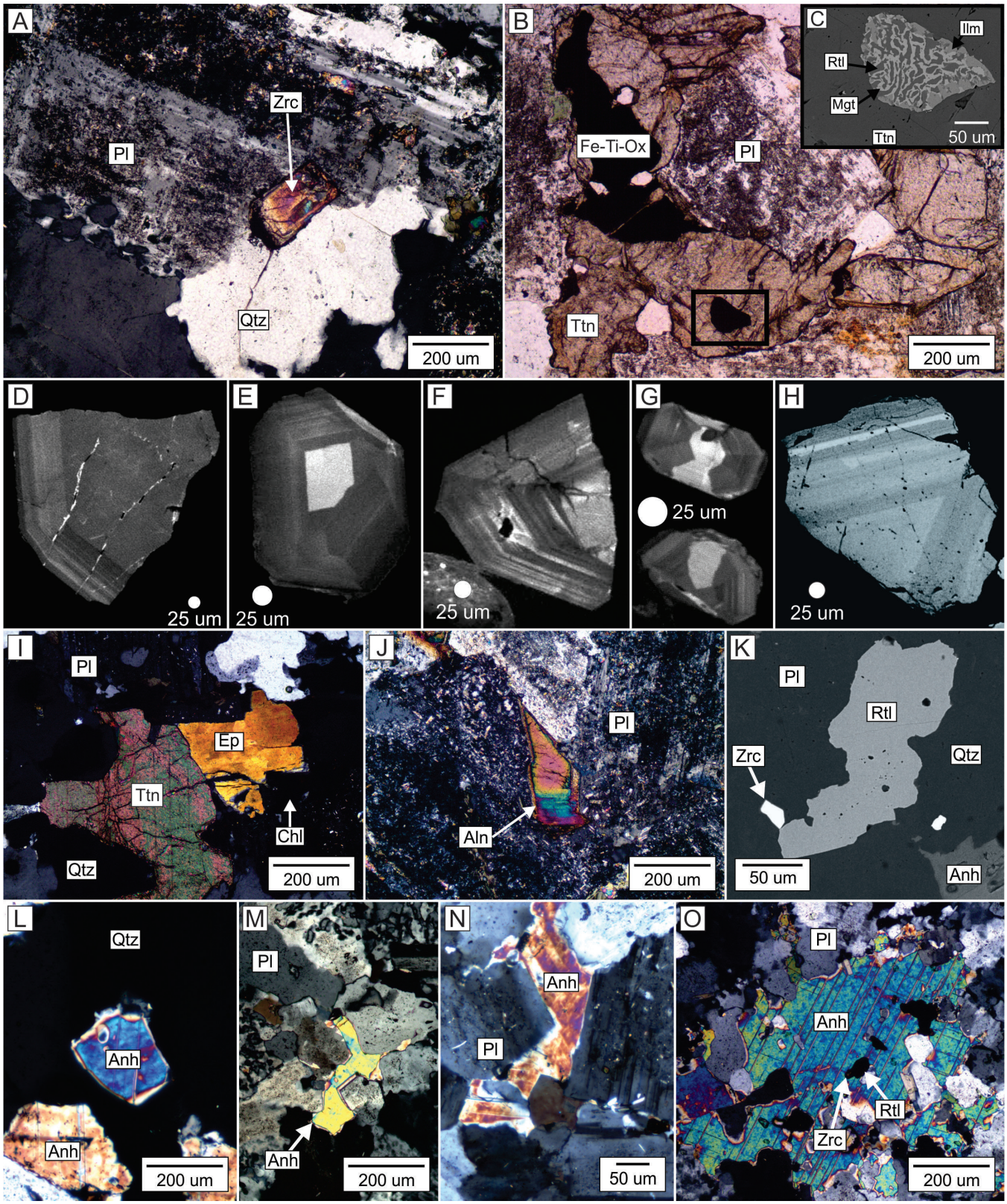
A
Zrc
Pl
Qtz
200 um
B
Fe-Ti-Ox
Pl
Ttn
200 um
C
Ilm
Rtl
Mgt
Ttn
50 um
D
25 um
E
25 um
F
25 um
G
25 um
H
25 um
I
Pl
Ep
Ttn
Chl
Qtz
200 um
J
Pl
Aln
200 um
K
Pl
Rtl
Zrc
Qtz
50 um
Anh
L
Qtz
Anh
Anh
200 um
M
Pl
Anh
200 um
N
Anh
Pl
50 um
O
Pl
Anh
Rtl
Zrc
200 um

Figure 4: Representative photomicrographs and cold CL images of accessory minerals in various phases from the Mooshla Intrusive Complex. A) Interstitial, tabular zircon from Phase D Tonalite (Sample = Stop 10; cross polarized light [XPL]). B) Interstitial titanite with inclusions and partial inclusions of Fe-Ti-oxides (see frame C) from Phase D Tonalite (Sample = Stop 10; plane polarized light [PPL]). C) Fe-Ti-oxide inclusion composed of rutile, ilmenite, and magnetite in titanite (Sample = Stop 10; SEM-BSE image). D) Zircon from Phase C Quartz Diorite showing an unzoned core with oscillatory zoning on the rim. Late fractures (bright lines) cut through both core and rim (Sample = MSK-6-810-493.7; cold CL image). E) Zircon from Phase B Gabbro showing an unzoned core with oscillatory and sector zoning on the rim (Sample MSK-6-810-715.6; cold CL image). F) Oscillatory zoned zircon from Phase D Tonalite (Sample = Stop 11; cold CL image). G) Sector and oscillatory zoned zircon grains from Phase I Trondhjemite (Sample = 1106-86-1444.5; cold CL image). H) Titanite displaying oscillatory zoning (Sample = Stop 11; SEM-BSE image). I) Interstitial titanite and epidote sharing a mutual grain boundary in Phase D Tonalite (Sample = Stop 11; XPL). J) Interstitial allanite from Phase D Tonalite (Sample = Stop 10; XPL). K) Fine-grained zircon located on the edge of an interstitial rutile grain from Phase I Trondhjemite (Sample = 1106-86-534.8; SEM-BSE). L) Inclusion of anhydrite in quartz and interstitial anhydrite located on the edge of quartz from Phase I Trondhjemite (Sample = 1106-86-534.8; XPL). M-N) Anhydrite interstitial to plagioclase Phase I Trondhjemite (Sample = 1106-86-534.8; XPL). Note the planar grain boundaries anhydrite forms with plagioclase and the relatively unaltered appearance of plagioclase. O) Coarse-grained interstitial anhydrite with inclusions of rutile and zircon from Phase I Trondhjemite (Sample = 1106-86-534.8; XPL).

anhydrite. The second variety of rutile (Rtl2) forms anhedral aggregates composed of multiple grains, up to 700 µm in diameter, occurring proximal to miarolitic cavities and/or biotite-chlorite alteration patches. Where zircon is observed with rutile, it is mainly Rtl1, and rarely Rtl2.

Phase I contains accessory anhydrite, with up to 5-8 vol% in one sample (1106-96-534.8). Anhydrite occurs as inclusions within magmatic quartz and plagioclase and shows planar crystal boundaries with other (igneous) minerals (Figure 4L). Anhydrite also occurs interstitial to quartz and plagioclase (Figure 4M, N, O). Plagioclase in these associations is relatively unaltered, showing clear twinning with only trace inclusions and patches of secondary micas (Figure 4N). Interstitial anhydrite patches vary from ~50 µm to ~600 µm in diameter, whereas inclusions within quartz and plagioclase range from ~10 µm to ~100 µm in diameter. Subhedral inclusions of zircon and rutile occur in anhydrite (Figure 4O).

Mineral trace element chemistry

Quartz

Quartz from Phases B, C, D, and I of the MIC were analysed by LA-ICP-MS to determine the Ti concentration in order to apply the TitaniQ thermometer (i.e., Ti-in-quartz; Thomas et al., 2010). Quartz from Phase B (MSK-6-810-715.6) and Phase C (MSK-6-810-493.7) have average Ti contents of 84 ± 27 ppm (n=27) and 118 ± 30 ppm (n=62), respectively. Quartz from two samples of Phase D have average Ti contents of 140 ± 31 ppm (n=20) and 110 ± 26 ppm (n=9), for samples Stop 10 and Stop 11 respectively. Quartz from three different samples of Phase I were analyzed. Samples 1106-96-534.8, 1106-96-1323, and 1106-96-1444.5 have average Ti contents of 75 ± 31 (n=17), 177 ± 33 ppm (n=20), and 155 ± 41 ppm (n=21), respectively. Average Ti-in-quartz concentrations for all samples is summarized in Appendix 1.

Table 1. Summary of zircon grain size and zoning types

Sample	Mooshla Phase	Size (µm)	Form	Aspect Ratio	Zoning type(s)
MSK-6-810-715.6	B	90 - 500	Eu-subhedral	1:1 - 2:1	Oscillatory, sector
MSK-6-810-493.7	C	100 - 620	Eu-subhedral	1:1 - 3:1	Oscillatory, sector
Stop 10	D	120 - 560	Eu-subhedral	1:1 - 3:1	Oscillatory, sector
Stop 11	D	120 - 540	Eu-subhedral	1:1 - 3:1	Oscillatory, sector
1106-96-1323	I	70 - 100	Eu-subhedral	1:1 - 2:1	Oscillatory, sector
1106-96-1444.5	I	50 - 160	Eu-subhedral	1:1 - 2:1	Oscillatory, sector

Zircon

Titanium and comprehensive trace element concentrations were determined for zircon from Phases B, C, D, and I of the MIC (Appendix 2). Titanium was measured in order to apply the Ti-in-zircon thermometer (Ferry and Watson, 2007). Zircon from Phase B (MSK-6-810-715.6) has Ti contents of 5.34 to 17.3 ppm (avg. 9.97 ± 2.43 ppm; n=70). Zircon from Phase C (MSK-6-810-493.7) has Ti contents of 6.14–18.8 ppm (avg. 11.5 ± 2.70 ppm; n=66). Zircon from two samples of Phase D were analyzed. Samples Stop 10 and Stop 11 have Ti contents between 5.44 and 17.2 ppm (avg. 9.34 ± 2.34 ppm; n=46) and 6.82 and 20.1 ppm Ti (avg. 10.3 ± 2.41 ppm; n=555), respectively. Zircon from two samples of Phase I were analyzed. Sample 1106-96-1323 and 1106-96-1444.5 have ranges in Ti concentrations of 7.87 to 11.1 ppm (avg. 9.18 ± 1.03 ppm; n=19) and 7.63 to 12.0 ppm (avg. 9.54 ± 1.45 ppm; n=20), respectively.

Representative zircon and titanite chondrite-normalized REE plots are presented in Figure 5. Zircon REE patterns (Figure 5A-G) are very similar for all lithologies, showing typical patterns for magmatic zircon (LREE<HREE) with positive Ce and negative Eu anomalies (cf Lu et al., 2016). However, the magnitude of the Eu anomaly ($Eu/Eu^* = Eu_N/[Sm_N \times Gd_N]^{½}$) in zircon varies across the different Phases of the MIC. Phase B has a slightly lower Eu anomaly (avg. 0.25 ± 0.03; n=70) than Phase C (avg. 0.32 ± 0.02; n=66). Both samples from Phase D have similar Eu anomalies of 0.36 ± 0.01 (n=46) and 0.37 ± 0.02 (n=55) for Stop 10 and 11, respectively. The Eu anomaly for the two Phase I samples are basically identical, being 0.26 ± 0.02 (n=19) and 0.26 ± 0.03 (n=20) for 1106-96-1323 and 1106-96-1444.5, respectively.

Titanite

Comprehensive trace element and zirconium concentrations were determined for titanite from two samples (Stop 10 and Stop 11) from Phase D of the MIC (Appendix 3). Zirconium was measured in order to apply the Zr-in-titanite thermometer (Hayden et al., 2008). The Zr-in-titanite content is highly variable in both samples, ranging from 26 to 82 ppm (avg. 51 ± 17.6 ppm; n=18) and from 85 to 524 ppm (avg. 241 ± 126 ppm; n=14) in Stop 10 and 11, respectively. Titanite

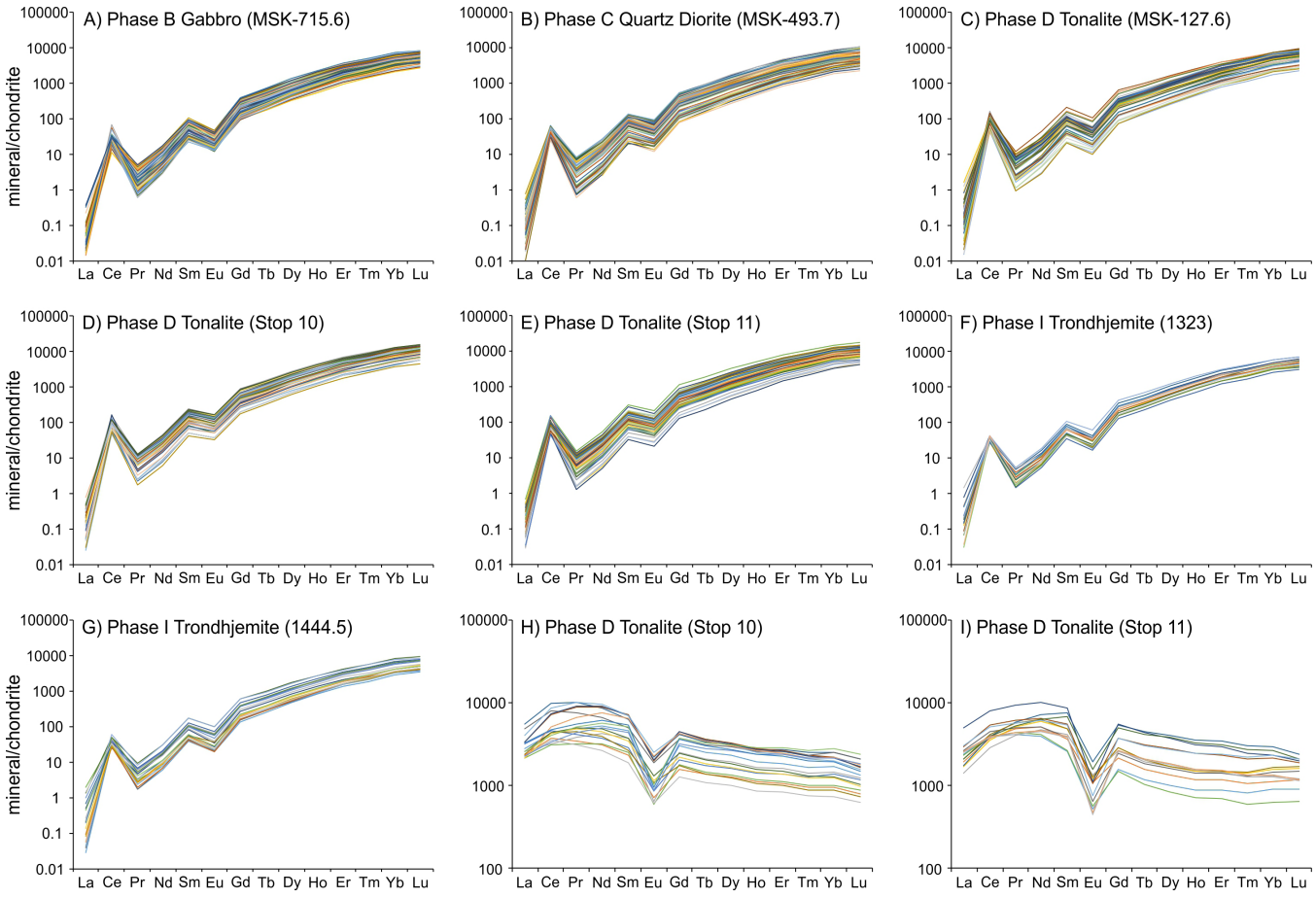

Figure 5: Chondrite-normalized REE graphs of zircon (A-G) and titanite (H-I) from the Mooshla Intrusive Complex. Note the patterns for zircon and titanite are consistent with a magmatic origin (cf Lu et al., 2016, Kohn, 2017). Normalization values for CI from McDonough and Sun (1995).

shows chondrite normalized REE patterns characteristic of magmatic origin with a pronounced negative Eu anomaly, and LREE < MREE > HREE (Figure 5H-I; *cf* Kohn, 2017).

Rutile

Approximately 13 Rtl1 grains from Phase I (1106-96-534.8) of the MIC were analyzed by LA-ICP-MS for trace elements, primarily to obtain the concentration of zirconium to apply the Zr-in-rutile thermometer (Ferry and Watson, 2007; Tomkins et al., 2007). The Zr-in-rutile concentration ranged between 470 and 1070 ppm (710 ± 195 ppm; n=13; Appendix 4). Significant enrichments in V (4110 ± 870 ppm; n=13), Ni (24.3 ± 5.57 ppm; n=13), Cu (18.3 ± 14.2 ppm; n=13), Sn (420 ± 138 ppm; n=13), W (98.9 ± 42.5 ppm; n=13), and Sb (2.58 ± 1.09 ppm; n=10) are also present.

Mineral Thermometry

The results of mineral LA-ICPMS analyses used to constrain PT conditions of their crystallization in various units of the MIC are summarized in Appendix 1-4.

The Ti-in-zircon thermometer is dependent on the activity of silica ($aSiO_2$) and activity of titanium ($aTiO_2$) of the magmatic system (Ferry and Watson, 2007). This study implemented an $aSiO_2 = 1$ because quartz is present in all samples (cf Large et al., 2018) and an aTiO2 = 0.7 because either titanite or titanomagnetite are present in the analyzed samples (cf Chelle-Michou et al., 2014). Uncertainty in $aTiO_2$ of ±0.1 results in an error of ±15°C over the calculated temperature range. Resulting temperature calculations of zircon from Phase B give 778 ± 25°C (n=70) and 792 ± 25°C (n=66) for zircon from Phase C. The samples from Phase D give relatively consistent temperatures of 771 ± 24°C (n=46) and 781 ± 22°C (n=56) for zircons from Stop 10 and 11, respectively. Both samples from Phase I have almost identical temperatures with 1106-86-1323 and 1106-86-1444.5 giving 771 ± 11°C (n=19) and 775 ± 15°C (n=20), respectively. A summary of average calculated temperatures are presented in Table 2. Rutile crystallization temperatures were calculated for Rtl1 from Phase I using the non-pressure dependant Zr-in-rutile thermometer of Ferry and Watson (2007). For the calculation, $aSiO_2$ was set to 1.0 because rutile occurs interstitial to quartz, therefore the system would have been saturated in quartz at the time of rutile formation. Resulting temperatures ranged from 680° to 760° (avg. 715 ± 25°C; n=13), which are slightly lower than Ti-in-zircon temperatures from other samples of Phase I.

Other thermometers require constraints on the $aSiO_2$ and aTiO2 but are also significantly dependant on crystallization pressure. The Ti-in-Quartz, Zr-in-titanite, and Zr-in-rutile thermometers (Tomkins et al., 2007; Hayden et al., 2008; Thomas et al., 2010) are pressure sensitive and since pressure is currently not constrained for the MIC direct application of these thermometers cannot be applied to the samples. However, using the method of intersecting isopleths, the point where these two independent isopleths intersect provides an estimate of crystallization temperature as well as pressure (cf Thomas et al., 2010). The Zr-in-titanite thermometer is dependent on the $aSiO_2$ and $aTiO_2$ of the magmatic system and $aSiO_2$ was set to 1 because quartz is present in all samples (cf Large et al., 2018) and $aTiO_2 = 0.7$ to reflect titanite crystallization (cf Chelle-Michou et al., 2014). Uncertainty in $aTiO_2$ of ±0.1 results in an error of ±5°C over the calculated temperature range. The Ti-in-quartz thermometer relies on $aTiO_2$ and was set to 0.7 similar to the Zr-in-titanite and Ti-in-zircon thermometers. Uncertainty in $aTiO_2$ of ±0.1 results in an error of ±12°C over the calculated temperature range.With these constraints, graphical integration of isotherms (solved independent of pressure) is the best approach to accurately constraining crystallization conditions for the MIC (see below).

In Situ Oxygen Isotopes of Zircon

The oxygen isotope composition of zircon was determined by SIMS at the University of Manitoba. Zircon from Phase C (MSK-6-810-493.7) has $\delta^{18}O_{V\text{-}SMOW} = 5.7 \pm 1.4$ ‰ (n=11; 1σ) with no core-to-rim variations evident. The data are summarized in Table 3. This overlaps wholly with the compositional zircons from across the Superior Province ($\delta^{18}O_{V\text{-}SMOW} = 5.50 \pm 0.51$ ‰; n=82; cf King et al., 1998, 2000) but the overall range in $\delta^{18}O_{V\text{-}SMOW}$ in zircon from Phase C ranges from magmatic (mantle-like) values to supracrustal values (higher than ~ 8‰; e.g., Watts and Mercer, 2020) and inter- and intragrain variations in $\delta^{18}O_{V\text{-}SMOW}$ are large suggesting that, while the zircon is magmatic (based on REE systematics, textural associations, and the presence of melt inclusions in zircon), its oxygen isotope systematics records the variable assimilation of supracrustal material by the MIC magma prior to or during it crystallization and emplacement (cf King et al., 1998, 2000).

INTERPRETATION

Implications of trace element chemistry of zircon and titanite

Scatter plots of various trace element and thermometry parameters for zircon (Figure 6A-D) show significant variations in composition within and between MIC lithologies that reflect real variations in magma composition and/or fO_2. For example:

Table 2: Ti-in-zircon concentrations and resulting temperature calculations[1]

Sample	MIC Phase	Avg. Ti (ppm; 1σ)	T (°C)	n
MSK-6-810-715.6	B	9.97 ± 2.43	778 ± 25	70
MSK-6-810-493.7	C	11.5 ± 2.70	792 ± 25	66
Stop 10	D	9.34 ± 2.34	774 ± 30	46
Stop 11	D	10.3 ± 2.41	782 ± 22	55
1106-96-1323	I	9.18 ± 1.03	771 ± 11	19
1106-96-1444.5	I	9.54 ± 1.45	775 ± 11	20
[1]temperatures calculated based on the equation of Ferry and Watson, 2007				

Table 3: Summary of zircon oxygen isotopes analyses

Sample	MIC Phase	$\delta^{18}O_{V\text{-}SMOW}$ (‰)
MSK-6-810-493.7	C	8.4
MSK-6-810-493.7	C	7.3
MSK-6-810-493.7	C	7.3
MSK-6-810-493.7	C	6.4
MSK-6-810-493.7	C	6.0
MSK-6-810-493.7	C	5.8
MSK-6-810-493.7	C	5.6
MSK-6-810-493.7	C	5.6
MSK-6-810-493.7	C	5.3
MSK-6-810-493.7	C	4.5
MSK-6-810-493.7	C	4.4
MSK-6-810-493.7	C	4.3
MSK-6-810-493.7	C	3.8

(i) Ti-in-zircon temperature vs. Hf content shows a weak inverse correlation reflecting the cooling growth of zircon, and shows that zircons in all lithologies grew over a similar crystallization temperature window (Figure 6A). Applying the Ti-in-zircon thermometer (Ferry and Watson, 2007) to the Ti concentration map of zircon produced by LA-ICP-MS shows a decrease in temperature with an increase in Hf content from the core outwards recording a prolonged cooling history for the zircons (Figure 6A-F).

(ii) Different lithologies of the MIC show distinct differences in Eu/Eu* but with no correlation with crystallization temperature (Figure 6B).

(iii) Hf/Y vs. Th/U ratios show that large variations in Hf/Y observed in some lithologies of the MIC reflecting titanite ± apatite ± amphibole fractionation as these phases remove Y from the melt relative to Hf and in the case of titanite and apatite, remove Th from the melt more readily compared to U (Figure 6C; cf Lee et al., 2020).

(iv) A plot of Dy vs. Yb/Dy ratio (Figure 6D) shows an inverse correlation between Dy and Yb/Dy that reflects the significant influence of titanite ± apatite removal, but also the spread in data from a strong correlation reflects zircon crystallization (*cf* Schaltegger and Davies, 2017). Like Figure 6C, this reasserts that titanite, like zircon is a magmatic mineral.

In modern porphyry systems the Eu anomaly of zircon has been used as a redox indicator of the crystallizing magma, with Eu anomalies approaching 1 signifying more oxidizing conditions (e.g., Dilles et al., 2015; Bissig et al., 2017). A compilation of all zircon analyses on a Eu/Eu* vs Hf plot from the various phases of the MIC shows the Eu anomaly increases in the Mouska stage of the MIC from Phase B through to D, followed by a significant decrease of the Eu anomaly in Phase I of the Doyon stage of the MIC (Figures 6B, 7G). This fluctuation in Eu anomaly likely records variations in the oxidation state of the magma over the history of the MIC, suggesting the magmatic system became

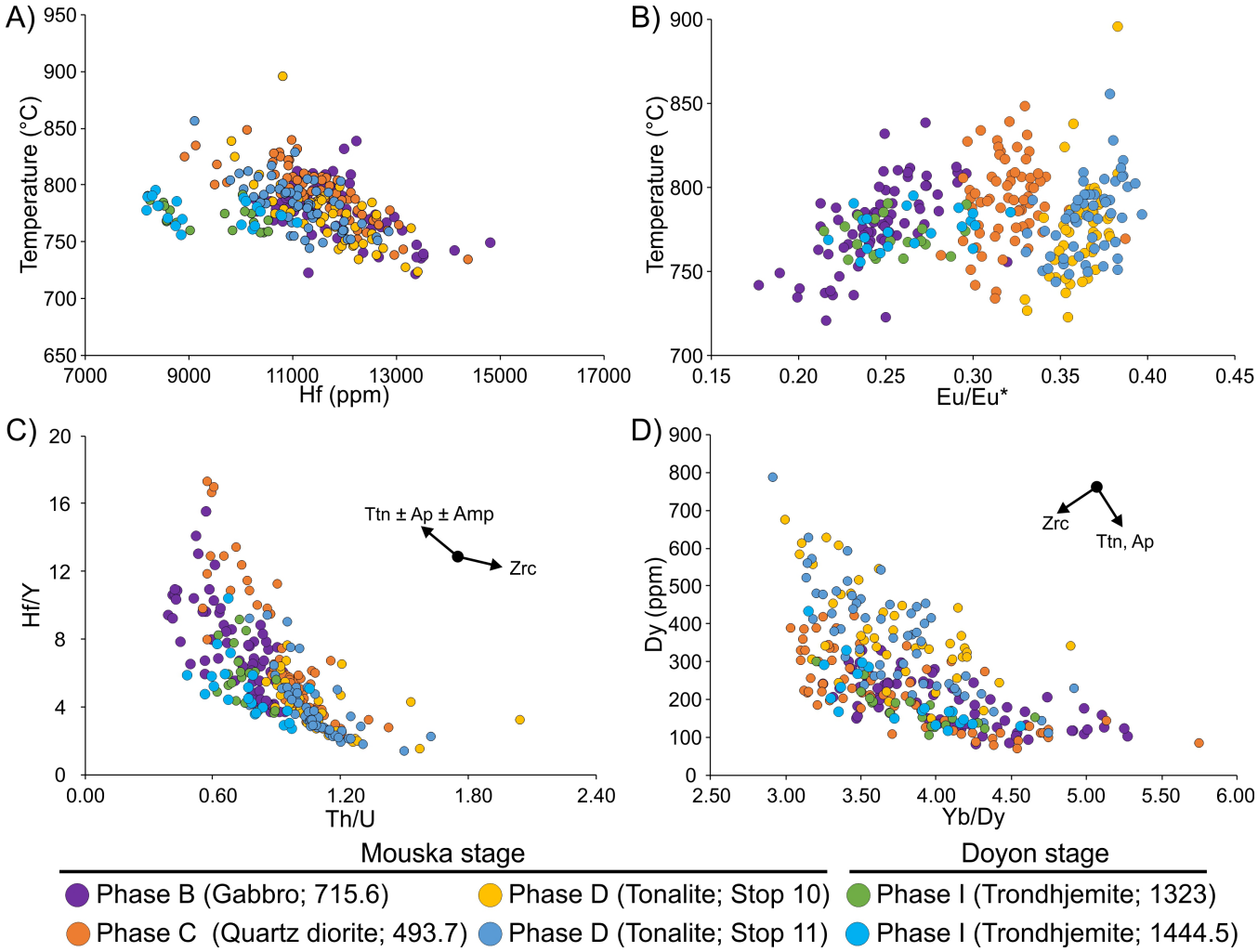

Figure 6: Zircon compositional scatter plots from the Mooshla Intrusive Complex. A) Temperature (as a function of Ti concentration; cf Ferry and Watson, 2007) vs Hf concentrations in zircon. Note the increase of Hf concentration with a decrease in temperature. B) Temperature vs Eu/Eu* of zircon. Note the increase in Eu/Eu* from Phase B to Phase D of the Mouska stage. C) Hf/Y vs Th/U ratios in zircon. Note the relatively higher Hf/Y ratios in Phase B and C compared to all other phases, suggesting amphibole is fractionating prior to or coeval to zircon fractionation removing Y from the melt (cf Lee et al., 2020). The shallower slope of Phases D and I likely suggests titanite and/or apatite are fractionating. D) Dy concentration vs Yb/Dy ratio in zircon. Note the relatively large range Yb/Dy ratios suggesting titanite and/or apatite are fractionating causing the Yb/Dy ratio to increase (cf Schaltegger and Davies, 2017).

more oxidized as it evolved from Phase B to D and then system became more reduced during the crystallization of Phase I. This is important with respect to the magmas ability to transport gold because higher fO_2 conditions lead to an increase in the solubility of sulphur in the melt and with increasing sulphur content, gold solubility increases (Jugo, 2009; Zajacz et al., 2012). It is interesting to note that titanite also shows large, negative Eu/Eu* and small, positive Ce/Ce* (Figure 5H-I). However, the Eu/Eu* reflects the lower compatibility of Eu in titanite relative to Sm and Gd and does not reflect magma oxidation state (Loader et al., 2017).

Comparison of the Eu/Eu* vs. Hf data for zircon from the MIC to compositional fields for zircon from pre-mineralized and mineralized magmatic phases in porphyry Cu-Au-Mo systems (Figure 7G; *cf* Dilles, 2015) shows that the zircon from the MIC have compositional overlap with both pre-mineralized and mineralized stages.

Significance of magmatic anhydrite and epidote

Similar textural characteristics for anhydrite (e.g., straight planar crystal boundaries and associated fresh plagioclase) in Phase I have also been reported in the "Porphyry A" stock at the El Teniente Cu-Mo deposit, Chile (Stern et al., 2007). These authors suggested that the anhydrite at El Teniente is magmatic and not a result of secondary hydrothermal alteration. Therefore, given the textural characteristics of anhydrite observed in the MIC (i.e., inclusions in silicates, sharp grain boundaries), it is suggested that MIC anhydrite

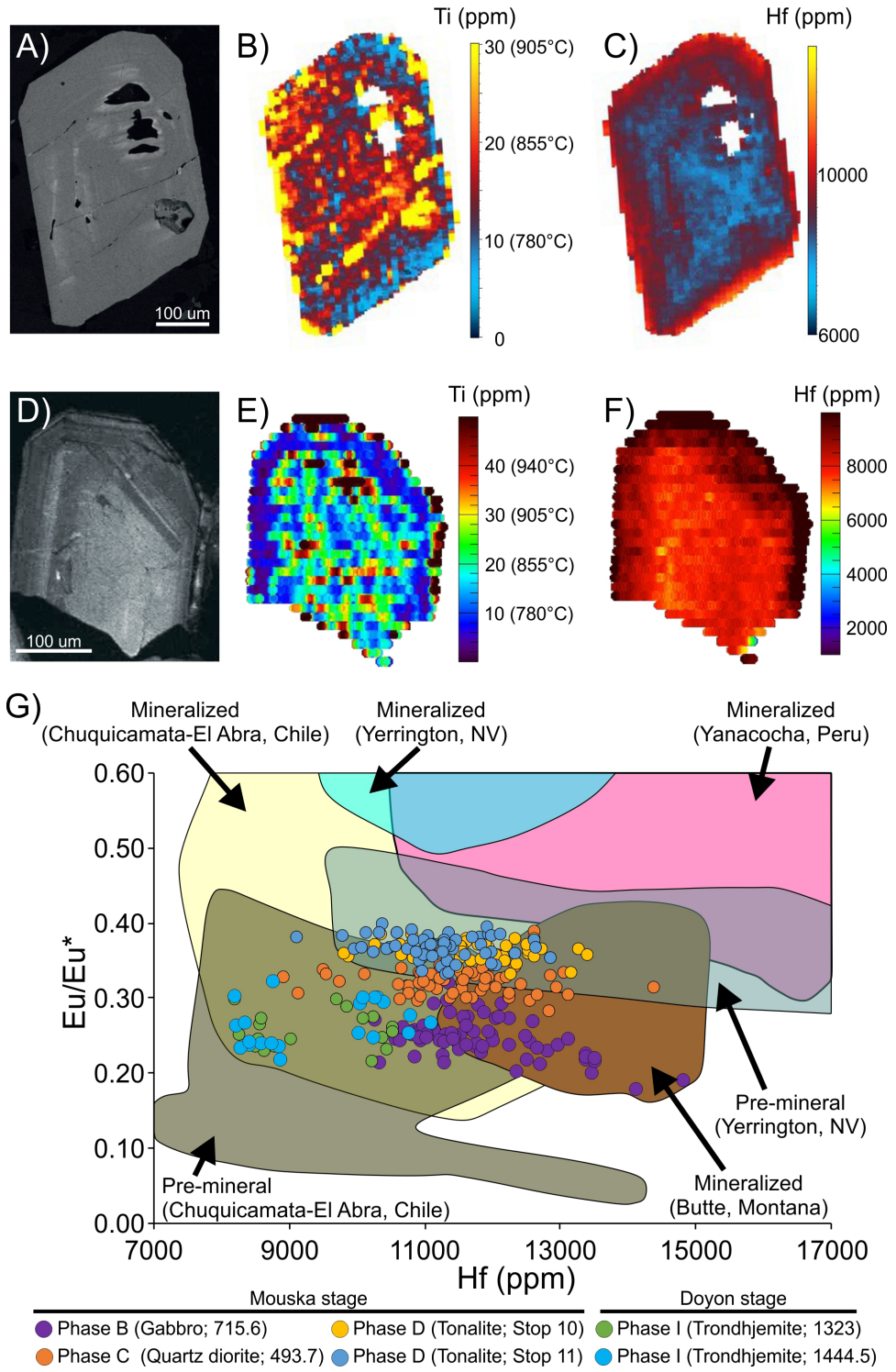

Figure 7: Eu/Eu* vs Hf concentration of zircon from various phases of the Mooshla Intrusive Complex and zircon LA-ICPMS trace element maps from Phase C and Phase D. A) Eu/Eu* vs Hf concentration of zircon from various phases of the Mooshla Intrusive Complex compared to various pre-mineralized and mineralized rocks from various porphyry systems (all fields from Dilles, 2015). Note, the overlap of Mooshla zircons with both pre-mineralized and mineralized systems. B) Cold CL image of a zircon from Phase C Quartz Diorite. C) Ti concentration map of zircon in frame C. Temperature estimates based on the equation of Ferry and Watson, 2007. Note the decrease in temperature (i.e., Ti concentration) from core to rim. D) Hf concentration map of zircon in frame C. Note the increase in Hf concentration from core to rim. Black patches (white in map) are silicate mineral inclusions or melt inclusions. E) Cold CL image of a zircon from Phase D Tonalite. F) Ti concentration map of zircon in frame E. Note the decrease in temperature (i.e., Ti concentration) from core to rim. G) Hf concentration map of zircon in frame E. Note the increase in Hf concentration from core to rim.

is a magmatic mineral. The presence of magmatic anhydrite, combined with a low Eu/Eu* anomaly in texturally-earlier zircon suggests significant variability in fO_2 conditions during the crystallization and emplacement of Phase I. This may have implications for Au exsolution and transport (discussed above).

Similarly, the variable occurrence (in some lithologies and not others) of magmatic epidote and titanite in the MIC also has important implications for fluctuations in the fO_2 of the MIC magmas (above and below FMQ; Wones, 1989; Schmidt and Poli, 2004) but also indicates a relatively high P of crystallization (e.g., >5-6 kbar; Zen and Hammarstrom, 1984).

Insight into the crystallization conditions of the MIC

The best approach to accurately constrain the crystallization conditions of quartz, zircon, rutile, and titanite is to integrate the thermometry calibrations for coeval phases (e.g., Thomas et al., 2010). Figure 8 summarizes this approach using data from all analyzed minerals. In Figure 8, pressure-temperature fields (coloured rhombs) are shown that represent the intersections of isopleths calculated using the Zr-in-titanite, Ti-in-quartz, Ti-in-zircon, and Zr-in-rutile thermometer calibrations. The results of this exercise show:

(i) For all MIC phases, the crystallization temperature window of the coeval mineral phases is constrained between 695° and 790°C. This temperature range is similar to the estimated temperature for tonalite-trondhjemite-granite (TTG)-suite melt generation reported in the literature (grey field in Figure 8; Condie, 2005; Clemens et al., 2006, De Almeida et al., 2011, Getsinger et al. 2009, and Hoffman et al., 2014).

(ii) With the exception of one titanite-bearing sample of Phase D (Stop 10) for which Zr-in-titanite yields an anomalously high crystallization pressure, all the other MIC lithologies yield crystallization pressures ranging from ~5-16 kbar through the method of intersecting isopleths (Figure 8). The upper part of this range (i.e., > 12 kbar) overlaps with the lower pressure range of TTG-suite magma generation (Figure 8). This would indicate that either the crystallization of these accessory phases in the MIC occurred over a significant window of ascent in the crust, or that they preserve conditions associated with the region of partial melting ± crystallization and, therefore, the lithologies of the MIC are polyphase containing xenocrystic or xenolithic phases. The tightest ranges in pressure come from intersections between Ti-in-quartz and Ti-in-zircon with multiple lithologies giving P ranges between ~5-13 kbar.

(iii) Crystallization conditions for the various igneous accessory minerals record much higher pressure and temperature conditions compared to the maximum metamorphic pressure-temperature conditions estimated from previous studies (grey, black, and hatched fields in Figure 8; ~2-4 kbar and ~400-550°C; Tourigny et al., 1989; Marquis et al., 1990; Mercier-Langevin, 2005; Yergeau, 2015).

NEXT STEPS

Future work will integrate the trace element chemistry of melt inclusions in quartz and zircon from the MIC with the trace element, thermobarometric, and stable isotope systematics of the accessory minerals described here with the goal of: (i) constraining the depth of origin of the MIC magmas; (ii) constraining the melt evolution of the MIC during its emplacement history through comparison of silicate melt inclusions obtained for different phases of the intrusion; (iii) determine the fertility (with respect to metal enrichment) of the MIC magmas relative to younger magmas in porphyry and intrusion-related gold settings globally by taking a more thorough examination of the Eu and Ce anomalies in zircon from different phases of the MIC (e.g., Dilles et al., 2015; Smythe and Brenan, 2016) and consideration of the emplacement history of the different MIC lithologies; and (iv) understanding the influence other accessory minerals (titanite, apatite) may have had on zircon chemistry (e.g., Loader et al., 2017). Clearly there were variations in the mineralizing potential (i.e., fertility) of different phases of the MIC based on their mineralogy and mineral chemistry, as shown here.

Scientific Impact and Conclusions

The emerging trace element and oxythermobarometric database for accessory minerals in the MIC represents the first examination of such parameters in an Archean magmatic complex in a world-class mineralized district. Even though temperature estimates are preliminary and accurate pressure constraints are needed to provide more reliable estimates, some preliminary conclusions can be made in conjunction with trace element and isotopic signatures of certain minerals. Given that the peak metamorphic conditions in the DBL camp are in the mid greenschist to lower amphibolite range (~400-550°C; ~2-4 kbar; Tourigny et al., 1989; Marquis et al., 1990; Mercier-Langevin, 2005; Yergeau, 2015), and that the applied mineral thermometers here record temperatures well above these conditions. This, together with textural and compositional (i.e., trace element patterns and zonation, and trace element correlations related to fractionation of accessory mineral phases) reassert that studied minerals are of magmatic origin and not a product of metamorphism. Recognizing that these accessory phases are of magmatic origin (e.g., zircon, titanite, and quartz) validates their application in understanding the physicochemical evolution of the MIC, and therefore, its relevance as both a heat and metal source for potentially genetically linked mineral deposits in the region.

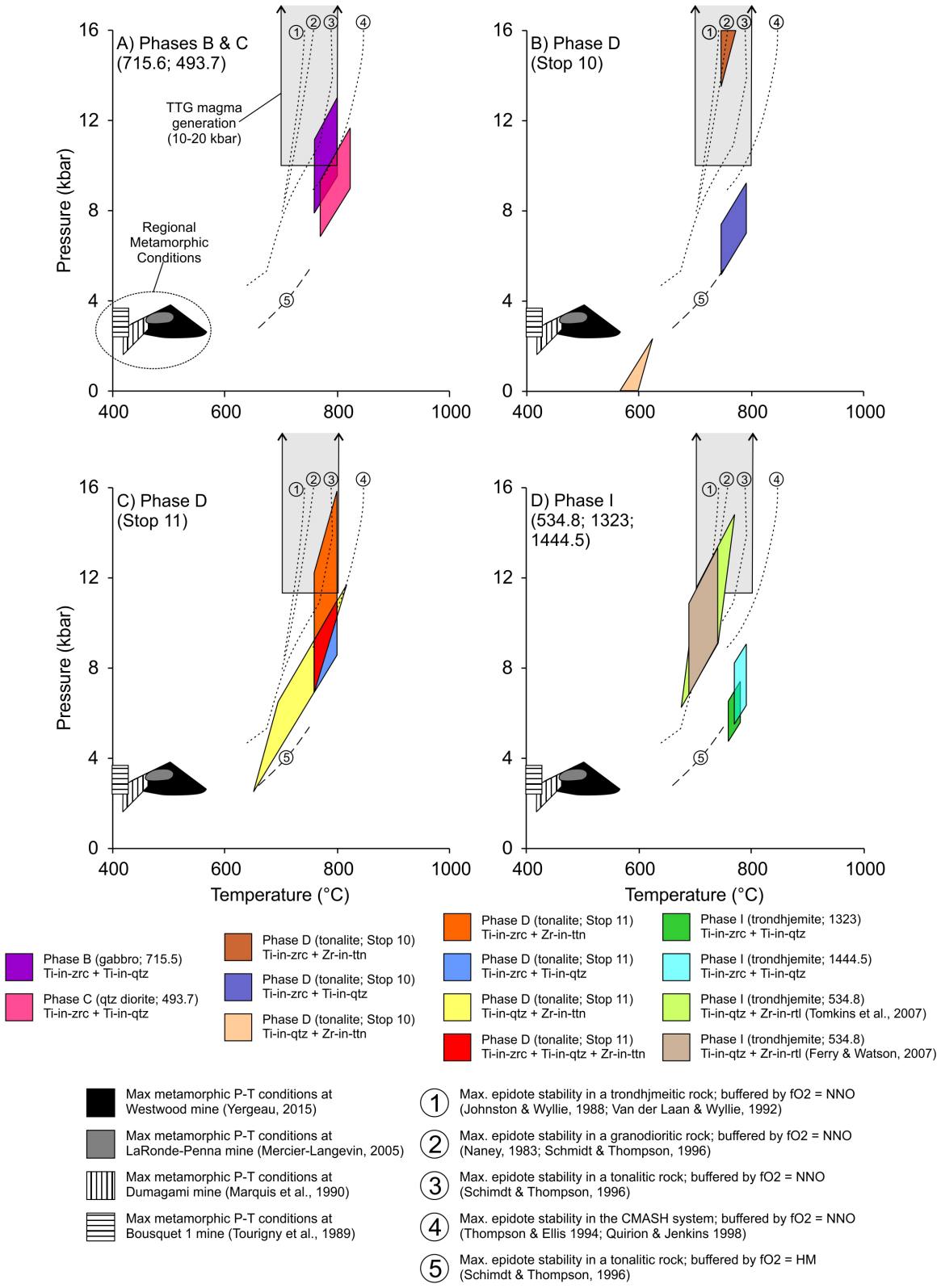

Figure 8. Pressure-temperature constraints for the crystallization of accessory phases (zircon, rutile, titanite) and quartz for various phases of the MIC. PT fields (coloured rhombs) for various MIC lithologies are based on the overlap of calculated Zr-in-titanite, Ti-in-quartz, Ti-in-zircon, and Zr-in-rutile temperatures (see text for explanation and references). Constraints for the maximum metamorphic P-T are shown in grey, black and hatched fields, and range from ~2-4 kbar and ~400-550oC (mid greenschist to lower amphibolite; references listed in legend). The PT field for TTG suite magma generation is taken from Condie (2005), Clemens et al (2006), De Almeida et al. (2011), Getsinger et al. (20) and Hoffman et al. (2014). Also shown are epidote stability boundaries in magmatic systems of various compositions and at various fO2 (references in legend).

The data presented provides first constraints on the depth and other conditions of melt generation and crystallization of the MIC. The P-T estimates and qualitative fO_2 constraints have significant implications for the overall model for formation (crystallization, emplacement) of the MIC and potentially related mineral deposits. First, the depths of crystallization are well below the final emplacement level of the MIC units, and consistent with the conditions of TTG suite magma genesis and felsic MASH (melting-assimilation-storage-homogenization) processes (e.g., Schwindinger and Weinberg, 2017). Evidently, the MIC units were largely crystallized and distinct (i.e., in terms of composition) at significant depths, and prior to shallow-level emplacement (Galley and LaFrance, 2014). Second, the MIC magmas were not unusually oxidizing, unlike some more modern arc magmas that endow porphyry deposits with Au. Attempts to link causative MIC magmatic processes and mineral deposit metal endowment in the Doyon-Bousquet-LaRonde district should consider (i) deep-seated, trans-crustal magmatic processes (e.g., fractionation/volatile exsolution) as important controls on deposit genesis, and not focus solely on processes occurring at the depth of final emplacement and solidification, and (ii) that less oxidizing magmas may still have the potential to carry and supply metals to hydrothermal systems related to Archean TTG suites.

ACKNOWLEDGEMENTS

The authors thank A. Tsay (University of Toronto), B. Boucher (University of New Brunswick) and J. Crowley (Boise State University) for their valuable contribution to LA-ICP-MS trace element analysis of accessory phases and sample preparation. Patrick Mercier-Langevin, Al Galley and David Yergeau provided critical assistance in the field during sample collection and provided key information about the regional and local geology of the MIC. This report benefited from the reviews of Jan Peter, Michael Gadd, and Ian Honsberger.

REFERENCES

Almeida, J.A.C.. Dall'Agnol, R., Oliveira, M.A., Macambira, M.J.B., Pimentel, M.M., Rämö, O.T., Guimarães, F.V., and Leite, A.A.S., 2011, Zircon geochronology, geochemistry and origin of the TTG suites of the Rio Maria granite-greenstone terrane: Implications for the growth of the Archean crust of the Carajás province, Brazil: Precambrian Research, v. 187, p. 201-221

Audétat, A., and Pettke, T., 2006, Evolution of a porphyry-Cu mineralized magma system at Santa Rita, New Mexico (USA): Journal of Petrology, v. 47, p. 2021-2046.

Ballard, J.R., Palin, J.M., and Campbell, I.H., 2002, Relative oxidation states of magmas inferred from Ce(IV)/Ce(III) in zircon: Application to porphyry copper deposits of northern Chile: Contributions to Mineralogy and Petrology, v. 144, p. 347–364.

Belkabir, A., and Hubert, C., 1995, Geology and structure of a sulfide-rich gold deposit: an example from the Mouska gold mine, Bousquet district, Canada: Economic Geology, v. 90, p. 1064-1079.

Bissig, T., Leal-Mejia, H., Stevens, R.B., and Hart, C.J.R., 2017, High Sr/Y magma petrogenesis and the link to porphyry mineralization as revealed by garnet-bearing I-type granodiorite porphyries of the Middle Cauca Au-Cu belt, Columbia: Economic Geology, v. 112, p. 551-568.

Black, L.P., Kamo, S.L., Allen, C.M., Davis, D.W., Aleinkoff, J.N., Valley, J.W., Mundil, R., Campbell, I.H. Korsch, R.J., Williams, I.S., and Foudoulis, C., 2004, Improved 206Pb/238U microprobe geochronology by the monitoring of a trace-element-related matrix effect: SHRIMP, ID-TIMS, ELA-ICP-MS and oxygen isotope documentation for a series of zircon standards: Chemical Geology, v. 205, p. 115-140.

Botcharnikov, R.E., Linnen, R.L., Wilke, M., Holtz, F., Jugo, P.J., and Berndt, J., 2011, High gold concentrations in sulphide-bearing magma under oxidizing conditions: Nature Geoscience, v. 4, p. 112-115.

Condie, K.C., 2005, TTGs and adakites: are they both slab melts?: Lithos, v. 80, p. 33-44.

Clemens, J.D., Yearron, L.M., Stevens, G., 2006, Barberton (South Africa) TTG magmas: geochemical and experimental constraints on source-rock petrology, pressure of formation and tectonic setting: Precambrian research, v. 151, p. 53-78.

Chambefort, I., Dilles, J.H., and Kent, A.J.R., 2008, Anhydrite-bearing andesite and dacite as a source for sulfur in magmatic-hydrothermal mineral deposits: Geology, v. 36, p. 719-722.

Chelle-Michou, C., Chiaradia, M., Ovtcharova, M., Ulianov, A., and Wotzlaw, J-F., 2014, Zircon petrochronology reveals the temporal link between porphyry systems and the magmatic evolution of their hidden plutonic roots (the Eocene Coroccohuayco deposit, Peru): Lithos, v. 198-199, p. 129-140.

Cherniak, D.J., Watson, E.B., and Wark, D.A., 2007, Ti diffusion in quartz: Chemical Geology, v. 236, p. 65-74.

Davis, D.W., 2002, U-Pb geochronology of Archean metasedimentary rocks in the Pontiac and Abitibi subprovinces, Quebec, constraints on timing, provenance, and regional tectonics: Precambrian Research, v. 115, p. 97−117.

Dilles, J.H., Kent, A.J.R., Wooden, J.L., Tosdal, R.M., Koleszar, A., Lee, R.G., and Farmer, L.P., 2015, Zircon compositional evidence for sulfur-degassing from ore-forming arc magmas: Economic Geology, v. 110, p. 241-251.

Dube, B., Mercier-Langevin, P., Hannington, M.D., Davis, D.W., and Lafrance, B., 2004, Le gisement de sulfures massifs volcanogenes auriferes LaRonde, Abitibi, Quebec: Alteration, mineralisations, genese et implications pour l'exploration: Ministere des Ressources naturelles, de la Faune et des Parcs, Quebec Report MB 2004-03, 112 p.

Ferry, J.M., and Watson, E.B., 2007, New thermodynamic models and revised calibrations for the Ti-in-zircon and Zr-in-rutile thermometers: Contributions to Mineralogy and Petrology, v. 154, p. 429-437.

Fillion, M., Vallee, M., and Lavoie, C., 1977, Les gisements d'or de la SOQUEM Silverstack, Canton Bousquet, Quebec: CIM Bulletin, v. 70, p. 159−172.

Gagnon, J., Fryer, B., Samson, I.M. and Williams-Jones, A.E., 2008, Quantitative analysis of silicate certified reference materials by LA-ICPMS with and without an internal reference standard: Journal of Analytical Atomic Spectroscopy, v. 23, p. 1529-1537.

Galley, A.G., and Lafrance, B., 2014, Setting and evolution of the Archean synvolcanic Mooshla Intrusive Complex, Doyon-Bousquet-LaRonde mining camp, Abitibi greenstone belt: emplacement history, petrogenesis, and implications for Au metallogenesis: Economic Geology, v. 109, p. 205-229.

Getsinger, A., Rushmer, T., Jackson, M.D., and Baker, D., 2009, Generating High Mg-numbers and Chemical Diversity in Tonalite-Trondhjemite-Granodiorite (TTG) Magmas during Melting and Melt Segregation in the Continental Crust: Journal of Petrology, v. 50, p. 1935-1954.

Götze, J., Plötze, M., and Habermann, D., 2001, Origin, spectral characteristics and practical applications of the cathodoluminescence (CL) of quartz - a review: Contributions to Mineralogy and Petrology, v. 71, p. 225-250.

Guillong, M.M., Maier, D.L., Allan, M.M., Heinrich, C.A., and Yardley, B.W.D., 2008, Appendix A6: SILLS: a MATLAB based program for the reduction of laser ablation ICP-MS data of homogeneous materials and inclusions. In Laser Ablation ICP-MS in the Earth Sciences: Current Practices and Outstanding Issues. Edited by P. Sylvester. Mineralogical Association of Canada Short Course Series v. 40.

Gunning, H.C., 1941, Region de Bousquet-Joannes, Quebec: Geological Survey of Canada Memoir 206, 80 p.

Hayden, L.A., Watson, B.E., and Wark, D.A., 2008, A thermobarometer for sphene (titanite): Contributions to Mineralogy and Petrology, v. 155, p. 529-540.

Hellstrom, J., Paton, C., Woodhead, J., and Hergt, J., 2008, Iolite: software for spatially resolved LA-(quad and MC) ICPMS analysis: Mineralogical Association of Canada Short Course, v. 40, p. 343-348

Hoffman, J.E., Nagel, T.J., Münker, C., Naeraa, T., and Rosing, M.T., 2014, Constraining the process of Eoarchean TTG formation in the Itsaq Gneiss Complex, southern West Greenland: Earth and Planetary Science Letters, v. 388, p. 374-386.

Humphris, S.E., 1998, Rare earth element composition of anhydrite: implications for deposition and mobility within the active TAG hydrothermal mound: Proceedings of the Ocean Drilling Program, v. 158, p. 143-159.

Jugo, P.J., 2009, Sulfur content at sulfide saturation in oxidized magmas: Geology, v. 37, p. 415-418.

Kelly, J.L., Fu, B., Kita, N.T., and Valley, J.W., 2007, Optically continuous silcrete quartz cements of the St. Peter Sandstone: High precision oxygen isotope analysis by ion microprobe: Geochimica et Cosmochimica Acta, v. 71, p. 3812–3832.

King, E.M., Valley, J.W., Davies, D.W., and Edwards, G.R., 1998, Oxygen isotope ratios of Archean plutonic zircons from granite-greenstone belts of the Superior Province: indicator of magmatic source: Precambrian Research, v. 92, p. 365-387.

King, E.M., Valley, J.W., and Davies, D.W., 2000, Oxygen isotope evolution of volcanic rocks at the Sturgeon Lake volcanic complex, Ontario: Canadian Journal of Earth Science, v. 37, p. 39-50.

Kohn, M.J., 2017, Titanite petrochronology: Reviews in Mineralogy and Geochemistry, v. 83, p. 419-441.

Lafrance, B., Moorhead, J., and Davis, D.W., 2003, Cadre geologique du camp minier de Doyon-Bousquet-LaRonde: Ministere des Ressources naturelles, de la Faune et des Parcs, Quebec Reports ET 2002-07, 45 p., and ET 2002-07 C001 1:20,000 map sheet.

Lafrance, B., Davis, D.W., Goutier, J., Moorhead, J., Pilote, P., Mercier-Langevin, P., Dube, B., and Galley, A., 2005, Nouvelles datations isotopiques dans la portion quebecoise du Groupe de Blake River et des unites adjacentes: Ministere des Ressources naturelles et de la Faune, Quebec Report RP 2005-01, 26 p.

Langshur, A., 1990, The geology, geochemistry and structure of the Mooshla intrusion, Bousquet mining centre, Quebec: Unpublished M.Sc. thesis, Ottawa, Canada, University of Ottawa, 172 p.

Large, S.J.E., von Quadt, A., Wotzlaw, J-F., Guillong, M., and Heinrich, C.A., 2018, Magma evolution leading to porphyry Au-Cu mineralization at the Ok Tedi deposit, Papua New Guinea: trace element geochemistry and high-precision geochronology of igneous zircon: Economic Geology, v. 113, p. 39-61.

Lee, R.G., Byrne, K, D'Angelo, M., Hart, C.J.R., Hollings, P., Gleeson, S.A., Alfaro, M., 2020, Using zircon trace element composition to assess porphyry copper potential of the Guichon Creek batholith and Highland Valley Copper deposit, south-central British Columbia: Mineralium Deposita, v. 119.

Loader, M.A., Wilkinson, J.J., and Armstrong, R.N., 2017, The effect of titanite crystallisation on Eu and Ce anomalies in zircon and its implication for the assessment of porphyry Cu deposit fertility: Earth and Planetary Science Letters, v. 472, p. 107-119.

Lu, Y.-J., Loucks, R. R., Fiorentini, M., McCuaig, T. C., Evans, N. J., Yang, Z.-M., Hou, Z.-Q., Kirkland, C. L., Parra-Avila, L. A., and Kobussen, A., 2016, Zircon compositions as a pathfinder for porphyry Cu±Mo±Au deposits: Economic Geology Special Publication, v. 19, p. 329-347.

Luhr, J.F., 1990, Experimental phase relations of water- and sulfur-saturated arc magmas and the 1982 eruptions of El Chichon volcano: Journal of Petrology, v. 31, p. 1071-1114.

Luhr, J.F., 2008, Primary igneous anhydrite: progress since its recognition in the 1982 El Chichón trachyandesite: Journal of Volcanology and Geothermal Research, v. 175, p. 394-407.

Marquis, P., Hubert, Brown, A.C., and Rigg, D.M., 1990, An evaluation of genetic models for gold deposits of the Bousquet district, Quebec, based on their mineralogical, geochemical and structural characteristics: Canadian Institute of Mining and Metallurgy Special volume 24, p. 383−399.

McDonough, W.F., and Sun, S.-S., 1995, The composition of the Earth: Chemical Geology, v. 120, p. 223-253.

McNicoll, V., Goutier, J., Dube, B., Mercier-Langevin, P., Ross, P-S., Dion, C., Monecke, T., Legault, M., Percival, J., and Gibson, H., 2014, U-Pb geochronology of the Blake River Group, Abitibi greenstone belt, Quebec, and implications for base metal exploration: Economic Geology, v. 109, p. 27–59.

Mercier-Langevin, P., 2005, Geologie du gisement de sulfures massifs volcanogenes auriferes LaRonde, Abitibi, Quebec: Unpublished Ph.D. thesis, Quebec, Canada, Institut National de la Recherche Scientifique, Centre Eau, Terre et Environnement, 689 p.

Mercier-Langevin, P., Dube, B., Hannington, M.D., Davis, D.W., Lafrance, B., 2004, Contexte geologique et structural des sulfures massifs volcanogenes auriferes du Gisement LaRonde, Abitibi: Ministere des Ressources naturelles, de la Faune et des Parcs, Quebec, Report ET 2003-03, 47 p.

Mercier-Langevin, P., Dube, B., Hannington, M.D., Davis, D.W., Lafrance, B., and Gosselin, G., 2007a, The LaRonde Penna Au-rich volcanogenic massive sulfide deposit, Abitibi greenstone belt, Quebec: Part 1. Geology and geochronology: Economic Geology, v. 102, p. 585−609.

Mercier-Langevin, P., Dube, B., Lafrance, B., Hannington, M., Galley, A., Moorhead, J., and Gosselin, P., 2007b, Metallogeny of the Doyon-Bousquet-LaRonde mining camp, Abitibi greenstone belt, Quebec: Geological Association of Canada, Mineral Deposits Division, Special Publication 5, p. 673−701.

Mercier-Langevin, P., Dube, B., Hannington, M.D., Richer-Lafleche, M.,and Gosselin G., 2007c, The LaRonde Penna Au-rich volcanogenic massive sulfide deposit, Abitibi greenstone belt, Quebec: Part 2. Lithogeochemistry and paleotectonic setting: Economic Geology, v. 102, p. 611−631.

Mercier-Langevin, P., Ross, P.-S., Lafrance, B., and Dube, B., 2008, Volcaniclastic rocks of the Bousquet scoriaceous tuff units north of the LaRonde Penna mine, Doyon-Bousquet-LaRonde mining camp, Abitibi greenstone belt, Quebec : Geological Survey of Canada Current Research Paper 2008-11, 19 p.

Mercier-Langevin, P., Wright-Holfeld, A., Dube, B., Bernier, C., Houle, N., Savoie, A., and Simard, P., 2009, Stratigraphic setting of the Westwood-Warrenmac ore zones, Westwood project, Doyon-Bousquet-LaRonde mining camp, Abitibi, Quebec: Geological Survey of Canada Current Research Paper 2009-03, 20 p.

Mercier-Langevin, P., Goutier, J., Ross, P.-S., McNicoll, V., Monecke, T., Dion, C., Dube, B., Thurston, P., Becu, V., Gibson, H., Hannington, M., and Galley, A., 2011, The Blake River Group of the Abitibi greenstone belt and its unique VMS and gold-rich VMS endowment: Geological Survey of Canada Open File Report 6869, 61 p.

Paton, C., Hellstrom, J., Paul, B., Woodhead, J., and Hergt, J., 2011, Iolite: freeware for the visualisation and processing of mass spectrometric data: Journal of Analytical Atomic Spectrometry, v. 26, p. 2508-2518.

Piercey, S.J., Chaloux, E.C., Péloquin, A.S., Hamilton, M.A., and Creaser, R.A., 2008, Synvolcanic and younger plutonic rocks from the Blake River Group: Implications for regional metallogenesis: Economic Geology, v. 103, p. 1243-1268.

Riciputi, L.R., Paterson, B.A., and Ripperdan, R.L., 1998, Measurement of light stable isotope ratios by SIMS: Matrix effects for oxygen, carbon, and sulfur isotopes in minerals: International Journal of Mass Spectrometry, v. 178, p. 81112.

Savoie, A., Trudel, P., Sauve, P., Hoy, L., and Lao, K., 1991, Geologie de la mine Doyon (region de Cadillac): Ministere de l'Energie et des Ressources, Quebec, Report ET 90-05, 80 p.

Schaltegger, U., and Davies, J., 2017, Petrochronology of zircon and baddeleyite in igneous rocks: reconstructing magmatic processes at high temporal resolution: Reviews in Mineralogy and Geochemistry, v. 83, p. 297-328.

Schmidt, M.X. and Poli, S., 2004, Magmatic epidote: Reviews in Mineralogy and Geochemistry, v. 56, p. 399-430.

Schwindinger, M. and Weinberg, R.F., 2017, A felsic MASH zone of crustal melts – Feedback between granite magma intrusion and *in situ* crustal anataxis. Lithos, 284-285, pp. 109-121.

Sheahan, C., Fayek, M., Quirt, D., and Jefferson, C.W., 2016, A combined ingress-egress model for the Kianna unconformity-related uranium deposit, Shea Creeek Project, Athabasca Basin, Canada: Economic Geology, v. 111, p. 225-257.

Sláma, J., Košler, J., Condon, D.J., Crowley, J.L., Gerdes, A., Hanchar, J.M., Horstwood, M.S.A., Morris, G.A., Nasdala, L., Norberg, N., Schaltegger, U., Schoene, B., Tubrett, M.N., and Whitehorse, M.J., 2008, Plešovice zircon-a new natural reference material for U-Pb and Hf isotopic microanalysis: Chemical Geology, v. 249, p. 1-35.

Smythe, D.J., and Brenan, J.M., 2016, Magmatic oxygen fugacity estimated using zircon-melt partitioning of cerium: Earth and Planetary Science Letters, v. 453, p. 260-266.

Stern, C.R., Funk, J.A., Skewes, M.A., and Arévalo, A., 2007, Magmatic anhydrite in plutonic rocks at the El Teniente Cu-Mo deposit, Chile, and the role of sulfur- and copper-rich magmas in its formation: Economic Geology, v. 102, p. 1335-1344.

Student, J.J., and Bodnar, B.J., 1996, Melt inclusion microthermometry: petrologic constraints from the H2O-saturated haplogranite system: Journal of Petrology, v. 40, p. 1509-1525.

Sun, S.-S., and McDonough, W.F., 1989, Chemical and isotopic systematics of oceanic basalts: implications for mantle composition and processes. In: Saunders, A.D., Norry, M.J. Eds., Magmatism in Ocean Basins. Geol. Soc. Spec. Publ., London, pp. 313–345.

Tan, W., Wang, C.Y., He, H., Xing, C., Liang, X, and Dong, H., 2015, Magnetite-rutile symplectite derived from ilmenite-hematite solid solution in the Xinjie Fe-Ti oxide-bearing mafic-ultramafic layered intrusion (SW China): Americal Mineralogist, v. 100, p. 2348-2351.

Thomas, J.B., Watson, E.B., Spear, F.S., Shemella, P.T., Nayak, S.K., and Lanzirotti, A., 2010, TitaniQ under pressure: the effect of pressure and temperature on the solubility of Ti in quartz: Contributions to Mineralogy and Petrology, v. 160, p. 743-759.

Tomkins, H.S., Powell, R., and Ellis, D.J., 2007, The pressure dependence of the zirconium-in-rutile thermometer: Journal of Metamorphic Petrology, v. 25, p. 703-713.

Tourigny, G., Hubert, C., Brown, A.C. and Crépeau, R., 1989, Structural control of gold mineralization at the Bousquet mine, Abitibi, Quebec: Canadian Journal of Earth Sciences, v. 26, p. 157-175.

Trail, D., Watson, E.B., and Tailby, N., 2012, Ce and Eu anomalies in zircon as proxies for oxidation state of magmas: Geochimica et Cosmochimica Acta v. 97, p 70-87.

Trudel, P., Sauve, P., Tourigny, G., Hubert, C., and Hoy, L., 1992, Synthese des caracteristiques geologiques des gisements de la region de Cadillac (Abitibi): Ministere des Ressources naturelles, Quebec, Report MM 91-01, 106 p.

Valiant, R.I., and Hutchinson, R.W., 1982, Stratigraphic distribution and genesis of gold deposits, Bousquet region, northwestern Quebec: Canadian Institute of Mining and Metallurgy Special Volume 24 p. 27−40.

Watts, K.E., and Mercer, C.N., 2020, Zircon-hosted melt inclusion record of silicic magmatism in the Mesoproterozoic St. Francois Mountains terrane, Missouri: Origin of the Peak Ridge iron oxide-apatite-REE deposit and implications for regional crustal pathways of mineralization: Geochimica et Cosmochimica Acta, v. 272, p. 54-77.

Wones, D.R., Significance of the assemblage titanite + magnetite + quartz in granitic rocks: American Mineralogist, v. 74, p. 744-749.

Wiedenbeck, M., Hanchar, J.M., Peck, W.H., Sylvester, P., Valley, J., Whitehouse, M., Kronz, A., Morishita, Y., Nasdala, L., 2004, Further characterisation of the 91500 zircon crystal: Geostandards and Geoanalytical Research, v. 28, p. 9-39.

Yergeau, D., 2015, Géologie du gisement synvolcanique aurifère atypique Westwood, Abitibi, Québec: Unplublished Ph.D. thesis, Quebec, Canada, Canada, Institut National de la Recherche Scientifique, Centre Eau, Terre et Environnement, 671 p.

Zen E., and Hammarstrom, J.M., 1984, Magmatic epidote and its petrologic significance: Geology, v. 12, p. 515-518.

APPENDIX 1: Revised_8a_Appendix 1 - Ti-in-quartz.xlsx

APPENDIX 2: Revised_8a_Appendix 2 - Zircon_Chem.xlsx

APPENDIX 3: Revised_8a_Appendix 3 - Titanite_Chem.xlsx

APPENDIX 4: Revised_8a_Appendix 4 - Rutile_Chem.xlsx

Pyrite and pyrrhotite in a prograde metamorphic sequence, Hyland River region, SE Yukon: implications for orogenic gold

C.D.W. Padget[1], D.R.M. Pattison[1], D.P. Moynihan[2], and O. Beyssac[3]

Padget, C.D.W., Pattison, D.R.M., Moynihan, D.P., and Beyssac, O., 2021. Pyrite and pyrrhotite in a prograde metamorphic sequence, Hyland River region, SE Yukon: implications for orogenic gold; in *Targeted Geoscience Initiative 5:grant program final reports (2018-2020), Geological Survey of Canada, Open File 8755, p. 169–200. https://doi.org/10.4095/328987*

Abstract: The distribution of pyrite and pyrrhotite is documented within an andalusite-sillimanite type (high-temperature, low-pressure) metasedimentary succession exposed in the Hyland River region of southeastern Yukon, Canada. The following metamorphic zones are recognized: chlorite, biotite, cordierite/staurolite (porphyroblast-in), andalusite, sillimanite, and K-feldspar + sillimanite. Pyrite occurs in the chlorite zone through the biotite zone, while pyrrhotite occurs from the chlorite zone to K-feldspar + sillimanite zone. The pyrite-pyrrhotite transition, therefore, occupies an interval in the chlorite and lower biotite zones that is terminated upgrade by a pyrite-out isograd in the upper part of the biotite zone or lowest grade part of the cordierite/staurolite zone. Pressure and temperature conditions of the rocks were estimated from phase equilibrium modelling and from Raman spectroscopy of carbonaceous material (RSCM) thermometry. Modelling indicates pressures of 3.7–4.1 kbar with temperatures of ~425 °C at the biotite isograd, 560–570 °C for chlorite-out/porphyroblast-in, ~575 °C for andalusite-in, 575–600 °C for the sillimanite isograd, and 645–660 °C at the K-feldspar + sillimanite isograd. RSCM temperatures are ≥ 420 °C in the Chl zone, 500 °C at the Bt isograd, 525-550 °C for porphyroblast-in isograd, ~550 °C at the And isograd, and 580 °C at the Sil isograd. These results suggest the pyrite-pyrrhotite transition occurs from ≤420°C to ~560 °C. Thermodynamic modelling shows 0.6 wt. % H_2O is released during metamorphism over the ~140 °C interval of the pyrite-pyrrhotite transition. The gradual release of fluid in the biotite zone is interpreted to have broadened the pyrite-pyrrhotite transition compared to other studies that predict a small interval of vigorous fluid release associated with volumetric chlorite consumption. Samples from the pyrite-pyrrhotite transition zone contain lower whole rock and pyrite Au values than samples from unmetamorphosed/lower rocks, suggesting that Au was removed from the rock at conditions below the pyrite-pyrrhotite transition (<420 °C). The chlorite zone and higher-grade metamorphic rocks of the Hyland River area do not appear to be a plausible source region for orogenic gold.

[1]University of Calgary, Department of Earth Sciences, 2500 University Drive Northwest, Calgary, AB T2N 1N4
[2]Yukon Geological Survey, 91807 Alaska Hwy, Whitehorse, YT Y1A 0R3
[3]IMPMC, UMR 7590, Sorbonne Université-CNRS-MNHN-IRD, Paris, France

INTRODUCTION

Orogenic gold deposits (Bohlke, 1982) are a group of gold-bearing quartz and quartz-carbonate vein-type deposits hosted in low-grade (greenschist facies) igneous or sedimentary rocks. Several models have been suggested for the source of mineralizing fluids and metals (see Kerrich, 1983; Goldfarb and Groves, 2015). The most widely agreed upon is the metamorphic fluid model (e.g., Cox et al., 1991; Phillips and Powell, 2010; Tomkins, 2013; Goldfarb et al., 2005), in which the breakdown of hydrous minerals (e.g., clays, chlorite, micas) generates fluids capable of scavenging metals from the rock and transporting them to higher levels in the crust.

Diagenetic pyrite contained in carbonaceous shales often contain elevated concentrations of gold and other metals (e.g., Large et al., 2011; Thomas et al., 2011) making these an optimal source rock for the metals in orogenic gold deposits (Gaboury, 2013; Tomkins, 2013). The pyrite in the original sediments is formed through a sequence of steps beginning with the reduction of seawater sulphate by bacteria under anoxic conditions to produce sulphide in the form of H_2S (Berner, 1984). This reduced S mixes with available iron in the sediment to form a series of precursory iron sulphide minerals (e.g., mackinawite—$FeS_{0.9}$, greigite—Fe_3S_4; Berner, 1984; Hunger and Benning, 2007). The final conversion to pyrite (FeS_2) occurs during diagenesis, and this newly formed pyrite contains higher mean trace element concentrations than later-formed or recrystallized pyrite (Large et al., 2007). Increasing pressure and temperature conditions associated with continued diagenesis and progressive metamorphism eventually results in the conversion of pyrite to pyrrhotite (Toulmin and Barton, 1964; Carpenter, 1974). During this conversion, Au and other metals able to reside within the pyrite crystal structure, but not that of pyrrhotite, are released (Thomas, 2011).

The pyrite-pyrrhotite transition is also considered a major control on the release of sulphur to metamorphic fluids (Toulmin and Barton, 1964; Tomkins, 2010; Zhong et al., 2015) by the reaction:

$$FeS_{2(pyrite)} + H_2O = FeS_{(pyrrhotite)} + H_2S_{(aq)} + \frac{1}{2}O_{2(aq)} \quad (1)$$

This desulphidation reaction promotes the transport and dissolution of gold because the metal complexes with HS^- in low-salinity, mixed H_2O-CO_2 metamorphic fluids (Powell et al., 1991; Phillips, 1993). Such fluids are thought to be generated most voluminously at the greenschist-amphibolite facies transition where chlorite reacts out of the rock to generate metamorphic porphyroblasts such as garnet and staurolite in metapelites and hornblende in metabasites (e.g., Powell et al., 1991; Phillips, 1993; Tomkins, 2010, Starr and Pattison, 2019).

The position of the pyrite-pyrrhotite transition with respect to major silicate reactions has been documented in several metamorphic sequences. The first appearance of pyrrhotite in Barrovian-type metasedimentary rocks of Tennessee and North Carolina occurs slightly below the biotite isograd and was mapped as a regional metamorphic isograd (Carpenter, 1974). Ferry (1981) investigated the pyrite-pyrrhotite transition in a sequence of graphitic, sulphide-rich rocks in south-central Maine subjected to Buchan-type metamorphism. There, pyrrhotite was reported coexisting with pyrite from lower-greenschist to upper-amphibolite facies with estimated pressure and temperature conditions of ~3.5 kbar and 375–575 °C. In the metaturbidites of the Otago schist in New Zealand, pyrite is converted to pyrrhotite under sub-greenschist to upper-greenschist facies conditions (Pitcairn et al., 2010). Finch and Tomkins (2017) investigated the pyrite-pyrrhotite transition in graphitic rocks sampled through the well-studied metamorphic sequence of the contact aureole surrounding the Ballachulish igneous complex in western Scotland (Neumann, 1950; Pattison & Harte, 1985, 1997, 2001). There, diagenetic pyrite is absent in rocks above the cordierite isograd associated with the contact aureole. Pyrite is documented only outside the aureole, where regional metamorphic conditions reached ~500 °C and ~7 kbar. This is interpreted to reflect an upper limit of the pyrite-pyrrhotite transition of 500–550 °C.

The goal of this research is (1) to document the nature of the pyrite-pyrrhotite transition relative to major, fluid-producing, silicate reactions in metapelitic rocks of the Hyland River region of southeastern Yukon and (2) assess to what degree sulphur, gold, and other metals are mobilized through the metamorphic sequence. We use field and petrographic observations combined with phase equilibrium modelling and quantitative thermometry based on Raman spectroscopy of carbonaceous material (RSCM) to provide pressure and temperature constraints on the pyrite-pyrrhotite transition. The whole rock geochemistry and trace element content of pyrite and pyrrhotite are compared against published data for samples from lower metamorphic grades in the Hyland River area to evaluate broad trends in element mobility in the region. Phase equilibrium modelling was performed to assess fluid generation (temperature and volumes) in the rocks. We compare our findings with other similar studies worldwide to assess implications for the genesis of orogenic gold.

GEOLOGIC SETTING

The Hyland River region is located within the Selwyn fold belt of the northern Canadian Cordillera (Fig. 1). The area is underlain by rocks of the Neoproterozoic to Paleozoic Hyland Group (Gordey and Anderson, 1993), which includes >3 km of mixed-clastic and lesser carbonate rocks deposited during the formation of the western Laurentian (Cordilleran) continental margin. The region also includes abundant mid-Cretaceous (98–107 Ma) felsic to intermediate intrusions (Moynihan, 2020).

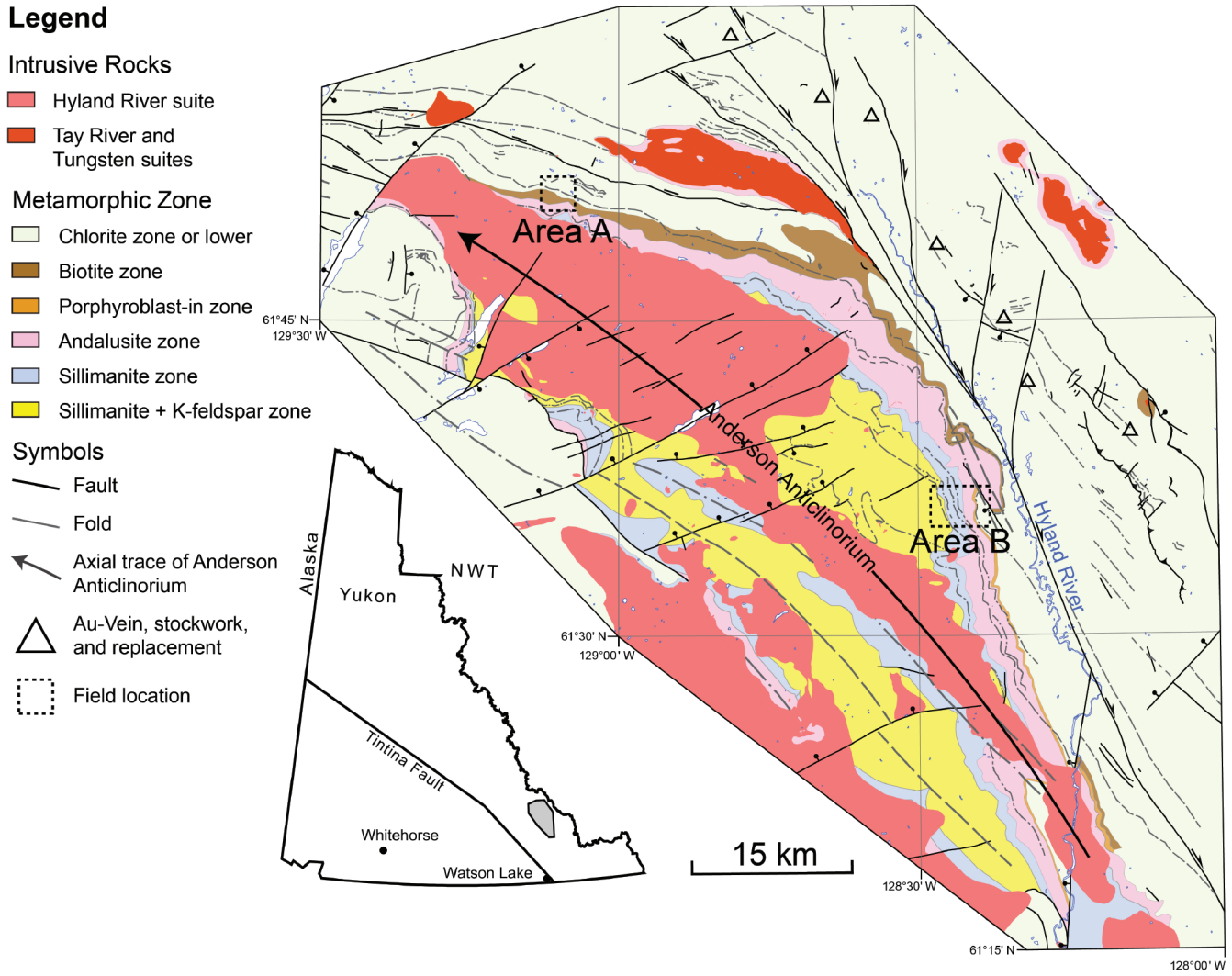

Figure 1. Metamorphic map of the Hyland River region of southeastern Yukon Territory, Canada. Field areas for this study are marked as dashed boxes and labelled Area A & B. Figure modified after Moynihan (2020).

The study area underwent polyphase deformation during development of the Cordilleran orogen (Monger and Gibson, 2019). The dominant structures (D2) in the area are a series of high amplitude (10–15 km), SW-vergent recumbent folds (F2) that arch over a NW-SE trending structural culmination, termed the Anderson anticlinorium (Fig. 1). The anticlinorium is ~50 km wide, 90 km long and hosts many upright parasitic (F3) folds. Formation of the recumbent (F2) folds was accompanied by development of an axial planar cleavage/schistosity (S2), and by greenschist to upper amphibolite-facies, low pressure regional metamorphism. The following metamorphic zones, in order of increasing grade, are recognised: chlorite, biotite, porphyroblast-in (cordierite or staurolite), andalusite, sillimanite, and K-feldspar + sillimanite. The highest-grade rocks are in the centre of the anticlinorium and metamorphic grade decreases gradationally to the north and east (Fig. 1). Regional metamorphic isograds on the northeast flank of the Anderson Anticlinorium are condensed due to high metamorphic field gradients and are crosscut by intrusions of the Hyland River suite (107–105.5 Ma) intrusions. U-Th-Pb monazite dates of 110–108 Ma from metapelitic schist suggest peak metamorphic conditions occurred just prior to the emplacement of these intrusive bodies at the current level of exposure (Moynihan, 2020).

The region has several features favourable for the generation of orogenic gold deposits, including a compressional/transpressional tectonic environment leading to large-scale faulting; high-temperature/low-pressure metamorphism, which promotes the generation of S-rich hydrothermal fluids; and thick sequences of sedimentary rocks with abundant intervals of sulphide-bearing, carbonaceous shales (e.g., Goldfarb et al., 1988; Tomkins, 2010). In addition, the Hyland River region host numerous Au occurrences (Fig. 1; triangles) in chlorite zone or lower grade metasedimentary

rocks. In these occurrences, gold is found in quartz-vein systems associated with pyrite, arsenopyrite, and galena (Hart and Lewis, 2006).

PETROGRAPHY

Two study areas were chosen to investigate the distribution of pyrite and pyrrhotite across the range of metamorphic grades exposed in the region (Fig. 1). Area A was chosen for a detailed investigation of the pyrite-pyrrhotite transition, while area B was chosen to extend the study of sulphide evolution to higher metamorphic grades. Both locations are underlain by the same stratigraphy as the Au occurrences to the east but are separated from these occurrences by the dextral-slip Hyland fault, a regional-scale fault system with tens of kilometres of offset (Moynihan, 2017). Fifty samples were collected from area A and seventeen from area B. Weathered samples and those close to or containing veins were avoided where possible.

Many samples from both areas A and B contain evidence for local alteration. Examples in silicate minerals include near complete pinitisation of cordierite and local replacement of biotite by chlorite. The most common alteration products of sulphides are iron hydroxides (e.g., goethite), which form around, within, or entirely replace grains of pyrite and pyrrhotite (Fig. 10a, b). Pyrite interpreted as retrograde after pyrrhotite forms small, inclusion-free cubes within or along the margin of pyrrhotite grains. Marcasite (FeS_2), the orthorhombic dimorph of pyrite, forms along fractures and grain boundaries of pyrrhotite (Fig. 10e & f). Two samples contain retrograde pyrite after pyrrhotite, and five contain marcasite.

The silicate and sulphide mineral assemblages for each metamorphic zone are described separately for areas A and B below. Mineral modes and relative abundances are visual estimates from thin section petrography. Zone widths are from map distance along the surface and represent apparent thicknesses of the zones because isograds dip moderately to the northeast (see Figs. 2 & 3). Table 1 lists silicate and sulphide mineral assemblages; all mineral abbreviations are after Kretz (1983).

Area A

Area A (Fig. 2) includes rocks of the chlorite, biotite, 'outer porphyroblastic' (cordierite ± staurolite) and andalusite zones. The dominant sulphide phase varies with metamorphic grade; pyrite is more abundant than pyrrhotite in chlorite zone rocks, while pyrrhotite is the primary sulphide phase above the biotite isograd. Subordinate quantities of chalcopyrite, sphalerite, and galena are present in all metamorphic zones but occur in the greatest abundance with samples containing pyrrhotite.

Chlorite zone

The chlorite zone is the lowest metamorphic grade in the region and is defined by the assemblages Chl + Ms + Qtz + Pl in variably carbonaceous metapelitic and semipelitic rocks (Fig. 4d; CP075). Most are well-foliated phyllites with compositional banding at the mm to cm scale. Muscovite in the matrix defines S2 at this and higher metamorphic grades. Chlorite generally forms parallel to foliation as fine-grained aggregates intergrown with muscovite. Locally, samples contain 200-300 μm chlorite knots (Fig 4e inset; CP047). Rounded, detrital, quartz grains of up to 8 mm in maximum dimension are preserved in non-porphyroblastic (chlorite and biotite zone) samples. Ilmenite is present in 26 samples from area A and six from area B and forms tabular laths parallel to sub-parallel to the foliation. Rutile occurs in 30 samples from area A and 8 samples from area B as a matrix phase. Rutile does not show any preferential alignment with respect to the dominant foliation. The two minerals coexist in 11 samples from area A and 3 from area B and exhibit these same characteristics throughout.

The most abundant sulphide phase is pyrite. It is present in 17 of 32 chlorite zone samples and occurs as 10-50 μm, isolated or clustered, sub- to euhedral crystals. Larger, >100 μm grains are uncommon (Fig. 5a; CP075). Rarely, pyrite contains rounded, inclusion-rich diagenetic cores. Pyrrhotite is the sole sulphide phase in 5 of 32 chlorite zone samples and coexists with pyrite in eight samples. Pyrrhotite forms either around pyrite grains (Fig. 5b; CP056) or as isolated 50–100 μm blocky grains. Trace chalcopyrite occurs as 25–100 μm blebs often included in or along the margins of pyrrhotite grains. Nine samples from the chlorite zone do not contain sulphide.

Biotite zone

The biotite zone is ~500 m wide and defined by the assemblage Bt ± Chl + Ms + Qtz ± Pl. Most samples are well foliated phyllites or fine-grained mica schists (Fig. 6a). At the biotite isograd, biotite occurs as small (<100 μm), foliation-parallel flakes distributed throughout the matrix. Biotite coarsens and becomes more abundant with proximity to the outer porphyroblast zone, where it occurs parallel to the dominant foliation (S2). Pyrrhotite is present in 4 of 7 samples and is the most abundant sulphide phase above the biotite isograd. Pyrrhotite forms foliation parallel stringers up to 2 cm in length and typically contains inclusions of quartz, chlorite, and (or) biotite (Fig. 5d; CP059). Four samples contain pyrite, which hosts fewer inclusions and are slightly larger than those of the chlorite zone; pyrite under 25 m is rare or absent. Where both pyrite and pyrrhotite are present in the rock, pyrite abundance is always subordinate. Chalcopyrite occurs as described for chlorite zone rocks. Sphalerite and galena are rare and, where present, always occur in contact with pyrrhotite.

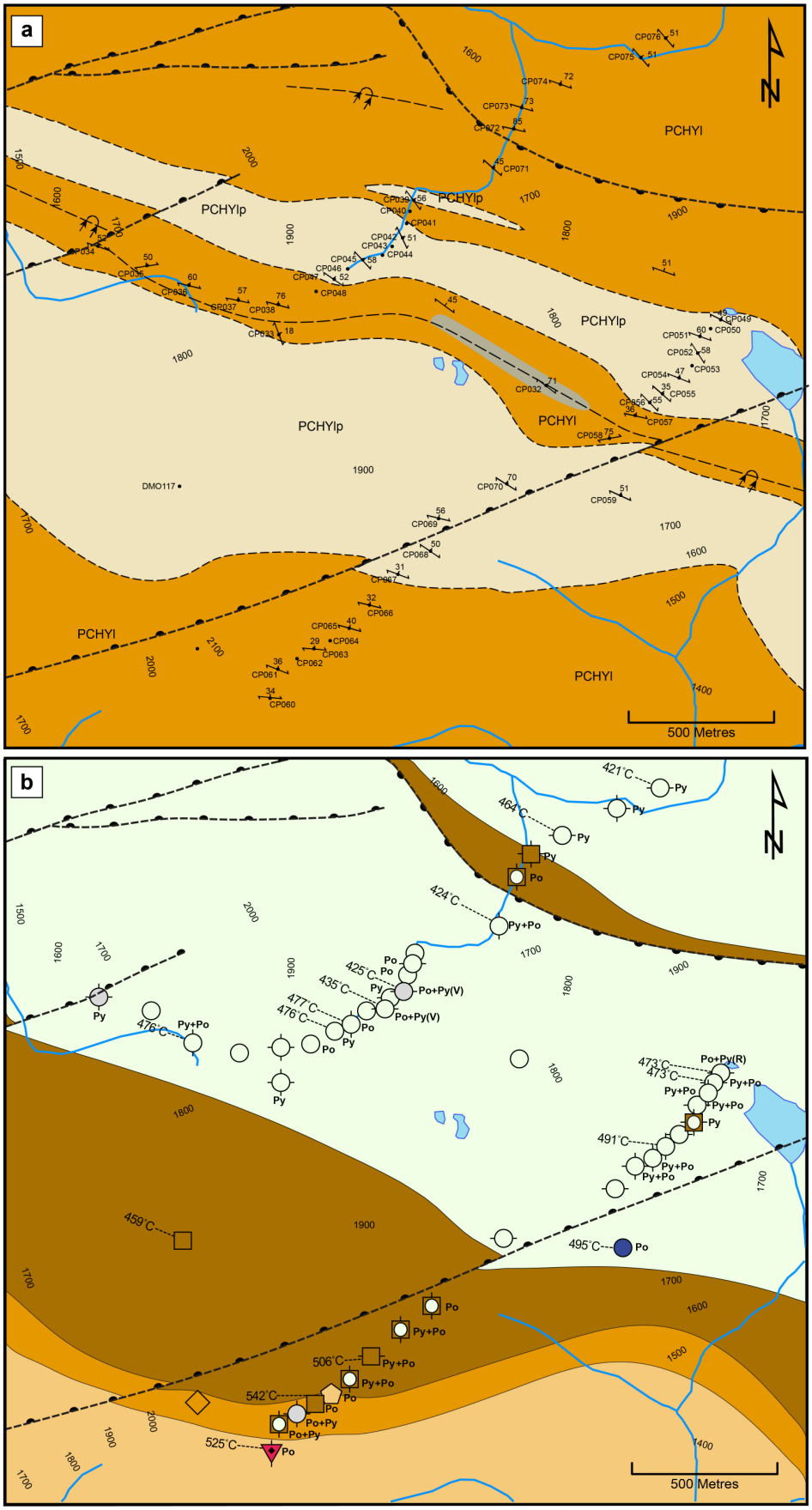

Figure 2. a) Bedrock geology map of area A with sample locations and ID; only samples discussed in text are labelled. **b)** Metamorphic map of area A showing mineral assemblages, metamorphic zones, and RSCM temperature estimates. Legend provided on separate page.

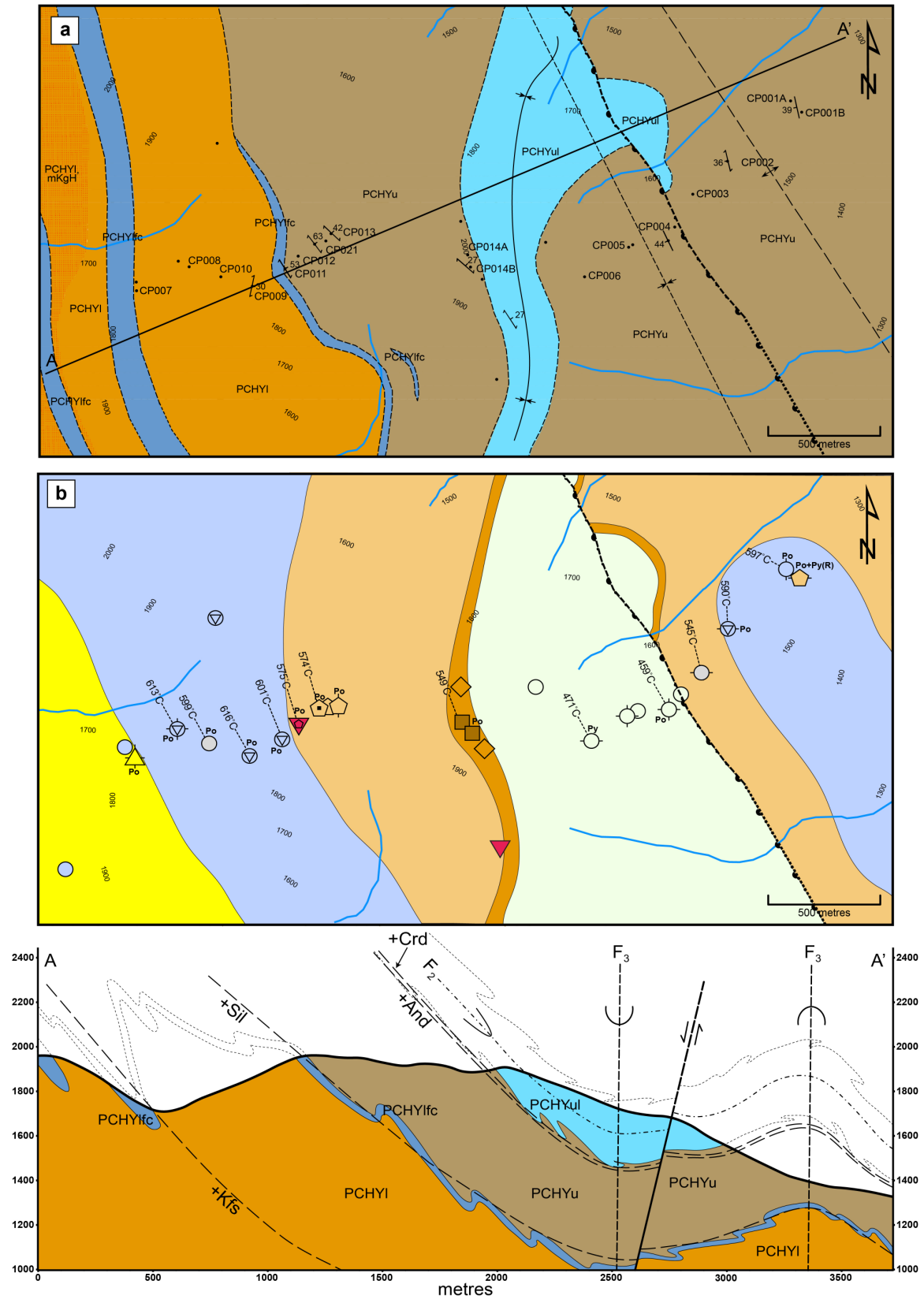

Figure 3. a) Bedrock geology map of area B with sample locations and ID; only samples discussed in text are labelled. **b)** Metamorphic map of area B showing mineral assemblages, metamorphic zones, and RSCM temperature estimates. Cross-section A-A' demonstrates the folding of isograds by F_3 and sub-parallel nature of isograds to lithological boundaries. Legend provided on separate page.

LEGEND FOR FIGURES 2 & 3

METASEDIMENTARY ROCKS

PCHYul — **YUSEZYU FORMATION, UPPER, limestone:** *thin to medium bedded, grey and buff, planar and cross-laminited limestone*

PCHYu — **YUSEZYU FORMATION, UPPER, undivided:** *grey and pale green phyllite, sandstone, granule-pebble conglomerate*

PCHYlfl — **YUSEZYU FORMATION, LOWER, fetid limestone:** *thin to medium bedded, medium to dark grey fetid limestone*

PCHYl — **YUSEZYU FORMATION, LOWER, undivided:** *grey, rusty-brown- weathering phyllite, sandstone, granule-pebble conglomerate*

PCHYlp — **YUSEZYU FORMATION, LOWER, pelitic:** *rusty-brown-weathering phyllite and schist*

PCHYlcs — **YUSEZYU FORMATION, LOWER, calcsilicate:** *dark grey, sulphide-rich marble, calcsilicate, phyllite*

SYMBOLS

geologic contacts (approximate, inferred)...

normal fault.....

antiform.....

synform.....

anticline (overturned).....

sample location.....

compositional layering..... 39

dominant foliation..... 36

RSCM temperature..... 471°C

pyrite, pyrite (vein), pyrite (retrograde)..... Py, Py(v), Py(R)

pyrrhotite..... Po

quartzo-feldspathic / caclsilicate samples... (not used in mineral assemblage maps)

METAMORPHIC ZONE

- Chlorite zone
- Biotite zone
- Outer porphyroblast zone (Cordierite ± Staurolite)
- Andalusite zone
- Sillimanite zone
- Sillimanite + K-feldspar zone

MINERAL ASSEMBLAGES

+ Ms + Qtz + Pl

- chlorite
- chlorite + biotite
- biotite

+ Bt + Ms + Qtz + Pl

- cordierite
- staurolite
- staurolite + cordierite
- andalusite
- andalusite + cordierite
- andalusite + staurolite
- andalusite + staurolite + cordierite
- sillimanite
- sillimanite + andalusite
- K-feldspar + sillimanite

Fe-Ti oxides

- ilmenite
- rutile
- ilmenite + rutile

Table 1. Silicate and sulphide mineral assemblages for Area A and Area B. R=retrograde, Det=detrital, P=pseudomorphed, VH=vein-hosted, N/I=not identified.

Sample #	Map Zone	UTM E	UTM N	Elev. (m)	Grt	Kfs	Sil	St	And	Crd	Bt	Chl	Ms	Qtz	Pl	Ilm	Rt	Ttn	Tur	Py	Po	Ap	Ccp	Mc	Sp
Area A																									
18-CP-033	Chlorite	494098	6857918	1844								x	x	x	x	x	x			x					
18-CP-034	Chlorite	493458	6858238	1698								x	x	x	x	x	x			x					
18-CP-036A	Chlorite	493651	6858134	1709								x	x	x	x	x	x			x	x	x	x		
18-CP-036B	Chlorite	493651	6858134	1709								x	x	x	x	x	x			x					
18-CP-037A	Chlorite	493782	6858094	1706								x	x	x	x		x					x			
18-CP-037B	Chlorite	493782	6858094	1706								x	x	x	x		x					x			
18-CP-038	Chlorite	493954	6858061	1802								x	x	x	x	--N/I--									
18-CP-040	Chlorite	494583	6858388	1706								x	x	x	x	--N/I--	-				x	x			
18-CP-041	Chlorite	494569	6858352	1743								x	x	x	x		x		x		x	x			
18-CP-042	Chlorite	494554	6858314	1729								x	x	x	x	--N/I--				VH	x		x	R	
18-CP-043A	Chlorite	494542	6858265	1717								x	x	x	x		x			x		x	x		
18-CP-043B	Chlorite	494542	6858265	1717								x	x	x	x		x					x			
18-CP-044A	Chlorite	494510	6858230	1761								x	x	x	x		x		x		x	x	x		
18-CP-045A	Chlorite	494475	6858194	1770								x	x	x	x		x					x			
18-CP-045B	Chlorite	494475	6858194	1770								x	x	x	x		x				x	x	x		
18-CP-046	Chlorite	494406	6858188	1773								x	x	x	x	x	x		x	x			x		
18-CP-047	Chlorite	494348	6858149	1800								x	x	x	x	x			x		x	x	x		
18-CP-048	Chlorite	494297	6858115	1802								x	x	x	x	x	x					x			
18-CP-049A	Chlorite	495654	6857958	1712								x	x	x	x		x		x	R	x				
18-CP-049B	Chlorite	495654	6857958	1712								x	x	x	x		x			x		x			
18-CP-050A	Chlorite	495632	6857936	1710								x	x	x			x			x	Det				
18-CP-050B	Chlorite	495632	6857936	1710								x	x	x	x	x	x		x	x		x			x
18-CP-051A	Chlorite	495600	6857901	1701								x	x	x	x		x			x	Det		x		
18-CP-052A	Chlorite	495586	6857850	1728								x	x	x	x		x		x	x	Det				
18-CP-053	Chlorite	495569	6857800	1733					x			x	x	x	x	x	x			x					
18-CP-054C	Chlorite	495518	6857759	1731								x	x	x	x	x						x			
18-CP-055	Chlorite	495462	6857699	1727								x	x	x	x	x									
18-CP-056	Chlorite	495418	6857666	1756								x	x	x		x				x	x		x		
18-CP-057A	Chlorite	495365	6857624	1745								x	x	x	x	x	x		x	x	x		x		
18-CP-58	Chlorite	495271	6857544	1762								x	x	x	x		x								
18-CP-59	Chlorite	495317	6857342	1826					x				x	x	x	--N/I--					x	x	x		x
18-CP-070	Chlorite	494904	6857389	1948								x	x	x			x								
18-CP-071	Chlorite	494870	6858499	1650								x	x	x	x	x				x	x	x	x		
18-CP-074	Chlorite	495102	6858811	1592								x	x	x	x		x			x					

Table 1. (cont.) Silicate and sulphide mineral assemblages for Area A and Area B. R=retrograde, Det=detrital, P=pseudomorphed, VH=vein-hosted, N/I=not identified.

Sample #	Map Zone	UTM E	UTM N	Elev. (m)	Grt	Kfs	Sil	St	And	Crd	Bt	Chl	Ms	Qtz	Pl	Ilm	Rt	Ttn	Tur	Py	Po	Ap	Ccp	Mc	Sp
18-CP-075	Chlorite	495315	6858907	1577								x	x	x	x	x	x			x		x	x		
18-CP-076	Chlorite	495452	6858985	1604								x	x	x	x		x			x					
18-CP-065A	Biotite	494345	6856870	2045					x			x		x	x	x				x	x	x	x		
18-CP-066	Biotite	494418	6856955	2031					x					x	x		x			x	x	x	x		x
18-CP-067	Biotite	494519	6857062	2010					x			x	x	x		x				x	x		x		
18-CP-068A	Biotite	494635	6857144	2006					x			x	x	x	x	x						x			
18-CP-068B	Biotite	494635	6857144	2006					x			x	x	x	x	x									
18-CP-072	Biotite	494946	6858661	1634					x			x	x	x	x	x					x	x		R	
18-CP-073	Biotite	494997	6858745	1598					x			x	x	x	x	x	x			x					
18-CP-60A	Andalusite	494092	6856630	2058			x	P	x			x	x	x	x	x			x		x	x	x		x
18-CP-61	Porphyroblast	494092	6856726	2102					x			x	x	x	x	x			x	x	x	x	x		x
18-CP-62A	Porphyroblast	494161	6856764	2073								x	x	x	x	x	x		x			x			
18-CP-62B	Porphyroblast	494161	6856764	2073								x	x	x	x		x			x	x		x		x
18-CP-063A	Porphyroblast	494220	6856802	2056					x				x	x	x	--N/I--			x		x		x	R	x
18-CP-063B	Porphyroblast	494220	6856802	2056					x			R	x	x	x	x		x	x	x	x	x	x		
18-CP-064	Porphyroblast	494273	6856826	2028			x		x				x	x	x	--N/I--					x		x		x
Area B																									
18-CP-004	Chlorite	532323	6830644	1690								x	x	x	x	x	x		x		x				
18-CP-005	Chlorite	532169	6830629	1733								x	x	x	x	x	x								
18-CP-006	Chlorite	531962	6830486	1803								x	x	x	x		x		x	x					
18-CP-014A	Porphyroblast	531477	6830528	1995					x			R	x	x	x	--N/I--			x						
18-CP-014B	Porphyroblast	531477	6830528	1995					x				x	x	x	--N/I--		x	x		x		x		
18-CP-003	Andalusite	532428	6830848	1610					x				x	x			x		x						
18-CP-012	Andalusite	530735	6830583	1990			x x	P	x				x	x	x	--N/I--					x		x		
18-CP-013	Andalusite	530823	6830646	1995			x		x				x	x	x	--N/I--			x		x		x		
18-CP-021	Andalusite	530863	6830664	1989	x		x		x				x	x	x	x			x						
18-CP-001A	Sillimanite	532853	6831234	1507	x	x	x x		x			R		x	x	x			x		x				
18-CP-001B	Sillimanite	532853	6831234	1507			x	P	x			R	x	x	x		x	x	x	R	x		x	R	
18-CP-002	Sillimanite	532578	6830994	1565		x	x		x			R	x	x	x		x				x			R	
18-CP-008	Sillimanite	530220	6830563	1763	x	x	x x		x				x	x	x	x	x		x		x				
18-CP-009	Sillimanite	530462	6830411	1840								R	x	x	x	--N/I--					x				
18-CP-010	Sillimanite	530535	6830451	1906	x	x	x x		x				x	x	x	--N/I--					x				
18-CP-011	Sillimanite	530667	6830528	1992		x	x x		x				x	x	x	--N/I--			x		x				
18-CP-007	K-feldspar	530036	6830453	1759	x	x x			x				x	x	x	x					x				

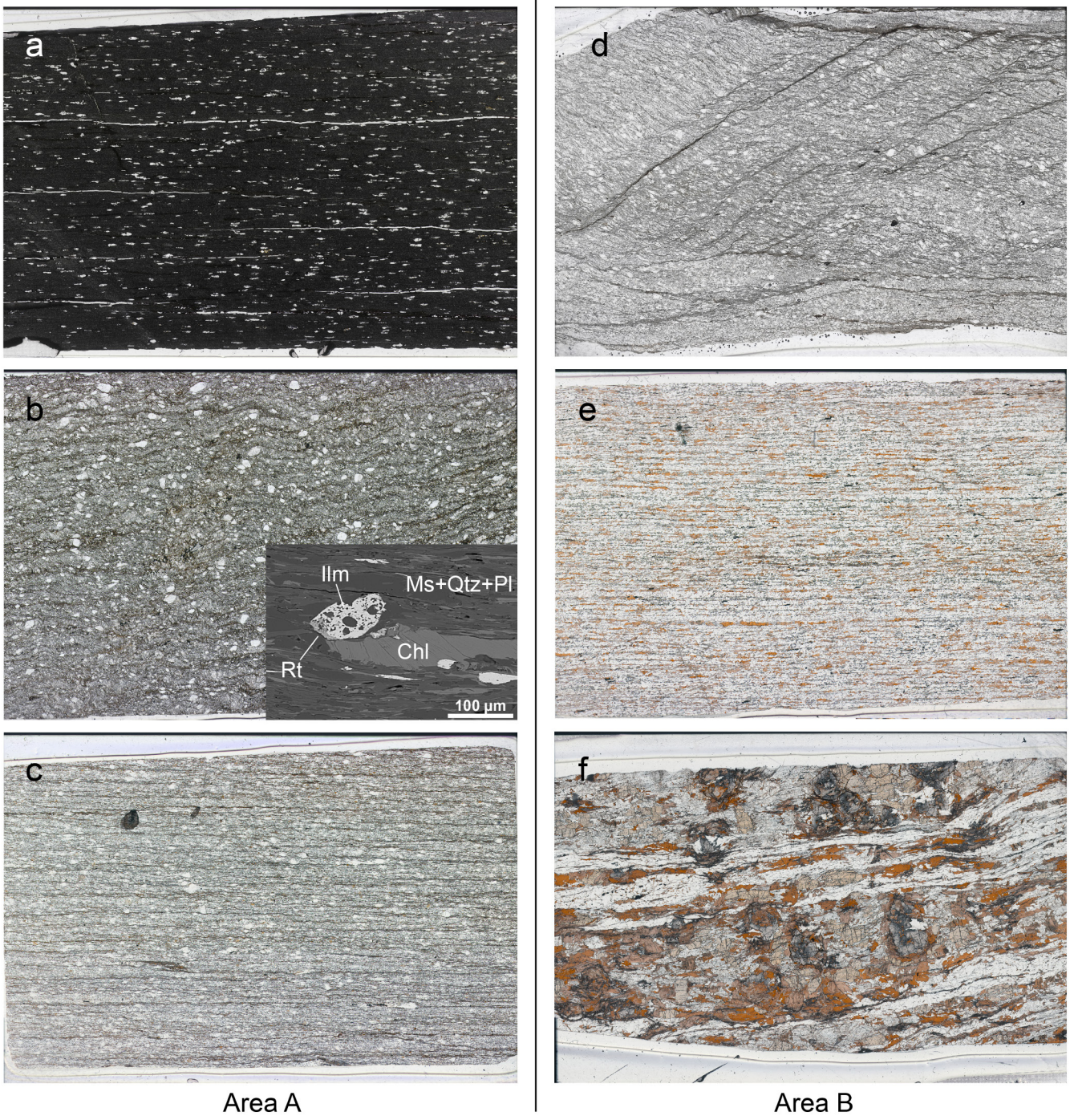

Figure 4. Polished thin section scans showing representative rock textures for Area A **(a, b, and c)** and Area B **(d, e, and f)**. **a)** Chlorite zone, carbonaceous pelitic sample (CP075). Fine-grained chlorite and abundant carbonaceous material. Pyrite as sulphide phase. **b)** Chlorite zone, semipelitic sample (CP047), abundant chlorite along phyllitic partings. Sulphides are pyrrhotite and chalcopyrite. **c)** Andalusite zone, psammitic sample. Andalusite and cordierite (not visible) present as small (< 100 µm) porphyroblasts within thin, phyllitic horizons. Sample contains minor pyrrhotite. **d)** Chlorite zone, semipelitic sample (CP006). Dominant foliation (S_2) deformed by later crenulation. Trace pyrite as the sole sulphide phase. **e)** Staurolite zone, pelitic sample (CP013). Abundant fine grained staurolite (see inset); foliation parallel stringers of pyrrhotite (black in image). **f)** Sillimanite zone, pelitic sample (CP008). Large garnet porphyroblasts surrounded by biotite, staurolite, and sillimanite; + andalusite. Minor fine grained pyrrhotite. Field of view for all images is ~4.5 cm.

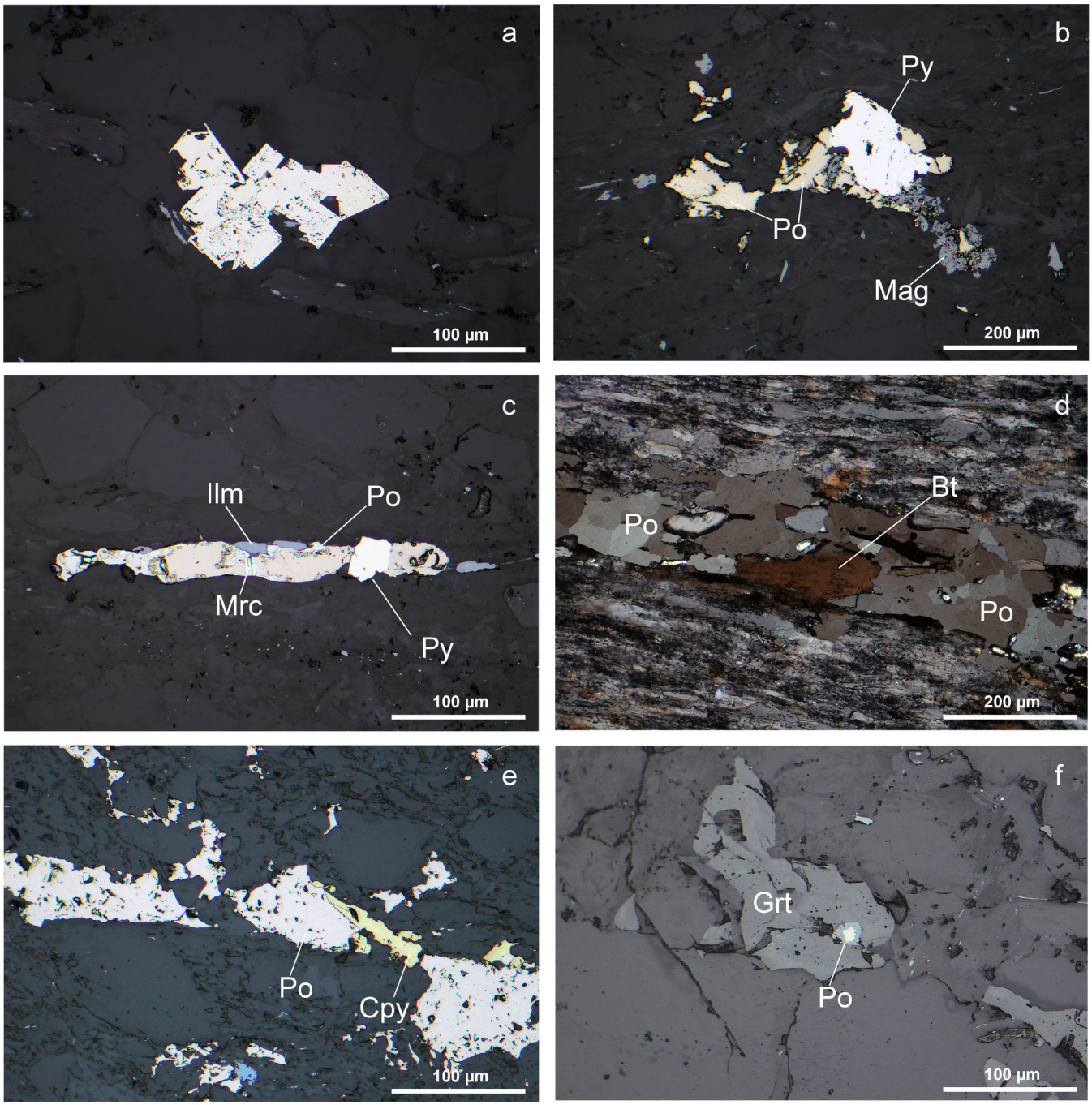

Figure 5. Reflected light photomicrographs of common pyrite and pyrrhotite textures. **a)** Cluster of euhedral pyrite crystals from area A chlorite-zone phyllite with inclusion-rich cores. **b)** Area A chlorite zone sample showing pyrrhotite around pyrite with magnetite. **c)** Subhedral pyrite crystal interpreted as retrograde after pyrrhotite in area B sillimanite zone sample. Pyrrhotite is shown growing parallel to the dominant foliation with small tabular ilmenite (grey). Marcasite alteration along fractures and margins of pyrrhotite. **d)** Coarse, area A biotite zone, pyrrhotite with inclusions of biotite and quartz under partially cross-polarized light showing characteristic anisotropy of pyrrhotite. **e)** Pyrrhotite with chalcopyrite from area A chlorite zone. **f)** Area B sample showing pyrrhotite inclusion in garnet. Pyrrhotite is rimmed by Fe-hydroxide.

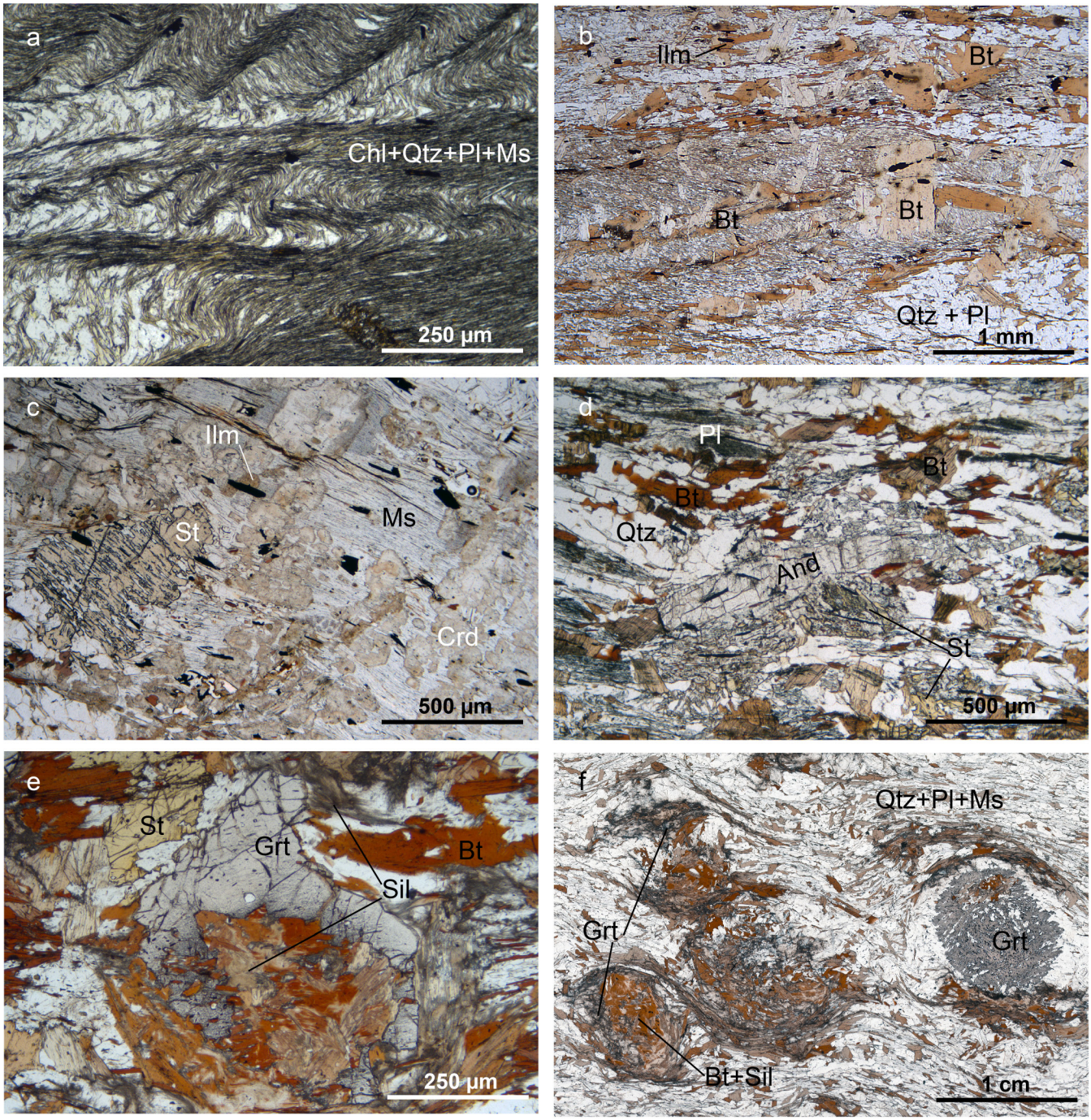

Figure 6. Transmitted-light photomicrographs showing representative textures and mineralogy for each metamorphic zone in area B. **a)** crenulations developed in a Chl-Ms-Qtz bearing phyllite (CP005) of the chlorite zone. **b)** Bt-Chl-Ms-Qtz bearing schist (CP014B). **c)** St+Crd bearing schist (CP012) from Staurolite ± Andalusite zone. Poikilitic, subhedral staurolite with inclusion trails following S_2 foliation. Subhedral cordierite is almost completely pseudomorphed by pinite. **d)** And+St bearing schist (CP011). Andalusite is shown replacing staurolite. Plagioclase contains abundant carbonaceous material causing a dusty appearance. **e)** Sil+And+St+Grt bearing schist (CP008) from the sillimanite zone. Biotite is locally replaced by sillimanite, and garnet is extensively replaced by Bt and Sil. **f)** Kfs+Sil+Grt schist (CP007). Large, poikilitic garnet porphyroblasts are wrapped by S_2 defined by aligned sillimanite and biotite. Abundant foliation parallel, coarse muscovite.

Outer Porphyroblast zone

The outer porphyroblast zone is ~125 m wide and defined by the first appearance of cordierite or staurolite. Two of the five samples collected are porphyroblastic: one contains the assemblage Crd + Bt + Ms + Qtz + Pl and the other contains St + Bt + Ms + Qtz + Pl. The three remaining samples contain Bt + Ms + Qtz + Pl. Staurolite occurs as sub-200 μm crystals along thin micaceous partings within a metapsammite. The cordierite-bearing sample contains ovoid, poikilitic cordierite porphyroblasts pseudomorphed by pinite. Biotite is like that described for the biotite zone. Pyrrhotite forms foliation parallel stringers and is present in 4 of 5 samples. Two of these samples contain trace pyrite, which occurs as sub-50 μm, isolated, subhedral grains included within quartz. Chalcopyrite occurs in association with pyrrhotite as small blebby inclusions or along pyrrhotite grain boundaries.

Andalusite zone

Andalusite is present in only one sample (CP060) with the assemblage And + Crd + Bt + Ms + Qtz + Pl. Andalusite and cordierite form sub-100 μm grains along thin micaceous partings (Fig. 4c) and were identified by EDS following BSE imaging on the thin section. Pyrrhotite is the dominant sulphide phase with trace amounts of chalcopyrite and sphalerite forming along pyrrhotite grain boundaries. The sample contains no pyrite.

Area B

Area B (Fig. 3) includes rocks of the chlorite, 'outer porphyroblastic' (cordierite ± staurolite), andalusite, sillimanite, and K-feldspar + sillimanite zones; unlike area A, there is no separate biotite zone. Minor faulting interrupts the metamorphic sequence at the eastern end of the transect, where upright F3 folds fold the metamorphic isograds (see Fig. 3 cross-section). All sulphide-bearing samples above the porphyroblast-in isograd contain pyrrhotite; pyrite is only present in one chlorite zone sample. Trace quantities of chalcopyrite and sphalerite occur in pyrrhotite-bearing samples only.

Chlorite zone

The chlorite zone in area B is defined by the assemblages Chl + Ms + Qtz + Pl in carbonaceous metapelites. The characteristics of silicate and oxide phases are as described for the chlorite zone in area A. Two out of six chlorite zone samples contain sulphides; one contains only pyrite and the other only pyrrhotite. Pyrite occurs as 10–50 μm, isolated sub- to euhedral crystals. There is no pyrite above this grade in area B. Pyrrhotite forms 50–100 m blocky grains.

Biotite zone

There is no biotite zone in area B; the first appearance of biotite is coincident with the development of porphyroblasts of cordierite.

Outer Porphyroblast zone

The outer porphyroblast zone in area B is defined by the assemblage Crd + Bt + Ms + Qtz + Pl in metapelitic rocks, which occurs in two of the four samples collected within this zone. The other two samples contain Bt + Ms + Qtz + Pl. This zone is ~100 m wide. Cordierite occurs as ovoid, poikilitic porphyroblasts typically completely replaced by pinite. Biotite in this zone forms small foliation parallel grains and larger porphyroblasts with no preferred orientation (Fig. 6b). Trace amounts of pyrrhotite and chalcopyrite were observed in one of the four samples from the porphyroblast zone.

Andalusite zone

The andalusite zone is ~700 m wide and defined by the assemblage And ± St + Bt + Ms + Pl + Qtz. Garnet occurs in two samples and one sample contains cordierite with the assemblage And + St + Crd + Bt + Ms + Pl + Qtz. Andalusite forms large, blade-like, poikilitic porphyroblasts up to 20 cm long, which overprint the dominant foliation and only locally exhibit a preferred orientation. Staurolite forms small grains aligned parallel to foliation (Fig. 4b; inset) or as poikilitic, sub- to euhedral porphyroblasts up to 1 cm in maximum dimension (Fig 6c; CP012). In some samples, staurolite is partially replaced by andalusite (Fig. 6d) and often includes the dominant foliation (S2), suggesting syn- to post-kinematic mineral growth.

A single sample from this zone contains cordierite, which is partially pseudomorphed by pinite and forms together with staurolite in domains of coarse, foliation parallel muscovite (Fig. 6c). Garnet is present in one sample (CP021) as 100–200 μm, anhedral porphyroblasts within the matrix. Pyrrhotite occurs in 3 of 5 samples and forms small (<50 μm) an- to subhedral grains, foliation parallel stringers, or blocky aggregates. Chalcopyrite is present in one sample as inclusion within pyrrhotite.

Sillimanite zone

The sillimanite zone is ~600 m wide and defined by the assemblage Sil + And + St ± Grt + Bt + Ms + Qtz + Pl (Fig. 4c & 6e; CP008). Sillimanite forms fine needles within biotite grains or as large mats of hair-like fibres (fibrolite). Garnet forms sub- to euhedral porphyroblasts up to 1 cm in maximum dimension and contains abundant inclusions of plagioclase and quartz. Garnet is typically embayed and partially replaced by biotite, sillimanite, and (or) plagioclase (Fig. 6e). Locally, garnets have a zoned, dusty appearance with dark rims and lighter coloured cores. Pyrrhotite forms as foliation parallel stringers/blebs or isolated grains and is the most abundant sulphide. Only trace amounts of chalcopyrite and sphalerite ae present. Pyrite occurs in one sample (CP001B) as small, euhedral grains hosted within, or along the margins of, pyrrhotite and is interpreted to be retrograde.

K-feldspar + Sillimanite zone

The K-feldspar + sillimanite zone is defined by a single sample with the assemblage Kfs + Sil + Grt + And + Bt + Ms + Qtz + Pl. K-feldspar occurs as small crystals distributed throughout the rock. Fibrolitic sillimanite forms within or surrounding garnet porphyroblasts. Garnet is inclusion-rich and partially to completely replaced by sillimanite and biotite (Fig. 6f). Biotite occurs as foliation-parallel porphyroblasts and as randomly oriented, coarser, red-brown patches associated with garnet and sillimanite. Muscovite forms parallel to the dominant foliation and as larger, irregularly aligned crystals interpreted to be retrograde. Small (<30 μm) inclusions of pyrrhotite within quartz and garnet represent the only sulphide phase (Fig. 5f).

Fe-Ti oxides

Figures 2 and 3 show the distribution of ilmenite ($FeTiO_3$) and rutile (TiO_2) within areas A and B, respectively. Ilmenite occurs as 80–300 μm long tabular laths or as anhedral, inclusion-rich grains, while rutile forms small (sub-200 μm) sub-to-euhedral grains locally intergrown with ilmenite. Rutile locally forms partial rims around ilmenite grains in area A (Fig. 4e inset; CP047) providing textural evidence for replacement of ilmenite by rutile. However, there is no systematic change in the distribution of ilmenite or rutile with metamorphic grade, nor any correlation to the distribution of pyrite and pyrrhotite. Sagenitic biotite above the andalusite isograd in area B contains fine intersecting needles of rutile, which are interpreted to be retrograde.

ANALYTICAL METHODS

Whole Rock Geochemistry

Whole rock geochemical analyses of 21 samples from area A were performed by Activation Laboratories Ltd. in Ancaster, Ontario. Samples were analyzed by LA-ICP-MS following a lithium tetraborate fusion. Reanalysis of samples by INAA was performed to improve detection limits for As, Au, Br, Cr, Mo, Sb, Sc and Se. Additionally, Ga, Pb, Sn, Nb, and Rb were analysed by pressed pellet XRF. Detection limits for major elements were between 0.001–0.01% and trace element detection limits ranged from 0.1 to 5 ppm. Au detection limits were 1 ppb. Five certified reference materials were used to calibrate the data (DNC-1 & BIR-1—Flanagan, 1984; SY-4—Bowman, 1984; W-2a—Govindaraju, 1995). FeO was obtained separately by titration. To facilitate comparison with other studies, which did not directly analyse Fe^{2+} and Fe^{3+}, FeO* in text represents all iron as FeO.

LA-ICP-MS Trace Elements

The Trace element concentration of pyrite and pyrrhotite was obtained by laser ablation inductively coupled plasma mass spectrometry (LA-ICP-MS) using a Resonetics M-50 193 nm excimer laser system connected to an Agilent 7700x quadrupole ICP-MS at the University of New Brunswick. Both samples and standards were loaded into an S155 Lauren Technic sample cell and run through a purge routine after each sample load. Samples were ablated in spot mode using a 33 μm spot size operating at a 3 Hz repetition rate and a laser energy (fluence) of 2.5 J/cm^2. Each spot was ablated for 30 s following 30 s of gas background collection. Carrier gasses were set to a constant flow of 300 ml/min He mixed downstream with 2 ml/min N_2 and 930 ml/min Ar. NIST 610 and MASS-1 (Wilson et al., 2002) were used as external standards and analysed throughout a run, surrounding groups of natural samples. ^{56}Fe was used as an internal standard and derived stoichiometrically for the respective sulphide phase. To assess within sample heterogeneity of trace elements in pyrite and pyrrhotite, between 10–20 grains were analysed where grain size and sulphide abundance allowed. Off-line data reduction was performed using the software Iolite 3 (Hellstrom et al., 2008).

Raman spectroscopy

Raman Spectroscopy was completed using a Renishaw InVia Raman microspectrometer at the Institut de Minéralogie, Physique des Matériaux et Cosmochimie (Paris, France). A circularly polarized, 514.5 nm, argon laser was focused on the sample using a Leica DMLM optical microscope with a 100x objective lens (numerical aperture = 0.85) providing a spot size of ~1 μm in diameter. Laser power was set to 1 mW at the sample surface using neutral density filters and Rayleigh diffusion was removed with notch filters. A 1200 gr/mm grating dispersed the signal prior to analysis by a Peltier cooled RenCam CCD detector. A silicon standard was used for calibration.

Measurements of carbonaceous material were done on polished thin sections. As polishing may damage the structure of the CM at the surface of the sample, all measurements are taken on CM below an adjacent transparent mineral. A minimum of 15 spectra were collected per sample to assess within sample structural heterogeneity. Detrital graphite, present in many samples, was identified by morphology and its high crystallinity compared to CM in the matrix; detrital graphite spectra were not retained. Collected spectra were processed using the software Peakfit following the procedure from Beyssac, Goffé, et al. (2002) and Beyssac and Lazzeri (2012). The uncertainty on temperature estimates is ±50 °C, though work by Beyssac et al. (2004) suggests ±10–15 °C for relative differences in temperature between samples.

RESULTS

Whole Rock Geochemistry

Major and trace element compositions for 21 samples from area A are provided in Table 2 and select scatter plots are presented in Figure 7. Whole rock SiO_2 concentrations range between 44–84 wt. % reflecting the pelitic, semipelitic,

Table 2. Concentrations of major and select trace elements in samples from the upper Hyland River region, southeastern Yukon Territory. Fe^{2+}/Fe^{3+} by titation. *LOI 1 and Total 1 are determined by weight difference following ignition of the sample at 1000°C. LOI 2 and Total 2 have been corrected for ferrous-iron oxidation during ignition using the ferric/ferrous ratio determined by Fe-titration. FeO* is all Fe as FeO.

Sample UTM E UTM N	18CP049A 495654 6857958	18CP049B 495654 6857958	18CP050A 495632 6857936	18CP051A 495600 6857901	18CP052A 495586 6857850	18CP053 495569 6857800	18CP054C 495518 6857759	18CP055 495462 6857699	18CP056 495418 6857666	18CP058 495271 6857544	18CP059 495317 6857342	18CP070 494904 6857389	18CP068A 494635 6857144	18CP067 494519 6857062	18CP066 494418 6856955	18CP065A 494345 6856870	18CP064 494273 6856826	18CP063B 494220 6856802	18CP062 494161 6856764	18CP061 494092 6856726	18CP060A 494092 6856630	Average area A pelite
SiO_2	72.93	44.12	65.73	54.91	53.42	61.12	63.52	72.55	64.10	60.39	35.73	84.28	63.89	56.27	56.92	55.98	58.20	55.15	56.88	55.19	79.23	58.35
Al_2O_3	11.87	31.79	17.75	22.26	24.58	20.04	19.22	11.63	18.52	20.45	9.62	7.49	17.16	22.43	16.91	17.52	15.05	15.41	23.25	14.40	8.70	20.77
FeO	4.40	3.00	4.40	5.80	3.90	4.00	3.40	6.40	4.50	4.80	4.20	3.50	4.90	4.80	5.20	6.70	5.20	7.80	3.30	7.70	4.80	4.52
Fe_2O_3	1.05	2.1	0.3	1.69	1.59	1.92	0.97	1.06	0.43	1.31	0.50	< 0.01	0.83	0.34	2.00	1.51	2.91	0.97	1.07	0.91	0.47	1.31
FeO*	5.35	4.89	4.67	7.32	5.33	5.73	4.27	7.35	4.89	5.98	4.65	3.50	5.65	5.11	7.00	8.06	7.82	8.67	4.26	8.52	5.22	5.69
MnO	0.03	0.02	0.04	0.05	0.03	0.04	0.04	0.06	0.05	0.04	0.21	0.03	0.04	0.05	0.16	0.08	0.07	0.15	0.03	0.14	0.10	0.04
MgO	2.46	2.44	1.92	3.31	1.91	2.09	2.04	1.75	1.40	2.22	2.52	0.96	2.26	2.41	3.64	4.40	3.25	4.76	1.89	6.51	1.84	2.43
CaO	0.15	0.11	0.07	0.14	0.08	0.06	0.16	0.03	0.23	0.05	25.54	0.05	0.17	0.10	7.39	1.62	2.19	6.96	0.10	6.81	0.33	0.39
Na_2O	0.65	0.47	0.82	0.73	0.99	0.83	1.66	0.82	1.42	1.34	0.64	1.07	0.77	0.61	0.63	3.28	0.20	2.39	1.00	3.74	0.21	1.09
K_2O	2.12	8.85	4.59	5.13	5.97	4.61	4.42	1.64	4.11	4.37	2.34	1.03	4.19	5.97	1.74	2.05	5.00	1.19	5.83	0.45	1.82	5.01
TiO_2	0.46	1.03	0.63	1.01	0.87	0.78	0.82	0.54	0.78	0.84	0.43	0.26	0.74	0.81	0.79	1.17	2.23	2.19	0.86	2.09	0.47	0.97
P_2O_5	0.08	0.2	0.1	0.11	0.11	0.09	0.13	0.03	0.06	0.08	0.11	0.03	0.08	0.11	0.17	0.23	0.63	0.59	0.12	0.41	0.08	0.16
S	0.21	0.02	0.02	0.04	0.02	0.05	0.01	0.02	0.05	0.02	1.24	0.02	0.01	0.44	1.88	0.19	0.74	0.29	0.03	0.20	0.03	0.13
LOI 1	3.13	5.73	3.42	4.56	4.52	4.27	3.40	2.71	3.05	4.02	15.98	1.49	3.14	4.13	2.75	3.47	2.95	2.01	3.94	1.23	1.87	3.89
LOI 2*	3.62	6.07	3.91	5.21	4.96	4.72	3.78	3.42	3.55	4.56	16.45	1.88	3.69	4.67	3.33	4.22	3.53	2.88	4.31	2.09	2.41	4.40
Total 1	99.32	99.90	99.79	99.68	97.97	99.86	99.79	99.23	98.64	99.90	97.82	100.10	98.18	98.03	98.30	98.00	97.90	99.57	98.25	99.59	99.93	98.91
Total 2*	99.81	100.20	100.30	100.30	98.40	100.30	100.20	99.94	99.14	100.40	98.30	100.50	98.73	98.57	98.90	98.75	98.48	100.40	98.62	100.40	100.50	99.41
Au (ppb)	< 1	< 1	< 1	< 1	< 1	< 1	< 1	< 1	< 1	3	< 1	< 1	3	< 1	3	< 1	5	< 1	< 1	3	< 1	4
As	19	6	8	29	19	16	< 1	< 1	2	3	9	3	4	< 1	2	< 1	< 1	< 1	< 1	1	8	11
Ba	443	1821	704	821	1126	857	822	272	755	712	456	206	656	1070	755	464	1738	346	937	133	261	960
Bi	< 2	3	< 2	4	8	< 2	< 2	< 2	< 2	< 2	< 2	< 2	< 2	5	5	< 2	7	4	< 2	5	< 2	5
Co	7	4	2	7	4	5	3	6	11	6	13	2	15	24	20	19	31	33	5	43	17	11
Ni	12	7	7	23	11	8	10	14	22	10	23	5	33	47	40	42	45	83	7	105	42	21
Cr	48	110	61	97	113	89	78	45	82	80	45	32	81	103	82	119	38	90	95	134	40	88
Cu	32	8	8	21	30	24	11	13	47	13	31	4	12	42	55	15	36	20	12	43	33	21
Pb	7	8	9	8	13	23	7	7	16	16	10	6	23	21	35	23	< 5	8	27	11	8	16
Sb	0.3	0.8	0.6	0.5	0.7	0.6	0.5	0.3	0.2	0.2	0.3	0.2	0.3	0.3	0.4	0.2	0.2	< 0.1	0.2	0.3	0.3	0.4
Sn	< 5	8	< 5	< 5	7	6	< 5	< 5	< 5	< 5	< 5	< 5	< 5	< 5	8	< 5	< 5	< 5	5	< 5	< 5	7
Zn	103	62	64	107	64	76	64	84	65	75	53	47	107	178	136	116	139	126	55	111	106	90

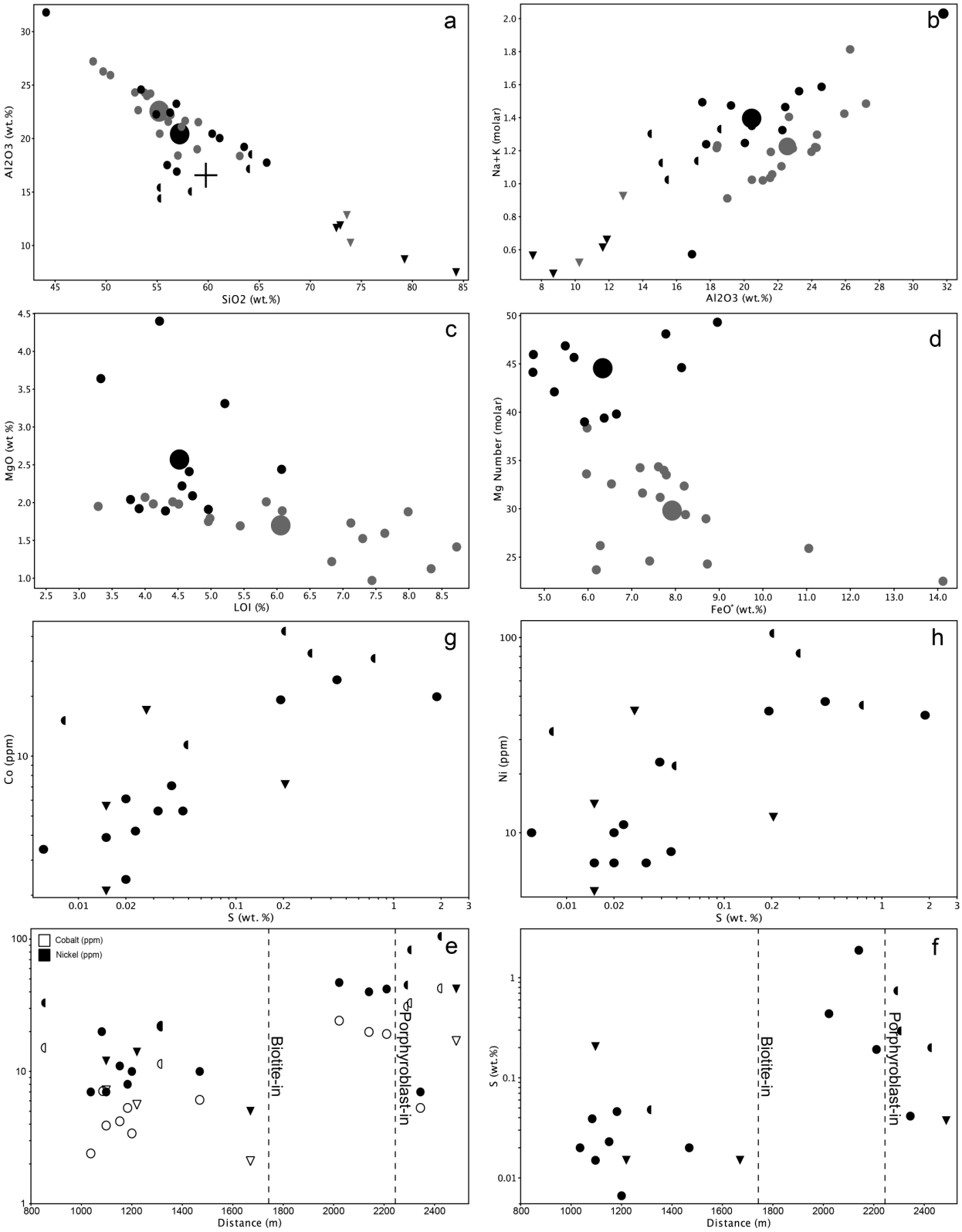

Figure 7. (a) to **(f)**: Select scatter plots from area A whole-rock geochemical data. Distance is surface distances. Data from: black (this study), dark-grey (Sack et al., 2018). Large circles show mean values for each dataset. For all plots, circles represent pelitic samples, half-circles are semi-pelites, and triangles show data for psammitic samples. The + in (a) represents values from the “average pelite” of Ague (1991).

and psammitic lithologies representative of lower Yusezyu Formation stratigraphy. Ferrous iron ranges from 3.0 to 7.8 wt. % with a mean of 4.9 wt. %. The ratio of ferric to ferrous iron (molar $Fe^{3+}/\Sigma Fe$) for pelitic samples in area A is 0.09 ± 0.06 (n = 16, 1SD), much lower than the Ague (1991) average of 0.30 for pelitic rocks.

To remove the bulk compositional effects of varying amounts of detrital plagioclase and quartz in the original sediments, rock compositions are plotted on a molar AFM diagram (Fig. 8) after projections from Ms, Qtz, Ap, the Ab and An components of plagioclase, and depending on the minerals present, Ru/Ilm and Py/Po. On this diagram, [A] = Al_2O_3 - $3K_2O$ - Na_2O - (CaO - [$10/3P_2O_5$]), [F] = FeO* - TiO_2 – SO_3), [M] = MgO. The use of measured FeO values in place of FeO* displaces points on the AFM to higher values of Mg/(Mg+Fe). All samples plot between the low- and high-Al pelite fields of Spear (1993) with [A] values of 0.12–0.26 (mean, 0.19; St. Dev., 0.04), higher than global average of 0.04 for greenschist facies metapelites (Ague, 1991). Mg# ranges from 0.31 to 0.56 (mean, 0.44; St. Dev., 0.07), compared with a global average of 0.44. Sulphur ranges from 0.01 to 0.44 wt. % (mean, 0.07; St. Dev., 0.11), and is comparable to average pelitic S content of 0.10% (average Nelson pelite from Pattison and Vogl, 2005).

Whole rock Au is low in all samples with only 5 of 21 reporting values above detection limits. These range from 1 ppb (detection limit) to a maximum value of 5 ppb. Mean Ag, Mo, and W are below detection in all samples and As ranges from below detection to a maximum concentration of 29 ppm (mean, 11 ppm). Copper ranges from 4 to 47 ppm (mean, 20 ppm), Sb from 0.2 to 0.8 ppm (mean, 0.4 ppm), and Cr from 32 to 119 ppm (mean, 77 ppm). Co ranges from 2 to 31 ppm (mean, 10 ppm) and Ni from 5 to 47 ppm (mean, 20 ppm). Higher values of Co and Ni correlate with higher bulk S (Fig. 7e-h).

Pyrite and Pyrrhotite Trace Element Chemistry

The trace element contents of pyrite and pyrrhotite is presented in Table 3 and select scatter plots are shown in Figure 9. Forty-eight pyrite grains were analyzed from four samples from the chlorite zone of area A. Three hundred and twenty-eight pyrrhotite grains were analyzed from twenty-nine samples collected across all metamorphic zones in area A.

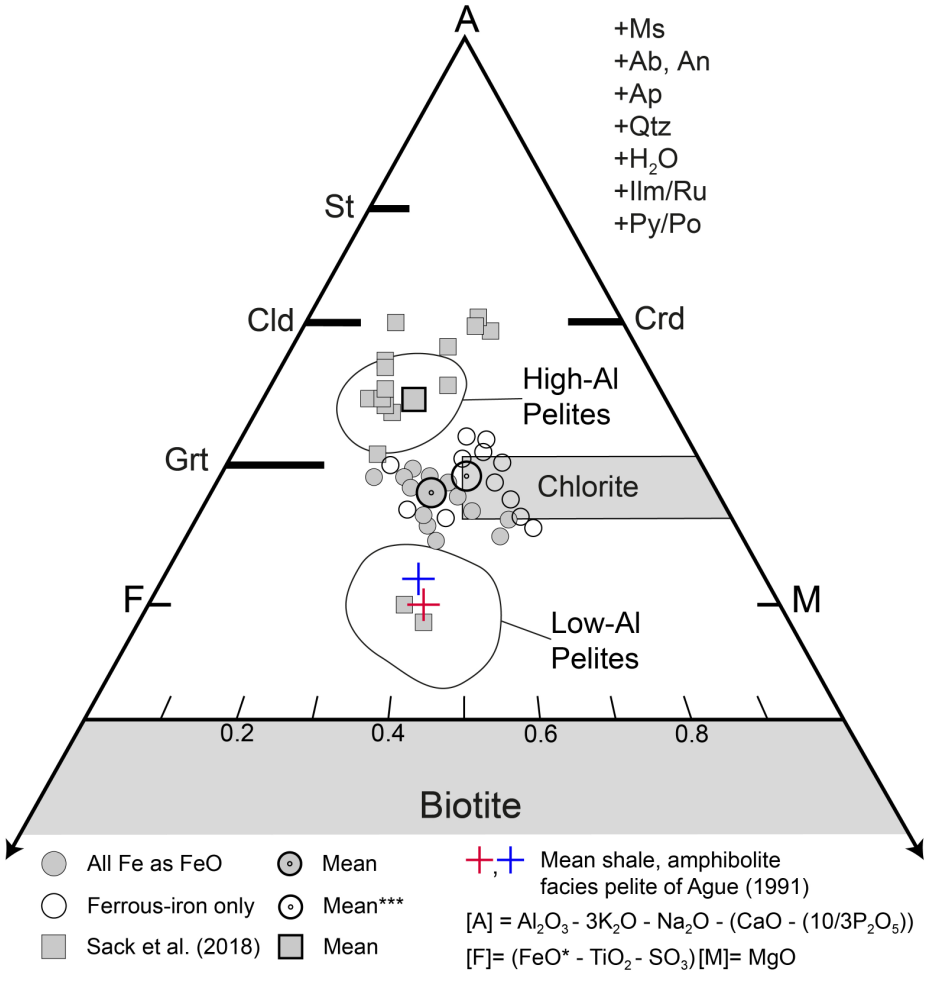

Figure 8. AFM diagram after Thompson (1957) showing compositional variation between samples from area A of this study and those of Sack et al. (2018). The same data from this work is plotted twice to demonstrate the effects of assuming all Fe as Fe^{2+}. Representative compositional range of minerals and high/low Al pelite zones from Spear (1993). Projections from pyrite (Py), pyrrhotite (Po), ilmenite (Ilm), and rutile (Ru) are based on the observed phase in the rock. Ilmenite assumed for projection where Fe-Ti oxide unknown. *** Composition used for phase equilibrium and fluid modelling in Figure 12.

Table 3. LA-ICP-MS trace element chemistry of pyrite and pyrrhotite.

Mean Detection Limit					**0.019**	**0.037**	**0.342**	**0.230**	**0.515**	**2.206**	**2.540**	**0.087**	**0.044**	**0.181**	**0.178**	**0.515**	**0.031**	**0.026**
Sample	Mineral	n	T(°C)		Au	Co	Ni	Cu	Zn	As	Se	Mo	Ag	Cd	Sb	Te	Pb	Bi
CP040	Po	7	422	Min		532.00	1384.00	0.39	0.77	8.10	13.00		0.10	4.91	0.19		0.59	0.09
				Max	BDL	611.00	1656.00	4.59	203.00	24.30	57.00	BDL	0.42	7.20	0.30	BDL	6.70	5.46
				Mean		562.57	1485.29	1.09	52.69	14.59	35.67		0.26	6.06	0.25		2.85	1.50
				St.Dev.		30.64	103.21	1.55	100.22	5.55	14.58		0.23	1.62	0.06		2.42	1.88
CP041	Po	13	422	Min		160.60	130.60	0.44	0.59	3.00	6.00	BDL	0.05		0.22	0.74	0.40	0.11
				Max	BDL	262.00	1195.00	35.40	208.00	28.60	39.00	0.23	1.61	BDL	2.64	1.56	161.00	23.38
				Mean		200.95	445.62	5.11	37.45	9.99	19.57	-	0.78		1.15	1.15	33.35	8.35
				St.Dev.		23.15	268.59	9.80	70.12	7.61	12.42	-	0.55		0.73	0.58	49.32	8.47
CP042	Po	13	423	Min		254.00	582.00	0.40	BDL	3.20	10.00		0.08		BDL		0.28	0.16
				Max	BDL	558.00	1906.00	3.40	298.00	17.60	33.00	BDL	3.17	BDL	0.98	BDL	37.40	23.40
				Mean		382.16	1151.31	0.85	31.20	11.18	19.11		0.81		0.45		9.42	4.23
				St.Dev.		84.50	321.21	0.80	93.75	5.11	8.33		0.89		0.30		12.46	6.39
CP071	Po	7	424	Min	BDL	313.00	5160.00	BDL	19.80	7.60	BDL		0.22		0.35		4.75	0.31
				Max	0.02	498.00	7290.00	172.00	3120.00	17100.00	25.00	BDL	2.51	BDL	11.60	BDL	69.20	10.00
				Mean	-	393.17	6095.71	28.91	1092.40	2460.90	12.50		1.35		4.02		26.33	3.13
				St.Dev.	-	73.20	778.01	70.10	1358.47	6455.25	9.88		0.95		4.23		25.08	3.40
CP043A	Py	14	425	Min	BDL	29.60	10.50	0.41	BDL	44.30	4.00		0.12		0.30	BDL	2.03	0.60
				Max	0.05	2380.00	1916.00	24.00	6.90	820.00	23.00	BDL	0.33	BDL	6.55	6.40	36.50	13.05
				Mean	0.03	761.61	216.40	4.15	2.13	318.84	13.08		0.20		2.96	3.40	15.15	4.82
				St.Dev.	0.01	781.13	516.83	6.19	2.38	227.18	6.92		0.08		1.90	2.81	12.06	3.91
CP043B	Po	6	425	Min		509.00	1184.00	0.44	BDL	3.60	16.00		0.15		0.21		0.41	0.22
				Max	BDL	1390.00	1306.00	0.61	0.83	1640.00	44.00	BDL	0.80	BDL	0.68	BDL	6.55	8.99
				Mean		671.00	1245.83	0.53	0.64	278.43	27.00		0.49		0.41		2.08	2.48
				St.Dev.		352.50	48.81	0.07	0.26	667.03	14.93		0.34		0.25		2.31	3.67
CP044A	Po	13	429	Min		269.00	559.00	BDL	6.20	4.60	4.00		BDL		0.26		0.16	0.07
				Max	BDL	333.00	879.00	15.10	28.00	14.00	81.00	BDL	0.39	BDL	0.63	BDL	8.49	3.54
				Mean		289.07	737.38	3.47	15.40	8.37	22.91		0.17		0.39		2.21	0.94

Table 3. (cont.) LA-ICP-MS trace element chemistry of pyrite and pyrrhotite.

Mean Detection Limit					**0.019**	**0.037**	**0.342**	**0.230**	**0.515**	**2.206**	**2.540**	**0.087**	**0.044**	**0.181**	**0.178**	**0.515**	**0.031**	**0.026**
Sample	Mineral	n	T(°C)		Au	Co	Ni	Cu	Zn	As	Se	Mo	Ag	Cd	Sb	Te	Pb	Bi
				St.Dev.		19.91	100.80	5.50	9.46	3.68	22.06		0.13		0.21		2.99	1.17
CP045B	Po	12	436	Min		641.00	1451.00	0.29	1.12	6.30	3.00		0.33		BDL		0.71	0.52
				Max	BDL	876.00	5600.00	1.50	1960.00	19.80	44.00	BDL	0.88	BDL	1.36	BDL	215.00	34.20
				Mean		786.00	3567.42	0.83	398.00	13.45	20.27		0.64		0.69		33.77	12.85
				St.Dev.		92.10	1517.53	0.36	589.41	4.27	12.83		0.26		0.50		60.04	12.81
CP072	Po	15	442	Min	BDL	497.00	1293.00	BDL	0.68	8.40	4.00	0.27	0.05		0.32		0.55	0.13
				Max	0.02	602.00	2117.00	1.38	2250.00	22.30	55.00	0.27	0.80	BDL	0.75	BDL	76.00	10.86
				Mean	-	531.43	1517.73	0.50	334.25	13.97	20.92	-	0.36		0.52		11.38	3.34
				St.Dev.	-	29.20	205.87	0.46	625.46	4.36	13.35	-	0.31		0.16		19.87	3.96
CP075	Py	20	443	Min		BDL	47.80	BDL	BDL	9.90	BDL		BDL		BDL	BDL	BDL	BDL
				Max	BDL	1129.00	1840.00	451.00	31.00	662.00	32.00	BDL	0.65	BDL	2.01	1.45	22.30	1.82
				Mean		259.51	565.25	42.70	7.09	180.28	19.16		0.27		1.13	0.95	2.95	0.50
				St.Dev.		335.93	486.87	122.59	13.39	189.06	6.96		0.27		0.69	0.45	5.65	0.65
CP049A	Po	21	470	Min		200.80	697.00	0.32	BDL	6.00	8.00		0.14		0.29	BDL	1.31	0.33
				Max	BDL	609.00	1500.00	0.96	88.00	362.00	44.00	BDL	0.94	BDL	1.90	0.38	42.10	8.11
				Mean		247.48	890.48	0.59	7.65	31.86	17.71		0.48		0.90	-	10.30	3.21
				St.Dev.		90.29	187.26	0.19	20.83	75.89	10.78		0.26		0.51	-	10.29	2.52
CP032	Py	13	475	Min	0.02	3.97	1.04	0.38	BDL	337.00	14.00		0.07		BDL	1.01	0.08	0.03
				Max	0.10	152.80	455.00	15.30	72.00	2480.00	42.00	BDL	0.44	BDL	10.97	4.75	100.60	11.39
				Mean	0.04	46.13	56.63	3.74	15.11	898.09	24.33		0.22		5.15	2.90	40.20	3.86
				St.Dev.	0.03	52.88	132.69	4.22	26.57	601.17	9.50		0.13		3.78	1.54	35.90	3.55
CP036A	Po	9	477	Min	BDL	436.00	1713.00	0.39	0.70	2.30	11.00		0.38		0.52		3.29	2.63
				Max	0.05	1229.00	3150.00	2.04	80.00	7.70	46.00	BDL	1.06	BDL	2.45	BDL	258.00	11.00
				Mean	-	630.56	2337.33	1.09	24.44	4.74	28.75		0.62		1.17		73.66	5.87
				St.Dev.	-	259.21	567.53	0.63	28.90	2.11	10.71		0.22		0.89		87.18	2.48

Table 3. (cont.) LA-ICP-MS trace element chemistry of pyrite and pyrrhotite.

Mean Detection Limit					**0.019**	**0.037**	**0.342**	**0.230**	**0.515**	**2.206**	**2.540**	**0.087**	**0.044**	**0.181**	**0.178**	**0.515**	**0.031**	**0.026**
Sample	Mineral	n	T(°C)		Au	Co	Ni	Cu	Zn	As	Se	Mo	Ag	Cd	Sb	Te	Pb	Bi
CP047	Po	18	477	Min		788.00	2679.00	0.32	0.59	6.00	4.00		0.08		BDL		0.09	0.06
				Max	BDL	1604.00	4530.00	60.50	121.00	15.90	32.00	BDL	1.70	BDL	0.37	BDL	201.00	13.70
				Mean		1012.29	3229.89	4.15	24.09	10.28	15.36		0.81		0.28		24.10	3.40
				St.Dev.		290.06	533.38	14.52	45.39	3.03	8.26		0.57		0.12		56.79	4.91
CP057A	Po	5	490	Min	BDL	1442.00	2510.00	0.37	0.57	5.00	3.00	0.49			0.42	BDL	0.30	0.08
				Max	0.03	2905.00	18430.00	1.46	2130.00	18.00	38.00	BDL	0.49	BDL	0.74	2.20	55.50	9.81
				Mean	-	1755.60	7102.00	0.88	485.57	11.52	26.40		0.49		0.58	-	19.79	3.16
				St.Dev.	-	642.99	6416.16	0.40	923.69	5.36	13.61		BDL		0.23	-	21.13	4.34
CP056	Po	11	491	Min	BDL	1050.00	5130.00	0.45	1.34	13.70	23.00	BDL	0.29	0.70	0.39	BDL	8.60	0.77
				Max	0.02	2991.00	13660.00	162.20	1020.00	110.00	58.00	0.17	8.25	3.57	9.38	28.80	467.00	81.00
				Mean	-	1444.36	6531.82	17.79	156.18	46.27	44.90	-	2.47	1.95	2.14	8.02	128.92	16.98
				St.Dev.	-	548.03	2440.00	50.76	298.45	32.03	12.13	-	2.45	1.47	2.76	13.88	142.92	23.69
CP059	Po	22	495	Min		241.40	743.00	0.65	BDL	4.90	BDL		0.07		0.20		0.38	0.06
				Max	BDL	344.00	935.00	1.36	1.60	14.60	24.00	BDL	0.94	BDL	3.40	BDL	45.00	5.28
				Mean		281.96	811.41	1.00	0.66	8.29	13.07		0.32		0.91		8.07	1.87
				St.Dev.		25.48	42.26	0.18	0.48	2.47	7.25		0.24		1.05		10.94	1.89
CP067	Po	11	499	Min	BDL	563.00	1405.00	0.45	0.90	3.10	4.00		0.09	0.33	0.66		0.38	0.16
				Max	0.09	773.00	2011.00	19.90	3730.00	12.30	42.00	BDL	0.99	0.94	1.06	BDL	27.20	11.24
				Mean	-	651.40	1708.91	4.80	406.35	9.23	17.78		0.46	0.64	0.82		9.43	2.84
				St.Dev.	-	53.23	219.25	6.79	1169.86	3.05	14.02		0.28	0.43	0.21		9.43	2.98
CP066	Po	21	506	Min		249.00	575.00	0.26	BDL	4.80	5.00		0.06		BDL	1.78	0.12	0.06
				Max	BDL	356.00	1098.00	0.62	8.10	15.50	37.00	BDL	3.73	BDL	5.41	3.60	2290.00	29.50
				Mean		299.64	780.14	0.41	1.30	10.02	18.32		0.92		1.98	2.69	161.51	9.21
				St.Dev.		26.12	136.34	0.11	1.85	3.21	7.99		0.85		1.62	1.29	495.10	9.17
CP060A	Po	7	522	Min		586.00	3780.00	0.40	0.97	3.20	136.00		0.22	BDL	BDL	BDL	2.55	0.59
				Max	BDL	5170.00	8590.00	7.10	427.00	17.90	173.00	BDL	0.69	22.70	0.54	1.32	598.00	22.90
				Mean		1642.43	6175.71	1.86	83.35	9.10	152.86		0.45	-	-	-	111.35	4.68
				St.Dev.		1751.48	1781.40	2.37	159.50	5.02	14.12		0.19	-	-	-	217.25	8.11

Table 3. **(cont.)** LA-ICP-MS trace element chemistry of pyrite and pyrrhotite.

Mean Detection Limit					**0.019**	**0.037**	**0.342**	**0.230**	**0.515**	**2.206**	**2.540**	**0.087**	**0.044**	**0.181**	**0.178**	**0.515**	**0.031**	**0.026**
Sample	Mineral	n	T(°C)		Au	Co	Ni	Cu	Zn	As	Se	Mo	Ag	Cd	Sb	Te	Pb	Bi
CP061	Po	7	526	Min		418.00	4940.00	0.59	6.18	BDL	8.00	BDL	0.08		0.30		0.30	0.32
				Max	BDL	4820.00	10610.00	1.33	439.00	11.80	44.00	0.09	0.69	BDL	0.67	BDL	22.10	9.29
				Mean		2042.00	7705.71	0.87	106.45	6.71	26.75	-	0.30		0.50		11.23	4.55
				St.Dev.		1620.72	2128.61	0.27	162.60	3.17	17.46	-	0.22		0.14		7.43	3.40
CP065A	Po	18	528	Min	BDL	978.00	4290.00	0.25	0.56	3.60	10.00		0.07	0.16	BDL		1.48	0.36
				Max	0.32	4854.00	27420.00	1.73	171.00	19.40	29.00	BDL	0.83	5.20	9.70	BDL	124.00	10.20
				Mean	0.17	1577.53	7659.44	0.59	34.44	9.18	20.63		0.40	2.68	2.39		21.43	3.02
				St.Dev.	0.22	952.33	5619.13	0.41	50.83	4.52	6.67		0.22	3.56	3.05		29.61	2.51
CP065B	Po	8	528	Min		1370.00	10620.00	BDL	2.39	5.90	6.00		0.24		0.28	0.54	0.95	0.80
				Max	BDL	1670.00	14180.00	0.75	1460.00	14.40	21.00	BDL	3.13	BDL	0.83	10.50	3040.00	39.00
				Mean		1462.88	11382.50	0.39	491.30	9.03	13.33		0.95		0.49	4.41	442.40	9.74
				St.Dev.		94.72	1150.95	0.24	677.51	3.14	5.32		0.99		0.24	5.34	1145.48	12.14
CP062B	Po	3	533	Min		625.00	2656.00	BDL	BDL	BDL	BDL		0.21		0.63		15.80	3.57
				Max	BDL	742.00	2839.00	59.40	3.38	538.00	21.00	BDL	0.45	BDL	1.64	BDL	172.80	9.24
				Mean		683.50	2747.50	-	-	-	-		0.33		1.14		94.30	6.41
				St.Dev.		82.73	129.40	-	-	-	-		0.17		0.71		111.02	4.01
CP063A	Po	18	537	Min		185.90	463.00	0.35	BDL	10.40	6.00		0.06	BDL	BDL	BDL	0.43	0.05
				Max	BDL	408.00	1456.00	160.90	245.00	2400.00	39.00	BDL	0.92	1.55	9.38	1.23	35.70	3.58
				Mean		218.51	659.06	9.41	32.39	173.64	25.29		0.28	-	1.88	-	8.58	1.04
				St.Dev.		54.65	227.72	37.81	85.95	574.81	8.62		0.22	-	2.55	-	10.72	0.90
CP063B	Po	10	537	Min		965.00	2258.00	0.24	BDL	5.80	18.00		0.13		BDL		0.27	0.16
				Max	BDL	1103.00	5340.00	0.54	277.00	21.60	23.00	BDL	1.17	BDL	0.47	BDL	14.70	3.61
				Mean		1030.80	2754.00	0.42	57.85	13.58	20.50		0.44		0.29		4.13	1.06
				St.Dev.		44.43	953.75	0.12	102.01	4.87	3.54		0.36		0.16		4.47	1.04
CP064	Po	14	542	Min		384.00	511.00	0.30	0.52	4.50	5.00		0.05				0.17	0.11
				Max	BDL	651.00	1194.00	1.26	7.60	13.50	15.00	BDL	0.65	BDL	BDL	BDL	8.43	2.82
				Mean		497.07	857.79	0.75	2.93	9.24	9.45		0.30				2.02	0.92
				St.Dev.		70.08	217.58	0.29	4.05	2.34	3.33		0.16				2.37	0.88

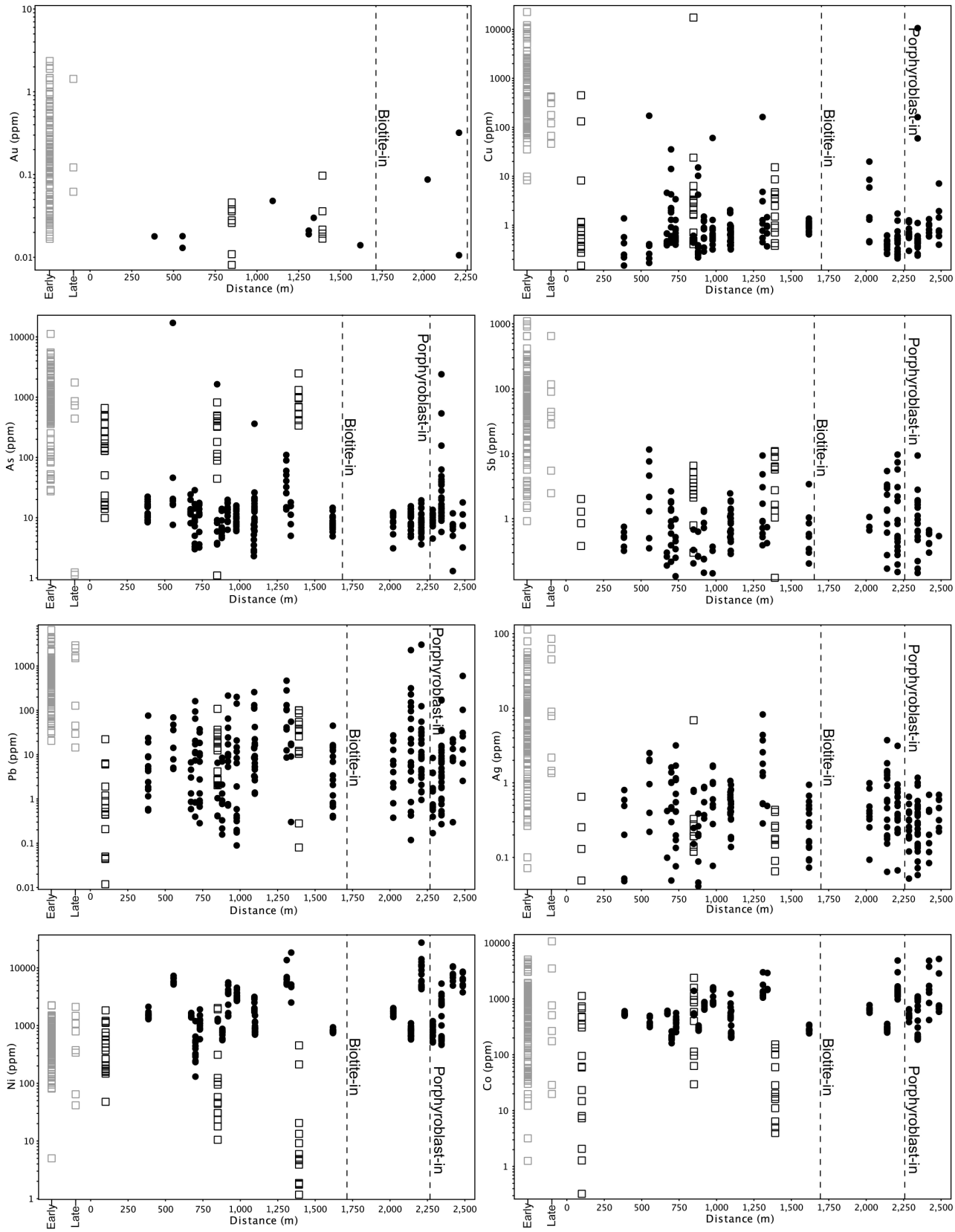

Figure 9. Scatter plots of trace element concentrations in pyrite (squares) and pyrrhotite (filled circles) versus temperature (°C). Data in black from this study; Grey from Sack et al. (2018). "Early" and "Late" are early diagenetic and late diagenetic pyrite as they are given in the Sack study for the Hyland Group samples. Distance is surface distance.

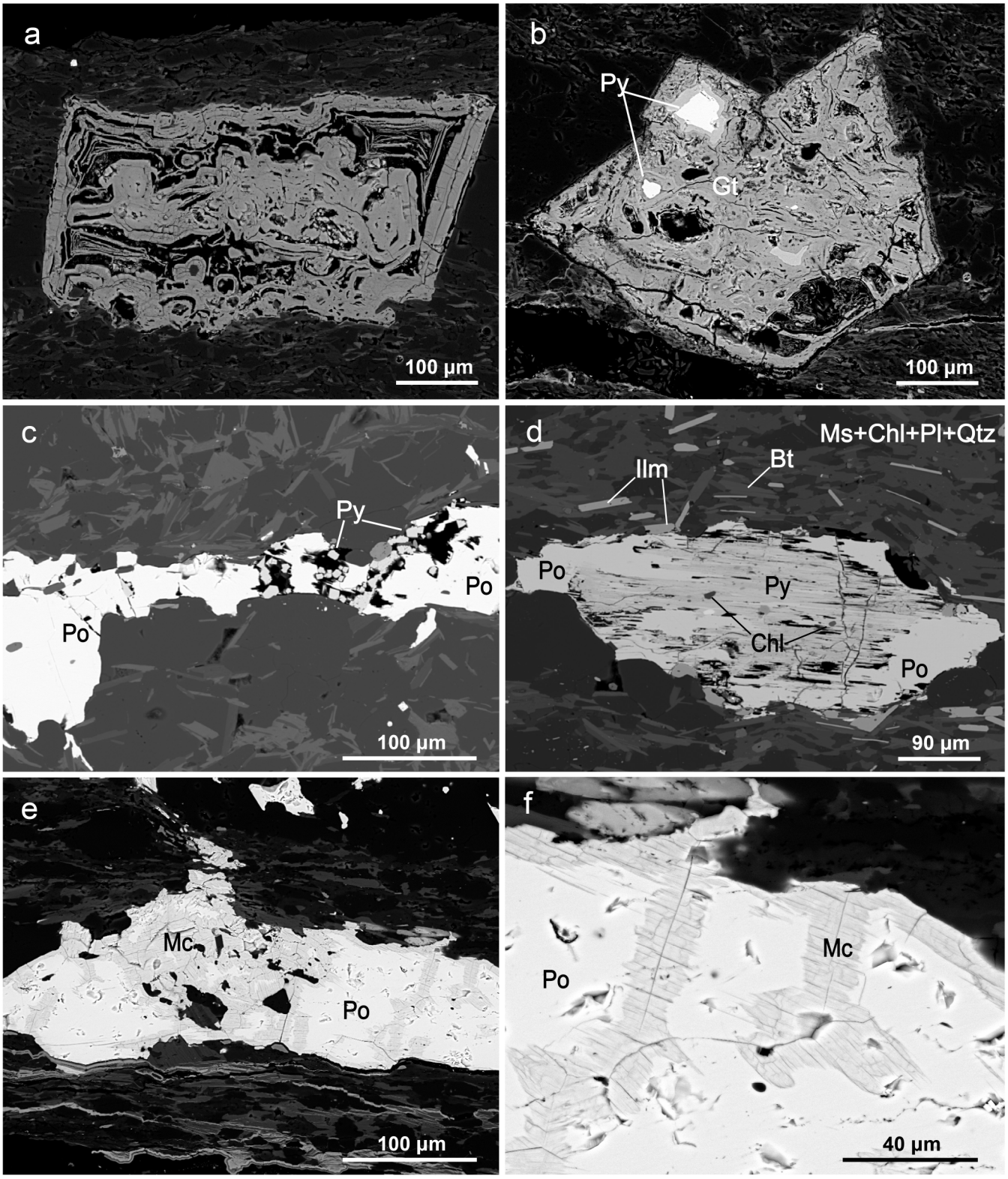

Figure 10. Backscattered electron (BSE) images of common sulphide alteration textures. **a)** complete replacement of Fe-hydroxide (goethite) interpreted to have formed after pyrite. **b)** Partial replacement of pyrite by goethite, brighter grey rim around pyrite grain is hematite. **c)** Retrograde pyrite after pyrrhotite. **d)** Replacement of inclusion-rich pyrite by pyrrhotite. **e, f)** Marcasite formed at the margins and along fractures of pyrrhotite.

Cadmium, Mo, Te, Tl, and W are below detection for all analyses. Arsenic concentrations in pyrite are strongly heterogeneous ranging from 10 to 2480 ppm with a mean of 402 ppm (St. Dev., 453 ppm). Mean Cu content is 17 ppm (St. Dev., 73 ppm) and mean Sb is 3.7 ppm (St. Dev., 3.1 ppm) though >50% of Sb analyses were below detection. Ag is below 1 ppm in all analyses. Values of Zn range from 0.26 to 72 ppm though most analyses were below detection. Concentrations of Co and Ni show strong inter- and intra-sample heterogeneity with Co:Ni ratios between 0.46–3.52. Mean values for Co and Ni are 322 ± 519 ppm and 322 ± 475 ppm, respectively.

Arsenic, Cu, and Sb concentrations are lower in pyrrhotite than pyrite with mean values of 31 ppm As (St. Dev., 179 ppm), 4 ppm Cu (St. Dev., 18 ppm), and 1.3 ppm Sb (St. Dev., 1.9 ppm). Mean Ag in pyrrhotite is 0.63 ppm (St. Dev., 0.83 ppm), higher than the mean concentration of 0.22 in pyrite. Pyrrhotite contains significantly more Co, Ni, and Zn than in pyrite with concentrations of 700 ppm Co (St. Dev., 684 ppm), 2773 ppm Ni (St. Dev., 3268 ppm), and 156 ppm Zn (St. Dev., 500 ppm). Co:Ni ratios in pyrrhotite range from 0.06 to 1.23.

Au in pyrite and pyrrhotite

Gold values were above detection limits (0.019 ppm) in 12 of 48 pyrite grains (25%) and 12 of 328 pyrrhotite grains analyzed (3.7%). Calculations of the mean and geometric mean (G.M.) only incorporate data above the Au detection limit. Mean Au in pyrite is 0.032 ppm (G.M., 0.026 ppm) with a maximum concentration of 0.1 ppm. Mean Au in pyrrhotite is 0.06 (G.M., 0.030 ppm) with a maximum value 0.32 ppm. This maximum value is anomalous for pyrrhotite and when removed as an outlier, pyrrhotite contains lower Au concentrations than pyrite with values from below detection to 0.087 ppm (mean, 0.029; St. Dev., 0.023; G.M., 0.022).

Phase equilibrium Modelling

Phase equilibrium modelling was performed using the mean bulk composition of Hyland metapelites from area A (composition is plotted on AFM in Fig. 8 and listed in Table 2). Modelling was performed in the chemical system MnNCKFMASHT ($MnO–Na_2O–CaO–K_2O–FeO–MgO–Al_2O_3–SiO_2–H_2O–TiO_2$), assuming the presence of a free C-O-H fluid phase in equilibrium with graphite (Connolly and Cesare, 1993). Phase diagrams were calculated using the Gibbs free energy minimization software Theriak-Domino (de Capitani and Brown, 1987; de Capitani and Petrakakis, 2010) in combination with version ds5.5 of the thermodynamic database of Holland and Powell (1998). The solution models employed are those listed in Beyssac, Pattison & Bourdelle (2018). Uncertainty, primarily associated with the thermodynamic data, is on the order of ±20 °C for most reactions (Beyssac, Pattison & Bourdelle, 2018). For biotite-in reactions uncertainty is ±50 °C.

To satisfy an isograd sequence sequence containing andalusite and sillimanite zones downgrade of the development of K-feldspar, modelling predicts pressures of between ~3.1–4.1 kbar (Fig. 12A; dashed area). For staurolite-bearing samples, this is further constrained to pressures of 3.7–4.1 kbar (grey band), which satisfies the observed sequence of metamorphic zones (chlorite; biotite; staurolite; andalusite; sillimanite; K-feldspar + sillimanite). Modelling predicts a wide biotite zone between 425–560 °C at these pressures. The chlorite consuming reactions that produce staurolite or andalusite occur within a narrow temperature window between 560–570 °C. Sillimanite is stable above 575 °C. K-feldspar first appears with muscovite-out at ~650 °C. Cordierite is not predicted to be stable at these pressures in this bulk composition. In Figure 12a, the first appearance of cordierite occurs at a maximum pressure of ~3 kbar and the observed prograde metamorphic sequence of cordierite, andalusite, and sillimanite (all with muscovite) is not predicted at any pressure. Thermodynamic modelling of cordierite-bearing bulk compositions awaits future study.

At the 3.7–4.1 kbar pressures consistent with the staurolite-bearing assemblages, fluid modelling predicts ~0.6 wt. % H_2O is released from the rock across the biotite zone from 425 to 560 °C. At 560 °C, the consumption of chlorite to produce staurolite releases an additional 0.3 wt. % H_2O over a <10 °C temperature interval. The next significant release of H_2O is predicted at the terminal breakdown of muscovite, which releases ~1 wt. % H_2O over a <5 °C interval.

RSCM Thermometry

RSCM thermometry data including R2 values and calculated temperatures for samples from areas A and B are found in Table 4. RSCM temperature estimates are plotted on a summary diagram in Figure 11 and on maps for each area in Figures 2 and 3. Temperature estimates range from 421 to 542 °C for samples from chlorite to andalusite zone in area A, while temperatures for samples from the chlorite to sillimanite zones of Area B range from 459 to 616 °C.

Chlorite zone samples record estimated temperatures down to 420°C. The biotite-in isograd occurs at ~500 °C, with chlorite-out/porphyroblast-in at between 525–550 °C. The first appearance of andalusite is at ~550 °C, and the sillimanite isograd at 580 °C. The K-feldspar + sillimanite zone sample did not contain carbonaceous material. For all but the biotite isograd, RSCM temperatures show excellent agreement with the phase equilibrium modelling. The RSCM temperature for the biotite isograd is more reliable given the consistent up-grade progression for 12 RSCM temperatures from 420 to 495 °C through the chlorite zone in area A.

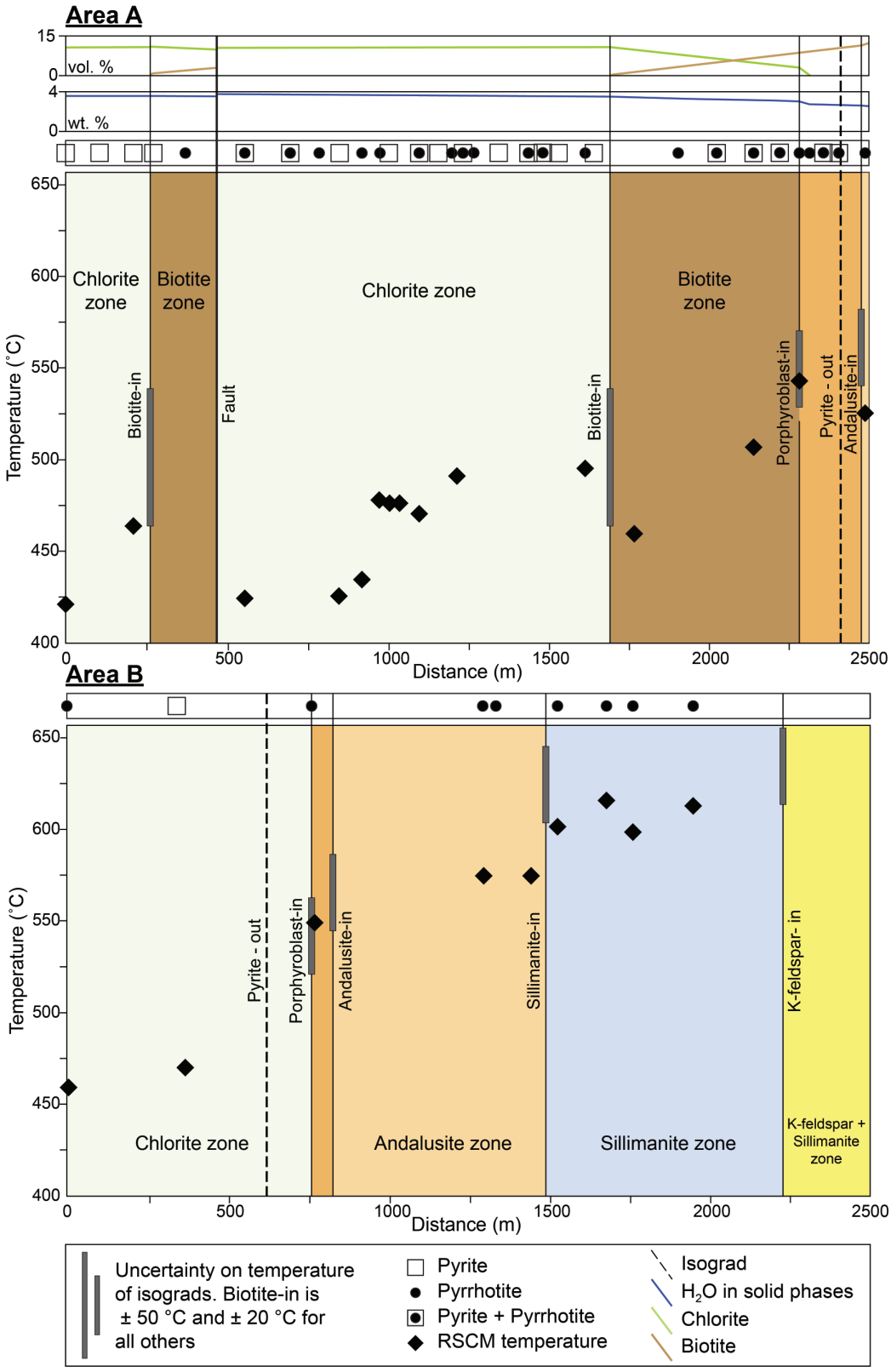

Figure 11. RSCM temperature estimates vs. distance. Zero distance in each diagram is first chlorite zone sample along each transect moving up grade. Isograd positions are based on map positions in Figs. 2 and 3. Isograd temperatures from Fig. 12 along isobaric path at 3.9 kbar except biotite-in for which the RSCM temperature of 500 °C is used. Band above each diagram indicates presence of pyrite/pyrrhotite. Subsequent bands above diagram for area A show calculated wt. % H_2O in solids and vol. % chlorite and biotite. Uncertainty on RSCM temperatures is ± 50 °C.

Table 4. Estimated temperatures from RSCM thermometry. TB_{02} is temperature calculated after Beyssac et al. (2002). Distance along transect is calculated using first chlorite zone sample as the origin. No distance is calculated for samples separated by major faulting.

Sample	Assemblage	Distance (m)	n	R2 (avg)	SD	TB_{02} (°C)	SD	SE
Area A								
18-CP-004	Ms+Chl (Po)	0	25	0.41	0.04	459	18	4
18-CP-006	Ms+Chl (Py)	357	24	0.38	0.04	471	16	3
18-CP-014b	Ms+Bt (Po)	757	19	0.21	0.06	549	27	6
18-CP-021	Ms+Bt+Gt+St	1290	20	0.15	0.10	575	42	9
18-CP-012	Ms+Bt+St+And (Po)	1438	23	0.15	0.04	574	16	3
18-CP-011	Ms+Bt+St+And+Sil (Po)	1520	23	0.09	0.05	601	22	5
18-CP-009	Ms (po)	1674	25	0.06	0.06	616	28	6
18-CP-010	Ms+Bt+Gt+St+And+Sil (Po)	1757	22	0.09	0.04	599	18	4
18-CP-008	Ms+Bt+Gt+St+And+Sil (Po)	1944	18	0.06	0.06	613	25	6
18-CP-003	Ms+Bt	-	23	0.22	0.05	545	23	5
18-CP-002	Ms+Bt+And+Sil (Po)	-	20	0.11	0.07	590	33	7
18-CP-001b	Ms+Bt+St (Po+Py(R))	-	25	0.10	0.08	597	36	7
Area B								
18-CP-076	Ms+Chl (Py)	0	21	0.50	0.02	421	10	2
18-CP-074	Ms+Chl (Py)	205	24	0.40	0.03	464	11	2
18-CP-071	Ms+Chl (Py+Po)	554	24	0.49	0.04	424	16	3
18-CP-043	Ms+Chl (Py)	849	18	0.49	0.02	425	11	3
18-CP-045	Ms+Chl (Po)	919	25	0.47	0.02	434	9	2
18-CP-047	Ms+Chl (Po)	977	24	0.37	0.05	477	22	5
18-CP-048	Ms+Chl	1003	20	0.37	0.04	476	16	4
18-CP-037b	Ms+Chl	1037	19	0.37	0.05	476	22	5
18-CP-049	Ms+Chl (Py+Po)	1098	20	0.38	0.05	470	24	5
18-CP-055	Ms+Chl	1220	25	0.34	0.03	491	15	3
18-CP-059	Ms+Bt (Po)	1619	25	0.33	0.04	495	19	4
17-DMO-117	Ms+Chl+Bt	1769	25	0.41	0.02	459	7	1
18-CP-066	Bt (Py+Po)	2140	20	0.30	0.04	506	16	4
18-CP-064	Ms+Chl+Bt+St (Po)	2286	19	0.22	0.06	542	25	6
18-CP-060a	Ms+Chl+Bt+Crd+And (Po)	2486	30	0.27	0.07	525	31	6

DISCUSSION

The Pyrite-Pyrrhotite Transition

The transition from pyrite to pyrrhotite is controlled by many factors including pressure and temperature conditions, the type and availability of fluids, the mobility of these fluids, and possible competing reactions for sulphur (Tomkins, 2010). Observations from areas A and B show pyrite occurs in rocks of the chlorite, biotite, and lowermost outer porphyroblast zones, while pyrrhotite occurs in chlorite to K-feldspar + sillimanite zone rocks. Because pyrrhotite occurs in the lowest grade samples collected, the pyrite-pyrrhotite transition must occupy a minimum temperature interval of 140 °C, largely restricted to the chlorite and biotite zones. Similar ranges in metamorphic conditions are reported elsewhere (e.g., Carpenter, 1974; Ferry, 1981; Pitcairn et al., 2010, 2015b). However, thermodynamic modelling by Zhong et al (2015) in an average pelite bulk composition predicted that the pyrite-pyrrhotite transition occurs over a discrete temperature interval (<10 °C) between ~360–400 °C at pressures of 1–5 kbar, with a pressure dependency of ~8 °C/kbar (Zhong et al, 2015). Higher S content (>1% S vs. 0.24% in average pelite) broadens this range slightly, however, lower Fe content has the greatest effect on pyrite desulphidation extending the range to >420 °C when Fe content is reduced by half from the average.

Fluids

The abrupt release of fluid due to chlorite breakdown over a small temperature interval is commonly thought to promote pyrite desulphidation and therefore to localise the pyrite-pyrrhotite transition (e.g., Powell et al., 1991; Craig and Vokes, 1993; Phillips, 1993; Tomkins, 2010). The amount, composition, and rate that fluids are released all play critical roles in pyrite desulphidation and the related mobility of metals and sulphur (Zhong, 2015). In area A, fluid is generated from the progressive metamorphism of variably carbonaceous pelitic to semi-pelitic rocks. Modelling shows most fluid (0.6 wt. % H_2O) is released gradually across the biotite zone in response to changes in the composition and modal abundance of chlorite and biotite (see top panel of Fig. 11a). Examples of biotite-producing reactions include:

$$Chl + Kfs_{detrital} = Bt + Ms + Qtz + H_2O \quad 3)$$

$$Ms + Ank + Chl + Qtz = Bt + Pl + CO_2 + H_2O \quad 4)$$

Going through the biotite zone, modal chlorite is predicted to decreases from 12 to 3 vol. % as modal biotite rises to ~11.6 vol. % (Fig. 11a). Fluid subsequently produced during the first growth of porphyroblasts (chlorite-out reactions) results in less (~0.3 wt. %) H_2O production but the fluid is released over a much smaller (~10 °C). Therefore, any pyrite remaining pyrite prior to the onset of these reaction, is predicted to be consumed over this interval.

The predicted gradual release of fluid going through the biotite zone in area A is one possible factor contributing to the breadth of the observed pyrite-pyrrhotite transition there. For a metamorphic sequence with a narrow or absent biotite zone down-grade of the porphyroblast-in isograd such as in area B, a greater fluid flux would be expected at the porphyroblast-in isograd because chlorite would not have been consumed at lower grade. This might result in a more abrupt transition from pyrite to pyrrhotite concurrent with the loss of chlorite at the porphyroblast-in isograd. This possibility is the subject of future work.

Fe and S

Sulphur-conserving reactions occur when Fe-bearing phases in the rock react with fluid-borne sulphur (released from pyrite as H_2S) to form pyrrhotite (Ferry, 1981; Nesbitt, 1982; Newton & Mohr, 1983; Nesbitt & Essene, 1983; Slotznick et al., 2018). In area A, pyrrhotite is commonly found in contact with or surrounding grains of chlorite and (or) biotite suggesting the pyrrhotite may have formed from reaction of S-bearing fluid with the Fe in these phases. The removal of sulphur from the fluid promotes additional breakdown of pyrite by reaction [1] and may lower the temperature required for the complete consumption of pyrite (Tomkins, 2010).

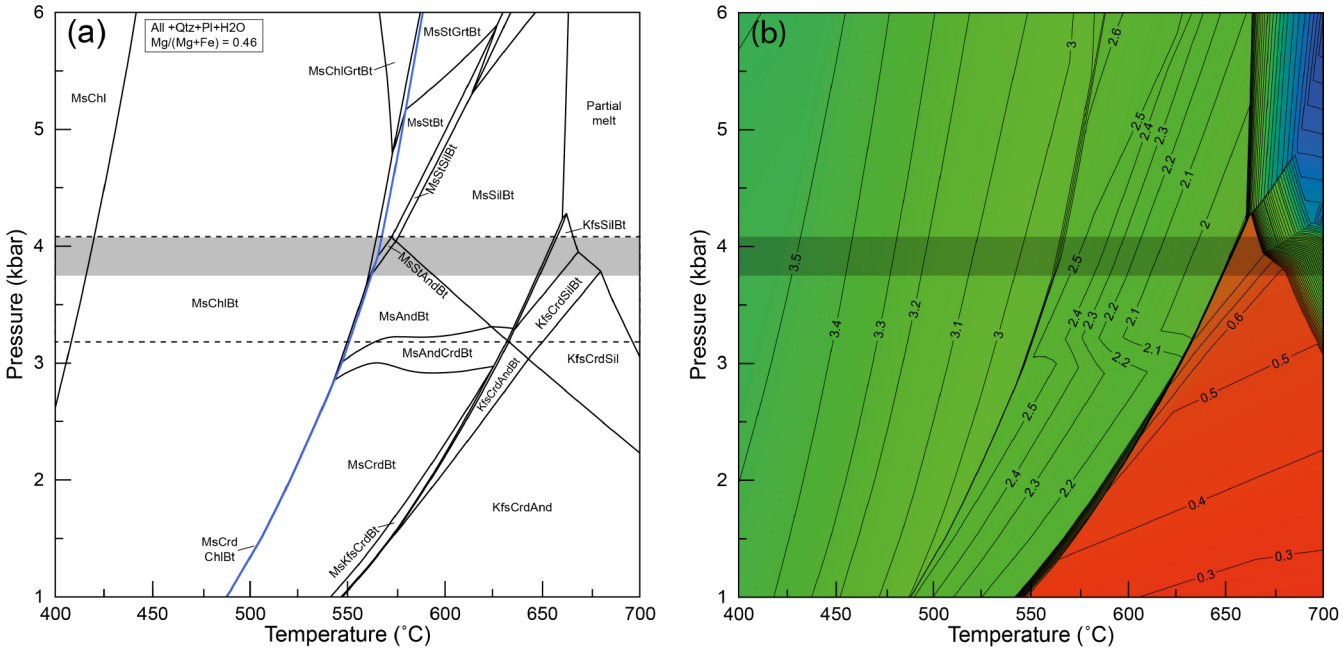

Figure 12. Thermodynamic modelling. **a)** Calculated P-T phase diagram for the average pelitic bulk composition from area A. Iron values used are Fe^{2+} from titration (composition given in Table 2 and plotted on an AFM in Fig. 8). Dashed lines show range in pressure for an andalusite to sillimanite (+ muscovite) sequence. Grey band represents estimated pressure range the region for a sequence containing a staurolite zone (see text for discussion). The blue line is chlorite-out. **b)** 300 x 300 pixel map and contours calculated in Theriak-Domino for the same bulk composition as in A showing wt. % H_2O in solids with contours of 0.1 wt. %. Colour scale from red to blue with lowest H_2O content in red.

Fe-Ti oxides may also react pyrite and pyrrhotite according to the S conserving reaction ilmenite + pyrite = pyrrhotite + rutile (Connolly and Cesare, 1993). Rutile is present in 12 of 34 pyrrhotite-bearing samples in areas A and B, and locally, rutile replaces ilmenite in the pyrrhotite-bearing samples from area A, possibly indicating the localized operation of this reaction. Overall, however, there is no clear relationship between the distribution of oxide and sulphide phases (Figs. 2a and 3a), suggesting that this is not a controlling process in the Hyland River area.

Deformation

Metamorphic rocks often have low porosity and permeability, which limits fluid-rock interactions and allows only small volumes of rock to equilibrate with any newly produced metamorphic fluid (Yardley, 2009). In the case of fluid-driven pyrite breakdown, this may allow only limited desulphidation of pyrite if the fluid becomes saturated in H_2S prior to the total consumption of pyrite (Tomkins, 2010). Faults and fractures generated during deformation promote fluid mobility and allow for flow within and out of a source rock (Groves et al., 1998; Goldfarb et al., 2005; Cox, 2005). Additionally, the fracturing of the rock increases the available surface area able to interact with a fluid promoting more extensive desulphidation of pyrite (Tomkins, 2010). Due to the limited amount and only gradual production of metamorphic fluid over the biotite zone in area A, concurrent deformation may have been necessary for near complete pyrite desulphidation and the growth of pyrrhotite at these metamorphic conditions.

GEOCHEMISTRY

Here, we compare compositional trends of whole rock and sulphide trace element data with shale and pyrite data from Sack et al. (2018). The metamorphic grade of the samples collected by these authors is low (sub-greenschist facies; Read et al., 1991), and the rocks exhibit characteristic early- to late-diagenetic pyrite morphologies (e.g., framboids, bedding parallel masses, pyrite aggregates, and nodular pyrite). We limit comparison to 10 of 19 Yusezyu Fm. samples with bulk S values below 1 wt. % as all samples above 1% S were collected from drill holes associated with gold-bearing quartz veins within which Au mineralisation is linked to pyrite, galena, and arsenopyrite. Removing the 9 samples with S > 1%, mean S becomes 0.29 ± 0.28 wt.% (1 SD; G.M., 0.19). These results are more similar to an average shale (0.23 wt. % S; Clarke, 1900) and supports the use of the Sack et al., (2018) data as a low-grade comparator to data from this study.

Trace Elements in Pyrite and Pyrrhotite

Au

Pyrite from Sack et al. (2018) contain Au concentrations between 0.017–3.167 ppm (mean, 0.445; St. Dev., 0.629; G.M., 0.217) compared to the much lower values of 0.019–0.1 ppm (mean, 0.039; St. Dev., 0.023; G.M., 0.034) for chlorite zone pyrite from this study. Likewise, As shows a similar trend with maximum concentrations of 2480 ppm (mean, 566; St. Dev., 541; G.M., 314) for pyrite from this work against a maximum of 5259 ppm (mean, 1081; St. Dev., 1169; G.M., 471) for pyrite from the Sack study.

Pyrite from area A has been largely recrystallised during metamorphism and holds lower concentrations of many trace metals and Au than pyrite in Sack et al. (2018; see Fig. 9). These authors show the highest pyrite Au concentrations in the Hyland River area belong to early diagenetic morphologies, with pyrite identified as late diagenetic hosting significantly less. One possible explanation for these variations in Au content is that the chlorite zone pyrite analyzed in this study was never enriched in Au and does not represent the higher grade equivalent to pyrite analyzed by Sack et al. Alternatively, much of the Au contained in Sack et al. pyrite may have been mobilised at metamorphic grades below the upper chlorite zone conditions of area A (~420 °C).

Similar mobilisation or prograde depletion of trace elements in pyrite is well documented (e.g., Large et al., 2007; Pitcairn et al., 2006, 2010, 2015; Gregory et al., 2015). For Au, Large et al. (2007) suggest the metal is confined to the crystal structure (invisible gold) in earlier formed pyrite and redistributed as micro-inclusions or along fractures in later generations of newly formed/recrystallised pyrite. This leaves the later pyrite largely devoid of lattice-bound Au and results in the loss of some Au with each progressive change.

Co and Ni in pyrrhotite

The relative abundance of Co and Ni in sulphides has been documented extensively (e.g., Neumann, 1950; see Bralia et al. (1979) for a syntheses of historical work). In pyrite, Co:Ni ratios have been used to interpret the source of the pyrite with different signatures attached to various deposit types and sedimentary environments (Bajwah et al., 1987). These authors showed that sedimentary pyrite typically has Co:Ni ratios of <1, which increases during prograde metamorphism. Going through the pyrite-pyrrhotite transition, Ni is preferentially incorporated into the crystal lattice of pyrrhotite over Co (Bajwah et al., 1987). The resultant Co:Ni ratios for pyrrhotite are therefore lower than those of the precursor pyrite as is the case in this study. Analyses of coexisting pyrite and pyrrhotite in sample CP043 show lower concentrations of Co and Ni in pyrite than pyrrhotite. The geometric mean for Co is 351 ppm and 65 ppm Ni in

pyrite versus 619 ppm Co and 1245 ppm Ni in pyrrhotite. This is contrary to findings in the studies discussed above, and while the analytical heterogeneity documented for the pyrite of this study is a common feature of hydrothermal pyrite (Bajwah et al., 1987), pyrite may not be the sole source of Co and Ni. Possible alternate sources (or sinks) of these transition metals are other sulphides such as cobaltite (CoAsS), pentlandite ($(Fe,Ni)_9S_8$), galena (PbS), sphalerite (Zn,Fe)S, and chalcopyrite ($CuFeS_2$) or silicate phases such as chlorite.

Neither cobaltite nor pentlandite were present in any samples from this study but trace quantities are documented elsewhere in similar prograde metamorphic sequences and protoliths (e.g., Pitcairn et al., 2006), and so may be present but undetected. Galena and sphalerite may contain minor concentrations of Co and Ni through divalent substitution for Pb in galena or Zn in sphalerite. Co and Ni concentrations in galena are generally <50 ppm and often much lower (Blackburn & Schwendeman, 1977). Sphalerite may contain up to 25 ppm Co and 300 ppm Ni, however, where sphalerite coexists with pyrite or pyrrhotite, the Fe-sulphide phase will preferentially incorporate Co and Ni, which are more readily substituted for divalent Fe than for Zn (Czamanske & Goff, 1973) Chalcopyrite is the most abundant sulphide after pyrite and pyrrhotite but commonly develops with or after pyrrhotite.

Alternatively, chlorite may represent a poorly studied reservoir for Co, Ni, and other transition metals at low metamorphic grade. Though there is a general paucity of data on the trace metal content of low-grade metamorphic chlorite, Wilkinson et al. (2015) demonstrated hydrothermal chlorite associated with porphyry deposits was able to incorporate sufficient concentrations of several transition metals, including up to 243 ppm Co and 427 ppm Ni, for use as a geochemical exploration tool. Though the metal content of chlorite associated with porphyry deposits is likely elevated compared to metamorphic chlorite in average metasediments, the Wilkinson et al. study shows that chlorite could be a plausible reservoir for Ni and Co and perhaps other trace elements. Further study is needed to better understand the potential role for chlorite, and perhaps other phyllosilicates, in the trace metal budget of low-grade metasediments.

Implications for Orogenic Gold

The gold content of pyrite, pyrrhotite, and whole rock samples, and the link between the pyrite-pyrrhotite transition and fluid-producing silicate reactions, has been evaluated for rocks of the upper Hyland River area in SE Yukon. We find (1) overall low Au concentration in all whole rock and sulphide samples analysed and (2) that pyrite desulphidation occurs predominantly within the upper chlorite and biotite zones and in advance of terminal chlorite breakdown. At Hyland River, pyrite consumption is likely controlled by a gradual release of fluid as chlorite is gradually consumed to produce biotite. For bulk compositions like those from area A, biotite producing reactions may consume enough chlorite to reduce the fluid released during terminal chlorite breakdown when chlorite reacts over a small interval to form porphyroblasts like staurolite or cordierite. Similar results were obtained by Starr et al. (2019) for metabasites near Flin Flon, Manitoba, where pyrite breakdown did not correlate with intervals of significant devolatilisation of chlorite through the greenschist to amphibolite transition; in that study, bulk composition was the primary control on the volume of fluid produced. Overall, the results of this study suggest that this part of the Hyland River area is not a plausible Au source for orogenic gold deposits.

CONCLUSIONS

The distribution of pyrite and pyrrhotite is documented within an andalusite-sillimanite type (high-temperature, low-pressure) metasedimentary succession in the upper Hyland River region of SE Yukon. Mapping shows the following metamorphic zones: chlorite, biotite, porphyroblast-in (cordierite or staurolite), andalusite, sillimanite, and K-feldspar + sillimanite. Pyrrhotite occurs at all metamorphic grades, while pyrite is restricted to the chlorite, biotite, and the lowermost porphyroblast-in zone. The pyrite-pyrrhotite transition, therefore, occupies an interval within the chlorite and biotite zones, with pyrite largely absent from rocks above the biotite zone.

Whole rock geochemistry combined with in-situ pyrite and pyrrhotite trace element data show lower concentrations of most trace elements including S, Au, and As, in the metamorphic rocks of the Hyland River area compared with unmetamorphosed/sub-chlorite zone samples in the region. This difference is most pronounced in the comparison of Au concentrations in pyrite with maximum values of 0.1 ppm Au in chlorite zone pyrite of this study and ~3.2 ppm Au for sub-chlorite zone pyrite in Sack et al. (2018).

Combined phase equilibrium modelling and RSCM thermometry suggest regional metamorphic conditions of 3.7–4.1 kbar and temperatures of up to 660 °C with the pyrite-pyrrhotite transition extending from ≤420 °C to ~560 °C. Fluid modelling shows a gradual release of 0.6 wt. % H_2O over this ~140 °C interval of pyrite desulphidation. This gradual fluid release in biotite zone rocks may have contributed to the observed breadth of the pyrite-pyrrhotite reaction window.

The upper chlorite zone and higher metamorphic rocks of the Hyland River area do not appear to be a plausible source region for orogenic gold. Samples from the pyrite-pyrrhotite transition zone in this study show no grade-related variation in whole rock or sulphide Au content. Whole rock and pyrite Au concentrations are lower than in samples from unmetamorphosed/lower grade rocks suggesting that Au was removed from the rock at conditions below the pyrite-pyrrhotite transition (<420 °C).

ACKNOWLEDGEMENTS

This report is a contribution to the NRCan Targeted Geoscience Initiative Phase 5 Program (TGI-5). Field and logistical support was generously supported by the Yukon Geological Survey. The authors would like to thank Patrick Sack and Murray Allan for discussions beneficial to this project. We thank Golden Predator Mining Corp. (3Aces Project: Jeff Cary and Mark Shutty) for logistical support and property access and Stratabound Minerals Corp. (Golden Culvert Project: Kim Tyler) for supplying an excellent property tour and site access. Furthermore, the authors acknowledge ongoing analytical support from Rob Marr (EPMA), Chris Debuhr (FE-SEM), and Brandon Boucher (LA-ICP-MS). DEMs were created from DigitalGlobe, Inc. imagery (ArcticDEM—Polar Geospatial Center) funded under National Science Foundation awards 1043681, 1559691, and 1542736. This work is further supported through an NSERC CGS-D to Padget and discovery grant # 037233 to Pattison.

REFERENCES

Ague, J. J. (1991). Evidence for major mass transfer and volume strain during regional metamorphism of pelites. *Geology*, 19(8), 855-858.

Alpers, C. N., Jambor, J. L., & Nordstrom, D. (Eds.). (2018). Sulfate minerals: Crystallography, geochemistry, and environmental significance. *Reviews in Mineralogy and Geochemistry*, 40. Walter de Gruyter GmbH & Co KG. 620 pp.

Angiboust, S., & Harlov, D. (2017). Ilmenite breakdown and rutile-titanite stability in metagranitoids: Natural observations and experimental results. *American Mineralogist*, 102(8), 1696-1708.

Bajwah, Z. U., Seccombe, P. K., & Offler, R. (1987). Trace element distribution, Co: Ni ratios and genesis of the Big Cadia iron-copper deposit, New South Wales, Australia. *Mineralium Deposita*, 22(4), 292-300.

Berner, R. A. (1984). Sedimentary pyrite formation: An update. *Geochimica et cosmochimica Acta*, 48(4), 605-615.

Beyssac, O., Pattison, D. R., & Bourdelle, F. (2019). Contrasting degrees of recrystallization of carbonaceous material in the Nelson aureole, British Columbia and Ballachulish aureole, Scotland, with implications for thermometry based on Raman spectroscopy of carbonaceous material. *Journal of Metamorphic Geology*, 37(1), 71-95.

Beyssac, O., & Lazzeri, M. (2012). Application of Raman spectroscopy to the study of graphitic carbons in the Earth Sciences. Applications of Raman spectroscopy to earth sciences and cultural heritage. *EMU Notes in Mineralogy*, 12, 415-454.

Beyssac, O., Goffé, B., Chopin, C., & Rouzaud, J. N. (2002). Raman spectra of carbonaceous material in metasediments: A new geothermometer. *Journal of metamorphic Geology*, 20(9), 859-871.

Beyssac, O., Bollinger, L., Avouac, J. P., & Goffé, B. (2004). Thermal metamorphism in the lesser Himalaya of Nepal determined from Raman spectroscopy of carbonaceous material. *Earth and Planetary Science Letters*, 225(1-2), 233-241.

Blackburn, W. H., & Schwendeman, J. F. (1977). Trace-element substitution in galena. *The Canadian Mineralogist*, 15(3), 365-373.

Bohlke, J. K. (1982). Orogenic (metamorphic-hosted) gold-quartz veins. U.S. *Geological Survey Open-File Report*, 795, 70-76.

Bralia, A., Sabatini, G., & Troja, F. (1979). A revaluation of the Co/Ni ratio in pyrite as geochemical tool in ore genesis problems. *Mineralium Deposita*, 14(3), 353-374.

Carpenter, R. H. (1974). Pyrrhotite isograd in southeastern Tennessee and southwestern North Carolina. *Geological Society of America Bulletin*, 85(3), 451-456.

Clarke, F. W. (1900). Analyses of rocks. U.S. *Geological Survey. Bulletin*, 168.

Cox, S. F., Etheridge, M. A., Cas, R. A. F., & Clifford, B. A. (1991). Deformational style of the Castlemaine area, Bendigo-Ballarat Zone: Implications for evolution of crustal structure in central Victoria. *Australian Journal of Earth Sciences*, 38(2), 151-170.

Craig, J. R., & Vokes, F. M. (1993). The metamorphism of pyrite and pyritic ores: An overview. *Mineralogical Magazine*, 57(386), 3-18.

Czamanske, G. K., & Goff, F. E. (1973). The character of Ni (2+) as demonstrated by solid solutions in the Ni-Fe-Zn-S system. *Economic Geology*, 68(2), 258-268.

de Capitani, C., & Petrakakis, K. (2010). The computation of equilibrium assemblage diagrams with Theriak/Domino software. *American Mineralogist*, 95(7), 1006-1016.

de Capitani, C., & Brown, T. H. (1987). The computation of chemical equilibrium in complex systems containing non-ideal solutions. *Geochimica et Cosmochimica Acta*, 51(10), 2639-2652.

Ferry, J. M. (1981). Petrology of graphitic sulfide-rich schists from south-central Maine: An example of desulphidation during prograde regional metamorphism. *American Mineralogist*, 66(9-10), 908-930.

Finch, E. G., & Tomkins, A. G. (2017). Pyrite-pyrrhotite stability in a metamorphic aureole: Implications for orogenic gold genesis. *Economic Geology*, 112(3), 661-674.

Fleet, M. E. (1978). The pyrrhotite-marcasite transformation. *The Canadian Mineralogist*, 16(1), 31-35.

Gaboury, D. (2013). Does gold in orogenic deposits come from pyrite in deeply buried carbon-rich sediments?: Insight from volatiles in fluid inclusions. *Geology*, 41(12), 1207-1210.

George, L. L., Cook, N. J., Crowe, B. B., & Ciobanu, C. L. (2018). Trace elements in hydrothermal chalcopyrite. *Mineralogical Magazine*, 82(1), 59-88.

Gregory, D. D., Large, R. R., Halpin, J. A., Baturina, E. L., Lyons, T. W., Wu, S., & Bull, S. W. (2015). Trace element content of sedimentary pyrite in black shales. *Economic Geology*, 110(6), 1389-1410.

Goldfarb, R. J., & Groves, D. I. (2015). Orogenic gold: Common or evolving fluid and metal sources through time. *Lithos*, 233, 2-26.

Goldfarb, R., Baker, T., Dube, B., Groves, D. I., Hart, C. J., & Gosselin, P. (2005). Distribution, character and genesis of gold deposits in metamorphic terranes. In: Hedenquist, J.W., Thompson, J.F.H., Goldfarb, R.G., and Richards, J.P., (eds.) Economic geology 100th Anniversary volume. Society of Economic Geologists, Littleton, Colorado, USA, pp. 407-450.

Goldfarb, R. J., Leach, D. L., Pickthorn, W. J., & Paterson, C. J. (1988). Origin of lode-gold deposits of the Juneau gold belt, southeastern Alaska. *Geology*, 16(5), 440-443.

Gordey, S. P., Anderson, R.G. (1993). Evolution of the northern Cordilleran miogeocline, Nahanni map area (105I), Yukon and Northwest Territories. *Geological Survey of Canada Memoir*, 428, 214.

Gordey, S. P. (2013). Evolution of the Selwyn basin region, Sheldon Lake (105J) and Tay River (105K) map areas, central Yukon Territory. *Geological Survey of Canada, Bulletin,* 599, 274.

Hart, C. J., Goldfarb, R. J., Lewis, L. L., & Mair, J. L. (2004). The northern Cordilleran mid-Cretaceous plutonic province: ilmenite/magnetite-series granitoids and intrusion-related mineralisation. Resource *Geology*, 54(3), 253-280.

Hart, C., & Lewis, L. L. (2005). Gold mineralization in the upper Hyland River area: A non-magmatic origin. In *Yukon Exploration & Geology* 2005 (pp. 109-125). Yukon Geological Survey.

Hall, A. J., Boyce, A. J., & Fallick, A. E. (1987). Iron sulphides in metasediments: Isotopic support for a retrogressive pyrrhotite to pyrite reaction. *Chemical Geology: Isotope Geoscience Section*, 65(3-4), 305-310.

Hellstrom, J., Paton, C., Woodhead, J., Hergt, J., (2008). Iolite: software for spatially resolved LA– (quad and MC) ICPMS analysis. *Mineralogical association of Canada short course series* 40, 343–348.

Holland, T. J. B., & Powell, R. T. J. B. (1998). An internally consistent thermodynamic data set for phases of petrological interest. *Journal of metamorphic Geology*, 16(3), 309-343.

Hunger, S., & Benning, L. G. (2007). Greigite: A true intermediate on the polysulfide pathway to pyrite. *Geochemical transactions*, 8(1), 1.

Kerrich, R. (1983). Geochemistry of gold deposits in the Abitibi greenstone belt. *Canadian Institute of Mining and Metallurgy Special*, *27*, 75 pp.

Kretz, R. (1983). Symbols for rock-forming minerals. *American mineralogist*, 68(1-2), 277-279.

Large, R. R., Bull, S. W., & Maslennikov, V. V. (2011). A carbonaceous sedimentary source-rock model for Carlin-type and orogenic gold deposits. *Economic Geology*, 106(3), 331-358.

Large, R. R., Danyushevsky, L., Hollit, C., Maslennikov, V., Meffre, S., Gilbert, S., & Singh, B. (2009). Gold and trace element zonation in pyrite using a laser imaging technique: Implications for the timing of gold in orogenic and Carlin-style sediment-hosted deposits. *Economic Geology*, 104(5), 635-668.

Large, R. R., Maslennikov, V. V., Robert, F., Danyushevsky, L. V., & Chang, Z. (2007). Multistage sedimentary and metamorphic origin of pyrite and gold in the giant Sukhoi Log deposit, Lena gold province, Russia. *Economic Geology*, 102(7), 1233-1267.

Mohr, D. W., & Newton, R. C. (1983). Kyanite-staurolite metamorphism in sulfidic schists of the Anakeesta formation, Great Smoky Mountains, North Carolina. *American Journal of Science*, 283(2), 97-134

Monger, J. W., & Gibson, H. D. (2019). Mesozoic-Cenozoic deformation in the Canadian Cordillera: the record of a "Continental Bulldozer"?. Tectonophysics, 757, 153-169.

Moynihan, D., (2012). A preliminary assessment of low pressure, amphibolite-facies metamorphism in the upper Hyland River area (NTS 105H), southeast Yukon. Yukon Exploration and Geology, 99-114.

Moynihan, D., (2017). Progress report on geological mapping in the upper Hyland River region of southeastern Yukon (parts of NTS 105H / 08, 09, 10, 15, 16 and 105I / 02). Yukon Exploration and Geology, 163-180.

Moynihan, D., (2020; *in prep*). Geology of the upper Hyland River region of southeastern Yukon Territory. Yukon Geological Survey, *Bulletin*.

Neumann, H. (1950). Pseudomorphs of pyrrhotine after pyrite in the Ballachulish slates. *Mineralogical Magazine and Journal of the Mineralogical Society, 29*(210), 234-238.

Nesbitt, B. E. (1982). Metamorphic sulfide-silicate equilibria in the massive sulfide deposits at Ducktown, Tennessee. *Economic Geology, 77*(2), 364-378.

Nesbitt, B. E., & Essene, E. J. (1983). Metamorphic volatile equilibria in a portion of the southern Blue Ridge Province. *American Journal of Science, 283*(2), 135-165.

Padget, C., (2018). Bedrock geology and metamorphism of the Anderson Lake area, parts of NTS 105H07, 105H/10, and 105H/11, southeastern Yukon. Tech. rep., Yukon Geological Survey, Open File 2018-19.

Pattison, D. R. (2001). Instability of Al2SiO5 "triple-point" assemblages in muscovite+ biotite+ quartz-bearing metapelites, with implications. *American Mineralogist, 86*(11-12), 1414-1422.

Pattison, D.R.M., and Harte, B., (1985), A petrogenetic grid for pelites in the Ballachulish and other Scottish thermal aureoles: *Journal of the Geological Society*, 142, 7–28.

——(1997), The geology and evolution of the Ballachulish igneous complex and aureole: *Scottish Journal of Geology*, v. 33, p. 1–29.

——(2001), The Ballachulish igneous complex and aureole: A field guide: Edinburgh, *Edinburgh Geological Society*, 148 p.

Pattison, D.R.M. and Tracy R.J. (1991) Phase equilibria and thermobarometry of metapelites. In: Kerrick, D.M. (ed) Contact Metamorphism. *Mineralogical Society of America Reviews in Mineralogy 26*, 105-206.

Pattison, D. R. M., Spear, F. S., & Cheney, J. T. (1999). Polymetamorphic origin of muscovite+ cordierite+ staurolite+ biotite assemblages: implications for the metapelitic petrogenetic grid and for PT paths. *Journal of Metamorphic Geology, 17*, 685-704.

Phillips, G. N., & Powell, R. (2010). Formation of gold deposits: A metamorphic devolatilization model. *Journal of Metamorphic Geology, 28*(6), 689-718.

Pitcairn, I. K., Teagle, D. A., Craw, D., Olivo, G. R., Kerrich, R., & Brewer, T. S. (2006). Sources of metals and fluids in orogenic gold deposits: insights from the Otago and Alpine Schists, New Zealand. *Economic Geology, 101*(8), 1525-1546.

Pitcairn, I. K., Olivo, G. R., Teagle, D. A., & Craw, D. (2010). Sulfide evolution during prograde metamorphism of the Otago and Alpine Schists, New Zealand. *The Canadian Mineralogist, 48*(5), 1267-1295.

Pitcairn, I. K., Craw, D., & Teagle, D. A. (2015a). Metabasalts as sources of metals in orogenic gold deposits. *Mineralium Deposita, 50*(3), 373-390.

Pitcairn, I. K., Skelton, A. D., & Wohlgemuth-Ueberwasser, C. C. (2015b). Mobility of gold during metamorphism of the Dalradian in Scotland. *Lithos, 233*, 69-88.

Phillips, G. N. (1993). Metamorphic fluids and gold. *Mineralogical Magazine, 57*(388), 365-374.

Powell, R., Will, T. M., & Phillips, G. N. (1991). Metamorphism in Archaean greenstone belts: Calculated fluid compositions and implications for gold mineralization. *Journal of Metamorphic Geology, 9*(2), 141-150.

Qian, G., Xia, F., Brugger, J., Skinner, W. M., Bei, J., Chen, G., & Pring, A. (2011). Replacement of pyrrhotite by pyrite and marcasite under hydrothermal conditions up to 220 C: An experimental study of reaction textures and mechanisms. *American Mineralogist, 96*(11-12), 1878-1893.

Rasmussen, K., 2013. The timing, composition, and petrogenesis of syn-to post-accretionary magmatism in the northern Cordilleran miogeocline, eastern Yukon and southwestern. Ph.D. thesis, University of British Columbia.

Read, P. B., Woodsworth, G. J., Greenwood, H. J., Ghent, E. D., & Evenchick, C. A. (1991). Metamorphic map of the Canadian Cordillera: Geological Survey of Canada. *Map 1714A, scale, 1:2 000 000*.

Sack, P. J., Large, R. R., & Gregory, D. D. (2018). Geochemistry of shale and sedimentary pyrite as a proxy for gold fertility in the Selwyn basin area, Yukon. *Mineralium Deposita, 53*(7), 997-1018.

Shaw, D. M. (1956). Geochemistry of pelitic rocks. Part III: Major elements and general geochemistry. *Geological Society of America Bulletin, 67*(7), 919-934.

Slotznick, S. P., Eiler, J. M., & Fischer, W. W. (2018). The effects of metamorphism on iron mineralogy and the iron speciation redox proxy. *Geochimica et Cosmochimica Acta, 224*, 96-115.

Spear, F. S. (1993). Metamorphic phase equilibria and pressure-temperature-time paths, Mineral. *Soc. Am. Monogr, 1*, 799.

Starr, P. G., Pattison, David, R. M. (2019). Metamorphic devolatilization of basalts across the greenschist- amphibolite facies transition zone: insights from isograd mapping, petrography, and thermodynamic modelling. *Lithos*, 342-343, 295-314.

Thomas, H. V., Large, R. R., Bull, S. W., Maslennikov, V., Berry, R. F., Fraser, R., & Moye, R. (2011). Pyrite and pyrrhotite textures and composition in sediments, laminated quartz veins, and reefs at Bendigo gold mine, Australia: Insights for ore genesis. *Economic Geology, 106*(1), 1-31.

Tomkins, A. G. (2010). Windows of metamorphic sulfur liberation in the crust: Implications for gold deposit genesis. *Geochimica et Cosmochimica Acta, 74*(11), 3246-3259.

Tomkins, A. G. (2013). On the source of orogenic gold. *Geology, 41*(12), 1255-1256.

Toulmin III, P., & Barton Jr, P. B. (1964). A thermodynamic study of pyrite and pyrrhotite. *Geochimica et Cosmochimica Acta, 28*(5), 641-671.

Whelan, S., 2014. Orogenic gold mineralization at 3Ace and geochemical characteristics of quartz monzonite dikes at Sprogge, southeast Yukon. Master's thesis, unpublished, University of Alberta.

Wilkinson, J. J., Chang, Z., Cooke, D. R., Baker, M. J., Wilkinson, C. C., Inglis, S., & Gemmell, J. B. (2015). The chlorite proximitor: A new tool for detecting porphyry ore deposits. *Journal of Geochemical Exploration, 152*, 10-26.

Wilson, S.A., Ridley, W.I., Koenig, A.E., 2002. Development of sulphide calibration standards for the laser ablation inductively coupled plasma mass spectrometry technique. *Journal of Analytical Atomic Spectrometry* 17, 406–409.

Wood, B. L., & Popov, N. P. (2006). The giant Sukhoi log gold deposit, Siberia. *Russian Geology and Geophysics, 47*(3), 315-341.

Yardley, B. W. (2009). The role of water in the evolution of the continental crust. *Journal of the Geological Society, 166*(4), 585-600.

Zhong, R., Brugger, J., Tomkins, A. G., Chen, Y., & Li, W. (2015). Fate of gold and base metals during metamorphic devolatilization of a pelite. *Geochimica et Cosmochimica Acta, 171*, 338-352.

Nd-Hf Isotope Geochemistry and Lithogeochemistry of the Rambler Rhyolite, Ming VMS Deposit, Baie Verte Peninsula, Newfoundland: Evidence for Slab Melting and Implications for VMS Localization

S.J. Piercey[1*] and J.-L. Pilote[2]

Piercey, S.J. and Pilote, J.-L., 2021. Nd-Hf Isotope Geochemistry and Lithogeochemistry of the Rambler Rhyolite, Ming VMS Deposit, Baie Verte Peninsula, Newfoundland: Evidence for Slab Melting and Implications for VMS Localization; in *Targeted Geoscience Initiative 5:grant program final reports (2018-2020): Geological Survey of Canada, Open File 8755, p. 201–215. https://doi.org/10.4095/328988*

Abstract: New high precision lithogeochemistry and Nd and Hf isotopic data were collected on felsic rocks of the Rambler Rhyolite formation from the Ming volcanogenic massive sulphide (VMS) deposit, Baie Verte Peninsula, Newfoundland. The Rambler Rhyolite formation consists of intermediate to felsic volcanic and volcaniclastic rocks with U-shaped primitive mantle normalized trace element patterns with negative Nb anomalies, light rare earth element-enrichment (high La/Sm), and distinctively positive Zr and Hf anomalies relative to surrounding middle rare earth elements (high Zr-Hf/Sm). The Rambler Rhyolite samples have εNdt = -2.5 to -1.1 and εHf_t = +3.6 to +6.6; depleted mantle model ages are T_{DM}(Nd) = 1.3-1.5 Ga and T_{DM}(Hf) = 0.9-1.1Ga. The decoupling of the Nd and Hf isotopic data is reflected in εHft isotopic data that lies above the mantle array in εNd_t -εHf_t space with positive $\Delta\varepsilon Hf_t$ values (+2.3 to +6.2). These Hf-Nd isotopic attributes, and high Zr-Hf/Sm and U-shaped trace element patterns, are consistent with these rocks having formed as slab melts, consistent with previous studies. The association of these slab melt rocks with Au-bearing VMS mineralization, and their FI-FII trace element signatures that are similar to rhyolites in Au-rich VMS deposits in other belts (e.g., Abitibi), suggests that assuming that FI-FII felsic rocks are less prospective is invalid and highlights the importance of having an integrated, full understanding of the tectono-magmatic history of a given belt before assigning whether or not it is prospective for VMS mineralization.

[1]Department of Earth Sciences, Memorial University of Newfoundland, Alexander Murray Building, 9 Arctic Ave, St. John's, Newfoundland and Labrador, Canada A1B 3X5
[2]Geological Survey of Canada, 490 rue de la Couronne, Québec, QC, G1K 9A9
*Corresponding author (e-mail: spiercey@mun.ca)

INTRODUCTION

The utilization of felsic volcanic geochemistry has been a crucial tool in VMS exploration for over 40 years (e.g., Spitz and Darling, 1978; Lesher et al., 1986). Lithogeochemistry of felsic volcanic rocks has been used to understand the relationships between primary petrology, tectonic setting, and VMS tectono-magmatic environment definition (e.g., Piercey, 2011), but also for delineating hydrothermal footprints around VMS deposits (e.g., Barrett and MacLean, 1999). The usage of radiogenic isotopes for understanding the petrology and origin of VMS-host rocks is much less widespread (e.g., Barrie et al., 1999), despite their utility in understanding primary petrological histories of rocks. Moreover, radiogenic isotopes paired with lithogeochemical data allow for more refined petrological models for VMS host rocks (e.g., Pilote and Piercey, 2018) and facilitate a more robust understanding of the tectono-magmatic relationships between host rock formation and VMS deposit genesis.

In many VMS districts, felsic rocks are the predominant host to mineralization (Franklin et al., 2005; Galley et al., 2007) and there has been extensive study of felsic volcanic petrology and geochemistry. In a classic study of felsic volcanic prospectivity, Lesher et al. (1986) documented the FI-FIII classification for rocks from the Superior Province, which was subsequently expanded upon by Hart et al. (2004), and included a fourth classification (FIV). In these classifications, the most prospective units were those with relatively low Zr/Y and La/Yb ratios (and high Y and Yb contents), which were interpreted to have formed via crustal melting at shallow levels (<10km) where plagioclase or amphibole are stable in the residue with the FIII and FIV being the most prospective units. They interpreted that melting at shallow levels resulted in magmas that reached the surface with much of their heat of fusion intact and correspondingly they would be associated with more robust hydrothermal circulation. In contrast, the FII and FI suite of felsic rocks were interpreted to reflect melting at greater depths where amphibole/hornblende and garnet were stable in the residue, resulting in higher Zr/Y and La/Yb ratios and lower Y and Yb contents. They argued these were less prospective because they formed at depth and would lose much of their heat upon transition from depth to the near surface and thus would be less prospective for forming VMS deposits. While this worked well for VMS districts in the Archean and those that are floored by mafic crust, many Phanerozoic VMS deposits, including many giant and super-giant deposits that are partially to fully underlain by continental crust are associated with FII rhyolites (e.g., Lentz, 1998; Piercey, 2011). Further, many Au-enriched VMS deposits in the ancient record are associated with FI rhyolites (Mercier-Langevin et al., 2007; Gaboury and Pearson, 2008; Pilote and Piercey, 2018).

In a recent study of the Ming deposit, Pilote and Piercey (2018) demonstrated that the rhyolites hosting Au-enriched mineralization were similar to FI rhyolites. These rocks are spatially associated with boninitic rocks of the Pacquet complex (Skulski et al., 2010; Skulski et al., 2015) and were interpreted to have formed at depths >10km. However, unlike previous models for FI rhyolites, Pilote and Piercey (2018) using numerous petrological arguments suggested that the FI rhyolites at the Ming VMS deposit were a direct result of slab melting. Slab melting is generally rare in subduction zones, only occurring where the subducting oceanic crust is young and hot (Drummond and Defant, 1990; Gutscher et al., 2000; Peacock, 2004); under normal conditions the slab dehydrates, rather than melts (e.g., Pearce and Parkinson, 1993; Pearce and Peate, 1995).

To test the slab melting hypothesis and its importance for Au-rich VMS deposit formation, we have obtained new, ultra-high precision trace element geochemical data and radiogenic Nd and Hf isotope data on the Rambler Rhyolite formation. Nd and Hf isotope data (and associated trace element data) are ideal for testing slab melting models. In particular, Nd and Hf isotopes are decoupled from one another during slab melting (Pearce et al., 1999; Barry et al., 2006; Cai et al., 2014), thus they provide an ideal tool for evaluating the potential contributions of slab melting to the formation of the Rambler Rhyolite (hereafter shorten for brevity). Thus, in this paper we will present new geochemical, Nd and Hf isotope data for the Rambler Rhyolite to evaluate a model for its petrogenesis and how that potentially relates to the genesis of the Ming VMS deposit and its Au-enrichment.

Geological and Stratigraphic Setting

The Ming VMS deposit is hosted within the Baie Verte oceanic tract (BVOT), which consists of peri-Laurentian rocks that formed during the Cambrian-Ordovician closure of the Taconic seaway (Figs. 1-2)(Waldron and van Staal, 2001; van Staal, 2007; van Staal and Barr, 2012). The BVOT consists of four partial to full ophiolite complexes that are ~488-487 Ma (Dunning and Krogh, 1985) that host both Cu(-Au)-rich VMS deposits (Betts Cove ophiolite) and Au-enriched VMS deposits (Pacquet complex)(Figs. 1-2)(Sangster et al., 2007; Brueckner et al., 2014; Pilote et al., 2017). The cover sequence to mineralization, the Snooks Arm Group, also hosts younger (Silurian-Devonian) orogenic Au-type mineralization (Figs. 1-2)(Ramezani et al., 2000).

The Ming deposit is hosted by the Pacquet complex, which consists of a lowermost unit, the Betts Head Formation, that includes variably spherulitic and amygdaloidal pillow lavas, massive flows, and volcaniclastic rocks that have boninitic affinities (Fig. 2) (Hibbard, 1983; Bedard et al., 2000; Skulski et al., 2009; Skulski et al., 2010). This is overlain by the Mount Misery Formation, which contains variably plagioclase- and pyroxene-phyric pillow lavas with island arc tholeiitic affinities interbedded with those with boninitic affinities (Fig. 2) (Hibbard,

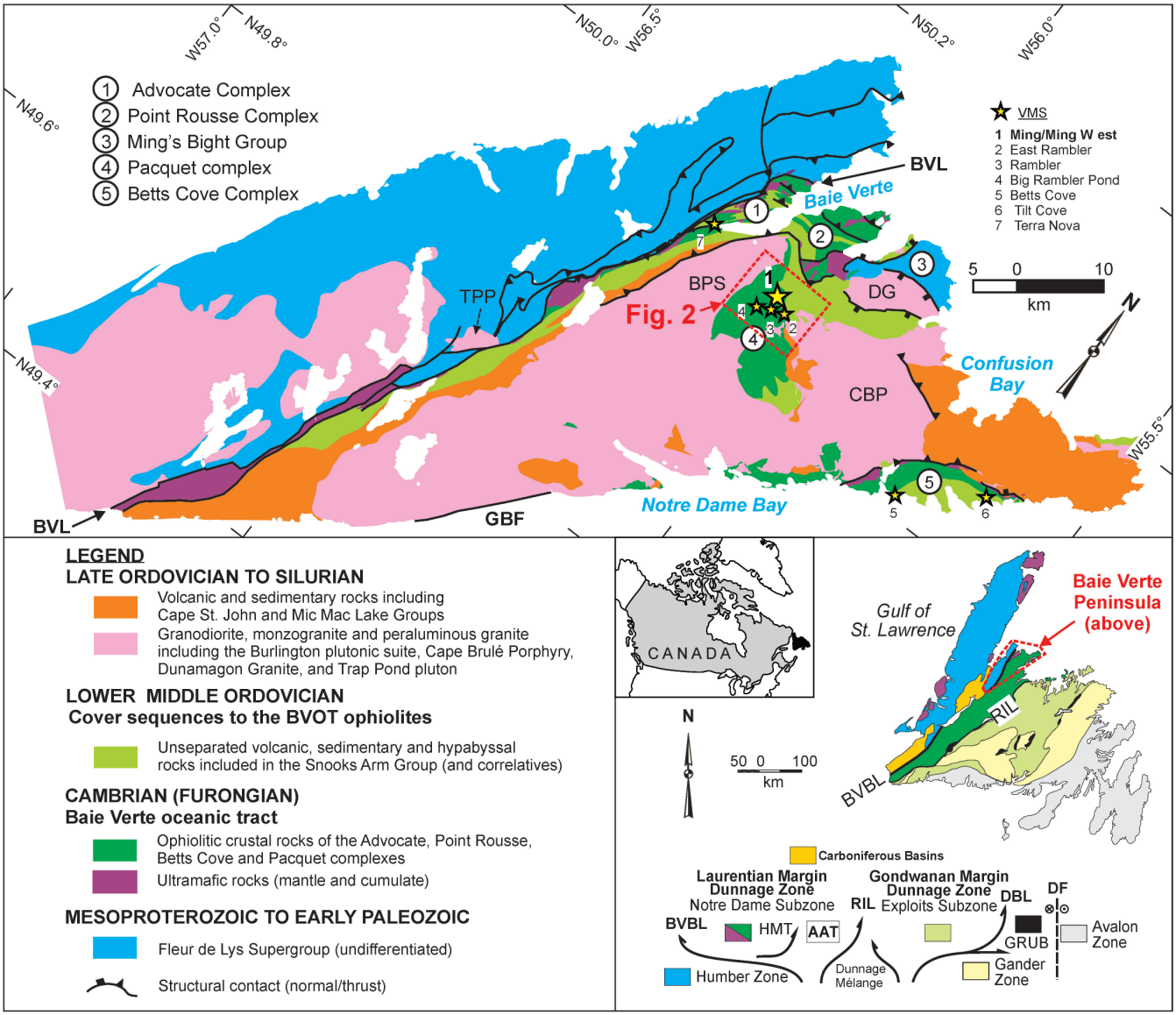

Figure 1. Simplified geology of the Baie Verte Peninsula with the tectonostratigraphic zones of the Appalachian orogenic in Newfoundland (modified from Castonguay et al., 2014, and references therein; and Pilote and Piercey, 2018). Location of major VMS deposits as yellow stars. AAT - Annieopsquotch Accretionary Tract, BPS - Burlington plutonic Suite, BVBL - Baie Verte-Brompton Line, BVBL - Baie Verte-Brompton Line, CB - Cape Brule, DBL - Dog Bay Line, DF - Dover Fault, DG - Dunamagon Granite, GBF - Green Bay Fault, GRUB - Gander River Ultramafic Belt, TPP - Trap Pond pluton, RIL - Red Indian Line, HMT - Hungry Mountain Thrust.

1983; Bedard et al., 2000; Skulski et al., 2009; Skulski et al., 2010). The spatially restricted Rambler Rhyolite lies stratigraphically above these units and consist of quartz-phyric rhyolite to rhyodacitic flows interbedded with tuff, lapilli tuff, and tuff breccia (Fig. 2)(Hibbard, 1983; Skulski et al., 2009; Skulski et al., 2010; Pilote et al., 2017; Pilote and Piercey, 2018). The latter is overlain by rocks of the Snooks Arm Group (the cover sequence) that contains intercalated felsic and mafic volcanic and volcaniclastic rocks that have chemistry ranging from tholeiitic, calc-alkalic, and non-arc affinities (Fig. 2)(e.g., E-MORB and OIB)(Hibbard, 1983; Bedard et al., 2000; Skulski et al., 2009; Skulski et al., 2010). These rocks were subject to polyphase deformation in the Ordovician and Silurian-Devonian (Fig. 2)(Castonguay et al., 2009; Castonguay et al., 2014).

In map view, the Rambler Rhyolite has a dome shape that may have been accentuated by polyphase deformation and fold interference (Fig. 2) (Castonguay et al., 2009; Castonguay et al., 2014). The Rambler Rhyolite consists of three lithofacies that are ~1km thick, from top to bottom they are (Pilote et al., 2017): 1) unit 1.1 – coherent facies of quartz-phyric to aphanitic felsic volcanic rocks that have a sharp transitions to; 2) unit 1.2 - quartz-bearing bedded to massive felsic volcaniclastic rocks with variable fragment

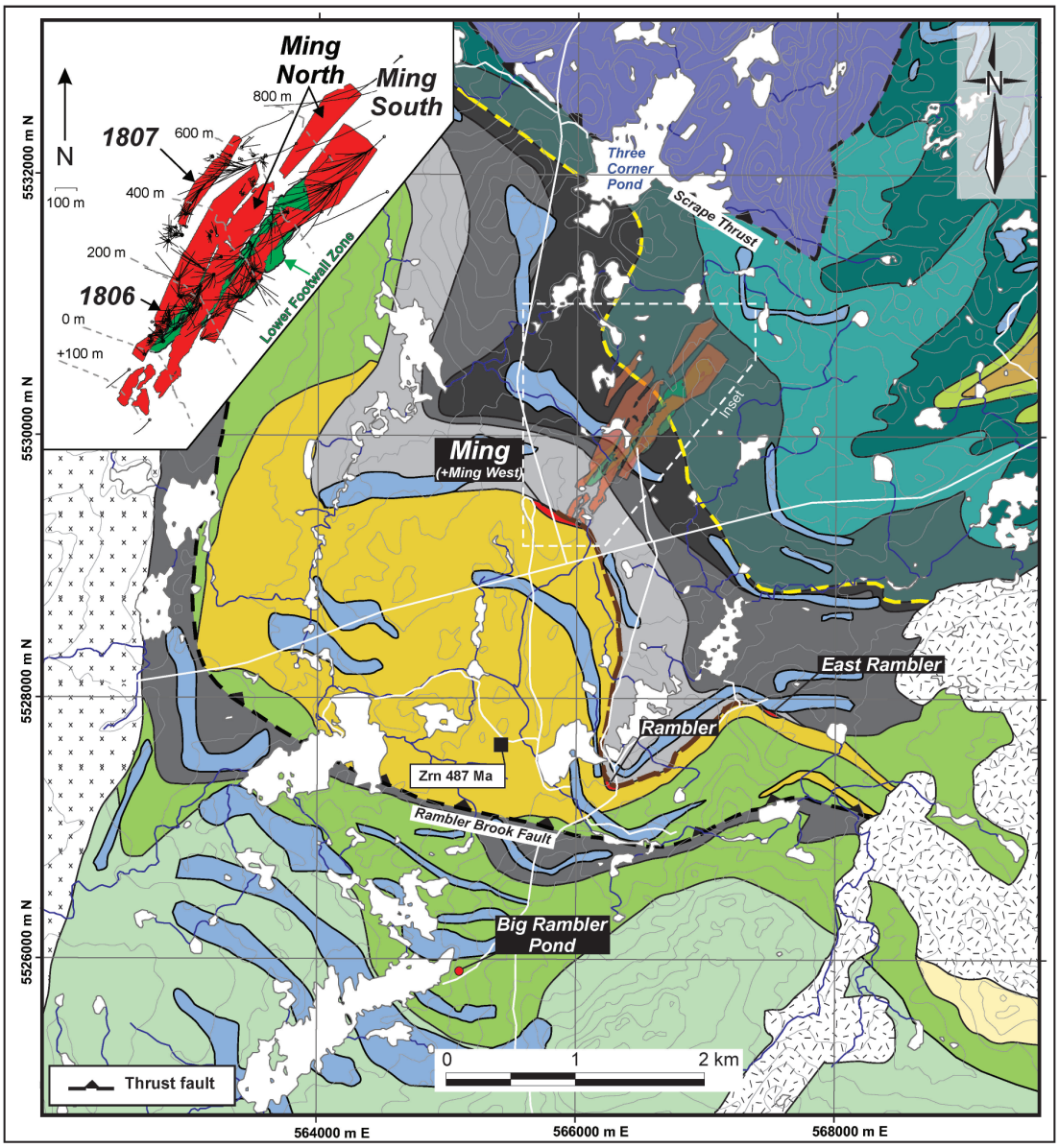

Silurian Cape St. John Group (unseparated)

Clastic, pinkred sedimentary rocks, mafic and/or felsic volcanic rocks.

Burlington Granodiorite (434 430 Ma)

Cape Brulé Porphyry (430 Ma)
Porphyritic granodiorite, quartzfeldspar porphyry.

EarlyMiddle Ordovician Snooks Arm Group (479467 Ma)

Tholeiitic gabbro sills/dikes, include plagioclasephyric to finegrained gabbro. Minor mediumgrained equigranular diorite.

Basalm Bud Cove Formation

Volcanogenic turbidite, siltstone, felsic tuffs, basalts.

Calcalkaline felsic tuf f, lapilli tuff.

Venam's Bight Formation
Tholeiitic pillowed basalt, porphyritic and vesicular basalt, siliceous mudstone.

Bobby Cove Formation
Chert, iron formation, volcanogenic sedimentary rocks, minor felsic tuffs.

Mafic tuff, lapilli tuff, epiclastic rocks, interbedded basalt flows.

Clinopyroxenephyric crystal tuf f, lapilli tuff, and tuff breccia (Prairie Hat member).

Calkalkaline plagioclasephyric pillow basalt and andesite.

Scrape Point Formation
Mafic volcaniclastic rocks, tuff, lapilli tuff, epiclastic sandstone, shale, interbedded pillow basalt.

Pillowed, massive, amygdaloidal, plgioclasephyric basalt flows. Tholeiitic affinities.

Magnetiterich iron formation, chert beds, volcanogenic siltstone (Nugget Pond horizon).

CambroOrdovician Pacquet complex

Rambler Rhyolite formation (487 Ma)
Calcalkalic quartzphyric rhyolite to rhyodacite flows interbedded with intermediate to felsic tuff, lapilli tuffs, and tuff breccia.

Mt. Misery Formation
Plagioclase and pyroxenephyric pillow basalt with tholeiitic affinities, interbedded with boninite.

Betts Head Formation
Spherulitic, amygdaloidal, porphyritic boninitic pillow lavas with aphanitic darkgreen groundmass.

Point Rousse ophiolite (490 Ma)

Undifferentiated serpentinized ultramafic rocks with tholeiitic and boninitic affinities.

sizes; and 3) unit 1.3 – an uppermost unit of blue quartz-phyric to quartz-megacrystic coherent felsic lava flows that transition into bedded quartz-bearing tuffs (Fig. 3). The lithofacies show distinct variations in thickness related to synvolcanic faults that controlled the localization of mineralization in the various zones of the Ming deposit and there is a clear spatial (and genetic?) relationship between VMS mineralization and felsic magmatism in the Ming deposit (Pilote et al., 2017).

LITHOGEOCHEMISTRY AND RADIOGENIC ISOTOPE GEOCHEMISTRY

Samples for lithogeochemistry are those collected from drill core and from underground and surface mapping from lithofacies units 1.1, 1.2, and 1.3 of the Rambler Rhyolite. Major element data were previously reported in Pilote and Piercey (2018), whereas new trace element, Nd and Hf isotope data were collected as part of this study. In the case of this study least altered to weakly altered samples were chosen; however, it is assumed that all samples exhibit mobility of alkali elements and low field strength element (LFSE); thus, our interpretations are focused on the utilization of elements that are immobile during most hydrothermal alteration and metamorphism, namely Al_2O_3, TiO_2, high field strength elements (HFSE: Zr, Hf, Nb, Ta, Th), and rare earth elements (REE)(e.g., MacLean and Barrett, 1993). Further, Lu-Hf and Sm-Nd isotope systems are chosen because they contain immobile REE (Sm, Nd, Lu) and HFSE (Hf) and thus provide the best method to delineate the primary isotopic values of the Rambler Rhyolite at the time of formation.

METHODS

Rock samples were pulverized using a mild still mill and major elements were determined using a lithium metaborate fusion that was subsequently dissolved in HF-HNO^3 and then analyzed using an inductively coupled plasma emission spectrometer (ICP-ES) at Activation Laboratories in Ancaster, ON, Canada (see Pilote and Piercey, 2018 for details). Trace elements Li, Cs, Rb, Ba, Sr, Pb, U, Th, Nb, Ta, Zr, Hf, Y, Ga, Cu, Zn, Mo, Cd, Sn, Sb, W, Bi, V, Cr, Co, Ni, Sc, and REE were determined at the Pacific Centre for Isotopic and Geochemical Research (PCIGR) in the Department of Earth and Ocean Sciences at the University of British Columbia. Sample powders were prepared following the methods of Pretorius et al. (2006). Sample powders (~ 0.1 g) were digested in a HF-HNO_3-$HClO_4$ mixture at 190°C in steel-jacketed high-pressure PTFE vessel. The solutions were then dried down and re-fluxed in sub-boiled 6N HCl on a hotplate at 120-130°C for at least 24 hours. After digestion, samples were diluted ~5000× with a 1% HNO_3-0.05% HF solution for concentrations measurements. Analyses were carried out on a Thermo Finnigan Element2 HR-ICP-MS using In (concentration of 10 ppb) to monitor instrumental drift and the USGS BCR-2 reference material for external calibration of the signal. Data were corrected following blank subtraction and sample-standard bracketing, where BCR-2 was analyzed following every 6 unknown samples. The reference materials AGV-1 (andesite; n = 12) and AGV-2 (andesite; n = 4) and G-3 (granite; n=4) were run during the course of the analytical program. In AGV-1 the relative standard deviation (%RSD) measurements for precision are <2% for all LFSE and HFSE, <5% for REE, with the exception of W, all metals and metalloids are <5% RSD. For AGV-2, %RSD varies from 1.7-7.5% for HFSE, 1.9-4.3% for LFSE (except Li = 12.2%), 1.5-7.5% for REE, and 1.8-5.0% for metals and metalloids, except W (12.1%) and Mo (8.2%). For G-3, the %RSD is <4% for HFSE, ~1-10% for REE (except Lu ~12%), 1-7% for LFSE (except Li ~10%), and <8% for metals except Mo, W, and Bi. Accuracy, given as % relative difference (%RD) compared to known values, for AGV-1 ranges from -2.7% to +1.54% for HFSE, -1.7% to +3.8 for LFSE, -4.4% to +3.7% for REE, and +/-7%RD for metals, except C, Sb, W, and Bi. For AGV-2, %RD values range from -1.4% to +1.0% for HFSE, -1.9% to +1.8% for LFSE (except Li = -4.7%), -2.7% to +3.5% for REE, and -0.6% to 2.3% for Metals, except W and Mo. For G-3, %RD values range from -5.9% to +3.5% for HFSE, -5.2% to +7.8% for LFSES (except Li = -8.9% and Ba = -10.9%), -6.5% to +0.1% for REE, and +/-12% for metals, except Mo, Cr, Sn, Sb and W.

Radiogenic isotope determinations were also obtained at the PCIGR following the methods of Weis et al. (2006) and Weis et al. (2007). Approximately 100 to 150 mg of sample rockpowder is loaded into a steel-jacketed acid-washed high-pressure PTFE bomb with 5.0 mL of 48% HF and 1.0 mL of ~14 N HNO_3, and then dissolved for 5 days at 190°C. Digested samples are dried down on a hotplate overnight at ~130°C, reconstituted in 6.0 mL of 6 N HCl and re-bombed for 24 hours at 190°C. These solutions were then evaporated to dryness on hotplate prior to re-dissolution for ion exchange purification of Hf and Nd. Separation procedures for Nd followed Weis et al. (2006; 2007). and was then separated from the other rare earth elements using HDEHP-coated Teflon resin. Hafnium separations were conducted using TODGA resin following a method modified after Connelly et al. (2006). The Nd and Hf isotope ratios were measured by MC-ICP-MS (Nu Instruments Ltd., Nu

Figure 2. Geological map of the Ming VMS deposit area, Baie Verte Peninsula, with VMS orebodies projected to surface (also in the inset) and shown in light red and light green (Lower Footwall Zone stockwork). Datum is UTM 21N NAD 83. Map from Pilote and Piercey (2018 and references therein).

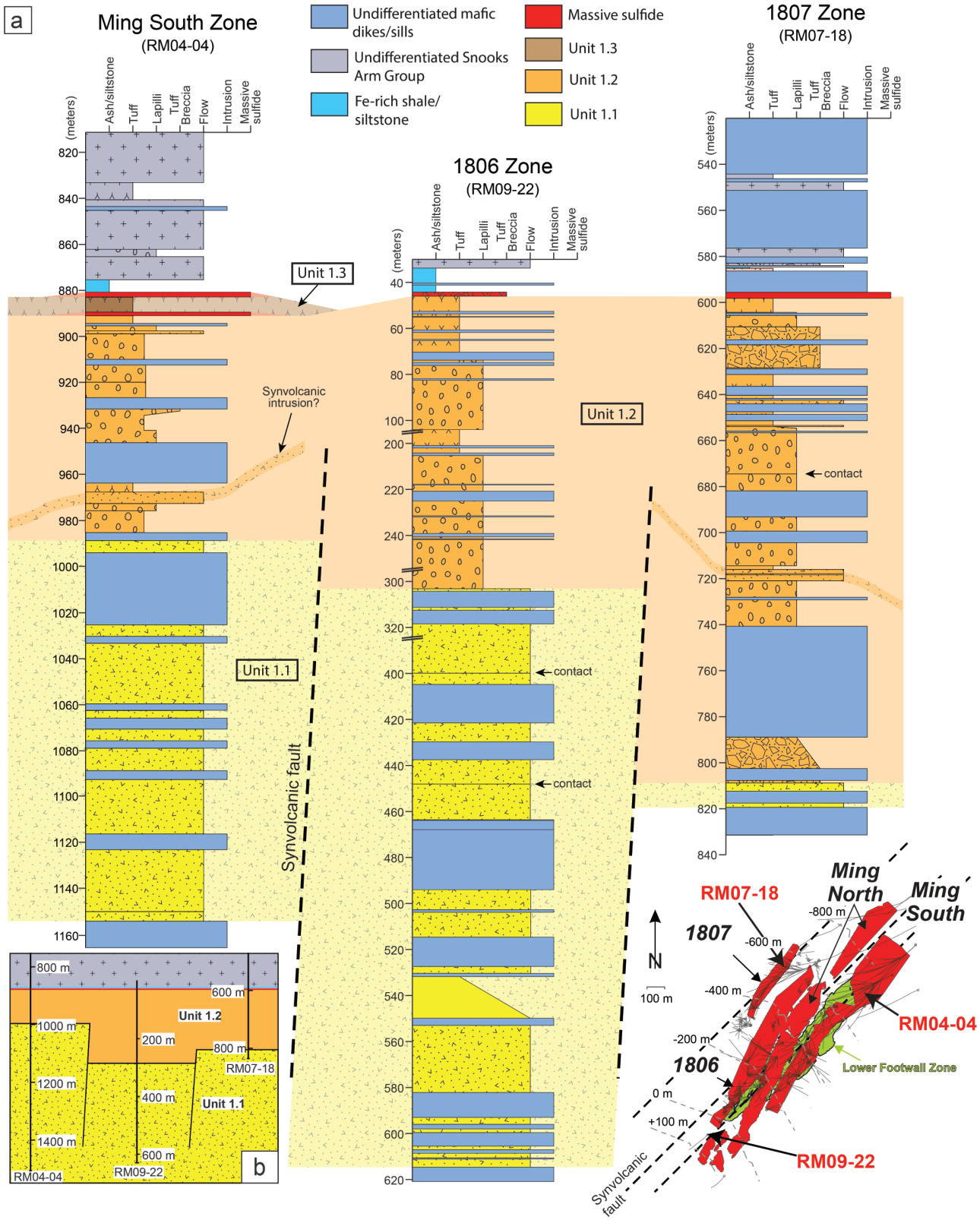

Figure 3. Stratigraphic columns for various zones in the Ming VMS deposits, including the Ming South (DDH RM04-04), 1806 (RM09-22), and 1807 (RM07-18) zones with the various lithofacies of the Ming deposit. These illustrate the volcaniclastic lithofacies associated with all zones. Sharp lateral variations in facies thickness and association of these changes with chlorite alteration are interpreted to reflect synvolcanic faults. Diagram after Pilote et al. (2017) and Pilote and Piercey (2018).

II 214 or Nu 1700) following Weis et al. (2006; 2007), and normalized to the JNDi (Nd) and JMC 475 (Hf) standards using sample-standard bracketing. Normalization values are $^{143}Nd/^{144}Nd$ = 0.512116 for JNDi (Tanaka et al., 2000) and $^{176}Hf/^{177}Hf$ = 0.282160 for JMC 475 (Blichert-Toft et al., 1997). Repeat analyses of the JNDi and JMC 475 standards during two sample batches in 2018 yielded mean isotopic compositions of $^{143}Nd/^{144}Nd$ = 0.512059 0.000008 (2SE, n=30) and 0.512095 0.000007 (2SE, n=13), and $^{176}Hf/^{177}Hf$ = 0.282191 0.000005 (2SE, n=27) and 0.282165 0.000004 (2SE, n=13), respectively. Sm, Nd, Lu, and Hf concentrations were determined as outlined above. Reference materials analyzed in this study include AGV-2 and G-3, which yielded isotopic compositions of $^{143}Nd/^{144}Nd$ = 0.512799 0.000007 (2SE; n=2) and 0.512249 0.000007 (2SE; n=2), respectively, and overlap the PCIGR lab averages of AGV-2 (0.512794 0.000019) and G-3 (0.512241 0.000016) and the values of Weis et al. (2006; 2007). The analysis of AGV-2 and G-3 yielded $^{176}Hf/^{177}Hf$ values of 0.282979 0.000004 (2SE; n=1) and 0.282513 0.000005, respectively, which overlaps the long term PCIGR lab values for AGV-2 (0.282978 0.000016) and G-3 (0.282515 0.000012) and the values of Weis et al. (2006; 2007).

Epsilon Nd and Hf values at the time of rock formation (εNdt and εHft) were calculated at ~485 Ma, the rough mid-point of U-Pb ages for Rambler Rhyolite rocks and correlatives in the Baie Verte oceanic tract (Dunning and Krogh, 1985; Ramezani et al., 2000; Skulski et al., 2010). Present day chondrite uniform reservoir (CHUR) values used for epsilon calculations include $^{143}Nd/^{144}Nd$ = 0.512630 and $^{147}Sm/^{144}Nd$ = 0.1960, and $^{176}Hf/^{177}Hf$ = 0.282785 and $^{176}Lu/^{176}Hf$ = 0.0336 (Bouvier et al., 2008). Depleted mantle model ages were calculated using $^{143}Nd/^{144}Nd$ = 0.513163 and $^{147}Sm/^{144}Nd$ = 0.2137 (Goldstein et al., 1984) and $^{176}Hf/^{177}Hf$ = 0.283238 and $^{176}Lu/^{176}Hf$ = 0.03976 (Vervoort and Blichert-Toft, 1999). The decay constants used for ^{147}Sm is $6.54x10^{-12}$ yr^{-1} (Lugmair and Marti, 1978) and ^{176}Lu is 1.876x10-11 yr^{-1} (Soederlund et al., 2004).

RESULTS

Results for the lithogeochemical data are presented in Figures 4-7. The majority of samples within the study have Na_2O between 2 and 5% and Al_2O_3/Na_2O <10, consistent with rocks that are relatively fresh or only weakly altered (Fig. 4). Moreover, key trace element ratios of the HFSE and REE have no correlation with the Al_2O_3/Na_2O alteration index (Fig. 5), suggesting that their behavior is controlled by processes other than alteration and that the HFSE and REE were immobile during alteration, as has been shown in many studies (e.g., MacLean and Barrett, 1993). Immobile element discrimination diagrams for the units from the Rambler Rhyolite suggest they have subalkaline Nb/Y ratios and are andesitic to dacitic in affinity, have M-type affinities in Nb-Y space, and plots close to the FI to FII fields in felsic volcanic VMS-prospectivity diagrams (Fig. 6). The primitive mantle normalized multi-element plots for the Rambler Rhyolite samples have distinctive U-shaped patterns with negative Nb anomalies relative to Th and La, light rare earth element enrichment (i.e., high La/Sm) and a distinctive positive Zr-Hf anomaly, relative to the surrounding elements (Fig. 7a). The high Zr-(Hf) anomalies (high Zr/Sm) and LREE-enrichments (La/Sm) in these rocks lies above the typical mantle array (N-MORB to OIB) and is even higher than upper continental crust (Fig. 7b).

The Sm-Nd and Lu-Hf isotopic data for the Rambler Rhyolite samples are plotted on Figures 8-9. The Rambler Rhyolite samples have $^{147}Sm/^{144}Nd$ ratios <0.14 and εNd_t = ~ -1.0 to -2.5 and $^{176}Lu/^{177}Hf$ ratios <0.0175 and εHf_t = ~ +3.5 to +6.5 (Fig. 8). In εNd_t-εHf_t space there is a clear decoupling of the Nd-Hf isotopic data with all Rambler Rhyolite samples having excess εHf_t relative to εNd_t and lying well above the mantle array with positive ΔεHf [= εHf_t – (1.33*εNdt +3.19)] values (Vervoort et al., 1999)(Fig 8). There is also a decoupling of the depleted mantle model ages with the T_{DM}(Nd) ages ranging from ~1.3-1.5Ga, whereas the T_{DM}(Hf) ages range from ~0.9-1.1 Ga (Fig. 9).

DISCUSSION AND SUMMARY

The melting of the subducted slab is not common to most subduction zone environments, as the slab is typically cold and dehydrates rather than melts, leading to the typical "arc" signatures found in volcanic arc rocks through time (e.g., Pearce and Peate, 1995; Tatsumi and Eggins, 1995; Stern, 2002). Slab melting is much rarer and occurs either during subduction zone initiation (Pearce et al., 1992; Pearce et al., 1999) and/or when the subducted slab is young and hot (Drummond and Defant, 1990; Tatsumi, 2000). For the rocks of the BVOT, current tectono-magmatic models argue that the Pacquet complex and correlative rocks in the Betts Cove Complex formed during Cambro-Ordovician (~488-487 Ma) eastward subduction zone initiation within the Taconic Seaway where there was formation of boninites, island arc tholeiites, and high Zr-(Hf)/Sm rhyolites of the Betts Head, Mount Misery, and Rambler Rhyolite formations, respectively (Bedard et al., 2000; van Staal, 2007; Skulski et al., 2010; van Staal and Barr, 2012; Pilote and Piercey, 2018). The association of boninites and high Zr-(Hf)/Sm rhyolites found the Pacquet complex are consistent with slab melting. For example, Pearce et al. (1992) demonstrated that the U-shaped REE pattern and high Zr-(Hf)/Sm patterns found in fore-arc boninites were in part due to slab melt-related metasomatism of ultra-depleted mantle. Similarly, Pilote and Piercey (2018) demonstrated using field arguments and geochemical modeling that the Rambler Rhyolite also formed via slab melting.

The new trace element data and Hf-Nd isotopic data for the Rambler Rhyolite are consistent with them having formed from slab melts. In particular, they have the high Zr-(Hf)/Sm

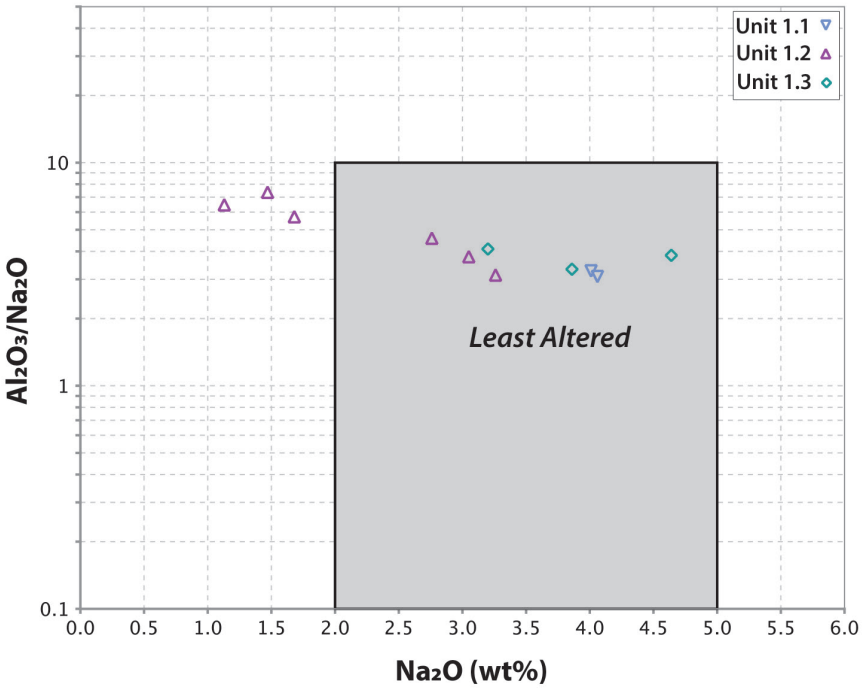

Figure 4. Al_2O_3/Na_2O index (Spitz and Darling, 1978) versus Na_2O illustrating that the Rambler Rhyolite samples from this study are fresh to weakly altered. Diagram from Ruks et al. (2006).

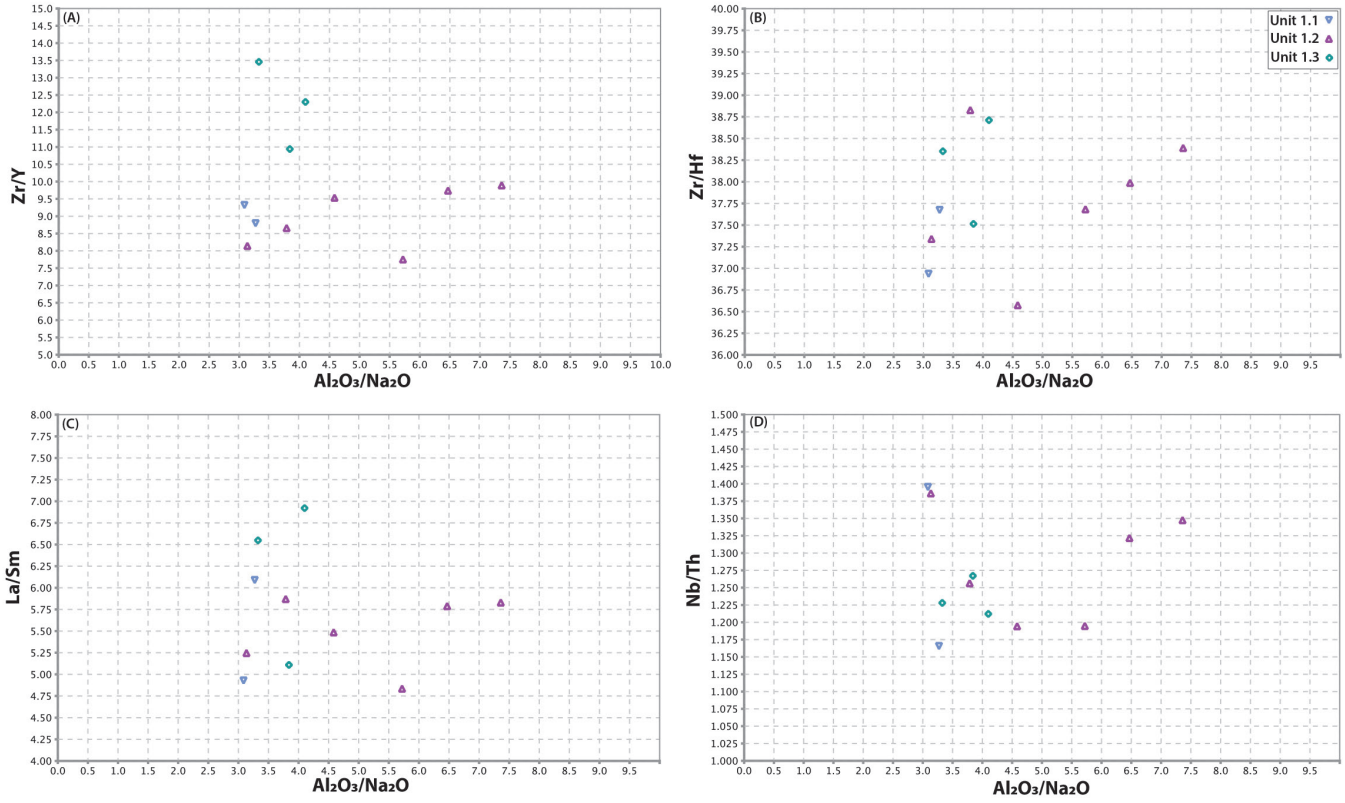

Figure 5. Spitz-Darling index (Spitz and Darling, 1978) against high field strength element and rare earth element ratios. **A)** Zr/Y. **B)** Zr/Hf. **C)** La/Sm. **D)** Nb/Th. The lack of correlation between the alteration index and these ratios suggests that these elements and ratios are not controlled by alteration, were immobile, and controlled by processes other than alteration (i.e, primary igneous processes).

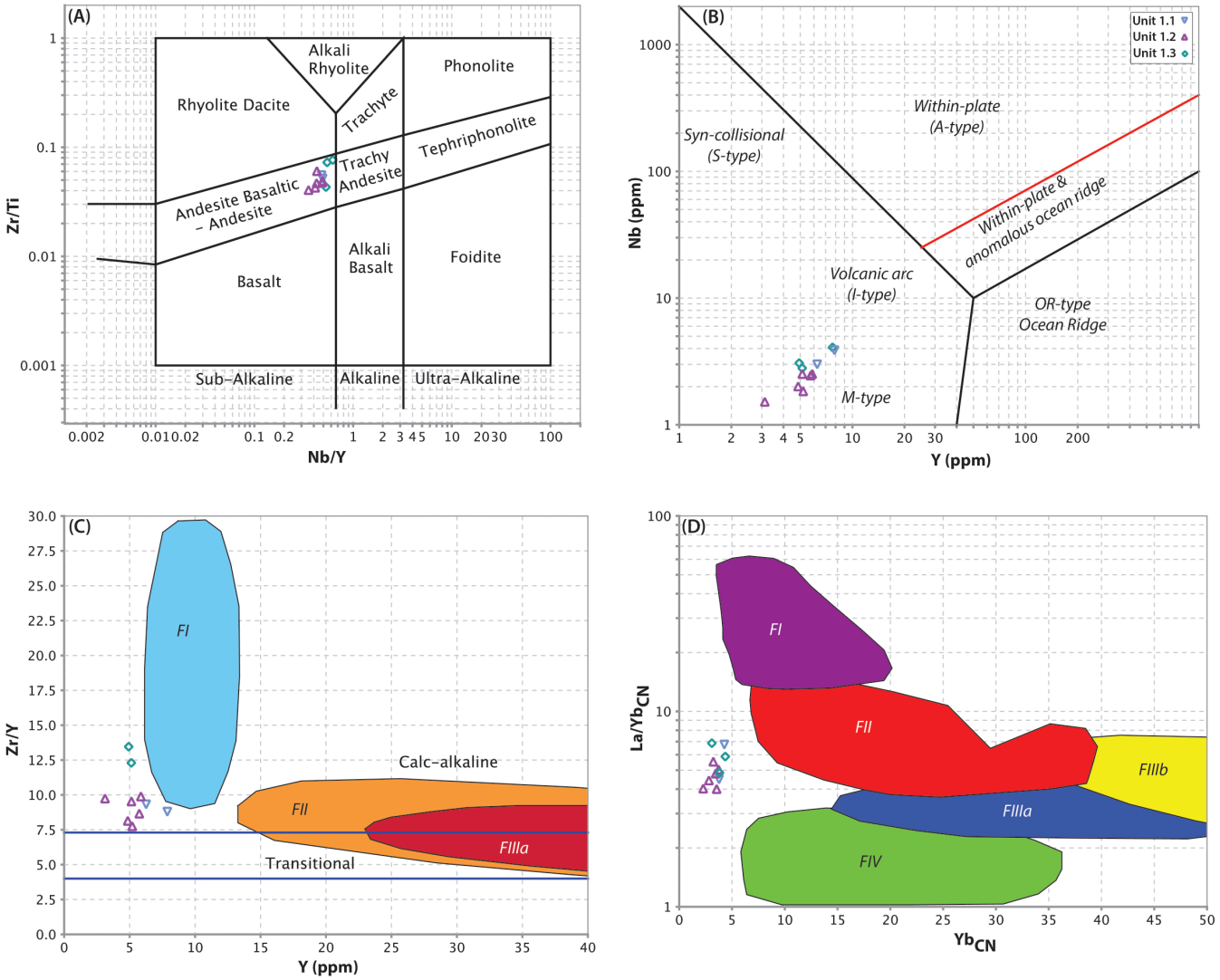

Figure 6. Discrimination diagrams for Rambler Rhyolite felsic rocks. **A)** Zr/TiO_2-Nb/Y diagram of Pearce (modified after Winchester and Floyd, 1977; 1996). **B)** Nb-Y felsic discrimination diagram of Pearce et al. (1984). **C)** Zr/Y-Y rhyolite fertility diagram of Lesher et al. (1986). **D)** La/Yb-Yb rhyolite fertility diagram of Hart et al. (2004).

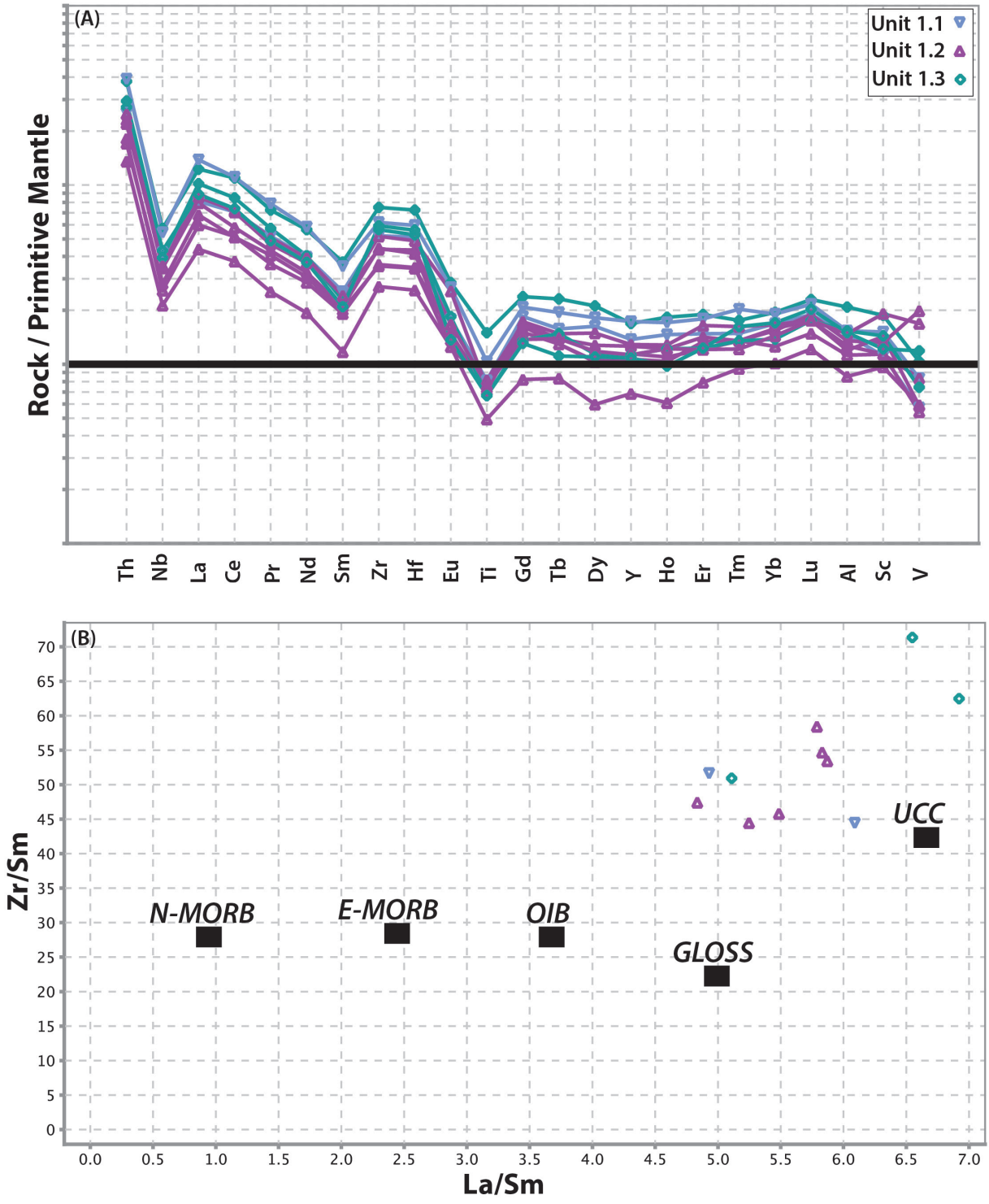

Figure 7. A) Primitive mantle normalized multi-element plot of Rambler Rhyolite samples (primitive mantle values from Sun and McDonough, 1989). **B)** Zr/Sm-La/Sm diagram illustrating the high Zr/Sm ratios of the Rambler Rhyolite rocks in comparison to normal mantle rocks and other reservoirs (diagram after Pearce et al., 1992). Reservoirs show including: N-MORB – normal mid-ocean ridge basalt, E-MORB – enrichment mid-ocean ridge basalt, and OIB – ocean island basalt (from Sun and McDonough, 1989); UCC – upper continental crust (from McLennan, 2001); and GLOSS – global subducted sediment (from Plank and Langmuir, 1998).

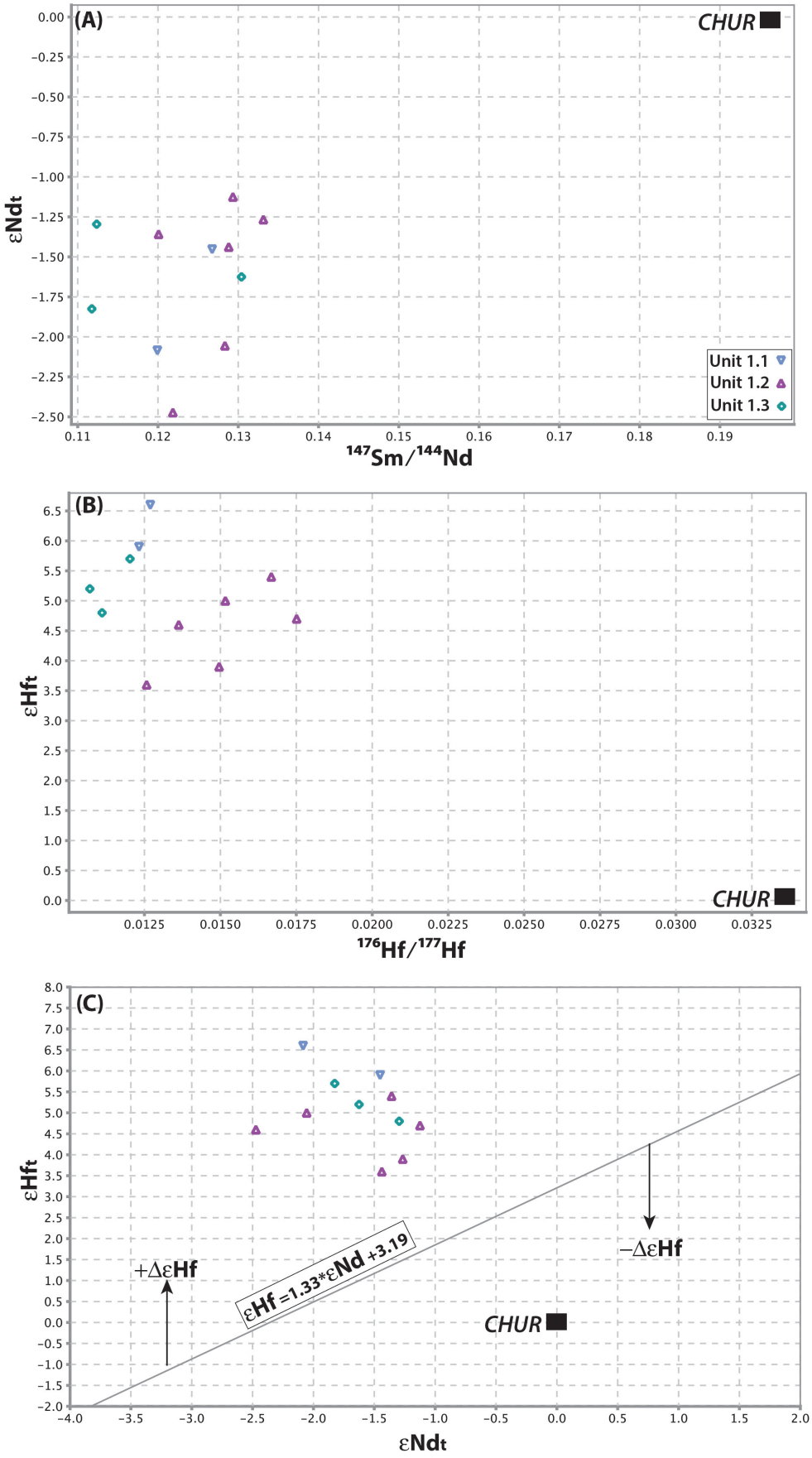

Figure 8. Nd-Hf isotopic data. **A)** εNdt versus $^{147}Sm/^{144}Nd$. **B)** εHd_t-$^{176}Lu/^{177}Hf$. C) εHf_t-$\Delta\varepsilon Nd_t$. In **C)** the mantle array from Vervoort et al. (1999) is shown where εHft = 1.33*εNd_t+3.19. Values that lie above or below the mantle array have positive or negative ΔεHf values where ΔεHf = [εHft – (1.33*εNd_t+3.19)]. CHUR = chondrite uniform reservoir.

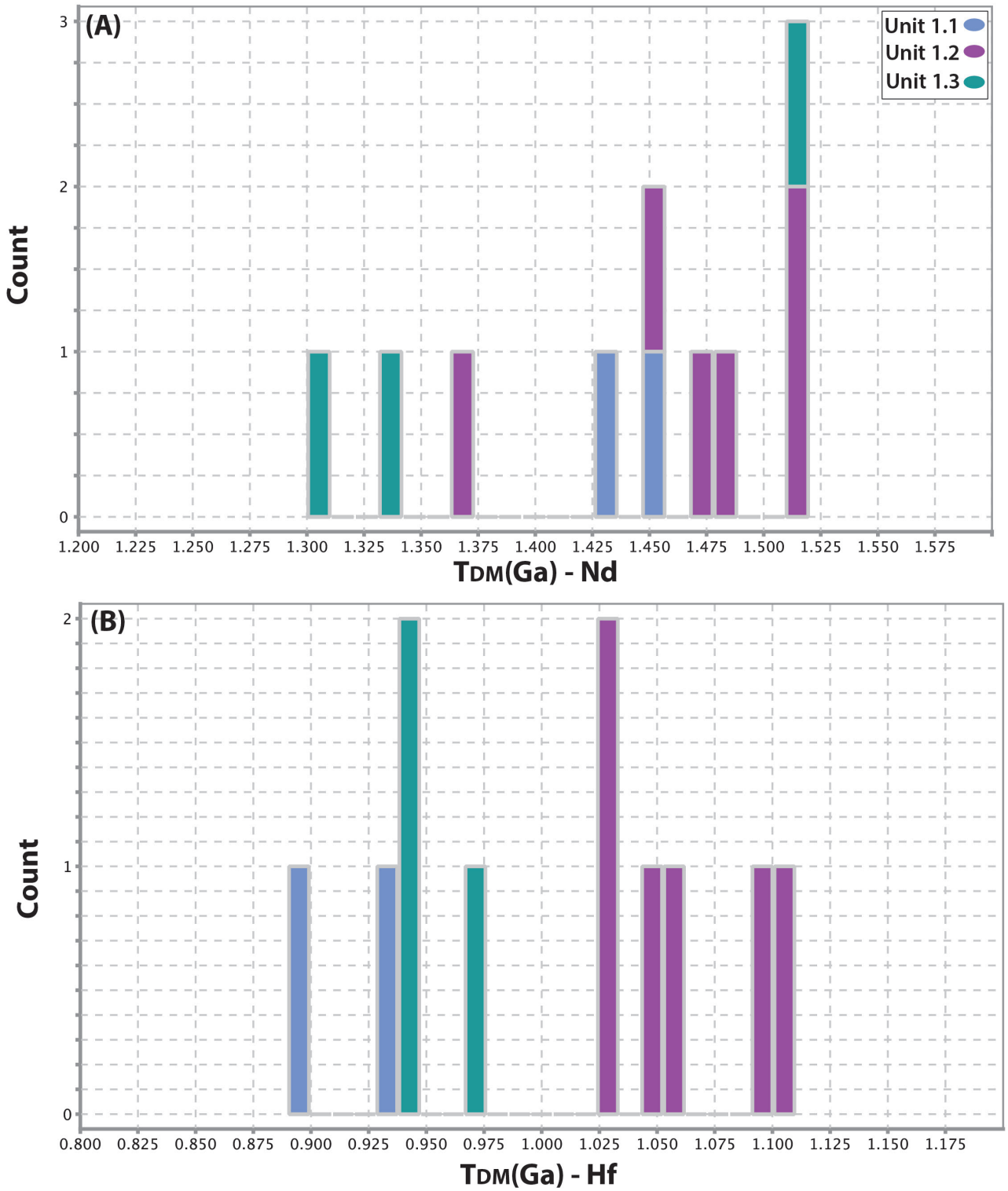

Figure 9. Frequency histograms of depleted mantle model ages for Rambler Rhyolite samples. **A)** T_{DM}(Nd). **B)** T_{DM}(Hf).

ratios that are common to melts derived from the subducted slab (e.g., Fig. 7)(Pearce et al., 1992). Further, decoupling of εHf_t and εNd_t like that found in the Rambler Rhyolite is also a feature of slab melt-derived felsic magmas. In particular, during slab melting Nd is not quantitatively transferred from the slab to the mantle wedge (Pearce and Parkinson, 1993; Pearce and Peate, 1995), such that the εNdt reflects the mantle wedge, or the crust that the rocks interacted with en route to the surface (Pearce et al., 1999). In contrast, samples with excess Hf and Zr, relative to Sm-Nd and excess εHft relative to εNdt are consistent with derivation of Hf and Zr via melting of the subducted slab and/or the sedimentary material atop it (Pearce et al., 1999; Barry et al., 2006; Yogodzinski et al., 2010; Cai et al., 2014). The results from the Rambler Rhyolite are clearly consistent with slab melting.

Slab melt rocks from the Rambler Rhyolite are hosts to VMS mineralization and they have features, including high Zr/Y and La/Yb and relative low Y and Yb, features that are attributed to some of the least prospective felsic rocks associated with VMS mineralization (similar to FI and FII rhyolites)(Lesher et al., 1986; Hart et al., 2004). These results add to other studies that suggests that many Au-bearing VMS deposits are associated with FI and FII rhyolites (Mercier-Langevin et al., 2007; Gaboury and Pearson, 2008) and that they should not be considered as "unprospective" as previously suggested. Moreover, it illustrates the importance of fully integrated, process-oriented, tectono-magmatic models to decipher mineral prospectivity of a terrain, rather than reliance on singular method approaches.

ACKNOWLEDGEMENTS

We would like to thank Larry Pilgrim, Paul Legrow, and the staff of Rambler Metals and Mining Canada Ltd. for access to the Ming VMS deposit and for collaboration on research in the region. We acknowledge discussions with our colleagues on the geology and mineralization in the Baie Verte region and its VMS deposits, including Stefanie Brueckner, Sebastien Castonguay, Greg Dunning, John Hanchar, Patrick Mercier-Langevin, and Tom Skulski. Dominque Weis and staff at the Pacific Centre for Isotopic and Geochemical Research (PCIGR) at UBC are thanked for completion of the trace element and Nd-Hf isotopic analyses. This research was funded by grants to Piercey from the Targeted Geoscience Initiative 5 (TGI5) program from Natural Resources Canada (NRCan) and an NSERC Discovery Grant; these funding agencies are gratefully acknowledged. This manuscript was reviewed by Dr. Alex Zagorevski and we thank him for his comments and suggestions as they helped improve the manuscript.

REFERENCES

Barrett, T. J., and MacLean, W. H., 1999, Volcanic sequences, lithogeochemistry, and hydrothermal alteration in some bimodal volcanic-associated massive sulfide systems: Reviews in Economic Geology, v. 8, p. 101-131.

Barrie, C. T., Cousens, B. L., Hannington, M. D., Bleeker, W., and Gibson, H. L., 1999, Lead and neodymium isotope systematics of the Kidd Creek Mine stratigraphic sequence and ore, Abitibi Subprovince, Canada: Economic Geology Monographs, v. 10, p. 497-510.

Barry, T. L., Pearce, J. A., Leat, P. T., Millar, I. L., and le Roex, A. P., 2006, Hf isotope evidence for selective mobility of high-field-strength elements in a subduction setting: South Sandwich Islands: Earth and Planetary Science Letters, v. 252, p. 223-244.

Bedard, J. H., Lauziere, K., Tremblay, A., Sangster, A., Douma, S. L., and Dec, T., 2000, Betts Cove Ophiolite and its cover rocks, Newfoundland. Bulletin - Geological Survey of Canada., 76 p.

Blichert-Toft, J., Chauvel, C., and Albarede, F., 1997, Separation of Hf and Lu for high-precision isotope analysis of rock samples by magnetic sector-multiple collector ICP-MS: Contributions to Mineralogy and Petrology, v. 127, p. 248-260.

Bouvier, A., Vervoort, J. D., and Patchett, P. J., 2008, The Lu-Hf and Sm-Nd isotopic composition of CHUR: Constraints from unequilibrated chondrites and implications for the bulk composition of terrestrial planets: Earth and Planetary Science Letters, v. 273, p. 48-57.

Brueckner, S. M., Piercey, S. J., Sylvester, P. J., Maloney, S., and Pilgrim, L., 2014, Evidence for Syngenetic Precious Metal Enrichment in an Appalachian Volcanogenic Massive Sulfide System: The 1806 Zone, Ming Mine, Newfoundland, Canada: Economic Geology, v. 109, p. 1611-1642.

Cai, Y., LaGatta, A., Goldstein, S. L., Langmuir, C. H., Gómez-Tuena, A., Martín-del Pozzo, A. L., and Carrasco-Núñez, G., 2014, Hafnium isotope evidence for slab melt contributions in the Central Mexican Volcanic Belt and implications for slab melting in hot and cold slab arcs: Chemical Geology, v. 377, p. 45-55.

Castonguay, S., Skulski, T., van Staal, C., and Currie, M., 2009, New insights into the structural geology of the Pacquet Harbour Group and Point Rousse Complex, Baie Verte Peninsula, Newfoundland: Current Research - Newfoundland and Labrador Department of Natural Resources, Geological Survey, v. Report 09-01, p. 147-158.

Castonguay, S., Van Staal, C. R., Joyce, N., Skulski, T., and Hibbard, J. P., 2014, Taconic Metamorphism Preserved in the Baie Verte Peninsula, Newfoundland Appalachians: Geochronological Evidence for Ophiolite Obduction and Subduction and Exhumation of the Leading Edge of the Laurentian (Humber) Margin During Closure of the Taconic Seaway: Geoscience Canada, v. 41, p. 459.

Connelly, J. N., Ulfbeck, D. G., Thrane, K., Bizzarro, M., and Housh, T., 2006, A method for purifying Lu and Hf for analyses by MC-ICP-MS using TODGA resin: Chemical Geology, v. 233, p. 126-136.

Drummond, M. S., and Defant, M. J., 1990, A model for trondhjemite-tonalite-dacite genesis and crustal growth via slab melting; Archean to modern comparisons: Journal of Geophysical Research, B, Solid Earth and Planets, December, v. 95, p. 21,503-21,521.

Dunning, G. R., and Krogh, T. E., 1985, Geochronology of ophiolites of the Newfoundland Appalachians: Canadian Journal of Earth Sciences, v. 22, p. 1659-1670.

Franklin, J. M., Gibson, H. L., Galley, A. G., and Jonasson, I. R., 2005, Volcanogenic Massive Sulfide Deposits, in Hedenquist, J. W., Thompson, J. F. H., Goldfarb, R. J., and Richards, J. P., eds., Economic Geology 100th Anniversary Volume: Littleton, CO, Society of Economic Geologists, p. 523-560.

Gaboury, D., and Pearson, V., 2008, Rhyolite geochemical signatures and association with volcanogenic massive sulfide deposits: examples from the Abitibi Belt, Canada: Economic Geology, v. 103, p. 1531-1562.

Galley, A. G., Hannington, M., and Jonasson, I., 2007, Volcanogenic massive sulphide deposits, *in* Goodfellow, W. D., ed., Mineral Deposits of Canada: A Synthesis of Major Deposit-types, District Metallogeny, the Evolution of Geological Provinces, and Exploration Methods, Special Publication 5, Mineral Deposits Division, Geological Association of Canada, p. 141-161.

Goldstein, S. L., O'Nions, R. K., and Hamilton, P. J., 1984, A Sm-Nd isotopic study of atmospheric dusts and particulates from major river systems: Earth and Planetary Science Letters, v. 70, p. 221-237.

Gutscher, M.-A., Maury, R., Eissen, J.-P., and Bourdon, E., 2000, Can slab melting be caused by flat subduction?: Geology (Boulder), v. 28, p. 535-538.

Hart, T. R., Gibson, H. L., and Lesher, C. M., 2004, Trace element geochemistry and petrogenesis of felsic volcanic rocks associated with volcanogenic massive Cu-Zn-Pb sulfide deposits: Economic Geology, v. 99, p. 1003-1013.

Hibbard, J., 1983, Geology of the Baie Verte Peninsula, Newfoundland. Memoir - Government of Newfoundland and Labrador, Department of Mines and Energy, Mineral Development Division, Vol. 2, 279 p.

Lentz, D. R., 1998, Petrogenetic evolution of felsic volcanic sequences associated with Phanerozoic volcanic-hosted massive sulfide systems: the role of extensional geodynamics: Ore Geology Reviews, v. 12, p. 289-327.

Lesher, C. M., Goodwin, A. M., Campbell, I. H., and Gorton, M. P., 1986, Trace element geochemistry of ore-associated and barren felsic metavolcanic rocks in the Superior province, Canada: Canadian Journal of Earth Sciences, v. 23, p. 222-237.

Lugmair, G. W., and Marti, K., 1978, Lunar initial 143Nd/144Nd: Differential evolution of the lunar crust and mantle: Earth and Planetary Science Letters, v. 39, p. 349-357.

MacLean, W. H., and Barrett, T. J., 1993, Lithogeochemical techniques using immobile elements: Journal of Geochemical Exploration, v. 48, p. 109-133.

McLennan, S. M., 2001, Relationships between the trace element composition of sedimentary rocks and upper continental crust: Geochemistry, Geophysics, Geosystems, v. 2, p. 24 (Paper 2000GC000109).

Mercier-Langevin, P., Dube, B., Hannington, M. D., Richer-Lafleche, M., and Gosselin, G., 2007, The LaRonde Penna Au-Rich Volcanogenic Massive Sulfide Deposit, Abitibi Greenstone Belt, Quebec: Part II. Lithogeochemistry and Paleotectonic Setting: Economic Geology, v. 102, p. 611-631.

Peacock, S. M., 2004, Thermal Structure and Metamorphic Evolution of Subducting Slabs: Inside the Subduction Factory, p. 7-22.

Pearce, J. A., 1996, A user's guide to basalt discrimination diagrams, *in* Wyman, D. A., ed., Trace element geochemistry of volcanic rocks: Applications for massive sulphide exploration, Short Course Notes, Volume 12, Geological Association of Canada, p. 79-113.

Pearce, J. A., Harris, N. B. W., and Tindle, A. G., 1984, Trace element discrimination diagrams for the tectonic interpretation of granitic rocks: Journal of Petrology, v. 25, p. 956-983.

Pearce, J. A., Kempton, P. D., Nowell, G. M., and Noble, S. R., 1999, Hf-Nd element and isotope perspective on the nature and provenance of mantle and subduction components in Western Pacific arc-basin systems: Journal of Petrology, v. 40, p. 1579-1611.

Pearce, J. A., and Parkinson, D., 1993, Trace element models for mantle melting: applications to volcanic arc petrogenesis, *in* Prichard, H. M., Alabaster, T., Harris, N. B. W., and Neary, C. R., eds., Magmatic Processes and Plate Tectonics, Special Publication 76, Geological Soceity of London, p. 373-403.

Pearce, J. A., and Peate, D. W., 1995, Tectonic implications of the composition of volcanic arc magmas: Annual Reviews of Earth and Planetary Science, v. 23, p. 251-285.

Pearce, J. A., van der Laan, S. R., Arculus, R. J., Murton, B. J., Ishii, T., Peate, D. W., and Parkinson, I. J., 1992, Boninite and harzburgite from Leg 125 (Bonin-Mariana forearc); a case study of magma genesis during the initial stages of subduction: Proceedings of the Ocean Drilling Program, Scientific Results, July, v. 125, p. 623-659.

Piercey, S., 2011, The setting, style, and role of magmatism in the formation of volcanogenic massive sulfide deposits: Mineralium Deposita, v. 46, p. 449-471.

Pilote, J.-L., and Piercey, S. J., 2018, Petrogenesis of the Rambler Rhyolite Formation: Controls on the Ming VMS Deposit and geodynamic implications for The Taconic Seaway, Newfoundland Appalachians, Canada: American Journal of Science, v. 318, p. 640-683.

Pilote, J.-L., Piercey, S. J., and Mercier-Langevin, P., 2017, Volcanic and Structural Reconstruction of the Deformed and Metamorphosed Ming Volcanogenic Massive Sulfide Deposit, Canada: Implications for Ore Zone Geometry and Metal Distribution: Economic Geology, v. 112, p. 1305-1332.

Plank, T., and Langmuir, C. H., 1998, The chemical composition of subducting sediment and its consequences for the crust and mantle: Chemical Geology, v. 145, p. 325-394.

Pretorius, W., Weis, D., Williams, G., Hanano, D., Kieffer, B., and Scoates, J., 2006, Complete trace elemental characterisation of granitoid (USGS G-2, GSP-2) reference materials by high resolution inductively coupled plasma-mass spectrometry: Geostandards and Geoanalytical Research, v. 30, p. 39-54.

Ramezani, J., Dunning, G. R., and Wilson, M. R., 2000, Geologic setting, geochemistry of alteration, and U-Pb age of hydrothermal zircon from the Silurian Stog'er Tight gold prospect, Newfoundland Appalachians, Canada: Exploration and Mining Geology, v. 9, p. 171-188.

Ruks, T. W., Piercey, S. J., Ryan, J. J., Villeneuve, M. E., and Creaser, R. A., 2006, Mid- to late Paleozoic K-feldspar augen granitoids of the Yukon-Tanana terrane, Yukon, Canada: Implications for crustal growth and tectonic evolution of the northern Cordillera: Geological Society of America Bulletin, v. 118, p. 1212-1231.

Sangster, A. L., Douma, S. L., and Lavigne, J., 2007, Base metal and gold deposits of the Betts Cove Complex, Baie Verte Peninsula, Newfoundland, *in* Goodfellow, W. D., ed., Mineral Deposits of Canada: A Synthesis of Major Deposit-types, District Metallogeny, the Evolution of Geological Provinces, and Exploration Methods, Special Publication 5, Mineral Deposits Division, Geological Association of Canada, p. 703-721.

Skulski, T., Castonguay, S., Kidd, W. S. F., McNicoll, V., van Staal, C. R., and Hibbard, J. P., 2015, Baie Verte and parts of Fleur de Lys, Newfoundland and Labrador, NTS 12-H/16 and part of NTS 12-I/1. Canadian Geoscience Map 159.: Ottawa, ON, Canada, Geological Survey of Canada.

Skulski, T., Castonguay, S., McNicoll, V., van Staal, C., Kidd, W., Rogers, N., Morris, W., Ugalde, H., Slavinski, H., Spicer, W., Moussallam, Y., and Kerr, I., 2010, Tectonostratigraphy of the Baie Verte Oceanic Tract and its ophiolite cover sequence on the Baie Verte Peninsula: Current Research - Newfoundland and Labrador Department of Natural Resources, Geological Survey, v. Report 10-1, p. 315-225.

Skulski, T., Castonguay, S., van Staal, C., Rogers, N., McNicoll, V., Kerr, A., and Escayloa, M., 2009, Baie Verte Peninsula: An evolving geological story: St. John's, NL, Geological Association of Canada Newfoundland and Labrador Section, 76 p.

Soederlund, U., Patchett, P. J., Vervoort, J. D., and Isachsen, C. E., 2004, The (super 176) Lu decay constant determined by Lu-Hf and U-Pb isotope systematics of Precambrian mafic intrusions: Earth and Planetary Science Letters, v. 219, p. 311-324.

Spitz, G., and Darling, R., 1978, Major and minor element lithogeochemical anomalies surrounding the Louvem copper deposit, Val d'Or, Quebec: Canadian Journal of Earth Sciences, v. 15, p. 1161-1169.

Stern, R. J., 2002, Subduction zones: Reviews of Geophysics, v. 40, p. 3.1-3.38.

Sun, S.-s., and McDonough, W. F., 1989, Chemical and isotopic systematics of oceanic basalts: implications for mantle composition and processes, in Saunders, A. D., and Norry, M. J., eds., Magmatism in the Ocean Basins, Geological Society Special Publication 42, p. 313-345.

Tanaka, T., Togashi, S., Kamioka, H., Amakawa, H., Kagami, H., Hamamoto, T., Yuhara, M., Orihashi, Y., Shigekazu, Y., Shimuzu, H., Kunimaru, T., Takahashi, K., Yanagi, T., Nakano, T., Fujimaki, H., Shinjo, R., Asahara, Y., Tanimizu, M., and Dragusanu, C., 2000, JNdi-1: a neodymium isotopic reference in consistency with LaJolla neodymium: Chemical Geology, v. 168, p. 279-281.

Tatsumi, Y., 2000, Slab melting: Its role in continental crust formation and mantle evolution: Geophysical Research Letters, v. 27, p. 3941-3944.

Tatsumi, Y., and Eggins, S., 1995, Subduction Zone Magmatism, Blackwell Science, 211 p.

van Staal, C., and Barr, S. M., 2012, Lithospheric architecture and tectonic evolution of the Canadian Appalachians and associated Atlantic margin. Chapter 2 *in* Percival, J. A., Cook, F. A., and Clowes, R. M., eds., In Tectonic Styles in Canada: the LITHOPROBE Perspective, Special Paper 49: St. John's, NL, Canada, Geological Association of Canada, p. 41-96.

van Staal, C. R., 2007, Pre-Carboniferous tectonic evolution and metallogeny of the Canadian Appalachians, *in* Goodfellow, W. D., ed., Mineral Deposits of Canada: A Synthesis of Major Deposit-types, District Metallogeny, the Evolution of Geological Provinces, and Exploration Methods, Special Publication 5, Mineral Deposits Division, Geological Association of Canada, p. 793-818.

Vervoort, J. D., and Blichert-Toft, J., 1999, Evolution of the depleted mantle; Hf isotope evidence from juvenile rocks through time: Geochimica et Cosmochimica Acta, v. 63, p. 533-556.

Vervoort, J. D., Patchett, P. J., Blichert-Toft, J., and Albarede, F., 1999, Relationships between Lu-Hf and Sm-Nd isotopic systems in the global sedimentary system: Earth and Planetary Science Letters, v. 168, p. 79-99.

Waldron, J. W. F., and van Staal, C. R., 2001, Taconian Orogeny and the accretion of the Dashwoods Block; a peri-Laurentian microcontinent in the Iapetus Ocean: Geology, v. 29, p. 811-814.

Weis, D., Kieffer, B., Hanano, D., Silva, I. N., Barling, J., Pretorius, W., Maerschalk, C., and Mattielli, N., 2007, Hf isotope compositions of US Geological Survey reference materials: Geochemistry Geophysics Geosystems, v. 8, p. 15.

Weis, D., Kieffer, B., Maerschalk, C., Barling, J., de Jong, J., Williams, G. A., Hanano, D., Pretorius, W., Mattielli, N., Scoates, J. S., Goolaerts, A., Friedman, R. M., and Mahoney, J. B., 2006, High-precision isotopic characterization of USGS reference materials by TIMS and MC-ICP-MS: Geochemistry, Geophysics, Geosystems, v. 7, p. 30.

Winchester, J. A., and Floyd, P. A., 1977, Geochemical discrimination of different magma series and their differentiation products using immobile elements: Chemical Geology, v. 20, p. 325-343.

Yogodzinski, G. M., Vervoort, J. D., Brown, S. T., and Gerseny, M., 2010, Subduction controls of Hf and Nd isotopes in lavas of the Aleutian island arc: Earth and Planetary Science Letters, v. 300, p. 226-238.

Stratigraphy and Lithogeochemistry of Rocks from the Nugget Pond Deposit Area, Baie Verte Peninsula, Newfoundland

C. Mueller[1], S.J. Piercey[1]*, M.G. Babechuk[1], and D. Copeland[2]

Mueller, C., Piercey, S.J. Babechuk, M.G., and Copeland, D., 2021. Stratigraphy and Lithogeochemistry of Rocks from the Nugget Pond Deposit Area, Baie Verte Peninsula, Newfoundland; in *Targeted Geoscience Initiative 5:grant program final reports (2018-2020); Geological Survey of Canada, Open File 8755, p. 217–234. https://doi.org/10.4095/328989*

Abstract: Stratigraphic and lithogeochemical data were collected from selected drill core from the Nugget Pond gold deposit in the Betts Cove area, Newfoundland. The stratigraphy consists of a lower unit of basaltic rocks that are massive to pillowed (Mount Misery Formation). This is overlain by sedimentary rocks of the Scrape Point Formation that consist of lower unit of turbiditic siltstone and hematitic cherts/iron formations (the Nugget Pond member); the unit locally has a volcaniclastic rich-unit at its base and grades upwards into finer grained volcaniclastic/turbiditic rocks. This is capped by basaltic rocks of the Scrape Point Formation that contain pillowed and massive mafic flows that are distinctively plagioclase porphyritic to glomeroporphyritic. The mafic rocks of the Mount Misery Formation have island arc tholeiitic affinities, whereas Scrape Point Formation mafic rocks have normal mid-ocean ridge (N-MORB) to back-arc basin basalt (BABB) affinities. One sample of the latter formation has a calc-alkalic affinity. All of these geochemical features are consistent with results and conclusions from previous workers in the area. Clastic sedimentary rocks and Fe-rich sedimentary rocks of the Scrape Point Formation have features consistent with derivation from local, juvenile sources (i.e., intra-basinal mafic rocks). The Scrape Point Formation sedimentary rocks with the highest Fe/Al ratios, inferred to have greatest amount of hydrothermally derived Fe, have positive Ce anomalies on Post-Archean Australian Shale (PAAS)-normalized trace element plots. These features are consistent with having formed via hydrothermal venting into an anoxic/sub-oxic water column. Further work is needed to test whether these redox features are a localized feature (i.e., restricted basin) or a widespread feature of the late Cambrian-early Ordovician Iapetus Ocean, as well as to delineate the role that these Fe-rich sedimentary rocks have played in the localization of gold mineralization within the Nugget Pond deposit.

[1]Department of Earth Sciences, Memorial University of Newfoundland, Alexander Murray Building, 9 Arctic Ave, St. John's, Newfoundland and Labrador, Canada A1B 3X5

[2]Anaconda Mining Inc., Elizabeth Business Centre, 55 Elizabeth Avenue, St. John's, Newfoundland and Labrador, Canada A1A 1W9

*Corresponding author (e-mail: spiercey@mun.ca)

INTRODUCTION

The Baie Verte Peninsula (BVP) is host to numerous volcanogenic massive sulfide (VMS) and orogenic Au deposits within ophiolitic and cover sequence rocks of the Baie Verte oceanic tract (BVOT) (Hibbard, 1983; van Staal, 2007; Skulski et al., 2009; Skulski et al., 2010; van Staal and Barr, 2012). There is a well-defined regional stratigraphy throughout the BVP, with older (~488-487 Ma) ophiolitic units hosting variably Cu- and Au-enriched VMS deposits (e.g., Betts Cove and Pacquet Complexes), whereas orogenic Au deposits are hosted in younger units (~479-467 Ma) of the Snooks Arm Group cover sequence (e.g., Goldenville, Nugget Pond, Pine Cove, Stog'er Tight)(Bédard et al., 1999; Bedard et al., 2000; Sangster et al., 2007). The Goldenville-Nugget Pond iron formation is located at the transition from the underlying Cambro-Ordovician ophiolitic rocks and the overlying cover sequence rocks of the Snooks Arm Group. The stratigraphic horizon is a marker throughout the peninsula and has features similar to hydrothermal Algoma-style iron formations found in other volcanic belts globally (e.g., Peter, 2003). Further, this unit was a chemical trap and host for orogenic Au mineralization associated with the past producing Nugget Pond and Goldenville deposits (Evans, 2004; Sangster et al., 2007).

In this report we provide preliminary lithogeochemical data for rocks from the Nugget Pond member and associated rocks in the Betts Cove region of the Baie Verte Peninsula. The goals of this contribution are to provide basic stratigraphic relationships, as derived from drill core, as well as utilize the lithogeochemical data to understand the chemostratigraphy and correlations of these rocks to regional units on the BVP and to compare to previous work in the region.

GEOLOGICAL AND STRATIGRAPHIC SETTING

The Nugget Pond gold deposit and associated stratigraphy are hosted within rocks of the BVOT, which consists of peri-Laurentian rocks that formed during the Cambrian-Ordovician evolution of the Taconic seaway (Waldron and van Staal, 2001; van Staal, 2007; van Staal and Barr, 2012). The BVOT consists of four partial to full ophiolite complexes that are ~488-487 Ma (Dunning and Krogh, 1985) that host both Cu-Au-rich VMS deposits (Betts Cove Complex) and Au-enriched VMS deposits (Pacquet Complex) (Figs. 1-3) (Bédard et al., 1999; Bedard et al., 2000; Sangster et al., 2007; Brueckner et al., 2014; Pilote et al., 2017). The cover sequence to mineralization, the Snooks Arm Group, is the host to younger (Silurian-Devonian) orogenic Au mineralization both in the Nugget Pond member (Sangster et al., 2007; Skulski et al., 2009; van Staal and Barr, 2012), but also in correlative rocks of the Goldenville iron formation, and in gabbroic to basaltic rocks of the group found in the interior of the BVP (Figs. 1-3) (Ramezani et al., 2000; Skulski et al., 2009; Skulski et al., 2010).

The Nugget Pond deposit is located within sedimentary units of the Scrape Point Formation above the contact between the underlying Mount Misery Formation (Figs. 2-4) (Bédard et al., 1999; Bedard et al., 2000; Sangster et al., 2007). The Mount Misery Formation footwall rocks are predominantly basalt that is variably variolitic and overprinted with varying intensity of chlorite, hematite, epidote, quartz, and carbonate alteration. The formation often has a breccia zone at the top that is locally faulted and intercalated with red siltstone, magnetite-rich units, and basaltic fragments (Fig. 4). The overlying Scrape Point Formation has a lower sedimentary lithofacies and upper basaltic lithofacies (Bédard et al., 1999; Bedard et al., 2000; Sangster et al., 2007). The sedimentary lithofacies consists of fine to coarse grained turbiditic sedimentary rocks that are variably graded, are green-black to purple, locally hematitic, and have varying abundances of magnetite, pyrite, and pyrrhotite (Figs. 2 and 4). The sedimentary lithofacies has previously been divided into a lower and upper unit. The lower unit is comprised of massive to weakly bedded red siltstone and sandstone. The upper unit is comprised of red and green argillite and green sandstone that is variably magnetic and is sometimes referred to as iron formation, and an upper green sedimentary unit dominated by variably limited volcanic-derived siltstones and turbidite beds (Fig. 4)(Sangster et al., 2007). The overlying basaltic facies of the Scrape Point Formation contains massive flows, pillowed flows, and a distinctive plagioclase porphyritic (glomeroporphyritic) unit that is intercalated with less plagioclase-phyric flows (Fig. 4). The plagioclase-rich unit does not exhibit chilled margins or other evidence for it being intrusive (i.e., it appears to be a massive flow intercalated with pillowed flows); however, similar units have been found as intrusive rocks regionally (Bedard et al., 2000).

The Nugget Pond deposit is hosted between the red and green sedimentary units where mineralization is associated with extension-related quartz-albite-carbonate veins and with distinctive pyrite- and magnetite-rich sedimentary units (Sangster et al., 2007). The deposit is spatially associated with faults and fault gouge and quartz-albite-carbonate alteration (Sangster et al., 2007).

LITHOGEOCHEMISTRY

Samples from all major units were collected from representative drill holes for lithogeochemical analysis to document the chemostratigraphy of the Nugget Pond area, facilitate comparisons to regional chemostratigraphic units, and to evaluate the chemistry of sedimentary rocks and the "iron formations" within the Nugget Pond member. Samples

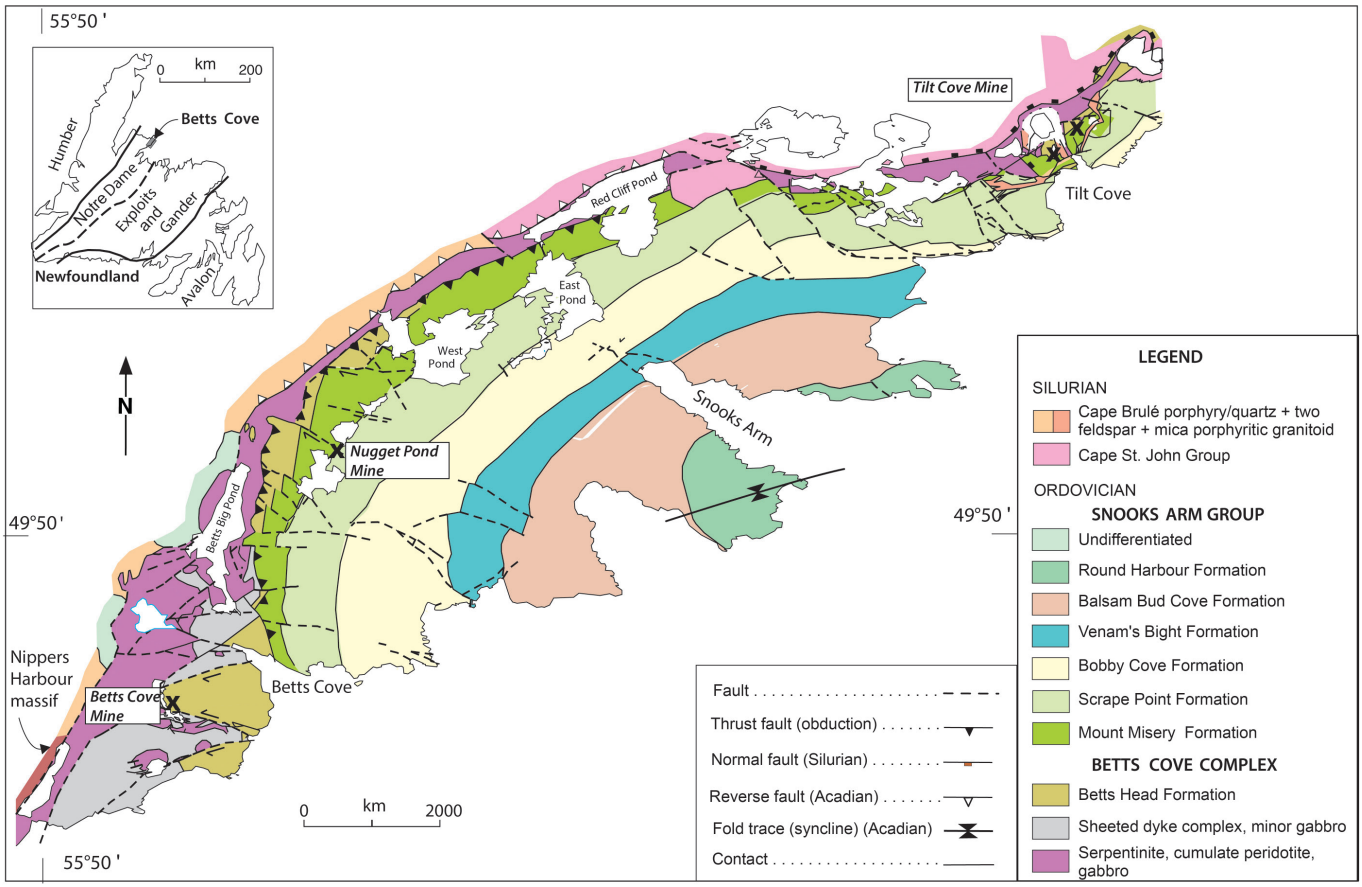

Figure 1. Geology of the Betts Cove Complex and associated rocks with contained mineral deposits (from Bédard et al., 1999; Bedard et al., 2000; Sangster et al., 2007).

were crushed and then pulverized in agate. Major elements were determined by inductively coupled plasma emission spectroscopy (ICP-ES), whereas all trace elements were determined by inductively coupled plasma mass spectrometry (ICP-MS). For both analyses, samples were prepared into a solution by lithium metaborate fusion and acid dissolution. C and CO_2 were determined by infrared methods. All analytical work was undertaken at ALS Minerals Ltd. in Vancouver, BC. An internal basalt reference material was analyzed during the program for quality control and quality assurance and results are shown in Table A1 in Appendix A.

Although representative samples were chosen from areas with minimal alteration, it is assumed that all samples have experienced some level of element mobility. In particular, we assume that the alkali elements and low field strength element (LFSE) were variably mobilized, which limits their utility for understanding primary features in the rocks. Thus, most interpretations are focused on the immobile elements Al_2O_3, TiO_2, high field strength elements (HFSE: Zr, Hf, Nb, Ta, Th), and rare earth elements (REE) (e.g., MacLean and Barrett, 1993).

Results: Mafic Volcanic Rocks

Lithogeochemical data for mafic volcanic rocks from the Nugget Pond area are presented in Table 1 and Figures 5-7. Most volcanic samples cluster within the least altered field in Al_2O_3/Na_2O-Na_2O, with a few samples exhibiting Na-depletion (Na_2O <2%) and higher Al_2O_3/Na_2O ratios, and one sample exhibiting Na-enrichment (Na_2O >5%; albite alteration) (Fig. 5).

The rocks in the lowermost part of stratigraphy in the Nugget Pond area, interpreted Mount Misery Formation, are subalkalic with Nb/Y<0.7, have tholeiitic affinities in La-Yb and Th-Yb space, and have Ti-V ratios <10 consistent with island arc tholeiitic affinities (Fig. 6). Features consistent with an island arc tholeiitic (IAT) signature are also evident from primitive mantle normalized plots as samples exhibit light rare earth element (LREE)-depletion, flat heavy rare earth element (HREE) distribution, and a distinctive negative Nb anomaly relative to Th and La (Fig. 7a). These are features similar to those found by Bedard et al. (2000) for the Mount Misery Formation.

The rocks interpreted to be from the Scrape Point Formation are predominantly subalkalic with Nb/Y<0.7, and have tholeiitic affinities in La-Yb and Th-Yb space, with the exception of the one outlier sample, which has a more

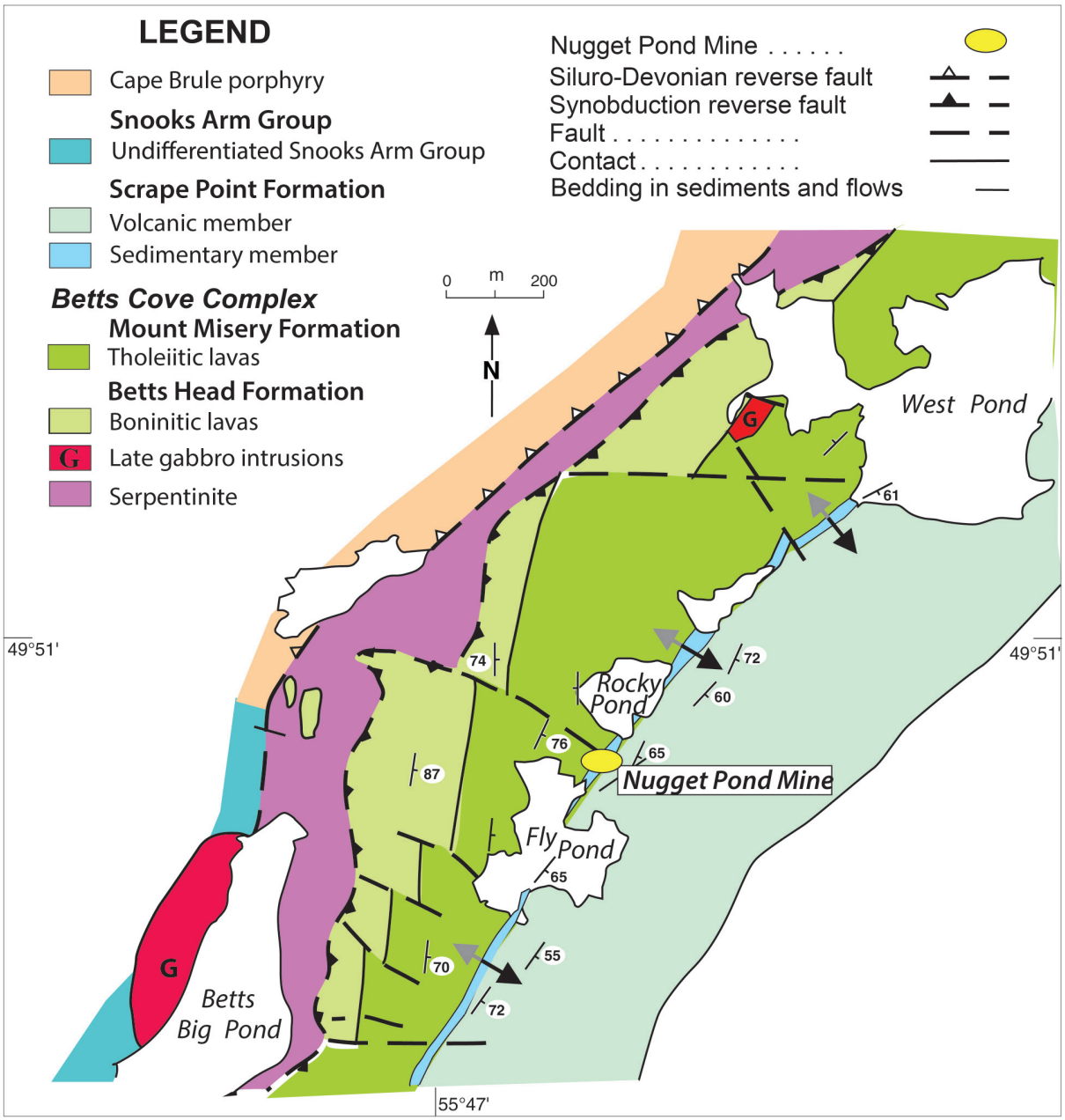

Figure 2. Geology of the Nugget Pond deposit area (modified after Bédard et al., 1999; Bedard et al., 2000; Sangster et al., 2007).

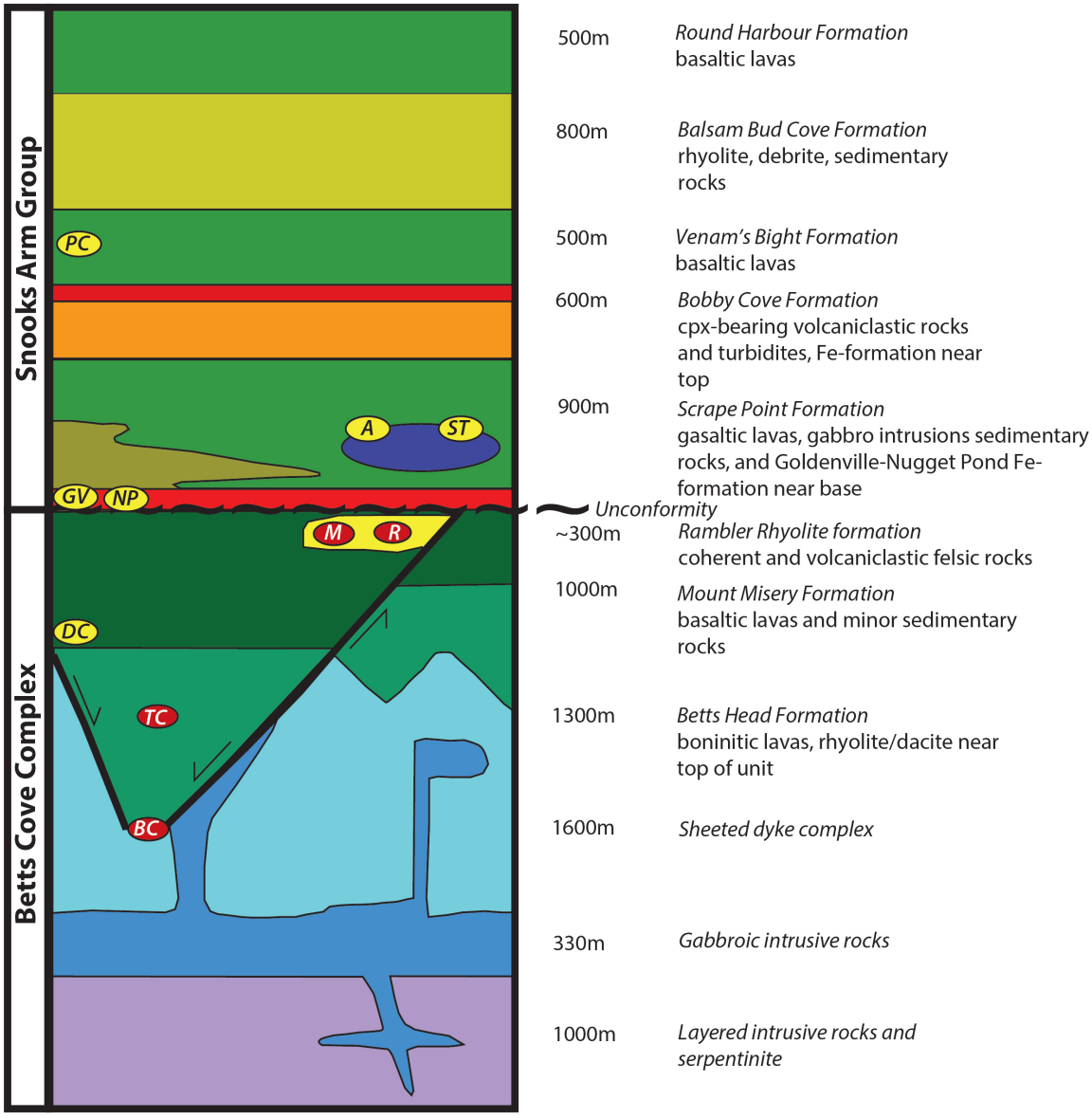

Figure 3. Stratigraphy of the Betts Cove Complex and Snooks Arm Group cover sequence. Mineral deposits are from both within the Betts Cove area and from the Baie Verte Peninsula regionally. Red ovals are VMS deposits and include: BC – Betts Cove, TC – Tilt Cove, R = Rambler, M = Ming. Yellow ovals are orogenic Au deposits and include: DC – Deer Cove, GV = Goldenville, NP = Nugget Pond, ST = Stog'er Tight, A = Argyle, PC = Pine Cove. Diagram modified after Bedard et al. (2000) and Kessler and Bedard (2000).

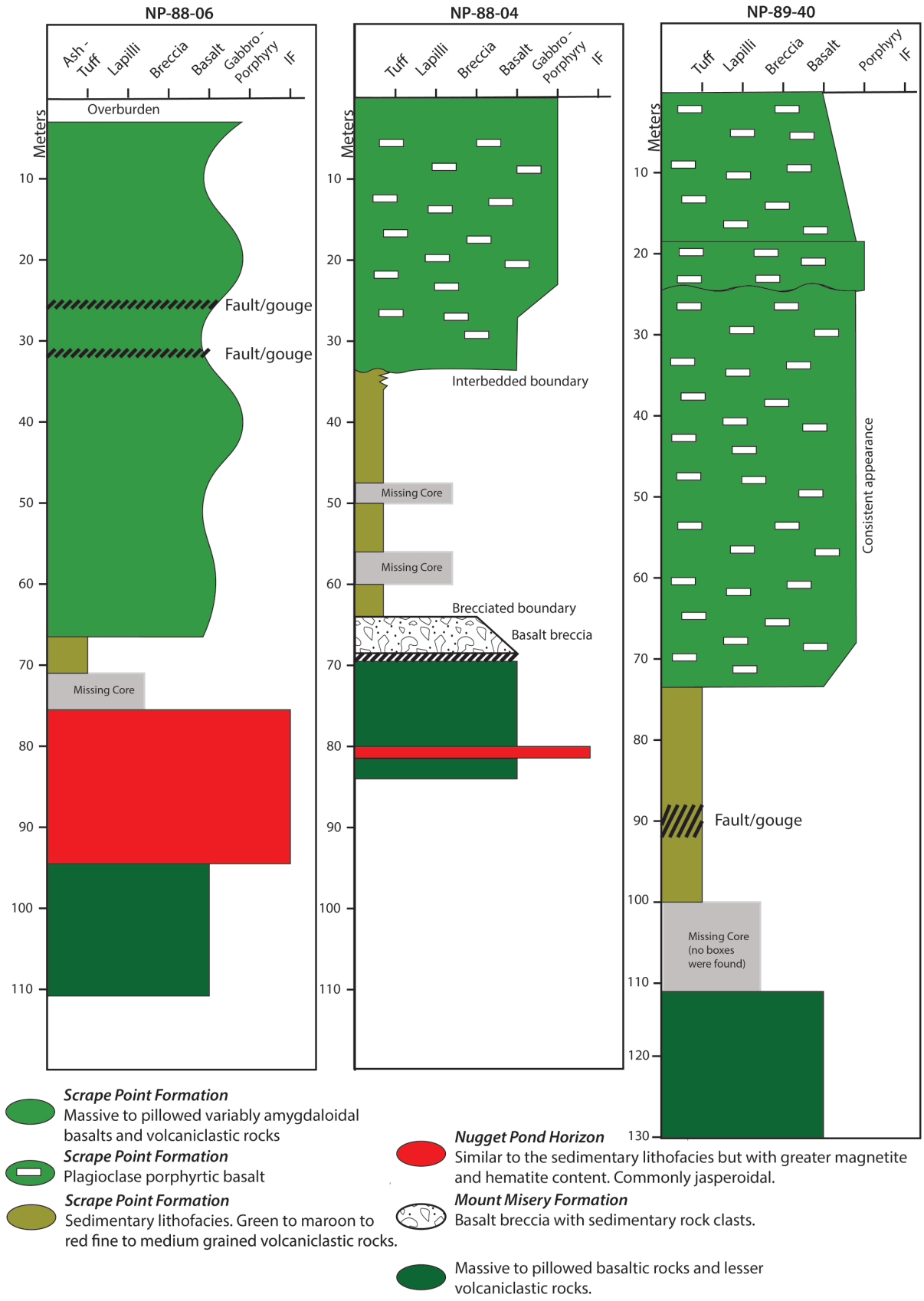

Figure 4. Graphic logs of select drill holes from the Nugget Pond deposit illustrating the host stratigraphy and lithological variability present in the deposit.

Table 1. Lithogeochemical data for rocks from the Nugget Pond deposit area.

Sample	407001	407002	407006	407007	407008	407013	407003	407009	407010	407014	407004	407015	407005	407011	407016
Hole ID	NP-88-06	NP-88-06	NP-88-13	NP-88-13	NP-88-13	NP-89-26	NP-88-06	NP-88-13	NP-88-13	NP-88-22	NP-88-06	NP-88-22	NP-88-06	NP-88-13	NP-88-22
From	9.56	65.95	9.10	18.87	43.20	29.30	71.90	84.40	103.90	165.10	86.60	182.00	104.80	128.90	204.10
To	9.65	66.20	9.40	19.10	43.50	29.60	72.20	84.70	104.20	165.40	89.00	182.30	105.10	129.20	204.25
Lithology	Basalt - HW	Basalt - HW	Basalt - HW	Basalt - HW	Plag-rich porphyry	Plag rich porphyry	Sediments	Sediments	Sediments	Sediments	Iron FM	Iron FM	Basalt	Basalt	Basalt
Stratigraphic Unit	Scrape Point	Scrape Point	Scrape Point	Scrape Point	Scrape Point	Scrape Point	Scrape Point	Scrape Point	Scrape Point	Scrape Point	Scrape Point/ Goldenville-Nugget Pond Horizon	Scrape Point/ Goldenville-Nugget Pond Horizon	Mount Misery	Mount Misery	Mount Misery
SiO_2	46.60	47.80	46.20	41.30	46.20	43.20	46.70	44.20	57.40	44.60	53.60	57.80	46.10	47.80	49.70
Al_2O_3	18.05	16.70	15.65	15.35	17.00	18.60	15.45	13.45	13.20	13.55	12.45	12.30	15.25	14.75	15.05
Fe_2O_3	9.30	9.29	10.25	9.75	9.49	8.99	14.85	8.80	10.65	8.24	11.40	12.50	12.45	10.35	10.55
CaO	12.75	4.25	10.40	9.63	12.95	11.80	2.93	9.29	1.50	10.00	3.74	2.81	6.91	8.52	9.90
MgO	6.09	6.71	9.20	6.81	6.69	6.90	5.11	8.43	3.37	7.42	2.43	3.14	8.47	8.05	7.14
Na_2O	2.28	6.37	2.80	4.14	2.01	1.91	5.40	3.10	6.88	3.33	6.58	1.13	3.98	4.17	2.24
K_2O	0.09	0.36	0.16	0.66	0.09	0.20	2.85	0.09	0.94	0.25	0.80	3.30	0.38	0.59	0.14
Cr_2O_3	0.04	0.05	0.04	0.04	0.04	0.04	0.06	0.05	0.01	0.06	0.01	0.01	0.02	0.01	0.01
TiO_2	1.20	0.81	1.17	1.24	1.28	1.02	0.82	0.83	0.65	0.83	0.63	0.59	0.99	0.73	0.73
MnO	0.13	0.29	0.16	0.17	0.14	0.13	0.29	0.20	1.32	0.26	1.92	1.17	0.18	0.18	0.15
P_2O_5	0.10	0.12	0.09	0.11	0.12	0.09	0.15	0.13	0.11	0.11	0.13	0.18	0.08	0.07	0.05
SrO	0.02	<0.01	0.02	0.01	0.03	0.03	<0.01	0.01	<0.01	0.02	<0.01	<0.01	0.01	0.01	0.01
BaO	<0.01	<0.01	<0.01	0.04	<0.01	<0.01	0.02	<0.01	0.06	0.01	0.05	0.05	0.01	0.01	<0.01
LOI	2.72	5.36	3.99	9.86	3.10	6.08	4.37	10.10	3.95	10.25	5.26	4.94	4.99	4.97	4.10
Total	99.37	98.11	100.13	99.11	99.14	98.99	99.00	98.68	100.04	98.93	99.00	99.92	99.82	100.21	99.77
C (wt%)	0.12	0.72	0.17	1.75	0.32	0.66	0.51	1.73	0.27	1.78	0.80	0.72	0.45	0.64	0.32
CO_2 (wt%)	0.40	2.70	0.60	6.40	1.20	2.40	1.90	6.30	1.00	6.50	3.00	2.60	1.60	2.30	1.20
Ba (ppm)	19.00	22.40	21.40	307.00	17.70	25.00	131.50	23.50	462.00	46.10	452.00	394.00	54.10	104.50	19.90
Cs	0.07	2.31	0.07	0.31	0.06	0.14	15.05	0.05	11.10	0.10	14.80	2.29	0.47	0.31	0.11
Rb	1.90	19.00	3.20	12.60	1.70	4.40	190.50	1.80	41.00	5.70	50.00	112.50	8.30	12.70	3.70
Cr	270.00	370.00	260.00	260.00	270.00	250.00	420.00	360.00	50.00	400.00	60.00	60.00	150.00	90.00	70.00
Cs	0.07	2.31	0.07	0.31	0.06	0.14	15.05	0.05	11.10	0.10	14.80	2.29	0.47	0.31	0.11
Ga	18.20	17.10	16.90	16.50	19.10	16.50	16.50	15.70	12.70	16.30	12.70	18.10	18.60	16.60	17.60

Table 1. (cont.) Lithogeochemical data for rocks from the Nugget Pond deposit area.

Sample	407001	407002	407006	407007	407008	407013	407003	407009	407010	407014	407004	407015	407005	407011	407016
Hole ID	NP-88-06	NP-88-06	NP-88-13	NP-88-13	NP-88-13	NP-89-26	NP-88-06	NP-88-13	NP-88-13	NP-88-22	NP-88-06	NP-88-22	NP-88-06	NP-88-13	NP-88-22
From	9.56	65.95	9.10	18.87	43.20	29.30	71.90	84.40	103.90	165.10	86.60	182.00	104.80	128.90	204.10
To	9.65	66.20	9.40	19.10	43.50	29.60	72.20	84.70	104.20	165.40	89.00	182.30	105.10	129.20	204.25
Lithology	Basalt - HW	Basalt - HW	Basalt - HW	Basalt - HW	Plag-rich porphyry	Plag rich porphyry	Sediments	Sediments	Sediments	Sediments	Iron FM	Iron FM	Basalt	Basalt	Basalt
Stratigraphic Unit	Scrape Point	Scrape Point	Scrape Point	Scrape Point	Scrape Point	Scrape Point	Scrape Point	Scrape Point	Scrape Point	Scrape Point	Scrape Point/ Goldenville-Nugget Pond Horizon	Scrape Point/ Goldenville-Nugget Pond Horizon	Mount Misery	Mount Misery	Mount Misery
Hf	2.40	2.40	2.10	2.40	2.50	2.00	2.20	1.90	2.70	2.20	3.10	3.40	1.40	1.10	1.20
Ho	0.78	0.38	0.78	0.77	0.87	0.69	0.46	0.52	0.94	0.61	0.76	1.22	0.90	0.62	0.68
La	4.30	10.10	3.20	3.90	3.90	3.20	10.30	9.70	28.20	8.40	31.20	35.80	1.80	1.60	1.70
Ce	11.30	23.80	8.60	10.40	10.60	8.60	21.60	20.20	108.50	18.60	91.30	99.30	5.60	5.00	5.20
Pr	1.70	2.91	1.43	1.60	1.69	1.35	2.56	2.59	7.11	2.34	7.07	8.42	0.88	0.74	0.77
Nd	9.10	12.20	7.30	8.10	8.40	6.60	10.60	10.30	27.00	10.00	25.10	32.70	5.20	3.70	4.00
Sm	3.02	2.40	2.79	2.68	2.97	2.34	2.57	2.43	6.15	2.81	5.41	7.00	1.98	1.49	1.47
Eu	1.05	0.63	1.07	0.99	1.15	0.90	0.66	0.77	1.04	0.86	1.10	1.70	0.76	0.65	0.75
Gd	4.00	2.34	3.88	3.43	3.94	3.31	2.78	2.63	5.38	2.92	4.76	6.84	3.66	2.38	3.09
Tb	0.61	0.38	0.65	0.63	0.67	0.54	0.38	0.44	0.80	0.46	0.71	1.05	0.66	0.43	0.48
Dy	4.17	2.40	4.08	3.79	4.20	3.19	2.50	2.65	4.83	3.00	4.05	6.40	4.52	2.99	3.38
Er	2.56	1.34	2.39	2.37	2.57	2.09	1.62	1.66	2.97	1.94	2.39	3.47	2.87	2.12	2.05
Lu	0.32	0.20	0.30	0.29	0.38	0.27	0.21	0.20	0.35	0.26	0.33	0.41	0.49	0.30	0.33
Nb	2.70	8.80	2.10	2.90	2.90	2.20	4.80	6.10	8.00	5.00	8.20	10.00	0.70	0.60	0.60
Sn	1.00	1.00	1.00	1.00	1.00	1.00	2.00	1.00	1.00	1.00	2.00	2.00	1.00	1.00	1.00
Sr	253.00	62.80	200.00	87.40	267.00	245.00	50.60	124.50	31.90	199.50	62.10	42.50	121.00	120.50	171.00
Ta	0.20	0.40	0.20	0.30	0.20	0.20	0.40	0.40	0.70	0.30	0.60	0.70	0.10	0.10	0.10
Th	0.29	2.24	0.15	0.17	0.21	0.20	2.26	1.87	7.10	1.76	6.80	7.08	0.14	0.15	0.19
Tm	0.32	0.19	0.34	0.31	0.33	0.29	0.19	0.23	0.38	0.25	0.32	0.51	0.42	0.29	0.34
U	0.12	1.46	0.07	0.07	0.11	0.20	1.59	1.02	1.15	1.21	1.10	1.33	0.18	0.12	0.07
V	242.00	174.00	247.00	232.00	256.00	197.00	197.00	231.00	78.00	213.00	70.00	97.00	348.00	305.00	316.00
W	3.00	5.00	2.00	2.00	2.00	2.00	3.00	3.00	7.00	3.00	2.00	7.00	3.00	3.00	3.00
Y	21.80	11.50	22.00	20.90	23.10	18.00	12.80	14.00	24.40	16.40	18.90	32.50	26.20	17.80	19.30
Yb	2.12	1.46	2.32	1.98	2.26	1.69	1.24	1.53	2.68	1.72	2.06	3.23	2.98	1.85	2.09
Zr	86.00	76.00	74.00	84.00	90.00	68.00	84.00	71.00	103.00	73.00	107.00	125.00	49.00	35.00	36.00

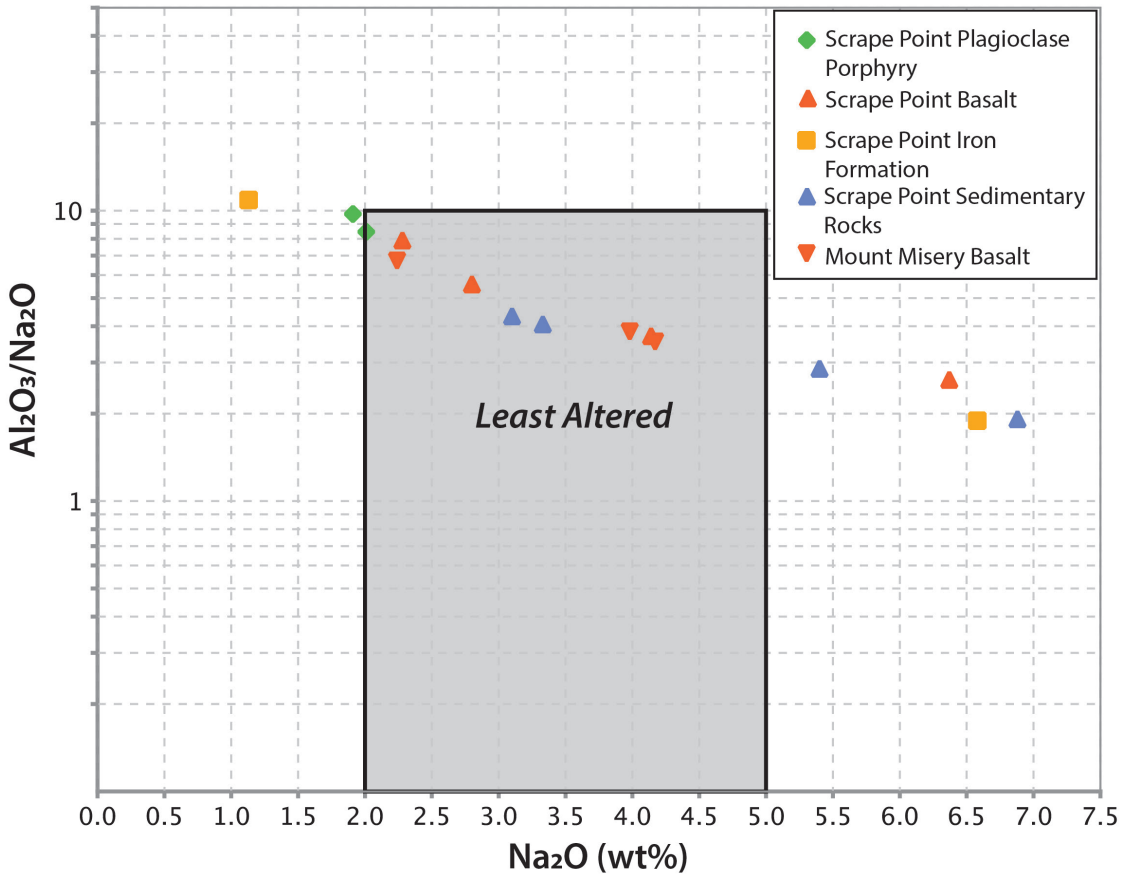

Figure 5. Al_2O_3/Na_2O index (Spitz and Darling, 1978) versus Na_2O illustrating that the samples from the Nugget Pond area are generally fresh to weakly altered. Diagram from Ruks et al. (2006).

calc-alkalic affinity (Fig. 6a-c). The samples have Ti/V ratios >20 and suggest a mid-ocean ridge basalt (MORB)/back-arc basin basalt (BABB) affinity (Fig. 6d). The majority of the samples have primitive manle normalized trace element patterns that exhibit LREE-depletion, flat HREE distribution, and smooth Th-Nb-La patterns or very weak Th-enrichment (Fig. 7b), similar to normal-MORB (N-MORB) to back-arc basin basalts (BABB). One sample has a more calc-alkalic affinity and exhibits LREE-enrichment, a downward sloping profile with moderate HREE-depletion, and a very weak negative Nb anomaly relative to Th and La (Fig. 7b). These features are similar to calc-alkalic basalts, albeit with less Ti depletion. The signatures above are similar to those found by Bedard et al. (2000) for the Scrape Point Formation.

Results: Iron Formation and Sedimentary Rocks

Lithogeochemical data for Scrape Point Formation sedimentary rocks from the Nugget Pond region are presented in Table 1 and Figures 5, 8-10. The sedimentary rocks and Fe-rich sedimentary rocks (i.e., >10% Fe_2O_3) have a wide range of Na_2O wt.% and Al_2O_3/Na_2O, spanning across the fields of weakly Na-depleted, least altered, and Na-enriched in Al_2O_3/Na_2O-Na_2O space (Fig. 5). On Böstrom-type plots (Boström et al., 1972) all samples lie well outside the hydrothermal fields with low Fe/Ti ratios, elevated Al/(Al+Fe+Mn) and overlap fields from sedimentary rocks (Fig. 8). While having some enrichments in Fe (8.20-14.85% Fe_2O_3), they do not exhibit hydrothermal Fe-enrichment common to many Algoma-type iron formations (Peter, 2003). Moreover, they have elevated Al_2O_3 (12.30-15.45%), Zr (73-125 ppm), and La (9.75-38.50 ppm) indicative of a dominantly detrital sedimentary component within them (Table 1). On immobile element discrimination diagrams the Scrape Point Formation sedimentary rocks and Fe-rich sedimentary rocks cluster near the fields for intra-oceanic and continental arcs (Fig. 9a). The samples also exhibit values that lie below unity on an upper crust normalized La-Sm plot which suggests derivation from sources that are more juvenile than the continental crust (i.e., local mafic sources) (Fig. 9b). Post-Archean Australian Shale (PAAS)-normalized REE+Y plots for the Fe-rich sedimentary rocks show that the samples have generally flat patterns but with a distinctive positive Ce anomaly (Fig. 10a). The positive Ce anomaly is also echoed

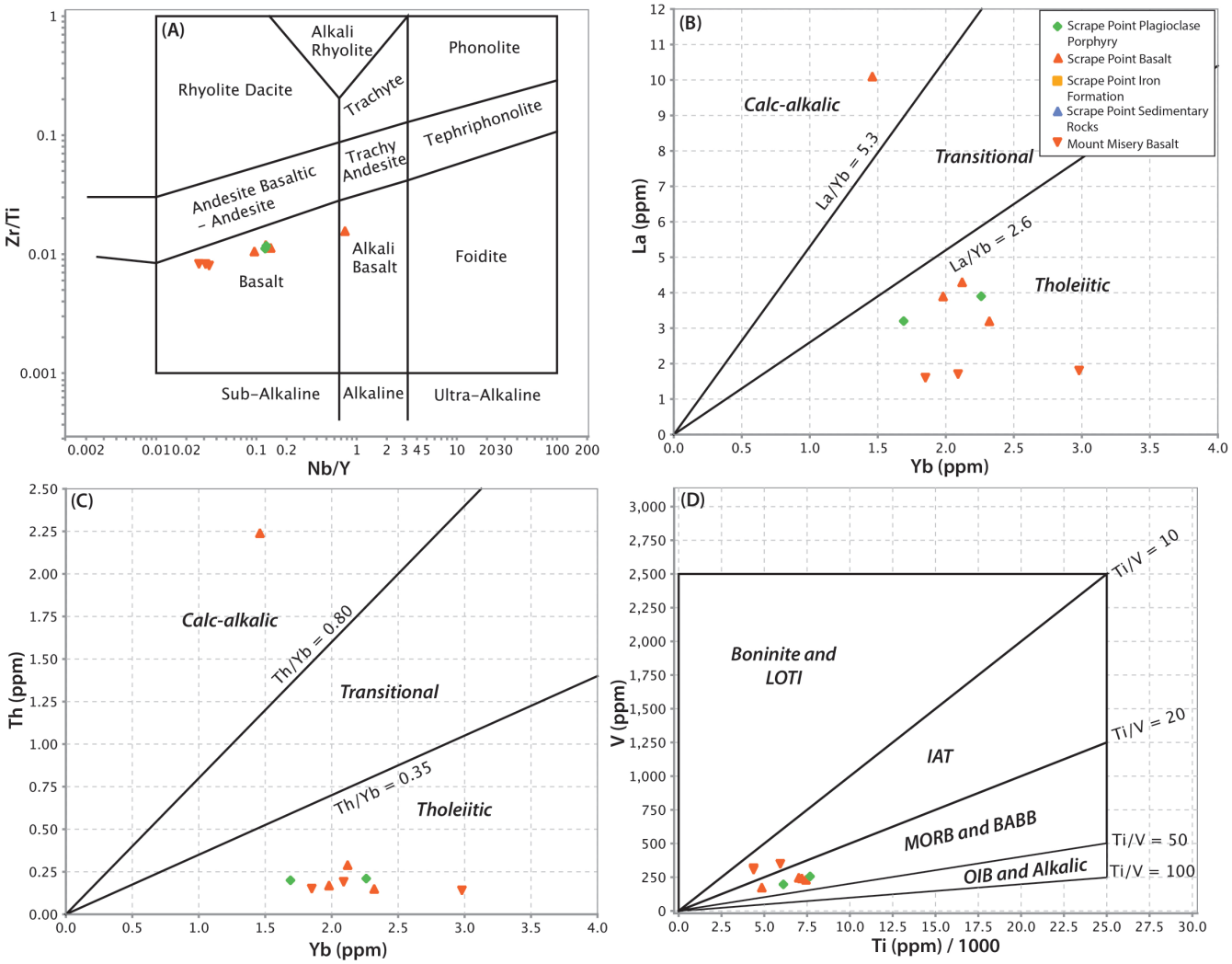

Figure 6. Discrimination diagrams for basaltic rocks. **A)** Zr/TiO_2-Nb/Y diagram of Pearce (modified after Winchester and Floyd, 1977; 1996). **B)** La-Yb and **C)** Th-Yb magma affinity diagrams of Ross and Bedard (2009). **D)** Ti-V diagram of Shervais (1982).

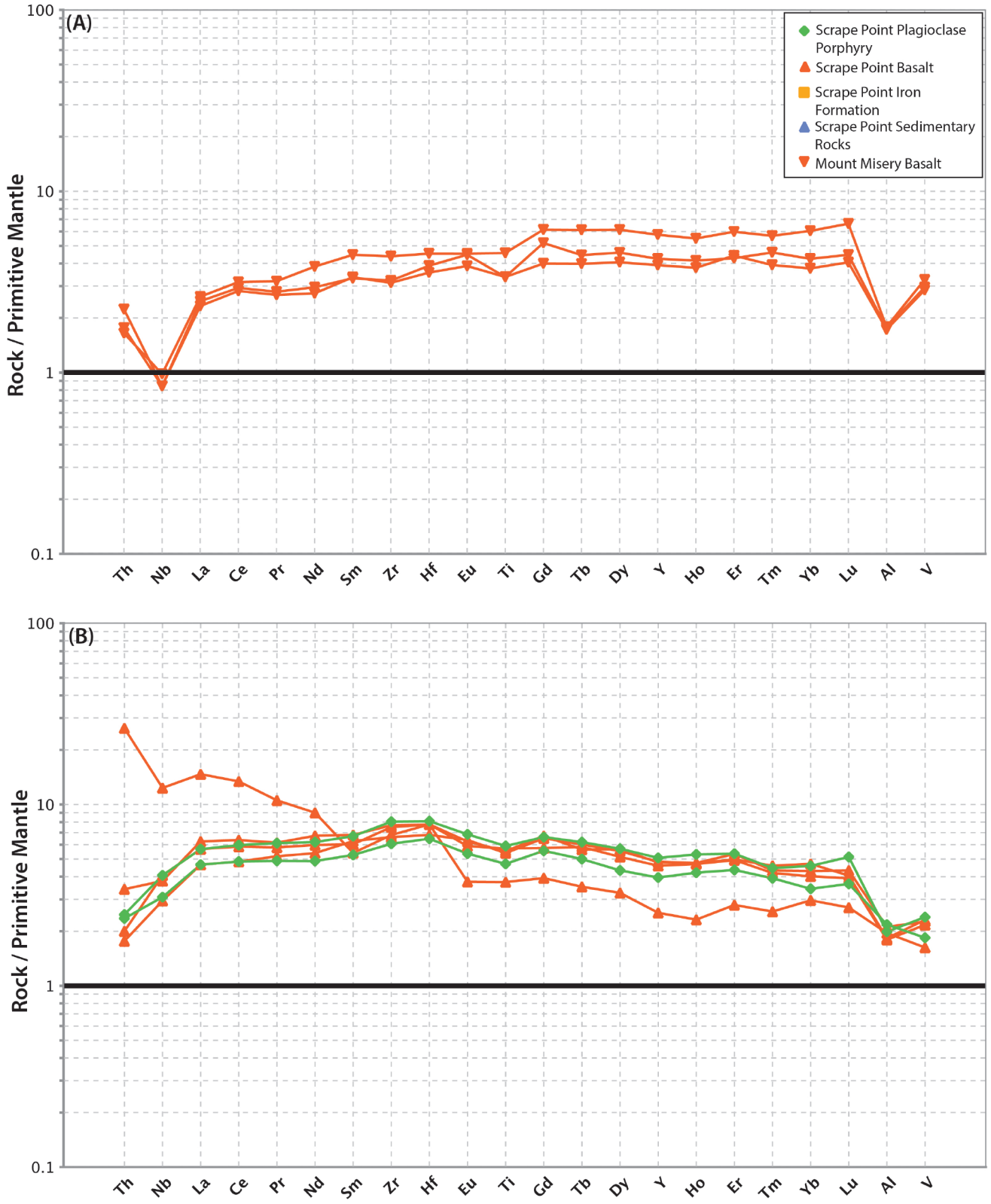

Figure 7. Primitive mantle normalized multi-element plots for mafic rocks from the Nugget Pond area. **A)** Lower stratigraphic unit, Mount Misery Formation, exhibiting island arc tholeiitic (IAT) affinities. **B)** Uppermost stratigraphic unit, Scrape Point Formation, exhibiting both normal mid-ocean ridge basalt (N-MORB) to back-arc basin basalt (BABB) signatures, with one sample having LREE-enriched signatures similar to calc-alkalic basalts. Primitive mantle values from Sun and McDonough (1989).

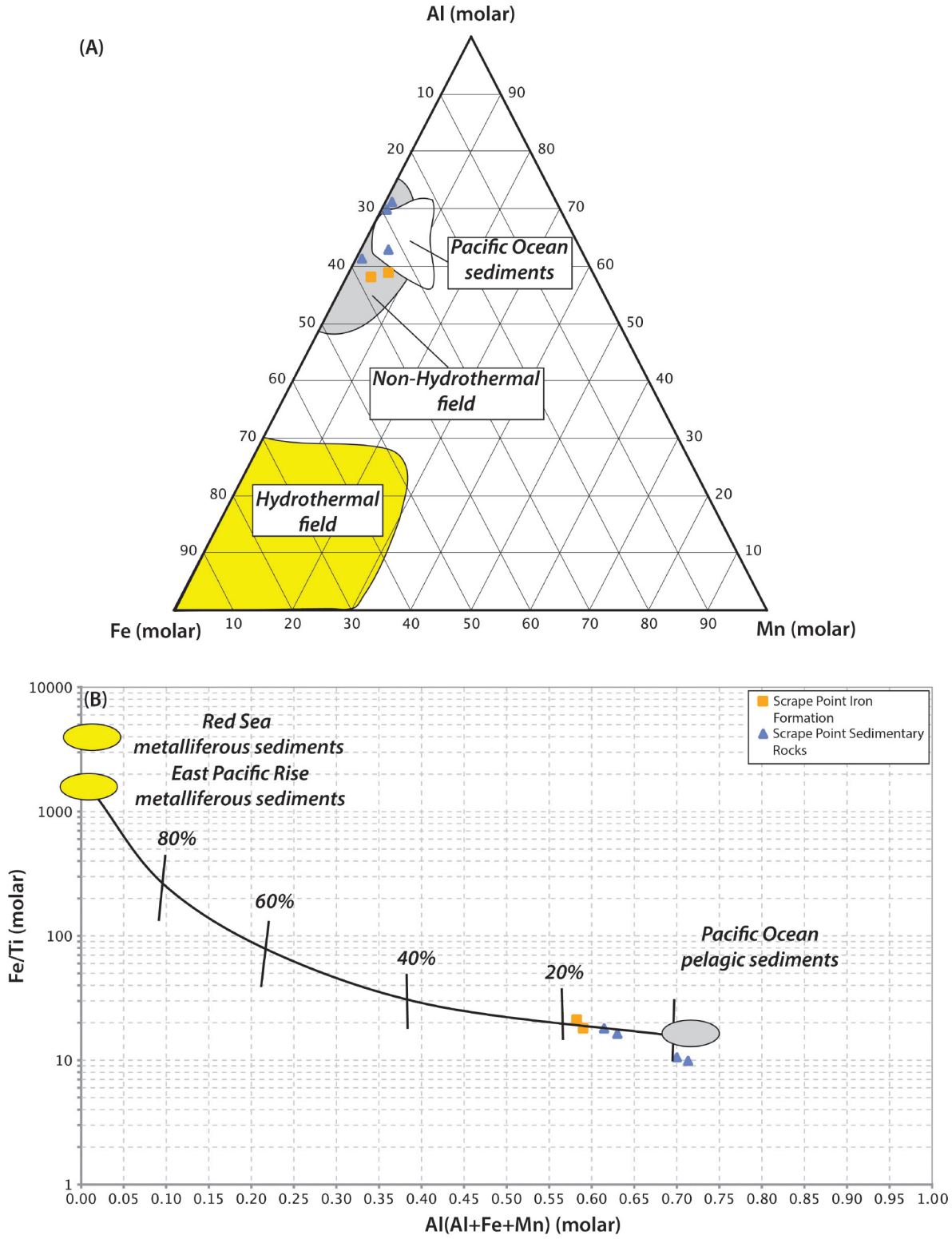

Figure 8. Böstrom-type plots for the sedimentary and iron formation samples from the Scrape Point formation. **A)** Molar Fe-Al-Mn diagram illustrating that most samples are dominated by detrital material and do not lie in the hydrothermal field. **B)** Molar Fe/Ti-Al/(Al+Fe+Mn) diagram with mixing lines between hydrothermal sources and background sedimentary materials. Most samples lie closer to the sedimentary end of this mixing line with up to 20% hydrothermal input permissible with the assumed end-member compositions, similar to vent-distal hydrothermal sedimentary rocks (e.g., Peter, 2003). Diagrams from Boström et al. (1972).

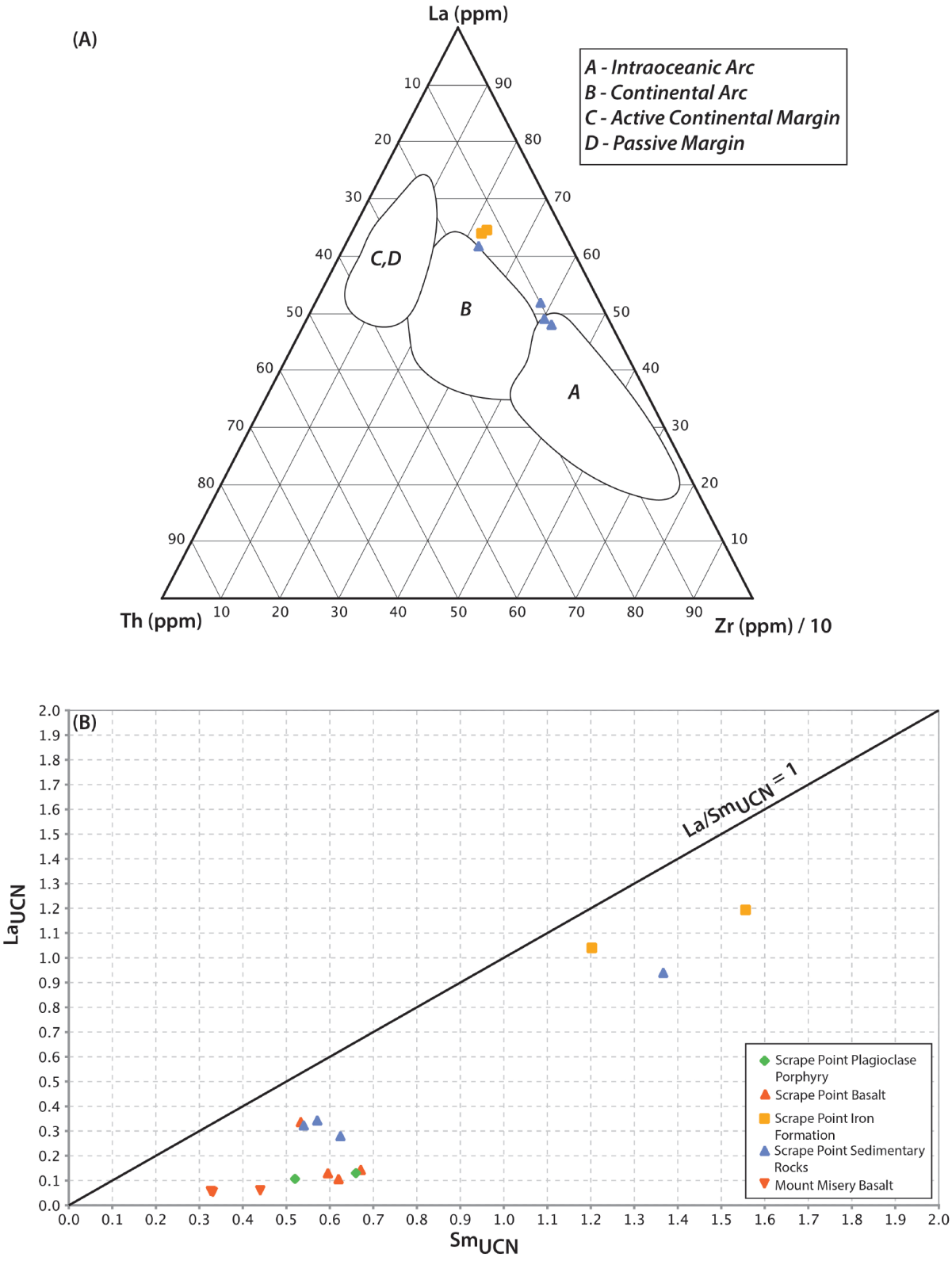

Figure 9. Immobile element discrimination diagrams for sediment provenance. **A)** Th-La-Zr/10 diagram demonstrating that most samples lie proximal to the intra-oceanic to continental arc fields. Diagram from Bhatia and Crook (1986). **B)** Upper crust normalized La-Sm diagram illustrating most samples have values less than 1 indicating derivation from sources more juvenile than the upper continental crust (i.e., local mafic sources). Diagram from Piercey and Colpron (2009). Upper crust values from McLennan (2001).

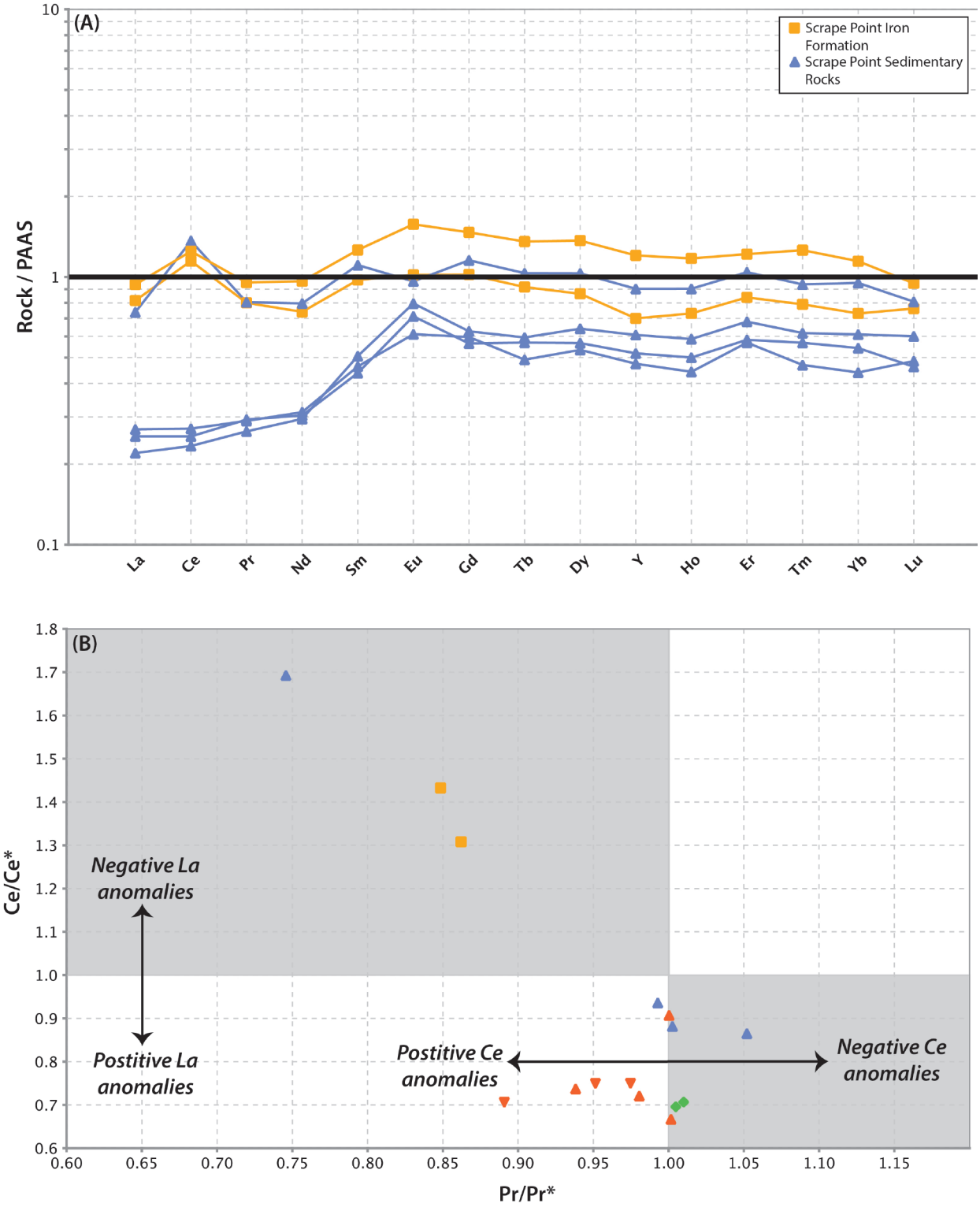

Figure 10. A) Post-Archean Australian Shale (PAAS) normalized rare earth element and Y (REE+Y) plot for sedimentary rocks and iron formation. The iron formation and some sedimentary rocks from the Scrape Point Formation have flat REE+Y patterns with distinctive positive Ce anomalies, other samples are LREE-depleted suggesting derivation from sources more juvenile than typical upper crust. **B)** Ce/Ce*-Pr/Pr* plot demonstrating that the iron formation and some sedimentary samples have true positive Ce anomalies. Diagram after Bau and Dulski (1996) and Kamber and Webb (2001). Ce/Ce* = Ce_{SN}/ ($0.5La_{SN}$ + $0.5Pr_{SN}$) and Pr/Pr* = Pr_{SN}/($0.5Ce_{SN}$ + $0.5Nd_{SN}$); SN = PAAS-normalized values (Kamber and Webb, 2001). PAAS values for (A) and (B) from McLennan (1989).

by the sample positions in Ce/Ce*-Pr/Pr* space (Fig. 10b). PAAS-normalized REE+Y plots for the sedimentary rocks show that the majority of samples have flat HREE+Y and depletions in LREE without a Ce anomaly (Fig. 10a,b), consistent with a sediment source more juvenile than average upper crustal shales. However, one sample has a pattern similar to the iron formations with a flatter REE+Y profile and a positive Ce anomaly.

DISCUSSION AND SUMMARY

Selected drill holes through the Nugget Pond deposit in the Baie Verte Peninsula illustrate a distinctive stratigraphic sequence that is correlative both physically and chemically with regional stratigraphic units. The lowermost unit consists of pillowed and massive mafic lavas that have island arc tholeiitic affinities that are similar to the Mount Misery Formation both in the Betts Cove Complex and regionally throughout the BVP (Bedard et al., 2000; Skulski et al., 2009; Skulski et al., 2010). Similarly, the mafic rocks of the Scrape Point Formation have units that in some cases are diagnostic, including the plagioclase porphyritic unit, and have N-MORB to BABB signatures like those found elsewhere in this unit regionally (Bedard et al., 2000; Skulski et al., 2009; Skulski et al., 2010). The sedimentary facies of the Scrape Point formation is distinctive with units that range from green-black turbiditic units near the top, variably chert-, hematite-, and magnetite-rich units throughout the middle and lower sections, and in some cases near the upper contact with the Mount Misery Formation there are volcaniclastic breccias. These rocks have immobile element signatures that imply intra-basinal and local derivation from juvenile units, likely the underlying Mount Misery Formation or coeval mafic rocks from the Scrape Point Formation (e.g., Fig. 9).

Despite having minor Fe enrichment and a significant detrital component, the iron formation and sedimentary rock samples from the Scrape Point Formation with the highest Fe/Al ratios (presumably greatest hydrothermal contribution) exhibit distinctive Ce anomalies on PAAS-normalized plots (Fig. 10). This REE+Y feature can provide insight into the nature of the ocean redox state at the time of deposition. Iron formations and chemical sedimentary rocks are interpreted to form via hydrothermal venting in which iron rich particles emanate from hydrothermal vents, interact to varying degrees with overlying seawater, and are subsequently deposited as hydrothermal sediment upon the seafloor (e.g., German et al., 1993; German and Von Damm, 2003; Peter, 2003; Bekker et al., 2010). During this process, Fe-rich particles can adsorb the REE+Y from seawater prior to deposition and consequently provide an indicator of the REE+Y signature of seawater at the time of formation (e.g., German et al., 1993; Bau, 1999; German and Von Damm, 2003; Peter, 2003; Bekker et al., 2010). The REE+Y signature of seawater, and particularly the Ce/Ce* of seawater, has varied through geological time, in part reflecting varying redox conditions in the oceans (Elderfield and Greaves, 1981, 1982; Elderfield et al., 1988; Bau and Dulski, 1996; Planavsky et al., 2010). In modern hydrothermal sediments, where Fe-oxide/oxyhydroxide particles have interacted with oxygenated seawater, the sediments inherit a distinctive negative Ce anomaly common to modern and fully oxygenated seawater (e.g., German et al., 1993). This feature is also found in ancient hydrothermal sedimentary rocks that have vented into oxygenated seawater (e.g., Lode et al., 2015; Piercey et al., 2018). In contrast, hydrothermal sedimentary rocks that have vented into sub-oxic or redox-stratified seawater (anoxic water underlain by more oxygenated water) can result in positive Ce anomalies being preserved in iron formation (e.g., Slack et al., 2007). The positive Ce anomalies recorded in the Scrape Point sedimentary rocks and iron formation (Fig. 10) could therefore suggest hydrothermal particles interacted with sub-oxic seawater. The larger question arising from this is whether this was a restricted, oxygen-limited basin within the Iapetus Ocean, for example, like modern restricted basins like the Caraico Trench or Saanich Harbour (e.g., de Baar et al., 1988; Calvert and Pedersen, 1993), or if limited oxygenation (relative to modern seawater) was a feature of the entire Iapteus Ocean (i.e., a late Cambrian-early Ordovician stratified ocean). Further work is required to test these hypotheses.

The association of gold mineralization with the Fe-rich units in the Scrape Point Formation is similar to some other orogenic gold districts globally (e.g., Homestake, Lupin, Meadobank)(Poulsen et al., 2000; Goldfarb et al., 2001; Gourcerol et al., 2016). In the case of the Nugget Pond deposit, there are numerous interpretations for its formation, including synvolcanic (VMS-style) accumulation of gold coupled with deformation post-gold formation (Kretschmar and McBride, 2015), magmatic-hydrothermal Manto-style mineralization (Sangster et al., 2007), and orogenic Au mineralization (Evans, 2004). The association with fault gouge, typical orogenic Au alteration assemblages (quartz-albite-carbonate), and sulfidation of a chemically reactive host rock is generally is consistent with the latter model, but further work is required to test the various deposit models above by using ore and alteration mineral petrology and both alteration mineral and lithogeochemical mapping.

ACKNOWLEDGEMENTS

We would like to thank staff from Anaconda Mining for their logistical support and for discussions during this project, including Steve Barrett, Dean Courage, Alison Cox, Michelle English, Linsey Gale, and Paul McNeill. Discussions regarding the geology of the Baie Verte Peninsula with Sebastien Castonguay, Greg Dunning, Graham Layne, and Tom Skulski are also acknowledged. This research was funded by grants to Piercey and Babechuk from the Targeted Geoscience Initiative 5 (TGI5) program from Natural Resources Canada (NRCan); Anaconda Mining Inc.; an NSERC Collaborative Research and Development

Grant and NSERC Discovery Grants. These funding agencies are thanked for their support of our research. We thank GSC reviewer Dr. Jean Bedard for thoughtful and helpful comments that improved this manuscript.

REFERENCES

Bau, M., 1999, Scavenging of dissolved yttrium and rare earths by precipitating iron oxyhydroxide; experimental evidence for Ce oxidation, Y-Ho fractionation, and lanthanide tetrad effect: Geochimica et Cosmochimica Acta, v. 63, p. 67-77.

Bau, M., and Dulski, P., 1996, Distribution of yttrium and rare-earth elements in the Penge and Kuruman iron-formations, Transvaal Supergroup, South Africa: Precambrian Research, v. 79, p. 37-55.

Bédard, J. H., Lauzière, K., Boisvert, É., Sangster, A., Tellier, M., Tremblay, A., and Dec, T., 1999, Geological map of the Betts Cove Ophiolitic Massif and its Cover Rocks. Geological Survey of Canada, Map 1969A: Ottawa, ON, Canada, Geological Survey of Canada.

Bedard, J. H., Lauzière, K., Tremblay, A., Sangster, A., Douma, S. L., and Dec, T., 2000, Betts Cove Ophiolite and its cover rocks, Newfoundland. Bulletin - Geological Survey of Canada., 76 p.

Bekker, A., Slack, J. F., Planavsky, N., Krapez, B., Hofmann, A., Konhauser, K. O., and Rouxel, O. J., 2010, Iron Formation: The Sedimentary Product of a Complex Interplay among Mantle, Tectonic, Oceanic, and Biospheric Processes: Economic Geology, v. 105, p. 467-508.

Bhatia, M. R., and Crook, K. A. W., 1986, Trace element characteristics of graywackes and tectonic setting discrimination of sedimentary basins: Contributions to Mineralogy and Petrology, v. 92, p. 181-193.

Boström, K., Joensuu, O., Valdés, S., and Riera, M., 1972, Geochemical history of South Atlantic Ocean sediments since Late Cretaceous: Marine Geology, v. 12, p. 85-121.

Brueckner, S. M., Piercey, S. J., Sylvester, P. J., Maloney, S., and Pilgrim, L., 2014, Evidence for Syngenetic Precious Metal Enrichment in an Appalachian Volcanogenic Massive Sulfide System: The 1806 Zone, Ming Mine, Newfoundland, Canada: Economic Geology, v. 109, p. 1611-1642.

Calvert, S. E., and Pedersen, T. F., 1993, Geochemistry of Recent oxic and anoxic marine sediments; implications for the geological record: Marine Geology, v. 113, p. 67-88.

de Baar, H. J. W., German, C. R., Elderfield, H., and van Gaans, P., 1988, Rare earth element distributions in anoxic waters of the Cariaco Trench: Geochimica et Cosmochimica Acta, v. 52, p. 1203-1219.

Dunning, G. R., and Krogh, T. E., 1985, Geochronology of ophiolites of the Newfoundland Appalachians: Canadian Journal of Earth Sciences, v. 22, p. 1659-1670.

Elderfield, H., Charnock, H., Lovelock, J. E., Liss, P. S., and Whitfield, M., 1988, The oceanic chemistry of the rare-earth elements: Philosophical Transactions of the Royal Society of London, Series A: Mathematical and Physical Sciences, v. 325, p. 105-124.

Elderfield, H., and Greaves, M. J., 1981, Negative cerium anomalies in the rare earth element patterns of oceanic ferromanganese nodules: Earth and Planetary Science Letters, v. 55, p. 163-170.

Elderfield, H., and Greaves, M. J., 1982, The rare earth elements in seawater: Nature (London), v. 296, p. 214-219.

Evans, D. T. W., 2004, Epigenetic Gold Occurrences, Baie Verte Peninsula (NTS 12H/09, 16 and 121/01, Newfoundland: St. John's, NL, Canada, Government of Newfoundland and Labrador, Department of Mines and Energy, Geological Survey, p. 157.

German, C. R., Higgs, N. C., Thomson, J., Mills, R., Elderfield, H., Blusztajn, J., Fleer, A. P., and Bacon, M. P., 1993, A Geochemical Study of Metalliferous Sediment From the TAG Hydrothermal Mound, 26o08'N, Mid-Atlantic Ridge: J. Geophys. Res., v. 98, p. 9683-9692.

German, C. R., and Von Damm, K. L., 2003, Hydrothermal Processes, Treatise on Geochemistry: Oxford, Pergamon, p. 181-222.

Goldfarb, R. J., Groves, D. I., and Gardoll, S., 2001, Orogenic gold and geologic time: a global synthesis: Ore Geology Reviews, v. 18, p. 1-75.

Gourcerol, B., Kontak, D. J., Thurston, P. C., and Duparc, Q., 2016, Do Magnetite Layers In Algoma-Type Banded Iron Formations (BIF) Preserve Their Primary Geochemical Signature? A Case Study of Samples From Three Archean BIF-Hosted Gold Deposits: The Canadian Mineralogist, v. 54, p. 605-624.

Hibbard, J., 1983, Geology of the Baie Verte Peninsula, Newfoundland. Memoir - Government of Newfoundland and Labrador, Department of Mines and Energy, Mineral Development Division, Vol. 2, 279 p.

Kamber, B. S., and Webb, G. E., 2001, The geochemistry of late Archaean microbial carbonate; implications for ocean chemistry and continental erosion history: Geochimica et Cosmochimica Acta, v. 65, p. 2509-2525.

Kessler, L. G., and Bedard, J. H., 2000, Epiclastic volcanic debrites; evidence of flow transformations between avalanche and debris flow processes, Middle Ordovician, Baie Verte Peninsula, Newfoundland, Canada: Precambrian Research, v. 101, p. 135-161.

Kretschmar, U., and McBride, D., 2015, The Metallogeny of Lode Gold Deposits: A Syngenetic Perspective: Amsterdam, Netherlands, Elsevier.

Lode, S., Piercey, S. J., and Devine, C. A., 2015, Geology, Mineralogy, and Lithogeochemistry of Metalliferous Mudstones Associated with the Lemarchant Volcanogenic Massive Sulfide Deposit, Tally Pond Belt, Central Newfoundland: Economic Geology, v. 110, p. 1835-1859.

MacLean, W. H., and Barrett, T. J., 1993, Lithogeochemical techniques using immobile elements: Journal of Geochemical Exploration, v. 48, p. 109-133.

McLennan, S. M., 1989, Rare earth elements in sedimentary rocks; influence of provenance and sedimentary processes: Reviews in Mineralogy, v. 21, p. 169-200.

McLennan, S. M., 2001, Relationships between the trace element composition of sedimentary rocks and upper continental crust: Geochemistry, Geophysics, Geosystems, v. 2, p. 24 (Paper 2000GC000109).

Pearce, J. A., 1996, A user's guide to basalt discrimination diagrams, in Wyman, D. A., ed., Trace element geochemistry of volcanic rocks: Applications for massive sulphide exploration, Short Course Notes, Volume 12, Geological Association of Canada, p. 79-113.

Peter, J. M., 2003, Ancient iron formations: their genesis and use in the exploration for stratiform base metal sulphide deposits, with examples from the Bathurst Mining Camp, *in* Lentz, D. R., ed., Geochemistry of Sediments and Sedimentary Rocks: Secular Evolutionary Considerations to Mineral Deposit-Forming Environments, GEOtext v.4., Geological Association of Canada, p. 145-176.

Piercey, S. J., and Colpron, M., 2009, Composition and provenance of the Snowcap assemblage, basement to the Yukon-Tanana terrane, northern Cordillera: Implications for Cordilleran crustal growth: Geosphere, v. 5, p. 439-464.

Piercey, S. J., Squires, G., and Brace, T., 2018, Geology and lithogeochemistry of hydrothermal mudstones from the upper block near the Duck Pond volcanogenic massive sulfide (VMS) deposit, Newfoundland, Canada: evidence for low-temperature venting into oxygenated mid-Cambrian seawater: Mineralium Deposita, v. 53, p. 1167-1191.

Pilote, J.-L., Piercey, S. J., and Mercier-Langevin, P., 2017, Volcanic and Structural Reconstruction of the Deformed and Metamorphosed Ming Volcanogenic Massive Sulfide Deposit, Canada: Implications for Ore Zone Geometry and Metal Distribution: Economic Geology, v. 112, p. 1305-1332.

Planavsky, N., Bekker, A., Rouxel, O. J., Kamber, B., Hofmann, A., Knudsen, A., and Lyons, T. W., 2010, Rare Earth Element and yttrium compositions of Archean and Paleoproterozoic Fe formations revisited: New perspectives on the significance and mechanisms of deposition: Geochimica et Cosmochimica Acta, v. 74, p. 6387-6405.

Poulsen, K. H., Robert, F., and Dube, B., 2000, Geological Classification of Canadian Gold Deposits, Bulletin 540: Ottawa, ON, Canada, Geological Survey of Canada, p. 113.

Ramezani, J., Dunning, G. R., and Wilson, M. R., 2000, Geologic setting, geochemistry of alteration, and U-Pb age of hydrothermal zircon from the Silurian Stog'er Tight gold prospect, Newfoundland Appalachians, Canada: Exploration and Mining Geology, v. 9, p. 171-188.

Ross, P.-S., and Bedard, J. H., 2009, Magmatic affinity of modern and ancient subalkaline volcanic rocks determined from trace-element discriminant diagrams: Canadian Journal of Earth Sciences, v. 46, p. 823-839.

Ruks, T. W., Piercey, S. J., Ryan, J. J., Villeneuve, M. E., and Creaser, R. A., 2006, Mid- to late Paleozoic K-feldspar augen granitoids of the Yukon-Tanana terrane, Yukon, Canada: Implications for crustal growth and tectonic evolution of the northern Cordillera: Geological Society of America Bulletin, v. 118, p. 1212-1231.

Sangster, A. L., Douma, S. L., and Lavigne, J., 2007, Base metal and gold deposits of the Betts Cove Complex, Baie Verte Peninsula, Newfoundland, *in* Goodfellow, W. D., ed., Mineral Deposits of Canada: A Synthesis of Major Deposit-types, District Metallogeny, the Evolution of Geological Provinces, and Exploration Methods, Special Publication 5, Mineral Deposits Division, Geological Association of Canada, p. 703-721.

Shervais, J. W., 1982, Ti-V plots and the petrogenesis of modern and ophiolitic lavas: Earth and Planetary Science Letters, v. 59, p. 101-118.

Skulski, T., Castonguay, S., McNicoll, V., van Staal, C., Kidd, W., Rogers, N., Morris, W., Ugalde, H., Slavinski, H., Spicer, W., Moussallam, Y., and Kerr, I., 2010, Tectonostratigraphy of the Baie Verte Oceanic Tract and its ophiolite cover sequence on the Baie Verte Peninsula: Current Research - Newfoundland and Labrador Department of Natural Resources, Geological Survey, v. Report 10-1, p. 315-225.

Skulski, T., Castonguay, S., van Staal, C., Rogers, N., McNicoll, V., Kerr, A., and Escayloa, M., 2009, Baie Verte Peninsula: An evolving geological story: St. John's, NL, Geological Association of Canada Newfoundland and Labrador Section, 76 p.

Slack, J. F., Grenne, T., Bekker, A., Rouxel, O. J., and Lindberg, P. A., 2007, Suboxic deep seawater in the late Paleoproterozoic: Evidence from hematitic chert and iron formation related to seafloor-hydrothermal sulfide deposits, central Arizona, USA: Earth and Planetary Science Letters, v. 255, p. 243-256.

Spitz, G., and Darling, R., 1978, Major and minor element lithogeochemical anomalies surrounding the Louvem copper deposit, Val d'Or, Quebec: Canadian Journal of Earth Sciences, v. 15, p. 1161-1169.

Sun, S.-s., and McDonough, W. F., 1989, Chemical and isotopic systematics of oceanic basalts: implications for mantle composition and processes, in Saunders, A. D., and Norry, M. J., eds., Magmatism in the Ocean Basins, Geological Society Special Publication 42, p. 313-345.

van Staal, C., and Barr, S. M., 2012, Lithospheric architecture and tectonic evolution of the Canadian Appalachians and associated Atlantic margin. Chapter 2 *in* Percival, J. A., Cook, F. A., and Clowes, R. M., eds., In Tectonic Styles in Canada: the LITHOPROBE Perspective, Special Paper 49: St. John's, NL, Canada, Geological Association of Canada, p. 41-96.

van Staal, C. R., 2007, Pre-Carboniferous tectonic evolution and metallogeny of the Canadian Appalachians, *in* Goodfellow, W. D., ed., Mineral Deposits of Canada: A Synthesis of Major Deposit-types, District Metallogeny, the Evolution of Geological Provinces, and Exploration Methods, Special Publication 5, Mineral Deposits Division, Geological Association of Canada, p. 793-818.

Waldron, J. W. F., and van Staal, C. R., 2001, Taconian Orogeny and the accretion of the Dashwoods Block; a peri-Laurentian microcontinent in the Iapetus Ocean: Geology, v. 29, p. 811-814.

Winchester, J. A., and Floyd, P. A., 1977, Geochemical discrimination of different magma series and their differentiation products using immobile elements: Chemical Geology, v. 20, p. 325-343.

Appendix A: Reference Material Data

Table A1. Lithogeochemical data for basalt reference material.

	SLV-MC This Study(n=1)	Long Term Average(n=29)	1s(n=29)
SiO2(wt%)	49.7	49.97	0.56
Al2O3	15.5	15.55	0.23
Fe2O3	12.95	12.85	0.21
CaO	8.61	8.59	0.13
MgO	7.63	7.55	0.12
Na2O	3.59	3.52	0.10
K2O	0.51	0.51	0.01
Cr2O3	0.031	0.03	0.00
TiO2	1.49	1.51	0.03
MnO	0.16	0.17	0.01
P2O5	0.24	0.24	0.01
SrO	0.05	0.05	0.00
BaO	0.02	0.02	0.00
LOI	-0.78	-0.66	0.17
Total	99.7	99.87	0.81
C(wt%)	<0.05	<0.05	<0.05
CO2(wt%)	<0.2	<0.2	<0.2
Ba(ppm)	154.5	159.17	5.17
Ce	21.3	21.23	0.91
Cr	220	233.48	11.52
Cs	0.09	0.07	0.02
Dy	3.58	3.59	0.22
Er	1.77	1.76	0.08
Eu	1.26	1.34	0.06
Ga	21	20.98	0.83
Gd	3.97	4.06	0.18
Hf	2.7	2.57	0.15
Ho	0.61	0.68	0.03
La	10.1	9.49	0.48
Lu	0.22	0.22	0.02
Nb	8.7	8.66	0.43
Nd	13.1	14.13	0.63
Pr	2.95	2.97	0.11
Rb	5.4	5.53	0.30
Sm	4.17	3.73	0.23
Sn	2	1.93	0.90
Sr	450	472.84	20.11
Ta	0.5	0.50	0.07
Tb	0.63	0.61	0.03
Th	0.81	0.83	0.09
Tm	0.21	0.24	0.01
U	0.28	0.26	0.08
V	190	193.10	8.77
W	2	1.07	0.27
Y	16.9	17.45	0.75
Yb	1.44	1.50	0.09
Zr	98	98.69	4.32

Stratigraphy and Lithogeochemistry of the Goldenville Horizon and Associated Rocks, Baie Verte Peninsula, Newfoundland

C. Mueller[1], S.J. Piercey[1]*, M.G. Babechuk[1], and D. Copeland[2]

Mueller, C., Piercey, S.J. Babechuk, M.G., and Copeland, D., 2021. Stratigraphy and Lithogeochemistry of the Goldenville Horizon and Associated Rocks, Baie Verte Peninsula, Newfoundland; in *Targeted Geoscience Initiative 5:grant program final reports (2018-2020); Geological Survey of Canada, Open File 8755, p. 235–249. https://doi.org/10.4095/328990*

Abstract: The Goldenville horizon in the Baie Verte Peninsula is an important stratigraphic horizon that hosts primary (Cambrian to Ordovician) exhalative magnetite and pyrite and was a chemical trap for younger (Silurian to Devonian) orogenic gold mineralization. The horizon is overlain by basaltic flows and volcaniclastic rocks, is intercalated with variably coloured argillites and cherts, and underlain by mafic volcaniclastic rocks; the entire stratigraphy is cut by younger fine-grained mafic dykes and coarser gabbro. Lithogeochemical signatures of the Goldenville horizon allow it to be divided into high-Fe iron formation (HIF; >50% Fe_2O_3), low-Fe iron formation (LIF; 15–50% Fe_2O_3), and argillite with iron minerals (AIF; <15% Fe_2O_3). These variably Fe-rich rocks have Fe-Ti-Mn-Al systematics consistent with element derivation from varying mineral contributions from hydrothermal venting and ambient detrital sedimentation. Post-Archean Australian Shale (PAAS)-normalized rare earth element (REE) signatures for the HIF samples have negative Ce anomalies and patterns similar to modern hydrothermal sediment deposited under oxygenated ocean conditions. The PAAS-normalized REE signatures of LIF samples have positive Ce anomalies, similar to hydrothermal sediment deposited under anoxic to sub-oxic conditions. The paradoxical Ce behaviour is potentially explained by the Mn geochemistry of the LIF samples. The LIF have elevated MnO contents (2.0–7.5 weight %), suggesting that Mn from hydrothermal fluids was oxidized in an oxygenated water column during hydrothermal venting, Mn-oxides then scavenged Ce from seawater, and these Mn-oxides were subsequently deposited in the hydrothermal sediment. The Mn-rich LIF samples with positive Ce anomalies are intercalated with HIF with negative Ce anomalies, both regionally and on a metre scale within drill holes. Thus, the LIF positive Ce anomaly signature may record extended and particle-specific scavenging rather than sub-oxic/redox-stratified marine conditions. Collectively, results suggest that the Cambro-Ordovician Taconic seaway along the Laurentian margin may have been completely or near-completely oxygenated at the time of Goldenville horizon deposition.

[1]Department of Earth Sciences, Memorial University of Newfoundland, Alexander Murray Building, 9 Arctic Ave, St. John's, Newfoundland and Labrador A1B 3X5
[2]Anaconda Mining Inc., Elizabeth Business Centre, 55 Elizabeth Avenue, St. John's, Newfoundland and Labrador A1A 1W9
*Corresponding author (e-mail: spiercey@mun.ca)

INTRODUCTION

The Baie Verte Peninsula hosts numerous volcanogenic massive sulphide (VMS) and orogenic Au deposits within ophiolitic and cover sequence rocks of the Baie Verte oceanic tract (BVOT) (Hibbard, 1983; van Staal, 2007; Skulski et al., 2009, 2010, 2015; van Staal and Barr, 2012). Cambro-Ordovician ophiolitic rocks (ca. 488–487 Ma) rocks host Cu-(Au)-bearing VMS deposits in both the Betts Cove and Pacquet complexes, whereas orogenic Au mineralization is hosted in the younger, chemically reactive rocks in the Snooks Arm Group cover sequence (Ramezani et al., 2000; Evans, 2004; Sangster et al., 2007; Ybarra et al., 2017). The past producing Nugget Pond and Goldenville Au deposits were hosted in iron formation proximal to the stratigraphic transition from underlying ophiolitic rocks of the Betts Cove Complex and equivalents and overlying rocks of the Snooks Arm Group (Evans, 2004; Sangster et al., 2007; Skulski et al., 2010). Despite the regional geological and metallogenic significance of this stratigraphic horizon no prior detailed modern study of the lithostratigraphy, lithofacies, and lithogeochemistry of the Goldenville–Nugget Pond horizon has been undertaken.

In this report we provide new geological, lithostratigraphy, and geochemical data for rocks from the Goldenville horizon with the goal to outline stratigraphic relationships and preliminary lithogeochemical interpretations. These results are part of an M.Sc. study by the senior author aimed at understanding the nature of the Goldenville horizon and its potential for orogenic Au and/or VMS-related base metal mineralization.

GEOLOGICAL AND REGIONAL STRATIGRAPHIC SETTING

The Goldenville gold deposit and associated stratigraphy are hosted within rocks of the BVOT, which consists of peri-Laurentian rocks that formed during the Cambro-Ordovician evolution of the Taconic seaway (Fig. 1–3) (Waldron and van Staal, 2001; van Staal, 2007; van Staal and Barr, 2012). The BVOT consists of four partial to full ophiolite complexes that are ca. 488 to 487 Ma (Dunning and Krogh, 1985) and host both Cu-Au-rich VMS deposits (Betts Cove ophiolite) and Au-enriched VMS deposits (Pacquet complex) (Fig. 1–3) (Sangster et al., 2007; Brueckner et al., 2014; Pilote et al., 2017). The cover sequence to mineralization, the Snooks Arm Group, is the host to younger (Silurian-Devonian) orogenic Au mineralization in iron formations (e.g. Goldenville and Nugget Pont) and in Fe-Ti-rich gabbroic to basaltic rocks (Fig. 1–3) (Ramezani et al., 2000; Sangster et al., 2007; Skulski et al., 2009; Skulski et al., 2010).

The Goldenville deposit is hosted within iron formations of the Scrape Point Formation and lies at the transition between the underlying Mount Misery Formation and the overlying Snooks Arm Group (Fig. 2–3). The Mount Misery Formation consists of basaltic volcanic and volcaniclastic rocks that have island arc tholeiitic affinities and are unconformably overlain by the Snooks Arm Group (Fig. 2–3) (Bedard et al., 2000; Skulski et al., 2010). The Goldenville horizon is interpreted to be correlative with the Nugget Pond member in the Betts Cove area and both are interpreted to represent a lowermost regional marker unit in the Scrape Point Formation of the Snooks Arm Group (Fig. 2–3) (Bedard et al., 2000; Skulski et al., 2010). However, there appear to be some stratigraphic differences between the two horizons (see below and companion paper by Mueller et al., 2021), and it is possible that there are multiple iron formation horizons in the Scrape Point Formation and underlying Mt. Misery Formation.

The Goldenville gold deposit consists of quartz-carbonate-sulphide replacement of the Goldenville horizon, where there is both wall rock sulphidation associated with shearing/faulting both in the iron formation and in footwall mafic rocks (Evans, 2004). The shearing in the Goldenville mine area results in the rocks exhibiting a mylonitic fabric that locally contain quartz-carbonate and chlorite veinlets within the mylonite; distal from the shear zone there are weakly pyrite-bearing quartz veins that contain Au (Evans, 2004). Where the veins have interacted with the iron formation they exhibit pyrite in the selvages around the veins (Evans, 2004), indicative of wall rock sulphidation of pre-existing magnetite. The Goldenville horizon also contains weakly laminated layers of pyrite intercalated with magnetite, potentially indicative of VMS-like exhalative mineralization.

STRATIGRAPHY AND LITHOFACIES IN THE GOLDENVILLE HORIZON

Recently drilled holes along the Goldenville horizon were logged to resolve the stratigraphy and lithofacies of the unit regionally and within mineralized zones. Holes were selected to provide regional coverage along the horizon and continuous stratigraphy.Representative holes along the horizon, documented using graphic logs, are shown in Figure 4.

The hanging wall to the Goldenville horizon is dominated by basaltic flows, whereas the footwall consists of intercalated basalt flows, mafic volcaniclastic rocks, and argillite. All of these units are cross-cut by gabbroic intrusive rocks (Fig. 4). While the rocks have been subject to deformation and metamorphism to greenschist facies, most exhibit primary textures. The stratigraphy is also preserved. Outlined below are the lithofacies found within the Goldenville stratigraphy.

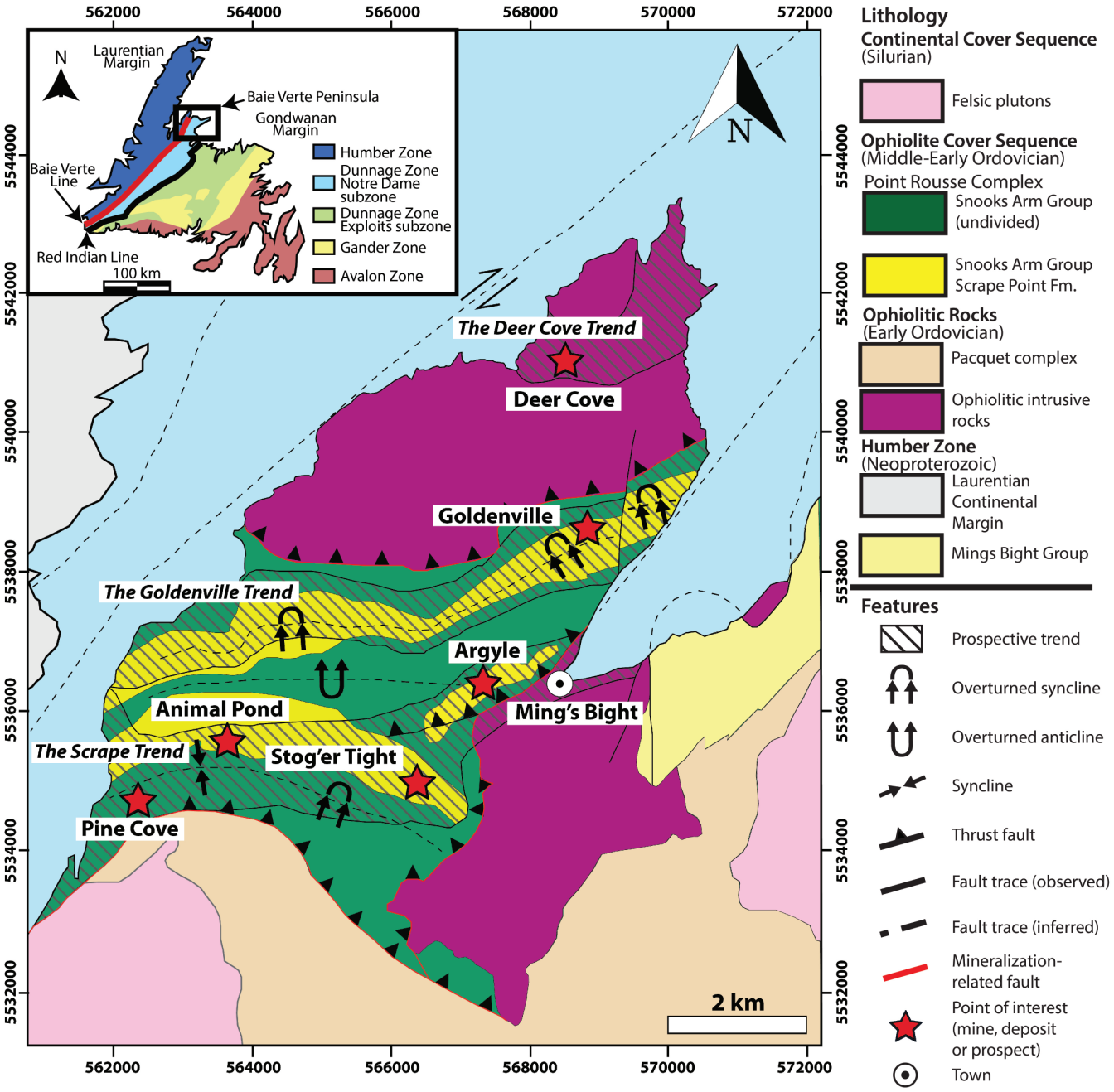

Figure 1. Simplified geological map of the Point Rousse Peninsula on the Baie Verte Peninsula. Positions of various gold projects are the red stars. Modified from Skulski et al. (2010; 2015) and Pawlukiewicz (2020). Inset shows the location of the Baie Verte Peninsula in Newfoundland.

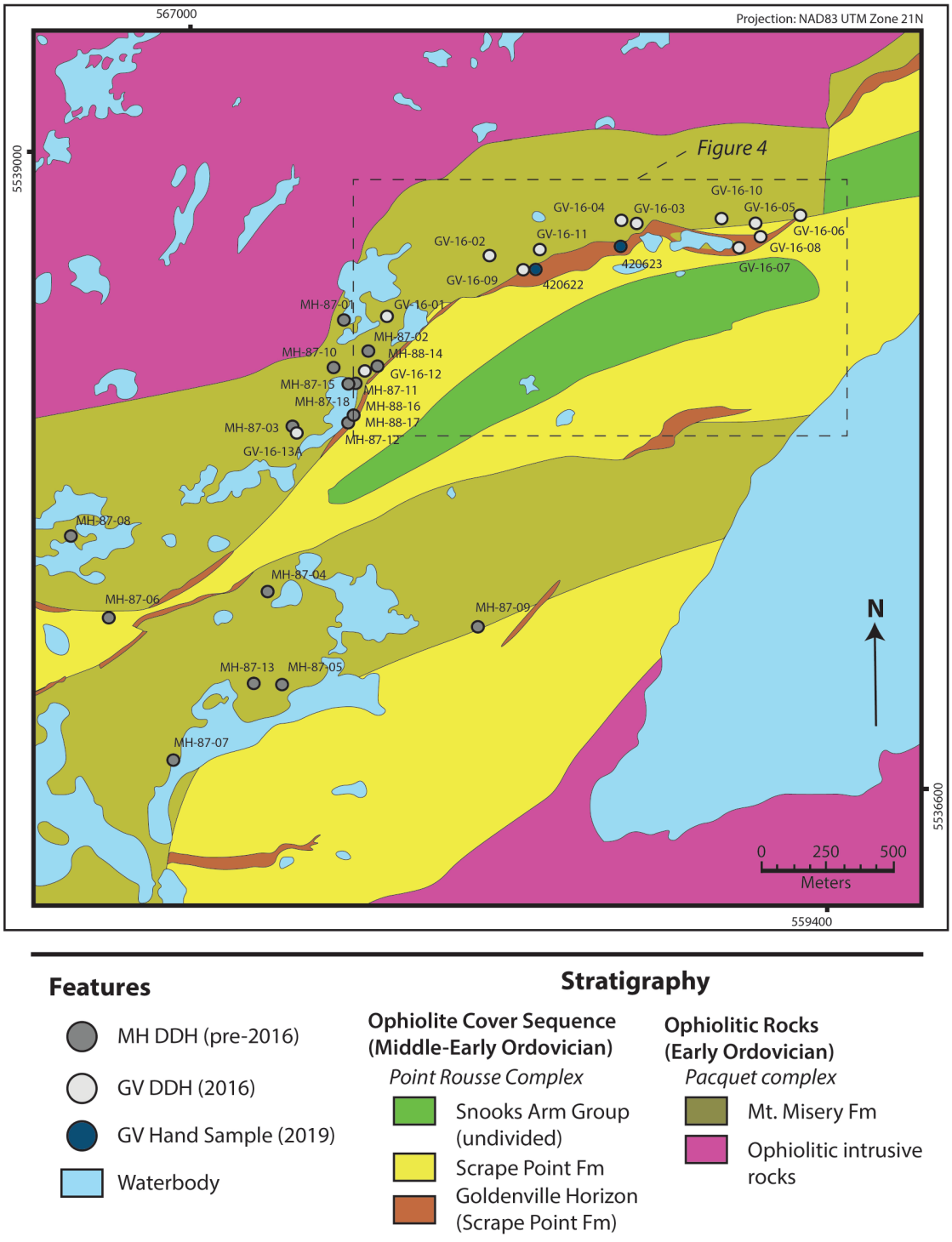

Figure 2. Geology of the Goldenville mine area with associated drill holes. Modified from Skulski et al. (2010; 2015) and Anaconda Mining Ltd. (unpub. rept., 2019).

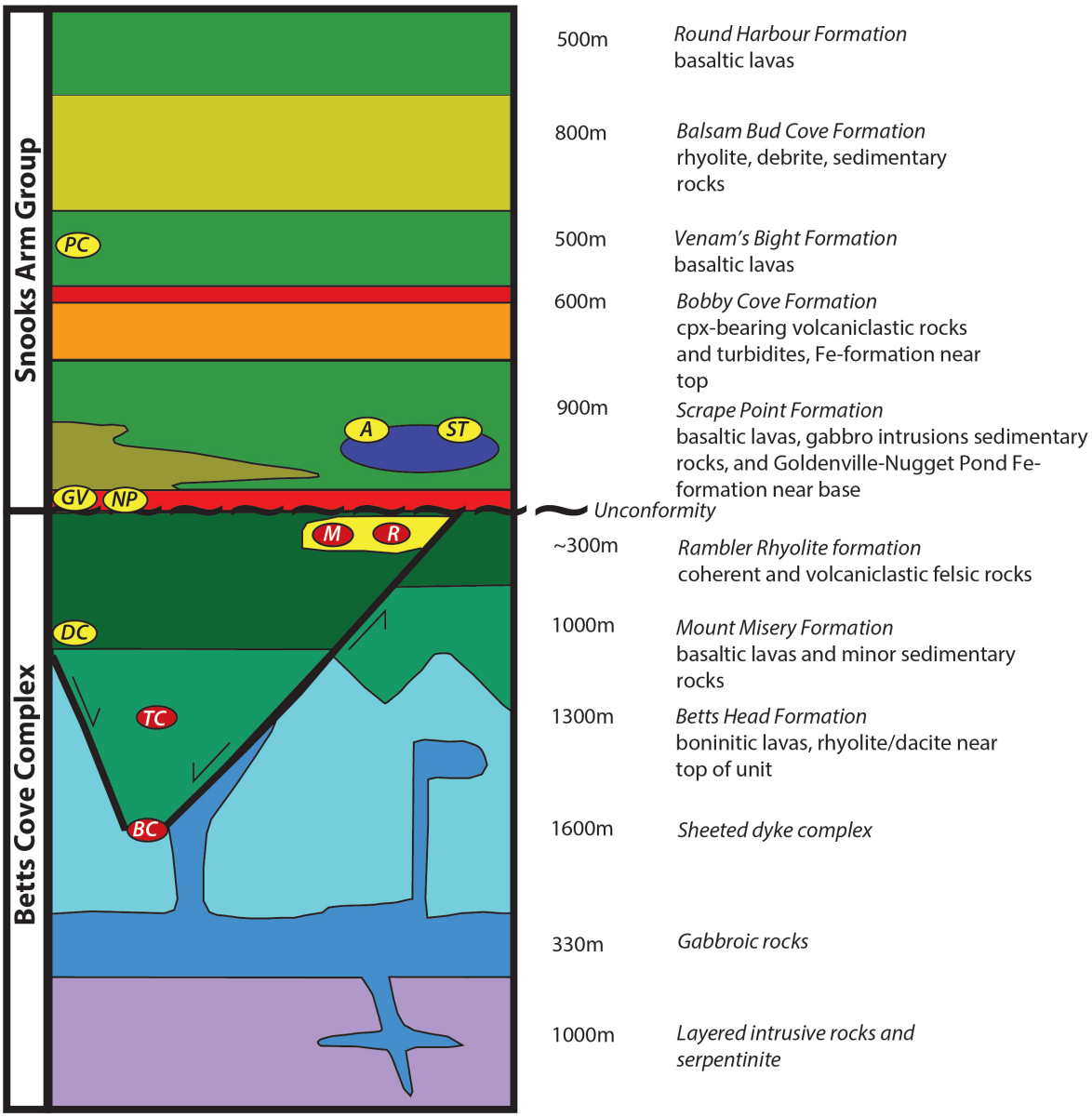

Figure 3. Stratigraphy of the Betts Cove Complex and Snooks Arm Group cover sequence. This is the regional stratigraphy representative of the Baie Verte Peninsula. Mineral deposits are from both within the Betts Cove area and from the Baie Verte Peninsula regionally. Red ovals are VMS deposits and include BC – Betts Cove, TC – Tilt Cove, R = Rambler, M = Ming. Yellow ovals are orogenic Au deposits and include: DC – Deer Cove, GV = Goldenville, NP = Nugget Pond, ST = Stog'er Tight, A = Argyle, PC = Pine Cove. Diagram modified after Bedard et al. (2000) and Kessler and Bedard (2000).

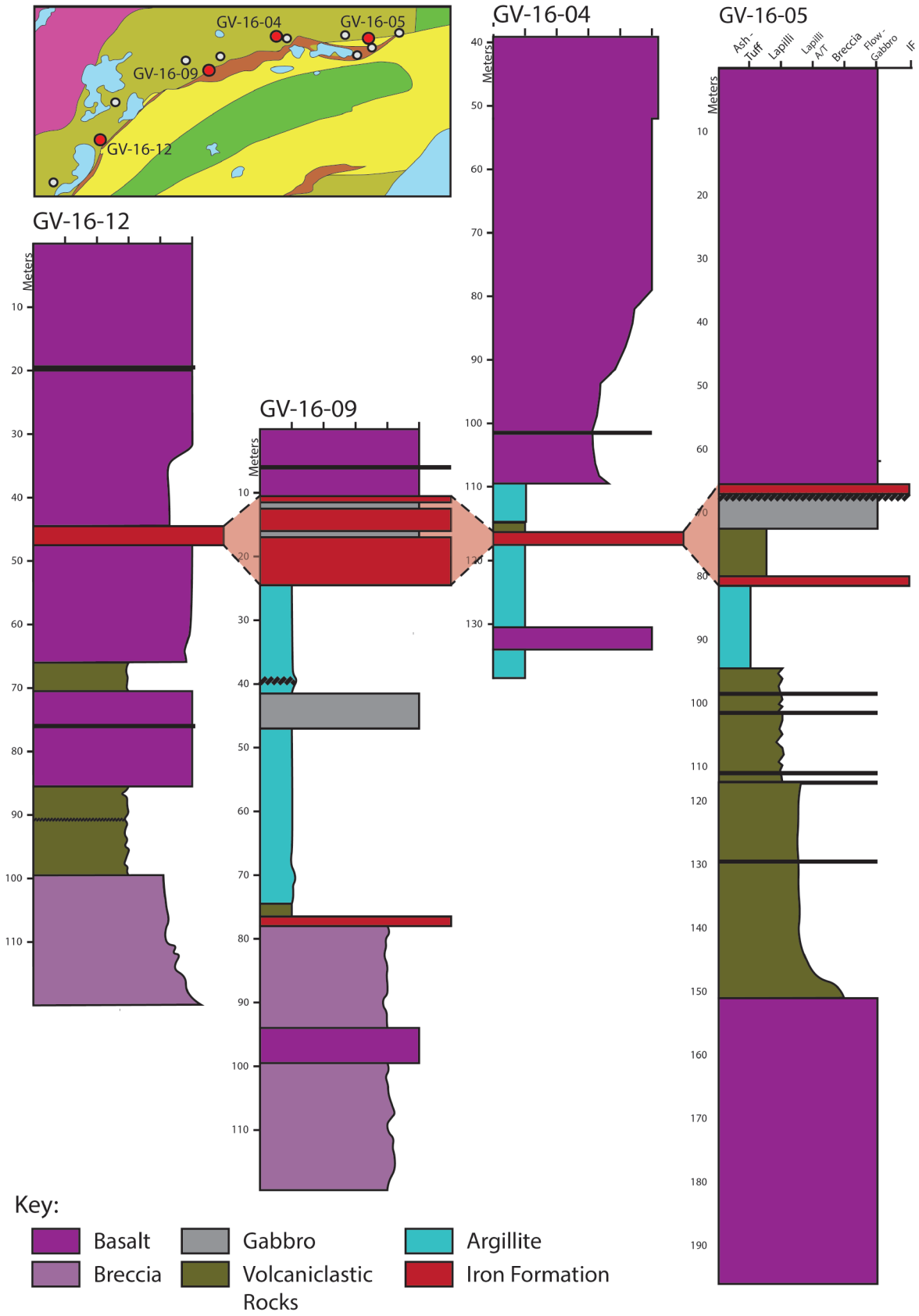

Figure 4. Graphic logs of select drill holes from the Goldenville deposit illustrating the host stratigraphy and lithological variability.

Volcanic, Volcaniclastic, Sedimentary, and Intrusive Lithofacies

Massive mafic flows, pillow lavas, and breccias: this facies consists of coherent basalt and associated breccias. Coherent facies rocks are massive to pillowed, contain amygdales, and locally hyaloclastite and varioles are preserved. They are light grey to green with amygdales and breccia that are partly to fully replaced by chlorite, epidote, calcite, and/or quartz. These rocks are locally cross cut by quartz-carbonate veins (< 4 cm) and millimetre-scale veinlets. There are no significant visible differences in the basalt flows above or below the Goldenville horizon.

Mafic volcaniclastic rocks: mafic volcaniclastic rocks, primarily lapilli tuff and lapillistone, are found throughout the stratigraphy, but predominantly in the (structural?) footwall to mineralization and are found proximal to iron formation (Fig. 4). The lapilli tuff is predominantly matrix-supported with sub-rounded to elongated clasts of mafic material. Clast supported, lapillistone zones are less abundant and contain angular clasts. The lapillistone does not have sharp boundaries to the surrounding stratigraphy, but grades into more matrix-supported lapilli tuff with rounded clasts. The ash within the volcaniclastic rocks is generally grey to green in colour. Clasts within the volcaniclastic rocks have been partially to fully replaced by chlorite and epidote. The ash-sized material in the volcaniclastic rocks has been partially to completely replaced with chlorite and epidote.

Mafic intrusive rocks: Coarse-grained gabbro and mafic intrusive rocks cross-cut many of the units logged, predominantly in the (structural?) footwall (Fig. 4). The gabbroic rocks are coarse grained, light tan to light grey and often contain leucoxene and disseminated pyrite. Mafic dykes are fine to medium grained, variably grey to light green, locally amygdaloidal. The gabbroic rocks are sericite altered with crosscutting millimetre-scale carbonate-quartz veinlets. The mafic dykes are variably chlorite altered and are crosscut by millimetre-scale epidote and carbonate-quartz veinlets. All the intrusive rocks are < 1 m to 5 m wide and exhibit sharp boundaries with surrounding lithologies.

Argillites: the argillite lithofacies is interbedded with and stratigraphically below the iron formation (Fig. 4). This unit varies from red/maroon to green, often grading from one colour to the other. The predominant lithology in this facies consists of fine-grained and well-laminated multicoloured argillite; complete turbidite sequences with clear graded bedding are rare, but locally present. Secondary chlorite and carbonate, lesser epidote and quartz, are associated with magnetite, hematite, and sulfides. Crosscutting quartz-carbonate ± albite veins to veinlets (2 cm to 2 mm, respectively) are observed throughout this unit.

Iron Formation Lithofacies

The Goldenville horizon iron formation varies from continuous intervals up to 8 m thick to multiple thinner lenses over a broader area (Fig. 4). The horizon contains alternating layers of magnetite and light to medium grey detrital volcanogenic material (ash), likely sourced from the surrounding basalts (e.g. Mount Misery Formation). This unit also contains dark red/brown to maroon zones that are laminated, magnetic, and locally contain chert nodules and detrital volcaniclastic/pelagic material. The iron formation mineral assemblage is predominantly magnetite, hematite, and pyrite, along with secondary chlorite, calcite, quartz, and variable epidote and muscovite. The iron formation is locally cut by milky-white quartz-carbonate veins (2–6 cm) that often contain albite and iron carbonate staining.

The iron formation lithofacies are subdivided following the James (1954) definition where iron formation contains at least 15 weight % Fe. Using Fe abundances (Fig. 5a), and textural relationships, the subdivision are broken down into high-Fe iron formation (HIF) (>50% Fe_2O_3), low-Fe iron formation (LIF) (approximately 15–50% Fe_2O_3), and argillites with Fe-minerals (AIF) (<15% Fe_2O_3). The argillite facies is as described above. The primary factor controlling these compositional differences between the HIF, LIF, and AIF are the relative proportion of magnetite/hematite to detrital minerals.

Mineralization: in the Goldenville iron formation there are various styles of mineralization. Finer grained, laminated pyrite is intercalated with magnetite and hematite; this mineralization style contains mm-scale up to 6cm layering and locally graded beds. This style is interpreted to reflect VMS-style exhalative mineralization (i.e. Cambro-Ordovician and primary) (e.g. Peter, 2003). The other style consists of coarser grained (>3 mm) euhedral pyrite in the selvages of crosscutting quartz-carbonate veins that are replacing magnetite and/or along the edges of chert nodules; these pyrite grains are interpreted to have formed from wall rock sulphidation related to orogenic Au mineralization (i.e. Silurian-Devonian and secondary) (e.g. Evans, 2004). Pyrite also occurs as: 1) pyrite replacement of amygdales (synvolcanic?); 2) within pillows and along their rims/rinds/cooled margins (synvolcanic?); 3) disseminated throughout coarse-grained gabbro intrusive rocks (magmatic?); and 4) less abundantly throughout argillite and lapilli tuff units (diagenetic?).

LITHOGEOCHEMISTRY

Samples of Goldenville area iron formation and argillite were collected from surface and diamond-drill core to evaluate the lithogeochemistry. Samples were crushed and then pulverized to a homogeneous powder in agate. Powders underwent lithium metaborate fusion followed by acid digestion in preparation for analysis using inductively coupled plasma emission spectroscopy (ICP-ES) for major elements and inductively

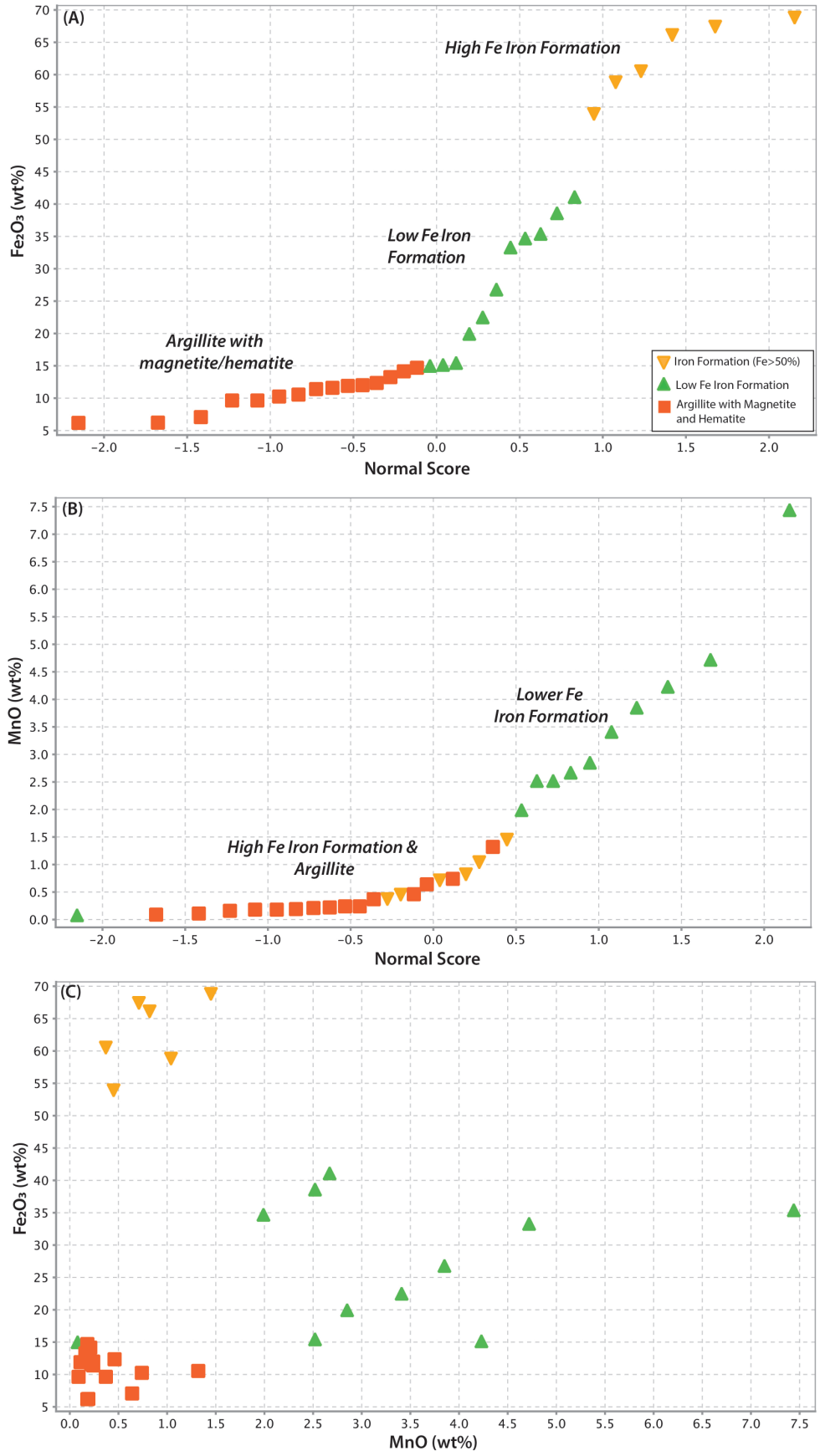

Figure 5. Probability plots of **A)** Fe_2O_3 and **B)** MnO for Fe-rich rocks in the Goldenville horizon. **C)** Fe_2O_3-MnO plot illustrating the various populations of Fe-rich rocks in the Goldenville stratigraphy.

coupled plasma mass spectrometry (ICP-MS) for trace elements. Total C and CO_2, were determined by infrared methods. All analytical work was undertaken at ALS Minerals Ltd., Vancouver, British Columbia. Additional trace element analytical work via ICP-MS was done at Geosciences Laboratories (Geo Labs) in Sudbury, Ontario, for transition metals, base metals, and semi-metals. A basalt (SLVMC) and iron formation reference material (IOC-1; CANMET) were analyzed during the program for quality control and quality assurance. Results for the basalt reference materials were presented in Mueller et al. (2021). These results provide estimates for the precision and accuracy of most trace elements. The IOC-1 iron formation certified reference material was selected due to its high-Fe matrix forming a closer match to the Goldenville iron formation; however, it is certified only for major elements and a limited number of trace elements. Results from 7 analyses of IOC-1 for major elements above the limit of quantification (3.3x limit of detection), include: 1) precision measured as percent relative standard deviation (%RSD) = SiO_2 (2.20%), Al_2O_3 (5.50%), Fe_2O_3 (0.90%), CaO (2.62%), MgO (1.86%), and MnO (1.66%); and 2) accuracy measured as percent relative difference from certified values (%RD) = SiO_2 (1.89%), Al_2O_3 (-6.06%), Fe_2O_3 (0.57%), CaO (2.86%), MgO (2.31%), and MnO (0.48%).

Despite trying to sample representative samples with minimal alteration, it is assumed that all samples underwent some element mobility during alteration and/or metamorphism. In particular, we assume that the alkali elements and low field strength element (LFSE) were mobile. This limits the elements that can be used for resolving primary rock characteristics, thus interpretations are focused on elements that are generally considered immobile: Al_2O_3, TiO_2, high field strength elements (HFSE: Zr, Hf, Nb, Ta, Th), and rare earth elements (REE) (e.g. MacLean and Barrett, 1993). Despite variable alteration, the Fe_2O_3 and MnO systematics of the iron formation and related rocks are coherent and appear to reflect original primary values (i.e., minimally affected by subsequent metamorphism and alteration).

RESULTS

Lithogeochemical data for the Goldenville horizon rocks are shown on Figures 5–9. A probability plot of Fe_2O_3 illustrates the three designated populations of iron formation and related rocks (HIF, LIF, and AIF; Fig. 5a). The three populations also show distinctive MnO relationships; the HIF and argillites having overlapping MnO contents (<1.5% MnO), whereas the LIF have MnO>1.5% and ranging from approximately 2.0 to 7.5 weight % (Fig. 5b). These units also form distinctive clusters in Fe_2O_3-MnO space (Fig. 5c).

On Böstrom-type plots (Boström et al., 1972) the HIF have >80% hydrothermal components, the LIF have approximately 40 to 60% hydrothermal contributions with dilution by some sedimentary material, and the AIF are dominated by detrital material; these rocks generally form a mixing trend between those with the highest hydrothermal components (HIF) towards those with dominantly detrital material (AIF) (Fig. 6a). In Fe-Al-Mn space a similar distribution exists where the HIF are exclusively in the hydrothermal field, the LIF straddle the hydrothermal to sedimentary fields, and the AIF are located predominantly in the non-hydrothermal field (Fig. 6b).

Post-Archean Australian Shale (PAAS)-normalized REE+Y plots of Goldenville horizon rocks are shown in Figure 7. All anomalies are calculated from PAAS-normalized (REE_n/REE_n^*) values (McLennan, 1989) and use of the Ce_n/Ce_n^*-Pr_n/Pr_n^* cross-plot in Figure 8 is as per Bau and Dulski (1996). The HIF have patterns that broadly parallel PAAS, but with slight depletions in LREE and distinctive negative Ce anomalies (Fig. 7a); these samples have true negative Ce anomalies ($Pr_n/Pr_n^*>1$) (Fig. 8a). The LIF have patterns that are similar to the HIF with flat HREE similar to PAAS, slight depletion in the LREE, and distinctly positive Ce anomalies (Fig. 7b); these samples have true positive Ce anomalies ($Pr_n/Pr_n^*<1$) (Fig. 8b). The AIF have PAAS-normalized patterns that range from samples that are strongly LREE-depleted (predominantly detrital) to those that have flat to weak positive Ce anomalies (Fig. 8c, 9c). When Ce anomalies, measured as Ce_n/Ce_n^*, are compared to MnO and Fe_2O_3 there are distinctive relationships. Those samples with the highest MnO contents and intermediate hydrothermal Fe signatures have the most positive Ce anomalies ($Ce_n/Ce_n^*>1$), whereas the samples with the highest Fe_2O_3 and hydrothermal Fe signature have the most negative Ce anomalies ($Ce_n/Ce_n^*<1$) (Fig. 9b, c).

DISCUSSION AND SUMMARY

The lithogeochemistry of the Goldenville iron formation and associated rocks confirms that they are hydrothermal in origin with varying contributions from detrital material (e.g. Fig. 6). It is generally accepted that Algoma-type iron formations form by exhalation of iron-rich fluids into ambient seawater either during the initial stages of hydrothermal venting and/or during the waning stages of hydrothermal activity (Grenne and Slack, 2003; Peter, 2003; Slack et al., 2007). As hydrothermal Fe particles vent into ambient seawater they are electrostatically charged and can adsorb various elements (e.g. REE+Y) dissolved in seawater (Elderfield and Greaves, 1981; Elderfield et al., 1981; German et al., 1993; Bau, 1999; German and Von Damm, 2006). Upon deposition on the seafloor as hydrothermal sediments the rocks contain a record of both hydrothermal venting, but also the ambient composition of seawater at the time of formation (e.g. Bau and Dulski, 1996; Slack et al., 2007). As a result, considerable research has demonstrated that such hydrothermal sedimentary rocks are excellent proxies for ancient ocean redox conditions (Elderfield and Greaves, 1981; Elderfield et al., 1981; Bau and Dulski, 1996; Grenne and Slack, 2003; Slack et al., 2007; Lode et al., 2015; Piercey et al., 2018). The

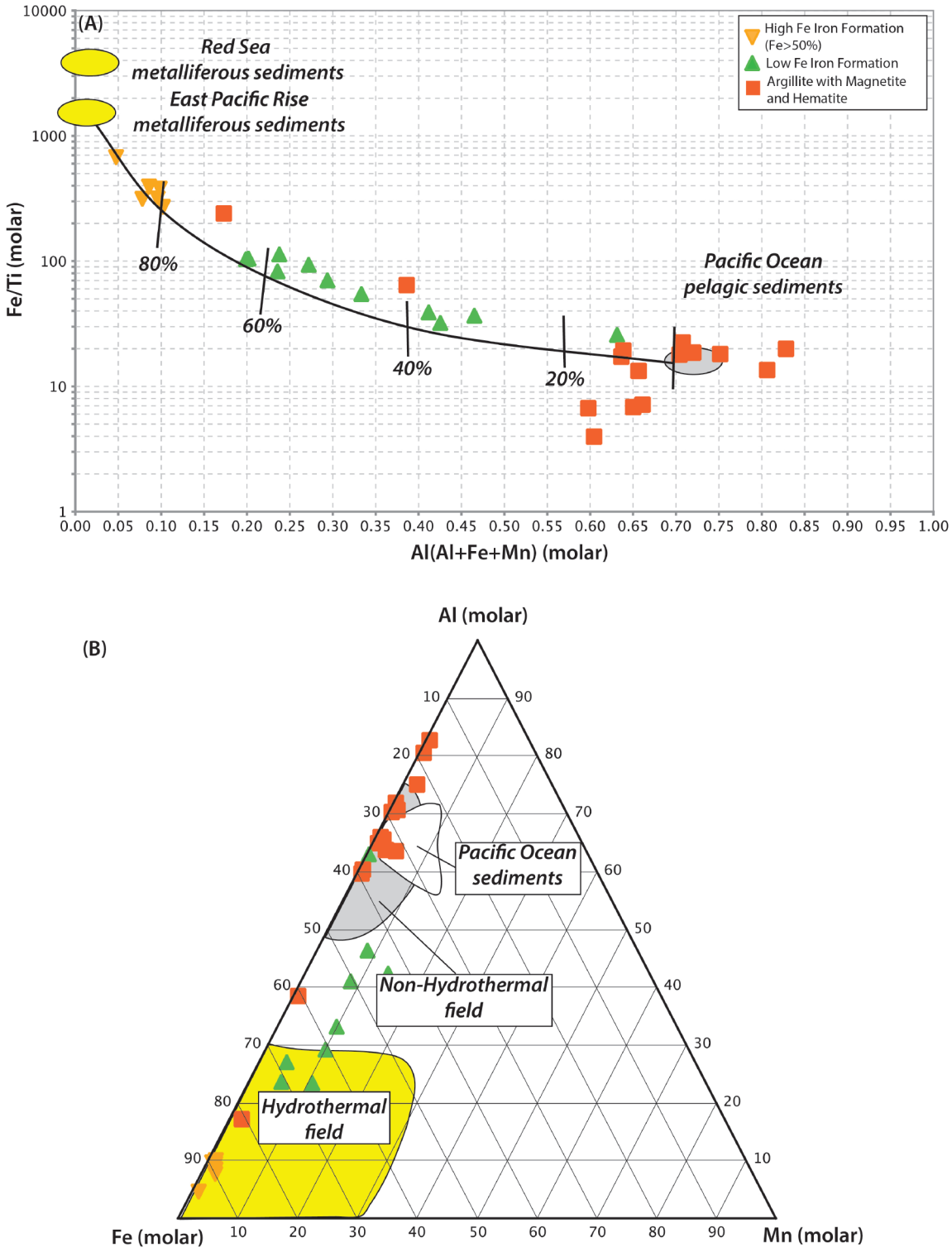

Figure 6. Böstrom-type plots for the sedimentary and iron formation samples from the Goldenville horizon. **A)** Molar Fe/Ti-Al/(Al+Fe+Mn) diagram with mixing lines between hydrothermal sources and background sedimentary materials. The iron formation population is predominantly comprised of hydrothermal Fe, whereas the argillites have predominantly sedimentary detritus; the low Fe iron formations have features intermediate between hydrothermal and sedimentary end members. **B)** Molar Fe-Al-Mn diagram illustrating that the iron formations lie in the hydrothermal field, the argillites predominantly cluster proximal to the sedimentary field, whereas the low Fe iron formations range from being dominated by hydrothermal material to those with an abundant detrital component. Diagrams from Boström et al. (1972).

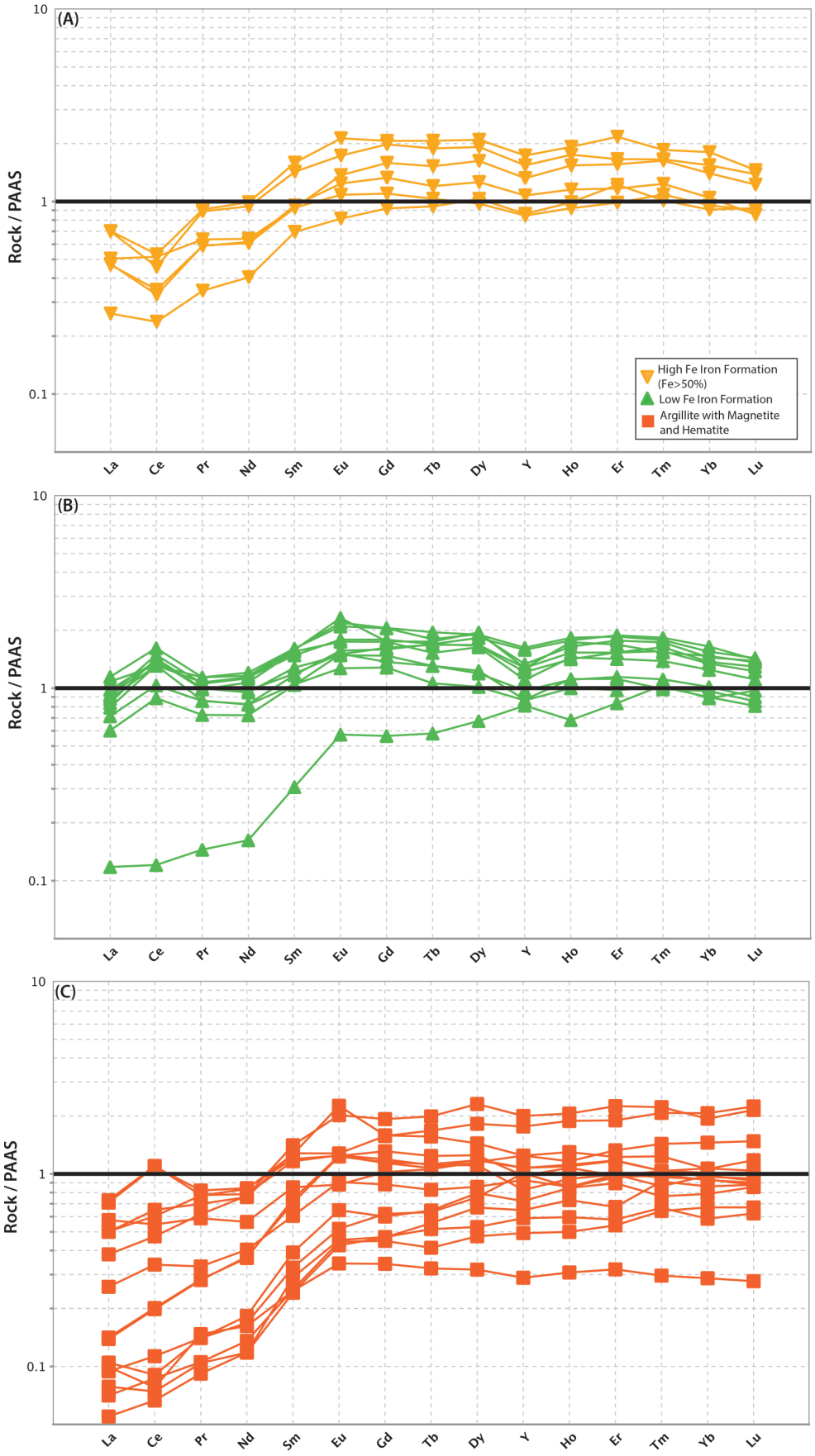

Figure 7. Post-Archean Australian Shale (PAAS) normalized REE-Y plots of Fe-rich rocks from the Goldenville horizon. **A)** High Fe iron formations (HIF group). **B)** low Fe iron formations (LIF group). **C)** Argillites with Fe-minerals (AIF group).

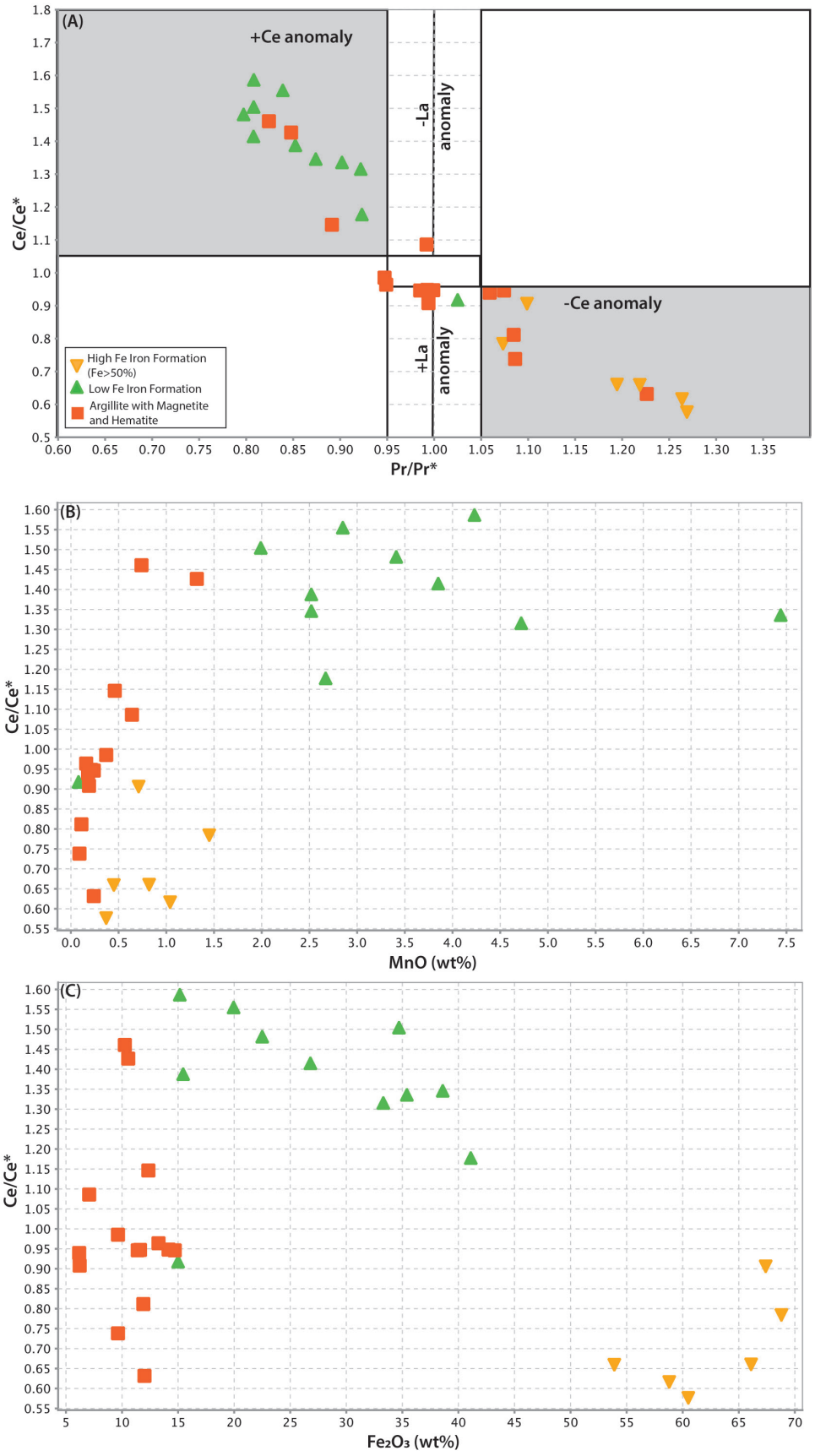

Figure 8. A) Ce_n/Ce_n^*-Pr_n/Pr_n^* plot demonstrating that the LIF and some AIF samples have true positive Ce anomalies, whereas the HIF and some AIF samples have true negative anomalies. Remaining AIF samples cluster near unity indicative of no Ce anomalies. Diagram after Bau and Dulski (1996) and Kamber and Webb (2001). $Ce_n^* = (0.5La_n + 0.5Pr_n)$ and $Pr_n^* = (0.5Ce_n + 0.5Nd_n)$; **B)** Ce_n/Ce_n^* versus MnO illustrating that the most positive Ce anomalies are generally associated with samples with the highest MnO content. **C)** Ce_n/Ce_n^* versus Fe_2O_3 illustrating that the most negative Ce anomalies are associated with samples with the highest Fe_2O_3 content. REE_n = PAAS-normalized values (McLennan, 1989).

geochemistry, and in particular the REE systematics, of the Goldenville iron formation can provide insight into the late Cambrian to early Ordovician (ca. 488–485 Ma) redox state of the Taconic seaway proximal to the Laurentian craton.

The REE signature of modern seawater has a distinctive Ce anomaly that is reflective of high oxygen levels (e.g. Elderfield and Greaves, 1982; de Baar et al., 1991). Under oxygenated ocean conditions, any Mn associated with hydrothermal venting results in deposition of Mn-oxides (e.g. Mn-nodules) and Ce is strongly adsorbed onto MnO particles effectively removing Ce from seawater. This process results in some pelagic sediments enriched in Ce (i.e. displaying positive Ce anomalies) and the remaining seawater depleted (negative Ce anomalies) (Elderfield et al., 1981; de Baar et al., 1988; Elderfield et al., 1988). Under anoxic conditions, hydrothermal Mn is not readily oxidized and the ambient reduced seawater can develop a positive Ce anomaly from the dissolution of oxides formed in shallow marine environments that scavenged REE (de Baar et al., 1988). Correspondingly, in contrast to fully oxygenated seawater, hydrothermal venting into sub-oxic to anoxic deep marine environments results in hydrothermal sedimentary rocks with Ce anomalies that are flat or positive (Slack et al., 2007).

The Goldenville iron formation exhibits variable Ce anomalies. Namely, the highest Fe_2O_3 iron formation samples (HIF group) have negative Ce anomalies, suggesting they vented into oxygenated seawater, whereas the lower Fe_2O_3 iron formation samples (LIF group) generally have positive Ce anomalies, which suggest they vented into anoxic or sub-oxic seawater (Fig. 7, 8). The presence of both positive and negative Ce anomalies in iron formations within the same stratigraphic unit, and in some cases between samples within metres of one another in the same drill hole, is paradoxical. However, this could be explained via the varying Fe_2O_3-MnO relationships of the different iron formations. In particular, those samples with the most positive Ce anomalies have the highest MnO contents (Fig. 8). Rather than being deposited under anoxic or sub-oxic conditions, these samples may record a greater extent of oxidation of Mn in an oxygenated water column, scavenging of Ce from seawater onto Mn-oxide particles, and then deposition into hydrothermal sediment. In essence, these samples record more extensive Mn-oxide particle-REE interaction and perhaps direct oxidation of Ce(III) on their surfaces relative to the lower MnO iron formation samples. These inferred conditions would be consistent with the negative Ce anomalies of the LIF group that point towards oxygen-rich bottom water conditions. Further research is required to test this working hypothesis, and better establish the Fe vs. Mn scavenging processes and relationships of Fe-Mn-REE to other particle-reactive metals soluble in oxygenated waters (e.g. V, Mo). Nevertheless, initial results suggest that during the formation of the Goldenville horizon in the late Cambrian - early Ordovician that the ocean was fully or near fully oxygenated and not unlike modern ocean conditions.

In addition to being a proxy for ocean oxygen conditions, the Goldenville horizon is both host to exhalative magnetite-pyrite and a chemical trap for subsequent orogenic Au mineralization. Further research will be focused on investigating the VMS and orogenic Au potential of this horizon.

ACKNOWLEDGMENTS

We would like to thank staff from Anaconda Mining for their logistical support and for discussions during this project, including Steve Barrett, Dean Courage, Alison Cox, Michelle English, Linsey Gale, and Paul McNeill. Discussions regarding the geology of the Baie Verte Peninsula with Sebastien Castonguay, Greg Dunning, Graham Layne, and Tom Skulski are also acknowledged. This research was funded by grants to Piercey and Babechuk from the Targeted Geoscience Initiative 5 (TGI5) program from Natural Resources Canada (NRCan); Anaconda Mining Ltd; an NSERC Collaborative Research and Development Grant and NSERC Discovery Grants. These funding agencies are thanked for their support of our research. We are particularly grateful for the thorough and thoughtful comments of Dr. Neil Rogers. His comments have improved the manuscript significantly.

REFERENCES

Bau, M., 1999. Scavenging of dissolved yttrium and rare earths by precipitating iron oxyhydroxide; experimental evidence for Ce oxidation, Y-Ho fractionation, and lanthanide tetrad effect; Geochimica et Cosmochimica Acta, v. 63, p. 67–77.

Bau, M. and Dulski, P., 1996. Distribution of yttrium and rare-earth elements in the Penge and Kuruman iron-formations, Transvaal Supergroup, South Africa; Precambrian Research, v. 79, p. 37–55.

Bédard, J.H., Lauzière, K., Tremblay, A., Sangster, A., Douma, S.L., and Dec, T., 2000. Betts Cove Ophiolite and its cover rocks, Newfoundland; Geological Survey of Canada, Bulletin 550, 76 p.

Boström, K., Joensuu, O., Valdés, S., and Riera, M., 1972. Geochemical history of South Atlantic Ocean sediments since Late Cretaceous; Marine Geology, v. 12, p. 85–121.

Brueckner, S.M., Piercey, S.J., Sylvester, P.J., Maloney, S., and Pilgrim, L., 2014. Evidence for Syngenetic Precious Metal Enrichment in an Appalachian Volcanogenic Massive Sulfide System: The 1806 Zone, Ming Mine, Newfoundland, Canada; Economic Geology, v. 109, p. 1611–1642.

de Baar, H.J.W., German, C.R., Elderfield, H., and van Gaans, P., 1988. Rare earth element distributions in anoxic waters of the Cariaco Trench; Geochimica et Cosmochimica Acta, v. 52, p. 1203–1219.

de Baar, H.J.W., Schijf, J., and Byrne, R.H., 1991. Solution chemistry of the rare earth elements in seawater; European Journal of Solid State Inorganic Chemistry, v. 28, p. 357–373.

Dunning, G.R. and Krogh, T.E., 1985. Geochronology of ophiolites of the Newfoundland Appalachians; Canadian Journal of Earth Sciences, v. 22, p. 1659–1670.

Elderfield, H., Charnock, H., Lovelock, J.E., Liss, P.S., and Whitfield, M., 1988. The oceanic chemistry of the rare-earth elements; Philosophical Transactions of the Royal Society of London, Series A: Mathematical and Physical Sciences, v. 325, p. 105–124.

Elderfield, H. and Greaves, M.J., 1981. Negative cerium anomalies in the rare earth element patterns of oceanic ferromanganese nodules; Earth and Planetary Science Letters, v. 55, p. 163–170.

Elderfield, H. and Greaves, M.J., 1982 The rare earth elements in seawater; Nature, v. 296, p. 214–219.

Elderfield, H., Hawkesworth, C.J., Greaves, M.J., and Calvert, S.E., 1981. Rare earth element geochemistry of oceanic ferromanganese nodules and associated sediments; Geochimica et Cosmochimica Acta, v. 45, p. 513–528.

Evans, D.T.W., 2004. Epigenetic Gold Occurrences, Baie Verte Peninsula (NTS 12H/09, 16 and 121/01, Newfoundland; Government of Newfoundland and Labrador, Department of Natural Resources, Geological Survey, Mineral Resources Report no. 11, 157 p.

German, C.R. and Von Damm, K.L., 2006. Hydrothermal Processes; in The Oceans and Marine Geochemistry: Treatise on Geochemistry, v. 6, (ed.) H. Elderfield. Pergamon, Oxford, United Kingdom, p. 181–222.

German, C.R., Higgs, N.C., Thomson, J., Mills, R., Elderfield, H., Blusztajn, J., Fleer, A.P., and Bacon, M.P., 1993. A Geochemical Study of Metalliferous Sediment From the TAG Hydrothermal Mound, 26o08'N, Mid-Atlantic Ridge; Journal of Geophysical Research, v. 98, p. 9683–9692.

Grenne, T. and Slack, J.F., 2003. Bedded jaspers of the Ordovician Lokken Ophiolite, Norway; seafloor deposition and diagenetic maturation of hydrothermal plume-derived silica-iron gels; Mineralium Deposita, v. 38, p. 625–639.

Hibbard, J., 1983. Geology of the Baie Verte Peninsula, Newfoundland; Memoir - Government of Newfoundland and Labrador, Department of Mines and Energy, Mineral Development Division, Vol. 2, 279 p.

Kamber, B.S., and Webb, G.E., 2001. The geochemistry of late Archaean microbial carbonate; implications for ocean chemistry and continental erosion history; Geochimica et Cosmochimica Acta, v. 65, p. 2509–2525.

Kessler, L.G., and Bedard, J.H., 2000. Epiclastic volcanic debrites; evidence of flow transformations between avalanche and debris flow processes, Middle Ordovician, Baie Verte Peninsula, Newfoundland, Canada; Precambrian Research, v. 101, p. 135–161.

Lode, S., Piercey, S.J., and Devine, C.A., 2015. Geology, Mineralogy, and Lithogeochemistry of Metalliferous Mudstones Associated with the Lemarchant Volcanogenic Massive Sulfide Deposit, Tally Pond Belt, Central Newfoundland; Economic Geology, v. 110, p. 1835–1859.

MacLean, W.H., and Barrett, T.J., 1993. Lithogeochemical techniques using immobile elements: Journal of Geochemical Exploration, v. 48, p. 109–133.

McLennan, S.M., 1989. Rare earth elements in sedimentary rocks; influence of provenance and sedimentary processes; Reviews in Mineralogy, v. 21, p. 169–200.

Pawlukiewicz, M., 2020. Hydrothermal Reconstruction and Lithogeochemistry of the Argyle Orogenic Gold Deposit, Baie Verte, Newfoundland; M.Sc. thesis, Memorial University of Newfoundland, St. John's, Newfoundland and Labrador, 412 p.

Peter, J.M., 2003. Ancient iron formations: their genesis and use in the exploration for stratiform base metal sulphide deposits, with examples from the Bathurst Mining Camp; *in* Geochemistry of Sediments and Sedimentary Rocks: Secular Evolutionary Considerations to Mineral Deposit-Forming Environments, GEOtext v.4., (ed.) D.R. Lentz. Geological Association of Canada, p. 145–176.

Piercey, S.J., Squires, G., and Brace, T., 2018. Geology and lithogeochemistry of hydrothermal mudstones from the upper block near the Duck Pond volcanogenic massive sulfide (VMS) deposit, Newfoundland, Canada: evidence for low-temperature venting into oxygenated mid-Cambrian seawater; Mineralium Deposita, v. 53, p. 1167–1191.

Pilote, J.-L., Piercey, S.J., and Mercier-Langevin, P., 2017. Volcanic and Structural Reconstruction of the Deformed and Metamorphosed Ming Volcanogenic Massive Sulfide Deposit, Canada: Implications for Ore Zone Geometry and Metal Distribution; Economic Geology, v. 112, p. 1305–1332.

Ramezani, J., Dunning, G.R., and Wilson, M.R., 2000. Geologic setting, geochemistry of alteration, and U-Pb age of hydrothermal zircon from the Silurian Stog'er Tight gold prospect, Newfoundland Appalachians, Canada; Exploration and Mining Geology, v. 9, p. 171–188.

Sangster, A.L., Douma, S.L., and Lavigne, J., 2007. Base metal and gold deposits of the Betts Cove Complex, Baie Verte Peninsula, Newfoundland; *in* Mineral Deposits of Canada: A Synthesis of Major Deposit-types, District Metallogeny, the Evolution of Geological Provinces, and Exploration Methods, (ed.) W.D. Goodfellow. Mineral Deposits Division, Special Publication 5, Geological Association of Canada, p. 703–721.

Skulski, T., Castonguay, S., van Staal, C.R., Rogers, N., McNicoll, V., Kerr, A., and Escayloa, M., 2009. Baie Verte Peninsula: An evolving geological story; Geological Association of Canada Newfoundland and Labrador Section, 76 p.

Skulski, T., Castonguay, S., McNicoll, V., van Staal, C., Kidd, W.S.F., Rogers, N., Morris, W., Ugalde, H., Slavinski, H., Spicer, W., Moussallam, Y., and Kerr, I., 2010. Tectonostratigraphy of the Baie Verte Oceanic Tract and its ophiolite cover sequence on the Baie Verte Peninsula; Current Research - Newfoundland and Labrador Department of Natural Resources, Geological Survey, Report 10-1, p. 315–225.

Skulski, T., Castonguay, S., Kidd, W.S.F., McNicoll, V., van Staal, C.R., and Hibbard, J.P., 2015. Baie Verte and parts of Fleur de Lys, Newfoundland and Labrador, NTS 12-H/16 and part of NTS 12-I/1; Canadian Geoscience Map 159, Geological Survey of Canada, 1 sheet.

Slack, J.F., Grenne, T., Bekker, A., Rouxel, O.J., and Lindberg, P.A., 2007. Suboxic deep seawater in the late Paleoproterozoic: Evidence from hematitic chert and iron formation related to seafloor-hydrothermal sulfide deposits, central Arizona, USA; Earth and Planetary Science Letters, v. 255, p. 243–256.

van Staal, C.R., and Barr, S.M., 2012. Lithospheric architecture and tectonic evolution of the Canadian Appalachians and associated Atlantic margin. Chapter 2; *in* Tectonic Styles in Canada: the LITHOPROBE Perspective, (ed.) J.A. Percival, F.A. Cook, and R.M. Clowes. Geological Association of Canada, Special Paper 49, p. 41–96.

van Staal, C.R., 2007. Pre-Carboniferous tectonic evolution and metallogeny of the Canadian Appalachians; *in* Mineral Deposits of Canada: A Synthesis of Major Deposit-types, District Metallogeny, the Evolution of Geological Provinces, and Exploration Methods, (ed.) W.D. Goodfellow. Mineral Deposits Division, Special Publication 5, Geological Association of Canada, p. 793–818.

Waldron, J.W.F., and van Staal, C.R., 2001. Taconian Orogeny and the accretion of the Dashwoods Block; a peri-Laurentian microcontinent in the Iapetus Ocean; Geology, v. 29, p. 811–814.

Ybarra, S., Piercey, S.J., Layne, G.D., Copeland, D.A., and McNeill, P., 2017. Alteration halo and lithostratigraphy of the Pine Cove orogenic gold deposit, Baie Verte Peninsula, Newfoundland, Canada; Proceedings of the 14th SGA Biennial Meeting, Quebec, Québec, Society of Geology Applied to Mineral Deposits, p. 219–222.

Whole-rock lithogeochemistry, Nd-Hf isotopes, and in situ zircon geochemistry of VMS-related felsic rocks, Finlayson Lake VMS district, Yukon

M.J. Manor[1*] and S.J. Piercey[1]

Manor, M.J., and Piercey, S.J., 2021. Whole-rock lithogeochemistry, Nd-Hf isotopes, and in situ zircon geochemistry of VMS-related felsic rocks, Finlayson Lake VMS district, Yukon; in *Targeted Geoscience Initiative 5:grant program final reports (2018-2020), Geological Survey of Canada, Open File 8755, p. 251–264. https://doi.org/10.4095/328992*

Abstract: The Finlayson Lake district in southeastern Yukon is composed of a Late Paleozoic arc–back-arc system that consists of metamorphosed volcanic, plutonic, and sedimentary rocks of the Yukon-Tanana and Slide Mountain terranes. These rocks host >40 Mt of polymetallic resources in numerous occurrences and styles of volcanogenic massive sulphide (VMS) mineralization. Geochemical and isotopic data from these rocks support previous interpretations that volcanism and plutonism occurred in arc-marginal arc (e.g., Fire Lake formation) and continental back-arc basin environments (e.g., Kudz Ze Kayah formation, Wind Lake formation, and Wolverine Lake group) where felsic magmatism formed from varying mixtures of crust- and mantle-derived material. The rocks have elevated high field strength element (HFSE) and rare earth element (REE) concentrations, and evolved to chondritic isotopic signatures, in VMS-proximal stratigraphy relative to VMS-barren assemblages. These geochemical features reflect the petrogenetic conditions that generated felsic rocks and likely played a role in the localization of VMS mineralization in the district. Preliminary *in situ* zircon chemistry supports these arguments with Th/U and Hf isotopic fingerprinting, where it is interpreted that the VMS-bearing lithofacies formed via crustal melting and mixing with increased juvenile, mafic magmatism; rocks that were less prospective have predominantly crustal signatures. These observations are consistent with the formation of VMS-related felsic rocks by basaltic underplating, crustal melting, and basalt-crustal melt mixing within an extensional setting. This work offers a unique perspective on magmatic petrogenesis that underscores the importance of integrating whole-rock with mineral-scale geochemistry in the characterization of VMS-related stratigraphy.

[1]Department of Earth Sciences, Memorial University of Newfoundland, Alexander Murray Building, 9 Arctic Ave, St. John's, Newfoundland and Labrador, Canada A1B 3X5
*Corresponding author (e-mail: mjmanor@mun.ca)

PURPOSE AND OBJECTIVES OF STUDY

The Finlayson Lake district, south-central Yukon, contains >40 Mt of polymetallic (Zn-Pb-Cu-Co-Au-Ag) volcanogenic massive sulphide (VMS) mineralization and represents one of northern Canada's most significant undeveloped base metal resources (Peter et al., 2007). The region is defined by a complex Paleozoic tectonic history that resulted in the formation of numerous VMS deposits related to mafic and felsic volcanism in the Upper Devonian to Early Mississippian (Murphy et al., 2006; Peter et al., 2007). Preliminary lithogeochemistry has identified distinct signatures of VMS-bearing and barren felsic volcanic rocks and proximal subvolcanic intrusions (Piercey et al., 2001; 2003; 2008), and recent use of bulk rock Nd-Hf isotopic geochemistry has addressed critical knowledge gaps related to the fertility and prospectivity of Yukon mineral belts (e.g., Wolverine VMS deposit; Piercey et al., 2017). These studies indicate that felsic rocks directly related to VMS formation contain more juvenile, mantle-derived (i.e., high-T) components relative to pre-VMS volcanic rocks and demonstrate that petrologic parameters (e.g., T, redox) may be more important to VMS genesis than previously considered. Despite these recent advances in geochemical fingerprinting within the Finlayson Lake district, the precise age of volcanic rock packages, subvolcanic intrusions, and VMS genesis, as well as fundamental magmatic petrological parameters that describe the melting, fractionation, and crystallization history of these felsic magmas, are poorly constrained.

The current research aims to provide a new perspective to three topics: 1) the formation of VMS deposits in the Yukon with applications to global models, including components of heat supply, fluid circulation, and timing/episodicity of mineralization events; 2) crustal evolution models for Cordilleran tectonics; and 3) the interplay of tectonics, magmatism, and ore formation. Integration of these topics can advance our scientific knowledge in ore deposit research with respect to specific tectonic environments which can be applied to discriminate prospective from less prospective stratigraphic sequences in other orogenic belts and deposit types globally (e.g., porphyry Cu and epithermal Au deposits; Piercey, 2011). The comparative mineral-scale petrology will ultimately redefine the chronostratigraphic framework of the Finlayson Lake district, add constraints on the timing and magmatic controls of VMS mineralization in the Yukon-Tanana terrane, and provide insight to existing models for VMS deposit genesis. This dataset will directly test the basaltic upwelling model hypothesis whereby mafic magmas are critical driving forces for VMS formation at continental margins (e.g., Piercey et al., 2008), and supply critical information to crustal growth models and terrane prospectivity and fertility for the North American Cordillera.

GEOLOGICAL SETTING

The Finlayson Lake VMS district of southeastern Yukon is a fault-bounded portion of the Devonian to Permian Yukon-Tanana and Slide Mountain terranes that formed off of the western peri-Laurentian continental margin (Fig. 1; Tempelman-Kluit, 1979; Mortensen and Jilson, 1985; Murphy et al., 2006). Rocks that comprise Yukon-Tanana terrane arc and back-arc assemblages are variably deformed and metamorphosed volcanic, plutonic, and sedimentary rocks that locally retain primary geological and geochemical characteristics; these rocks were deposited or intruded above a pre- to Late Devonian basement (Colpron et al., 2006b; Murphy et al., 2006; Piercey et al., 2006; Piercey and Colpron, 2009). The Jules Creek transform fault juxtaposes the Yukon-Tanana terrane adjacent to ophiolitic rocks of the Slide Mountain terrane (Murphy et al., 2006), which were then together thrust above North American miogeoclinal strata along the Inconnu thrust in the Late Jurassic (Murphy et al., 2002). The current geographical configuration of the Yukon-Tanana terrane in central Yukon was attained in the Eocene following ~430 km of displacement along the Tintina strike-slip dextral fault system, which ultimately resulted in the offset sliver now referred to as the Finlayson Lake district (Figs. 1 and 2; Gabrielse et al., 2006).

Yukon-Tanana terrane rocks within the Finlayson Lake district are hosted in three distinct structural panels (from structurally-deepest to shallowest): the Big Campbell, Money Creek, and Cleaver Lake thrust sheets (Fig. 2; Murphy et al., 2006). Pre-Upper Devonian metasedimentary rocks of the North River formation comprise the basement to both the Big Campbell and Money Creek thrust sheets, but is not observed beneath the Cleaver Lake thrust sheet. The Big Campbell thrust sheet is bounded below by the post-Late Triassic Big Campbell thrust fault and above by the Early Permian Money Creek thrust fault (Fig. 2). Rocks in the Big Campbell thrust sheet are predominantly Middle to Upper Devonian mafic and felsic metavolcanic and metasedimentary rocks of the Grass Lakes group, which includes the basal pre-Upper Devonian North River formation and overlying Fire Lake, Kudz Ze Kayah, and Wind Lake formations (Fig. 2). Late Devonian granitoid intrusions of the Grass Lakes plutonic suite cut the Grass Lakes group and were then both unconformably overlain by Lower Mississippian metaclastic and, mafic to felsic metavolcanic, rocks of the Wolverine Lake group (Fig. 2). The Grass Lakes group contains VMS mineralization at the Kudz Ze Kayah, GP4F, and Fyre Lake deposits, and the Wolverine Lake group contains the Wolverine deposit (Piercey et al., 2001; Sebert et al., 2004; Peter et al., 2007; Bradshaw et al., 2008; Piercey et al., 2016). Together, these deposits are interpreted to have formed in an evolving continental arc to back-arc basin tectonic setting (Piercey et al., 2001, 2002b, 2004, 2006; Murphy et al., 2006).

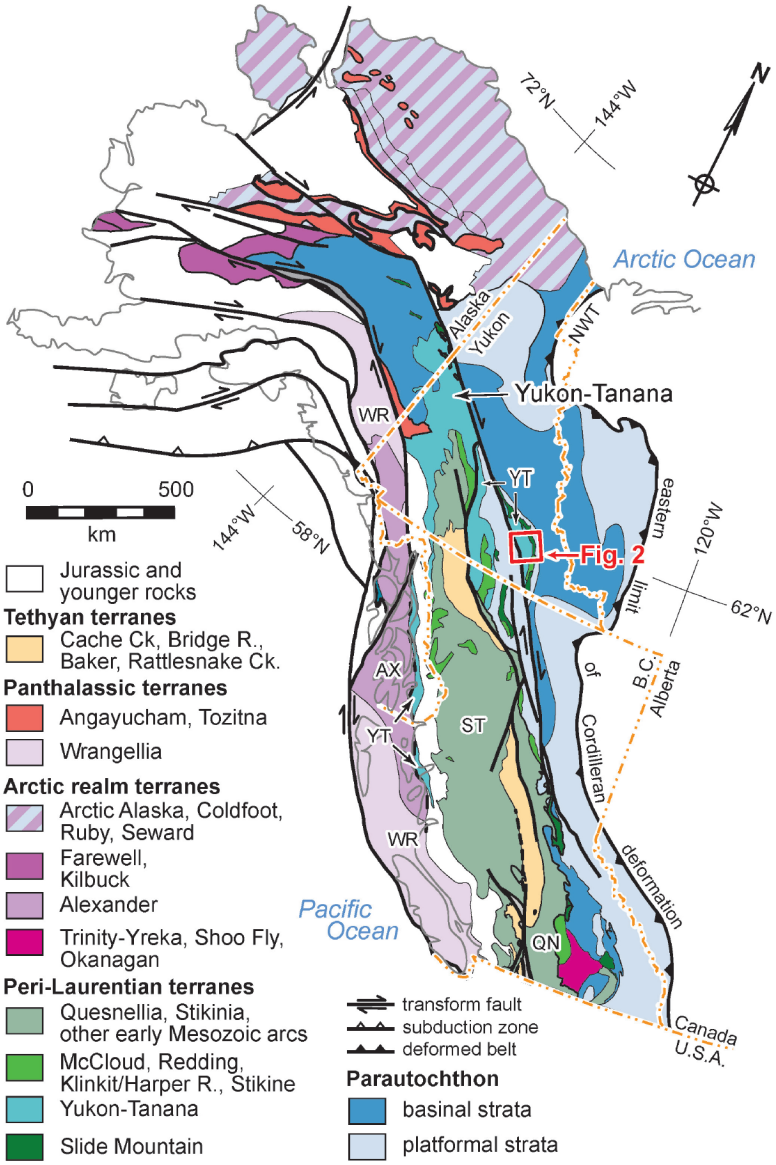

Figure 1. Paleozoic to early Mesozoic terranes of the northern Canadian Cordillera in British Columbia, Yukon, and Alaska (modified after Colpron and Nelson, 2011). AX=Alexander, QN=Quesnellia, ST=Stikinia, YT=Yukon-Tanana, WR=Wrangellia.

The Money Creek thrust sheet contains the pre-Upper Devonian North River formation that is overlain by Upper Devonian to Lower Mississippian felsic to intermediate metavolcanic and metasedimentary rocks (Waters Creek and Tuchitua River formations). These rock units are intruded by granitic rocks of the Late Devonian to Early Mississippian Simpson Range plutonic suite, then capped by Mississippian to Lower Permian limestone, mafic metavolcanic and metaclastic rocks (Fig. 2; Mortensen, 1992; Grant, 1997; Murphy et al., 2006). The Money Creek thrust sheet, which structurally underlies the Cleaver Lake thrust sheet, is comprised primarily of relatively undeformed and unmetamorphosed Late Devonian mafic and felsic volcanic rocks (Cleaver Lake formation) that overlie mafic and ultramafic rocks; these rock units are subsequently intruded by Early Mississippian granitoids of the Simpson Range plutonic suite (Tempelman-Kluit, 1979; Piercey and Murphy, 2000; Murphy et al., 2006). The Cleaver Lake thrust sheet was thrust above the Money Creek thrust sheet along the Early Permian Cleaver Lake thrust fault after the Early Permian (Murphy et al., 2006). The rocks in the Money Creek and Cleaver Lake thrust sheets were generated in a continental arc setting to the southwest of the Big Campbell thrust sheets and are not associated with any known VMS mineralization (Grant, 1997; Piercey et al., 2001, 2003, 2006; Murphy et al., 2006).

SAMPLING AND ANALYTICAL METHODS

During the 2017 and 2018 field seasons, samples of felsic and mafic volcanic, plutonic, and sedimentary rocks were taken from outcrops and drill core at different stratigraphic levels of the Big Campbell and Cleaver Lake thrust sheets (Fig. 2a). Drill core into the Kudz Ze Kayah formation

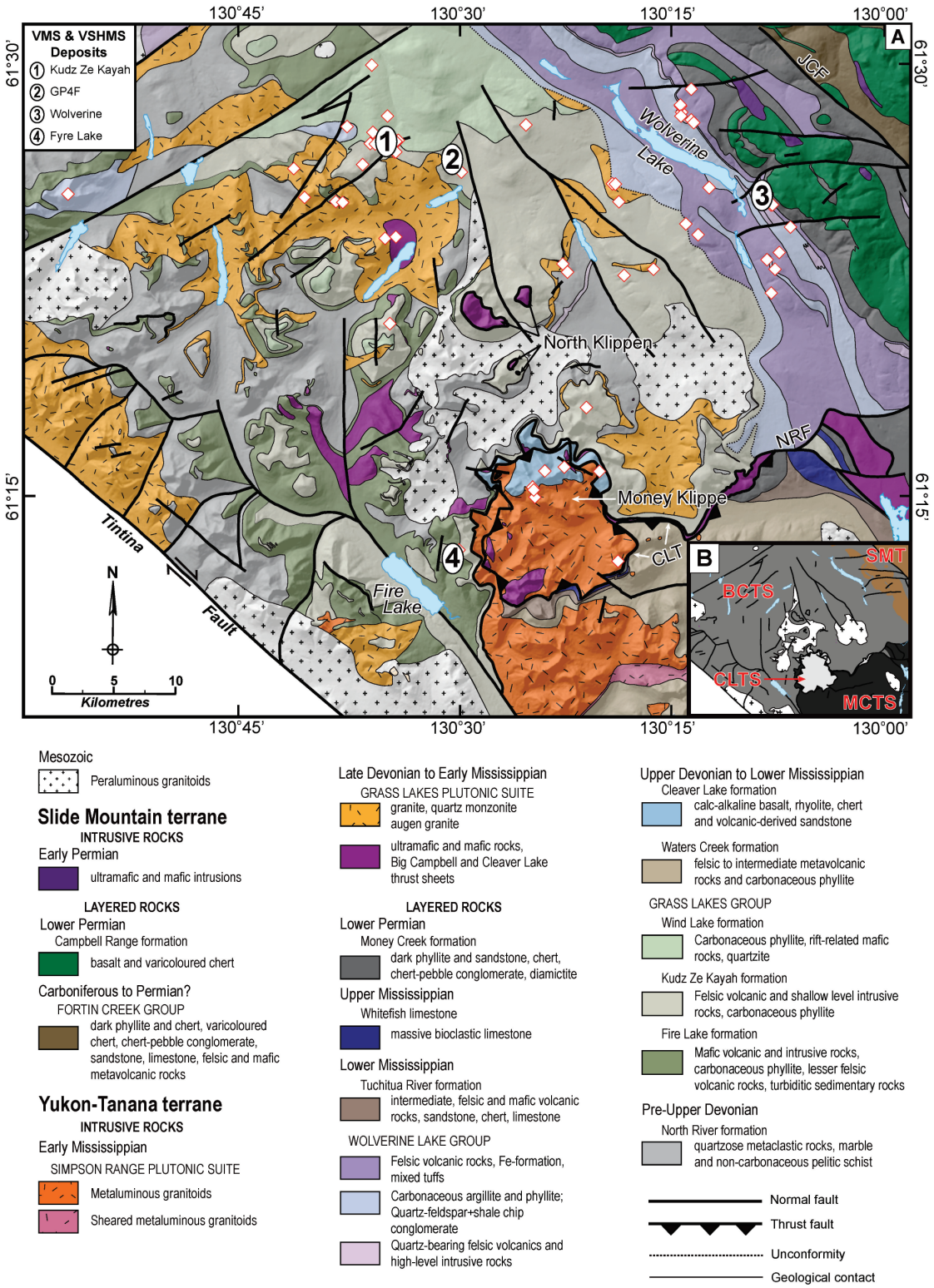

Figure 2. (A) Regional geologic setting of the south-central Finlayson Lake region, Yukon-Tanana terrane (modified after Piercey et al., 2003, and Yukon Geological Survey, 2018). The Money Creek thrust fault crops out south of the extent of the figure. Numbers indicate locations of prospective VMS deposits in the region. Diamonds indicate sample locations. VMS=volcanogenic massive sulphide; VSHMS=volcanic sediment-hosted massive sulphide; CLT=Cleaver Lake thrust; NRF=North River fault; JCF=Jules Creek fault. **(B)** Inset map, showing distribution of major thrust sheets containing Yukon-Tanana terrane rocks in the Finlayson Lake district. BCTS=Big Campbell thrust sheet; MCTS=Money Creek thrust sheet; CLTS=Cleaver Lake thrust sheet; SMT = Slide Mountain terrane.

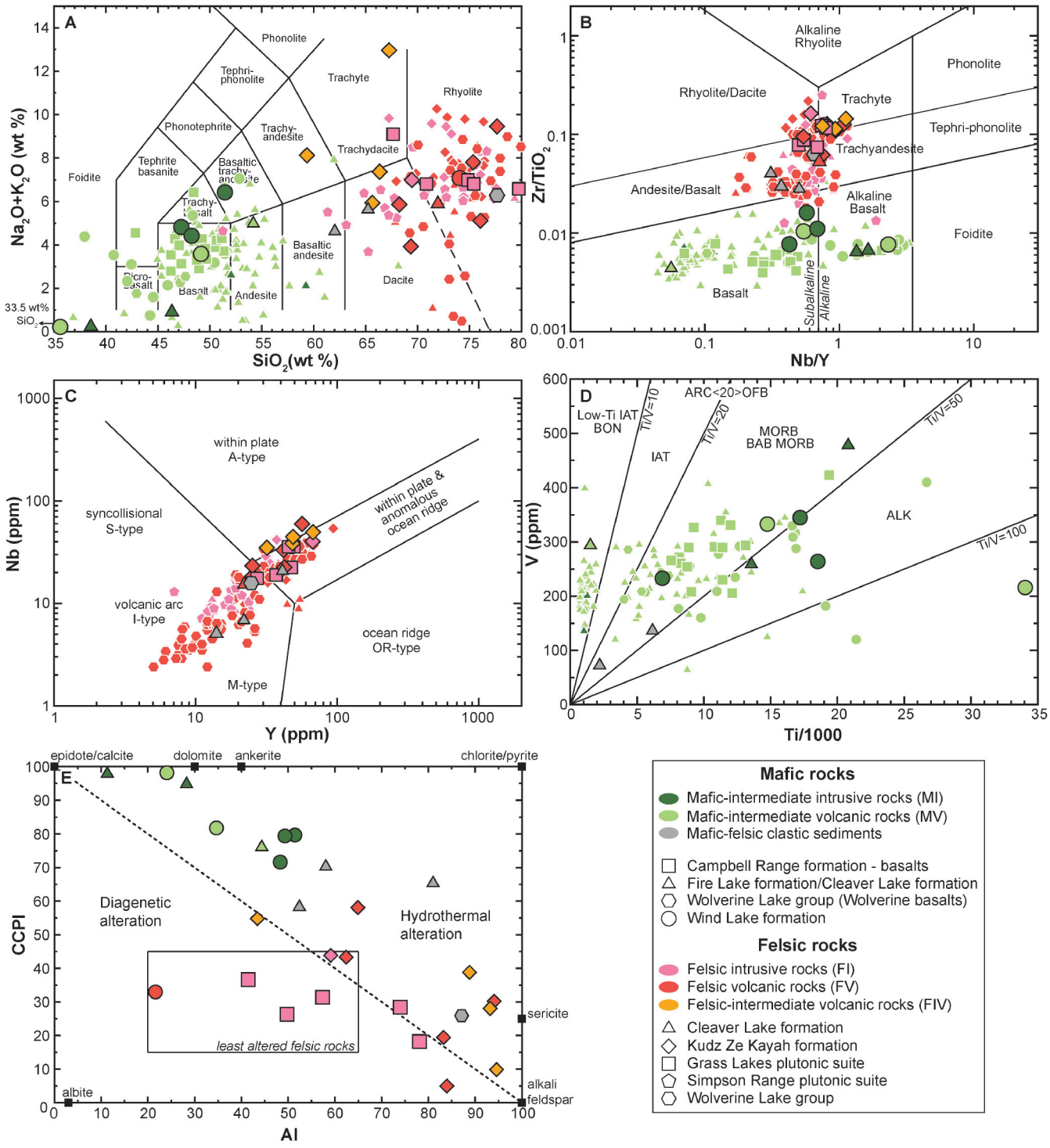

Figure 3. Major and trace element discrimination diagrams for felsic and mafic rocks in the Finlayson Lake region. Samples from this study are shown as the largest symbols with black outlines; archival data are smaller symbols with white outlines (Piercey, 2001; Piercey et al., 2001, 2002a, b, c, 2003, 2004, 2008, 2012). **(A)** SiO_2 vs. Na_2O+K_2O, analyses from the Wolverine deposit hanging wall have SiO_2 contents above 80 wt.% and are not included; **(B)** Nb/Y vs. Zr/TiO_2 (Pearce, 1996 after Winchester and Floyd, 1977) ; **(C)** Y vs. Nb (Pearce et al., 1984); **(D)** Ti/1000 vs. V (Shervais, 1982); **(E)** CCPI (chlorite-carbonate-pyrite index) vs. Al (Ishikawa alteration index; Ishikawa et al., 1976, from Large et al., 2001). IAT=island arc tholeiite; BON=boninite; OFB=ocean floor basalt; MORB=mid-ocean ridge basalt; BAB=back-arc basin; ALK=alkaline.

sampled previously inaccessible deeper parts of the formation and provide the means to evaluate its lithological and lithogeochemical character. At the Kudz Ze Kayah, GP4F, and Wolverine VMS deposits, felsic rocks were taken from the immediate footwall and hanging wall of mineralization to help identify additional geochemical prospectivity criteria in ancient, felsic-hosted VMS systems. Specifically, sampling was subdivided into two groups: 1) VMS-bearing, which includes rocks that directly host VMS mineralization, or are the same age as known VMS deposits; and 2) VMS-barren, which includes rocks with ages different from the VMS deposits, and arc-related stratigraphy.

Lithogeochemistry

Sample preparation and measurement of major and trace element data was performed at ALS Laboratories, North Vancouver, British Columbia. Rock samples were crushed and pulverized using steel plates and agate mills, respectively. Sample powders (~0.2 g) were fused with a lithium metaborate flux (0.9 g) at 1000°C. The fused bead was cooled and digested using 100 mL of a 4% HNO_3-2% HCl mixture. Analyses of the sample solutions were completed using inductively coupled plasma-atomic emission spectrometry (ICP-AES) for major elements and inductively coupled plasma-mass spectrometry (ICP-MS) for trace elements.

Whole-rock Hf-Nd isotopes

Whole-rock Hf and Nd isotope ratios were measured at the Pacific Centre for Isotopic and Geochemical Research, University of British Columbia, using separate aliquots of sample powders used for trace element analyses. Nd and Hf were purified using sequential ion-exchange column chemistry. Separation procedures for Nd followed Weis et al. (2006, 2007) and was then separated from the other rare earth elements using HDEHP-coated Teflon resin. Hafnium separations were conducted using TODGA resin following a method modified after Connelly et al. (2006). The Nd and Hf isotope ratios were measured by MC-ICP-MS (Nu Instruments Ltd., Nu II 214 or Nu 1700) following Weis et al. (2006, 2007), and normalized to the JNDi (Nd) and JMC 475 (Hf) standards using sample-standard bracketing. Normalization values are $^{143}Nd/^{144}Nd$ = 0.512116 for JNDi (Tanaka et al., 2000) and $^{176}Hf/^{177}Hf$ = 0.282160 for JMC 475 (Blichert-Toft et al., 1997). The present-day CHUR values used for age-corrections include $^{143}Nd/^{144}Nd$ = 0.512638 (Blichert-Toft and Albarède, 1997) and $^{176}Hf/^{177}Hf$ = 0.282785 (Bouvier et al., 2008), and parent-daughter ratios are $^{147}Sm/^{144}Nd$ = 0.1967 (Jacobsen and Wasserburg, 1980) and $^{176}Lu/^{176}Hf$ = 0.0336 (Bouvier et al., 2008).

In situ zircon geochemistry and Hf isotopes

Sample preparation and mineral separation procedures were carried out at Memorial University of Newfoundland (MUN). Zircon was extracted from rock samples following a series of traditional crushing, grinding, sieving, heavy liquid, and magnetic separation methods. The zircon grains were then hand-picked in ethanol and loaded into quartz crucibles, then placed into a furnace for annealing at 900°C for 60 hours (Mattinson, 2005). Annealed grains were mounted in epoxy and polished with 12 µm, 3 µm, and 1 µm steps. Samples were then carbon coated and imaged with cathodoluminscence (CL), backscatter electron (BSE), and secondary electron (SE) techniques on a JEOL JSM 7100F scanning electron microscope. Three spots per grain were then analyzed on a JEOL JXA-8230 SuperProbe for Zr, Si, Hf, Y, P, Ca, K, Na, and Al to screen for micro-inclusions and provide the ^{29}Si internal standard calibration for LA-ICP-MS analyses.

Laser ablation (LA)-ICP-MS analyses were performed at the Isotope Geology Laboratory at Boise State University, Idaho (BSU). Laser ablation was performed on each grain using a New Wave Research UP-213 Nd:YAG UV laser (213 nm) and ablated material was transferred to and analyzed in a ThermoElectron X-Series II quadrupole ICP-MS. Laser conditions were: 45 second analysis (15 sec gas blank, 30 sec ablation), 1.2 L/min He gas stream to the nebulizer flow of the plasma; quadrupole dwell times were 5 ms for Si and Zr, 200 ms for ^{49}Ti and ^{207}Pb, 80 ms for ^{206}Pb, 40 ms for ^{202}Hg, ^{204}Pb, ^{208}Pb, ^{232}Th, and ^{238}U and 10 ms for all other HFSE and REE; total sweep duration is 950 ms. Standards (Plešovice, Seiland, and Zirconia) were used throughout the run, four for every ten unknowns, to monitor for instrument drift. Data processing was completed with a BSU in-house Excel-based program.

Following trace element and U-Pb collection at BSU, Hf isotopes were measured at Memorial University using a ThermoFinnigan Neptune multi collector (MC)-ICPMS paired to a GeoLas Pro 193 nm ArF excimer laser under operating conditions of 10 Hz frequency, 5 J/cm^2 fluence, and a 40 m diameter spot size. Each LA-MC-ICPMS spot consisted of a 90 second analysis (30 s gas blank, 60 s ablation) that included a He flow rate in the sample cell of 0.9-1.0 L/min, N_2 flow rate of 0.012-0.020 L/min, Ar carrier gas flow rate of 0.7 L/min, and Ar auxillary flow rate of 1.0 L/min. Zircon standards (Plešovice, b142 synthetic, R33, and FC1) were used throughout the run, two for every eight unknowns, to monitor for instrument drift. Data correction and reduction are based on the framework of Fisher et al. (2011) using an in-house Excel-based reduction program. The present-day CHUR values used for age-corrections include $^{176}Hf/^{177}Hf$ = 0.282785 and $^{176}Lu/^{176}Hf$ = 0.0336 (Bouvier et al., 2008).

PRELIMINARY RESULTS

Lithogeochemistry and whole-rock Hf-Nd isotopes

We follow the methodology of Piercey et al. (2001) and use immobile elements and ratios that contain Al_2O_3, TiO_2, high field strength elements (HFSE; Zr, Hf, Nb, Ta, Y, Th), and rare earth elements (REE; La to Lu) to assess the primary geochemical characteristics of the rocks (Fig. 3). The alkali elements (e.g., Na, K, and Ca) and large ion lithophile elements (LILE; e.g., Cs, Ba, Rb, K, Sr, U) can be significantly affected by hydrothermal alteration and metamorphism (e.g., Fig. 3E); alteration of least-altered felsic rocks resulted in sericite, chlorite-pyrite, and alkali feldspar assemblages, while mafic rocks typically exhibit more abundant carbonate, epidote, and chlorite-pyrite alteration (Fig. 3E; Ishikawa et al., 1976; Lentz, 1999; Large et al., 2001). To illustrate the whole-rock geochemical results, the lithogeochemistry is presented in Figures 3–5 and Hf-Nd isotopes are shown in Figure 6.

Grass Lakes group

Fire Lake formation

Rock samples from the Fire Lake formation comprise mafic (metagabbro?) rocks, a single mafic tuff, intermediate–felsic clastic sedimentary rocks, and a felsic intrusive rock (Figs. 3–6; Table 1). The mafic rocks have low SiO_2 (38–46 wt.%) and show Nb/Y, Zr/Nb, Ti/V, and Zr/Y ratios indicative of an alkalic affinity, whereas the mafic tuff is more intermediate (SiO_2=54 wt.%) with lower Ti/V and Zr/Y and has an island-arc tholeiitic to boninitic affinity (Figs. 4 and 5; e.g., Piercey et al., 2002b, 2004). The mafic rocks have steep primitive mantle-normalized patterns with

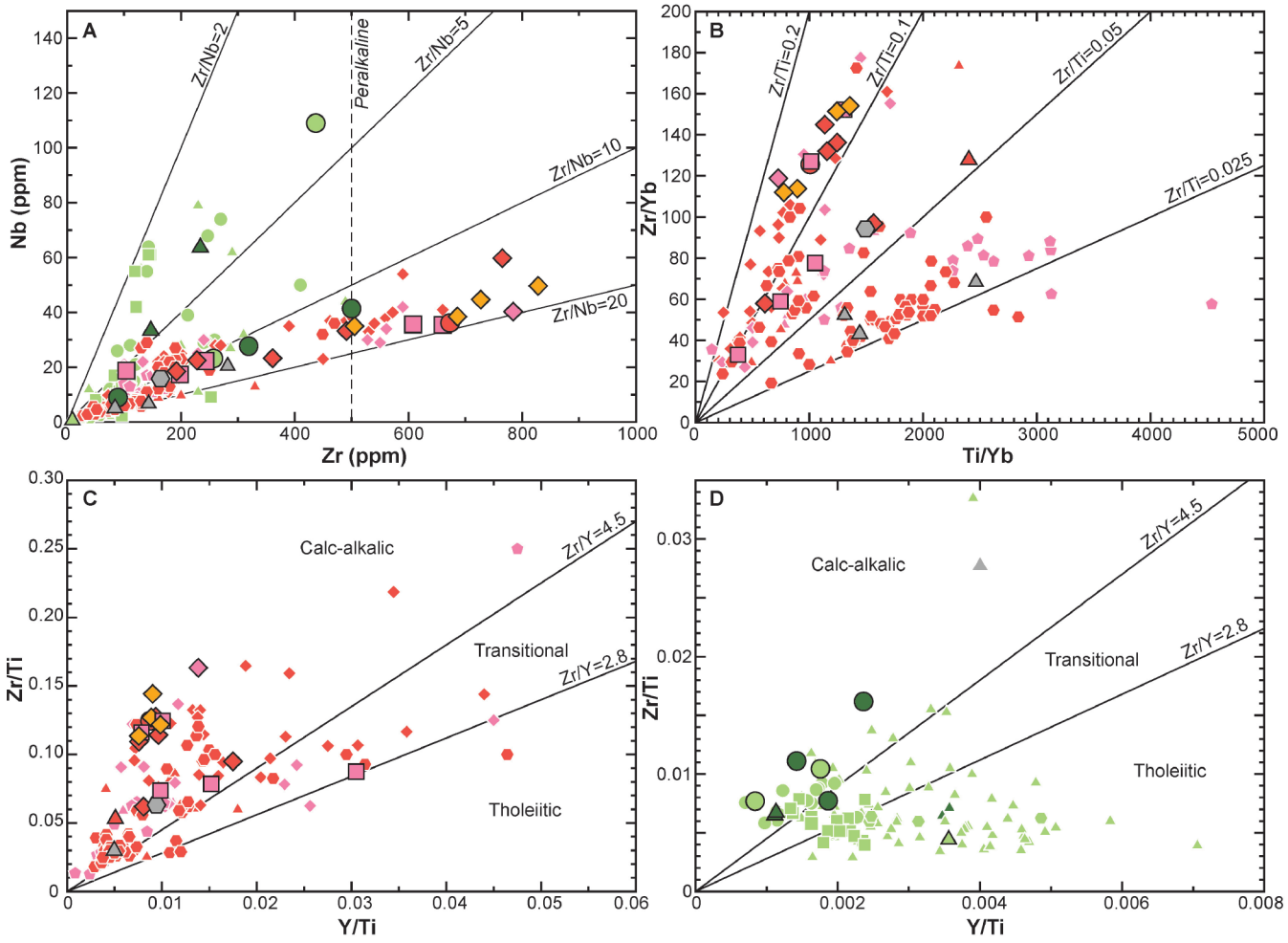

Figure 4. High field strength element diagrams for felsic and mafic rocks in the Finlayson Lake region. **(A)** Zr vs. Nb (Leat et al., 1986); **(B)** Ti/Yb vs. Zr/Yb; **(C)** Y/Ti vs. Zr/Ti for felsic rocks; **(D)** Y/Ti vs. Zr/Ti for mafic rocks. Panels C and D are modified after (Lentz, 1998, 1999); Zr/Y values defining magmatic affinity classes from Ross and Bédard (2009). Symbol styles as in Figure 3.

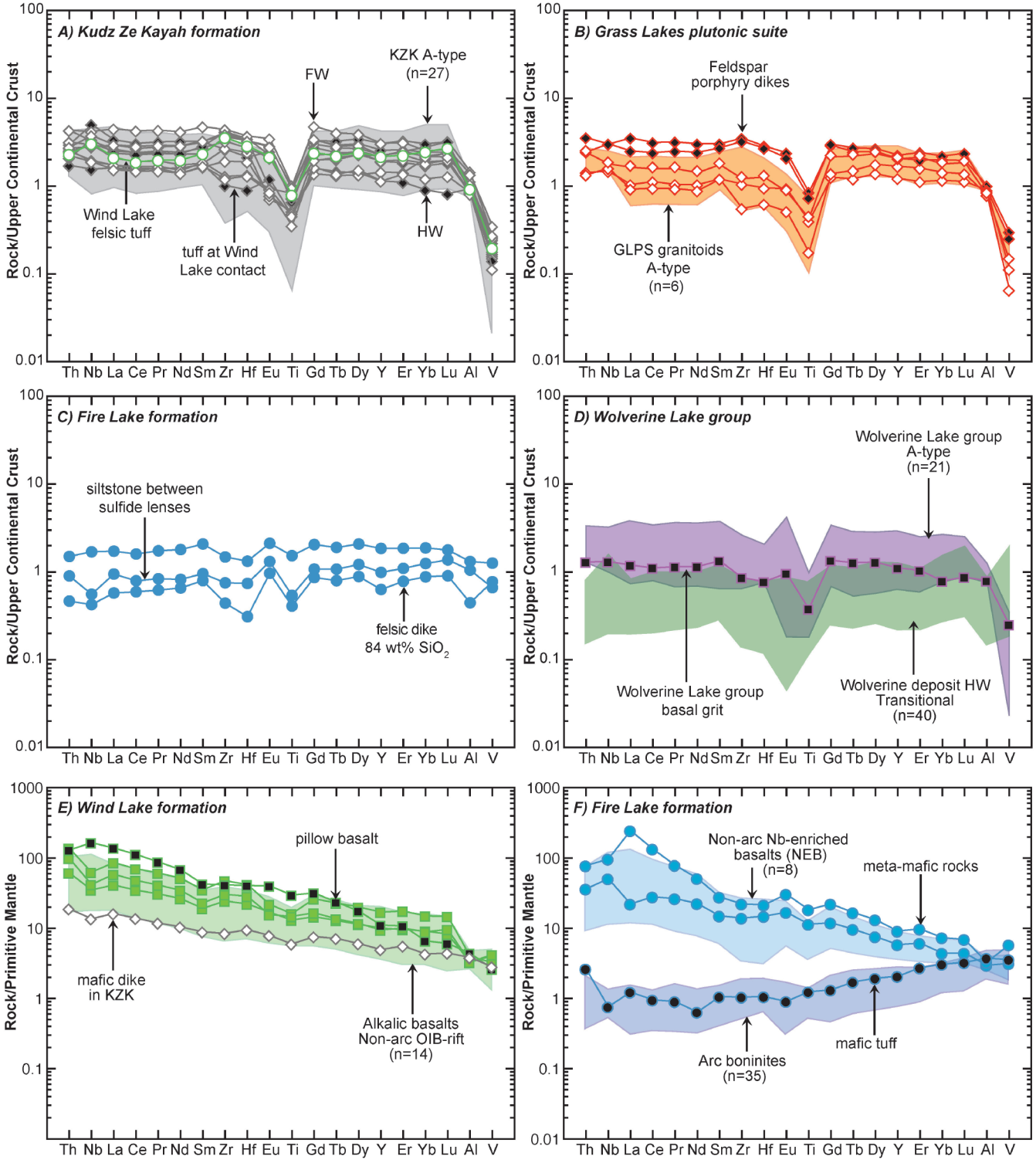

Figure 5. Immobile trace element variations for felsic rock (**A-D**) and mafic rock (**E-F**) suites in the Finlayson Lake region. Results for felsic and mafic rocks are normalized to upper continental crust (McLennan, 2001) and primitive mantle (McDonough and Sun, 1995), respectively. Shaded fields represent archival data with associated magmatic affinities (cf. references in Fig. 3). In panel (F), only results with similar trace element patterns are shown as fields (boninites and Nb-enriched basalts, 43 of 76 total analyses for the Fire Lake formation).

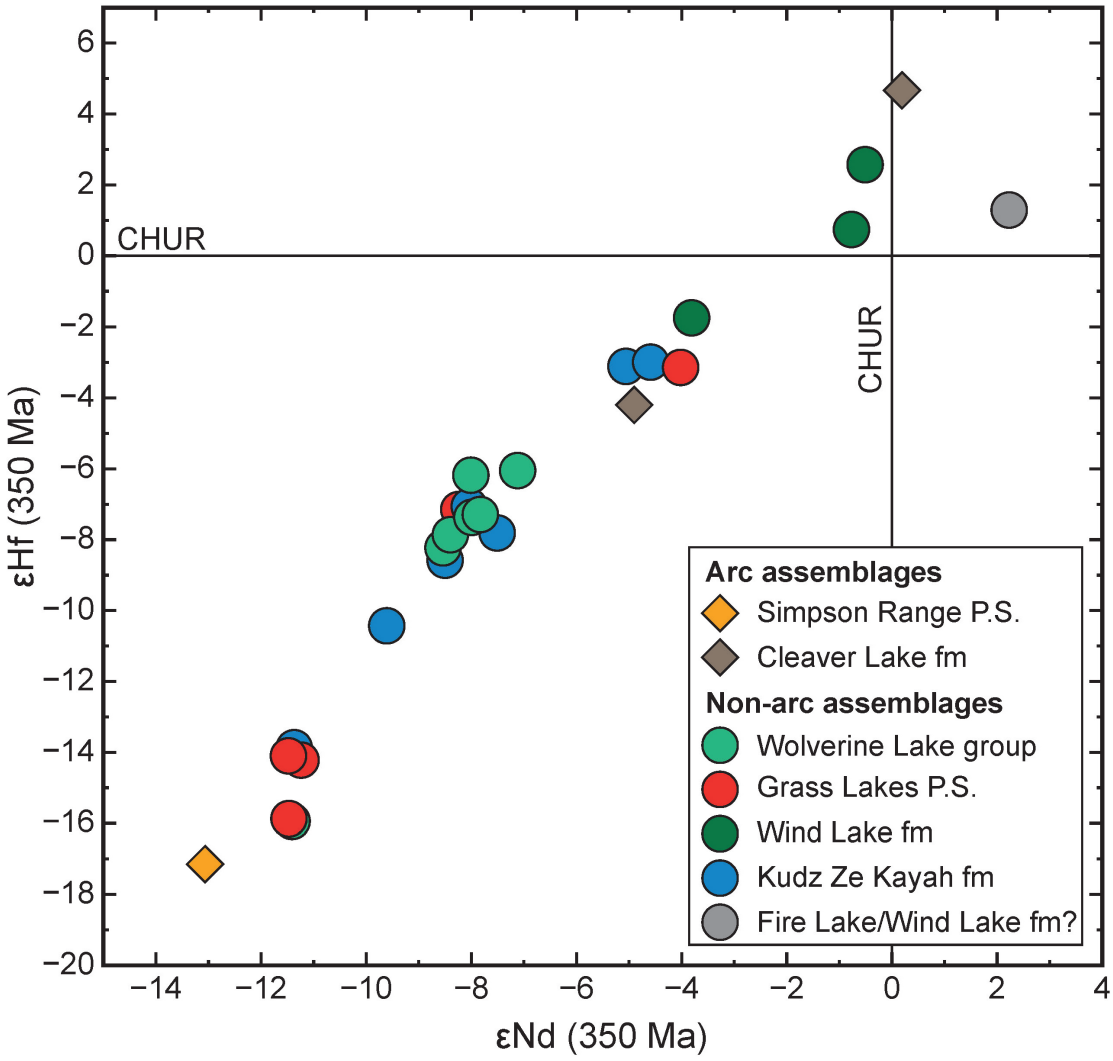

Figure 6. Whole-rock εHf versus εNd for rocks in the Finlayson Lake district (age-corrected to 350 Ma).

elevated LREE relative to HREE (La/Yb_{PM} = 5-34; La/Sm_{PM} = 1.5-9.1; Gd/Lu_{PM} = 2.7-3.2) similar to Nb-enriched basalts (NEB; Piercey et al., 2004); the mafic tuff has a relatively flatter pattern (La/Yb_{PM} = 0.4; La/Sm_{PM} = 1.2; Gd/Lu_{PM} = 0.4) and overlaps with the boninite field (Fig. 5F). The intermediate–felsic rocks comprise siltstones (SiO_2=62-65 wt.%) and one Si-rich felsic dike (SiO_2=84 wt.%) that occur proximal to massive sulphide mineralization at the Fyre Lake VMS deposit. Trace element ratios (Nb/Y and Zr/Y) distinguish these samples as derivatives of calc-alkaline arc rocks (Figs. 3 and 4) and have similar upper continental crust-al-normalized patterns (La/Yb_{UCN} = 0.65-0.91) and neutral to weakly negative Eu anomalies (Eu/Eu* = 0.75-1.0; Fig. 6C). The felsic dike is Permian in age (Manor, unpublished data) and cross-cuts mafic volcaniclastic rocks in the Fyre Lake VMS deposit hanging wall gave εHf_i and εNd_i are –4.7 and –7.3, respectively (Fig. 6). The meta-mafic intrusive rocks south of Kudz Ze Kayah has a juvenile isotopic composition (εHf_i = +1.5; εNd_i = +2.4), thus may be related to magmatism of the Fire Lake or Wind Lake formations (to be determined).

Kudz Ze Kayah formation

Felsic volcaniclastic rocks and coherent rhyolite flows of the Kudz Ze Kayah formation show similar geochemical compositions in the hanging wall and footwall of the Kudz Ze Kayah VMS deposits (Figs. 3–5; Table 1). The rocks display a range of SiO_2 contents (59–78 wt.%) and have variable alkali concentrations due to hydrothermal alteration (Fig. 3A). The lithofacies have dacite, rhyolite, and trachyte compositions with calc-alkalic to alkalic, within-plate affinities (Nb/Y=0.74-1.1; Zr/Y=7.7-16; Ross and Bédard, 2009) except for two samples from the immediate hanging wall and footwall of GP4F mineralization that have

subalkaline affinities (Nb/Y = 0.54-0.61; Zr/Y = 5.4-12; Figs. 3 and 4). Upper continental crust-normalized immobile elements yield relatively flat patterns with near-neutral LREE (La/Sm_{UCN} = 0.83-1.1) and relatively more abundant HREE (Gd/Lu_{UCN} = 0.57-1.9), and variably negative Eu (Eu/Eu* = 0.39-1.1) and Ti (Ti/Ti* = 0.32-1.0) anomalies (Fig. 5A) that overlap with A-type volcanic signatures from Piercey et al. (2001). Rocks from the Kudz Ze Kayah formation (n=8) gave a range of sub-chondritic isotopic compositions (εHf_i = –13.7 to –2.8; εNd_i = –11.2 to –4.5; Fig. 6). Rocks in the immediate hanging wall and footwall of VMS deposits (e.g., Kudz Ze Kayah and GP4F) have more chondritic isotopic compositions (εHf_i = –7.0 to –2.9; εNd_i = –7.3 to –4.9) relative to those rocks highest in the hanging wall (17MM-002) where εHf_i and εNd_i are –13.7 and –11.2, respectively.

Wind Lake formation

The Wind Lake formation is composed primarily of carbonaceous argillite, geochemically similar mafic volcaniclastic, volcanic, and intrusive rocks, and lesser felsic volcaniclastic units that are geochemically similar to the underlying Kudz Ze Kayah formation (Figs. 3–5; Table 1). The mafic rocks have low SiO_2 (34–51 wt.%) and correspond to basalt and alkaline basalt to basaltic trachyandesite compositions (Fig. 3A, B). They have back-arc basin MORB to alkalic geochemical affinities (Ti/V=30–160; Fig. 3D; Shervais, 1982) and straddle the subalkaline to alkaline boundary with Nb/Y=0.42–2.3 (Fig. 3B). Primitive mantle-normalized diagrams show steep patterns with LREE enrichment relative to HREE (La/Yb_{PM} = 3.9–22) and higher Eu and Ti (Eu/Eu* = 1.9–4.5; Ti/Ti* = 5.9–32) that are similar to non-arc, ocean island basalt, rift-related alkalic basalts (Fig. 5E; Piercey et al., 2002a). The felsic tuff sample has higher SiO_2 (74 wt.%) and similar geochemical characteristics to rocks from the Kudz Ze Kayah formation (Figs. 3–5). The sample exhibits a trachytic composition (Fig. 3B) and has an alkalic and peralkaline, within-plate geochemical affinity (Nb/Y=0.76; Zr/Y=14.2; Zr/Nb=125; Figs. 3 and 4). The upper continental crust-normalized pattern is relatively flat (La/Yb_{UCN} = 0.86) and overlaps directly with patterns from the Kudz Ze Kayah formation (Fig. 5A). The range of isotope values is more chondritic relative to the Kudz Ze Kayah formation, yielding εHf_i from –1.6 to +2.7 and εNd_i from –3.7 to –0.5, where the felsic tuff has the most negative values (Fig. 6).

Grass Lakes plutonic suite

Most samples of the Grass Lakes plutonic suite come from a batholith-sized intrusion lying south of and located beneath the Kudz Ze Kayah VMS deposit (Fig. 2). It is composed of high-silica, peraluminous alkali feldspar augen to megacrystic granitic rocks with apophyses of feldspar-porphyritic granitic rocks that are geochemically similar to, and contemporaneous with, the Kudz Ze Kayah strata (Figs. 3–5; e.g., Piercey et al., 2003; Murphy et al., 2006). Samples from the granitic pluton have high SiO_2 (68–79 wt.%) and HFSE concentrations which correspond to calc-alkalic, within-plate affinities (Zr/Y=2.9–14; Nb/Y=0.52–0.80; Figs. 3C and 4C). The upper continental crust-normalized diagrams show distinct trends for the pluton (La/Yb_{UCN} = 0.64–0.92) and feldspar porphyritic dikes (La/Yb_{UCN} = 1.1–1.8); the dikes contain higher concentrations of HFSE and REE compared to the pluton (e.g., Eu/Eu* = ~0.91 vs. 0.45; Zr/Zr* = ~1.4 vs. 0.55; Fig. 5B). These new results overlap with A-type, within-plate Grass Lakes granitic rocks of Piercey et al. (2003) and calc-alkalic to alkalic Kudz Ze Kayah volcanic rocks (Piercey et al., 2001; Fig. 5A). Granitoids from the Grass Lakes plutonic suite (n=5) give the largest range of evolved isotopic compositions across the district (εHf_i = –15.7 to –3.0; εNd_i = –11.4 to –3.9; Fig. 6).

Wolverine Lake group

The Wolverine Lake group overlies the Grass Lakes group above a marked angular unconformity (Murphy et al., 2002). One sample of quartzofeldspathic grit from immediately above the unconformity displays high SiO_2 (78 wt.%) and HFSE and REE compositions (Nb/Y=0.65; Zr/Y=6.7) that are similar to the underlying calc-alkalic, arc to intraplate rocks of the underlying Kudz Ze Kayah formation and Grass Lakes plutonic suite (Piercey et al., 2001; Figs. 3C, 4C, and 5). This sample exhibits a relatively flat upper continental crust-normalized pattern with relatively more abundant LREE (La/Sm_{UCN} = 0.89) than HREE (Gd/Lu_{UCN} = 1.5; Fig. 5D). The immobile element concentrations overlap with other intraplate rocks of the Wolverine Lake group, primarily from the footwall of the Wolverine VMS deposits, and are distinctly higher than those of the hanging wall felsic rocks (Fig. 5D; Piercey et al., 2001, 2008). The basal quartzofeldspathic grit yielded the most evolved isotopic compositions in the Wolverine Lake group (εHf_i = –15.8; εNd_i = –11.3), which broadly overlap with rocks in the Kudz Ze Kayah formation and Grass Lakes plutonic suite. Four samples from the lower footwall felsic volcaniclastic rock unit (Fig. 6) give a narrow range of sub-chondritic isotope compositions (εHf_i = –8.1 to –6.0; εNd_i = –8.5 to –7.0) that overlap with feldspar porphyritic rhyolites (n=2) from the Wolverine/Lynx zone (εHf_i = –7.3; εNd_i = –7.9) and the Fisher zone (εHf_i = –7.9; εNd_i = –7.8) in the upper footwall (Fig. 6).

Cleaver Lake thrust sheet

Three samples from the Cleaver Lake thrust sheet include felsic volcanic rocks of the Cleaver Lake formation (n=2) and a hornblende granodiorite from the Simpson Range plutonic suite (n=1). The Hf and Nd isotopic compositions for the Cleaver Lake formation are variable around chondrite

and correspond to the geochemical affinity of the rocks. Volcanic rocks of tholeiitic affinity yield superchondritic isotope compositions (εHf_i = +4.8; εNd_i = +0.25) relative those of calc-alkaline affinity, which give sub-chondritic values (εHf_i = –4.0; εNd_i = –4.8). The granodiorite yields a much more evolved isotopic signature where εHf_i and εNd_i are –17.1 and –13.1, respectively (Fig. 6).

Trace elements and Hf isotopes in zircon

Zircon crystals (n=789) from rocks in back-arc and arc environments were measured for both trace elements and Hf isotopes. Each grain was classified either as an autocryst (i.e., crystallized during the magmatic event) or a xenocryst (i.e., assimilated from surrounding wall rocks) to best assess primary petrologic characteristics; thus, autocrysts are discussed below and shown in Figure 7. In the back-arc, zircon chemistry in the Kudz Ze Kayah formation, Wolverine Lake group, and Grass Lakes plutonic suite generally overlap, which suggest similar petrogenetic processes in the crust during melting and crystallization of the zircon grains. These back-arc rocks contain zircon with Th and U concentrations between 20–3800 ppm and 40–1500 ppm, respectively, that correspond to Th/U = 0.1–5.4; these zircon also have Ti-in-zircon crystallization temperatures (T_{zrn}) of 630–960°C, and εHf_i = –18 to –3 (Fig. 7). Zircon from the Wind Lake formation gave lower Th (55–230 ppm) and U (130–370 ppm), Th/U of 0.4–0.6, T_{zrn} = 790–960°C, and the most chondritic εHf_i of all samples (–3.7 to –0.8). Arc rocks from the Cleaver Lake thrust sheet give similar Th and U concentrations (40–1400 ppm and 120–1300 ppm, respectively) that correspond to a narrow range of Th/U (0.4–1.3). The

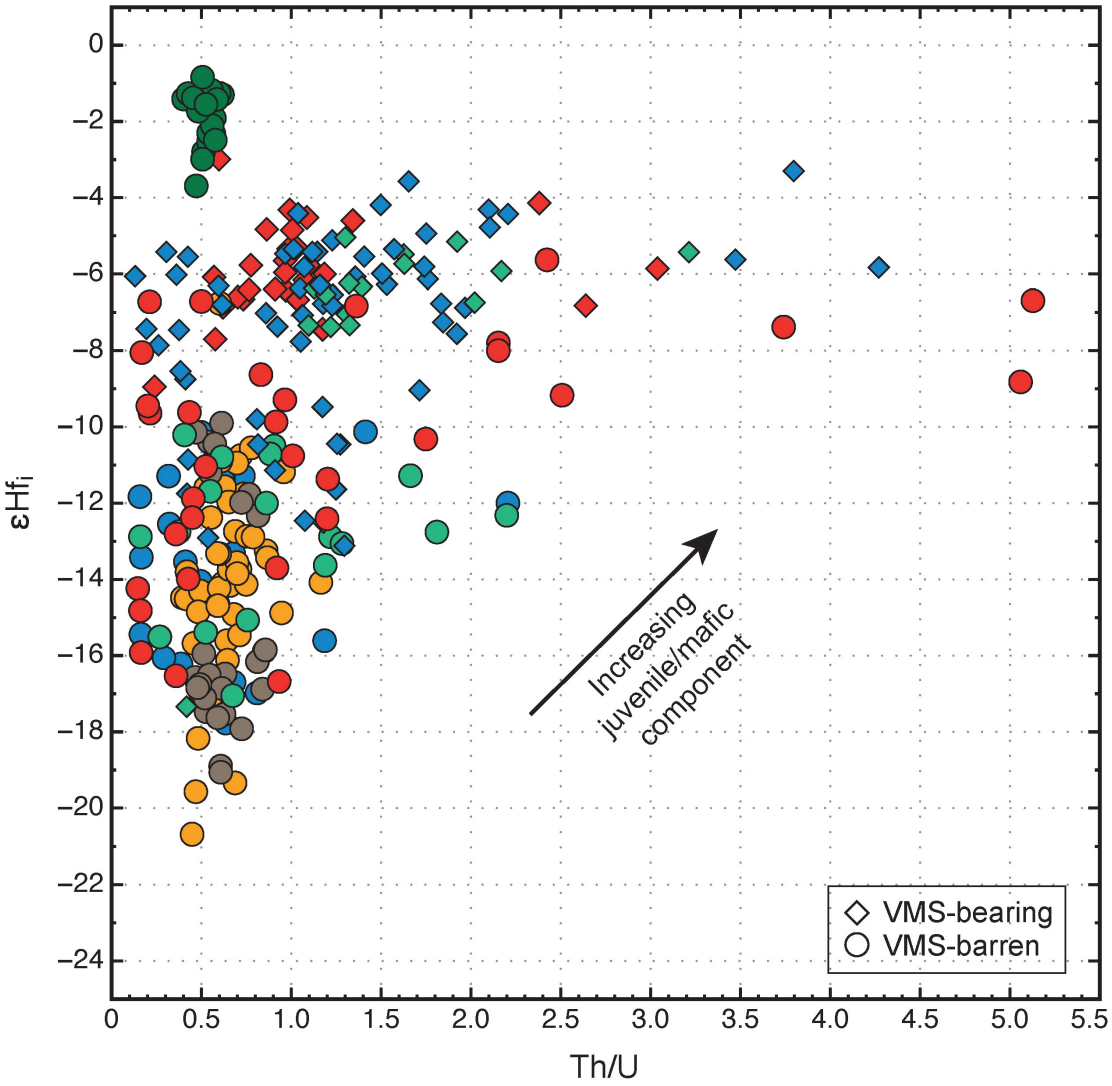

Figure 7. In situ zircon Th/U versus εHf_i. Symbol colours as in Figure 6, but markers indicate the location of the sample relative to known VMS deposits (i.e., VMS-bearing and VMS-barren).

T_{zrn} is noticeably lower than back-arc zircon at 470–710°C and yield significantly lower ranges of εHf_i (–20 to –10; Fig. 7). When subdivided based on their location to known VMS deposits (i.e., VMS-bearing or VMS-barren), zircon grains from VMS-bearing stratigraphy shows elevated geochemical signatures (Th/U = 0.1–5.4, mean = 1.4; εHf_i = –17 to –3, mean = –7.1; T_{zrn} = 680–960°C, mean = 790°C) relative to zircon of VMS-barren stratigraphy (Th/U = 0.1–2.5, mean = 0.7; εHf_i = –21 to –7, mean = –14; T_{zrn} = 470–930°C, mean = 690°C; Fig. 7).

CONCLUSIONS

The new geochemical and isotopic results presented here support the current interpretations of an evolving, mid-Paleozoic (ca. 365-355 Ma) continental arc, marginal arc, and back-arc basin configuration at the western Laurentian margin. Results from strata immediately above and below the Kudz Ze Kayah VMS deposit place new constraints on the HFSE and REE end-member compositions (e.g., Zr, Nb/Ta) and indicate a distinct period of high-temperature alkalic felsic volcanism within the Kudz Ze Kayah formation. Both whole-rock and *in situ* zircon isotopic data suggests that volcanic rocks in the district formed from varying abundances of crust–mantle-derived melts. Further, it is shown that slightly evolved isotopic signatures near known VMS deposits (i.e., VMS-bearing) contain elevated values closer to chondrite (i.e., $\varepsilon Hf_i > -10$) relative to rocks that are more distal to the deposits or located further in arc stratigraphy (i.e., VMS-barren; $\varepsilon Hf_i < -10$). We suggest these trace element and isotopic signatures arose from basaltic underplating of continental crust in a Late Devonian to Early Mississippian extensional tectonic setting. These high-temperature basalts facilitated extensive crustal anatexis evident by variable mixtures of mantle-derived basaltic melts and crustal melts, and supported elevated geothermal gradients to support long-lived hydrothermal circulation in the upper crust. Future work aims to identify additional mineral-scale (zircon and apatite) and whole-rock geochemical characteristics of VMS-bearing stratigraphy to develop prospectivity criteria for future exploration in orogenic belts globally.

ACKNOWLEDGEMENTS

We thank Corey Wall, Wanda Aylward, John Hanchar, Mark Schmitz, Jim Crowley, and Rebecca Lam for their assistance with mineral separation, SEM-EPMA, and LA-ICP-MS analyses. BMC Minerals is thanked for ongoing financial, logistical, and intellectual support of this project. Funding for this research was provided by the Yukon Geological Survey, BMC Minerals, a NSERC Discovery Grant, an NSERC Collaborative Research and Development Grant; and the Targeted Geoscience Initiative 5 (TGI-5) program of the Geological Survey of Canada (Piercey); and a GSA Graduate Student Research Grant and SEG Canada Foundation Student Research Grant (Manor).

REFERENCES

Blichert-Toft, J., Chauvel, C., and Albarède, F., 1997. Separation of Hf and Lu for high-precision isotope analysis of rock samples by magnetic sector-multiple collector ICP-MS; Contributions to Mineralogy and Petrology, v. 127, p. 248–260. doi: 10.1007/s004100050278.

Bradshaw, G.D., Rowins, S.M., Peter, J.M., and Taylor, B.E., 2008. Genesis of the Wolverine volcanic sediment-hosted massive sulfide deposit, Finlayson Lake District, Yukon, Canada: Mineralogical, mineral chemical, fluid inclusion, and sulfur isotope evidence; Economic Geology, v. 103, p. 35–60. doi: 10.2113/gsecongeo.103.1.35.

Colpron, M., and Nelson, J., 2011. A digital atlas of terranes for the Northern Cordillera; Yukon Geological Survey, www.geology.gov.yk.ca.

Colpron, M., Nelson, J.L., and Murphy, D.C., 2006. A tectonostratigraphic framework for the pericratonic terranes of the northern Canadian Cordillera; *in* Paleozoic Evolution and Metallogeny of Pericratonic Terranes at the Ancient Pacific Margin of North America, Canadian and Alaskan Cordillera, (eds.) M. Colpron and J.L. Nelson; Geological Association of Canada, Special Paper 45, p. 1–23.

Connelly, J.N., Ulfbeck, D.G., Thrane, K., Bizzarro, M., and Housh, T., 2006. A method for purifying Lu and Hf for analyses by MC-ICP-MS using TODGA resin; Chemical Geology, v. 233, p. 126–136. doi: 10.1016/j.chemgeo.2006.02.020.

Fisher, C.M., Hanchar, J.M., Samson, S.D., Dhuime, B., Blichert-Toft, J., Vervoort, J.D., and Lam, R., 2011. Synthetic zircon doped with hafnium and rare earth elements: A reference material for in situ hafnium isotope analysis; Chemical Geology, v. 286, p. 32–47. doi: 10.1016/j.chemgeo.2011.04.013.

Gabrielse, H., Murphy, D.C. and Mortensen, J.K., 2006. Cretaceous and Cenozoic dextral orogen-parallel displacements, magmatism, and paleogeography, north-central Canadian Cordillera; *in* Paleogeography of the North American Cordillera: Evidence For and Against Large-Scale Displacements, (eds.); J.W. Haggart, R.J. Enkin, and J.W.H. Monger, Geological Association of Canada, Special Paper 46, p. 255–276.

Grant, S.L., 1997. Geochemical, radiogenic tracer isotopic, and U-Pb geochronological studies of Yukon-Tanana terrane rocks from the Money klippe, southeastern Yukon, Canada; Unpublished MSc thesis, University of Alberta, Edmonton, 177 p.

Ishikawa, Y., Sawaguchi, T., Iwaya, S. and Horiuchi, M., 1976. Delineation of prospecting targets for Kuroko deposits based on modes of volcanism of underlying dacite and alteration halos; Mining Geology, 26, p. 105–117 (in Japanese with English abs.).

Large, R.R., Gemmell, J.B., and Paulick, H., 2001. The alternation box plot: A simple approach to understanding the relationship between alteration mineralogy and lithogeochemistry associated with volcanic-hosted massive sulfide deposits; Economic Geology, v. 96, p. 957–971. doi: 10.2113/gsecongeo.96.5.957.

Leat, P.T., Jackson, S.E., Thorpe, R.S., and Stillman, C.J., 1986. Geochemistry of bimodal basalt-subalkaline/peralkaline rhyolite provinces within the Southern British Caledonides; Journal of the Geological Society, v. 143, p. 259–273. doi: 10.1144/gsjgs.143.2.0259.

Lentz, D.R., 1998. Petrogenetic evolution of felsic volcanic sequences associated with Phanerozoic volcanic-hosted massive sulphide systems: the role of extensional geodynamics; Ore Geology Reviews, v. 12, p. 289–327. doi: 10.1016/S0169-1368(98)00005-5.

Lentz, D.R., 1999. Petrology, geochemistry, and oxygen isotope interpretation of felsic volcanic and related rocks hosting the Brunswick 6 and 12 massive sulfide deposits (Brunswick belt), Bathurst mining camp, New Brunswick, Canada; Economic Geology, v. 94, p. 57–86. doi: 10.2113/gsecongeo.94.1.57.

McDonough, W., and Sun, S., 1995. The composition of the Earth; Chemical geology, v. 120, p. 223–253. doi: 10.1016/0009-2541(94)00140-4.

McLennan, S.M., 2001. Relationships between the trace element composition of sedimentary rocks and upper continental crust; Geochemistry Geophysics Geosystems, v. 2, p. 1–30. doi: 10.1029/2000GC000109.

Mortensen, J.K., 1992, Pre-Mid-Mesozoic tectonic evolution of the Yukon-Tanana Terrane, Yukon and Alaska; Tectonics, v. 11, p. 836–853. doi: 10.1029/91TC01169.

Mortensen, J.K., and Jilson, G.A., 1985. Evolution of the Yukon-Tanana terrane: evidence from southeastern Yukon Territory; Geology, v. 13, p. 806–810. https://doi.org/10.1130/0091-7613(1985)13%3C806:EOTYTE%3E2.0.CO;2.

Murphy, D.C., Colpron, M., Roots, C.F., Gordey, S.P. and Abbott, J.G., 2002. Finlayson Lake Targeted Geoscience Initiative (southeastern Yukon), Part 1: Bedrock geology; *in* Yukon Exploration and Geology 2001, (eds.) D.S. Emond, L.H. Weston and L.L. Lewis; Exploration and Geological Services Division, Yukon Region, Indian and Northern Affairs Canada, p. 189–207.

Murphy, D.C., Mortensen, J.K., Piercey, S.J., Orchard, M.J. and Gehrels, G.E., 2006. Mid-Paleozoic to early Mesozoic tectonostratigraphic evolution of Yukon-Tanana and Slide Mountain terranes and affiliated overlap assemblages, Finlayson Lake massive sulphide district, southeastern Yukon; *in* Paleozoic Evolution and Metallogeny of Pericratonic Terranes at the Ancient Pacific Margin of North America, Canadian and Alaskan Cordillera, (eds.) M. Colpron and J.L. Nelson; Geological Association of Canada, Special Paper 45, p. 75–106.

Pearce, J.A., 1996. Sources and settings of granitic rocks; Episodes, v. 19, p. 120–125.

Pearce, J.A., Harris, N.B.W. and Tindle, A.G., 1984. Trace element distribution diagrams for the tectonic interpretation of granitic rocks; Journal of Petrology, 25, p. 956–983.

Peter, J.M., Layton-Matthews, D., Piercey, S.J., Bradshaw, G.D., Paradis, S. and Bolton, A., 2007. Volcanic-hosted massive sulphide deposits of the Finlayson Lake District, Yukon; *in* Mineral Deposits of Canada: A Synthesis of Major Deposit-Types, District Metallogeny, the Evolution of Geological Provinces, and Exploration Methods, (ed.) W.D. Goodfellow; Geological Association of Canada, Mineral Deposits Division, Special Publication No. 5, p. 471–508.

Piercey, S.J., 2001. Petrology and tectonic setting of felsic and mafic volcanic and intrusive rocks in the Finlayson Lake volcanic-hosted massive sulphide (VHMS) district, Yukon, Canada: A record of mid-Paleozoic arc and back-arc magmatism and metallogeny; Unpublished PhD dissertation, University of British Columbia, Vancouver, Canada, 324 p.

Piercey, S.J., 2011. The setting, style, and role of magmatism in the formation of volcanogenic massive sulfide deposits; Mineralium Deposita, 46, p. 449–471. doi: 10.1007/s00126-011-0341-z.

Piercey, S.J. and Colpron, M., 2009. Composition and provenance of the Snowcap assemblage, basement to the Yukon-Tanana terrane, northern Cordillera: Implications for Cordilleran crustal growth; Geosphere, 5, p. 439–464. doi: 10.1130/GES00505.S3.

Piercey, S.J. and Murphy, D.C., 2000. Stratigraphy and regional implications of unstrained Devono-Mississippian volcanic rocks in the Money Creek thrust sheet, Yukon-Tanana Terrane, Southeastern Yukon; *in* Yukon Exploration and Geology 1999, (eds.) D.S. Emond and L.H. Weston; Exploration and Geological Services Division, Yukon Region, Indian and Northern Affairs Canada, p. 67–78.

Piercey, S.J., Paradis, S., Murphy, D.C. and Mortensen, J.K., 2001. Geochemistry and paleotectonic setting of felsic volcanic rocks in the Finlayson Lake volcanic-hosted massive sulfide district, Yukon, Canada. Economic Geology, 96, p. 1877–1905. doi: 10.2113/gsecongeo.96.8.1877.

Piercey, S.J., Mortensen, J.K., Murphy, D.C., Paradis, S. and Creaser, R.A., 2002a. Geochemistry and tectonic significance of alkalic mafic magmatism in the Yukon-Tanana terrane, Finlayson Lake region, Yukon; Canadian Journal of Earth Sciences, 39, p. 1729–1744. doi: 10.1139/E02-090.

Piercey, S.J., Murphy, D.C., Mortensen, J.K. and Paradis, S., 2002b. Boninitic magmatism in a continental margin setting, Yukon-Tanana terrane, southeastern Yukon, Canada; Geology, vol. 29, p. 731–734. https://doi.org/10.1130/0091-7613(2001)029%3C0731:BMIACM%3E2.0.CO;2.

Piercey, S.J., Paradis, S.J., Peter, J.M. and Tucker, T.L., 2002c. Geochemistry of basalt from the Wolverine volcanic-hosted massive-sulphide deposit, Finlayson Lake district, Yukon Territory; Geological Survey of Canada, Current Research 2002-A3, 11 p.

Piercey, S.J., Mortensen, J.K. and Creaser, R.A, 2003. Neodymium isotope geochemistry of felsic volcanic and intrusive rocks from the Yukon-Tanana Terrane in the Finlayson Lake Region, Yukon, Canada; Canadian Journal of Earth Sciences, 40, p. 77–97. doi: 10.1139/e02-094.

Piercey, S.J., Murphy, D.C., Mortensen, J.K. and Creaser, R.A., 2004. Mid-Paleozoic initiation of the northern Cordilleran marginal backarc basin: Geologic, geochemical, and neodymium isotope evidence from the oldest mafic magmatic rocks in the Yukon-Tanana terrane, Finlayson Lake district, southeast Yukon, Canada; Bulletin of the Geological Society of America, 116, p. 1087–1106. doi: 10.1130/B25162.1.

Piercey, S.J., Nelson, J.L., Colpron, M., Dusel-Bacon, C., Simard, R.-L. and Roots, C.F., 2006. Paleozoic magmatism and crustal recycling along the ancient Pacific margin of North America, northern Cordillera; *in* Paleozoic Evolution and Metallogeny of Pericratonic Terranes at the Ancient Pacific Margin of North America, Canadian and Alaskan Cordillera, (eds.) M. Colpron and J.L. Nelson; Geological Association of Canada, Special Paper 45, p. 281–322.

Piercey, S.J., Peter, J.M., Mortensen, J.K., Paradis, S., Murphy, D.C. and Tucker, T.L., 2008. Petrology and U-Pb geochronology of footwall porphyritic rhyolites from the Wolverine volcanogenic massive sulfide deposit, Yukon, Canada: Implications for the genesis of massive sulfide deposits in continental margin environments; Economic Geology, 103, p. 5–33. doi: 10.2113/gsecongeo.103.1.5.

Piercey, S.J., Murphy, D.C. and Creaser, R.A., 2012. Lithosphere-asthenosphere mixing in a transform-dominated late Paleozoic backarc basin: Implications for northern Cordilleran crustal growth and assembly; Geosphere, 8, p. 716–739. doi: 10.1130/GES00757.1.

Piercey, S.J., Gibson, H.L., Tardif, N. and Kamber, B.S., 2016. Ambient redox and hydrothermal environment of the Wolverine volcanogenic massive sulfide deposit, Yukon: Insights from lithofacies and lithogeochemistry of Mississippian host shales; Economic Geology, 111, p. 1439–1463. doi: 10.2113/econgeo.111.6.1439.

Piercey, S.J., Beranek, L.P. and Hanchar, J.M., 2017. Mapping magma prospectivity for Cordilleran volcanogenic massive sulphide (VMS) deposits using Nd-Hf isotopes: Preliminary results; *in* Yukon Exploration and Geology 2016, (eds.) K.E. MacFarlane and L.H. Weston; Yukon Geological Survey, p. 197–205.

Ross, P.-S., and Bédard, J.H., 2009. Magmatic affinity of modern and ancient subalkaline volcanic rocks determined from trace-element discriminant diagrams; Canadian Journal of Earth Sciences, v. 46, p. 823–839. doi: 10.1139/E09-054.

Sebert, C., Hunt, J.A. and Foreman, I.J., 2004. Geology and lithogeochemistry of the Fyre Lake copper-cobalt-gold sulphide-magnetite deposit, southeastern Yukon; Yukon Geological Survey, Open File 2004-17, 46 p.

Shervais, J.W., 1982. TiV plots and the petrogenesis of modern and ophiolitic lavas; Earth and Planetary Science Letters, v. 59, p. 101–118. doi: 10.1016/0012-821X(82)90120-0.

Tanaka, T., Togashi, S., Kamioka, H., and Amakawa, H., 2000. JNdi-1: a neodymium isotopic reference in consistency with LaJolla neodymium; Chemical Geology, v. 168, p. 279–281.

Tempelman-Kluit, D.J., 1979. Transported cataclasite, ophiolite and granodiorite in Yukon: Evidence of arc-continent collision; Geological Survey of Canada, Paper 79-1, 27 p.

Weis, D., Kieffer, B., Hanano, D., Silva, I.N., Barling, J., Pretorius, W., Maerschalk, C., and Mattielli, N., 2007. Hf isotope compositions of U.S. Geological survey reference materials; Geochemistry, Geophysics, Geosystems, v. 8. doi: 10.1029/2006GC001473.

Weis, D., Kieffer, B., Maerschalk, C., Barling, J., De Jong, J., Williams, G.A., Hanano, D., Pretorius, W., Mattielli, N., Scoates, J.S., Goolaerts, A., Friedman, R.M., and Mahoney, J.B., 2006. High-precision isotopic characterization of USGS reference materials by TIMS and MC-ICP-MS; Geochemistry, Geophysics, Geosystems, v. 7. doi: 10.1029/2006GC001283.

Winchester, J.A., and Floyd, P.A., 1977. Geochemical discrimination of different magma series and their differentiation products using immobile elements; Chemical Geology, v. 20, p. 325–343. doi: 10.1016/0009-2541(77)90057-2.

Yukon Geological Survey, 2018. Yukon digital bedrock geology; <http://www.geology.gov.yk.ca/update_yukon_bedrock_geology_map.html>, accessed: 10 August 2018.

Alkaline magmatism in the Selwyn Basin, Yukon: Relationship to SEDEX mineralization

E.J. Scanlan[1]*, M. Leybourne[1,2], D. Layton-Matthews [1], A. Voinot[1,2], and N. van Wagoner[3]

Scanlan, E.J., Leybourne, M., Layton-Matthews, D., Voinot, A., and van Wagoner, N., 2021. Alkaline magmatism in the Selwyn Basin, Yukon: Relationship to SEDEX mineralization; in *Targeted Geoscience Initiative 5:grant program final reports (2018-2020), Geological Survey of Canada, Open File 8755, p. 265–279. https://doi.org/10.4095/328994*

Abstract: Several sedimentary exhalative (SEDEX) deposits have alkaline magmatism that is temporally and spatially associated to mineralization. This report outlines interim data from a study of potential linkages between magmatism and SEDEX mineralization in the Selwyn Basin, Yukon. This region is an ideal study site due to the close spatial and temporal relationships between SEDEX deposits and magmatism, particularly in the MacMillan Pass, where volcanic rocks have been drilled with mineralization at the Boundary deposit.

Alkaline volcanic samples were analysed from the Anvil District, MacMillan Pass, Keno-Mayo and the Misty Creek Embayment in the Selwyn Basin to characterise volcanism and examine the relationship to mineralization. Textural and field relationships indicate a volatile-rich explosive eruptive volcanic system in the MacMillan Pass region in comparison to the Anvil District, which is typically effusive in nature. High proportions of calcite and ankerite in comparison to other minerals are present in the MacMillan system. Cathodoluminescence imaging reveals zoning and carbonate that displays different luminescent colours within the same sample, likely indicating multiple generations of carbonate precipitation. Barium contents are enriched in volcanic rocks throughout the Selwyn Basin, which is predominately hosted by hyalophane with rare barite and barytocalcite. Thallium is positively correlated with Ba, Rb, Cs, Mo, As, Sb and the calcite-chlorite-pyrite index and is negatively correlated with Cu. Anvil District samples display a trend towards depleted mid-ocean ridge mantle on a plot of Ce/Tl versus Th/Rb. Hydrothermal alteration has likely led to the removal of Tl from volcanic rocks in the region.

Ongoing research involves: i) the analysis of Sr, Nd, Pb and Tl isotopes of volcanic samples; ii) differentiating magmatic from hydrothermal carbonate using O, C and Sr isotopes; iii) examining sources of Ba in the Selwyn Basin; iv) and constraining age relationships through U-Th-Pb geochronology.

[1]Department of Geological Sciences and Geological Engineering, Queen's University, 36 Union Street, Kingston, Ontario, Canada K7L 3N6
[2]McDonald Institute, Canadian Particle Astrophysics Research Centre, Department of Physics, Engineering Physics and Astronomy, Queen's University, 64 Bader Lane, Kingston, Ontario, Canada K7L 3N6
[3]Department of Physical Sciences, Thompsons Rivers University, 900 McGill Road, Kamloops, British Columbia, Canada V2C 0C8
*Corresponding author: (email: emma.scanlan@queensu.ca)

INTRODUCTION

Despite being one of the world's largest reserves and producers of lead and zinc, our understanding of the formation of sedimentary exhalative (SEDEX) deposits is poorly understood, with the genetic models changing over time. Broadly, these deposits are composed of finely laminated galena and sphalerite, form in intracratonic rift basins and are interbedded with deep marine sediments (Goodfellow, 2004; Leach et al., 2010). Massive base metal sulphides can be found where vent structures are preserved (Goodfellow and Lydon, 2007).

Early models for SEDEX deposit formation assumed all of these deposits formed through exhalation of metalliferous brines on the seafloor (e.g. Lydon, 1983). There were two models for the precipitation of finely laminated base metal sulphides. The plume model suggested that sulphides were deposited from an anoxic water column within the basin, whereas the brine pool model suggested that sulphides precipitated as fine laminae within hypersaline, bottom hugging hydrothermal fluids (Goodfellow and Lydon, 2007). However, what have been classified as SEDEX deposits do not necessarily always have an exhalative component (Leach et al., 2005). Several deposits have been found to form through sub-seafloor replacement and precipitation, such as the Red Dog deposit in Alaska (Kelley et al., 2004).

It is clear that each SEDEX deposit did not form through the exact same processes. Even within a basin or the same district, deposits can vary in mineral assemblages, chemistry and textures, fluid characteristics and host rock compositions. This is evident within the Selwyn Basin, where the Howard's Pass District, MacMillan Pass and Anvil District have different characteristics such as preservation of vent structures and presence of barite (Magnall et al., 2014). Within the MacMillan Pass, variations can be seen between the deposits themselves, with the Boundary Creek deposit showing different mineral textures than those in the Tom and Jason deposits (Turner and Rhodes, 1990; Magnall et al., 2014).

Although the research into the extent to which SEDEX deposits are actually exhalative is on-going, these deposits are typically considered to form through purely hydrothermal fluids, with no magmatic input (Lydon, 1983; Leach et al., 2010). However, there are a few SEDEX deposits that have been hypothesised to have a link to magmatism. The Sullivan deposit in the Belt-Purcell Basin is a Mesoproterozoic SEDEX deposit in British Columbia. Within the footwall stratigraphy of the Sullivan deposit are mafic volcanic rocks of the Moyie Sill Complex, which are a series of mafic sills that are of similar age to mineralization (Anderson and Goodfellow, 2000). Although these mafic sills themselves would not produce enough heat for hydrothermal circulation, their volume (50 000 km^3) implies involvement of feeder magma bodies that could have provided a heat engine (Anderson and Goodfellow, 2000). The Boundary deposit at MacMillan Pass in the Selwyn Basin, Yukon, has a spatial and temporal relationship to magmatism (Turner and Rhodes, 1990). The MacMillan volcanic rocks have been intersected in drill holes that also intersect mineralization. The Rosh Pinah SEDEX deposit in southern Namibia also has a temporal and spatial relationship with volcanism. In this case volcanism is dominantly felsic, although there is mafic volcanism in the area (Alchin and Moore, 2005).

Irish-type deposits are considered a hybrid between SEDEX and Mississippi Valley Type (MVT) deposits. Irish-type deposits have a structural control on their distribution, and there is increasing evidence that magmatism was also focused along these structures. In the Stonepark region of Ireland, mineralization is associated with diatremes, with fluids utilising the permeable diatreme structures as fluid conduits and precipitating base metal sulphides within and around these structures (Elliott et al., 2019). Helium isotopes across the Irish ore field have a mantle signature, with increased fluid temperatures and He isotopic ratios in the south and southeast of the orefield (Davidheiser-Kroll et al., 2014; Wilkinson et al., 2015).

Given the recognition that magmas are at least in some cases spatially and temporally associated with SEDEX and similar styles of mineralization, we set out to investigate the potential that magmatic rocks may be genetically related to SEDEX mineralization in the Selwyn Basin, Yukon (Fig. 1). The Selwyn Basin is an ideal location for this study because both SEDEX deposits and magmatic rocks occur at various stages during the Paleozoic, with both vent-proximal and bedded facies of SEDEX mineralization present. To investigate this potential, we are using a combination of approaches: 1) field studies focussing on physical volcanology; 2) detailed geochemical analyses of volcanic and intrusive rocks as although there have been some previous studies (e.g. Goodfellow et al., 1995) this is the first to emphasise trace metals and metalloids that have significance to mineralization; 3) age dating of the volcanic rocks, as there are few precise age controls on the volcanic rocks to determine their temporal relationship to mineralization; and 4) isotopic analyses.

For the isotopic work, we initiated analyses of radiogenic isotopes (Nd, Sr, Pb) to better understand mantle versus crustal influences, but have also deployed emerging isotope systems, in particular Tl and Ba in the volcanic rocks and SEDEX mineralization,. In-situ isotopes (C, O, Sr) in the carbonate-rich parts of the volcanic rocks of the MacMillan Pass district are used to determine the extent of magmatic CO_2, and therefore the volatile-rich nature of magmatism that might contribute gases and potentially metals to magmatic-hydrothermal fluids.

This report presents interim results, with the important caveat that some analytical work is ongoing. Here we summarize the work to date on: 1) field work and physical volcanology; 2) major and trace element geochemistry of

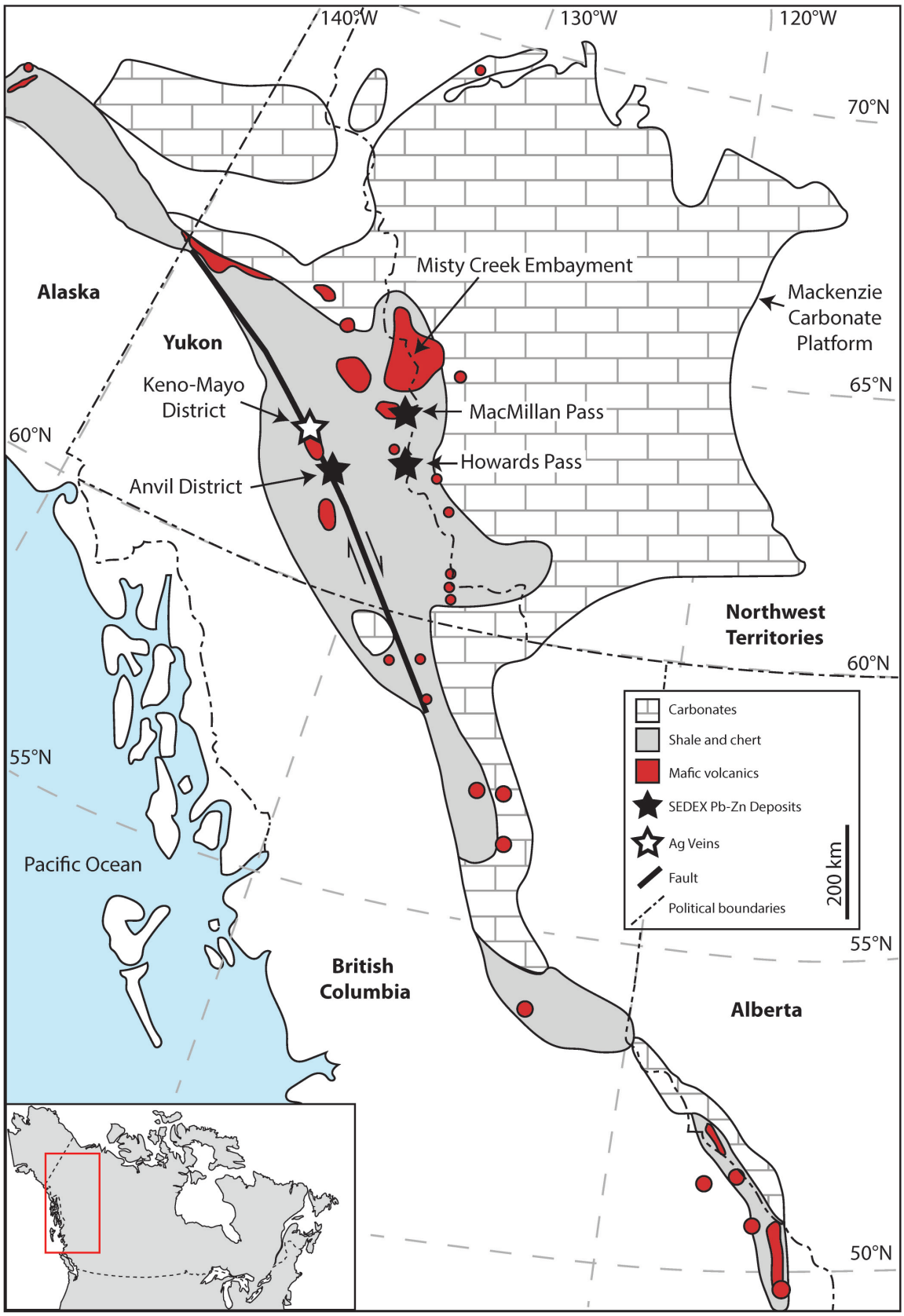

Figure 1: Location of mafic volcanic rocks and relevant SEDEX districts in the Selwyn Basin. Modified from Goodfellow et al. (1995).

volcanic rocks throughout the Selwyn Basin; 3) initial ages and plans for more age control; 4) preliminary Tl isotopic results and method development for the application of Ba isotopes to the study; and 5) a preliminary assessment of the potential for the volcanic rocks in the Selwyn Basin to have been an important genetic component of SEDEX mineralization.

REGIONAL GEOLOGY

The Selwyn Basin, near the border of the Yukon and Northwest Territories (Fig. 1), is a marine basin formed following the ca. 760 Ma initiation of rifting of Rodinia (Nelson and Colpron, 2007). Sedimentation began in the Neoproterozoic as syn-rift clastic sediments of the Windermere Supergroup (Nelson and Colpron, 2007). During the Cambrian, sedimentation transitioned to marine carbonate, chert and shale (Abbott, 1982; Goodfellow, 2004). After the Paleozoic, the tectonic regime shifted to collisional and terrane accretion to the Laurentian margin was initiated (Dusel-Bacon et al., 2002; Mair et al., 2006 Nelson and Colpron, 2007). This resulted in deformation and metamorphism of Paleozoic sedimentary rocks and intrusion of several granitoid bodies (Dusel-Bacon et al., 2002; Mair et al., 2006).

The MacMillan Pass deposits are located in the central block of the MacMillan fold belt. Within this central block there are five major Paleozoic sedimentary units (Abbott, 1982): Cambrian to Ordovician synrift clastic sedimentary rocks and shale of the Grit Unit; MacKenzie Platform carbonates (Lower Cambrian to Middle Devonian); Ordovician to Devonian shale, chert and rare limestone of the Road River Group; black clastic sedimentary rocks of the Devonian to Early Carboniferous Earn Group; and post Earn Group quartz arenite, chert, sandstone and shale. The SEDEX deposits in MacMillan Pass are hosted in the lower Earn Group. Alkaline volcanism is Middle to Late Devonian and occurs as tuff, breccia and flows that are interbedded with Earn Group marine sedimentation (Goodfellow et al., 1995).

The Anvil District is on the western margin of the Selwyn Basin (Fig. 1). The Paleozoic stratigraphy in this area contains four major units. Synrift clastic sediments of the Grit Unit are overlain by non-calcareous phyllite and schist, marble lenses and minor basalt of the Cambrian Mt Mye Formation. The Cambrian to Ordovician Vangorda Formation is composed of calcareous phyllite and schist, calc-silicate, and basalt. The overlying Menzie Creek Formation contains Ordovician to Silurian pillow basalts and massive volcanic flows, breccias, tuff, and interbedded black shales (Goodfellow, 2004). SEDEX deposits within the Anvil District (Faro, Grum, Vangorda, DY, Swim) are hosted in carbonaceous shales near the contact of the Mt Mye and Vangorda Formations (Goodfellow, 2004). There are minor VMS showings in the Menzie Creek Formation, such as the Rebel deposit, which was historically mined (Carne & Cathro, 1982). Alkaline volcanism in the Keno-Mayo area (Fig. 1) can be found within the Devonian-Carboniferous Earn Group, which is regionally metamorphosed up to greenschist facies. Within the Keno Hill area, the granitic Late Cretaceous Mayo Lake Pluton has an Ag-Pb-Zn hydrothermal vein system that extends up to 40 km from the pluton (Lynch, 1989). Ag is found in sulphide veins within the Early Carboniferous Keno Hill Quartzite (Lynch, 1989). Triassic diorite and gabbroic sills are also present in the region, cross-cutting the Keno Hill Quartzite (Sack et al., 2018).

Alkaline volcanic and volcaniclastic rocks within the Misty Creek Embayment (Fig. 1) occur in the Ordovician Marmot Formation. Lithologies include lapilli tuff to fine volcanic breccia, sandstone and argillite, massive flows, conglomerate, sills, and rare breccia (Cecile, 1982). The Marmot Formation has a variable thickness from one to tens of metres. In two mapped locations it is 250 to 500 m thick, with one of these locations interpreted as a volcanic centre. At the volcanic centre, volcanism began in a deep submarine environment and 'shoaled' to a shallow marine environment and perhaps subaerial volcanism (Cecile, 1982).

SAMPLES, FIELD WORK AND PHYSICAL VOLCANOLOGY

Samples were collected during a field season in 2016 from three regions in the Selwyn Basin: MacMillan Pass, Anvil District and the Keno-Mayo District (Fig. 1). This sample set was supplemented by MacMillan Pass samples provided by Fireweed Zinc and Misty Creek Embayment samples collected by Wayne Goodfellow (as reported in Goodfellow et al., 1995). MacMillan Pass samples came from Devonian MacMillan and Niddery Lake volcanic units, Anvil District samples are of the Ordovician-Silurian Menzie Creek volcanic rocks (Fig. 2), with metavolcanic rocks from the Devonian Earn Group sampled from the Keno-Mayo District.

MacMillan pass samples are typified by lapilli tuff and volcaniclastic breccia. Samples from the Menzie Creek volcanic rocks comprise basalt, tuff and lapilli tuff. Several mafic intrusive samples were also collected. The textures and mineralogy of these samples are described in Scanlan et al. (2019). The majority of the MacMillan Pass samples contain carbonates, typically calcite or ankerite. These carbonates are found as volcaniclastic breccia matrix, circular clusters and replacing phenocrysts in volcanic clasts (Scanlan et al., 2019). The high proportion of carbonate suggests that some is likely primary magmatic carbonate, indicating a volatile-rich magma produced explosive eruptions in MacMillan Pass. Isotopic analysis (C, O and Sr) of this carbonate is planned to determine if there is magmatic carbonate. Carbonate is less abundant in Anvil District samples. This carbonate is calcite and ankerite replacing

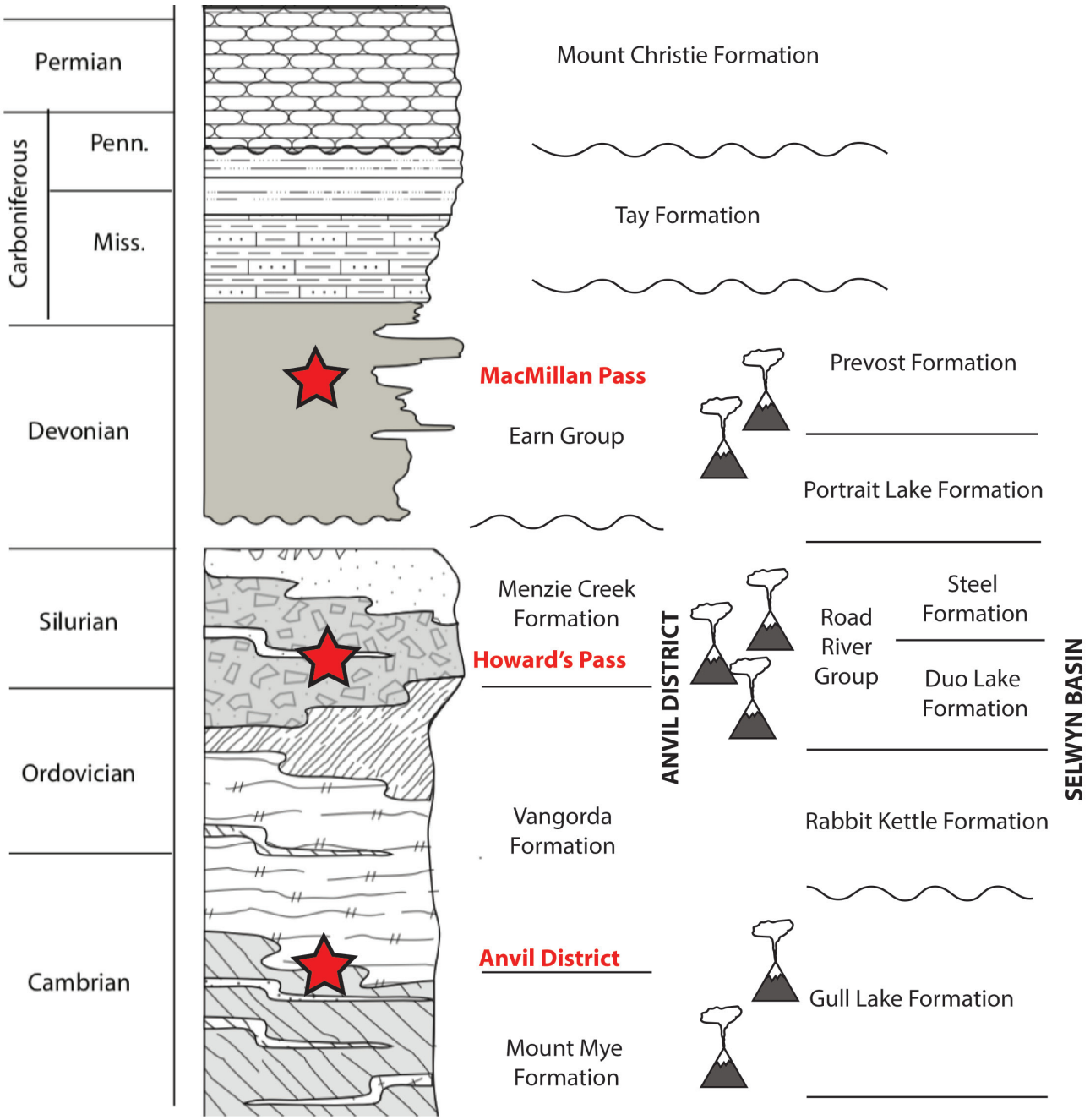

Figure 2: Paleozoic sedimentary strata of the Anvil District and the Selwyn Basin. From Cobbett (2016).

phenocrysts, filling vesicles and forming veins/lenses. Unlike the MacMillan Pass, no primary magmatic carbonate has been identified in the Anvil District samples.

Mineralogy and textures

Scanning electron microscopy (SEM) analysis was conducted on 40 samples to identify textures and mineralogy that could not be observed on a petrographic microscope. Scanning electron microscopy dispersive x-ray spectroscopy (SEM-EDS) analysis was carried out at the Queen's University Facility for Isotope Research (QFIR) using a FEI Quanta 650® field emission gun environmental SEM. Backscatter electron imaging and mineral analysis was carried out on polished thin sections under a low vacuum at 15 kV. Samples were not carbon coated.

Barium-bearing phases that have been identified include hyalophane ($(K,Ba)[Al(Si,Al)Si_2O_8]$), barite and barytocalcite. Goodfellow et al. (1995) also noted the presence of celsian (end-member = $BaAl_2Si_2O_8$) in some of these samples. One sample from MacMillan Pass contains primary hyalophane, a barium-potassium feldspar. This hyalophane is found as 10-50 µm subhedral crystals in the groundmass between circular clusters of coarse calcite (Fig. 3). This sample also contains barite inclusions and veinlets, with the barium likely sourced from breakdown of hyalophane.

Cathodoluminescence (CL) imaging was conducted on ten carbonate-bearing MacMillan Pass samples. The colour of the CL response of carbonate varies within between and samples (Fig. 4). The CL response varies from yellow, orange, red, blue, to purple in carbonate. Zoning is present within large carbonate grains, with bright growth zones, often near the edges of grains (Fig. 5). This zoning is present in large carbonate grains that luminesce the same orange colour, and has been observed in two samples (MP-09, MP-11). Zoning varies between gradual changes over a larger area and sharp changes in the CL response. One sample (MP-13) contains carbonate grains that do not luminesce, whereas the edges of these grains and smaller carbonate grains luminescing bright orange.

Geochemistry of Volcanic Rocks

Major elements and alteration

Whole rock lithogeochemistry of 140 samples was conducted by ALS Geochemistry, Vancouver, B.C. Full methods and data are outlined in Leybourne et al. (2018). Whole rock samples were crushed and prepared by in low-Cr-Mo mild steel ring mills. Major elements were measured using inductively coupled plasma-atomic emission spectrometry (ICP-AES) and trace elements were measured using inductively coupled plasma-mass spectrometry (ICP-MS).

Discussion of major and select trace elements is presented in more detail in Leybourne et al. (2018) and Scanlan et al. (2019). Most samples are compositionally within plate alkali basalt, with the exception of Keno-Mayo area Triassic dykes that are tholeiitic. Spidergrams show positive anomalies for Ba, Pb and Ti with negative anomalies in Rb, K, Pb, Sr and Ti (Scanlan et al., 2019).

On an alteration box plot (Ishikawa alteration index versus chlorite-carbonate-pyrite index of Large et al. (2001)) a large proportion of samples show a hydrothermal alteration signature; this is particularly so for those samples from the Anvil District (Scanlan et al., 2019). In contrast, samples from MacMillan pass have dominantly been subaerially weathered rather than hydrothermally altered (Scanlan et al., 2019). Many samples from the Anvil District plot within the least-altered basalt box, corresponding with the samples that display minimal alteration such as primary phenocrysts still present. Carbon contents in the volcanic samples varies from 0.02 to 9.83 weight %, and is higher in MacMillan Pass samples, with an average of 3.76 weight %. This reflects the high proportion of calcite and ankerite in the MacMillan Pass volcanic rocks. It is suspected that some of this carbonate is magmatic.

Trace element geochemistry

Thallium concentrations in volcanic samples vary from below detection limit (0.04 ppm) to 1.83 ppm, whereas barium is enriched (4.3 to >10 000 ppm). A positive correlation is recorded between Tl and Ba, that mimics the trend seen in Selwyn Basin mineralised samples ($R^2 = 0.467$; Fig. 6A–B). This trend is opposite to that of the Canol Formation, where Tl increases as Ba decreases (Fig. 6B). This may suggest some linkage between Tl in the volcanic and mineralising systems. Many thallium compounds are easily volatilised (Shaw, 1952) and thus Tl could be lost in a volatile-rich volcanic system, such as the MacMillan Pass volcanic rocks, making it a relevant element and isotope system to analyse. Rubidium and Cs show a positive correlation with Tl ($R^2 = 0.653$, 0.507; Fig. 6C-D) due to the behaviour of thallium as an alkali metal. When plotting Tl against Mo, As and Sb we see a slight positive trend ($R^2 = 0.032$, 0.036, 0.011; Fig. 6E–G). Copper tends to decrease with increasing Tl contents ($R^2 = 0.016$; Fig. 6H). There is no apparent trend between Tl and Zn, Pb or Cd. Thallium also shows a positive trend when plotted against the calcite-chlorite-pyrite index (CCPI) (Fig. 7).

Samples were chosen for Tl isotopic analysis. These show two distinct trends for samples from the Anvil District and MacMillan Pass when Ce/Tl is plotted against Th/Rb (Fig. 8). Samples from the Anvil District trend towards depleted mid-ocean ridge mantle values (Th/Rb = 0.09–0.19, Ce/Tl = 900–1300) and altered basalts of Nielsen et al. (2017). Thus, changes in the Tl content of the volcanic rocks is likely related to hydrothermal alteration, as suggested by the correlation between Tl and CCPI (Fig. 7).

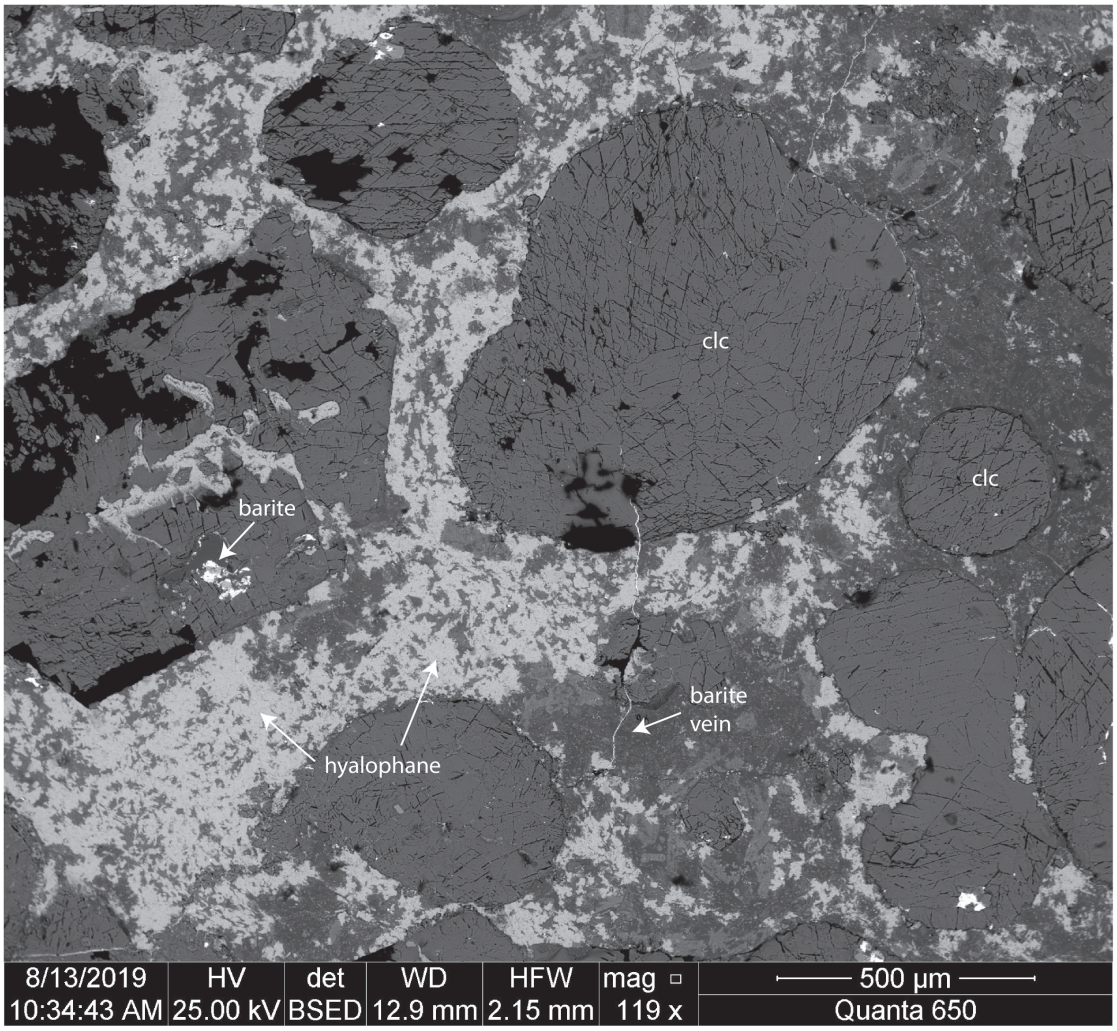

Figure 3: Backscattered electron image of hyalophane, which occurs in the groundmass between circular clusters of calcite. Small inclusions and veins of secondary barite are present. Clc = calcite.

Age Dating

Mineralization is hosted at the contact of the Mt Mye and Vangorda Formation in the Anvil District, within the Ordovician-Silurian Duo Lake Formation (Howard's Pass) and the Devonian Earn Group in MacMillan Pass (Norford and Orchard, 1985; Jennings and Jilson, 1986; Goodfellow, 2004) (Fig. 2). There are three major periods of alkaline magmatism in the Selwyn Basin: Cambrian, Ordovician-Silurian and Devonian (Goodfellow et al., 1995). The volcanic rocks studied are the Ordovician-Silurian Menzie Creek volcanic rocks in the Anvil District, Ordovician-Silurian Marmot Formation and Porter Puddle Complex in the Misty Creek Embayment and Devonian MacMillan and Niddery volcanic rocks and metavolcanic horizons in the Earn Group (Jennings and Jilson, 1986; Abbott and Turner, 1991; Goodfellow et al., 1995 Cecile and Norford, 2000; Pigage, 2004) (Fig. 2). Constraining the age relationships of mineralization and magmatism is important in understanding whether magmatism contributes to the genesis of SEDEX deposits. Geochronology in the Selwyn Basin is dominantly stratigraphic ages based on paleontological assemblage (e.g. Norford et al., 1993), along with U-Pb geochronology for the Kechika Group (Campbell et al., 2019). Radiometric ages of the volcanic units sampled in this project would contribute to the geochronology of Paleozoic units in the Selwyn Basin as well as constraining any relationships to mineralization. The MacMillan volcanic rocks, Menzie Creek Formation and Earn Group are the units targeted for age dating.

Preliminary TIMS date

A metavolcanic sample from the Keno-Mayo region was dated using chemical abrasion thermal ionisation mass spectrometry (TIMS) at Boise State University, Idaho. Selected zircon grains give an age of ca. 297 Ma. This sample was taken from what was assumed to be the Devonian Earn

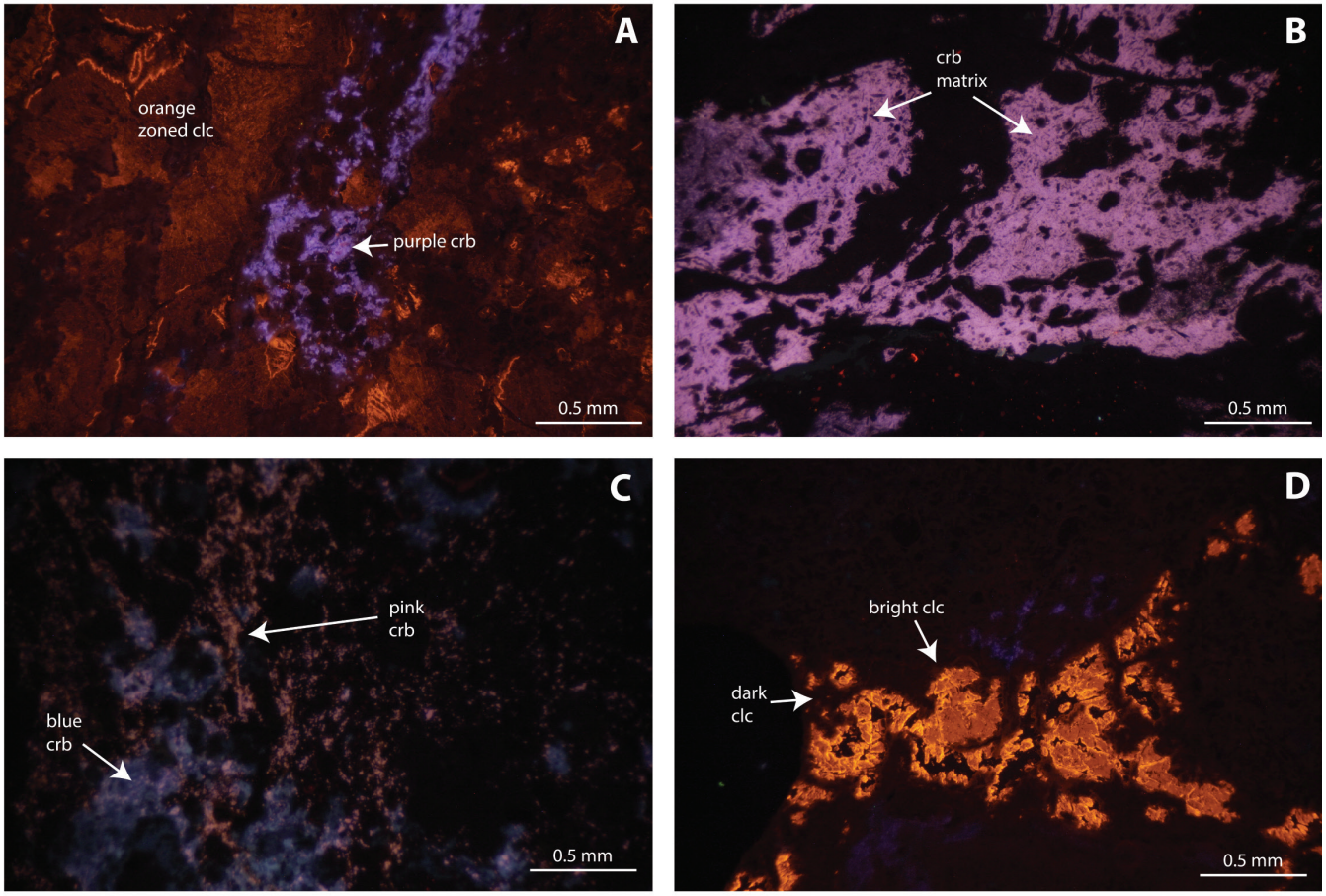

Figure 4: A. Cathodolumiscence image of zoned coarse orange calcite that is overprinted by anhedral purple carbonate. **B**. Carbonate matrix luminesces a purple colour. **C**. Intergrown blue and pink carbonate. **D.** Calcite that does not luminesce with a later generation of bright orange calcite grains.

Group. The much younger Triassic age indicates that either the stratigraphic unit this sample was taken from is not the Earn Group or the metavolcanic sample taken is an intrusion within the Earn Group. Analysis and interpretation of this age is ongoing.

Laser ablation ICP-MS dating

Sixteen samples were crushed using the SelFrag high voltage pulse power fragmentation system at Queen's University and sent to Overburden Drilling Management Ltd. (ODM) for zircon separation. The fraction that was greater than 1 mm was milled at ODM using a BICO crusher to less than 1 mm. The crusher was cleaned with quartz between each sample. Micropanning for zircons was carried out on the less than 1 mm fraction, with the remaining material refined through heavy liquid separation (specific gravity = 3.3). Full methods are described in McClenaghan (2011). The heavy mineral separates were set in a thin layer of epoxy resin under a vacuum for five minutes for removal of air bubbles. Following this, the remaining epoxy resin was added to the cast and set under a vacuum for an additional five minutes. The resulting grain mounts were polished to a 1 µm grit size.

Epoxy mounts were analysed using mineral liberation analysis (MLA) with extended backscattered electron (XBSE) liberation analysis (Fandrich et al., 2007) at QFIR. Mineral liberation analysis was completed to identify high density grains with resulting mineral spectra of these grains matched to the QFIR MLA database. Zircon, monazite and apatite were then identified and imaged (Scanlan et al., 2019).

Samples with suitable minerals will be dated using laser ablation inductively-coupled plasma mass spectrometry (LA-ICP-MS) at QFIR. Epoxy mounts will be analysed on a ThermoScientific X Series 2 quadrupole ICP-MS with a NewWave/ESI 193-nm ArF Excimer laser system. The measured isotopes will be ^{204}Pb, ^{206}Pb, ^{207}Pb, ^{208}Pb, ^{232}Th and ^{238}U, whereas ^{202}Hg will be monitored to correct of isobaric interference on ^{204}Pb; data reduction will be carried out using Iolite 3.0 (Paton et al., 2011).

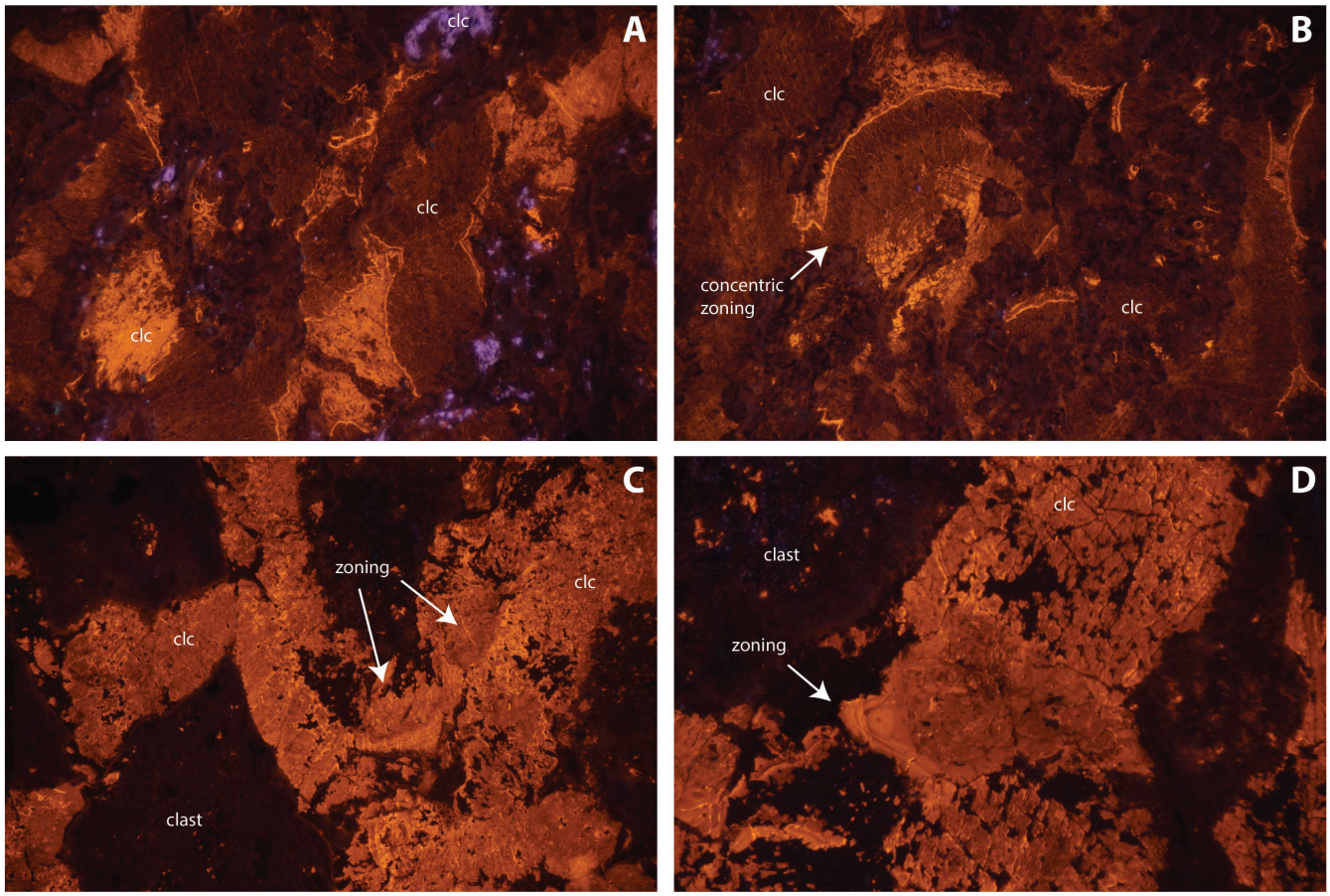

Figure 5: A. Coarse calcite that is zoned, showing differences in the CL response. Zoning is typically sharp in this sample. **B.** Concentric zoned calcite. **C.** Gradual zoning in calcite. **D.** Sharper zoning in a subhedral calcite termination.

Isotopic Studies

Tl isotopes

Thallium isotopes are being analysed to examine potential input of metalloids from magmas into the mineralising system. Thallium shows a correlation with several other metals in the volcanic rocks (Ba, Mo, Sb, As, Cu) and preferentially enters the volatile phase of a magma as it is a large ion lithophile element. Thallium isotopes of mineralised samples have been measured in the Selwyn Basin (Peter et al. 2017) and so a dataset already exists for comparison.

Fifteen samples were analyzed from the Anvil District and MacMillan Pass. Samples were digested, eluted and then analyzed on a Thermo-Finnigan Neptune® multi-collector ICP-MS at QFIR following the methods described in Peter et al. (2017). Six samples from MacMillan Pass give a ε^{205}Tl range of –14.2 ± 3.2 to –3.2 ± 1.8, with a large error on the most negative value. Five samples from the Anvil District have a less negative ε^{205}Tl range of –6.4 ± 1.2 to –0.9 ± 1.9 (Table 1; Scanlan et al., 2019). No trend was seen when the ε^{205}Tl values were plotted against Tl concentrations, but a negative correlation was present between ε^{205}Tl and Ba content (Scanlan et al., 2019). It was interpreted that the lighter isotopic values from MacMillan Pass represent low temperature hydrothermal alteration. Thallium isotope data of Crawford et al. (2019) for a Devonian hyper-enriched black shale deposit in the Yukon range from –8.1 to –5.2. The unmineralized black shale stratigraphically above and below the mineralization exhibit very similar ε^{205}Tl values of –4.8 to –4.4 (Crawford et al., 2019). These black shales overlap with the least negative values from the Devonian MacMillan volcanic rocks.

Ba Isotopes

There are seven naturally occurring stable isotopes of Ba (^{130}Ba, ^{132}Ba, $^{134\text{-}138}$Ba) with barium occurring in aqueous systems as Ba^{2+} (Charbonnier et al., 2018). Ba isotopes are reported as δ^{137}Ba where $\delta^{137}Ba = (^{137}Ba/^{134}Ba_{sample} / {}^{137}Ba/^{134}Ba_{standard} - 1) \times 1000$). The Barium standard solution used is typically NIST SRM 3104a. Barium isotopes are often measured using the double spike method, where

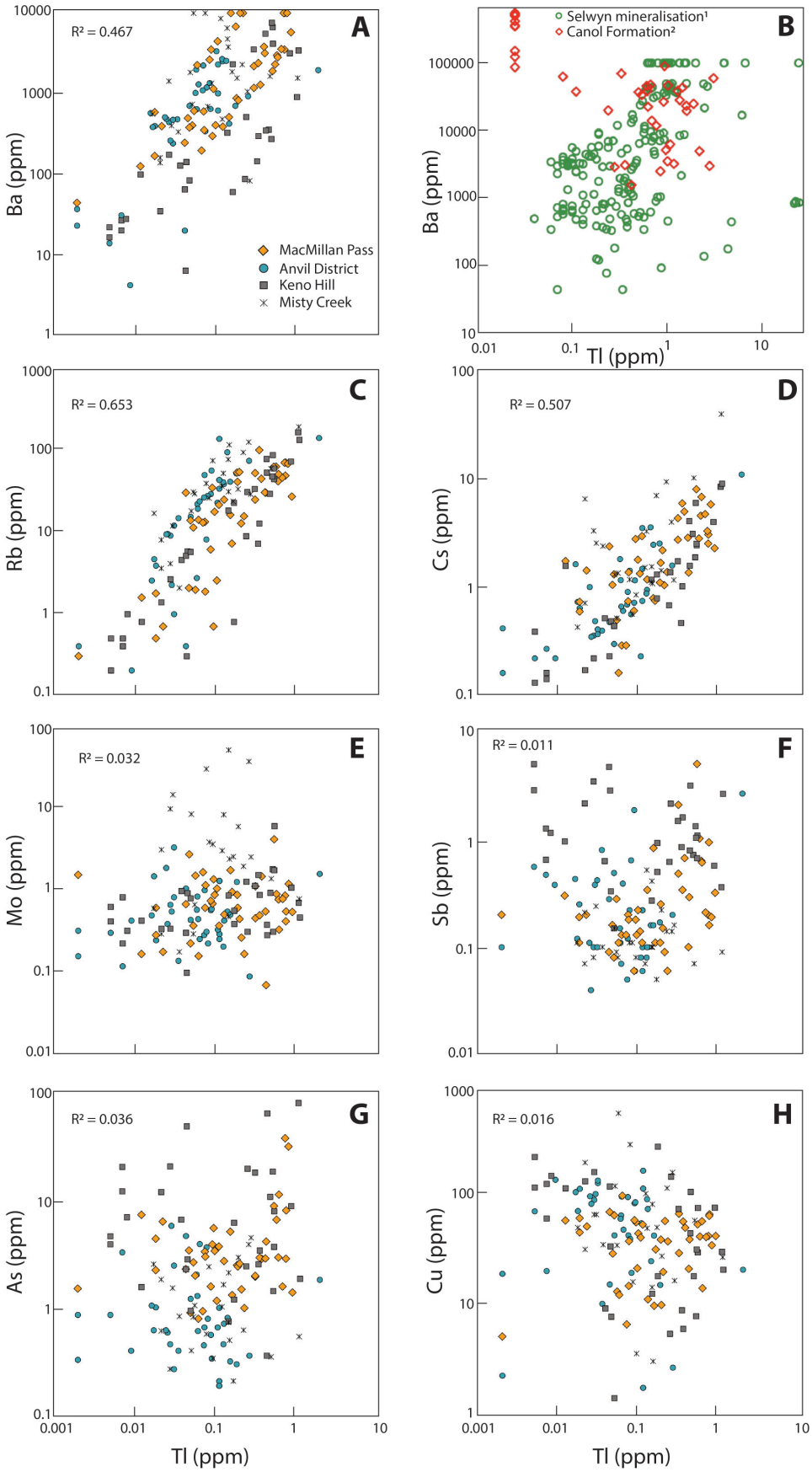
A
R² = 0.467
Ba (ppm)
MacMillan Pass
Anvil District
Keno Hill
Misty Creek
B
Selwyn mineralisation¹
Canol Formation²
Ba (ppm)
Tl (ppm)
C
R² = 0.653
Rb (ppm)
D
R² = 0.507
Cs (ppm)
E
R² = 0.032
Mo (ppm)
F
R² = 0.011
Sb (ppm)
G
R² = 0.036
As (ppm)
Tl (ppm)
H
R² = 0.016
Cu (ppm)
Tl (ppm)

Figure 6: A. Thallium and Ba are positively correlated. **B**. Mineralised samples from the Selwyn Basin show a similar trend to Selwyn Basin volcanic rocks (Peter, unpublished data referenced in Leybourne et al., 2018) whereas the Canol Formation shows decreasing Ba with increasing Tl (Fernandes et al., 2017). **C**. Rb and Tl contents are positively correlated. **D**. Cs and Tl are positively correlated. **E**. Molybdenum contents tend to increase with Tl. **F**. Sb displays a weak positive correlation with Tl. **G**. As is positively correlated with Tl. **H**. Copper contents decrease with increasing Tl.

a known mixture of $^{137}Ba/^{134}Ba$ is added to the sample. This allows for more accurate measurement of samples with low Ba and also to correct for instrumental mass fractionation without having to use the sample-standard bracketing technique (Charbonnier et al., 2018).

Barium has typically been used as a biogeochemical tracer and paleo productivity proxy due to the fact that Ba concentrations mimic ocean nutrients, with a Ba depletion at the surface and enrichment in deep and older waters (Chow and Goldberg, 1960; Paytan and Kastner, 1996). Barium isotopic fractionation is mass dependant. Precipitation of barite results in an enrichment of light Ba isotopes in sulphide minerals whereas removal of Ba from oceanic surface waters results in heavier Ba isotope enrichment (Horner et al., 2015; Bates et al., 2017; Hsieh and Henderson, 2017). However, Ba removal processes are slow and therefore the Ba isotope signature of ocean waters is dominantly controlled by basin-scale processes such as mixing of different waters and river inputs, with rivers having lighter isotopic signatures than oceans (Hsieh and Henderson, 2017.)

The Selwyn Basin is a barium-rich system. The volcanic samples are enriched in Ba, many of the SEDEX deposits contain barite, and there is sedimentary barite (Turner and Goodfellow, 1990). The source of Ba in the SEDEX deposits has been hypothesised as seawater derived. Measuring the Ba isotopes of these various Ba-bearing systems could elucidate the source of barium.

FUTURE WORK

Initial Ba isotope method development has begun at QFIR. Cup configuration has been set up on the MC-ICP-MS to measure ^{131}Xe, ^{132}Ba, ^{134}Ba, ^{135}Ba, ^{136}Ba, ^{137}Ba. Xenon 131 is measured to correct for Xe mass interferences on ^{132}Ba, ^{134}Ba and ^{136}Ba. An in-house Ba standard solution was created and measured at concentrations of 20, 50, 100, 200 and 500 ppb and 1 and 5 ppm. A Ba purification process of elution through Sr spec resin is currently in development.

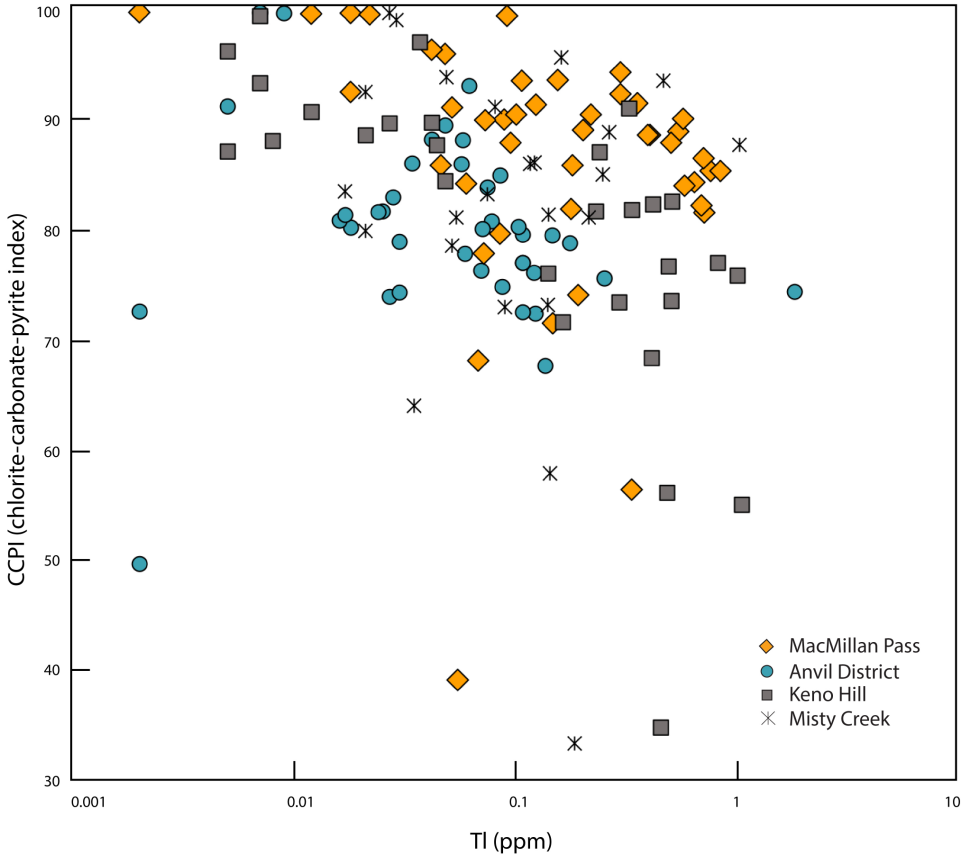

Figure 7: Thallium tends to have the lowest concentrations in samples with high CCPI (chlorite-carbonate-pyrite index) values.

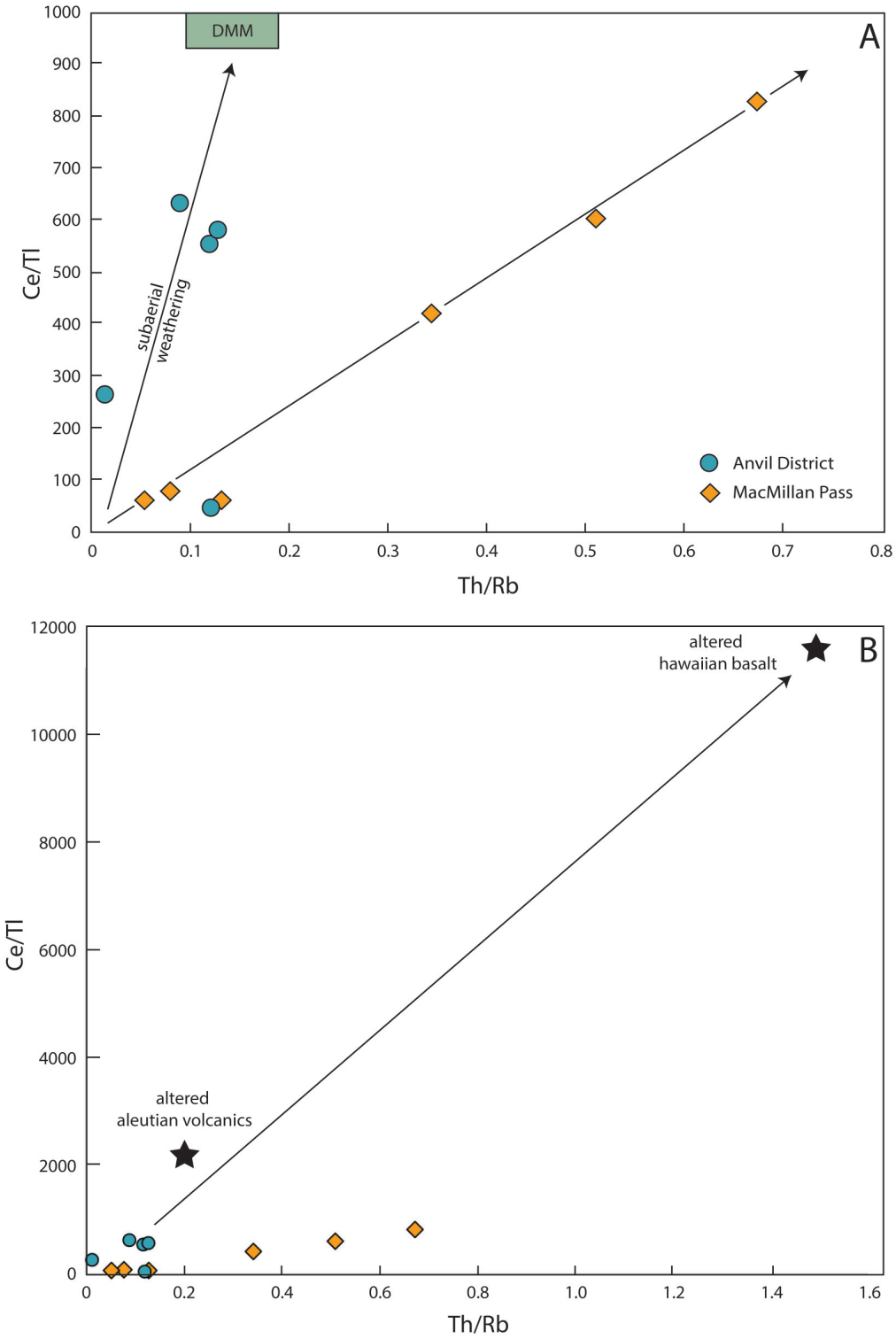

Figure 8: Anvil District volcanic samples trend towards depleted mid-ocean ridge mantle (DMM) and altered volcanic rocks from Nielsen et al. (2017). MacMillan Pass volcanic rocks have a distinct trend-line that differs from that of the Anvil District samples. Only samples that have been measured for Tl isotopes (see Scanlan et al., 2019) are displayed.

Table 1: Thallium isotopes of whole rock volcanic samples from MacMillan Pass and the Anvil District (Scanlan et al., 2019).

Sample #	Location	$\varepsilon^{205}Tl$	±	Tl (ppm)	Ba (ppm)
2016-MP-03	MacMillan Pass	-5.9	1.5	0.762	10000
2016-MP-11	MacMillan Pass	-14.2	3.2	0.299	2190
2016-MP-09	MacMillan Pass	-7.4	1.3	0.848	5790
2016-MP-47	MacMillan Pass	-3.2	1.8	0.187	901
2016-MP-18	MacMillan Pass	-7.1	2.2	0.155	10000
2016-MP-20	MacMillan Pass	-9.5	2.5	0.202	10000
2016-MC-10	Anvil District	-6.4	1.2	1.83	1965
2016-MC-41	Anvil District	-0.9	1.9	0.176	713
2016-MC-13	Anvil District	-5.2	1.7	0.103	3380
2016-MC-30	Anvil District	-4.2	1.8	0.059	648
2016-MC-29	Anvil District	-4.4	2.2	0.108	623

Future work will involve measurement of International Atomic Energy Agency (IAEA) Ba carbonate standard CO-9, and barium sulfate SO-5 and SO-6. Measurement of volcanic standards BHVO and AGV with and without a Ba double spike will also be carried out.

Other current work on this project includes measuring Sr, Nd, Pb and Tl isotopes of volcanic samples from MacMillan Pass and the Anvil District. Formation. U-Th-Pb geochronology will be carried out from zircon and apatite using LA-ICP-MS. C, O and Sr isotopes will be measured in-situ and using micro-drilled samples from carbonates to differentiate magmatic from hydrothermal carbonate.

INTERIM INTERPRETATIONS AND CONCLUSIONS

MacMillan Pass volcanic rocks are predominantly lapilli tuffs and volcaniclastic breccias that contain a large proportion of carbonate. These volcanic rocks represent explosive eruptive activity in a volatile-rich system. High Ba contents in the volcanic rocks is due to the presence of hyalophane and secondary barite and barytocalcite. Cathodoluminescence imaging shows zoning within large carbonate grains and the CL response of carbonate varies within and between samples. Carbonate that displays an orange CL response may represent late stage hydrothermal carbonate. In volcanic samples, Tl shows positive trends with Rb, Cs, Ba, Mo, As, Sb and is negatively correlated with Cu. Thallium shows positive trends with Rb and Cs due to the behaviour of Tl^+ (the predominant form of Tl in nature) as an alkali element. A positive relationship between Tl, As and Sb has been demonstrated before, where Tl^+ is found in pyrite associated with As^{3+} and Sb^{3+} (George et al., 2019). Low concentrations of Tl in the volcanic samples is likely due to removal of Tl through hydrothermal alteration or subaerial weathering, which is suggested by the correlation of Tl content and CCPI.

Our preliminary assessment is that there is likely a link between mineralization and magmatism in the Selwyn Basin. We base this assessment on: 1) the close spatial and temporal relationships, particularly in MacMillan Pass; 2) the volatile-rich nature of magmatism in MacMillan Pass; 3) the alkalic geochemistry of the volcanic rocks, particularly the high Ba contents, even in the least altered samples; and 4) the correlations of Mo, As, Sb, Tl, Cu and Ba. SEDEX deposits are hosted in intracratonic rift basins, which form through extension, resulting in the upwelling of mantle, partial melting and the formation of alkaline volcanic rocks. The tectonic setting of these deposits are linked to alkaline magmatism and increased heat flow from the upwelling mantle, suggesting that magmatism is part of SEDEX hydrothermal systems.

ACKNOWLEDGEMENTS

We would like to thank the following research technicians and students of QFIR, Agatha Dobozs for help with SEM analysis, Dr. Donald Chipley and Taylor Drake for Ba isotope method development, Jackson Malone for help with CL imaging. Thank you also to the TGI programme and Society of Economic Geology for funding for this project.

REFERENCES

Abbott, G., 1982. Structure and stratigraphy of the MacMillan Fold Belt: evidence for Devonian faulting; Open File Report, Exploration and Geological Services Division, Department of Indian Affairs and Northern Development, Whitehorse, Yukon, 16 p.

Abbott, J.G., and Turner, R.J., 1991. Character and paleotectonic setting of Devonian stratiform sediment-hosted Zn, Pb, Ba deposits, Macmillan fold belt, Yukon. *in* Mineral Deposits of the Northern Canadian Cordillera, Yukon – Northeastern British Columbia. Abbott, J.G. and Turner, R.J.W. (eds.) Open File 2169, p. 99-136.

Alchin, D.J., and Moore, J.M., 2005. A review of the Pan-African, Neoproterozoic Rosh Pinah Zn-Pb deposit, southwestern Namibia. South African Journal of Geology, v. 108, p. 71-86.

Anderson, H.E., and Goodfellow, W.D., 2000. Geochemistry and isotope chemistry of the Moyie Sills: Implications for the early tectonic setting of the Mesoproterozoic Purcell Basin. *in* The Geological Environment of the Sullivan Pb-Zn-Ag Deposit, British Columbia, (ed.) J.W. Lydon, T. Höy, J.F. Slack, and M.E. Knapp; Mineral Deposits Division of the Geological Association of Canada, Special Publication No. 1, p. 302-321.

Bates, S.L., Hendry, K.R., Pryer, H.V., Kinsley, C.W., Pyle, K.M., Woodward, E.M.S., and Horner, T.J., 2017. Barium isotopes reveal role of ocean circulation on barium cycling in the Atlantic. Geochimica et Cosmochimica Acta, v. 204, p. 286-299.

Campbell, R.W., Beranek, L.P., Piercey, S.J., and Friedman, R., 2019. Early Paleozoic post-breakup magmatism along the Cordilleran margin of western North America: New zircon U-Pb age and whole-rock Nd-and Hf-isotope and lithogeochemical results from the Kechika group, Yukon, Canada; Geosphere, v. 15, p.1262-1290.

Carne, R.C., and Cathro, R.J. 1982. Sedimentary exhalative (SEDEX) zinc lead deposits, northern Canadian Cordillera. Canadian Institute of Mining and Metallurgy Bulletin, v. 75, p. 66-78.

Cecile, M.P. 1982. The Lower Paleozoic Misty Creek Embayment, Selwyn Basin, Yukon and Northwest Territories. Canada GSo ed. 78 p.

Cecile, M.P., and Norford, B.S. 2000. Geology of the northeastern Niddery Lake map area, east-central Yukon and adjacent Northwest Territories. Geological Survey of Canada. v. 553, 119 p.

Charbonnier, Q., Moynier, F., and Bouchez, J. 2018. Barium isotope cosmochemistry and geochemistry. Science Bulletin, v. 63, p. 385-394.

Chow, T.J., and Goldberg, E.D. 1960. On the marine geochemistry of barium. Geochimica et Cosmochimica Acta, v. 20, p. 192-198.

Cobbett, R., 2016. Preliminary observations on the geology of Tay Mountain Area (parts of NTS 105K/12 and 13, 105L/09 and 16), central Yukon. *in* Yukon Exploration and Geology 2015, (eds.) K.E. MacFarlane and M.G. Nordling; Yukon Geological Survey, p. 79-98.

Crawford, I., Layton-Matthews, D., Peter, J.M., Gadd, M.G., and Voinot, A., 2019. Toward the application of molybdenum and thallium isotopes as indicators of paleoredox conditions and genesis of hyper-enriched black shale (HEBS) deposits, Peel River, Yukon; *in* Targeted Geoscience Initiative: 2018 report of activities, (ed.) N. Rogers; Geological Survey of Canada, Open File 8549, p. 139–161.

Davidheiser-Kroll, B., Stuart, F.M., and Boyce, A.J. 2014. Mantle heat drives hydrothermal fluids responsible for carbonate-hosted base metal deposits: evidence from 3 He/4 He of ore fluids in the Irish Pb-Zn ore district. Mineralium Deposita, v. 49, p.547-553.

Dusel-Bacon, C., Lanphere, M.A., Sharp, W.D., Layer, P.W., and Hansen, W.L., 2002. Mesozoic thermal history and timing of structural events for the Yukon-Tanana upland, east-central Alaska: 40Ar/39Ar data from metamorphic and plutonic rocks; Canadian Journal of Earth Sciences, v. 39, p. 1013–1051

Elliott, H.A., Gernon, T.M., Roberts, S., Boyce, A.J., and Hewson, C.. 2019. Diatremes act as fluid conduits for Zn-Pb mineralization in the SW Irish ore field. Economic Geology, v. 114, p.117-125.

Fandrich, R., Gu, Y., Burrows, D., and Moeller, K. 2007. Modern SEM-based mineral liberation analysis; International Journal of Mineral Processing, v. 84, p.310-320.

Fernandes, N.A., Gleeson, S.A., Magnall, J.M., Creaser, R.A., Martel, E., Fischer, B.J., and Sharp, R. 2017. The origin of Late Devonian (Frasnian) stratiform and stratabound mudstone-hosted barite in the Selwyn Basin, Northwest Territories, Canada; Marine and Petroleum Geology, v. 85, p. 1–15.

George, L.L., Biagioni, C., Lepore, G.O., Lacalamita, M., Agrosì, G., Capitani, G.C., Bonaccorsi, E., and d'Acapito, F. 2019. The speciation of thallium in (Tl, Sb, As)-rich pyrite. Ore Geology Reviews, v. 107, p. 364-380.

Goodfellow, W.D., Cecile, M.P., and Leybourne, M.I., 1995. Geochemistry, petrogenesis, and tectonic setting of lower Paleozoic alkalic and potassic volcanic rocks, northern Canadian Cordilleran Miogeocline; Canadian Journal of Earth Sciences, v. 32, p. 1236-1254.

Goodfellow, W.D. 2004. Geology, genesis and exploration of SEDEX deposits, with emphasis on the Selwyn Basin, Canada. *in* Deb, M. and Goodfellow, W.D. (eds.) Sediment-hosted Lead-Zinc sulphide deposits. New Dehli, India, Narosa Publishing House, pp. 24-100.

Goodfellow, W.D., and Lydon, J.W., 2007. Sedimentary exhalative (SEDEX) deposits. *in* Mineral deposits of Canada: A synthesis of major deposit types, district metallogeny, the evolution of geological provinces, and exploration methods (ed.) Goodfellow, W.D.; Geological Association of Canada, Mineral Deposits Division, Special Publication, 5, pp.163-183.

Horner, T.J., Kinsley, C.W., and Nielsen, S.G. 2015. Barium-isotopic fractionation in seawater mediated by barite cycling and oceanic circulation. Earth and Planetary Science Letters, v. 430, p. 511-522.

Hsieh, Y-T., and Henderson, G.M. 2017. Barium stable isotopes in the global ocean: Tracer of Ba inputs and utilization. Earth and Planetary Science Letters, v. 473, p. 269-278.

Jennings, D.S., and Jilson, G.A., 1986. Geology and sulphide deposits of the Anvil Range, Yukon; in Mineral Deposits of Northern Cordillera, (ed.) J.A. Morin, J.A.; Canadian Institute Mining and Metallurgy, p. 339-361.

Kelley, K.D., Leach, D.L., Johnson, C.A., Clark, J.L., Fayek, M., Slack, J.F., Anderson, V.M., Ayuso, R.A., and Ridley, W.I. 2004. Textural, compositional, and sulfur isotope variations of sulphide minerals in the Red Dog Zn-Pb-Ag deposits, Brooks Range, Alaska: Implications for ore formation; Economic Geology, v. 99, p. 1509-1532.

Large, R.R., Gemmell, J.B., Paulick, H., and Huston, D.L. 2001. The alteration box plot: A simple approach to understanding the relationship between alteration mineralogy and lithogeochemistry associated with volcanic-hosted massive sulphide deposits. Economic Geology, v. 96, p. 957-971.

Leach, D.L., Sangster, D.F., Kelley, K.D., Ross, R.L., Garven, G., and Allen, C.R. 2005. Sediment-hosted Pb-Zn deposits: a global perspective. Economic Geology, v. 100, p. 561-608.

Leach, D.L., Bradley, D.C., Huston, D., Pisarevsky, S.A., Taylor, R.D., and Gardoll, S.J. 2010. Sediment-hosted lead-zinc deposits in Earth history. Economic Geology, v. 105, p. 593-625.

Leybourne, M.I., Van Wagoner, N., Paradis, S., Layton-Matthews, D., and Moertle, J.A., 2018. Selwyn Basin magmatism and relationship to sediment-hosted Zn- Pb deposits. *in* Targeted Geoscience Initiative: 2017 report of activities, volume 2, (ed.) N. Rogers; Geological Survey of Canada, Open File 8373, p. 71–92.

Lydon, J.W. 1983. Chemical parameters controlling the origin and deposition of sediment-hosted stratiform lead-zinc deposits. *in* Short course in sediment-hosted stratiform lead-zinc deposits, (ed.) Sangster, D.F.,; Victoria, Mineralogical Association of Canada, p. 175-250.

Lynch, J.V.G. 1989. Large-scale hydrothermal zoning reflected in the tetrahedrite-freibergite solid solution, Keno Hill Ag-Pb-Zn district, Yukon. The Canadian Mineralogist, v. 27, p. 383-400.

Magnall, J.M., Gleeson, S.A., and Paradis, S., 2014. SEDEX mineralization, Macmillan Pass (Yukon): petrography, mineralogy and bulk geochemistry of the Tom and Nidd deposits. Natural Resources Canada. Open File 7457. doi:10.4095/293105

Mair, J.L., Hart, C.J., and Stephens, J.R., 2006. Deformation history of the northwestern Selwyn Basin, Yukon, Canada: Implications for orogen evolution and mid-Cretaceous magmatism; Geological Society of America Bulletin, v. 118 (3-4), pp.304-323.

McClenaghan, M.B. 2011. Overview of common processing methods for recovery of indicator minerals from sediment and bedrock in mineral exploration. Geochemistry: Exploration, Environment, Analysis, v. 11, p. 265-278.

Nelson, J.O., and Colpron, M.A., 2007. Tectonics and metallogeny of the British Columbia, Yukon and Alaskan Cordillera, 1.8 Ga to the present. *in* Mineral Deposits of Canada: A Synthesis of Major Deposit-Types, District Metallogeny, the Evolution of Geological Provinces, and Exploration Methods, (ed.) Goodfellow, W.D.; Geological Association of Canada, Mineral Deposits Division, Special Publication 5, p. 755-791.

Nielsen, S.G., Prytulak, J., Blusztajn, J., Shu, Y., Auro, M., Regelous, M. and Walker, J. 2017. Thallium isotopes as tracers of recycled materials in subduction zones: Review and new data for lavas from Tonga-Kermadec and Central America. Journal of Volcanology and Geothermal Research, v. 339, p. 23-40.

Norford, B.S., and Orchard, M.J., 1985. Early Silurian age of rocks hosting lead-zinc mineralization at Howards Pass, Yukon Territory and District of MacKenzie: local biostratigraphy of Road River Formation and Earn Group. Geological Survey of Canada. Paper 83-18, 35 p.

Norford, B.S., Orchard, M.J., Norris, A.W., Uyeno, T.T., Cecile, M.P., Abbott, J.G., Jackson, D.E., Fritz, W.H., Hofmann, H.J., Nowlan, G.S., and Tipnis, R.S. 1993. Paleontological identifications and correlations, Niddery Lakemap area, NTS 105-O, and immediately adjacent map areas. Geological Survey of Canada, Open File 2682, 88 p.

Paton, C., Hellstrom, J., Bence, P., Woodhead, J., and Hergt, J. 2011. Iolite: Freeware for the visualisation and processing of mass spectrometric data. Journal of Analytical Atomic Spectrometry, v. 26, p. 2508-2518

Paytan, A., and Kastner, M. 1996. Benthic Ba fluxes in the central Equatorial Pacific, implications for the oceanic Ba cycle. Earth and Planetary Science Letters, v. 142, p. 439-450.

Peter, J.M., Gadd, M.G., Layton-Matthews, D. and Voinot, A. 2017. Reconnaissance thallium isotope study of zinc-lead SEDEX mineralization and host rocks in the Howard's Pass district, Selwyn Basin, Yukon: Potential application to paleoredox determinations and fingerprinting of mineralization. *in* Targeted Geoscience Initiative: 2017 report of activities, volume 1, (ed.) N. Rogers; Geological Survey of Canada, Open File 8358, p. 179–191.

Pigage, L.C., 2004. Bedrock geology compilation of the Anvil District, (parts of NTS 105K/2, 3, 5, 6, 7 and 11), central Yukon. Yukon Geological Survey, Bulletin 15, 118 p.

Sack, R.O., Lynch, J.V.G., and Foit, F. 2018. Fahlore as a petrogenetic indicator: Keno Hill Ag-Pb-Zn District, Yukon, Canada. Mineralogical Magazine, v. 67, p. 1023-1038.

Scanlan, E.J., Leybourne, M., Layton-Matthews, D., Voinot, A., and van Wagoner, N. 2019. *in* Targeted Geoscience Initiative 5 Grant Program interim reports 2018–2019; Geological Survey of Canada, Open File 8620, p. 19-42

Shaw, D.M., 1952. The geochemistry of thallium. Geochimica et Cosmochimica Acta, v. 2, p. 118-154.

Turner, R. J. W., and Goodfellow, W.D. 1990. Barium carbonate bodies associated with the Walt (Cathy) stratiform barium deposit, Selwyn Basin, Yukon: a possible vent complex associated with a Middle Devonian sedimentary exhalative barite deposit. *in* Current Research, Part E, Geological Survey of Canada, Paper 90-lE, p. 309-319

Turner, R. J. W., and Rhodes, D. 1990. Boundary Creek zinc deposit (Nidd property), MacMillan Pass, Yukon: sub-seafloor sediment-hosted mineralization associated with volcanism along a late Devonian syndepositional fault. *in* Current Research, Part E, Geological Survey of Canada, Paper 90-IE, p. 321-335.

Wilkinson, J.J., Hitzman, M.W., Archibald, S.M., and Piercey, S.J., 2015. The Irish Zn-Pb orefield: the view from 2014. *in* Current Perspectives on Zinc Deposits. Irish Association for Economic Geology, Dublin, pp.59-72.

An experimental investigation of the solubility and speciation of uranium in hydrothermal ore fluids

K.U. Rempel[1], A.E. Williams-Jones[1], and K. Fuller[1]

Rempel, K.U., Williams-Jones, A.E., and Fuller, K., 2021. An experimental investigation of the solubility and speciation of uranium in hydrothermal ore fluids; in *Targeted Geoscience Initiative 5:grant program final reports (2018-2020); Geological Survey of Canada, Open File 8755, p. 281–288. https://doi.org/10.4095/328995*

Abstract: Experimental data on the solubility and speciation of uranium in hydrothermal solution is required to improve genetic models for the formation of ore deposits, yet very few data of this type have been published. Of particular interest is the oxidation state of the uranium in solution, as conventional wisdom suggests that U is dissolved in the oxidized U(VI) state and precipitated as reduced U(IV) minerals, yet recent experiments have shown ppm-level solubility for U(IV).

This study investigated the mobility of reduced U(IV) and oxidized U(VI) in acidic (pH = 2), fluoride-bearing and alkaline (pH = 10), chloride-bearing solutions at 100-200°C and 1 to 15.8 bars (0.1-1.58 MPa). Preliminary data for the mobility of U(IV) in pH 2 fluids with 0.01 m F^- show concentrations of 1.76 to 3.92 ppm U at 200°C, indicating that, contrary to common belief, the reduced U(IV) can be transported in solution. We have also conducted experiments on U(VI) solubility in pH 2 fluoride-bearing, and pH 10 chloride-bearing solutions. Uranium concentrations in the F^--bearing experiments ranged from 624 to 1570 ppm (avg. 825 ppm, n = 6) at 100°C, 670 to 1560 ppm (avg. 931 ppm, n = 4) at 150°C, and 3180 to 7550 ppm (avg. 5240, n = 9) at 200°C. In comparison, U concentrations in the Cl^--bearing runs range from 86.1 to 357 ppm (avg. 185 ppm, n = 15) at 200°C. Clearly, oxidized U(VI) is very readily mobilized in hydrothermal fluids. However, the measured concentrations of U(VI) are independent of those of F^- or Cl^-, suggesting the formation of U oxide or hydroxide species rather than U chlorides or fluorides.

These experimental data will be verified and supplemented in future experiments, which will be used to derive the stoichiometry and thermodynamic constants for the dominant uranium species in hydrothermal solutions. The data from this study will then be integrated into a comprehensive genetic model for uranium ore-forming systems.

[1]Department of Earth and Planetary Sciences, McGill University, 3450 University Street, Montreal, Quebec

INTRODUCTION

Uranium ore deposits are an increasingly important commodity in Canada and worldwide, yet these deposits are highly variable and numerous questions remain regarding the mechanisms for their formation. For example, in sediment-hosted, unconformity-type deposits, such as some of those of the Athabasca basin, Saskatchewan, U(VI)-bearing, oxidized basinal brines are thought to have reacted with an on-site reductant such as graphite to precipitate U(IV) ore (e.g., Komninou and Sverjensky, 1996; Fayek and Kyser, 1997; Jefferson et al., 2007). On the other hand, for magmatic-associated iron oxide-copper-gold (IOCG) deposits such as those of the Great Bear Magmatic Zone, NWT, there is no obvious evidence for a reducing agent and the depositional mechanism for uranium ore is unclear (Bastrakov et al., 2007; Montreuil et al., 2015). One reason for the lack of clarity on uranium mobility in hydrothermal fluids is a scarcity of experimental data on U solubility and speciation at elevated temperatures and pressures. Temperatures of mineralization reach up to ~250°C for unconformity-type deposits, and up to ~500°C for IOCG deposits (Bastrakov et al., 2007; Jefferson et al., 2007). However, existing genetic models for uranium ore formation (e.g., Grandstaff, 1976; Romberger, 1984) are mainly dependent on thermodynamic extrapolations of low-temperature (25°C) data, which are notoriously unreliable.

Previous investigations of the behaviour of uranium in aqueous solution and in mineral deposits suggests that U is typically dissolved as oxidized U(VI) species and precipitated as reduced U(IV) minerals, such as uraninite (UO_2; Langmuir, 1978; Romberger, 1984). Few experimental studies of U solubility have been carried out at elevated temperature and pressure, but extensive work has been conducted at ambient conditions (1 bar, 25°C). Applying Pearson's (1963) hard-soft-acid-base (HSAB) principle, both U(IV) and U(VI) are hard acids and will tend to bond to hard bases such as OH^- and F^-, though U is also known to form complexes with the softer yet commonly abundant Cl^- ligand (e.g., Bastrakov et al. 2010, Timofeev et al., 2018).

The relative predominance of the above species under hydrothermal conditions is debated. For example, thermodynamic models based on extrapolation of lower-temperature data to 200°C by Romberger (1984), Komninou and Sverjensky (1996) and Bastrakov et al. (2010) variably predict that U(VI) complexation in solutions of similar composition is dominated by fluoride, phosphate and carbonate species; oxychloride species; and phosphate and oxide species, respectively. Fluoride complexes were predicted only at 25 and 50°C and pH < 3 in the latter study, yet the association of uranium ore and fluorite commonly seen in natural systems (e.g., Cunningham et al., 1998; Jiang et al., 2006) is a compelling indicator of the importance of the fluoride ligand in uranium mobility.

Contrary to the prevailing theory regarding the immobility of U(IV), a study of uraninite solubility in alkaline solutions at temperatures up to 300°C by Tremaine et al. (1981) showed that U(IV) is relatively mobile as aqueous hydroxyl complexes. Furthermore, a recent experimental study at temperatures up to 350°C has shown that U(IV) is also highly soluble as chloride complexes in acidic fluids (Timofeev et al., 2018). These results have important implications for the existing uranium ore genesis models that assume transport of uranium as U(VI) and its immobility as U(IV). Despite these advances, considerable work remains to be done to understand the aqueous geochemistry of uranium at elevated temperature.

The objective of this study is to address the paucity of experimental data by conducting experiments at elevated temperature and pressure to determine the solubility and speciation of uranium in hydrothermal solutions and to evaluate the effects of fluid and host rock composition on uranium mineralization. Solubility studies involving the systematic variation of fluid pH, oxidation state and ligand concentration are being used to evaluate the optimal conditions for uranium transport and determine the dominant uranium complexes in solution. Work in progress and future experiments will optimize these preliminary results, and will be supplemented by fluid-rock reaction experiments to simulate uranium mineralization under a range of P-T-X conditions. The thermodynamic data produced from these studies will be integrated into a genetic model for uranium ore-forming systems.

EXPERIMENTAL METHODS

The early stages of this project were focused on method development for the uranium solubility studies. Because of the corrosive effect of HF on metal or glass components, solubility experiments in fluoride-bearing fluids were done in titanium autoclaves, but with all wetted parts made of Teflon (Fig. 1). Thus, method development included fabrication of gas-tight PTFE liners for the Ti autoclaves and holders for the solid phases (U oxide reagents and oxygen fugacity buffers). The hydroxide ion also causes the dissolution of silica, but OH^- is not detrimental to metals, so high-pH experiments were done in unlined Ti autoclaves with PTFE reagent holders.

For pH 2, fluoride-bearing experiments, $NaClO_4$ and $HClO_4$ were used to control ionic strength and pH, respectively, as perchlorate is known to be a non-complexing ligand (Choppin et al., 1966). In pH 10, chloride-bearing runs, ionic strength and pH were adjusted with NaCl and NaOH, respectively. The autoclaves were loaded with a sufficient volume of solution to ensure that saturated vapour pressure was attained and that sample volumes were adequate for analysis (10-15 ml). Depleted U(IV) oxide (UO_2) pellets and U(VI) oxide (UO_3) powder from IBI Labs were used as reagents for the U(IV) and U(VI) experiments,

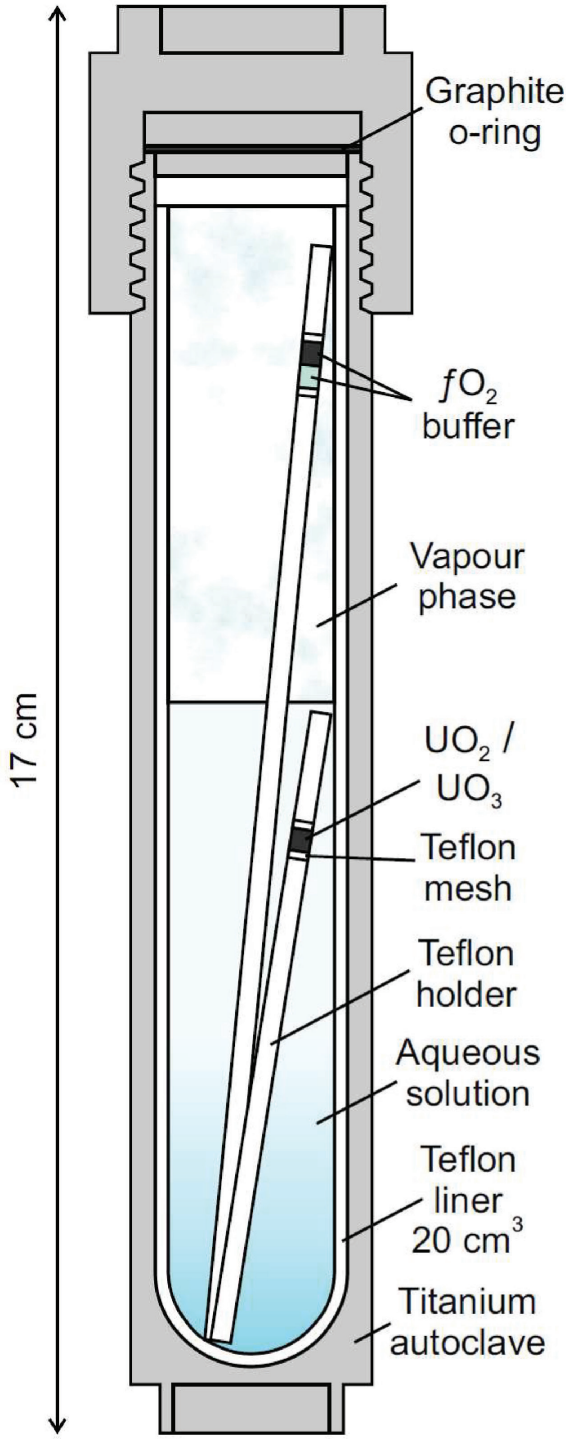

Figure 1. Schematic diagram of the Teflon-lined titanium autoclaves used for the solubility experiments at elevated temperature (100-200°C), illustrating the U oxide in contact with the solution and the oxygen fugacity buffer in contact with the vapour.

respectively. Oxygen fugacity (fO_2) was buffered using powdered MoO_2-MoO_3 for U(IV) and either Cu-CuO, MnO-MnO_2, or Mn_2O_3-MnO_2 for U(IV), in order to assess the effectiveness of different buffers. The fO_2 of each buffer at the temperatures employed, calculated using HCh (Shvarov, 1999), are given in Table 1. To eliminate oxygen and further ensure the activation of the fO_2 buffer, experiments using MnO-MnO_2 were loaded within a chamber purged with Ar gas.

Autoclaves were heated in an oven to the temperature of interest (100-200°C) until chemical equilibrium was reached, then quenched to ambient conditions in cold water. Thermal gradients in the ovens were found to be within about 2°C of the set temperature, and are predicted to be lower within the conductive Ti autoclaves. The experimental pressure was the saturated vapour pressure at the temperature of interest (1.0, 4.8 and 15.6 bar at 100, 150 and 200°C, respectively). Saturated vapour pressure was calculated for pure water using the National Institute of Standards and Technology (NIST) Steam Tables (Harvey, 2001). The concentrations of solutes added to the solutions (<1 wt%) will not significantly affect the calculated pressures, especially considering the scatter inherent in the experimental data.

After quenching, an aliquot of solution was removed for pH measurement and the remainder was acidified with 1 ml of concentrated aqua regia. The resulting solution was used to wash the walls of the autoclave to dissolve any precipitates formed during quenching. Uranium concentrations in the run products were analyzed using inductively-coupled plasma mass spectrometry (ICP-MS) or optical emission spectrometry (ICP-OES), with detection limits of about 1 ppt and 1 ppm, respectively. Uranium concentrations in blank experiments performed before and after U-bearing experiments were below detection, demonstrating that no appreciable environmental contamination occurred and that no residual U remained in autoclaves following the experiments.

A second experimental method, for flow-through, water-rock reaction experiments has also been developed. An externally-heated, Teflon-lined sampling autoclave made of stainless steel has been modified with a high-pressure liquid chromatography (HPLC) pump to allow a constant flow of U-bearing solution, which can be pumped into the vessel

Table 1: The logarithms of the oxygen fugacities (log fO_2), in bars, of the buffers employed in these experiments as a function of temperature.

Buffer	100°C	150°C	200°C
MoO_2-MoO_3	-36.32	-31.17	-27.11
Cu-CuO	-34.33	-29.14	-25.06
MnO-MnO_2	-26.32	-21.86	-18.34
MnO_2-Mn_2O_3	-11.53	-8.842	-6.729

through an input line at the desired flow rate and fluid:rock ratio (Fig. 2). Temperature and pressure within the vessel are monitored with an internal Type K thermocouple and Berghof pressure transducer, respectively, and gases to control oxygen fugacity are input via an independent gas line. The factory calibration of both the thermocouple and pressure transducer have been tested with boiling water. Throughout an experiment, in order to monitor reaction progress and changes in fluid composition, the solution is extracted through an output line fitted with an inline back-pressure regulator for sampling and analysis.

RESULTS AND DISCUSSION

The results of a kinetic study of UO_2 solubility in 0.01 m F^-, pH 2 solutions at 200°C, with fO_2 buffered with MoO_2-MoO_3, have relatively constant U(IV) concentrations, indicating that chemical equilibrium or steady-state conditions were attained within 3 days (i.e., before the first sample was quenched; Fig. 3). The solutions from these experiments were analyzed using ICP-MS. Error bars in these and subsequent experiments represent one standard deviation (1σ) of the data points from the slope of the line, assuming a slope of zero. Based on these results, all further experiments were conducted for at least 7 days. The U concentrations in this preliminary assessment of UO_2 solubility range from 1.76 to 3.92 ppm (avg 2.68 ppm, n = 5; Fig. 3).

In comparison, previous experimental studies of UO_2 solubility produced concentrations that were significantly lower or similar for ligand-free alkaline solutions at 200°C (8-30 ppb; Tremaine et al. 1981), and ppb- to ppm-level concentrations in chloride-bearing acidic solutions at 250°C (7 ppb-20 ppm, with higher concentrations attributed to the higher temperature employed; Timofeev et al. 2018). Our new results suggest that, as is the case with chloride, fluoride complexation may be of major importance for uranium (IV) transport in hydrothermal fluids, and that U(IV) is mobile in fluoride-bearing solutions.

On the other hand, UO_3 solubility in fluoride-bearing, pH 2 solutions is independent of fluoride concentration, as shown by near-zero slopes over a range of F concentrations (Figure 4). The U(VI) concentrations from these experiments range from 624 to 1570 ppm (avg 825 ppm, n = 6) at 100°C, 670 to 1560 ppm (avg 931 ppm, n = 4) at 150°C, and 3180 to 7550 ppm (avg 5240, n = 9) at 200°C. The U concentration levels are temperature-dependant, with higher solubility at higher T (Fig. 4a, b, c). Comparison of the results for the Cu-CuO and MnO-MnO_2 fO_2 buffers at 200°C (Fig. 4c) shows no statistically meaningful differences. Minor scatter in the data in these experiments may have been caused by trace contamination from the powdered UO_3 in the sample holders, so we have designed reagent pouches made from PTFE filter paper in order to resolve this issue in current and future experiments.

The independence of U(VI) and fluoride concentrations (Fig. 4) indicates that U(VI) fluoride complexes are not forming in solution. The thermodynamic model of Bastrakov et al. (2010), extrapolated from low-temperature data for pH 2 solutions containing F^-, Cl^-, PO_4^{3-}, and CO_3^{2-}, with oxygen fugacity near the Mn_2O_3-MnO_2 fO_2 buffer, also showed no evidence of U(VI) fluoride complexation. However, Bastrakov et al.'s (2010) model demonstrated a predominance of UO_2Cl^+ and UO_2(aq) at 100 and 200°C, respectively, indicating that U(VI) was not the dominant oxidation state at these conditions, despite the highly oxidized solutions. The post-experiment UO_3 charges from this study (initially yellow) displayed some evidence of recrystallization to other

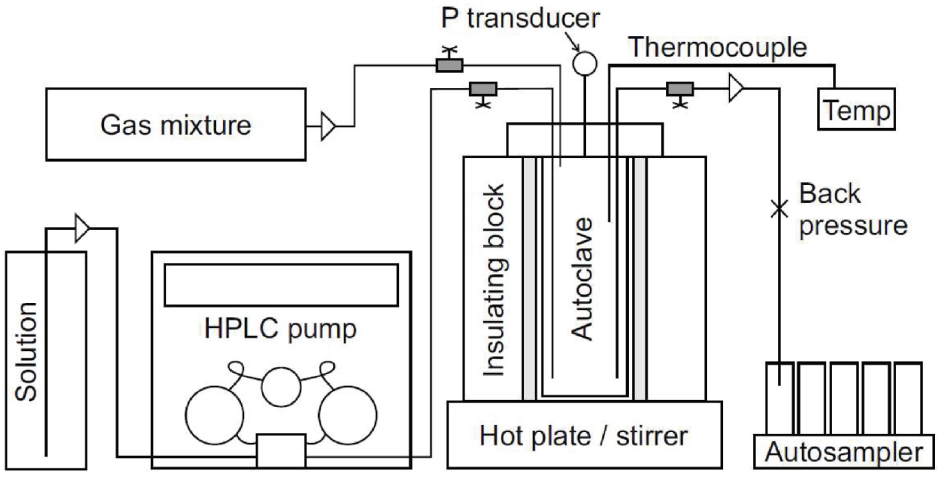

Figure 2. Schematic diagram of the flow-through system used for the water-rock reaction experiments, in which U-bearing solution and gas phases are pumped into the Teflon-lined stainless steel autoclave to be reacted with rock fragments, then extracted through an output line to an autosampler.

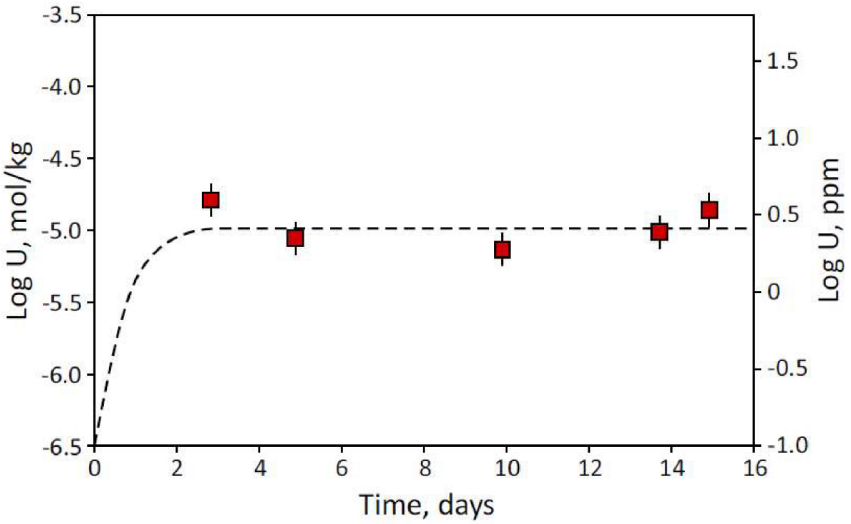

Figure 3. Results of a kinetic experiment evaluating the solubility of UO_2 in solutions with 0.01 m NaF, 0.05 m $NaClO_4$ and 0.01 m $HClO_4$ (pH 2) at 200°C and 15.6 bar, showing U concentration versus the duration of the experiment in days. The dotted line illustrates an idealized path to chemical equilibrium and the average U concentration of 2.68 ppm. Error bars represent one standard deviation (1σ) of the data points from the slope of the line.

phases in the form of colour changes to black or red, perhaps suggestive of the stability of U(IV) or U(V); these solid phases will be characterized in future work.

To assess the solubility and speciation of uranium in alkaline solutions, we have also conducted experiments using U(VI) oxide in chloride-bearing, pH 10 fluids at 200°C. Uranium concentrations range from 86.1 to 357 ppm (avg 185 ppm, n = 15). The results of these experiments show that U(VI) concentrations are again independent of the added ligand (Fig. 5), indicating that U(VI) chloride complexation does not occur at these conditions. These results are in good agreement with the model of Bastrakov et al. (2010), which predicts the predominance of the oxyacid HUO_4^- at pH 10. Future experiments in this chemical system will involve variable-pH runs to assess the dependence of U(VI) concentrations on those of the OH^- ligand and thus determine the stoichiometry of this species in the experimental fluids.

NEXT STEPS

A series of follow-up experiments are planned to verify and expand the results for the U(IV) and U(VI) experiments discussed above. Experiments involving U(VI) to verify speciation interpretations for low-pH, F^--bearing, and high-pH, Cl^--bearing solutions with variable OH concentrations are currently underway. These data will be used to derive thermodynamic constants for the dominant species in solution. Later experimental stages of the study will assess the importance of F^- and OH^- on U(IV) solubility and speciation, and then derive thermodynamic constants for modelling calculations.

Following extensive method development for the flow-through autoclave apparatus, water-rock interaction experiments issues have now been largely resolved, and experiments involving the reaction of U(IV) and (VI) with various host rock types are being planned. These experiments will be used to simulate the precipitation of uranium ore in natural systems under variable P-T-X conditions, and will be conducted using several host rock and fluid compositions (oxidizing and reducing fluids and rocks; acidic and alkaline fluids; temperatures from 150 to 250°C). Building on the results of the initial experiments, P-T-X parameters will be modified mid-experiment to promote mineralizing conditions. Both the unreacted and reacted host rocks will be investigated with scanning electron microscopy (SEM) to determine the mineralogy of precipitated uranium ores and other mineralization-related changes in mineralogy. These results will allow an assessment of the optimal fluid and rock compositions for uranium precipitation, as well as an evaluation of precipitation mechanisms.

Finally, the results will be integrated into a genetic model for the formation of uranium mineralization from hydrothermal fluids, e.g., for unconformity- and IOCG-type ore deposits. The thermodynamic constants determined for relevant aqueous uranium species will be used to input the species into thermodynamic modelling software (HCh; Shvarov 1999). The model will incorporate the results of

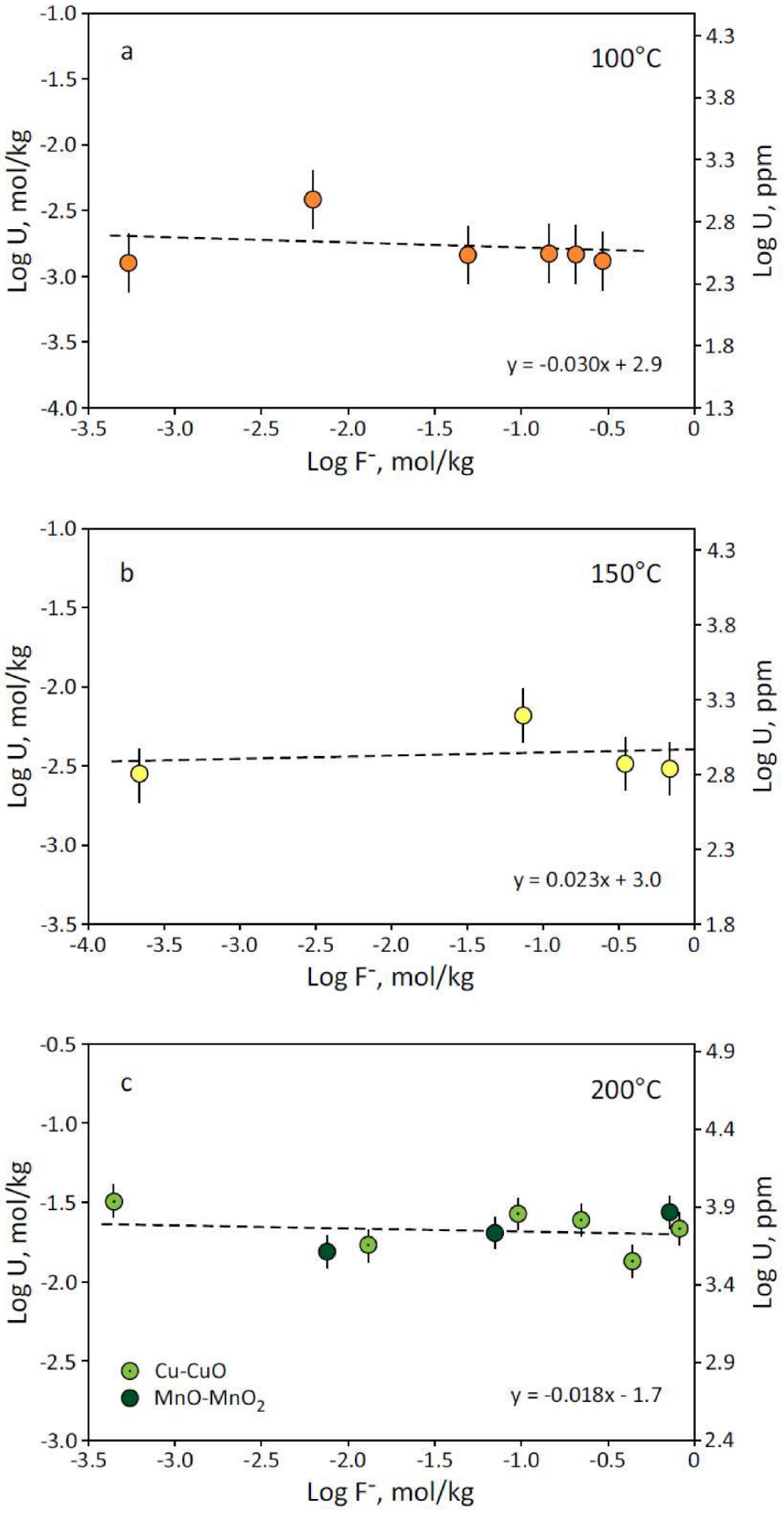

Figure 4. Results of UO_3 solubility experiments at pH 2 illustrating the near-zero slopes of uranium versus fluoride concentration. **a)** 100°C, 1 bar. **b)** 150°C, 4.8 bar. **c)** 200°C, 15.6 bar. This figure shows U concentrations at equilibrium with either the Cu-CuO oxygen fugacity buffer (dotted light green circles) or the MnO-MnO_2 buffer (dark green circles) used in experiments shown in (a) and (b). Error bars represent one standard deviation (1σ) of the data points from the slope of the line.

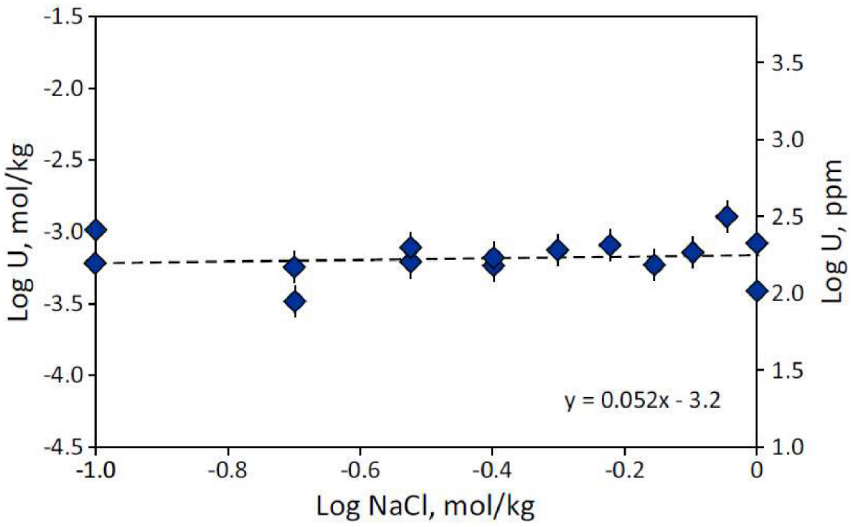

Figure 5. Results of UO_3 solubility experiments at 200°C and 15.6 bar in variable-chloride solutions at pH 10, showing a near-zero slope for uranium versus chloride concentration. Error bars represent one standard deviation (1σ) of the data points from the slope of the line.

solubility and flow-through experiments to predict the precipitation of uranium minerals from hydrothermal solutions in contact with a variety of host rock types. It is our expectation that the resulting predictions will provide a substantially improved genetic model incorporating uranium transport and precipitation at P-T-X conditions appropriate to the uranium ore-forming systems of interest.

KEY ACTIVITY HIGHLIGHTS

Contrary to the common perception that uranium is dissolved in the oxidized U(VI) state and precipitated as reduced U(IV) ore minerals, our new results reveal ppm-level concentrations of U(IV) in pH 2, fluoride-bearing solutions at 200°C, indicating that reduced ore fluids may be much more important than previously thought for the mobilization of uranium. Comprehensive genetic models for uranium ore formation therefore require the incorporation of mechanisms of deposition for reduced U, which will be simulated with water-rock interaction experiments in future work.

The concentrations of U(VI) in both low-pH, fluoride-bearing and high-pH, chloride-bearing solutions are high, particularly in comparison to the solubility of U(IV) species, suggesting that uranium is readily transported in either F^-- or Cl^--rich fluids. However, the chemical complexation of uranium in both of these chemical systems appears to be independent of the added ligand, suggesting that the U is forming oxide or hydroxide species. Given the relative softness of the chloride ligand compared to hydroxide, the lack of chloride speciation at high pH is not surprising, as Pearson's (1963) HSAB principles predicts that U will prefer to complex with hard ligands. The absence of fluoride complexation, on the other hand, is unexpected and brings into question the reasons for the common association of uranium ore and fluorite in natural systems.

ACKNOWLEDGMENTS

This report is a contribution to NRCan's Targeted Geoscience Initiative Program (TGI). Support for this study was provided through the Phase 2 Uranium Ore Systems Project. We also extend thanks to Dr A. Migdisov for invaluable input into the method development.

REFERENCES

Bastrakov, E.N., Skirrow, R., and Davidson, G.J., 2007. Fluid evolution and origins of iron oxide Cu-Au prospects in the Olympic Dam District, Gawler Craton, South Australia. Economic Geology, v. 102, p. 1415-1440.

Bastrakov, E.N., Jaireth, S., and Mernagh, T., 2010. Solubility of uranium in hydrothermal fluids at 25° to 300°C. Geoscience Australia, Record 2010/29, 95 p.

Choppin G. R., Kelly D. A., and Ward E. E., 1966. Effect of changes in the ionic medium on the stability constant of $Eu(NO_3)^{2+}$. United States Atomic Energy Commission, No. ORO-1797-2, CONF-660805-2, 21 p.

Cunningham, C.G., Rasmussen, J.D., Steven, T.A., Rye, R.O, Rowley, P.D., Romberger, S.B., and Selverston, J, 1998. Hydrothermal uranium deposits containing molybdenum and fluorite in the Marysvale volcanic field, west-central Utah. Mineralium Deposita v. 33, p. 477-494.

Fayek, M. and Kyser T.K., 1997. Characterization of multiple fluid-flow events and rare-earth-element mobility associated with formation of unconformity-type uranium deposits in the Athabasca Basin, Saskatchewan. Canadian Mineralogist v. 35, p. 627-658.

Grandstaff, D.E., 1976. A kinetic study of the dissolution of uraninite. Economic Geology v. 71, p. 1493-1506.

Harvey, A.H., 2001. Steam tables; in Encyclopedia of Physical Science and Technology, Third Edition, v. 16, p. 1-7.

Jefferson, C.W., Thomas, D.J., Gandhi, S.S., Ramaekers, P., Delaney, G., Brisbin, D., Cutts, C., Portella, P. and Olson, R.A., 2007. Unconformity-associated uranium deposits of the Athabasca Basin, Saskatchewan and Alberta. In EXTECH IV: Geology and Uranium EXploration TECHnology of the Proterozoic Athabasca Basin, Saskatchewan and Alberta, (ed.) C.W. Jefferson and G. Delaney; Geological Survey of Canada, Bulletin 588, p. 23-67.

Jiang, Y.-H., Ling, H.-F., Jiang, S.-Y., Shen, W.-Z., Fan, H.-H., and Ni, P., 2006. Trace element and Sr-Nd isotope geochemistry of fluorite from the Xiangshan uranium deposit, southeast China. Economic Geology v. 101, p. 1613-1622.

Komninou, A. and Sverjensky, D.A., 1996. Geochemical modeling of the formation of an unconformity-type uranium deposit. Economic Geology v. 91, p. 590-606.

Langmuir, D., 1978. Uranium solution-mineral equilibria at low temperatures with applications to sedimentary ore deposits. Geochimica et Cosmochimica Acta, v. 42, p. 547-569.

Montreuil, J.-F., Corriveau, L., and Potter, E.G., 2015. Formation of albitite-hosted uranium within IOCG systems: the Southern Breccia, Great Bear magmatic zone, Northwest Territories, Canada. Mineralium Deposita, v. 50, p. 293-325.

Pearson, R. G., 1963. Hard and soft acids and bases. Journal of the American Chemical Society v. 85, p. 3533-3539.

Romberger, S.B., 1984. Transport and deposition of uranium in hydrothermal systems of temperatures up to 300°C: geological implications; *in* Uranium Geochemistry, Resources, (ed.) B. de Vivo, F. Ippolito, G. Capaldi and P.R. Simpson; Institute of Mining and Metallurgy, London, p. 12-17.

Shvarov, Y.V., 1999. Algorithmization of the numerical equilibrium modelling of dynamic geochemical processes. Geochemistry International v. 37, p. 571-576.

Timofeev, A., Migdisov, A.A., Williams-Jones, A.E., Roback, R., Nelson, A.T., and Xu, H. (2018) Uranium transport in acidic brines under reducing conditions. Nature Communications v. 9, p 1469.

Tremaine, P.R., Chen, J.D., Wallace, G.J., and Boivin, W.A., 1981. Solubility of uranium (IV) oxide in alkaline aqueous solutions to 300°C. Journal of Solution Chemistry v. 10, p. 221-230.